



**INSTITUTO POTOSINO DE INVESTIGACIÓN  
CIENTÍFICA Y TECNOLÓGICA, A.C.**

**POSGRADO EN CIENCIAS APLICADAS**

**Polystyrene grafting of  $CN_x$  nanotubes for the  
elaboration of polystyrene-based nanocomposites**

Tesis que presenta

**Mariamne Dehonor Gómez**

Para obtener el grado de

**Doctora en Ciencias Aplicadas**

En la opción de

**Nanociencias y Nanotecnología**

**Codirectores de la Tesis:**

Prof. Mauricio Terrones Maldonado (IPICYT, Mexico)

Dra. Catherine Gauthier (INSA-Lyon, France)

Dr. Alfonso González Montiel (CID, Mexico)

San Luis Potosí, S.L.P., 29 de mayo de 2007



## Constancia de aprobación de la tesis

La tesis: “**Polystyrene grafting of  $CN_x$  nanotubes for the elaboration of polystyrene-based nanocomposites**” presentada para obtener el Grado de Doctora en Ciencias Aplicadas en la opción de Nanociencias y Nanotecnología fue elaborada por **Marianne Dehonor Gómez** y aprobada el **29 de mayo de 2007** por los suscritos, designados por el Colegio de Profesores de la División de Biología Molecular del Instituto Potosino de Investigación Científica y Tecnológica, A.C.

\_\_\_\_\_  
Prof. Mauricio Terrones Maldonado (IPICYT, Mex)  
*Codirector de la tesis*

\_\_\_\_\_  
Dra. Catherine Gauthier (INSA-Lyon, Fran)  
*Codirector de la tesis*

\_\_\_\_\_  
Dr. Alfonso González Montiel (CID, Mex)  
*Codirector de la tesis*

## Constancia de aprobación de la tesis

La tesis: "**Polystyrene grafting of CN<sub>x</sub> nanotubes for the elaboration of polystyrene-based nanocomposites**" presentada para obtener el Grado de Doctora en Ciencias Aplicadas en la opción de Nanociencias y Nanotecnología fue elaborada por **Marianne Dehonor Gómez** y aprobada el **29 de mayo de 2007** por los suscritos, designados por el Colegio de Profesores de la División de Materiales Avanzados del Instituto Potosino de Investigación Científica y Tecnológica, A.C.



---

Prof. Mauricio Terrones Maldonado (IPICYT, Mex)  
*Codirector de la tesis*



---

Dra. Catherine Gauthier (INSA-Lyon, Fran)  
*Codirector de la tesis*



---

Dr. Alfonso González Montiel (CID, Mex)  
*Codirector de la tesis*



## **Créditos Institucionales**

Esta tesis fue elaborada en los Laboratorios de:  
*la División de Materiales Avanzados para la Tecnología Moderna  
del Instituto Potosino de Investigación Científica y Tecnológica (IPICYT), Mex.*

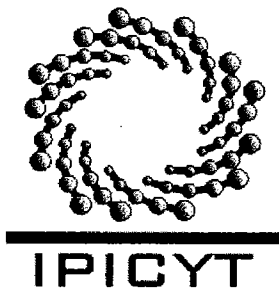
*el Materials, Engineering and Science Laboratory (MATEIS)  
del Institut National de Sciences Appliquées de Lyon (INSA de Lyon), Fr.*

*y*

*el Centro de Investigación y Desarrollo Tecnológico (CID), del grupo DESC, Mex.*

bajo la codirección de  
*Dr. Mauricio Terrones M. (IPICYT)  
Dra. Catherine Gauthier (INSA-Lyon)  
Dr. Alfonso González M. (CID)  
Dra. Karine Masenelli-Varlot (INSA-Lyon)*

Durante la realización del trabajo el autor recibió beca académica de:  
*Programa PCP del CONACYT-CNRS México-Francia,  
Estudios de doctorado de CONACYT y del IPICYT,  
Complemento de beca del MATEIS-INSA de Lyon y  
Complemento de beca de la Asoc. Nal. de Ing. Químicos (ANIQ), Méx.*



# Instituto Potosino de Investigación Científica y Tecnológica, A.C.

## Acta de Examen de Grado

El Secretario Académico del Instituto Potosino de Investigación Científica y Tecnológica, A.C., certifica que en el Acta 022 del Libro Primero de Actas de Exámenes de Grado del Programa de Doctorado en Ciencias Aplicadas en la opción de Nanociencias y Nanotecnología está asentado lo siguiente:

En la ciudad de San Luis Potosí a los 29 días del mes de mayo del año 2007, se reunió a las 08:30 horas en las instalaciones del Instituto Potosino de Investigación Científica y Tecnológica, A.C., el Jurado integrado por:

<b>Dr. Mauricio Terrones Maldonado</b>	<b>Presidente</b>	<b>IPICYT</b>
<b>Dr. Alfonso González Montiel</b>	<b>Secretario</b>	<b>CID-DESC</b>
<b>Dr. Humberto Terrones Maldonado</b>	<b>Sinodal</b>	<b>IPICYT</b>
<b>Dr. Pedro Jesús Herrera Franco</b>	<b>Sinodal externo</b>	<b>CICY</b>
<b>Dra. Yadira Itzel Vega Cantú</b>	<b>Sinodal</b>	<b>IPICYT</b>

a fin de efectuar el examen, que para obtener el Grado de:

**DOCTORA EN CIENCIAS APLICADAS  
EN LA OPCIÓN DE NANOCIENCIAS Y NANOTECNOLOGÍA**

sustentó la C.

**Mariamne Dehonor Gómez**

sobre la Tesis intitulada:

*Polystyrene grafting of CNx nanotubes for the elaboration of polystyrene-based nanocomposites*

que se desarrolló bajo la dirección de

**Dr. Mauricio Terrones Maldonado**  
**Dr. Alfonso González Montiel (CID-DESC)**  
**Dra. Catherine Gauthier (INSA-Lyon)**  
**Dra. Karine Masenelli-Varlot (INSA-Lyon)**

El Jurado, después de deliberar, determinó

**APROBARLA**

Dándose por terminado el acto a las 11:45 horas, procediendo a la firma del Acta los integrantes del Jurado. Dando fé el Secretario Académico del Instituto.

A petición de la interesada y para los fines que a la misma convengan, se extiende el presente documento en la ciudad de San Luis Potosí, S.L.P., México, a los 29 días del mes mayo de 2007.

**L.C.C. Ivonne Lizette Cuevas Velez**  
Jefa del Departamento de Asuntos Escolares

**Dr. Marcial Bonilla Martín**  
Secretario Académico



# **Polystyrene grafting of CN<sub>x</sub> nanotubes for the elaboration of polystyrene-based nanocomposites**

Mariamne Dehonor Gómez

Submitted for the Doctorate degree  
May 2007

## **Abstract**

This thesis is concerned to the development of novel engineered surface materials using nitrogen-doped carbon nanotubes (CN<sub>x</sub>) that were grafted with polystyrene (PS) chains using *in situ* radical polymerization controlled by nitroxides. The chemically modified carbon nanotubes were used in the preparation of polymer-nanotube composites with the aim of improving the dispersion of nanotubes within the matrix, but also the interfacial adhesion between them.

The *in situ* polymerization method to graft polymer chains over CN<sub>x</sub> nanotubes involved the radical attachment of a system initiator-controller that could follow a Nitroxide Mediated Radical Polymerization (NMRP) in solution. This technique take advantage of the enhance reactivity of CN<sub>x</sub> nanotubes, and their electrical and mechanical properties, producing low structural damage. An extensive characterization was performed on the obtained modified nanotubes in order to evaluate the covalent polymer-grafting, as well as the material structural changes and physico-chemical properties. Some of the used techniques mainly involved microscopy, spectroscopy and physico-chemical methods, among them SEM, HRTEM and allied techniques, FTIR, Raman spectroscopy, ESR, TGA, etc. The polymer-grafted nanotubes were produced at several reaction conditions, and compared to materials physically mixed.

The produced polymer-grafted CN<sub>x</sub> nanotubes were used as nanofillers to prepared polymer nanocomposites using several kinds of matrices (amorphous PS, semicrystalline polyethylene oxide (PEO) and immiscible blends PS-PEO). The structural and physical differences observed due to changes in dispersion and interactions were described for each polymer matrix. In addition, the polymer nanocomposites prepared with polymer-grafted CN<sub>x</sub> nanotubes were compared with sonicated MWNT and CN<sub>x</sub> nanotubes. The nanocomposite characterization involved morphological, thermal, electrical and mechanical properties using microscopy, TGA, DSC, dielectric spectroscopy and DMA. Interesting results were obtained, as elastic modulus enhancement and conductivity at low loadings in PS matrices. In other cases, a preparation challenges were found when producing PEO and PS-PEO, due to solution technique and immiscibility of the materials.

# Contents

<b>Abstract</b>	<b>ix</b>
<b>Acknowledgements</b>	<b>xi</b>
<b>List of Figures</b>	<b>xix</b>
<b>List of Tables</b>	<b>xxvii</b>
<b>Introduction</b>	<b>1</b>
References	4
<b>Chapter 1. Carbon nanotubes: an overview</b>	<b>7</b>
1.1. Introduction	7
1.1.1. Carbon-based materials	8
1.1.2. Discovery of fullerenes and other carbon-based materials	9
1.2. Structure of carbon nanotubes	
1.2.1. The single-walled carbon nanotube structure	10
1.2.2. Multi-walled carbon nanotube structure and dimensions	12
1.3. Methods for producing carbon nanotubes	13
1.3.1. Electric arc-discharge	13
1.3.2. Laser vaporization	14
1.3.3. Catalytic decomposition of hydrocarbons	15
1.3.4. Electrolysis	16
1.3.5. Other methods	16
1.4. Physico-chemical processing of carbon nanotubes	17
1.5. Physical properties of pure carbon nanotubes	19
1.5.1. Electrical properties	19
1.5.2. Mechanical properties	20
1.5.3. Thermal properties	21
1.6. Nitrogen-doped carbon nanotubes (CN <sub>x</sub> )	23
1.6.1. CN <sub>x</sub> nanotubes producing methods	23
1.6.2. Morphology, structure and composition of CN <sub>x</sub> nanotubes	23
1.6.3. C-N bonding in CN <sub>x</sub> nanotubes	23
1.6.4. Electrical properties of CN <sub>x</sub> nanotubes	26
1.7. Applications of carbon nanotubes	29
1.8. Conclusions	32
References	33

---

<b>Chapter 2. Chemical functionalization and polymer grafting of carbon nanotubes . . . . .</b>	<b>37</b>
2.1. Introduction . . . . .	38
2.2. Chemical reactivity of carbon nanotubes . . . . .	38
2.2.1. Local electronic structure and chemical reactivity . . . . .	38
2.2.2. Effect of bending and curvature in chemical reactivity . . . . .	39
2.2.3. Defective sites and chemical reactivity . . . . .	40
2.2.4. Nitrogen-doping sites and chemical reactivity . . . . .	41
2.3. Chemical modification of carbon nanotubes . . . . .	42
2.3.1. Types of chemical modification of carbon nanotubes . . . . .	42
2.3.2. Homogeneous dispersion of carbon nanotubes . . . . .	43
2.3.3. Chemical reactions of dispersed carbon nanotubes . . . . .	44
2.3.3.1. Covalent functionalization . . . . .	44
2.3.3.1.1. Oxidation reaction and subsequent functionalization . . . . .	44
2.3.3.1.2. Reduction, addition and other reactions . . . . .	46
2.3.3.1.3. Radical reactions . . . . .	47
2.3.3.2. Non-covalent functionalization . . . . .	49
2.3.3.3. Other functionalization types . . . . .	50
2.4. Polymer-grafting of carbon nanotubes . . . . .	50
2.4.1. Polymer-grafting of carbon black and fullerenes . . . . .	51
2.4.2. Polymer-grafting of carbon nanotubes by “grafting from” technique . . . . .	53
2.4.2.1. Polymer-grafting using carbon nanotube acid functionalization . . . . .	53
2.4.2.2. Polymer-grafting using living radical polymerization . . . . .	53
2.4.2.2.1. Anionic and cationic polymerization . . . . .	54
2.4.2.2.2. Controlled living radical polymerization . . . . .	55
2.5. Applications of functionalized and polymer-grafted carbon nanotubes . . . . .	56
2.6. Characterization of functionalized and polymer-grafted carbon nanotubes . . . . .	56
2.7. Conclusions . . . . .	57
References . . . . .	58
<b>Chapter 3. Polymer-carbon nanotubes composites . . . . .</b>	<b>65</b>
3.1. Introduction . . . . .	65
3.1.1. Carbon nanotube as nanofillers . . . . .	66
3.1.2. Types of carbon nanotubes composites . . . . .	66
3.2. Polymer-CNT composites . . . . .	67
3.2.1. Processing methods of polymer-CNT composites . . . . .	67
3.2.2. Critical issues in polymer-CNT composites processing . . . . .	69
3.2.2.1. Dispersion of CNTs within the matrix . . . . .	69
3.2.2.2. Interaction of CNTs with the polymer matrix . . . . .	70
3.2.2.3. Alignment and orientation of CNTs within the matrix . . . . .	72
3.2.3. Modification of CNT for composite processing . . . . .	72
3.2.3.1. Group functionalization of CNT . . . . .	73
3.2.3.2. Polymer attachment on CNT surface . . . . .	73
3.2.4. Physical properties of polymer-CNT composites . . . . .	74
3.2.4.1. Morphological properties . . . . .	74
3.2.4.2. Thermal properties of polymer-CNT composites . . . . .	74
3.2.4.3. Electrical properties of polymer-CNT composites . . . . .	75
3.2.4.4. Mechanical properties of polymer-CNT composites . . . . .	78
3.3. PS, PEO and PS-PEO blend and CNT composites . . . . .	80
3.4. Conclusions . . . . .	82
References . . . . .	83

<b>Chapter 4. Materials, methods and characterization techniques</b> . . . . .	<b>89</b>
4.1. Nanocomposite materials . . . . .	89
4.1.1. Carbon nanotubes . . . . .	89
4.1.2. Polymerization monomer, initiator and controllers . . . . .	92
4.1.3. Polymer matrices . . . . .	93
4.2. Preparation methods . . . . .	94
4.2.1. PS-grafted CN <sub>x</sub> nanotubes . . . . .	94
4.2.2. PS-PEO blend nanocomposites preparation . . . . .	95
4.3. Nanocomposite characterization . . . . .	96
4.3.1. Morphology, structure and composition characterization . . . . .	96
4.3.1.1. Electron Microscopy and allied techniques . . . . .	96
4.3.1.2. Raman Spectroscopy . . . . .	100
4.3.1.3. Infrared Spectroscopy (FTIR) . . . . .	103
4.3.2. Thermal properties characterization . . . . .	107
4.3.2.1. Thermogravimetric Analysis (TGA) . . . . .	107
4.3.2.2. Differential Scanning Calorimetry (DSC) . . . . .	109
4.3.3. Electromagnetic and electrical properties characterization . . . . .	
4.3.3.1. Electron Spin Resonance (EPR) . . . . .	112
4.3.3.2. Dielectrical measurements . . . . .	115
4.3.4. Dynamical Mechanical Analysis (DMA) . . . . .	118
4.3.5. Other characterization techniques . . . . .	120
4.4. Conclusions . . . . .	121
References . . . . .	122

## **Chapter 5. Polystyrene-grafting on nitrogen-doped carbon nanotubes by Nitroxide Mediated Radical Polymerization**

5.1. Introduction . . . . .	125
5.2. Results and discussion . . . . .	126
5.2.1. Disentanglement, dispersion and purification of the as-produced CN <sub>x</sub> nanotubes . . . . .	127
5.2.2. Variable screening of functionalized CN <sub>x</sub> nanotubes . . . . .	131
5.2.3. Radical functionalization of CN <sub>x</sub> nanotubes . . . . .	136
5.2.3.1. Electron Microscopy and allied techniques . . . . .	136
5.2.3.1.1. Structure and morphology of radical functionalized carbon nanotubes . . . . .	136
5.2.3.1.2. Chemical composition of radical functionalized carbon nanotubes . . . . .	137
5.2.3.2. Thermogravimetric Analysis . . . . .	143
5.2.3.3. FTIR Spectroscopy . . . . .	144
5.2.3.3.1. Carbon nanotubes spectra . . . . .	144
5.2.3.3.2. Carbon nanotubes and radicals spectra . . . . .	145
5.2.3.4. Raman Spectroscopy . . . . .	146
5.2.3.4.1. Carbon nanotubes spectra . . . . .	146
5.2.3.4.2. Carbon nanotubes and radical spectra . . . . .	147
5.2.3.5. Electron Paramagnetic Resonance . . . . .	150
5.2.3.5.1. Nitroxides spectra . . . . .	150
5.2.3.5.2. Carbon nanotubes spectra . . . . .	151
5.2.3.5.3. Carbon nanotubes and radicals spectra in solution . . . . .	152
5.2.3.6. Discussion . . . . .	160
5.2.4. Polystyrene-grafting of CN <sub>x</sub> nanotubes . . . . .	162
5.2.4.1. Synthesis results . . . . .	162
5.2.4.2. Thermogravimetric Analysis . . . . .	163
5.2.4.3. Electron Microscopy and allied techniques . . . . .	166
5.2.4.3.1. Arrangement and morphology of PS-grafted CN <sub>x</sub> nanotubes . . . . .	167

---

5.2.4.3.2. Chemical composition of PS-grafted CN <sub>x</sub> nanotubes . . . . .	168
5.2.4.4. Raman Spectroscopy . . . . .	172
5.2.4.5. FTIR Spectroscopy . . . . .	174
5.2.4.6. Separation . . . . .	175
5.2.4.7. Discussion . . . . .	175
5.3. Conclusions . . . . .	177
References . . . . .	179

## **Chapter 6. Preparation and morphological characterization of nanocomposites**

<b>of PS and PEO and PS-grafted CN<sub>x</sub> nanotubes . . . . .</b>	<b>183</b>
6.1. Introduction . . . . .	183
6.2. Results and discussion . . . . .	185
6.2.1. PS-based nanocomposites	
6.2.1.1. PS-nanotube composites processing . . . . .	185
6.2.1.2. PS-nanotube composites thermal properties . . . . .	186
6.2.1.3. PS-nanotube composites morphology . . . . .	188
6.2.1.4. Dispersion, adhesion and thermal behavior of PS-nanotube composites . . . . .	191
6.2.2. PEO-based nanocomposites	
6.2.2.1. PEO-nanotube composites processing . . . . .	193
6.2.2.2. PEO-nanotube composites thermal properties . . . . .	194
6.2.2.3. PEO-nanotube composites morphology . . . . .	199
6.2.2.4. Dispersion, adhesion and thermal behavior of PEO-nanotube composites . . . . .	202
6.2.3. PS-PEO-based nanocomposites	
6.2.3.1. PS-PEO nanotube composites processing . . . . .	203
6.2.3.2. PS-PEO nanotube composites thermal properties . . . . .	204
6.2.3.3. PS-PEO nanotube composites morphology . . . . .	206
6.2.3.4. Dispersion, adhesion and thermal behavior of PS-PEO nanotube composites . . . . .	211
6.3. Conclusions . . . . .	213
References . . . . .	215

## **Chapter 7. Electrical and mechanical characterization of nanocomposites**

<b>of PS, PEO and PS-grafted CN<sub>x</sub> nanotubes . . . . .</b>	<b>219</b>
7.1. Introduction . . . . .	219
7.2. Results and Discussion	
7.2.1. PS-based nanocomposites	
7.2.1.1. PS-nanotube composites electrical properties . . . . .	220
7.2.1.1.1. Carbon nanotubes conductivity measurement . . . . .	220
7.2.1.1.2. PS-nanotube composites conductivity measurement . . . . .	223
7.2.1.1.3. PS-nanotube composites conductivity modeling . . . . .	226
7.2.1.2. PS-nanotube composites mechanical properties . . . . .	232
7.2.1.2.1. PS-nanotube composites DMA measurements . . . . .	232
7.2.1.2.2. PS-nanotube composites mechanical modeling . . . . .	244
7.2.1.3. Analysis of the relation among electro-mechanical properties and microstructure of PS-nanotube composites . . . . .	248
7.2.2. PEO-based nanocomposites	
7.2.2.1. PEO-nanotube composites electrical properties . . . . .	251
7.2.2.2. PEO-nanotube composites mechanical properties . . . . .	256
7.2.2.3. Analysis of the relation among electro-mechanical properties and microstructure of PEO-nanotube composites . . . . .	261
7.3. Conclusions . . . . .	263
References . . . . .	265

---

<b>Conclusions and perspectives</b>	<b>269</b>
References .....	274
<b>Appendix</b>	
1.1. Discovery of carbon nanotubes .....	275
1.2. Growth mechanisms of carbon nanotubes .....	279
5.1. EFTEM spectra from the energy-filtered image series of $CN_x$ nanotubes .....	282
7.1. Imaginary part of the conductivity AC measurements in PS/CNTs composites .....	283
7.2. Modeling of electrical behavior of PS/CNTs composites using the Insulator-Conductor Transition Model .....	284
7.3. Conductivity exponent and percolation threshold in PS/CNTs composites calculated using the statistical percolation model .....	286
7.4. Loss Modulus of PS/CNTs composites at several CNT concentrations .....	288
7.5. Real and imaginary parts of the conductivity AC measurements in PEO210k/CNTs and PEO14k/CNTs composites .....	290
7.6. Conductivity exponent and percolation threshold in PEO14k/CNTs composites calculated using the Percolation Model .....	295
References .....	297

# Acknowledgments

This thesis was subscribed in the PCP Program of CONACYT-CNRS Mexico-France between the doctoral research programs of the Instituto Potosino de Investigación en Ciencia y Tecnología (IPICYT, Sn. Luis Potosi, Mexico), and the Materials, Engineering and Science Laboratory (MATEIS) at the Institut National de Sciences Appliquées (INSA de Lyon, France), with the collaboration of the Centro de Investigación y Desarrollo Tecnológico (CID, Lerma, Mexico). Therefore, I would like to acknowledge CONACYT-CNRS for the PCP scholarship to carry out the research stages at INSA de Lyon; to CONACYT-Mexico for the PhD student scholarship and the financial support grants: 45762 (HT), 45762 (MT), 41464-Inter American Collaboration (MT), 42428- Inter American Collaboration (HT), 2004-01-013/SALUD-CONACYT (MT), PUE-2004-CO2-9 Fondo Mixto de Puebla; to MATEIS Laboratory for complementary economical support for research events; and finally, to the Asociación Nacional de Ingenieros Químicos (ANIQ) for the student scholarship complement to performed the local stages at Lerma.

I would like to express a very special thankful to Dr. Alfonso González-Montiel for his scientific advice, teaching and personal guidance during these years. His motivation and scientific proposals were determinants in the course of my doctoral studies. In the same manner, I would like to acknowledge to Dr. Mauricio Terrones for his scientific advice, teaching and strong support all the time. I really appreciate their taught of enthusiasm by the knowledge, joy of scientific research, and the importance of the hard work. In both cases, I have the privilege to share with them an invaluable friendship.

In the chronological order of the project, I would like to acknowledge Dr. Jean-Yves Cavallé for accepting the research project, and for all the professional discussion that enriched the course of the work. In addition, I would like to thank to Dra. Catherine Gauthier and Dra. Karine Masenelli-Varlot for supervising the work, for their teaching and support along these years, and for the manuscript detailed revisions and brilliant opinions that enrich the project. Specially, I thank to Karine for her personal and professional guidance in all the thesis process. I really appreciate her human and scientific enthusiasm, her intelligence and disciplinary work, but specially her generous friendship.

In summary, I acknowledge all the advice and help I have received from my supervisors, with all of them I found a lot of pleasure to work. In addition, I want to thank the judicious reading of this work; they are not to be blamed for any remaining errors.

I also would like to grateful to the members of the Tutorial Comitte at IPICYT: Dr. Humberto Terrones and Dra. Yadira Vega, for their important commentaries along the thesis development that always enriched the work. In addition, I want to express my grateful to the other members of the jury: Dr. A. Peigney, Dr. C. Laurent, Dr. L. Ríos and Dr. P. Herrera, Dr. E. Saldívar for their enthusiastic and professional participation in the revision of the work.

I want to thank for the laboratory facilities of all the involved institutions CID, IPICYT, MATEIS at INSA de Lyon, Université Claude Bernard, UAM-I and IQ-UNAM. I also would like to thank to the researchers, technicians, and administrative personal of the institutions than gave me indispensable help at each scientific stage. Some of them are: G. C. Flores, C. R. López, M. D. Baeza, Dr. E. Muñoz, D. Ramírez, L. Chavez, G. Ramírez, A. L. Elías, G. Pérez-Assaf, F. Dalmas, and many others. I am also grateful to A. L. Elías, J. A. Rodríguez-Manzo, A. Zamudio for providing nanotube samples.

I want to specially thank to my colleagues and friends that were adorable and supportive all the time and, if the case, aid me with the inculturation process: E. Espinoza, O. González, P. Esparza, D. Meneses, B. Fragneaud, A. Vermogen, M. Vermogen, E. Munch, R. García, E. Dehonor, C. Camacho, J. Sánchez Pin, E. Miranda, among many others.

My sincere grateful to all of the members of my huge family for the great happiness they bring to my life, and their supportive presence in all of the important facts, as this professional step.

Finally and most importantly, I would like to express all my love and gratitude: to my parents Ma. Francisca and Israel, for their wonderful presence in my life, their guidance, support, dedication, and incommensurable love in all situations and moments; to my dear husband Luis for his magnificent love and devotion with multiple and varied demonstrations, for the amazing opportunity of sharing our lives, for always support and participate from my interests and projects; and to our growing little love Ana Paula for illumining us and became the reason of our life; finally, to God for their incredible and permanent blessings.

# List of Figures

## Chapter 1

- 1.1. Structure of crystalline carbon-based materials: (a) graphite, (b) diamond, (c) fullerene, and (d) SWNTs. (Molecular modeling images).
- 1.2. High resolution TEM Images of CNTs: left general view, right: (A) SWNTs and (B) MWNTs.
- 1.3. Molecular models of SWNTs exhibiting different achiral and chiral conformations: (a) armchair, (b) zigzag and (c) chiral; (d) graphene sheet mathematic description, using chiral vector ( $C_h$ ) with indexes ( $m,n$ ) and unitary vectors ( $\mathbf{a}_1$  and  $\mathbf{a}_2$ ). Fig. 2.3 (d) shows the mathematic description of a graphene sheet, introducing some definitions: carbon nanotube chiral vector, chiral angle and diameter.
- 1.4. Schematic representation of a) “Russian doll” and b) “Scroll-like” models for MWNTs. A mixed configuration is also represented (c).
- 1.5. Schematic representation of an electric-arc-discharge apparatus used to produce fullerenes and carbon nanotubes.
- 1.6. Representation of the laser vaporization method to produce SWNTs and MWNTs. In this particular case the process is carried out in a furnace and the nanotubes are collected in a Cu-cooled trap.
- 1.7. Schematic diagram of the pyrolysis set up used for the synthesis of CNTs.
- 1.8. Experimental set up of the electrolysis method used to synthesized CNTs in liquid phase.
- 1.9. Density of states (DOS) exhibiting the valence, the conduction band and the Fermi energy for (a) metallic armchair tubes and (b) a semiconducting zig zag tubes. In zigzag tubes an energy gap is clearly observed between the valence and conduction band.
- 1.10. Thermogravimetric Analysis of a MWNTs and  $C_{60}$ . As can be seen the nanotubes are more resistant than  $C_{60}$  to oxidation processes.
- 1.11. EEL spectra of  $CN_x$  nanotube showing the C-K and N-K ionization edges for C and N at (1) the nanotube edge and (2) in the center of the nanotube.
- 1.12. EELS spectra of a  $CN_x$  nanotube exhibiting K-shell ionization edges for C (~284.5 eV) and N (~400 eV). Inset shows (a) a sharp characteristic at ~401 eV corresponding to N bonded to C three C atoms within a hexagonal lattice, and (b) a weak shoulder at ~399 eV associated with pyridine-like N located in defective areas of the graphitic layers.
- 1.13. Calculated N1s binding energy loss-near edge fine structures.
- 1.14. Longitudinal cross-section of a fluorescent display with a field emission cathode constructed from MWNTs; (b) TV display prototype using CNTs.
- 1.15. (a) Charging-discharging mechanism of a Li battery; (b) basic composition of electrode and polymer  $Li^+$  composite of the battery.
- 1.16. SEM image of a standard AFM tip with MWNT attached.

- 1.17. C<sub>2</sub> addition to a cap of nanotube. (a) Numbers from 1 to 6 indicate the position of the six pentagons on the hemispherical cap. If there is an addition of one C<sub>2</sub> molecule, indicated by the open circles between 2 and 3, and if the new bonds denoted by dotted lines form, a new hexagon denoted in (b) by dark shading is obtained.
- 1.18. Growth mechanism of carbon nanotubes at an open end by the absorption of C<sub>2</sub> (dimers) and C<sub>3</sub> (trimers).
- 1.19. Growth mechanism proposed by Baker *et al* for the formation of carbon nanotubes by pyrolysis. In this model, the carbon particles from the precursor, C, diffuse through metal catalyst, M, precipitating in the other side in the form of graphite. As can be seen, fiber formation take place in the substrate side.
- 1.20. Model representation of carbon nanotubes growth mechanism from a substrate by the carbon diffusion over the metal catalyst particle, M. Vertical fibers of graphite are formed between metal and substrate.
- 1.21. Schematic diagram of fibrils growth from a substrate using pyrolysis method. In this particular case, carbon particles from the precursor Fe-Pt/C<sub>2</sub>H<sub>2</sub> diffuses the catalyst, but it remains close to the substrate.

### Chapter 2

- 2.1. Diagrams of (a) metallic (5,5) SWNT, (b) pyramidalization angle, and (c) misalignment angles ( $\phi$ ) along C1-C4 in the (5,5) SWNT and its capping fullerene C<sub>60</sub>.
- 2.2. The local chemical reactivity (hydrogenation energy) controlled by the carbon nanotube bending angle, that could be induced by mechanical deformations. The model considers only single bonds.
- 2.3. The most common defect sites in SWNTs: A) Five or seven membered rings within the carbon framework (inducing bending); B) sp<sup>3</sup>-hybridized defects (R=H and OH); C) Carbon framework damage by oxidation, which leaves -COOH groups; D) Open ended SWNTs terminated with -COOH, or other terminal groups, such as -NO<sub>2</sub>, -OH, -H and =O.
- 2.4. Nitrogen-doped carbon nanotube scheme. Molecular modeling of CN<sub>x</sub> nanotubes containing pyridine-like and highly coordinated N-atoms.
- 2.5. Some functionalization possibilities of SWNTs: (A) Defect-group functionalization, (B) Covalent sidewall functionalization, (C) Non-covalent exohedral functionalization with surfactants, (D) Noncovalent exohedral functionalization with polymers, and (E) Endohedral functionalization with, for example, C<sub>60</sub>.
- 2.6. Scheme of common covalent functionalization routes used to derive SWNTs at the ends and defect sites. As produced nanotubes are treated with an oxidative protocol to generate functional groups that react with SOCl<sub>2</sub> followed by amide or ester linkages. Amine and oxygenated functional groups are also effective sites for coordination to metal complexes and ions.
- 2.7. Covalent-sidewall functionalization reactions of carbon nanotubes.
- 2.8. Addition reactions of SWNTs. (a) attachment of radio-labeled ATP, (b) dichlorocarbene addition, and (c) hydrogenation.
- 2.9. Surface grafting onto carbon black by trapping polymer radicals formed by decomposition of TEMPO-polystyrene.
- 2.10. Surface grafting onto carbon black by trapping polymer radicals formed by redox reaction of ceric ions with polymer containing hydroxyl groups.

### Chapter 3

- 3.1. Types of nanocomposites prepared using carbon nanotubes.
- 3.2. Key mechanisms of energy dissipation have been identified in the fracture of short as well as continuous fiber-reinforced composites.

*Chapter 4*

- 4.1. SEM images of raw  $CN_x$ : (a) nanotubes bundles and (b) top-view of flakes showing the catalyst particles at the free ends of the nanotubes.
- 4.2. HRTEM images of raw  $CN_x$  after sonication in ethanol: (a) global view, (b) nanotube crystalline planes and carbon amorphous layer.
- 4.3. Core-loss EEL spectra of the as prepared- $CN_x$ , showing the C and N edges.
- 4.4. D and G peak position and their relative intensities ( $I_D/I_G$ ) of  $CN_x$  Raman Spectra from samples of different batches production.
- 4.5. Weight loss and degradation temperatures of as received carbon nanotubes: i) MWNTs, ii)  $CN_x$ .
- 4.6. Polymer brushes reaction scheme: functionalization of  $CN_x$  (1) with the NMRP initiator (2) and controller (3), and synthesis of polymer brushes of polystyrene (4).
- 4.7. Elastic and Inelastic Interactions between incident electron beam and atom.
- 4.8. Electron ray path of a Transmission Electron Microscope equipped with an in-column energy filter.
- 4.9. Comparative EEL spectra of graphite, bundle of SWNTs and MWNTs carbon nanotubes in energy ranges of (a) 0 to 45 eV (plasmon region) and (b) 280-300 eV (carbon K-edge).
- 4.10. Energy level diagram for Raman scattering: (a) Stokes Raman scattering, and (b) anti-Stokes Raman scattering.
- 4.11. Schematics of molecular vibration of polyatomic molecules.
- 4.12. FTIR experimental set up.
- 4.13. Experimental set up of a Thermogravimeter.
- 4.14. TGA of purified SWNTs.
- 4.15. Experimental device of a DS Calorimeter.
- 4.16. Differential Scanning Calorimetry curve for a polymer which shows the glass transition temperature ( $T_g$ ), crystallization temperature ( $T_c$ ), melting temperature ( $T_m$ ), heat of crystallization ( $\Delta H_{cryst}$ ), heat of melting ( $\Delta H_{melt}$ ), heat of degradation ( $\Delta H_{decom}$ ) and heat of crystallization from the melt ( $\Delta H_{melt-cryst}$ ).
- 4.17. Dielectric relaxation processes as a function of the frequency.
- 4.18. Conductivity zones of a material.
- 4.19. Polymer modulus evolution as a function of the temperature.

*Chapter 5*

- 5.1. Polymer brushes reaction scheme: functionalization of  $CN_x$  (1) with the NMRP initiator (2) and controller (3), and synthesis of polymer brushes of polystyrene (4).
  - 5.2. Effect of sonication time in thermal degradation of  $CN_x$  nanotubes: samples were sonicated (a) 0, (b) 1, (c) 2, (d) 3, (e) 4 and (f) 5 hr in xylene and dried in a vacuum oven for 15 hrs at 70-80°C. TGA in N from 20-900°C at 10°C/min.
  - 5.3. Effect of the dried time in thermal degradation of  $CN_x$  sonicated in xylene (1 hr) and dried for (a) 2, (b) 6, (c) 10 and (d) 15 hr in a vacuum oven at 70-80°C. TGA in N from 20-900°C at 10°C/min.
- Fig. 5.4. Thermal degradation of: (a) as-received  $CN_x$  nanotubes, (b) dried  $CN_x$  nanotubes (15 hr), (c)  $CN_x$  nanotubes dispersed in xylene without sonication and dried (15 hr), (d)  $CN_x$  nanotubes sonicated in xylene (1 hr) and dried (15 hr). The drying step was performed in oven for 15 hr at 70-80°C.
- 5.5. Schematic experimental design.
  - 5.6. Thermal degradation of radical functionalized reactor samples from the PPRs column 3, synthesized in benzene at 130°C using three nitroxides types: BPO/TEMPO ((a)A3 and (b)B3), BPO/OHTEMPO ((c) C3 and (d) D3) and PR CGX 505 ((e) E3 and (f) F3). A3, C3 and E3 consider high initiator concentration, whereas B3, D3 and F3 low initiator concentration.

- 5.7. Thermal degradation of radical functionalized reactor sample from the PPRs3, corresponding to F3 synthesized in benzene at 130°C using PR CGX 505 and low initiator concentration. The variables displayed are weight loss and its first derivative.
- 5.8. HRTEM images of radical functionalized carbon nanotubes with BPO and TEMPO after dispersion by sonication in ethanol: (a) global view, (b) zoom.
- 5.9. Filtered images of (a) CN<sub>x</sub> nanotubes, and (b) CN<sub>x</sub>-RNO<sub>x</sub>. Each group of images is presented in the following order: zero loss, carbon, nitrogen and oxygen maps.
- 5.10. EFTEM spectra extracted from the energy-filtered image series, sorted by element and the parameters used for the calculation of the elemental maps in CN<sub>x</sub> nanotubes (1): (a) carbon map, (b) nitrogen map and (c) oxygen map.
- 5.11. EFTEM spectra extracted from the energy-filtered image series, sorted by element and the parameters used for the calculation of the elemental maps in CN<sub>x</sub>-RNO<sub>x</sub> (3): (a) carbon map, (b) nitrogen map and (c) oxygen map.
- 5.12. Thermal degradation of CN<sub>x</sub> nanotubes reacted with solutions of (b) BPO, (c) PR CGX505 and (d) BPO-PR CGX505 at same reaction conditions than F3 sample, but with twice of CN<sub>x</sub> nanotubes.
- 5.13. FTIR spectra of CN<sub>x</sub> nanotubes and radical functionalized CN<sub>x</sub> nanotubes.
- 5.14. Raman spectra of (a) CN<sub>x</sub> nanotubes, and radical functionalized CN<sub>x</sub> nanotubes with: (b) BPO/TEMPO and (c) BPO/PR CGX505 solutions.
- 5.15. EPR Spectra of PR CGX505 nitroxide recorded at several temperatures 20, 80 and 120°C in xylene as solvent.
- 5.16. Spin concentration as a function of time in samples of CN<sub>x</sub> nanotubes and BPO/TEMPO radicals reacted in benzene at 105°C.
- 5.17. Spin concentration as a function of time in samples of MWNT and CN<sub>x</sub> nanotubes with BPO/PR CGX505 radicals reacted in xylene at 120°C.
- 5.18. Stability and solubility differences between (a) physical blend of PS and sonicated-CN<sub>x</sub> nanotubes, PS-CN<sub>x</sub>, (left hand side), and (b) *in situ* polymerized PS in the presence of radically functionalized CN<sub>x</sub> (right hand side) in toluene. The former dispersion is not stable, whereas the second is stable over weeks.
- 5.19. Thermal degradation of reaction products of *in situ* polymerized CN<sub>x</sub> nanotubes using BPO/PR CGX 505 (reactor F3), separated by filtration: (a) as-produced CN<sub>x</sub> nanotubes, (b) over filter sample, corresponding to the PS-grafted from radical functionalized CN<sub>x</sub> nanotubes, and (c) under filter sample, corresponding to PS.
- 5.20. Thermal degradation of reaction products of functionalized and polymer-grafted CN<sub>x</sub> nanotubes (reactor F3): (a) as-produced CN<sub>x</sub> nanotubes, (b) radical functionalized-CN<sub>x</sub> nanotubes (CN<sub>x</sub>-RNO<sub>x</sub>), where the weight loss mainly corresponding to the BPO/PR CGX505 attachment, and (c) polymer-grafted-CN<sub>x</sub> (PS-g-CN<sub>x</sub>) nanotubes where the weight loss corresponded to polymer attachment.
- 5.21. Thermal degradation of reaction products of polymer-grafted CN<sub>x</sub> nanotubes at the conditions of reactor F3 using several radical functionalized samples: (a) CN<sub>x</sub>-BPO (CN<sub>x</sub>-R), (b) CN<sub>x</sub>-PR CGX505 (CN<sub>x</sub>-NO<sub>x</sub>), and (c) CN<sub>x</sub>-BPO/PR CGX505 (CN<sub>x</sub>-RNO<sub>x</sub>).
- 5.22. STEM images of *in situ* polymerized PS-g-CN<sub>x</sub> nanotubes samples at several magnification (a) 32676X and (b) 8000X.
- 5.23. HRTEM micrographs of the (a) and (b) *in situ* polymerized PS in the presence of CN<sub>x</sub> nanotubes produced using the NMRP method, and (c) and (d) physical blend of PS with CN<sub>x</sub> nanotubes.
- 5.24. EEL comparative spectra of the PS, raw CN<sub>x</sub> nanotubes, PS-g-CN<sub>x</sub>, and the physical blend of PS and CN<sub>x</sub> nanotubes.
- 5.25. High energy-loss EELS spectra of PS-g-CN<sub>x</sub> amorphous layer and relative elemental composition.

- 5.26. Filtered images of (a) PS-g-CN<sub>x</sub> and (b) physical blend of PS and CN<sub>x</sub> nanotubes. Each group of images is presented in the next order: zero loss, carbon, nitrogen and oxygen maps.
- 5.27. EFTEM spectra extracted from the energy-filtered image series, and parameters used for the calculation of the elemental maps for the physical blend of PS and CN<sub>x</sub> nanotubes (PS/CN<sub>x</sub>): (a) carbon map, (b) nitrogen map and (c) oxygen map.
- 5.28. Raman spectra of (a) raw CN<sub>x</sub> nanotubes, and (b) *in situ* polymerized CN<sub>x</sub> nanotubes (PS-g-CN<sub>x</sub>) due to F3 reactor.
- 5.29. FTIR spectra of CN<sub>x</sub> nanotubes and PS-g-CN<sub>x</sub> nanotubes.
- 5.30. Diameter distribution (150 nanotubes) of PS-g-CN<sub>x</sub> and CN<sub>x</sub> nanotubes measured by TEM.
- 5.31. EFTEM spectra extracted from the energy-filtered image series, and parameters used for the calculation of the elemental maps for the CN<sub>x</sub> nanotubes: (a) carbon map, (b) nitrogen map and (c) oxygen map.

### Chapter 6

- 6.1. Reaction scheme of the preparation steps of the polymer-nanotube composites.
- 6.2. Glass transition temperature of PS matrix, PS-grafted CN<sub>x</sub> nanotube fillers alone (PS-g-CN<sub>x</sub>) and the PS-based nanocomposites with either CN<sub>x</sub> (PS/CN<sub>x</sub>), or PS-grafted CN<sub>x</sub> fillers (PS/PS-g-CN<sub>x</sub>) at 5 wt%.
- 6.3. SEM images of film-fractured polymer nanocomposites of PS and 2 wt% of MWNT prepared by solution casting and high temperature pressing at several magnifications and scan velocity: (a) high scan, (b) low scan.
- 6.4. TEM images of microtomed film of polymer nanocomposites of PS and 2 wt% of MWNT prepared by solution casting and high temperature pressing.
- 6.5. SEM images of film fractured polymer nanocomposites of PS and 2 wt% of CN<sub>x</sub> nanotubes prepared by solution casting and high temperature pressing.
- 6.6. TEM images of polymer nanocomposites of PS and 2 wt% of CN<sub>x</sub> nanotubes prepared by solution casting and high temperature pressing.
- 6.7. SEM images of polymer nanocomposites of PS and 2 wt% of PS-grafted CN<sub>x</sub> nanotubes (PS-g-CN<sub>x</sub>) prepared by solution casting and high temperature pressing.
- 6.8. TEM images of polymer nanocomposites of PS and 2 wt% of PS-grafted CN<sub>x</sub> nanotubes (PS-g-CN<sub>x</sub>) prepared by solution casting and high temperature pressing.
- 6.9. Melting temperature of (a) PEO polymer matrix, and PEO/MWNT nanocomposites at several filler content: (b) 0.5 wt% and (c) 2.0 wt%.
- 6.10. Melting temperature of (a) PEO polymer matrix, and PEO-based nanocomposites: (b) PEO/CN<sub>x</sub> at 0.5 wt%, (c) PEO/CN<sub>x</sub> at 2.0 wt%, (d) PEO/PS-g-CN<sub>x</sub> at 0.5 wt%, and (e) PEO/PS-g-CN<sub>x</sub> at 2.0 wt%.
- 6.11. Crystallization peak for (a) PEO polymer matrix, and PEO-based nanocomposites: PEO/CN<sub>x</sub> (b) with 0.5 wt%, and (c) with 2.0 wt%, PEO/PS-g-CN<sub>x</sub> (d) with 0.5 wt% and (e) with 2.0 wt%.
- 6.12. Crystallization temperature of (a) PEO polymer matrix, and PEO/MWNT nanocomposites at several filler content: (b) 0.5 wt% and (c) 2.0 wt%.
- 6.13. SEM images of polymer nanocomposites of PEO and 2 wt% of MWNT nanotubes prepared by solution casting and film pressing. Images (a) and (c) taken at normal scan and (b) and (d) at low scan.
- 6.14. SEM images of polymer nanocomposites of PEO and 2 wt% of CN<sub>x</sub> nanotubes prepared by solution casting and film pressing. Images (a) and (c) taken at normal scan and (b) and (d) at low scan.
- 6.15. TEM images of polymer nanocomposites of PEO and 2 wt% of CN<sub>x</sub> nanotubes prepared by solution casting and film pressing.
- 6.16. SEM images of polymer nanocomposites of PEO and 2 wt% of PS-g-CN<sub>x</sub> nanotubes prepared by solution casting and film pressing.

- 6.17. Melting temperature of (a) pure PS-PEO polymer blend, and PS-PEO/MWNT nanocomposites at several filler content: (b) 0.5 wt% and (c) 2.0 wt%.
- 6.18. SEM images of PS and PEO polymer blends at 35:65 w% relation.
- 6.19. SEM images of polymer nanocomposites of PS and PEO polymer blends (35:65 wt%) and 2 wt% MW nanotubes. Images (a) and (b) were taken at normal scan, whereas image (c) at low scan.
- 6.20. SEM images of polymer nanocomposites of PS and PEO polymer blends (35:65 wt%) and 2 wt% CN<sub>x</sub> nanotubes.
- 6.21. TEM images of polymer nanocomposites of PS and PEO blends (35:65 wt%) and 2 wt% of CN<sub>x</sub> nanotubes.
- 6.22. SEM images of polymer nanocomposites of PS and PEO blends (35:65 wt%) and 2 wt% of polymer grafted nanotubes (PS-g-CN<sub>x</sub>).
- 6.23. TEM images of polymer nanocomposites of PS and PEO blends (35:65 wt%) and 2 wt% of polymer grafted nanotubes (PS-g-CN<sub>x</sub>) at several magnifications.

### *Chapter 7*

- 7.1. Conductivity measures of several carbon nanotube fillers, and their correspondent PS-based nanocomposites filled at 5 wt% of filler.
- 7.2. Schematic representation of the percolation behavior dependence on the filler dispersion. Example of the (a) PS/MWNT, (b) PS/CN<sub>x</sub>, and (c) PS/PS-g-CN<sub>x</sub> nanocomposites.
- 7.3. Real conductivity of PS/MWNT nanocomposites vs. frequency at filler weight fractions of 0.1 to 5.0 wt% and applied voltage of 0.1 V.
- 7.4. Imaginary conductivity of PS/MWNT nanocomposites vs. frequency at filler weight fractions of 0.1 to 5.0 wt% and applied voltage of 0.1 V.
- 7.5. Real conductivity of PS/CN<sub>x</sub> nanocomposites vs. frequency at filler weight fractions of 0.1 to 5.0 wt% and applied voltage 0.1 V.
- 7.6. Real conductivity of PS/PS-g-CN<sub>x</sub> nanocomposites vs. frequency at filler weight fractions of 0.1 to 7.7 wt% and applied voltage 0.1 V.
- 7.7. Real part of the AC electrical conductivity at 1 Hz for nanocomposites of PS and nanotubes at several filler contents. Comparison with the statistical percolation theory (solid lines).
- 7.8. Storage modulus of PS/MWNT nanocomposite vs. temperature at filler weight fractions of (a) 0, (b) 0.3, (c) 0.5, (d) 1.0, (e) 2.0 and (f) 5.0 wt%.
- 7.9. Loss modulus of PS/MWNT nanocomposites vs. temperature at filler weight fractions of: (a) 0, (b) 0.3, (c) 0.5, (d) 1.0, (e) 2.0 and (f) 5.0 wt%.
- 7.10. Tan  $\delta$  of PS/MWNT nanocomposites vs. temperature at filler weight fractions of (a) 0, (b) 0.3, (c) 0.5, (d) 1.0, (e) 2.0 and (f) 5.0 wt%.
- 7.11. Storage modulus of PS/CN<sub>x</sub> nanocomposites vs. temperature at filler weight fractions of (a) 0, (b) 0.3, (c) 0.5, (d) 1.0, (e) 2.0, and (f) 5.0 wt%.
- 7.12. Tan  $\delta$  of PS/CN<sub>x</sub> nanocomposites vs. temperature at filler weight fractions of (a) 0, (b) 0.3, (c) 0.5, (d) 1.0, (e) 2.0, and (f) 5.0 wt%.
- 7.13. Storage modulus of PS/PS-g-CN<sub>x</sub> nanocomposites vs. temperature at filler weight fractions of 0.1 to 5.0 wt%.
- 7.14. Tan  $\delta$  of PS/PS-g-CN<sub>x</sub> nanocomposites vs. temperature at filler weight fractions of (a) 0, (b) 0.1, (c) 0.3, (d) 0.5, (e) 0.7, (f) 1.0, (g) 2.0, (h) 5.0, and (i) 7.7 wt%.
- 7.15. Loss factor (tan  $\delta$ ) of the PS/CNTs composites at several volume fractions of: ( $\diamond$ ) MWNT, ( $\square$ ) CN<sub>x</sub> and ( $\circ$ ) PS-g-CN<sub>x</sub> nanotubes.
- 7.16. Schematic representation of (a) the entanglement of the nanotube fillers, and (b) the contact between nanotube fillers (PS/MWNT, PS/CN<sub>x</sub>, and PS-g-CN<sub>x</sub>).
- 7.17. Comparison of the Storage Modulus of (a) PS and PS-based composite with (b) MWNT, (c) CN<sub>x</sub> and (d) PS-g-CN<sub>x</sub> nanotubes at a concentration of 5.0 wt%.

- 7.18. Comparison of the  $\tan \delta$  of (a) PS and PS-based composite with (b) MWNT, (c)  $\text{CN}_x$  and (d) PS-g- $\text{CN}_x$  nanotubes at a concentration of 5.0 wt%.
- 7.19. Storage modulus of the PS/CNTs composites at several volume fractions of: ( $\diamond$ ) MWNT, ( $\square$ )  $\text{CN}_x$  and ( $\circ$ ) PS-g- $\text{CN}_x$  nanotubes. Lines show the Halpin-Kardos Model calculated values.
- 7.20. Storage modulus of the PS/CNTs composites at several volume fractions of: ( $\diamond$ ) MWNT, ( $\square$ )  $\text{CN}_x$  and ( $\circ$ ) PS-g- $\text{CN}_x$  filler. Lines show the fits obtained with the Percolation Model.
- 7.21. Real conductivity of PEO210k/MWNT nanocomposites vs. frequency at filler weight fractions of 0.1 to 5.0 wt% and applied voltage of 0.1 V.
- 7.22. Real conductivity of PEO210k/ $\text{CN}_x$  nanocomposites vs. frequency at filler weight fractions of 0.1 to 5.0 wt% and applied voltage of 0.1 V.
- 7.23. Real conductivity of PEO210k/PS-g- $\text{CN}_x$  nanocomposites vs. frequency at filler weight fractions of 0.1 to 5.0 wt% and applied voltage of 0.1 V.
- 7.24. Real part of the AC electrical conductivity at 1 Hz and 0.1 V for PEO14k/CNT at several filler contents. Comparison with statistical percolation theory (solid lines).
- 7.25. Storage modulus of PEO/MWNT nanocomposite vs. temperature at filler weight fractions of (a) 0, (b) 0.5, and (c) 2.0 wt%.
- 7.26.  $\tan \delta$  of PEO/MWNT nanocomposite vs. temperature at filler weight fractions of (a) 0, (b) 0.5, and (c) 2.0 wt%.
- 7.27. Comparison of the Storage Modulus of (a) PEO and PEO-based composite with (b) MWNT, (c)  $\text{CN}_x$  and (d) PS-g- $\text{CN}_x$  nanotubes at a filler concentration of 2.0 wt%.
- 7.28. Comparison of the  $\tan \delta$  of (a) PEO and PEO-based composite with (b) MWNT, (c)  $\text{CN}_x$  and (d) PS-g- $\text{CN}_x$  nanotubes at a concentration of 2.0 wt%.
- 7.29. Imaginary conductivity of PS/ $\text{CN}_x$  nanocomposites vs. frequency at filler weight fractions of 0.1 to 5.0 wt% and applied voltage of 0.1 V.
- 7.30. Imaginary conductivity of PS/PS-g- $\text{CN}_x$  nanocomposites vs. frequency at filler weight fractions of 0.1 to 5.0 wt% and applied voltage of 0.1 V.
- 7.31. Insulator-conductor transition model applied to PS/CNTs composites.
- 7.32. Real part of the AC electrical conductivity at 1 Hz and applied voltage of 0.1 V for PS/MWNT at several filler contents. Comparison with statistical percolation theory (solid lines).
- 7.33. Real part of the AC electrical conductivity at 1 Hz and 0.1 V for PS/ $\text{CN}_x$  at several filler contents. Comparison with statistical percolation theory (solid lines).
- 7.34. Real part of the AC electrical conductivity at 1 Hz and applied voltage of 0.1 V for PS/PS-g- $\text{CN}_x$  at several filler contents. Comparison with statistical percolation theory (solid lines).
- 7.35. Loss Modulus of PS/ $\text{CN}_x$  nanocomposites vs. temperature at filler weight fractions of: (a) 0, (b) 0.1, (c) 0.3, (d) 0.5, (e) 1.0, (f) 2.0 and (g) 5.0 wt%.
- 7.36. Loss Modulus of PS/PS-g- $\text{CN}_x$  nanocomposites vs. temperature at filler weight fractions of: (a) 0, (b) 0.1, (c) 0.3, (d) 0.5, (e) 0.7, (f) 1.0, (g) 2.0, (h) 5.0 and (i) 7.7 wt%.
- 7.37. Comparison of the loss modulus of (a) PS and PS-based composite with (b) MWNT, (c)  $\text{CN}_x$  and (d) PS-g- $\text{CN}_x$  nanotubes at a concentration of 5.0 wt%.
- 7.38. Imaginary conductivity of PEO210k/MWNT nanocomposites vs. frequency at filler weight fractions of 0.1 to 5.0 wt% and applied voltage of 0.1 V.
- 7.39. Imaginary conductivity of PEO210k/ $\text{CN}_x$  nanocomposites vs. frequency at filler weight fractions of 0.1 to 5.0 wt% and applied voltage of 0.1 V.
- 7.40. Imaginary conductivity of PEO210k/PS-g- $\text{CN}_x$  nanocomposites vs. frequency at filler weight fractions of 0.1 to 5.0 wt% and applied voltage of 0.1 V.
- 7.41. Real conductivity of PEO14k/MWNT nanocomposites vs. frequency at filler weight fractions of 0.1 to 5.0 wt% and applied voltage of 0.1 V.
- 7.42. Imaginary conductivity of PEO14k/MWNT nanocomposites vs. frequency at filler weight fractions of 0.1 to 5.0 wt% and applied voltage of 0.1 V.

- 7.43. Real conductivity of PEO14k/CN<sub>x</sub> nanocomposites vs. frequency at filler weight fractions of 0.1 to 5.0 wt% and applied voltage of 0.1 V.
- 7.44. Imaginary conductivity of PEO14k/CN<sub>x</sub> nanocomposites vs. frequency at filler weight fractions of 0.1 to 5.0 wt% and applied voltage of 0.1 V.
- 7.45. Real conductivity of PEO14k/PS-g-CN<sub>x</sub> nanocomposites vs. frequency at filler weight fractions of 0.1 to 5.0 wt% and applied voltage of 0.1 V.
- 7.46. Imaginary conductivity of PS-g-CN<sub>x</sub> nanocomposites vs. frequency at filler weight fractions of 0.1 to 5.0 wt% and applied voltage of 0.1 V.
- 7.47. Real part of the AC electrical conductivity at 1 Hz and applied voltage of 0.1 V for PEO14k/MWNT composites at several filler contents. Comparison with model (solid lines).
- 7.48. Real part of the AC electrical conductivity at 1 Hz and applied voltage of 0.1 V for PEO14k/CN<sub>x</sub> composites at several filler contents. Comparison with model (solid lines).
- 7.49. Real part of the AC electrical conductivity at 1 Hz and applied voltage of 0.1 V for PEO14k/PS-g-CN<sub>x</sub> at several filler contents. Comparison with model (solid lines).

# List of Tables

## *Chapter 1*

- 1.1. Physico-chemical characteristics of carbon-based materials.
- 1.2. Single-walled carbon nanotube structural parameters: chiral angle, chiral vector and the shape of the cross-section for arm-chair, zigzag and chiral conformations.
- 1.3. Fabrication methods of N-doped carbon nanotubes.
- 1.4. Electrical resistivity of different carbon materials.
- 1.5. Progress in carbon allotropes until the discovery of carbon nanotubes.
- 1.6. Discovery of carbon structure materials.

## *Chapter 3*

- 3.1. Microscopy and Spectroscopy techniques most used in morphological characterization of nanocomposites and their corresponding size range.

## *Chapter 4*

- 4.1. Characteristics bands associated to functionalized CNTs.

## *Chapter 5*

- 5.1. Values of the average weight losses at 600°C for ultrasonicated (1 hr in xylene), and dried (15 hr at 70-80°C) as-produced CN<sub>x</sub> nanotube samples.
- 5.2. Peak to peak analysis of weight losses of radical functionalized reactor samples from the PPRs column 3, synthesized in benzene at 130°C using two levels of initiator and three nitroxide types: BPO/TEMPO (A3 and B3), BPO/OHTEMPO (C3 and D3) and PR CGX 505 (E3 and F3).
- 5.3. Radical functionalization efficiency of reactor samples from the PPRs column 3, synthesized in benzene at 130°C using two levels of initiator and three nitroxide types: BPO/TEMPO (A3 and B3), BPO/OHTEMPO (C3 and D3) and PR CGX 505 (E3 and F3).
- 5.4. N and O averages relative concentrations of as-produced (**1**), radical functionalized (**3**) and polymer-grafted carbon nanotubes (**4**) corresponding to F3 sample and measured by EELS at high energy losses.
- 5.5. Parameters of Raman spectra of CN<sub>x</sub> nanotubes and radical functionalized products using BPO/TEMPO (A3) and BPO/PR CGX505 (F3) radicals.
- 5.6. EPR sample preparation of sonicated-CN<sub>x</sub> nanotubes in benzene reacted with BPO and TEMPO. The experiment considered dispersions of 10 mg of nanotubes in 15 ml of solvent and 1 ml of initiator/controller radical solution.
- 5.7. EPR sample preparation of sonicated-MWNT and sonicated-CN<sub>x</sub> nanotubes in xylene reacted with BPO and PR CGX505. The experiment considered dispersions of 1mg of nanotubes in 1 ml and 0.25 ml of initiator/controller radical solution.

- 5.8. EPR spectra parameters of  $CN_x$  nanotubes samples and BPO/TEMPO solutions reacted in benzene at several temperatures.
- 5.9. EPR spectra parameters of MWNT and  $CN_x$  nanotube samples and BPO/PR CGX505 solutions reacted in xylene at several temperatures.
- 5.10. Parameters of Raman spectra of  $CN_x$  nanotubes and polystyrene-grafted  $CN_x$  nanotubes.

#### *Chapter 6*

- 6.1. Characteristics of PS-based nanocomposites at several observational scales.
- 6.2. Thermal properties of PEO-based nanocomposites.
- 6.3. Characteristics of PEO-based nanocomposites at several observational scales.
- 6.4. Thermal properties of the PS-PEO blend nanocomposites with MWNT,  $CN_x$  and PS-g- $CN_x$  carbon nanotubes.

#### *Chapter 7*

- 7.1. Conductivity values of sonicated CNTs and PS/CNTs composites filled at 5 wt% of filler with and without additional pressure on the films at 1 Hz.
- 7.2. Experimental conductivity values measured for PS/CNTs composites compared with calculated values by the simple mixing law.
- 7.3. Conductivity exponent  $t$  and the percolation threshold  $p_c$  of PS/CNT composites using the statistical percolation model.
- 7.4. Literature reports of conductivity in composites modeling by percolation theory.
- 7.5. Mechanical properties of PS/CNTs composites at several concentrations of MWNT,  $CN_x$  and PS-g- $CN_x$  fillers.
- 7.6. Storage modulus of PS/CNTs composites at 60°C and several filler and nanotube content from 0 to 5.0 wt%.
- 7.7. Maximum conductivity values at 1 Hz and cristallinity for PEO210k/CNTs at 2 wt%.
- 7.8. Experimental conductivity values and statistical percolation parameters for PEO14k/CNT composites.
- 7.9. Mechanical properties of PEO/CNTs composites at several concentrations of MWNT,  $CN_x$  and PS-g- $CN_x$  fillers.

# Introduction

Nanoscience and nanotechnology are new trend of phenomena involving the manipulation, design, fabrication and engineering of nanostructured materials. Nanostructured materials are broadly defined as materials of zero to three dimensions, with at least one dimension in the nanometer range (1-100 nm). Nanomaterials could be metals, ceramic, polymers and biomolecules synthesized by different methods. These kinds of materials exhibit interesting properties involving multidisciplinary field due to their size and the assembly of the components. Particularly, this thesis is concerned to the study of carbon nanotubes, as nanostructured materials, in the fabrication of polymer composites.

A composite is a system consisting of two or more components, which properties complement each other to produce a single hybrid material. The composites are formed by a matrix and filler. The matrix is the major component in the composite and is usually a metal, ceramic or polymer. The filler can be any metal, organic or inorganic material ranging from macroscopic to nanoscales entities. In the recent years, nanocomposites or composites containing nanostructured fillers have generated a lot of interest [1-3]. Some of the basic reasons are that they often display superior properties to macro-sized filler counterparts, and they enable the realization of desired properties at lower loadings due to their high surface area [4].

Nanofillers are considered high as interesting filler materials to conventional polymers and polymer blend materials. The main idea in this nanocomposite materials deals with the improvement of polymer physical properties and processing behavior at same time. The polymer-nanofiller composite properties are induced by the physical presence of the nanofillers, their dispersion and the interaction of the polymer with the particle [3, 5, 6]. Some advantages of nano-scaled fillers are their high surface area, which can act as interface for stress-transfer, and their high aspect ratio, which affect the percolation threshold. Several types of nanofillers are being used, including fillers based on carbon, as carbon black [7-9], fullerenes [10-12], nanotubes [3].

Carbon nanotubes (CNTs) consist in graphene sheets rolled up into cylinders with half-fullerene caps at each end. Because of the carbon nanotubes size, assembly and composition (carbon-carbon covalent bonds), they could be considered as one of the strongest material in the nature with amazing properties [13]. The discovery of CNTs in 1991 [14], and their controlled production since 1993 [15], led to increasing investigations

into applications in almost all fields of science [16, 17]. Particularly, the synthesis of modified carbon nanotubes using nitrogen to create doped carbon nanotubes ( $CN_x$ ), that exhibit an intrinsic surface reactivity, and attractive electronic properties [18-21], favors an increment in the CNT engineering applications.

Carbon nanotubes (diameter of 2-80 nm and length of 10  $\mu\text{m}$ ) [1, 3, 22-24] and nanofibers (diameter of 70-200 nm and length of 50-100  $\mu\text{m}$ ) [3, 25, 26] with their high aspect ratio and specific surface area [27], high Young modulus [28], tensile strength, electrical conductivity and thermal conductivity [2, 13] are ideal fillers for composite systems for the development of advanced multifunctional materials. In fact, as-produced single-walled (SWNTs) and multi-walled carbon nanotubes (MWNTs) have been successfully using as fillers in polymer nanocomposites [29] using matrices such as epoxy [30-32], poly(methyl methacrylate) [33], polycarbonate [34], polypropylene, polyethylene [35, 36], several polymer blends [37], among others. A variety of property enhancement, including mechanical, electrical, optical, and thermal properties, have been achieved by incorporating nanotubes into suitable polymer matrices.

In all nanocomposite cases, an efficient exploitation of the carbon nanotube properties in order to improve the materials performance is generally related to the degree of dispersion, the interaction of nanotubes with the host polymer (interfacial adhesion and interfacial strength) [35, 38] and the alignment and orientation of the nanotubes in the polymer matrix. Processing is a challenge because of the arrangement of as-produced crystalline nanotube in ropes due to strong inter-tubular van der Waals attractions, the poor solubility of nanotubes in most solvents, and the weak matrix-nanotube interaction. Thus, exfoliation of nanotube bundles into individual tubes is necessary for taking advantage of their aspect ratios. In addition, the interface between the nanotubes and the polymer has to be engineered in order to maximize load transfer.

The chemical functionalization of carbon nanotubes with suitable groups was proposed to enhance the solubility, to induce a better dispersion, and the strength of the bonding between the nanotubes and the polymer matrix [12, 39]. Even more, functionalizing nanotubes with a compatible polymer with the matrix [3] ideally provides the best possible interface with the host polymer. Among several routes to covalently graft polymer chains on the nanotube surface, the ones that use the carbon nanotube scavenging properties begin to be used because their potential applications. Therefore, radical controlled polymerization techniques as nitroxide-mediated radical polymerization could be useful in the *in situ* synthesis of polymer chains because of the possibility to control the molecular weight, molecular weight distribution and composition.

In summary, a mechanical reinforcement, and electrical and thermal properties enhanced of polymers by carbon nanotubes can only be performed by the optimization of processing variables to allow better filler dispersion and nanotube-polymer interactions.

This study aims to contribute towards understanding and overcoming some of the challenges involved in the synthesis of PS-grafted  $CN_x$  nanotubes by *in situ* radical polymerization using nitroxides, and the fabrication of nanocomposites with PS, PEO or a PS-PEO blend as matrices, and  $CN_x$  or PS-grafted  $CN_x$  nanotubes as fillers, to aid designing multifunctional materials. Thus, this thesis presents the work performed on the development of a technique that enables the grafting of polymer chains onto carbon nanotube surfaces using a nitroxide mediated polymerization approach without affecting

the original nanotube structure. These polymer brushes could be prepared by the covalent attachment of styrene monomer to radically initiated and *in situ* growing PS chains on nanotube functionalized surface.

Furthermore, the thesis described the effort to develop synthetic protocols for creating composites of polymer matrices and PS-grafted  $CN_x$  nanotubes with good interfacial properties and dispersion, while retaining the structural integrity (including the aspect ratio) of the carbon nanotubes. Also of interest was to study the thermal, electrical and mechanical properties of such composite systems with the aim of delineating the effects of nitrogen doping, functionalization and polymer-grafting of carbon nanotubes used as rein forcers; and also the effects of the polymer matrices.

All these ideas allowed determining the following main objectives of the research project:

- (i) Grafting of PS on the surface of nitrogen-doped carbon nanotubes ( $CN_x$ ) by nitroxide mediated radical polymerization.
- (ii) Preparation of nanocomposites of PS, PEO and PS-PEO polymer blends and several kinds of nanotubes as fillers by the solution method. Among the fillers, multiwalled carbon nanotubes (MWNTs), nitrogen-doped carbon nanotubes ( $CN_x$ ) and polymer-grafted nitrogen-doped carbon nanotubes (PS-g- $CN_x$ ) were considered.
- (iii) Evaluation of the morphology of the prepared polymer-nanotube composites, as well as the dispersion and interfacial behavior.
- (iv) Determination of the thermal, electrical and mechanical properties of the prepared polymer-nanotube composites.

Therefore, the thesis is organized as follows. Chapter 1 presents in detail an introduction to the structure, synthesis and physical properties of raw and nitrogen-doped carbon nanotubes. In Chapter 2, the main techniques for nanotube surface modification, in particular radical functionalization methodologies, as well as polymer-grafting will be reviewed. Chapter 3 presents the fundamentals in the field of nanocomposites, especially related to the polymer-nanotube composites. These background chapters were written as reviews from the corresponding field. The synthesis protocol for nanotube chemical modification by radical functionalization and polymer-grafting methods, as well as polymer-nanotube composites preparation will be explained in Chapter 4. In addition, the various characterization techniques employed in this thesis will be also outlined and explained in the same Chapter. In the following chapters the obtained experimental results and their analysis will be described as follows. The carbon nanotube functionalization and polymer-grafting results will be presented in Chapter 5. The experimental results of the synthesis of nanocomposite preparation will be shown in Chapter 6 along with the results concerning the dispersion and thermal properties of the composites. Chapter 7 deals with the characterization of nanocomposites by their electrical and mechanical properties. Finally, the last chapter is devoted to conclusions and perspectives. Some other points are present in detail in Annexes.

## References

1. Breuer, O. and U. Sundararaj, *Big returns from small fibers: a review of polymer/carbon nanotube composites*. Polymer composites, 2004. **25**(6): p. 630-645.
2. Harris, P.J.F., *Carbon nanotubes and related structures New materials for the twenty-first century*. 2001, Cambridge: Cambridge University Press. 279.
3. Thostenson, E.T., *Nanocomposites in context*. Composites Science and Technology, 2005. **65**: p. 491-516.
4. Viswanathan, G., *Polymer grafted single-walled carbon nanotube composites*. 2004, Rensselaer Polytechnic Institute: Troy, NY, USA. p. 163.
5. Fischer, H., *Polymer nanocomposites: from fundamental research to specific applications*. Materials Science and Engineering, 2003. **C23**: p. 763-772.
6. Schmidt, G. and M.M. Malwitz, *Properties of polymer-nanoparticle composites*. Current Opinion in Colloid and Interface Science, 2003. **8**: p. 103-108.
7. Donnet, J.B., *Structure and reactivity of carbons: from carbon black to carbon composites*. Carbon, 1982. **20**: p. 267-282.
8. Hayashi, S., A. Naitoh, S. Machida, M. Okazaki, K. Maruyama, and N. Tsubokawa, *Grafting of polymers onto a carbon black surface by the trapping of polymer radicals*. Applied Organometallic Chemistry, 1998. **12**: p. 743-748.
9. Del Rio, C., M.C. Ojeda, and J.L. Acosta, *Carbon black effect on the microstructure of incompatible polymer blends*. European Polymer Journal, 2000. **36**: p. 1687-1695.
10. Chen, X.L. and S.A. Jenekhe, *Solubilization and Encapsulation of Fullerenes by Amphiphilic Block Copolymers*. Langmuir, 1999. **15**: p. 8007-8017.
11. Wang, C., Z.-X. Guo, S. Fu, W. Wu, and D. Zhu, *Polymers containing fullerene or carbon nanotube structures*. Progress in Polymer Science, 2004. **29**: p. 1079-1141.
12. Goh, H.W., S.H. Goh, G.Q. Xu, K.P. Pramoda, and W.D. Zhang, *Crystallization and dynamic mechanical behavior of double-C<sub>60</sub>-end-capped poly(ethylene oxide)/multi-walled carbon nanotube composites*. Chemical Physics Letters, 2003. **379**: p. 236-241.
13. Terrones, M., *Science and technology of the twenty-first century: synthesis, properties and applications of carbon nanotubes*. Annual Reviews Materials Research, 2003. **33**: p. 419-501.
14. Iijima, S., *Helical microtubules of graphitic carbon*. Nature, 1991. **354**: p. 56.
15. Iijima, S. and T. Ichihashi, *Single-shell carbon nanotubes of 1 nm diameter*. Nature, 1993. **363**: p. 603.
16. Terrones, M., *Science and Technology of the twenty-first century: synthesis, properties, and applications of carbon nanotubes*. Annual Reviews Materials Research, 2003. **33**: p. 419-501.
17. Ajayan, P.M., *Nanotubes from carbon*. Chemical Reviews, 1999. **99**(7): p. 1787-1799.
18. Terrones, M., *Advances on the growth and properties of N- and B-doped carbon nanotubes*. AIP Conference proceedings (Electronic Properties of Molecular Nanostructures), 2001. **591**: p. 212-216.
19. Czerw, R., M. Terrones, and J.C. Charlier, *Identification of electron donor states in N-doped carbon nanotubes*. Nanoletters, 2001. **1**(9): p. 457-460.
20. Terrones, M., P.M. Ajayan, F. Banhart, X. Blase, D.L. Carroll, J.C. Charlier, R. Czerw, B. Foley, N. Grobert, R. Kamalakaran, P. Kohler-Redlich, M. Rühle, T. Seeger, and H. Terrones, *N-doping and coalescence of carbon nanotubes: synthesis and electronic properties*. Applied Physics A, 2002. **74**: p. 355-361.
21. Ajayan, P.M. and L.S. Schadler, *Carbon nanotube filled polymer nanocomposites*. Polymer Preprints, 2001. **42**(2): p. 35.

22. Thostenson, E.T., Z. Ren, and T.-W. Chou, *Advances in the science and technology of carbon nanotubes and their composites: a review*. Composites Science and Technology, 2001. **61**: p. 1899–1912.
23. Xie, X.-L., Y.-W. Mai, and X.-P. Zhou, *Dispersion and alignment of carbon nanotubes in polymer matrix: A review*. Materials Science and Engineering, 2005. **R49**: p. 89-112.
24. Tasis, D., N. Tagmatarchis, A. Bianco, and M. Prato, *Chemistry of Carbon Nanotubes*. Chemical Reviews, 2006. **106**(3): p. 1105-1136.
25. Tsubokawa, N., *Preparation and properties of polymer-grafted carbon nanotubes and nanofibers*. Polymer Journal, 2005. **37**(9): p. 637-655.
26. Wu, G., S. Asai, and M. Sumita, *Entropy Penalty-Induced Self-Assembly in Carbon Black or Carbon Fiber Filled Polymer Blends*. Macromolecules, 2002. **35**: p. 945-951.
27. Gojny, F.H., M.H.G. Wichmann, B. Fiedler, W. Bauhofer, and K. Schulte, *Influence of nano-modification on the mechanical and electrical properties of conventional fibre-reinforced composites*. Composites: Part A, 2005. **36**(11): p. 1525-1535.
28. Poncharal, P., Z.L. Wang, D. Ugarte, and W.A. de Heer, *Electrostatic deflections and electromechanical resonances of carbon nanotubes*. Science, 1999. **283**: p. 1513-1516.
29. Zhou, C. and S. Kumar. *Study of interaction between various carbon nanotubes and polymer matrices*. in *Abstracts of Papers, 231st ACS National Meeting*. 2006. Atlanta, GA, United States: American Chemical Society.
30. Song, Y.S. and J.R. Youn, *Influence of dispersion states of carbon nanotubes on physical properties of epoxy nanocomposites*. Carbon, 2005. **43**: p. 1378-1385.
31. Allaoui, A., S. Bai, H.M. Cheng, and J.B. Bai, *Mechanical and electrical properties of a MWNT/epoxy composite*. Composites Science and Technology, 2002. **62**: p. 1993-1998.
32. Wong, M., M. Paramsothy, X.J. Xu, Y. Ren, S. Li, and K. Liao, *Physical interactions at carbon nanotube-polymer interface*. Polymer, 2003. **44**: p. 7757-7764.
33. Yao, Z., N. Braidy, G.A. Botton, and A. Adronov, *Polymerization from the Surface of Single-Walled Carbon Nanotubes - Preparation and Characterization of Nanocomposites*. Journal of American Chemical Society, 2003. **125**: p. 16015-16024.
34. Chen, L., X.-J. Pang, M.-Z. Qu, Q.-T. Zhang, B. Wang, B.-L. Zhang, and Z.-L. Yu, *Fabrication and characterization of polycarbonate/carbon nanotubes composites*. Composites Part A, 2005. **37**(9): p. 1485-1489.
35. McNally, T., P. Potschke, P. Halley, M. Murphy, D. Martin, S.E.J. Bell, G.P. Brennan, D. Bein, P. Lemoine, and J.P. Quinn, *Polyethylene multiwalled carbon nanotube composites*. Polymer, 2005. **46**: p. 8222-8232.
36. Tong, X., C. Liu, H.-M. Cheng, H. Zhao, F. Yang, and X. Zhang, *Surface Modification of Single-Walled Carbon Nanotubes with Polyethylene via In Situ Ziegler–Natta Polymerization*. Journal of Applied Polymer Science, 2004. **92**: p. 3697–3700.
37. Doleman, B.J., R.D. Sanner, E.J. Severin, R.H. Grubbs, and N.S. Lewis, *Use of Compatible Polymer Blends To Fabricate Arrays of Carbon Black-Polymer Composite Vapor Detectors*. Analytical Chemistry, 1998. **70**: p. 2560-2564.
38. Wagner, H.D., *Nanotube-polymer adhesion: a mechanics approach*. Chemical Physics Letters, 2002. **361**: p. 57-61.
39. Niyogi, S., M.A. Hamon, H. Hu, B. Zhao, P. Bhowmik, R. Sen, M.E. Itkis, and R.C. Haddon, *Chemistry of single-walled carbon nanotubes*. Accounts of Chemical Research, 2002. **35**: p. 1105-1113.

# Chapter 1.

## Carbon nanotubes: an overview

The chapter reviews some research advances in carbon nanotube science since the early 90's. It is noticeable that an increasing experimental and theoretical work has been developed due to the fascinating structure and properties of carbon nanotubes (CNTs). The materials could be used in the fabrication of nanoelectronic devices, flat panel displays, gas storage devices, toxic gas sensors, Lithium ion batteries, robust and lightweight composites, and conducting paintings.

This chapter deals with the structural identification of carbon nanotubes and synthetic methods for producing them. This work also reviews the production of nitrogen-doped carbon nanotubes (CN<sub>x</sub>) and their physico-chemical properties. Finally, it will be discussed the possible applications of these novel doped nanostructures.

### 1.1. Introduction

Carbon is a nonmetallic and tetravalent element. Carbon has a ground-state configuration of  $1s^2 2s^2 2p^2$ . The carbon atom could exhibit various configurations of the electronic states (hybridization of atomic orbitals). Three possible orbital hybridizations could occur:  $sp$ ,  $sp^2$  and  $sp^3$ . In general, for  $sp^n$  hybridization,  $n+1$  electron belong to the carbon atom occupied in the hybridized  $\sigma$  orbital, and  $4-(n+1)$  electrons are in  $\pi$  orbital. The  $sp^n$  hybridization is essential for determining the dimensionality of the carbon-based materials. Thus, carbon is the only element in the periodic table that could possess different isomers ranging from 0-dimension (0D) to 3 dimensions (3D) [1]. These carbon isomers determine different allotropic forms: diamond, graphite, amorphous carbon, and the newly discovered fullerenes and CNTs.

### 1.1.1. Carbon-based materials

Among the carbon allotropes (illustrated in Fig. 1.1), diamond and graphite are two natural crystalline forms. In diamond, each carbon atom is bonded to four carbon atoms forming a tetrahedral structure with a C-C bond length of  $1.56\text{\AA}$ . Diamond exhibits  $sp^3$  hybridization and tends to form robust three dimensional networks (Fig. 1.1 (a)).

In graphite, each carbon atom is bonded trigonally to other carbon atoms in the  $xy$  plane with an angle of  $120^\circ$ , and exhibits weak  $\pi$  bonding in the  $z$  axis. Therefore graphite possesses a  $sp^2$  hybridization, in which the C-C  $sp^2$  bond length is  $1.42\text{\AA}$ , and forms hexagonal lattices (honeycomb), as depicted in Fig. 1.1 (b). These graphene planes are weakly bonded by van der Waals forces and are spaced by  $3.35\text{\AA}$ . The free electrons in the  $p_z$  orbital are delocalized and are responsible for the electron transport in graphite; contrarily to diamond which behaves as an insulator because all its electrons are localized within bonds [2].

Other carbon allotropes include amorphous carbon, carbynes, and carbon fibers. Amorphous carbon could be defined as an arrangement of carbon molecules in non-crystalline and irregular bonds. Amorphous carbon is considered as a three dimensional material in which  $sp^2$  and  $sp^3$  hybridization are randomly present. Carbynes are linear chains of carbon which have  $sp$  bonding arranged in different orientations with respect to the fiber axis. Carbon fibers are macroscopic one-dimensional materials. They consist of many graphitic planes and microscopically exhibit electronic properties that are predominantly two-dimensional.

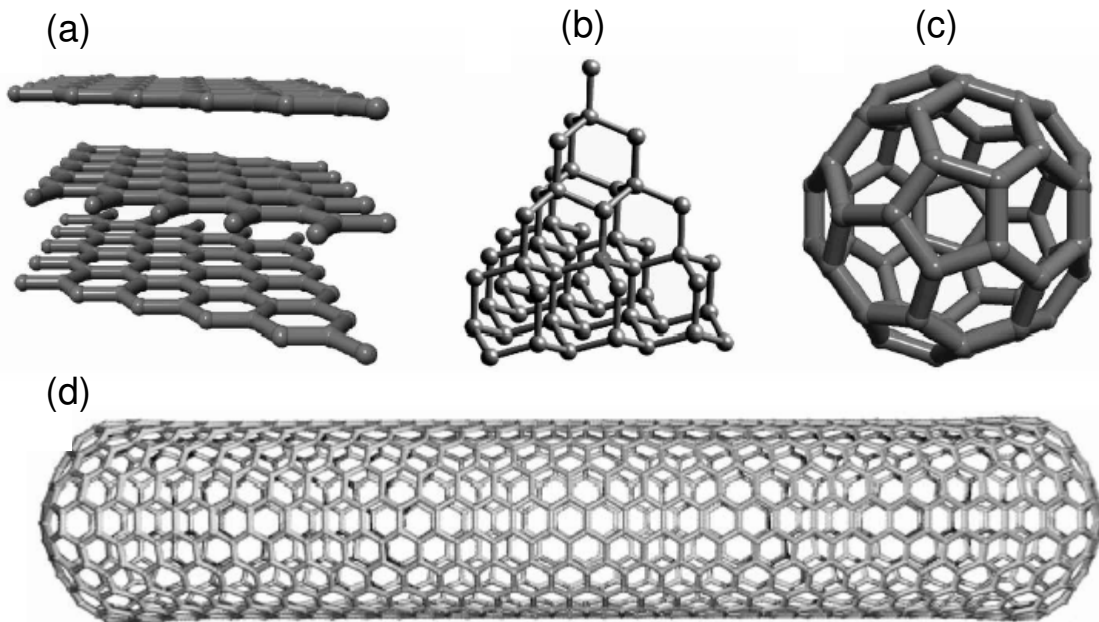


Fig. 1.1. Structure of crystalline carbon-based materials: (a) graphite, (b) diamond, (c) fullerene, and (d) SWNTs. (Molecular modeling images) [3].

New forms of pure carbon, carbon nanotubes [4] and fullerenes [5], have recently emerged. Fullerenes are large and hollow molecules formed by carbon atoms bonded trigonally, see Fig. 1.1 (c) and (d). Carbon nanotubes (CNTs) can be viewed as graphene sheets wrapped up into cylinders that are capped by the presence of pentagonal carbon rings. Due to their high aspect-ratio (similar to that of carbon fibers), they can be considered as one-dimensional nanostructures (Fig. 1.1 (d)).

Graphite, fullerenes and carbon nanotubes are also known as  $\pi$ -electron materials, which are defined as those displaying extended  $\pi$ -electron clouds in the solid state. Consequently, these materials could show unusual properties derived from their structure, such as high electron mobility as well as chemical/biological activities.

The structures of several carbon-based materials are summarized in Fig. 1.1 and Table 1.1 describes their physico-chemical characteristics. CNTs will be the topic of the entire chapter.

Table 1.1. Physico-chemical characteristics of carbon-based materials [1].

<b>Dimension</b>	<b>0-D</b>	<b>1-D</b>	<b>2-D</b>	<b>3-D</b>
Isomer	C <sub>60</sub> fullerenes	nanotubes carbyne chains	graphite fibers	diamond amorphous carbon
Hybridization	sp <sup>2</sup> -like	sp <sup>2</sup> (sp)	sp <sup>2</sup>	sp <sup>3</sup>
Density [g/cm <sup>3</sup> ]	1.72	1.2-2.0 2.68-3.13	2.26 ~2	3.515 2-3
Bond length [Å]	1.40 (C=C) 1.46 (C-C)	1.44 (C=C)*	1.42 (C=C) 1.44 (C=C)	1.54 (C-C)
Electronic properties	semiconductor E <sub>g</sub> = 1.9eV	metal or semiconductor	semimetal	insulating E <sub>g</sub> = 5.47 eV

\* Carbyne should have alternating triple, double and single bonds.

### 1.1.2. Discovery of fullerenes and carbon nanotubes

Carbon structures research was triggered many years ago with the study of carbon fibers, diamond and graphite. Nevertheless, the new era of carbon science began when fullerenes and CNTs were discovered and identified. In the following paragraphs, a brief chronological description of their discovery will be presented. Additional information related to the chronological progress in carbon allotropes is summarized in Appendix 1.1.

Fullerenes (C<sub>60</sub>, Fig. 1.1 (c)) were discovered using mass spectrometry by Harold Kroto, Richard Smalley and Robert Curl in 1985 [5] when they were performing experiments of graphite vaporization. Years later, in 1992 the same team reported [6] the first isolation of C<sub>60</sub> and C<sub>70</sub> using chromatography. Subsequent experimental work related to the synthesis of fullerenes lead to the structural identification of CNTs [4].

Carbon nanotubes can be considered as elongated fullerenes (Fig. 1.1 (d)). There exist several types of CNTs depending on the number of graphitic walls that conforms them: single-walled (SWNTs), double-walled (DWNTs) and multi-walled (MWNTs).

Morinobu Endo in the mid-1970s [7] probably obtained the first clear images of SWNTs and MWNTs produced by pyrolysis, using Transmission Electron Microscopy (TEM). Sumio Iijima in 1991 [4] reported the existence of MWNTs prepared by arc-discharge methods. The High Resolution TEM images of nanotubes consisted of graphene tubules that exhibit different helicities and chiralities. Soon after, Thomas Ebbesen and Pulickel Ajayan synthesized MWNTs in bulk quantities using arc-discharge techniques [8].

The first report related to the synthesis of SWNTs appeared in 1993 by Iijima and Ichihashi [9]. The authors used the arc-electric method in the presence of metal catalysts. Additional arc experiments using Fe-Co-Ni graphite mixtures in a He atmosphere were carried out by Bethune *et al* [10].

Saito, Dresselhaus *et al* [1], among others, predicted the theoretical properties of SWNTs and the possibility of producing DWNTs. Experimentally, DWNTs have recently been synthesized by several research teams using arc-discharge technique and Chemical Vapor Deposition [11-13].

At present, various scientific groups are studying fullerene and carbon nanotube structure and their physico-chemical properties. In particular, the thesis research will focus on the use of doped-MWNTs as fillers in the fabrication of polymer composites. A novel grafting route will be presented and the mechanical and electronic properties of these materials will be explained in detail.

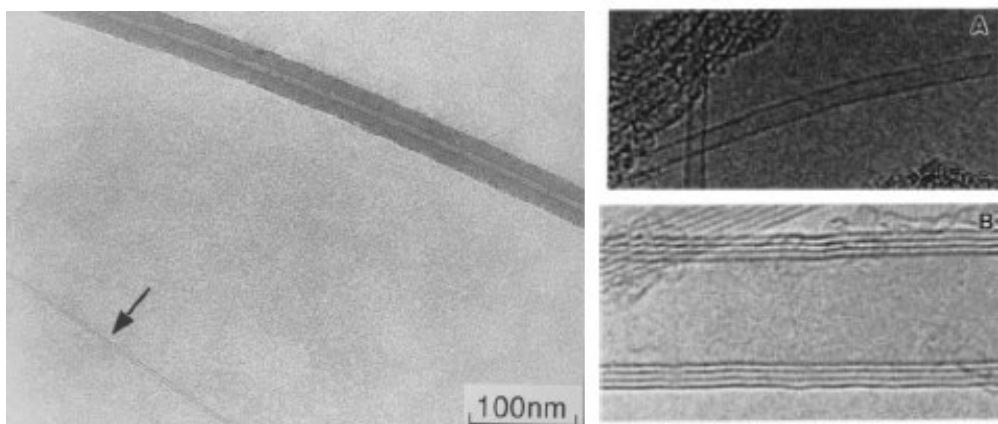


Fig. 1.2. High resolution TEM Images of CNTs: left general view, right: (A) SWNTs and (B) MWNTs. Edited from references [14] and [15].

## 1.2. Structure of carbon nanotubes

### 1.2.1. The single-walled carbon nanotube structure

This section is devoted to the importance of single-walled carbon nanotube chirality and nanotube capping. In addition, some useful mathematical definitions will be presented.

### Nanotube chirality

As explained earlier, SWNTs can be described as a rolled graphene sheet into a cylindrical shape. The nanotube chirality is characterized by the orientation of the six-membered carbon rings in the honeycomb lattice. This concept provides many possible nanotube structures: achiral (symmorphic) or chiral (non-symmorphic) carbon nanotubes. There are only two cases of achiral nanotubes: armchair and zigzag. These conformations are defined by the shape of the tube cross-section (Fig. 1.3 (a) and (b)). In addition, chiral nanotubes exhibit spiral symmetry and then the honeycomb is not parallel to the nanotube axis, Fig. 1.3 (c) [16].

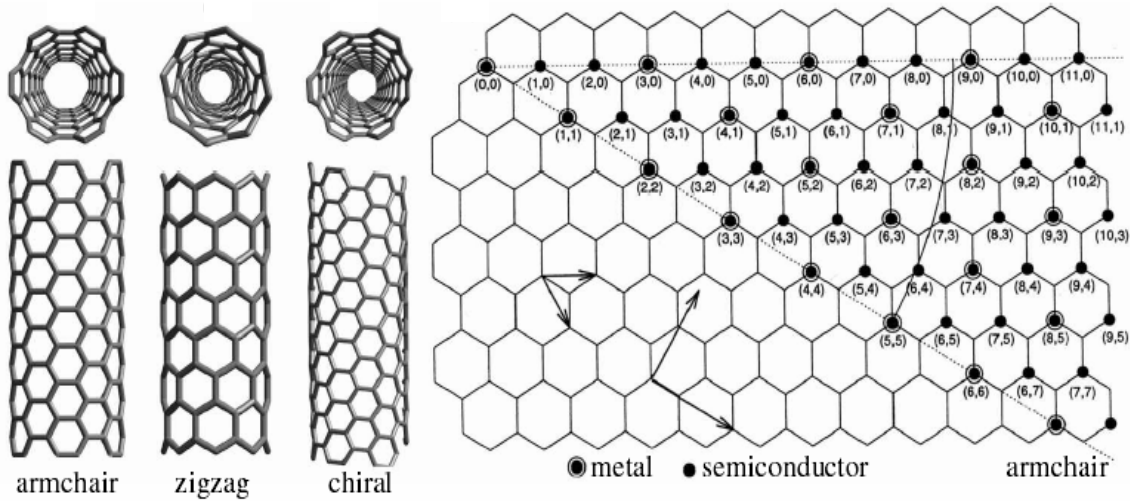


Fig. 1.3. Molecular models of SWNTs exhibiting different achiral and chiral conformations: (a) armchair, (b) zigzag and (c) chiral; (d) graphene sheet mathematic description, using chiral vector ( $C_h$ ) with indexes ( $m,n$ ) and unitary vectors ( $\mathbf{a}_1$  and  $\mathbf{a}_2$ ).

(d) shows the mathematic description of a graphene sheet, introducing some definitions: carbon nanotube chiral vector, chiral angle and diameter [3].

The diameter of any SWNT can be expressed as  $d_t = L/\pi$ , with  $L$  the circumferential length, defined by  $L = |C_h| = \sqrt{C_h \cdot C_h}$ . In addition,  $C_h = n\mathbf{a}_1 + m\mathbf{a}_2$  (chiral vector) corresponds to a section perpendicular to the nanotube axis with  $\mathbf{a}_1$  and  $\mathbf{a}_2$  are not orthogonal unitary vectors and ( $n,m$ ) are lattice points. The chiral vector determines the rolling direction and diameter. Therefore,  $d = \frac{|C_h|}{\pi} = \frac{a\sqrt{n^2 + m^2 + nm}}{\pi}$ , where

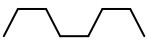
$a = 1.42 \times \sqrt{3} \text{ \AA}$  that corresponds to the lattice constant of a graphene sheet and to C-C distance for  $sp^2$  hybridized carbon. The chiral angle is defined as the angle between vectors

$C_h$  and  $\mathbf{a}_1$ , thus  $\theta = \arctan\left[-\frac{\sqrt{3}n}{2m+n}\right]$ , with  $0 \leq |\theta| \leq 30^\circ$ , and denotes the tilt angle

between the hexagons and the nanotube axis. Chiral angle determines the spiral symmetry.

In Table 1.2, the SWNT structural parameters are presented schematically. These values provide information related to their SWNT electronic properties. Armchair nanotubes are metallic, as well as zigzag cylinders when  $\frac{(2m+n)}{3} = \text{integer}$ . All other nanotube conformations exhibit a semiconductor behavior. Thus, it is possible to have metallic or semiconducting CNTs by varying the (n,m) value.

Table 1.2. Single-walled carbon nanotube structural parameters: chiral angle, chiral vector and the shape of the cross-section for arm-chair, zigzag and chiral conformations [1].

Type	$\theta$	$C_h$	Shape cross-section
Arm-chair	$30^\circ$	(n,n)	
Zig-zag	$0^\circ$	(n,0)	
Chiral	$0^\circ <  \theta  < 30^\circ$	(n,m)	combination

### 1.2.2. Multi-walled carbon nanotube structures and dimensions

In general, as-produced CNTs, i.e. SWNTs, DWNTs and MWNTs, preferentially aggregate into bundles or ropes. The characteristics (dimensions, organization, shape and quantity of individual nanotubes) of the bundles strongly depend on the nanotube fabrication method.

Individual DWNTs and MWNTs consist of two and several (3 to 30 approx.) concentric graphene cylinders, respectively. Thus, in these nanotubes, the arrangement and structural relationship between successive cylinders becomes important. There are two general theories explaining the layered structure in DWNTs and MWNTs: concentric (Russian doll) and scroll-like walls arrangement (see Fig. 1.4). The model of concentric layers is mostly retained as it provides more favorable arguments to explain the multi-walled carbon structures. In fact, the equal number of fringes on either side of the nanotube central cavity, the presence of internal caps or closed compartments, and also the behavior at opening and filling carbon structure (the nanotubes preferentially react in the caps) are some of experimental pieces of evidence of the concentric model.

Regarding nanotube dimension, SWNTs usually exhibit average diameters of ca. 0.7-3 nm, MWNTs (Fig. 1.2) display average outer diameters from 2.5 to 60 nm. In both cases, CNTs length can vary from a few tens of nanometers to several micrometers. For MWNTs, the interlayer spacing was determined as 3.4Å, and it was also observed that the concentric tubes exhibited different chiralities.

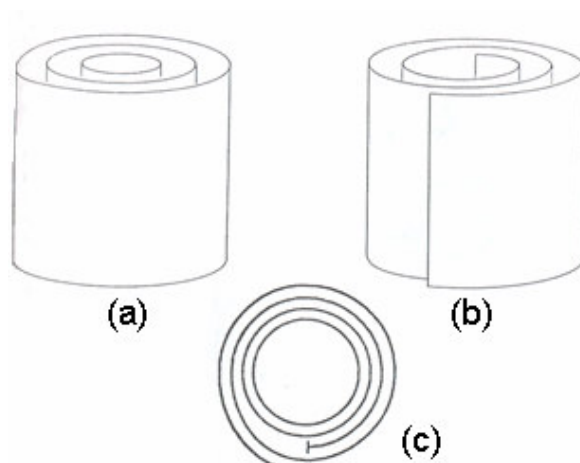


Fig. 1.4. Schematic representation of a) “Russian doll” and b) “Scroll-like” models for MWNTs [17]. A mixed configuration is also represented (c).

### 1.3. Methods for producing carbon nanotubes

MWNTs were first synthesized as a by-product when using the arc-discharge method during the synthesis of fullerenes. At present, they are prepared by numerous methods including arc-discharge, laser vaporization of graphite targets, catalytic decomposition of hydrocarbons, electrolysis of carbon electrodes in molten ionic salts and solar carbon vaporization, ball milling, among others [1, 2, 16]. In almost all cases, CNTs synthesis methods mainly involve gas phase processes, except in the electrolysis technique.

It is worth mentioning that the production method determines the carbon nanotube structural surface, sample homogeneity, purity, yield and cost. In particular, the surface structure and defective sites on MWNTs are determinant in their physico-chemical properties (further discussed in chapter 3).

#### 1.3.1. Electric arc-discharge

This technique is similar to the one used in the fullerene production by Krätschmer & Huffman [6]. In electric arc-discharge technique, a DC voltage is applied to two high purity graphite electrodes to generate a current between them by varying their separation distance. The high electrode temperatures (2500-3000°C) and the voltage lead to the formation of a plasma so that carbon atoms from the anode are deposited on the cathode in the form of CNTs. The process is always carried out in an inert gas atmosphere. In Fig. 1.5, a typical scheme of the technique is shown. The main parameters to control the nanotube production are the distance between electrodes, the gas pressure, and the electrical current density. Also, it was observed that the arc discharge stability and the electrode cooling are effective to increase the product quantity.

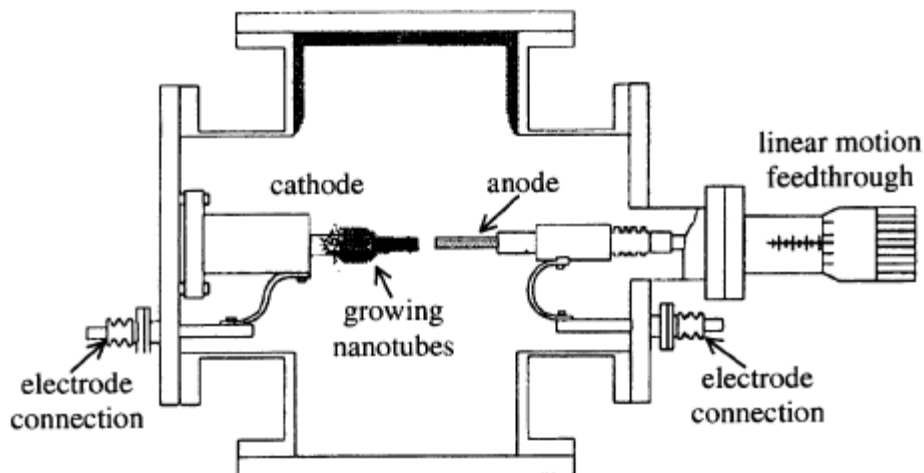


Fig. 1.5. Schematic representation of an electric-arc-discharge apparatus used to produce fullerenes and carbon nanotubes [18].

The electric-arc discharge can be used to synthesize either MWNTs or ropes of SWNTs. However, SWNTs can only be synthesized by the co-evaporation of carbon and a metal catalyst, i.e. Fe-graphite, Ni-graphite, Co-graphite and others. It should be noted that MWNTs are synthesized using the carbon anode without catalyst. The general mechanism for the CNTs formation from a chaotic carbon plasma still remains a great challenge. Nevertheless, some theories have been postulated and are reviewed in Appendix 1.2.

The arc-discharge method is able to produce highly crystalline SWNTs and MWNTs; nevertheless, in a typical sample, the CNTs could be accompanied by a large number of foreign particles, including nanoparticles (hollow and fullerene-related structures), encapsulated metal particles and some disordered carbon. Consequently, a purification process becomes necessary. Additionally, arc-discharge does not favor the control of the tubes dimensions because of the violent reaction involved.

### 1.3.2. Laser vaporization

The process involves firing a high power laser (YAG type) towards a graphite target inside a furnace at 1200°C in the presence of argon [3]. A typical device is presented in Fig. 1.6.

Laser ablation could be used to produce fullerenes, single-walled carbon nanotubes and multi-walled carbon nanotubes. SWNTs can be obtained using a graphite catalysts mixture as target. In the case of MWNTs, the length of the tubes is much shorter than that of those produced by the arc-discharge method. In general, the CNTs obtained by this method are almost free of nanoparticles and amorphous carbon. Laser power and target porosity play a role in the CNTs generation.

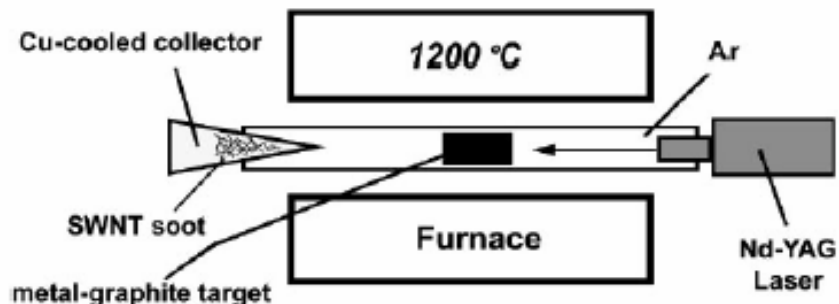


Fig. 1.6. Representation of the laser vaporization method to produce SWNTs and MWNTs. In this particular case the process is carried out in a furnace and the nanotubes are collected in a Cu-cooled trap [2].

### 1.3.3. Catalytic decomposition of hydrocarbons

This technique is also known as carbon vapor deposition (CVD) or pyrolysis. It consists of heating (650-1000°C) hydrocarbons or carbon organic precursors (e.g. methane, benzene, acetylene, ethylene, etc.) in the presence of metal catalysts (transition metals, rare earths and combinations of them), deposited on silicon, alumina, graphite, or silica substrates under gas flow. A schematic representation of the technique is shown in Fig. 1.7.

Using the CVD technique, it is possible to produce fullerenes, SWNTs, DWNTs, and MWNTs. In fact, this method is suitable for mass production because it is a continuous method with high yields. In addition, the morphology, shape, length, diameter and alignment of tubes could be controlled by changing the experimental conditions, such as the type of hydrocarbons, the metal catalysts, the catalyst particle size, the carrier gases, and the temperature. Moreover, the organization and shape of the nanotubes in ropes can be controlled. Three main growth mechanisms are proposed for the production of CNTs by pyrolysis; all of them can be extended to explain the SWNTs and MWNTs growth (see Appendix 1.2).

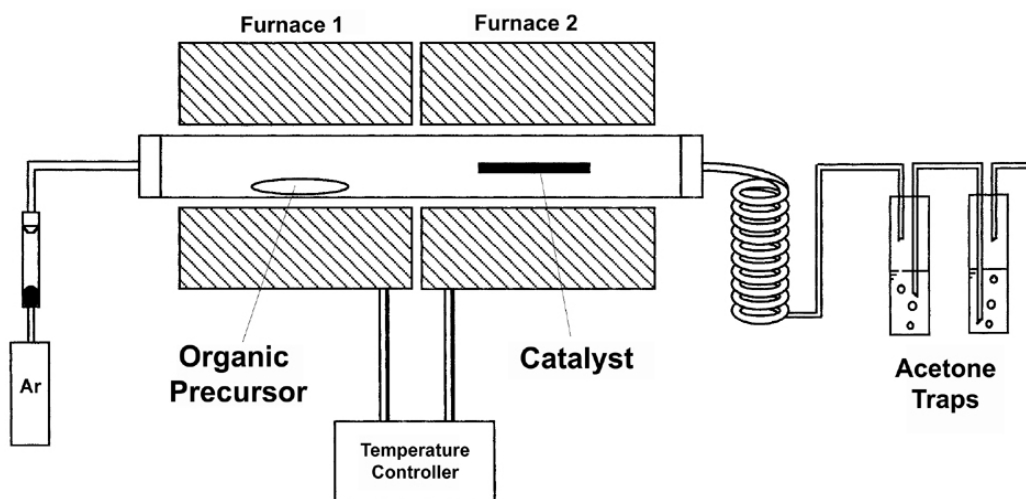


Fig. 1.7. Schematic diagram of the pyrolysis set up used for the synthesis of CNTs [2].

### 1.3.4. Electrolysis

This technique involves graphite electrodes immersed in molten salts (LiCl, KCl, NaCl, LiBr, etc) under an argon or air atmosphere. A DC voltage is then applied between the electrodes leading to the nanotube formation. In this method, the controllable variables are the depth of the cathode in the molten salt, the current, the molten salts and the temperature of the electrolyte. An electrolysis device is depicted in Fig. 1.8. The electrolysis method is useful for the MWNTs production, but with low control yields. Unfortunately, SWNTs can not be synthesized.

### 1.3.5. Other methods

Alternative methods involving the solar energy have been used to evaporate the carbon-catalyst target in an inert atmosphere. Hence, fullerenes and nanotubes were produced. Various improvements of this technique are still under investigation in order to obtain higher yields of CNTs. Further research is needed. Another proposed method to synthesize CNTs from nanoporous microstructures by thermal annealing is ball milling. The method consists of placing graphite powder into a stainless steel container along with steel balls. The container was purged and the milling is carried out at room temperature. The powder was annealed under an inert gas flow at high temperatures. The mechanism of this process is not known exactly, but it is thought that the ball milling forms nanotube nuclei, and the annealing process activates nanotube growth.

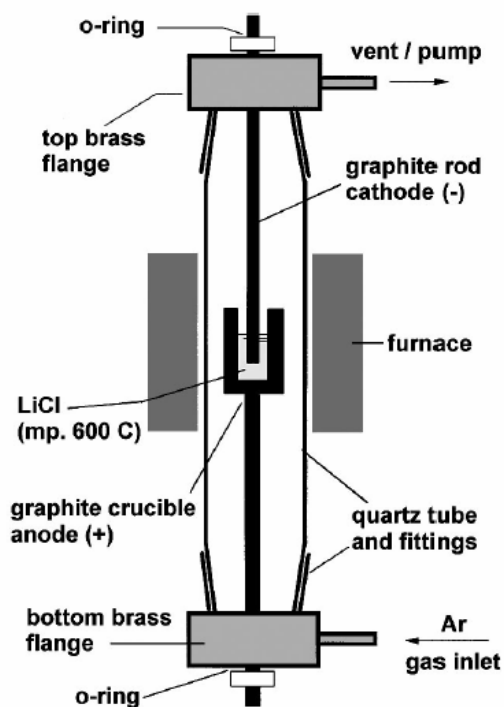


Fig. 1.8. Experimental set up of the electrolysis method used to synthesize CNTs in liquid phase [2].

## 1.4. Physico-chemical processing of carbon nanotubes

### *Purification, separation and deagglomeration*

In most of the nanotube synthesis methods (i.e. electric arc discharge, electrolysis, etc.), the tubes are produced with other foreign materials, such as nanoparticles (polyhedral-like and amorphous graphite particles).

Purification procedures refer to the elimination of particular by-products and catalyst residues from the carbon nanotube samples. There are many procedures to purify raw CNTs. Some of them are preferable from others depending on the carbon nanotube type, the carbon nanotubes synthesis method, and the extend of damage and changes that could be induced.

In some cases the purification method also involves i) the separation of SWNTs by length, diameter and chirality and/or ii) the deagglomeration of the synthesized CNTs ropes into individual CNTs. Nevertheless, more specific techniques for selective separation and deagglomeration can be found in the literature.

In the following paragraphs the most popular methods used to purify, separate and/or deagglomerate CNTs ropes are presented.

- i) *Physical separation: filtration, centrifugation and size exclusion chromatography.* The CNTs are dispersed in a non-reactive solvent with or without sonication. Subsequently, the nanotubes are physically separated. These methods are efficient to deagglomerate the nanotube ropes and to remove the big graphite particles, but it is not efficient enough to remove nanoparticles or amorphous carbon [16]. Nevertheless some diameter/length tube separation can be induced using the size exclusion chromatography.
- ii) *Thermal Oxidation.* The as-produced samples of CNTs are subjected to high temperatures (440-1100°C) in an oxygen or air atmosphere. This process favors the degradation of the amorphous layers and amorphous particles, thus leaving pure crystalline nanotube structures. This method uses the property of nanoparticles to burn out faster than CNTs. Nevertheless, the process can neither destroy the ropes (CNTs deagglomeration), nor remove metals or their oxides in MWNTs. Furthermore, the air oxidation method is disadvantageous because more than 95% of the starting material could be destroyed and the remaining nanotubes become more reactive at their ends due to the presence of dangling bonds (open caps). The dangling bonds can be eliminated using a subsequent high-temperature annealing (2800°C) [2, 16].  
As an alternative technique, the thermal oxidation in the presence of other gases or chemical compounds has been also performed. In particular, the microwave-assisted purification of MWNTs at 130°C in the presence of 20% hydrogen peroxide was recently reported to efficiently remove CNTs defects [19].
- iii) *Chemical Oxidation by acid treatments.* CNTs are oxidized by refluxing the material in concentrated acid solutions (i.e. HNO<sub>3</sub>, H<sub>2</sub>O<sub>2</sub>/NH<sub>4</sub>OH, HNO<sub>3</sub>/H<sub>2</sub>SO<sub>4</sub>). This procedure separates the CNTs from amorphous graphite particles, but partially damages their crystalline surface structure. It was also

reported that this technique separates individual CNTs from the ropes, negatively charges their surfaces, opens their caps and functionalizes CNTs with carboxylic groups, among other functional groups [20, 21].

Some combined methods have also been reported [22, 23]. Among them, the thermal oxidation in oxygen which results in the formation of iron oxide in the CNTs surfaces. This is followed by the removal of oxide particles using diluted solutions of HCl [24]. A similar method was reported using hydrogen at high temperatures (700-1000°C) after the acid treatment. In this case, the acid reflux dissolves the metal particles whereas the hydrogen treatment removes the amorphous carbon [25].

- iv) *Chemical reactions: Intercalation.* Nanoparticles, fullerenes and other contaminants can be removed using chemicals, such as  $\text{KMnO}_4$ ,  $\text{CuCl}_2$  or  $\text{CuCl}_2/\text{KCl}$ . The nanotubes which have closed structures are not affected [1]. Therefore, subsequent chemical removal of the intercalated species can be carried out.
- v) *Colloid suspensions of tubes/particles coupled with surface-active agent treatments (surfactants, polymers or other colloidal particles)* [26]. Subsequent filtration of the suspensions, using porous filters and size exclusion chromatography results in pure nanotube samples [2]. This is considered as a non destructive method to separate CNTs from carbon nanoparticles, to efficiently suspend CNTs in solvents, and to disentangle the CNTs ropes. This technique could also be useful to separate SWNTs by diameter and length, because it was observed that the polymer chains interact more efficiently with nanotubes of specific diameters, whereas the size exclusion chromatography separates the tubes according to their lengths [27].
- vi) *Plasma irradiation.* There are several versions. Radio-frequency plasma irradiation of MWNTs is performed in order to modify the structural defects and to vaporize contamination. It was observed that Ar plasmas did not chemically interact with CNTs [28]. In other works the CNTs were IR irradiated in air at high temperatures [29, 30].

It was experimentally observed that up to some extent the gas uptake, chemical, thermal, mechanical and electronic properties of CNTs vary significantly according to the purification and deagglomeration treatments [20, 31]. In particular, little damage is required on the CNT surface for polymer nanocomposite applications in order to achieve efficient load transfer.

From the different purification processes, the physical separation using filtration in conjunction with ultrasonication treatments with a non-reactive organic solvent is mainly used in the thesis. This method guarantees the deagglomeration of nanotube bundles and the carbon particles removal.

## 1.5. Physical properties of pure carbon nanotubes

Carbon nanotubes exhibit extraordinary electrical, mechanical (strength, stiffness, and toughness) and thermal properties. In this section an overview is presented.

### 1.5.1. Electrical properties

As it was predicted [6] and then experimentally confirmed, the CNT electronic properties depend on their diameter and chirality, but also on the type of carbon nanotube (single or multi-walled).

SWNT behaves as pure quantum wires, in which electrical conduction occurs via well-separated, discrete electron states that are quantum-mechanically coherent over long distances. The electrons propagate along the CNT axis because of quantum confinement of electrons in the direction normal to CNT axis, i.e. in the radial direction electrons are restricted by the monolayer graphene sheet. In addition, the wave vector distribution points the axis direction. The resulting number of 1D conduction and valence bands effectively depends on the standing waves around the circumference of the CNT [16]. SWNT can be either a one-dimensional metal ( $1/3^{\text{rd}}$  of all SWNTs) or a semiconductor ( $2/3^{\text{rd}}$ ) with a band gap inversely proportional to the tube diameter. Graphite, on the contrary, behaves like a semimetal. As described earlier, an  $(n,m)$  CNT is metallic when  $|n-m|=3q$ , where  $q$  is an integer. Then, all arm-chair nanotubes and  $1/3^{\text{rd}}$  of zigzag nanotubes are metallic; whereas the others zigzag tubes are semiconductors or metallic. Contrary to conventional metals, the CNT density of states (DOS, Fig. 1.9) are characterized by a number of singularities, known as “van Hove” singularities which are an indicative of one-dimensional quantum conduction.

MWNT behaves as the ultimate carbon fiber. Experimental results of Scanning Tunneling Microscopy and Spectroscopy (STS) demonstrated that MWNTs behave similarly to nanowires, with a DOS inversely proportional to the tube diameter [32]. Furthermore, based on measurements of electrical resistance as a function of temperature, it appears that MWNTs are semi-metallic and behave similarly to rolled-up sheets of graphene. Thus, at high temperature their electrical conductivity could be described using semi-classical models. At low temperatures, they reveal 2D quantum transport characteristics (ballistic regime) where the propagation of an electron is directly related to the quantum probability of transmission across the global potential of the sample.

Several transport measurements on MWNTs bundles have been performed since 1994. Some results revealed the MWNTs temperature-dependent resistance of the bundle, and a thermally activated electrical behavior, whereas for SWNTs a temperature-independent conductivity was observed along the bundle axis. All these differences are related to the different transport response due to the sample preparation and measurement method used. It was reported that the direct 4-probe (or 2-probe) method avoids contact problems and favors individual measures. The reported resistivity values for individual MWNTs, exhibiting metallic and semiconducting behavior, correspond to  $1.2 \times 10^{-4}$  to  $5.1 \times 10^{-6}$  Ohm•cm at 300K and activation energies  $<300$  meV for semi-conducting tubes. In

addition, bundles of SWNTs have shown metallic behavior with resistivities of  $0.34 \times 10^{-4}$  and  $1.0 \times 10^{-4}$  Ohm•cm [2].

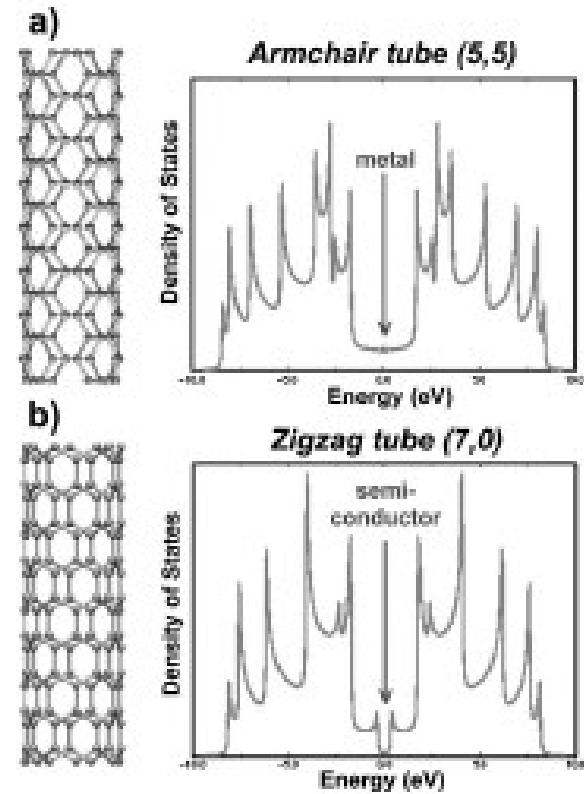


Fig. 1.9. Density of states (DOS) exhibiting the valence band, the conduction band and the Fermi energy for (a) metallic armchair tubes and (b) semiconducting zig-zag tubes. In zigzag tubes an energy gap is clearly observed between the valence and conduction band.

#### *Electronic Transport in doped-nanotubes: Defects, doping and Intercalation*

As in graphite and  $C_{60}$  crystals, van der Waals interactions govern the distances between sub-units in the crystalline structure of SWNTs ropes. It is thus possible to intercalate or dope nanotube with electron donors or acceptors. This leads to a charge transfer which allows the shifting of the Fermi level of nanotubes and modify their electronic properties [33]. Some ways to modify the CNTs electronic properties are the substitution of carbon atoms with other atoms, i.e. boron or nitrogen, or the introduction of structural defects (e.g. heptagon-pentagon pairs) into the hexagonal lattice.

### 1.5.2. Mechanical properties

Because the C-C bond in graphite is one of the strongest in nature, CNTs could be one of the stiffest materials ever synthesized [2]. A Young Modulus of  $\sim 1$  TPa has been predicted and experimentally measured for SWNTs and MWNTs [34]. Furthermore, measurements of MWNTs Young's moduli performed by recording the thermal vibration

amplitudes in a TEM [35] and by direct bending with AFM [36], revealed Young's moduli of 1.8 and 1.3 TPa, respectively. The compressive strength of CNTs is approximately two orders of magnitude higher than the compressive strength of any known fiber. CNT are also the stiffest structure ever made compared to carbon fibers, which typically have Young's moduli of up to 750 GPa, moduli of nanotubes range between 1 and 5 TPa. The most striking effect is the combination of the high flexibility and strength with high stiffness. Their fracture strains range between 10% and 30% which is better than most of the carbon fibers (0.1-2%) [37].

Hence, the theoretical and experimental results show that nanotubes are stiffer than any other known material. Nevertheless, it has been observed that these values could decrease significantly in the presence of defects (i.e. pentagons-heptagons pairs, vacancies and interstitials) within CNTs.

Carbon nanotubes behave elastically under large loads unlike all conventional materials, which either fracture or plastically deform [38]. MWNTs and SWNTs have been observed by TEM in the elongated state [39], and appear to behave as macroscopic elastic materials. Dai *et al* [40] used nanotubes as AFM tips. Using this experimental device, it was demonstrated that CNTs can be deformed without altering their structure. Other AFM measurements of force versus displacement of nanotubes tips provided more direct elastic measurements [36]. Their elastic modulus, a measure of their stiffness, could be as high as 4 TPa [38, 41].

Additionally, the carbon nanotube tubular structure is a closed structure which prevents the propagation of cracks and dislocations. Furthermore, the partial  $sp^2$ - $sp^3$  hybridization of the C-C bond should lead to a high flexibility.

It was observed that SWNTs display lower values of Young Modulus when compared to MWNTs [2]. In fact, mechanical strength measurements of SWNTs and MWNTs depend on the tube diameter (high diameter MWNTs approach graphite), crystallinity and number of defects. Additionally, the elastic properties measured on isolated tubes are decreasing when increasing the number of tubes within ropes [33].

In summary, it has been experimentally demonstrated that CNTs exhibit high elastic modulus, high tensile strength, and fracture toughness. These mechanical properties make nanotubes natural candidates for fabricating reinforced materials in composites, especially those expected to absorb heavy impacts (shock absorbers).

### 1.5.3. Thermal properties

The carbonization temperature (650-950°C) can be defined as the temperature at which the volatile species are driven off from carbon precursors. In the carbonization process, C-H, C-O, C-N, bonds are broken and C-C bonds begin to restructure. The graphitization temperature (2000-2800°C) is the temperature at which interplanar correlation (layer stacking among graphene sheets) exists. In the carbonization-graphitization temperature interval other reactions could occur. Oxygen and hydrogen atoms are removed above 700°C in the form of H<sub>2</sub>O, CO, CO<sub>2</sub> and CH<sub>x</sub> molecules. Oxidation reactions occur in the range between 800-1200°C when O<sub>2</sub>, H<sub>2</sub>O and CO<sub>2</sub> are present. The thermal purification process corresponds to the CO and CO<sub>2</sub> formation [1].

The thermal properties of carbon materials are closely related to the growth, and purification processes.

The thermal properties such as the thermal conductivity ( $k$ ) and specific heat ( $C_v$ ) for CNTs have been studied. Kim *et al* [42] reported that individual MWNTs present higher thermal conductivity than graphite ( $3000 \text{ W K}^{-1}$ ) at room temperature, and MWNTs bundles. Furthermore, in SWNTs and MWNTs, the phonon contribution dominates the thermal conductivity at all temperatures, but only above 20K for graphite. Yin *et al* found linear variations among thermal conductivity and temperature, and specific heat and temperature [2]. The phonon quantization has been observed during heat capacity and thermal conductivity measurements in SWNTs [2].

From the summary of Collins and Avouris [18]: the density of a SWNT is about  $1.33\text{-}1.40 \text{ g/cm}^3$ , which is just one-half of the density of aluminium. The elastic modulus of SWNT is comparable to that of diamond (1.2 TPa). The reported tensile strength of SWNT is much higher than that of high-strength steel (2 GPa). The tremendous resilience of SWNT in sustaining bending to large angles and restraightening without damage is distinctively different from the plastic deformation of metals and brittle fracture of carbon fibers at much lower strain when subjected to the same type of deformation. The electric current carrying capability is estimated to be  $1 \times 10^9 \text{ amp/cm}^2$ , whereas copper wires burn out at about  $1 \times 10^6 \text{ amp/cm}^2$ . The thermal conductivity of SWNT is predicted to be  $6000 \text{ W/m K}$  at room temperature; this is nearly double the thermal conductivity of diamond of  $3320 \text{ W/m K}$ . SWNT are stable up to  $2800^\circ\text{C}$  in vacuum and  $750^\circ\text{C}$  in air, whereas metal wires in microchips melt at  $600\text{-}1000^\circ\text{C}$ . SWNTs have great potential in field emission application because they can activate phosphors at 1-3V if electrodes are spaced  $1 \mu\text{m}$  apart. [43]

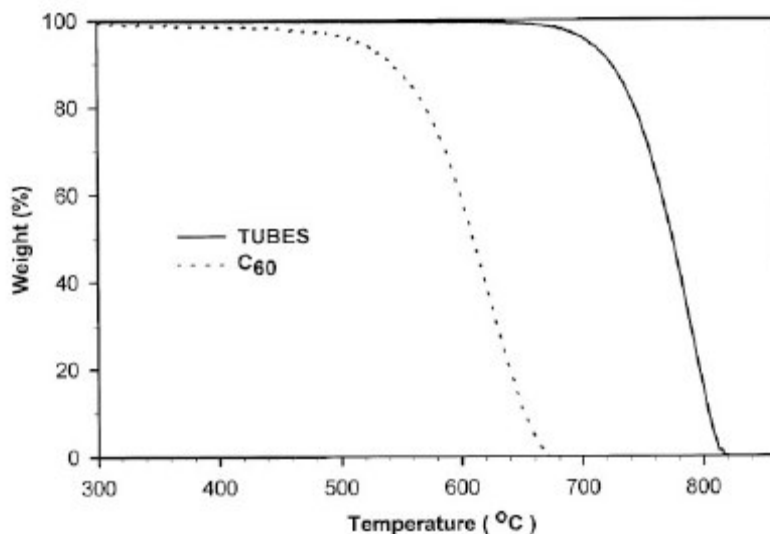


Fig. 1.10. Thermogravimetric Analysis of a MWNTs and  $C_{60}$ . As can be seen the nanotubes are more resistant than  $C_{60}$  to oxidation processes [2].

## 1.6. Nitrogen-doped carbon nanotubes (CN<sub>x</sub>)

The functionalization of CNTs has become an important issue for developing their potential applications [2, 3, 33, 44], in particular those related to polymer composites. Among various types of CNTs, the boron and nitrogen-doped MWNTs exhibit their intrinsic surface reactivity, and attractive electronic properties [15, 45-47]. In polymer nanocomposite applications, the nitrogen-nanotube surface reactivity could favor strong filler-matrix interactions without the use of acid treatments. Additionally, N-doped nanotubes (CN<sub>x</sub>) appear to be exclusively metallic conductors [48], so that conductive polymer composites could be prepared. Others nanocomposite applications, could take advantage of theoretical predictions of the existence of super hard materials when displaying the C<sub>3</sub>N<sub>4</sub> stoichiometry [49].

In this section, some details related to the synthesis, structure and properties of CN<sub>x</sub> nanotubes is summarized.

### 1.6.1. CN<sub>x</sub> nanotubes production methods

The nitrogen doping of CNTs are prepared by several methods, including CVD, templated technique and pyrolysis. The first reports on the synthesis of N-doped nanotubes dated after 1998. Table 1.3 presents the most representative fabrication methods of N-doped carbon nanotubes and related data.

### 1.6.2. Morphology, structure and composition of CN<sub>x</sub> nanotubes

Several reports established that the morphology and chemical composition of CN<sub>x</sub> nanotubes depend on the production methods and conditions (catalyst, temperature and gas flow, organic precursor, etc.).

Nitrogen-doping significantly alters the nanotube morphology, leading to compartmentalized bamboo structures [50]. Also, there was observed a strong dependence on the nitrogen concentration and the tube morphology. Trasobares *et al* [51] through spatially resolved EELS found that CN<sub>x</sub> nanotubes are made of carbon and nitrogen, inhomogeneously distributed. Carbon was located predominantly in the external surfaces, whereas N concentration is enhanced in the interior as N<sub>2</sub> gas (Fig. 1.11). Choi *et al* [52] found similar results.

### 1.6.3. C-N bonding in CN<sub>x</sub> nanotubes

In general, CN<sub>x</sub> nanotubes could be synthesized with different stoichiometries ( $x < 0.05$  to  $x < 0.32$ ) [48], principally during the carbon nanotube growth.

Some bonding pieces of information in CN<sub>x</sub> nanotubes have been obtained by monitoring the energy loss-near edge fine structures at the core edge (Fig. 1.12).

The spectra exhibit the C-K ionization edge for the  $\pi^*$  and  $\sigma^*$  transitions located at 285.5 eV and 293 eV, respectively. The position of the  $\pi^*$  peak is stable with different N

contents, nevertheless the intensity is diminished with increasing the N concentration. The  $\sigma^*$  band becomes relatively smooth as the N concentration increases. Thus, most authors suggest a transition from graphitic stacking on the tube outer layers to disorganized layers in the core region. Contrary results have been presented by Glerup *et al* [48], who suggested that the N-doped carbon nanotubes correspond only with a graphitic type network with  $sp^2$  bondings (substitutional nitrogen).

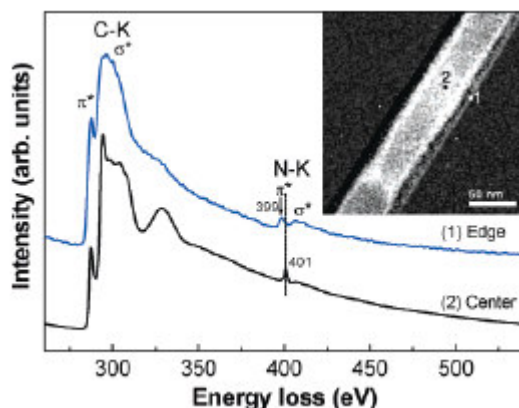


Fig. 1.11. EEL spectra of  $CN_x$  nanotube showing the C-K and N-K ionization edges for C and N (1) the nanotube edge and (2) in the center of the nanotube [52].

N-K edge peaks determine the C-N nature bonding in N-doped carbon nanotubes. In general, four different types of N structures have been reported in the literature, according to their  $\pi^*$  bands [52, 53] location.

- (i) *pyridine-like* at 398 eV, in which each N atom contributes with one p electron to the system and becomes significant in the inner walls.
- (ii) *pyrrolic site* at 399 eV, where each N atom contributes with two p electrons (C=N);
- (iii) *graphite-like* or *substitutional site*, at 401-403 eV, N atoms replace C in graphite layers (C≡N) becoming more visible in the inner walls; and,
- (iv) *Molecular  $N_2$* , that can be encapsulated in the hollow nanotube core.

A full description of each kind of functionality, predicted by N1s binding energies calculations, is presented in Fig. 1.13.

In general, N-doping (substitutional or pyridinic) in the inner regions of MWNTs is thermodynamically more favorable than in the outer walls. This incorporation of N atoms in the inner walls of MWNTs is driven during growth. Because the nanotube growth rate is mainly proportional to the saturated concentration and bulk diffusion rate of C atoms in the metal particle, higher concentrations of N atoms in the metal would lead to more N incorporation within the graphene cylinders. Using as Fe catalyst, the level of pyridine like structure is less according to the phase diagram which shows that saturation of N is 10% at 700°C. It was also observed [51] that the fine structure of N-K edge depends on the used catalyst [52].

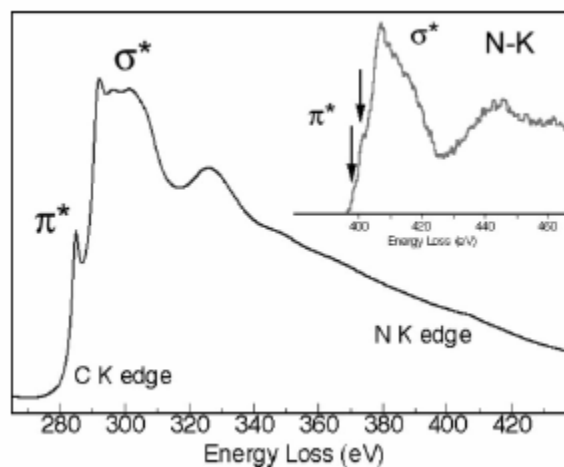


Fig. 1.12. EELS spectra of a  $CN_x$  nanotube exhibiting K-shell ionization edges for C ( $\sim 284.5$  eV) and N ( $\sim 400$  eV). Inset shows (a) a sharp characteristic at  $\sim 401$  eV corresponding to N bonded to C three C atoms within a hexagonal lattice, and (b) a weak shoulder at  $\sim 399$  eV associated with pyridine-like N located in defective areas of the graphitic layers [54].

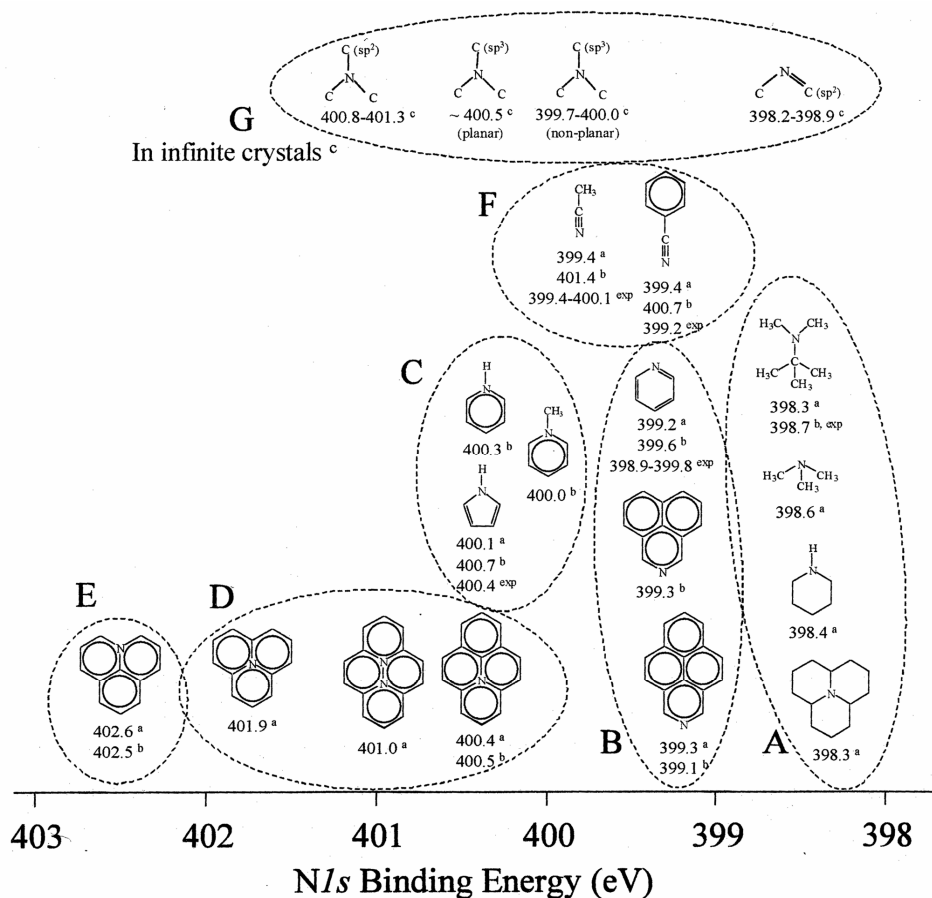


Fig. 1.13. Calculated N1s binding energy loss-near edge fine structures [55].

Interestingly, as the pyridine type N increases, the number of walls within the CNT decreases as well as the degree of crystallinity. Thus, defects in the inner wall are more favorable than in the outer wall. In fact, the fraction of pyridine-like N structures determines at some extent the degree of crystalline perfection of CNTs [52, 56].

Terrones *et al* [54] have observed a higher amount of pyridine-like N as the nitrogen concentration is increased; whereas, smaller concentrations of N generate straighter nanostructures with graphitic type N structures. This is because the pyridine-like N sites are responsible for the roughness and for interlinked morphologies.

Dos Santos *et al* [57] proposed that the graphitic structure maintains a planar morphology when the N content is less than 20%, but adopts a corrugated structure at higher N content.

Choi *et al* [58] using self-consistent charge-d.-functional-based tight-binding calculations of DWNTs, showed that the intercalation of N<sub>2</sub> is energetically possible and the graphite-like N structure becomes more stable when the inner wall is heavily doped.

The pyridine-like structure (deficiency of C resulting in “holes” within the tube) would exhibit more flexibility than pure graphite-like materials. The former can release more efficiently the strains of curved graphite layers of CNTs. Therefore, N-doping promotes the production of bamboo-like structure in the inner CNT shells. When the N content increases, the pyridine-like N structures become dominant when compared to the graphite-like structures and the tubes become less straight with reduced mechanical strength.

#### 1.6.4. Electrical properties of CN<sub>x</sub> nanotubes

The electronic densities of states (DOS) of these CN<sub>x</sub> nanotubes, using scanning tunneling spectroscopy (STS), reveals that doped nanotubes exhibit strong features in the conduction band close to the Fermi level (0.18 eV, above the E<sub>f</sub>). Using tight-binding and *ab initio* calculations, Czerw and Terrones *et al* [46] confirmed that pyridine-like N is responsible for introducing donor states close to the Fermi Level, i.e. induces a metallic behavior. These electron-rich structures are the first example of n-type nanotubes. Thus, the level of metallic properties can be controlled by manipulating the content of pyridine-like N.

Experimental conductance measurements indicate that bundles of N-doped CNTs exhibit higher conductivity when compared to undoped ones [56]. This may be due to the fact that lone pairs of electrons can conjugate with the delocalized p-system of the standard undoped graphene sheet [54].

In Table 1.4, electrical resistivities of some carbon materials are presented. In the common case, the less the crystallinity of graphene sheets, the higher the resistivity. In addition, the N doping lowers the resistivity. In less crystallized carbon materials the conduction occurs by a discontinuous hopping between localized states distributed in the mobility gap near a conduction band edge or the Fermi energy level. The doping of N (as donors) will change the electronic structure of the carbon layer, possibly shift the Fermi energy level and increase the electron density near the conduction band, thus promote the hopping conductance in the N-doped layer [56].

Table. 1.4. Electrical resistivity of different carbon materials.

Materials	Resistivity at room temp. ( $\rho$ , Ohm•cm)
Diamond	$\sim 10^{20}$
Graphite	$5 \times 10^{-5}$
Metallic SWNT	$(5-7) \times 10^{-4}$
MWNT	$5.3 \times 10^{-4}$ to $7.7 \times 10^{-3}$
B-doped MWNT	$7.4 \times 10^{-5}$ to $7.7 \times 10^{-4}$
undoped-CNT	$1.6 \times 10^3$
N-doped CNT	$2.2 \times 10$

In summary, nitrogen doping results in significant changes of the electronic and mechanical properties of the nanotubes. In particular, this thesis involves the use of  $CN_x$  nanotubes produced by pyrolysis demonstrating that is possible to fabricate polymer composites using polystyrene (PS).

Table 1.3. Fabrication methods of N-doped carbon nanotubes.

Authors	Technique	Description	Nanotubes	
			Characteristics	Structure
Yang et al	Template	Using porous anodic aluminium oxide	Double coaxial structure of N-doped CNT	N-doped layer less crystallized than non N-doped, that exhibit higher chemical reactivity toward O and higher conductivity.
Webster et al	CVD	Mixtures pyridine and pyridine-melanine	Well aligned materials	Pyridine and CNx
Liu et al	CVD	Reaction of pyridine (C <sub>5</sub> H <sub>5</sub> N) and pyrimidine (C <sub>4</sub> H <sub>4</sub> N <sub>2</sub> ) as precursors using ferrocene	N content 1-3.2%	Incorporation of N in the same form for both precursors
Yang et al	d.c.hot-filamnt. plasma-enhcd CVD.	NH <sub>3</sub> :C <sub>2</sub> H <sub>2</sub> (4:1) gas mixture as precursor on nickel-coated TiN/Si (100) substrates with/without N <sub>2</sub>	With N <sub>2</sub> were 2-5 times longer and morphology improved.	Nitrogen is in the CN <sub>x</sub> and C-NH <sub>2</sub> forms (XPS)
Jang et al	CVD	controlled NH <sub>3</sub> /C <sub>2</sub> H <sub>2</sub> flow ratio	N concentrations 0.4% to 2.4%.	N concentration increased the N-sp <sup>3</sup> C bonds as well as the deterioration of the crystallinity. For N>5%, N-sp <sup>3</sup> prevail over N-sp <sup>2</sup> .
Kozyol, et al	CVD	-	N doping of 3%	High internal order, graphene layers pure zigzag or armchair, space close to graphite
Choi et al	Pyrolysis	Reaction of iron phthalocyanine (FePc), cobalt phthalocyanine (CoPc), and nickel phthalocyanine (NiPc) in the temperature range of 750-1000 °C	Bamboo-like structures, diameter 15-80 nm, until 8% N content	Inhomogeneous distribution of concentration and electronic structure on their nitrogen atoms doped in the multiwalled carbon nanotubes. N inside of CNT.
Sadanadan et al	Pyrolysis	Reaction of xylene-ferrocene (99 at.% C:1 at.% Fe) with melamine (C <sub>3</sub> H <sub>6</sub> N <sub>6</sub> ) inside a quartz tube reactor operating at approximately 700 °C	Bamboo-like structures, 6-16 tube walls, 5% N content	Nitrogen doping of MWNTs renders them n-type
Terrones, M. et al	Pyrolysis	Thermolysis of ferrocene/melamine mixtyres (5:95) at 900-1000 °C in the presence of Ar	Arrays<2.5 cm2 of aligned CNx nanotubes (diameter 15-80 nm and <100 nm in length), N concentration 2-10%	N content varies from 2 to 10%, and can be bonded to C in two different fashions (double-bonded and triple-bonded nitrogen).
Reyes-Reyes et al	Thermolizing Ferrocene and benzylamine sol. at 850 °C		Bamboo-like structure encapsulating gaseous nitrogen	90% of these tubes contain molecular nitrogen in their cores
Terrones, M. et al	Pyrolysis	-	Synthesis of crystals of C <sub>3</sub> N <sub>4</sub> and CN nanotubes with small quantity of O	Two N bonding types within the hexagonal C network. . Difficult to generate highly ordered structures in which large concentrations of N are incorporated into the network

## 1.7. Applications of carbon nanotubes

Undoped-carbon nanotubes have been intensively studied and many applications have been developed as prototypes, or even more, as final products. Nevertheless, applications involving nitrogen doped-nanotubes are in their early stages.

In this section, general carbon nanotube applications will be discussed focusing in the fabrication of polymer-nanotube composites. In particular, those applications with  $CN_x$  nanotubes will be highlighted. An extended list, as well as detail description of applications could be found elsewhere [2].

### *Field emission sources*

Carbon nanotubes emit electrons from their tips when a potential is applied between the tube and an anode. The electrons are mainly emitted from the pentagons or dangling bonds located at the nanotube tips. MWNTs could be successfully used as field emitters because they exhibit sharp tips with a nanometer-scale radius of curvature, high aspect ratio, high mechanical stiffness, chemical inertness, high electrical conductivity, thermal stability and unique coaxial shape. In addition, high current electron emission at low operating voltages results in highly coherent, and monochromatic electron beams that could be used as cold cathode for flat panel displays, intense light sources or bright lamps and X-ray sources. Due to the advantages of field emission properties of CNTs over other materials (liquid crystals), some of those applications have already produced prototypes (Fig. 1.14). In particular,  $CN_x$  nanotubes could behave as stable field emitters operating at low voltages for the ultra low emission devices, due to the presence of surface defective sites. Nanotube emitting surfaces could be also fabricated with nanotube polymer composites (e.g. polyolefines).

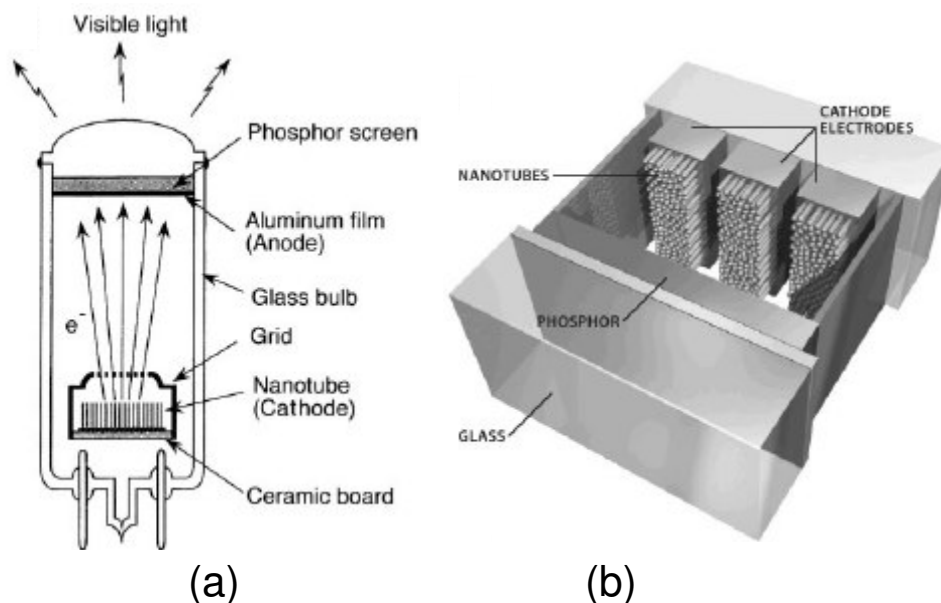


Fig. 1.14. Longitudinal cross-section of a fluorescent display with a field emission cathode constructed from MWNTs; (b) TV display prototype using CNTs [2].

### Lithium Ion Batteries

Battery prototypes have been fabricated using SWNTs and MWNTs (Fig. 1.15). Commercially available Li ions intercalated batteries now using graphite-like structures could incorporate vapor grown carbon fibers (VGCFs) and B-doped or N-doped carbon nanotubes. Li ions (usually from  $\text{LiCoO}_2$ ,  $\text{LiNiO}_2$  or  $\text{LiMn}_2\text{O}_4$ ) intercalate and de-intercalate from carbon material to charge and discharge the batteries. Li ions have high affinity to the B-doped sites which results in a higher energy storage of the battery. N-doped carbon nanotubes have an efficient reversible Li storage (480 mAh/g). In general, it is observed that doped nanotubes display higher reversible capacity when compared to highly crystalline undoped MWNTs (125 mAh/g). We should emphasize that the performance of this kind of batteries is superior to that of NiCd and NiMH batteries.

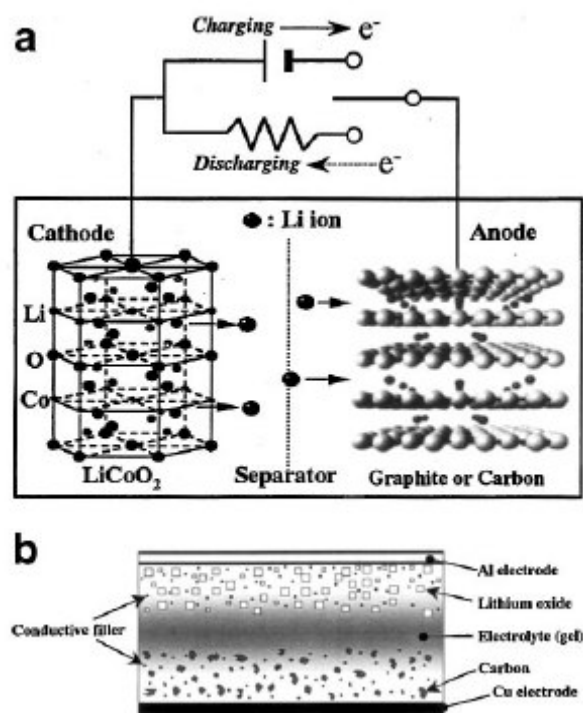


Fig. 1.15. (a) Charging-discharging mechanism of a Li battery; (b) basic composition of electrode and polymer  $\text{Li}^+$  composite of the battery [2].

### Chemical sensors

Carbon nanotubes can also be used as molecular sensors in Chemical Force Microscopes (CFM) or AFM sensors (Fig. 1.16), by introducing functional groups or polymers at the tip of SWNTs. Scanning probe tips are already produced and take advantage of the high stiffness and flexibility of CNTs. Proximal probe microscopes use CNTs tips with carboxylic functions that are chemically modified using amines or phenyl groups that are able to measure different adhesion forces when scanned over OH-terminated self-assembled monolayers.

SWNTs could behave as low concentration gas sensors ( $\text{NO}_2$  or  $\text{NH}_3$ ) considering changes in their transport properties. In addition, they are extremely sensitive to air and vacuum. This sensitivity could be measured as changes in resistivity.

Some other researches consider MWNT systems for detecting  $\text{NH}_3$ ,  $\text{H}_2\text{O}$ ,  $\text{CO}$ ,  $\text{CO}_2$ , and  $\text{NH}_3$ .

SWNTs can also be used to sense pressure under different liquid media (liquid immersion and polymer embedding), because of their deformation occurring property in the surrounding media.

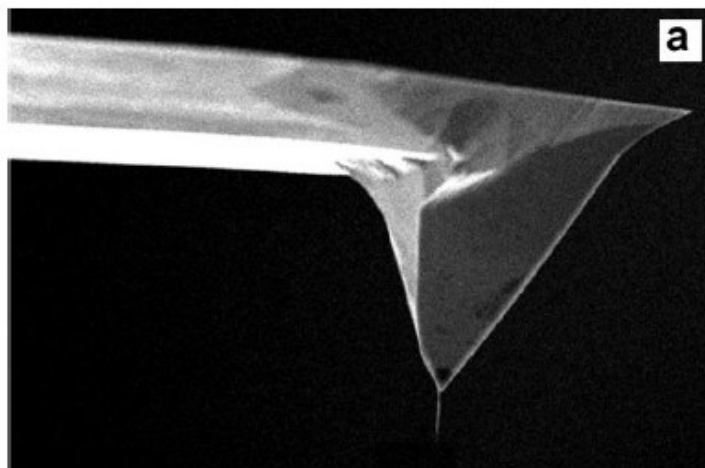


Fig. 1.16. SEM image of a standard AFM tip with a MWNT attached.

#### *Gas and liquid storage devices*

Carbon nanotubes are able to encapsulate metals and gases at high pressures. Metals, metal carbides, oxides, chlorides, etc can be introduced in CNTs using several methods such as chemical treatments, arc-discharge in the presence of metals, solid state reactions and electrochemical techniques. In particular, N-doped carbon nanotubes can store  $\text{N}_2$  gas.

The gas introduction inside CNTs generally involves the synthesis of the materials followed by the subsequent gas filling. Gases, such as  $\text{H}_2$ ,  $\text{He}$ ,  $\text{Ar}$ ,  $\text{N}_2$ , ammonia have successfully filled SWNTs and MWNTs. Therefore, CNTs could be used as fuel cells.

#### *Nanotube electronic devices*

Electronic devices can be constructed by the integration of CNTs, predominantly by molecular self-assembly, such as transistors or uncooled chips. In addition, voltage inverters can be fabricated using SWNTs (p-type transistor) and doped-nanotubes (n-type devices). MWNTs can be used as either n-type or p-type material, then novel p-n junctions can be created. N-doped nanotubes behave as n-type nanowires, whereas B-doped nanotubes act as p-type conductors. At higher temperatures the thermoelectric power of B-doped nanotubes is large and positive, indicating hole-like carriers. N-doped nanotubes show a large negative thermoelectric power, suggesting electron-like conduction [59].

### *Nanocomposites*

Carbon nanotubes can be used as fillers in ceramic, metallic and polymer nanocomposites because they combine high-aspect ratio, small size, stiffness, low density and high electrical conductivity.

SWNTs, DWNTs and MWNTs have been used to prepare composites with polystyrene, polycarbonate, poly(methyl methacrylate), epoxy, poly(vinyl alcohol), poly(aniline), etc using different approaches. It is important to emphasize that the preparation of  $CN_x$  nanotubes polymer nanocomposites is just beginning. Therefore, a great range of opportunities are opening, principally because they have proved to exhibit a higher surface reactivity, as well as good electrical and mechanical properties. Particularly, this thesis is devoted to the fabrication of polymer-nanotube composites using  $CN_x$  nanotubes. The main goal in the preparation of these composites is to enhance the dispersion and interface adhesion of nanofillers-matrix taking advantage of the  $CN_x$  nanotubes high reactivity and avoiding acid or other structural damaging processes, as acid treatment.

### *Other applications*

Others applications of CNTs include: electrochemical devices, supercapacitors and actuators, biomedical applications (no toxic effect for cells), such as coatings for prosthetics and anti-fouling coatings for ships, vascular stents and neuron growth and regeneration (chemically-modified CNTs), catalyst supports, etc. However, these are beyond the scope of this work.

## **1.8. Conclusions**

As stated in previous sections, CNTs (i.e. SWNTs and MWNTs) preferentially aggregate into bundles; could exhibit varied in lengths, diameters and chiralities; and could contain structural defects at their ends or on their sidewalls. Also, they present interesting physico-chemical properties that make them suitable materials for a great number of applications.

In addition, it was observed that structural characteristics are fundamental in chemical reactions. Therefore, more refined synthesis methods and efficient purification/separation process are searched to modify the chemistry of CNTs without uncontrolled parameters. Thus, it has been demonstrated that doping of CNTs (boron or nitrogen) modifies their physico-chemical properties, increase their surface reactivity, and enhances solvent dispersion. These modifications in addition preserve most of their characteristics and enables the synthesis of polymer nanocomposites [60].

## References

1. Saito, R., G. Dresselhaus, and M.S. Dresselhaus, *Physical properties of carbon nanotubes*. 1998, London: Imperial College Press. 279.
2. Terrones, M., *Science and Technology of the twenty-first century: synthesis, properties, and applications of carbon nanotubes*. Annual Reviews Materials Research, 2003. **33**: p. 419-501.
3. Terrones, M. and H. Terrones, *The carbon nanocosmos: novel materials for the twenty-first century*. Philosophical Trans Royal Society of London A, 2003. **361**: p. 2789-2806.
4. Iijima, S., *Helical microtubules of graphitic carbon*. Nature, 1991. **354**: p. 56.
5. Kroto, H.W., J.R. Heath, S.C. O'Brien, S.C. Curl, and R.E. Smalley, Nature, 1985. **318**: p. 162.
6. Dresselhaus, M.S., G. Dresselhaus, and P.C. Eklund, *Science of fullerenes and carbon nanotubes*, in *Science of fullerenes and carbon nanotubes*. 1996, San Diego: Academic. p. 1-505.
7. Oberlin, A., M. Endo, and T. Koyama, *Filamentous growth of carbon through benzene decomposition*. Journal of Crystal Growth, 1976. **32**: p. 335-349.
8. Terrones, M., W.K. Hsu, H.W. Kroto, and D.R.M. Walton, *Nanotubes: a revolution in material science and electronics.*, in *In Fullerenes and related structures: topics in chemistry series*, A. Hirsch, Editor. 1998, Springer: Berlin. p. 189.
9. Iijima, S. and T. Ichihashi, *Single-shell carbon nanotubes of 1 nm diameter*. Nature, 1993. **363**: p. 603.
10. Bethune, D.S., C.H. Kiang, M.S. de Vries, G. Gorman, R. Savoy, J. Vasquez, and R. Beyers, *Cobalt-catalysed growth of carbon nanotubes with single-atomic-layers walls*. Nature, 1993. **363**: p. 605.
11. Hutchison, J.L., N.A. Kiselev, E.P. Krinichnaya, A.V. Krestinin, R.O. Loutfy, A.P. Morawsky, V.E. Muradyan, E.D. Obraztsova, J. Sloan, S.V. Terehkov, and D.N. Zakharov, *Double-walled carbon nanotubes fabricated by a hydrogen arc discharge method*. Carbon, 2001. **39**(5): p. 761-770.
12. Peigney, A., P. Coquay, E. Flahaut, R.E. Vandenberghe, E. De Grave, and C. Laurent, *A Study of the Formation of Single- and Double-Walled Carbon Nanotubes by a CVD Method*. Journal of Physical Chemistry B, 2001. **105**(40): p. 9699-9710.
13. Morawsky, A.P. and R.O. Loutfy, *Synthesis of double-walled carbon nanotubes by carbon condensation in presence of iron-group metal catalysts*, in *PCT Int. Appl.* 2002, WO 2002030816 A1 20020418: USA. p. 70.
14. Terrones, M., *Synthetic routes to nanoscale BxCyNz architectures*. Carbon, 2002. **40**: p. 1665-1684.
15. Ajayan, P.M., *Nanotubes from carbon*. Chemical Reviews, 1999. **99**(7): p. 1787-1799.
16. Tanaka, K., T. Yamabe, and K. Fukui, *The science and technology of carbon nanotubes*. 1999, Amsterdam: Elsevier Science. 191.
17. Harris, P.J.F., *Carbon nanotubes and related structures New materials for the twenty-first century*. 2001, Cambridge: Cambridge University Press. 279.
18. Collins, P.G. and P. Avouris, *Nanotubes for electronics*. Scientific American, 2000. **283**(6): p. 62-69.
19. Ko, C., C.-Y. Lee, F.-H. Ko, H.-L. Chen, and T.-C. Chu, *Highly efficient microwave-assisted purification of multi-walled carbon nanotubes*. Microelectronic Engineering, 2004. **73-74**: p. 570-577.
20. Kim, Y.J., T.S. Shin, H.C. Choi, J.H. Kwon, Y.-C. Chung, and H.G. Yoon, *Electrical Conductivity of chemically modified multiwalled carbon nanotube/epoxy composites*. Carbon, 2005. **43**(1): p. 23-30.

21. Babaa, M.R., E. McRae, C. Gommès, S. Delpoux, G. Medjahdi, S. Blacher, and F. Beguin, *Characterization and gas adsorption on multi-walled carbon nanotubes before and after controlled chemical opening*. AIP Conference proceedings, 2004. **723**: p. 133-136.
22. Park, Y.S., Y.C. Choi, K.S. Kim, D.C. Chung, D.J. Bae, K.H. An, S.C. Lim, X.Y. Zhu, and Y.H. Lee, *High yield purification of multiwalled carbon nanotubes by selective oxidation during thermal annealing*. Carbon, 2001. **39**(5): p. 655-661.
23. Kneller, J.M., R.J. Soto, S.E. Surber, J.F. Colomer, A. Fonseca, J.B. Nagy, G. Van Tendeloo, and T. Pietrass, *TEM and Laser-Polarized  $^{129}\text{Xe}$  NMR Characterization of Oxidatively Purified Carbon Nanotubes*. Journal of American Chemical Society, 2000. **122**(43): p. 10591-10597.
24. Nguyen, C.V., L. Delziet, K. Matthews, B. Chen, and M. Meyyappan, *Purification process for vertically aligned carbon nanofibers*. Journal of Nanoscience and Nanotechnology, 2003. **3**(1/2): p. 121-125.
25. Vivekchand, S.R.C., A. Govindaraj, M.M. Seikh, and C.N.R. Rao, *New method of purification of carbon nanotubes based on hydrogen treatment*. Journal of Physical Chemistry B, 2004. **108**(22): p. 6935-6937.
26. Murphy, R., J.N. Coleman, M. Cadek, B. MacCarthy, M. Bent, A. Drury, R.C. Barklie, and W.J. Blau, *High-yield, non destructive purification and quantification method for multi-walled carbon nanotubes*. Abstracts of Papers, 227th ACS National Meeting, Anaheim, CA, United States, March 28-April 1, 2004.
27. Dalton, A.B., G. Chambers, H.J. Byrne, J.N. Coleman, B. McCarthy, M. in het Panhuis, W.J. Blau, G.S. Duesburg, S. Roth, P.M. Ajayan, and A. Maiti, *Non destructive methods to process and purify carbon nanotubes*. Recent Research Developments in Physical Chemistry, 2002. **6**: p. 327-349.
28. Ahn, K.S., J.S. Kim, C.O. Kim, and J.P. Hong, *Non-reactive rf treatment of multiwall carbon nanotube with inert argon plasma for enhanced field emission*. Carbon, 2003. **41**(13): p. 2481-2485.
29. Ando, Y., X. Zhao, and H. Shimoyama, *Structure analysis of purified multiwalled carbon nanotubes*. Carbon, 2001. **39**(4): p. 569-574.
30. Zhao, X.L., T.L. Guo, M. Ohkohchi, T. Okazaki, S. Iijima, and Y. Ando, *Production of highly graphitized multiwalled carbon nanotubes*. Acta Metallurgica Sinica, 1999. **12**(4): p. 345-352.
31. Lombardi, I., M. Bestetti, C. Mazzocchia, P.L. Cavallotti, and U. Ducati, *Electrochemical characterization of carbon nanotubes for hydrogen storage*. Electrochemical and solid-state letters, 2004. **7**(5): p. A115-A118.
32. Subramoney, S., *Novel nanocarbons-structure, properties and potential applications*. Advanced Materials, 1998. **10**: p. 1157-1171.
33. Petit, P. and A. Loiseau, *Carbon nanotubes: from science to applications*. C. R. Physique, 2003. **4**: p. 967-974.
34. Lu, J.P., *Elastic properties of carbon nanotubes and nanoropes*. Physical Reviews Letters, 1997. **79**: p. 1297-1300.
35. Treacy, M.M.J., T.W. Ebbesen, and J.M. Gibson, *Exceptionally high Young's modulus observed for individual carbon nanotubes*. Nature, 1996. **381**: p. 678-680.
36. Wong, E.W., P.E. Sheehan, and C.M. Lieber, *Nanobeam mechanics : Elasticity, strength, and toughness of nanorods and nanotubes*. Science, 1997. **277**: p. 1971-1975.
37. Breuer, O. and U. Sundararaj, *Big returns from small fibers: a review of polymer/carbon nanotube composites*. Polymer composites, 2004. **25**(6): p. 630-645.
38. Hafner, J.H., C.L. Cheung, A.T. Woolley, and C.M. Lieber, *Structural and functional imaging with carbon nanotube AFM probes*. Progress in Biophysics & Molecular Biology, 2001. **77**: p. 73-110.

39. Iijima, S., C. Brabec, A. Maiti, and J. Bernholc, *Structural flexibility of carbon nanotubes*. Journal of Chemical Physics, 1996. **104**: p. 2089-2092.
40. Dai, H., J.H. Hafner, A.G. Rinzler, D.T. Colbert, and R.E. Smalley, *Nanotubes as nanoprobes in scanning probe microscopy*. Nature, 1996. **384**: p. 147-151.
41. Lerner, E.J., *Putting nanotubes to work*. The Industrial Physicist, 1999. **5**(6): p. 22-25.
42. Kim, P., L. Shi, A. Majumdar, and P.L. McEuen, *Thermal transport measurements on individual multiwalled nanotubes*. Physical Reviews Letters, 2001. **87**: p. 215-218.
43. Thostenson, E.T. and T.-W. Chou, *Aligned multi-walled carbon nanotube-reinforced composites: processing and mechanical characterization*. Journal of Physics D: Applied Physics, 2002. **35**(16): p. L77-L80.
44. Rao, C.N.R., B.C. Satishkumar, A. Govindaraj, and M. Nath, *Nanotubes*. Chemical Physics and Physical Chemistry, 2001. **2**: p. 78-105.
45. Terrones, M., *Advances on the growth and properties of N- and B-doped carbon nanotubes*. AIP Conference proceedings (Electronic Properties of Molecular Nanostructures), 2001. **591**: p. 212-216.
46. Czerw, R., M. Terrones, and J.C. Charlier, *Identification of electron donor states in N-doped carbon nanotubes*. Nanoletters, 2001. **1**(9): p. 457-460.
47. Terrones, M., P.M. Ajayan, F. Banhart, X. Blase, D.L. Carroll, J.C. Charlier, R. Czerw, B. Foley, N. Grobert, R. Kamalakaran, P. Kohler-Redlich, M. Rühle, T. Seeger, and H. Terrones, *N-doping and coalescence of carbon nanotubes: synthesis and electronic properties*. Applied Physics A, 2002. **74**: p. 355-361.
48. Glerup, M., M. Castignolles, M. Holzinger, G. Hug, A. Loiseau, and P. Bernier, *Synthesis of highly nitrogen-doped multi-walled carbon nanotubes*. Chemical Communications, 2003: p. 2542-2543.
49. Liu, A.Y. and M.L. Cohen, *Prediction of new low compressibility solids*. Science, 1989. **245**: p. 841-842.
50. Ewels, C.P. and M. Glerup, *Nitrogen doping in carbon nanotubes*. Journal of Nanoscience and Nanotechnology, 2005. **5**(9): p. 1345-1363.
51. Trasobares, S., O. Stéphan, C. Colliex, W.K. Hsu, and H.W. Kroto, *Compartmentalized CN<sub>x</sub> nanotubes: Chemistry, morphology, and growth*. Journal of Chemical Physics, 2002. **116**(20): p. 8966-8972.
52. Choi, H.C., J. Park, and B. Kim, *Distribution and Structure of N Atoms in Multiwalled Carbon Nanotubes Using Variable-Energy X-Ray Photoelectron Spectroscopy*. Journal of Physical Chemistry B, 2005. **109**: p. 4333-4340.
53. Terrones, M., R. Kamalakaran, T. Seeger, and M. Rühle, *Novel nanoscale gas containers: encapsulation of N<sub>2</sub> in CN<sub>x</sub> nanotubes*. Chemical Communications, 2000: p. 2335-2336.
54. Terrones, M., H. Terrones, N. Grobert, W.K. Hsu, Y.Q. Zhu, J.P. Hare, H.W. Kroto, D.R.M. Walton, P. Kohler-Redlich, M. Rühle, J.P. Zhang, and A.K. Cheetham, *Efficient route to large arrays of CN<sub>x</sub> nanofibers by pyrolysis of ferrocene/melamine mixtures*. Applied Physics Letters, 1999. **75**(25): p. 3932-3934.
55. Helgren, N. 1999: Sweden.
56. Yang, Q., W. Xu, A. Tomita, and T. Kyotani, *Double Coaxial Structure and Dual Physicochemical Properties of Carbon Nanotubes Composed of Stacked Nitrogen-Doped and Undoped Multiwalls*. Chemical Materials, 2005. **17**(11): p. 2940-2945.
57. dos Santos, M.C. and F. Alvarez, *Nitrogen substitution of carbon in graphite: Structure evolution toward molecular forms*. Physical Review Letters B, 1998. **58**: p. 13918-13924.
58. Choi, H.C., S.Y. Bae, J. Park, K. Seo, C. Kim, B. Kim, H.J. Song, and H.-J. Shin, *Experimental and theoretical studies on the structure of N-doped carbon nanotubes: Possibility of intercalated molecular N<sub>2</sub>*. Applied Physics Letters, 2004. **85**(23): p. 5742-5744.
59. Choi, Y.M., D.S. Lee, R. Czerw, N. Grobert, and M. Terrones, Nanoletters, 2002.

60. Ahh, J.-H., Y. Paek, H.-S. Shin, and Y.-J. Kim, *Self-Organization of PEO-graft-Single-Walled Carbon Nanotubes in Solutions and Langmuir-Blodgett Films*. *Journal of Metastable and Nanocrystalline Materials*, 2004. **20-21**: p. 739-746.

# Chapter 2.

## Chemical functionalization and polymer grafting of carbon nanotubes

A great number of interesting carbon nanotube applications are related to polymer nanocomposites. Thus, many efforts have been carried out to enhance nanocomposite preparation methods aiming the production of homogeneous materials with desirable properties. Carbon nanotube surface reactivity and polymer-nanotube interaction have been improved by two main techniques, such as chemical functionalization (by elemental doping and/or functional group attachment) [1-4] and surface polymer-grafting [5-9]. The ability to manipulate carbon nanotubes enables their uniform dispersion in solvents, the subsequent functionalization reactions, and, the compatibilization with polymer, ceramic or metallic matrices for the fabrication of novel composites.

The main methods for modifying carbon nanotubes with polymers are: (i) *non-covalent attachment*, i.e. polymer wrapping and absorption, and (ii) *covalent attachment*, i.e. “grafting to”, “grafting from”, and functional groups reactions. In the case of covalent attachment, the resulting grafted polymer on CNTs is generically named polymer brush. Polymer brushes (polymer attached to different surfaces) have recently attracted considerable attention and there have been numerous studies describing their structure and novel properties [10-13]. So far, they have found application in a broad range of fields, such as cleaning, scrapping, applying and electronic contacts, among others [14].

In particular, this thesis considers the effect of chemical functionalization of carbon nanotubes, nitrogen-doping, radical surface functionalization and attachment of polymer chains on MWNTs used as fillers, in polymer composites. Therefore, this chapter reviews the structural and bonding characteristics that describe the chemical reactivity of carbon nanotubes. Additionally, most common chemical modifications of the carbon nanotubes are also described, as well as the preparation of polymer-brushes using carbon nanotubes as

surfaces via covalent attachment of polystyrene by the “grafting from” technique. Thus, this chapter will discuss the background and some basic concepts related to the polymer-grafting technique to functionalize carbon nanotubes, focusing on the nitroxide-mediated radical polymerization method.

## 2.1. Introduction

Carbon is the only element in the periodic table that is able to bond to itself in an extended network so as to form structures, such as fullerenes and carbon nanotubes. The delocalized  $\pi$ -electrons donated by each carbon atom in CNTs are free to move in the entire structure, and could give rise to electrical conductivity. In addition, the high frequency vibrations of the carbon-carbon bond provide a significant thermal conductivity in the carbon structures. The C-C strong bond determines the mechanical properties commonly expressed as strength, stiffness and toughness in materials. These fascinating properties promote the development of the carbon nanotube chemistry. This kind of chemistry considers the chemical reaction of carbon nanotubes and fullerenes with organic, inorganic, and organometallic molecules.

There are ways of forming chemical attachments to the walls or ends of carbon nanotubes. Generally, these chemical bonds might be used to join carbon nanotubes to other chemical molecules, such as solvents, polymers, ceramics, metals, solid substrates, or carbon nanotubes. Unfortunately chemical functionalized carbon nanotubes usually exhibit decreased mechanical or electrical properties when compared to as-produced carbon nanotubes.

## 2.2. Chemical reactivity of carbon nanotubes

Chemical reactivity of carbon nanotubes is due to structural modifications, such as: (i) local electronic structure, (ii) curvature and bending, (iii) superficial defective sites, and (iv) substitutional doping or functionalized sites. In particular, the presence of highly curved tubes (narrow diameter) could be reactive without the presence of defects. However, this type of reactivity only occurs with tubes of less <2nm in diameter.

### 2.2.1. Local electronic structure and chemical reactivity

Trigonal carbon bonds ( $sp^2$ -hybridization) strongly prefer a planar configuration with a pyramidalization angle of  $\theta_p = 0^\circ$ ; whereas tetragonal bonds ( $sp^3$ -hybridization) require  $\theta_p = 19.5^\circ$  (Fig. 2.1(b)). It has been observed that small fullerenes (e.g.  $C_{60}$ ,  $C_{70}$ ) exhibit  $\sim \theta_p = 11.6^\circ$ , thus the more appropriate geometry for them corresponds to tetragonal rather than trigonal hybridization. The chemical conversion of any trivalent carbon in  $C_{60}$  to a tetravalent carbon relieves the strain in the whole cage structure. Consequently, reactions that serve to saturate the carbon atoms in fullerene structures are chemically favorable. Fullerene double bonds with higher pyramidalization angles (characteristics of any

structure) are the most reactive. In this case, the  $C_{240}$  structure is the least reactive of all the fullerenes. Therefore, it can be concluded that the reactivity of fullerenes is primarily due to their spherical geometry and the strain generated by the pyramidalization angles of C-C conjugated bonds.

Carbon nanotubes and fullerenes are both curved structures; nevertheless, they present significant differences. Thus for a curved carbon nanotube (of diameters  $< 2\text{nm}$ ), the carbon atoms are restrained and could be more reactive. In fact, the strain energy of pyramidalization is proportional to  $\theta_p^2$ . As a consequence, reactions are energetically more probable in fullerenes which are highly curved. Carbon nanotubes can be divided in two regions: the end caps and the side walls. End caps look like fullerene hemispheres with  $\theta_p > 9.7^\circ$ , ensuring a good reactivity. The sidewalls of narrow diameter tubes (e.g.  $< 2\text{nm}$ ) could exhibit  $\theta_p \approx 6.0^\circ$ , representing a lower reactivity region. According to pyramidalization angles, narrow SWNTs reactivity is higher when compared to graphene sheets ( $\theta_p = 0^\circ$ ) [15].

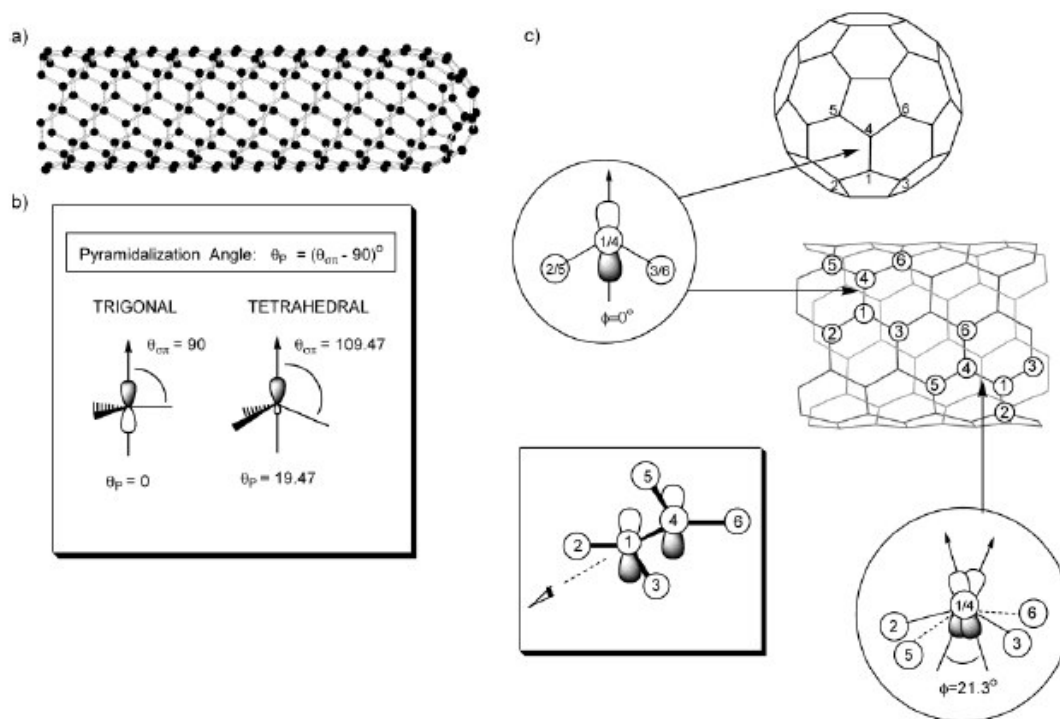


Fig. 2.1. Diagrams of (a) metallic (5,5) SWNT, (b) pyramidalization angle, and (c) misalignment angles ( $\phi$ ) along C1-C4 in the (5,5) SWNT and its capping fullerene  $C_{60}$  [15].

### 2.2.2. Effect of bending and curvature in chemical reactivity

Structural bending and curvature in carbon nanotubes are closely related with their chemical reactivity.

Bending of carbon nanotubes results in the formation of kinks and twists. These introduce local strain through conformational deformations [16]. This process has similar effects on the atomic orbitals, such as pentagonal defects. Therefore, bending of carbon nanotubes could be used to increase and control the reaction sites over the nanotube surface. In fact, selective schemes for carbon nanotubes derivatization that allow controlled reactions on specific sites, not only at end caps, would be useful. Experimentally it has been observed that bending of nanotubes can enhance the hydrogenation energy [17, 18], i.e. chemical reactivity, by introducing mechanical deformations. Park *et al* [19] developed an analytical model to determine the dependence of the chemical reactivity as a function of the local structure of a deformed carbon nanotube (Fig. 2.2).

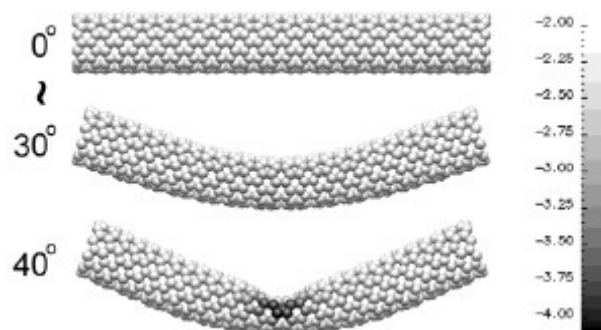


Fig. 2.2. The local chemical reactivity (hydrogenation energy) controlled by the carbon nanotube bending angle, that could be induced by mechanical deformations. The model considers only single bonds [19].

SWNTs and MWNTs are strongly differentiated by their curvature. Contrarily to SWNTs that exhibit high curvature radius (i.e. high reactivity), MWNTs possess low curvature radius on the sidewalls. The principal consequences of this fact are:

- (i) The chemical reactivity related to the local electronic structure in MWNTs is less effective when compared to SWNTs because MWNTs exhibit low curvature radius on the sidewalls. This means that the MWNTs behave chemically like graphite.
- (ii) The chemical reactivity on SWNTs strongly depends on their diameter [20].

### 2.2.3. Defective sites and chemical reactivity

Carbon nanotubes could possess different structural defects. Some of them are described below and presented in Fig. 2.3:

- A. Inclusion of five or seven membered rings within the carbon network,
- B.  $sp^3$ -hybridized defects, with R=H and OH groups,
- C.  $-COOH$  groups introduced by nanotube damage under oxidative conditions, and
- D. Open ends terminated with  $-COOH$  groups, or even other terminal groups such as  $-NO_2$ ,  $-OH$ ,  $-H$  and  $=O$ .

Defects in carbon nanotubes are important in the covalent chemistry, because they can serve as anchoring groups for achieving functionalization, mainly in the case of MWNTs sidewalls that have higher degree of planarity, and thus minor reactivity. In SWNTs, the curvature is the dominating factor explaining their reactivity. In addition, the chemical reactivity caused by impurities, open ends and dangling bonds (walls partial graphitization) in MWNTs could increase compared to SWNTs, if MWNTs are less perfect.

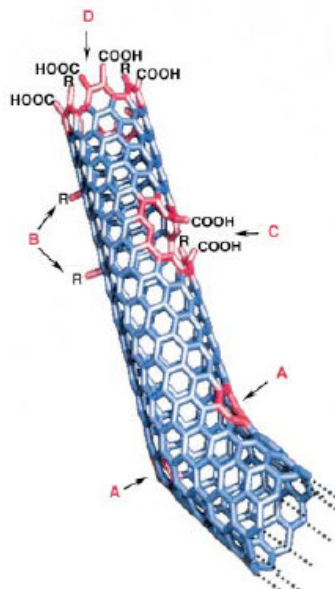


Fig. 2.3. The most common defect sites in SWNTs: A) Five or seven membered rings within the carbon framework (inducing bending); B)  $sp^3$ -hybridized defects ( $R=H$  and  $OH$ ); C) Carbon framework damage by oxidation, which leaves  $-COOH$  groups; D) Open ended SWNTs terminated with  $-COOH$ , or other terminal groups, such as  $-NO_2$ ,  $-OH$ ,  $-H$  and  $=O$  [4].

#### 2.2.4. Nitrogen-doping sites and chemical reactivity

Doped-carbon nanotubes exhibit other types of defective sites due to the functional groups added to the carbon network. In particular, several N-based structures have been reported in nitrogen-doped carbon nanotubes ( $CN_x$ ), among them: pyridine-like, pyrrolic site, and graphitic-like. These reactive sites are schematic represented in Fig. 2.4. As discussed above, the site number and structural location depend on several factors, as a function of the N concentration. In addition, experimental results have shown that  $CN_x$  nanotubes exhibit a higher reactivity when compared to un-doped tubes [21]. The N-doped nanotubes present higher reactivity towards reactants (like oxygen) due to the introduction of nitrogen species and the structural irregularity of carbon hexagonal rings [22]. The N substitution reactions are also able to create radicals over nanotube surfaces, which can react with suitable reactants. A detail description of the nitrogen-doped carbon nanotube structure and functionality is given in a previous section.

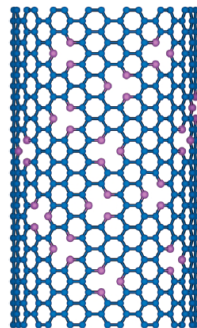


Fig. 2.4. Nitrogen-doped carbon nanotube scheme: molecular model of  $CN_x$  nanotubes containing pyridine-like and highly coordinated N-atoms. [23]

It is worth mentioning that the electrical, mechanical and thermal properties of carbon nanotubes could be modified if defects are introduced in the predominantly hexagonal network. In fact, it has been observed that carbon nanotubes can tolerate a limited number of defects before losing their properties.

## 2.3. Chemical modification of carbon nanotubes

Many of the chemical functionalization efforts have focused on SWNTs because they are characterized by strong covalent bonding and unique and almost perfect 1D structure. Because it was observed that MWNTs could exhibit higher mechanical properties, and several possibilities to chemical modifications (functionalized and doping) in comparison with SWNTs, different chemical functionalization of MWNTs have been carried out. In particular, because this study is interested in the chemical modification of MWNTs, some reports will be quoted.

### 2.3.1. Types of chemical modification of carbon nanotubes

The chemical modification of carbon nanotubes could be performed by covalent or non-covalent methods. The covalent modification considers the attachment of functional groups on the tube sides with chemical bonds, whereas non-covalent modifications use adsorbed molecules to modify the surface energy of carbon nanotubes. Thus, several mechanisms considering covalent and non-covalent modification can be described (Fig. 2.5):

- (i) Cap and sidewall functionalization, taking advantage of their local electronic structure induced by the bonds and curvature (mainly in SWNTs).
- (ii) Functionalization in defective sites and open ends, using the chemical group reactivity (Fig. 2.5 (A) and (B)),
- (iii) Functionalization in atom-doped sites, using the chemical group reactivity,
- (iv) Non-covalent functionalization using surfactants and polymers (Fig. 2.5 (C) and (E)), and
- (v) Endohedral functionalization using molecules (Fig. 2.5(E)).

In some cases, these functionalization reactions could induce the loss of the electronic structure in carbon nanotubes. The central dilemma of the functionalization field is to exploit the great potential reactivity of carbon nanotubes with the preservation of basic electronic and mechanical structure.

### 2.3.2. Homogenous dispersion of carbon nanotubes

There are important and practical aspects of nanotube composite preparation, such as disentanglement of bundles, separation-purification, and dispersion-solubilization of samples, prior to chemical reactions and polymerization [15].

Synthetic chemistry primarily takes place in solution. Thus, disentanglement and uniform dispersions of carbon nanotubes in several solvents have to be carried out in order to proceed with chemical reactions. Dispersion becomes difficult because SWNTs and MWNTs are extremely resistant to wetting and are difficult to separate due to strong van der Waals interactions. Nevertheless, it is possible to wet carbon nanotubes, i.e. thus favoring disentanglement and dispersion when using ultrasonic procedures in acids or solvents. In addition, surface modification (introducing dangling bonds and defects) could also be used to attach polymers covalently. Intercalated molecules play the role of disrupting and compensate the loss of van der Waals attractions between carbon nanotubes. In general, it was observed that ionic, covalent, non-covalent functionalization and polymer wrapping procedures could be effective when using uniform carbon nanotube dispersion.

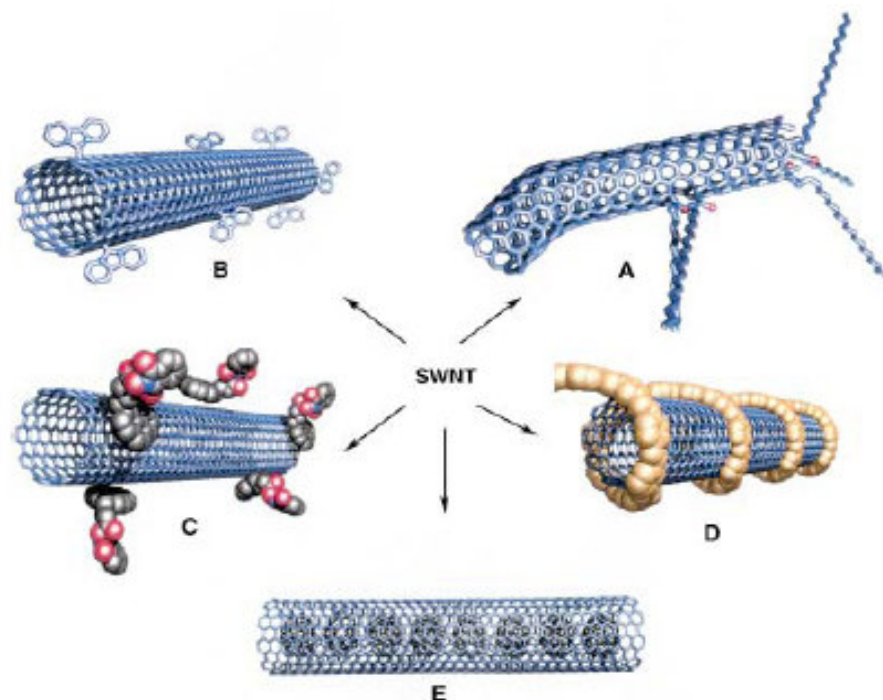


Fig. 2.5. Some functionalization possibilities of SWNTs: (A) Defect-group functionalization, (B) covalent sidewall functionalization, (C) non-covalent exohedral functionalization with surfactants, (D) non-covalent exohedral functionalization with polymers, and (E) endohedral functionalization with, for example,  $C_{60}$  [4].

Another important aspect of nanotube chemistry is the level of purity of the starting materials that was already commented in previous sections. Additional investigations related to the separation of carbon nanotubes by length, diameter and chirality could be useful. In fact, the control of extent, selectivity and localization of the chemical reactions, as well as the appropriate characterization and development of materials is desirable and could be established by the correct purification and separation of as-produced nanotube samples.

### 2.3.3. Chemical reactions of dispersed carbon nanotubes

The section is divided into covalent, non-covalent and other types of reactions (endohedral) with carbon nanotubes. Among the covalent functionalization methods two main strategies are employed: modifications based on surface-bound carboxylic acids on carbon nanotubes and direct sidewall modification. The covalent attachment of polymers (i.e. polymer-grafting) on the nanotube surface will be discussed in section 2.4.

#### 2.3.3.1. Covalent functionalization

Several covalent reactions with carbon nanotubes are originated in the chemistry of graphite, HOPG, and recently in the chemistry of fullerenes. In this context, many types of chemical reactions using carbon nanotubes have been investigated [1, 2, 15, 24]. Among them, oxidation, reduction and addition reactions have been performed to functionalize carbon nanotubes. In particular, the oxidation with their subsequent functionalization and the radical reactions approaches will be described in detail.

##### 2.3.3.1.1. Oxidation reaction and subsequent functionalization

The first reports related to the chemistry of SWNTs and MWNTs involved reactions under oxidizing conditions. The most common oxidation agents are  $\text{KMnO}_4/\text{H}_2\text{SO}_4$ ,  $\text{K}_2\text{Cr}_2\text{O}_7/\text{H}_2\text{SO}_4$ ,  $\text{OsO}_4$ , oxygen gas, and ozone. Other oxidation protocols deal with UV radiation, in addition to other physical modifications.

In the first steps of oxidation, the strong oxidizing agent intercalates reversibly in the nanotube bundles; using longer oxidation times, the reactant disorders and exfoliates the ropes into individual tubes. Finally, the extremely aggressive reagents can disrupt the aromatic ring system of the SWNTs and MWNTs.

In particular, concentrated acid solutions ( $\text{HNO}_3$ ,  $\text{H}_2\text{SO}_4$ ,  $\text{HCl}$ , among others, and their mixtures) produce functionalized sites (such as, carboxylic, sulfuric, anhydride, quinone, ketone, ester and hydroxyl, etc), defects in the hexagonal lattice, open ends, and impurity states at the Fermi level of the nanotubes. Furthermore, strong acid treatments with the aid of sonication, produces damage on the surface and results in the cutting of the tubes. In addition, the temperature rise in acid reactions increases the velocity and extents of structural damage within carbon nanotubes.

It is noteworthy that the oxidation rate is strongly dependent on the structure of the carbon layers, i.e. diameter and crystallinity.

First of all, various researchers observed that thinner tubes are more quickly consumed when compared to the thicker ones, because of their greater helical strain due to the narrow tube diameter.

In second place, less organized parts within carbon nanotubes appear to be more reactive when compared to highly crystalline regions. In general, functionalization of carbon nanotubes by oxidation takes place preferentially at end caps and defective sites [25].

#### *Subsequent functionalization after oxidation*

The literature presents numerous reaction protocols related to purification (see previous section) and functionalization of carbon nanotubes using acids. Usually in nanotube chemistry, the acid treatment is seen as a preliminary step to increase the carbon nanotube chemical reactivity by the introduction of functional groups labile for posterior modification. These modification steps consider several kinds of chemical reactions, predominantly at nanotube ends and defective sites (Fig. 2.6). Thus, this kind of nanotube chemistry is named, by some authors, end and defect-site chemistry.

Most of the carboxylic acid functional group react with thionyl chloride for activation with the subsequent reaction with amines ( $-\text{NH}_2$ ), alkyl amines, aniline derivatives, phenyl groups, etc. The ionic functionalization of the carboxylic acid groups in carbon nanotubes by octadecylamine has been reported and could form SWNTs-carboxylate zwitterions ( $\text{SWNT-COO}^- \text{NH}_3^+(\text{CH}_2)_{17}\text{CH}_3$ ) [2].

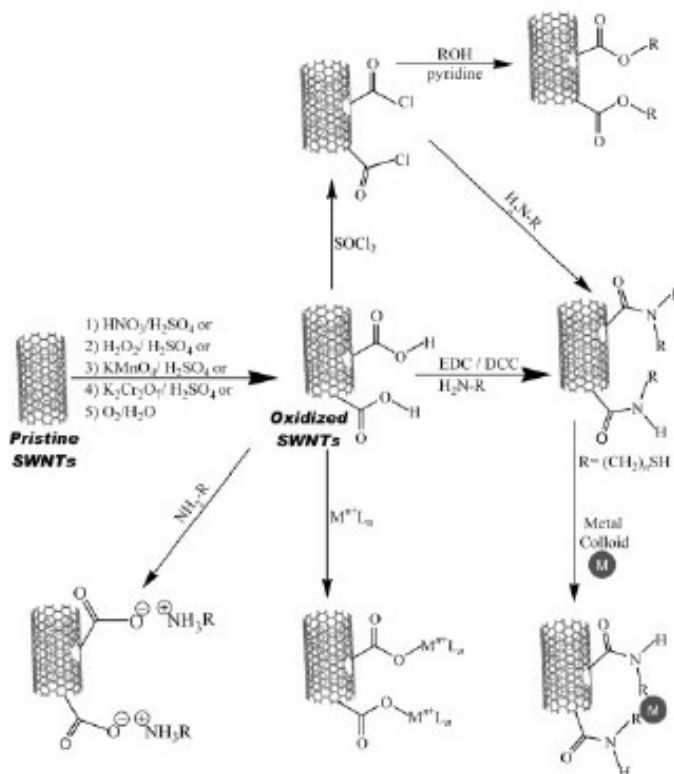


Fig. 2.6. Scheme of common covalent functionalization routes used to derive SWNTs at the ends and defect sites. As produced nanotubes are treated with an oxidative protocol to generate functional groups that react with  $\text{SOCl}_2$  followed by amide or ester linkages. Amine and oxygenated functional groups are also effective sites for coordination to metal complexes and ions [1].

Many efforts have been devoted to make carbon nanotubes biologically compatible. Thus, several water soluble molecules and macromolecules have been attached to acid functionalized-carbon nanotubes, as peptide nucleic acid, DNA, etc.

Nanoparticles (e.g. Au, Ag, etc) [26] and quantum dots (CdSe, TiO<sub>2</sub>, etc) have been bound to oxidized-carbon nanotubes in order to alter the optical and electronic properties of carbon nanotubes. Furthermore, coordination complexes of Ir, Pt and Pd, among others, have been synthesized by metal coordination in an  $\eta^2$  fashion to the carbon-carbon double bond in fullerenes. For SWNTs and MWNTs, the oxidized functional group appears to be a favorable mode of bonding of metals by complexation [1].

Finally, the addition of a long-chain hydrocarbon might render the acid functionalized-carbon nanotube soluble in organic solvents (such as chloroform (HCCl<sub>3</sub>), dichloromethane (CH<sub>2</sub>Cl<sub>2</sub>), benzene (C<sub>5</sub>H<sub>6</sub>), toluene (CH<sub>3</sub>-C<sub>6</sub>H<sub>5</sub>), carbon disulfide (CS<sub>2</sub>), etc.), when using octadecylamine (CH<sub>3</sub>(CH<sub>2</sub>)<sub>12</sub>NH<sub>2</sub>), alkyl-aryl amine 4-dodecyl-aniline (4-CH<sub>3</sub>(CH<sub>2</sub>)<sub>13</sub>C<sub>6</sub>H<sub>4</sub>NH<sub>2</sub>), among others. In addition, the functionalization of carbon nanotubes with polymers has also been carried out and will be discussed in following sections.

In summary, it could be mentioned some important aspects in the oxidation and subsequent functionalization of carbon nanotubes.

- The oxidation of carbon nanotubes could be successfully used in purification and exfoliation steps. Nevertheless, this technique is difficult to control and reproduce.
- The oxidation produces an improved solubility and an increment in the chemical reactivity of carbon nanotubes due to the creation of defects and functionalized sites on their surfaces. Nevertheless, it also produces dramatic structural damages with the tendency to destroy nanotubes.
- There are several chemical functionalization routes reported for carbon nanotubes using oxidation process. However, the functionalized carbon nanotubes predominantly exhibit the molecular attachment on defective sites and the end-caps. This could be a disadvantage for some applications, such as the nanocomposite preparation, among others.
- The induced structural damage affects seriously the mechanical, electronic and thermal properties of carbon nanotubes, thus affecting their possible applications.

To sum up, even though the oxidation of carbon nanotubes results in functionalized carbon nanotubes, this aggressive technique induces structural damage. Thus, a more effective and less aggressive method, such as the direct covalent functionalization, is preferred in nanotube functionalization processes.

#### 2.3.3.1.2. Reduction, addition and other reactions

There are several chemical processes able to modify carbon nanotubes by direct covalent functionalization. This method takes advantage of the nanotube chemical properties without the use of acids. Fig. 2.7 shows several chemical processes, such as nitrene addition, hydrogenation via Birch reduction, alkylation, arylation [27] and 1,3-

dipolar cycloaddition, among others. In particular, fullerene and carbon nanotube chemistry has shown that their structural properties favor addition reactions. In fact, efficient addition reactions take place with very reactive species, such as arynes, carbenes or halogens (i.e. iodine, bromine, etc) [15].

Chen *et al* [28] tested the reactivity of SWNTs using photolabeling of [ $\gamma^{32}\text{P}$ ]-benzophenone-ATP or [ $\gamma^{32}\text{P}$ ]2N<sub>3</sub>ATP solutions. Their results indicate that the radioactive probes become attached to the nanotube, but the mode of addition remains unknown. Further reactions were carried out using dichlorocarbene (electrophilic reagent) that adds to deactivated double bonds. Birch reduction conditions were applied to hydrogenate benzenoid rings of SWNTs. These reactions are schematically present in Fig. 2.8. References of functionalized SWNTs by the addition of nucleophilic carbenes have also been reported [15]. In this case, each added group is bound to one covalent bond of the tube (no cyclopropanation occurs), thus introducing a negative charge to the nanotube.

Fluorination was chosen during the initial studies of functionalization of carbon nanotubes because of the efficient chemical transformations of graphite. Margrave *et al* [29] reported the first extensive sidewall functionalization of SWNTs with F (Fig. X). Covalent C-F bond was detected by IR vibrations with stoichiometries of CF<sub>x</sub> ( $x \leq 0.4$ ) or CF<sub>2</sub>. It was also shown that fluorine substituents on SWNTs can be displaced using strong nucleophiles as Grignard, alkyllithium and metal alkoxides.

#### 2.3.3.1.3. Radical reactions

Several radical reactions have been performed with carbon structures (carbon black, fullerenes and carbon nanotubes) with organic peroxides and nitroxides. Experimental results reported addition of radicals to carbon structures using ESR [30, 31].

Donnet and colleagues [32] have studied the carbon black interaction with AIBN radicals. After characterization, it was found that the paramagnetic susceptibility of untreated and AIBN treated carbon black are almost the same. In addition, ESR results revealed that both samples are temperature independent. Finally they conclude that the observed reaction of free organic radicals with carbon black corresponds to chemical reactions and not to free radical coupling. The same authors, in another study, found that peroxides and carbon black can form macroinitiators labile to initiate *in situ* radical polymerization.

Several simulations were proposed to study the interactions of carbon nanotubes and radicals. In particular by molecular dynamics, the collision of benzene radicals with a SWNT has been considered by Ni and Sinnott [2]. Radical collisions at higher energies could create defects within the SWNTs walls, but also produce the scattering and adsorption of radicals or heavy fragments of radicals.

Peng *et al* [3] synthesized SWNTs and fluorinated-SWNTs and reacted them thermally with organic radicals from lauroyl and benzoyl peroxides. They reported the SWNT covalent sidewall attachment.

It has been also shown that nanotubes can coherently transport spin-polarized electrons over long distances (250 nm) [33]. In this context, Gallani *et al* [34] performed the grafting of TEMPO radicals to cut and polished SWNTs that were treated with oxalyl chloride.

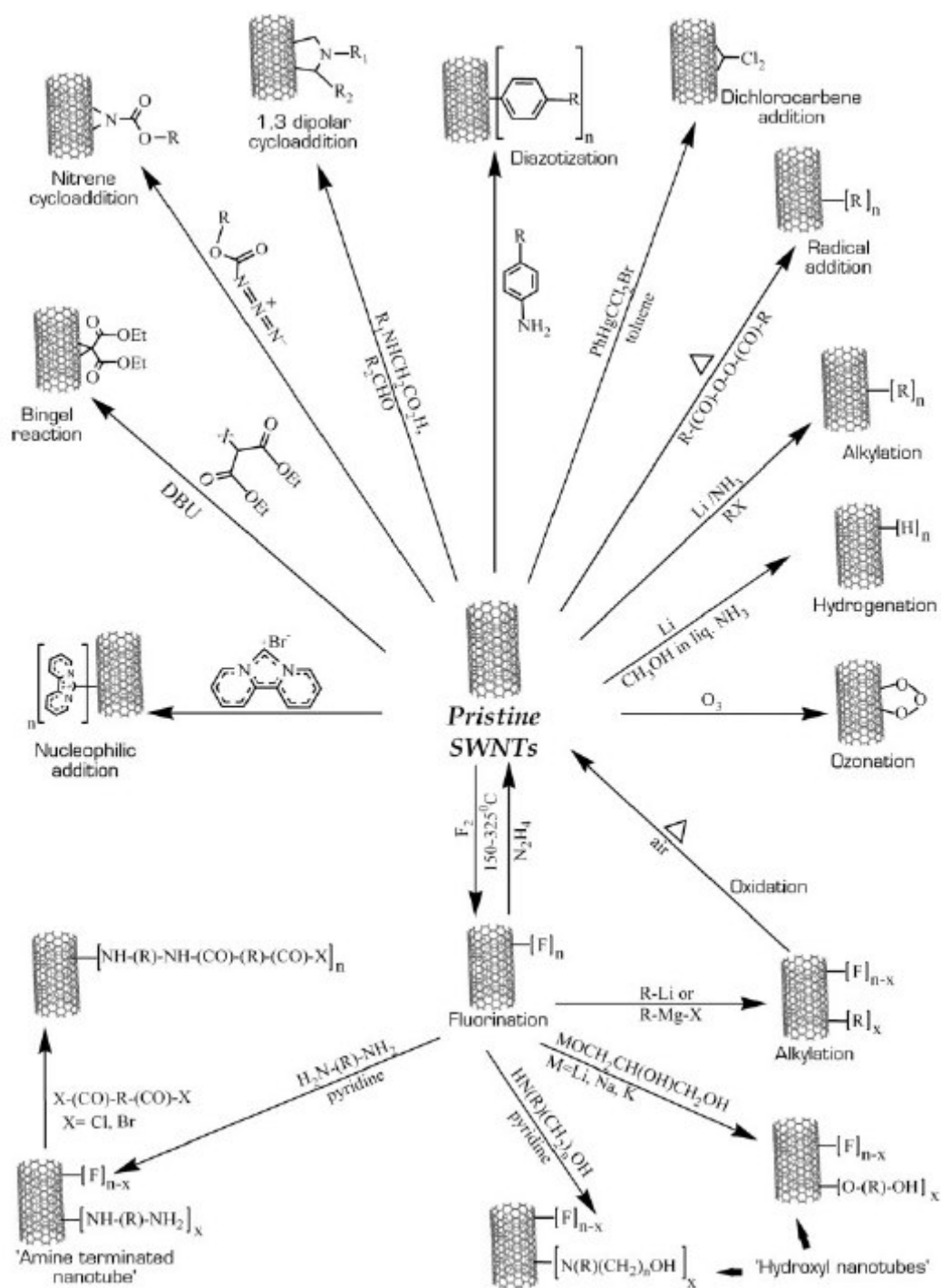


Fig. 2.7. Covalent-sidewall functionalization reactions of carbon nanotubes [1].

Shaffer *et al* [8] suggested that in solution polymerization systems of benzoyl peroxide, carbon nanotubes and monomer, the grafting mechanism involves growing polymer radicals attaching themselves to the defective and oxidized carbon surface of the nanotubes, although the small molecule initiators may also directly attack the nanotubes. Both effects have been observed in radical reactions with fullerenes and carbon black.

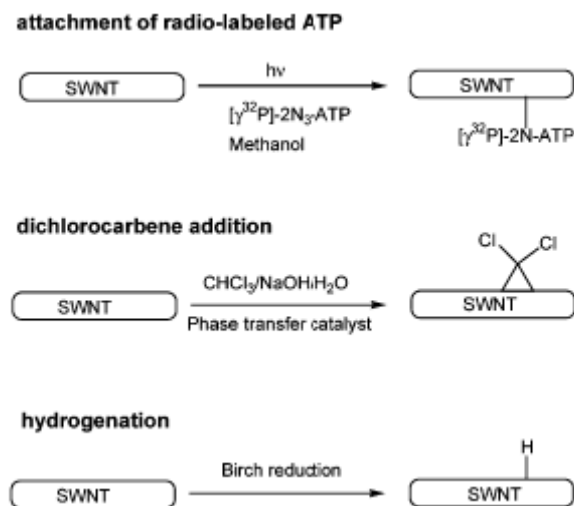


Fig. 2.8. Addition reactions of SWNTs. (a) attachment of radio-labeled ATP, (b) dichlorocarbene addition, and (c) hydrogenation [15].

These authors followed the radical attachment and the PmPV association by ESR. The authors observed that the radicals are either very weakly coupled, or not coupled. The explanation is related to finite size on the radical conductivity that could interfere and prevent the coupling, but also because of the steric impediments of the polymer chain.

Some other radical addition reactions with carbon nanotubes involve perfluoroalkyl and aryl radicals produced photochemically or by electrochemical reduction.

Therefore for carbon nanotubes, the chemical interaction with radicals, i.e. the fixation of molecular free radicals on carbon nanotubes, could be interpreted using two hypotheses:

- (i) It could be assumed by trapping radicals already present on the surface (nanotube scavenging properties); and,
- (ii) It could be proceeded by a chemical reaction of radicals with surface functional groups that could produce a stabilized radical.

In summary, the direct covalent functionalization of carbon nanotubes preserves the nanotube structure, and could favor a homogeneous and extended coverage of functionalized sites over the nanotube surface. In particular, radical reactions could be used to prepare further carbon nanotubes derivatives, such as polymer-grafting, and specifically the controlled radical polymer-grafting carbon nanotubes.

### 2.3.3.2. Non-covalent functionalization

Non-covalent functional carbon nanotubes can be prepared by: (i) adsorption of surfactants, amines, and molecules with large p-systems; and (ii) complexation with organometallic compounds or wrapping of polymers (Fig. 2.5 (C) and (D)). One of the main advantages of non-covalent functionalization is the conservation of the carbon nanotube electronic structure [1].

First of all, surface-active molecules, such as sodium dodecylsulfate (SDS) or benzylalkonium chloride, form stable suspensions of carbon nanotubes. The micelles formed contain carbon nanotubes in the hydrophobic region. If the hydrophobic interior of

the amphiphile contains an aromatic group, a strong interaction with the nanotubes is formed because of the  $\pi^*-\pi$  stacking interactions. Similar immobilizations on carbon nanotubes were observed with the hydrophobic part of proteins, anilines and amines. Evidence of these functionalizations is found by changes in solubility and electronic properties. Presumably donor-acceptor complexes are formed between surfactants-carbon nanotubes because of the curvature [4].

Interestingly, the suspension of purified carbon nanotubes with polymer solutions forms “molecular complexes”. Polymer wrapping around carbon nanotubes enhances solubility and modifies carbon nanotube and polymer properties. A range of polymers, mostly ionic polymers, are capable of coating SWNTs and MWNTs. Among them, polystyrene, poly(methyl methacrylate), poly(vinyl pyrrolidone), poly(styrene sulfonate), etc. It was observed that polymers, such as polyethylene glycol (PEG) and polyvinyl alcohol (PVA), are ineffective in wetting carbon nanotubes. Association and disassociation of polymers from carbon nanotubes can be controlled by varying the solvent polarity.

### 2.3.3.3. Other functionalization types

Endohedral functionalization takes advantage of the storage capacity of carbon nanotubes. Some of the molecules that can be inserted using the capillarity properties of carbon nanotubes are metals (for example, gold and platinum) and metal salts. The incorporation of fullerenes or metafullerenes has also been carried out (Fig. 2.5 (E)). The encapsulated fullerenes tend to form chains organized by van der Waals forces [4].

## 2.4. Polymer-grafting of carbon nanotubes

Polymer brushes refer to an assembly of polymer chains that are tethered to a substrate by one end. The substrate includes wafers, particles (such as carbon black, fullerenes and carbon nanotubes), and polymer backbones. The grafting of polymers onto a surface can be made by (a) “*grafting from*” *the surface method*, in which the polymerization is initiated from initiating groups (typically free radicals) introduced onto the substrate; (b) “*grafting onto*” *the surface method*, in which a polymer chain that is growing is trapped by the surface, rendering a covalent bond between the polymer and the surface, and, (c) *polymer reactions with functional groups on the surface*, in this approach a polymer exhibiting terminal functional groups reacts with other functional groups that are present on a specific surface.

Several studies have demonstrated the effectiveness of all these techniques when grafting polymers with solids. In the “grafting from” method, radical, cationic and anionic polymerization can be performed onto the desired surface. In addition, higher degree of surface functionalization is possible, but multiple synthetic steps must be carried out on the nanotubes, and polymer characterization is only possible for the grafted chains that are cleaved on the nanotube surface. Conversely, the “grafting to” method suffers from the low polymer loadings due to steric repulsion between grafted and propagating polymer chains. However, this technique allows the characterization of polymer chains prior to grafting. Furthermore, in both “grafting from” and “grafting to” procedures, a broad distribution of molecular weights and composition of the polymer chains are expected, if the polymerization proceeds by an uncontrolled method [35]. Additionally, polymer reactions

with functional groups present on the surface experience low chain polymer attachment due to steric repulsion; fortunately, the molecular weight, and a well defined polymer structure can be controlled [36].

In summary, the “grafting from” method is preferred over other methods, because of their possible advantages, such as higher degree of functionalization, that could be related to surface coverage, and the control of polymer molecular weight and the control of polymer weight and composition.

#### 2.4.1. Polymer-grafting of carbon black and fullerenes

Polymer-grafting has been carried out in carbon structures, such as carbon black, fullerenes, and carbon nanotubes. Previous, studies performed using carbon black and fullerenes constitute the pioneering work that evolved in the polymer grafting on CNT surfaces.

##### *Carbon black*

A permanent radical concentration [37], as well as a strong radical trapping behavior has been observed in carbon black [32, 38] and also both properties have been used to graft polymers onto its surface [36, 39, 40]. Polymer-grafting with carbon black has been achieved using the “grafting from”, “grafting onto” and “polymer-reactions with functional groups on the surface” techniques. The radical cationic and anionic polymerization by azo-[41] or peroxyester [42], acylium perchlorate [43] and potassium carboxylated [44] groups introduced on the carbon black surface are examples of “grafting from” technique. Additionally, it has been reported that free radical polymerization of vinyl monomers in the presence of carbon black (“grafting to” method), leads to the grafting of polymers onto the surface of carbon particles, but the percentage of grafting is less than 10%. This is because carbon black preferentially traps low-molecular-weight initiator fragments rather polymer radicals [45, 46].

Furthermore, it has been observed that, when carbon blacks are treated with conventional free radical initiators (benzoyl peroxide (BPO), or 2,2'-azobis(isobutyronitrile) (AIBN)), the corresponding radicals are bound on the surface forming polycondensed aromatic rings and quinonic oxygen groups on the surface [32, 47]. The free radicals formed on the carbon black surface by the addition of initiator radicals were considered to be stabilized by polycondensed aromatic rings. In most of these cases the increase of the number of surface radicals after the treatment with the initiators has been confirmed using Electron Spin Resonance (ESR) [32, 47]. From these studies, it is concluded that the polycondensed aromatic rings and quinonic oxygen groups of carbon black act as a strong radical trapping agents for polymer radicals.

Using the radical trapping behavior of carbon black, Hayashi *et al* [36] have reported the “grafting to” reaction of carbon black with polystyrene chains polymerized in the presence of (thus, end terminated) a nitroxide (TEMPO) at temperatures above 100°C. This reaction is summarized in Figure 2.9. The *in situ* polymerization experiments of the authors confirmed that carbon black traps more low-molecular-weight initiator fragments than growing polymer radicals. This behavior could be explained by the stability and the steric hindrance of the growing polymer radicals. They also found that polymers having

hydroxyl terminal groups could be grafted onto the carbon black surface in the presence of ceric ions, as depicted in Fig. 2.10. Complementary results by them determined that PEO could be also grafted onto carbon black without inducing gelation or crosslinking. This behavior revealed that radicals formed were not reacted with two carbon black particles.

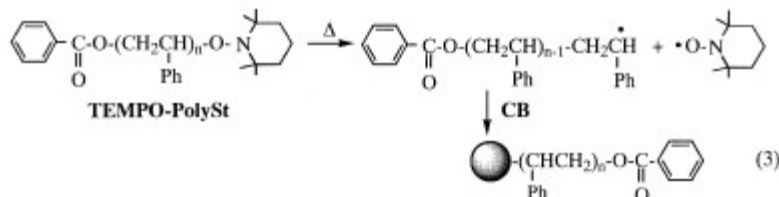


Fig. 2.9. Surface grafting onto carbon black by trapping polymer radicals formed by decomposition of TEMPO-polystyrene [36].



Fig. 2.10. Surface grafting onto carbon black by trapping polymer radicals formed by redox reaction of ceric ions with polymer containing hydroxyl groups [36].

### Fullerenes

Early studies on radical polymerization of vinyl monomers in the presence of  $\text{C}_{60}$  report very low yields of polymer formed in solution, or even complete inhibition [48]. From these cases, it has been suggested that for the case of styrene the free radicals are trapped by fullerene, and the resulting fullerene radicals do not propagate but instead can terminate. Nevertheless, there are pieces of evidence that if the polymerization is carried out in the presence of a large excess of initiator, the radicals undergo multiple additions on the fullerene surface, changing their nature sufficiently to not inhibit polymerization [49]. Other authors have reported on the grafting of polymer chains on fullerenes. Krusic *et al* [50] shown that free radical species can efficiently couple to the surface of  $\text{C}_{60}$ , resulting in a highly functionalized fullerenes. Mehrotra *et al* [48] reported that in the presence of  $\text{C}_{60}$ , the polymerization of vinyl monomers (methyl acrylate, methyl methacrylate, acrylonitrile, cyanovinyl acetate, vinyl acetate, 2-cyanoethyl acrylate, styrene and N-vinylpyrrolidone) in solution was inhibited, yielding 15% or less of polymer product. Therefore, it was concluded that the  $\text{C}_{60}$  intercepts the initiating radicals in the polymerization reaction. Furthermore, it was observed that monomers with high reactivity could form fullerene-based radicals by their addition to fullerene surface and continue the polymerization process. In fact, functionalization of fullerenes with well-defined polymers by living polymerization techniques (e.g. anionic polymerization, nitroxide mediated free radical polymerization, and atom-transfer free-radical polymerization) has been reported recently. With these living methods, both the architecture of the polymer-grafting on fullerenes surfaces and even more the architecture of the same polymer chains can be well-controlled [51]. As consequence, many kinds of polymer-grafted fullerenes have been reported, among them: side-chain polymers, main-chain polymers, dendritic fullerenes, star-shaped polymers and fullerene end-capped with polymers.

As can be seen, there are several experimental reports in the polymer-grafting of carbon black and fullerenes, by both the “grafting to” and the “grafting from” techniques. Furthermore, these techniques have been successfully applied to covalently bond polymer

chains using controlled radical polymerization. The free radical polymerization is possible by the chemical interaction of particle surface with the radicals and also by the polycondensed aromatic rings structure formed on the surface. The radicals stabilized on the surface of these carbon structures could in turn initiate the growth of polymer chains, forming an initiator.

#### 2.4.2. Polymer-grafting of carbon nanotubes by “grafting from” technique

The first synthesis of polymer-grafted multiwalled carbon nanotubes were reported by Jin *et al* in 2000 [5]. Since then, the number of papers has increased enormously. In most of these papers, the polymer-grafting of multiwalled carbon nanotubes have been achieved by either of the already mentioned techniques: “grafting from”, “grafting to”, and “polymer reactions with functional groups at nanotube surface” techniques. The advantages cited for the “grafting from” technique make interesting to consider it in the polymer-grafting of carbon nanotubes. Thus, in the next section, some of the experimental results in “grafting from” method applied to MWNTs will be described.

##### 2.4.2.1. Polymer-grafting using carbon nanotube acid functionalization

Several polymers have been successfully grafted onto MWNTs using the “grafting from” technique. Among them there are: polymethyl methacrylate grafted via emulsion polymerization [6, 7], sterification [52], and other methods [53]; polyethylenimine-grafted [54, 55]; hyperbranched polyetherketones [56, 57] via Friedel-Crafts acylation in polyphosphoric acid (PPA) [58]; PEO and PS [59]; polyureas, polyurethanes, and poly(urea-urethane) [60]; polyethers [61]; polyacetylene [62] and PS [63]. In all of these cases, the carbon nanotubes were chemically functionalized by acid treatment, to introduce initiator molecules by chemical reaction that could be used to carry out *in situ* polymerization of the different monomers.

The first covalent attachment of polystyrene chains onto carbon nanotubes was reported by Shaffer in 2002 [8]. Polystyrene and some of their copolymers (like poly(styrene-co-hydroxymethyl styrene) and poly(styrene-co-aminomethyl styrene) [64]) had been reported as grafts on carbon nanotubes by either of the three previously discussed methods, namely, “grafting from”, “grafting to”, and “polymer reactions with functional groups at nanotube surface”. In the case of acid functionalized carbon nanotubes, the grafting of polystyrene could be achieved by several reactions, such as esterification [65], amidation [66], acylation [67], Huisger cycloaddition [68], among others.

##### 2.4.2.2. Polymer-grafting using living radical polymerization

Polymer grafting techniques that use direct covalent functionalization methods, such as radical reactions, have been developed in order to avoid the problems associated with the functionalization of carbon nanotubes using acids. These grafting techniques eliminate the need for nanotube pretreatment prior to the functionalization and allow attachment of polymer molecules to pristine tubes without altering their original structure.

The grafting mechanism involves polymeric free radicals that attach themselves to the defective, doped and/or oxidized sites [8, 9] on the carbon nanotube surface, and also radical trapping mechanisms [9] of the CNTs. Both, the polymer “grafting from” and the “grafting to” methods on carbon nanotubes could be performed by radical reactions. In the “grafting from” technique the nanotubes are pretreated with a free radical initiator to give rise to “active” sites where the polymerization can be carried out, whereas in the “grafting to” technique a propagating polymer chain (bearing a free radical) reacts with the tubes directly. An alternative approach includes the use of a “regulator” molecule in addition to the initiator to give rise to a controlled radical polymerization (pseudo-living polymerization) where the free radicals are capped with a nitroxide molecule (the regulator) that is in essence a stable free radical and thus allows the controlled grafting of monomer molecules on the nanotube surface.

The use of a living radical polymerization approach allows a better control of molecular weight and molecular weight distribution of the tethered polymers onto the nanotube surface. Living polymerization methods in addition to the previously mentioned controlled radical polymerization include: anionic, carbocationic and ring-opening metathesis polymerization. All of these methods have been used in the synthesis of polymer brush in a “grafting from” approach, as will be detailed below.

In general, it is known that living free radical polymerization offers a high degree of control over the polymer architecture and is applicable to a broad spectrum of monomers, but there are very few instances where it has been used to graft polymer chains onto carbon nanotubes, for example, Nap *et al* [69] have considered how the strength and distance of the minimal interaction could be controlled by the choice of polymer chain length, surface coverage, and type of functional end-group; also, how the feed ratio of monomers controlled the quantity of the grafted polymer. Like these, many other factors need to be studied to reach an understanding on the formation of polymer brushes on nanotubes.

Some of the studied systems involved PMMA-grafting on carbon nanotubes. Park *et al* [70] reported the polymerization of PMMA over carbon nanotubes using 2,2'-azoisobutyronitrile (AIBN) as radical initiator. In this system, the authors have been observed that the induced radicals on the outer wall of the MWNTs by AIBN were found to initiate the grafting of PMMA [71]. Other authors observed that poly(4-vinylpyridine) grafts to single-walled carbon nanotubes (SWNTs) during *in situ* free radical polymerization of 4-vinylpyridine [72].

#### 2.4.2.2.1. Anionic and cationic polymerization

Anionic and cationic polymerization techniques can be used to graft polymer chains on carbon nanotubes surfaces. Some of the reported results are summarized in the following lines.

Mylvaganam *et al* [73] reported, with the aid of the density functional theory, that ethylene and epoxide functional groups could be grafted to carbon nanotubes using methoxy radicals and *sec*-Bu anion as initiators leading to polyethylene- and polyepoxide-grafted nanotubes. The study predicts that both free-radical and anionic functionalization methods are energetically favorable; that the resulting carbon nanotube-radical and the carbon nanotube anion can react with ethylene and epoxide functionalities, respectively; and that the resulting products have free electrons and negative charges on the carbon and oxygen atoms at the free ends of ethylene and epoxide, respectively. Hence, the *in situ* free-radical and anionic polymerizations can propagate to produce polymer-grafted carbon

nanotube. The cationic functionalization of carbon nanotubes using  $\text{BF}_3$  as an initiator was found to be infeasible. In addition, polystyrene chains were grafted onto SWNTs via anionic polymerization techniques [74].

#### 2.4.2.2.2 Controlled living radical polymerization

Particularly, the *in situ* surface-initiated controlled polymerization from the surface of carbon nanotubes was recently reported by several authors using Atom Transfer Radical Polymerization (ATRP) [75] and Nitroxide Mediated Radical Polymerization (NMRP) [35, 76, 77], among others. There exist a limited number of experimental pieces of evidence of these radical polymerization techniques to the polymer-grafting of carbon nanotubes. However, in these works there are some lacks in the demonstration of the polymer covering of the nanotube walls, and even more about the covalent attachment of the polymer chain to the surface.

##### *Reversible Addition and Fragmentation Chain Transfer (RAFT)*

Hong *et al* [78] reported the poly(N-isopropylacrylamide) grafting of MWNT via surface reversible addition and fragmentation chain transfer (RAFT) using the RAFT agent functionalized MWNTs as chain transfer. Using the same technique PS chains were grafted from the surface of MWNTs [79].

##### *Atom Transfer Radical Polymerization (ATRP)*

The ATRP reaction mechanisms proposed for nanotubes surface polymerization were: first the attachment of polymerization initiators via cycloaddition reaction, or the ring-opening metathesis polymerization (ROMP) [80], and; second the attachment of initiator by the carboxy group generated by chemical oxidation [81]. The polymers growing over nanotubes using this technique until now are principally poly(styrene) [75, 81-85], poly(methacrylate) [86, 87], poly(t-Bu acrylate) [88-90], poly(N-isopropylacrylamide) [91], and poly(acrylic acid) [92], as well as their copolymers [93].

##### *Nitroxide-mediated Radical Polymerization (NMRP)*

Nitroxide-mediated radical polymerization has been demonstrated on surfaces, nanoparticles and amphiphiles, and very recently on carbon nanotubes (by Ramirez *et al* [76]). This technique could be used in both “grafting to” and “grafting from” methods. In the first case, NMRP produces well-defined polymers that are end-capped with thermally labile nitroxide functionalities. Thus, this method could result in the controlled formation of polymer-centered radicals that could be utilized in the functionalization of carbon nanotubes [35, 94]. In the second case, the couple initiator-nitroxide could be attached to the nanotube to form a “macroinitiator”, susceptible of thermal initiation. The opening and closing mechanism for the free radical-controller pair favors the polymer chain growth.

The available literature on the grafting of polystyrene to CNTs using NMRP invariably includes the functionalization of the nanotubes using strong acids to attach the initiator to the nanotube ends and defective sites. Particularly, Ramirez *et al* [76] attached NMP initiator through carbodiimide or acid chloride chemistry with acid functionalized nanotubes. Adronov *et al* [35] proposed that polymers could be covalently attached to SWNTs through the radical coupling of the polymer to the nanotube walls. Datsyuk *et al* [77] synthesized double walled carbon nanotube-polymer brushes by in-situ nitroxide mediated polymerization.

Nitroxide-mediated Radical Polymerization is the less used controlled radical polymerization technique to graft polymer chains on carbon nanotubes; however, the technique is promising because of (i) the successful functionalization without any carbon nanotube surface damage, like in acid functionalized carbon nanotubes, and (ii) the minimal purification and separation problems, (when compared to a technique such as ATRP).

This thesis focuses on the use of the NMRP technique to graft polystyrene on nitrogen-doped carbon nanotubes. Furthermore, great opportunities and applications to this type of polymer brush are envisaged. A detailed review of the NMRP technique is available in several references [95, 96]. A detailed explanation of this technique is out of the scope of the present dissertation.

## **2.5. Applications of functionalized and polymer-grafted carbon nanotubes**

Numerous factors motivate the chemical modification, by functionalization or polymer grafting of carbon nanotubes, most of them are related with their applications. In general, the properties of carbon nanotubes could be differentiated by the intercalation, bonding, or even the doping of molecules with nanotubes.

The grafting of polymers onto carbon nanotubes could allow their assembly onto surfaces for electronic applications, permit the reaction of the grafted nanotubes with host matrices in composites, and finally could enable sensor applications that may require a variety of functional groups bound to carbon nanotubes with specific recognition sites (optical or transport properties) [24].

The polymer composites are the focus of this research. Thus it has to be said that the sidewall functional groups or polymer chains of carbon nanotubes polymer brushes could help the dispersion of the nanotubes in the polymer matrix and improve the mechanical properties of nanocomposites. In fact, the requirements of load transfer efficiency demand that nanotube surfaces should be compatible with the host matrix. In addition, tubes interconnected by chemical bonds could modify (increasing or decreasing) the contact resistance depending on the polymer that is grafted to the surface. Also, the polymer-grafting should avoid the tendency of the carbon nanotubes to form bundles and increase their specific surface area [77].

## **2.6. Characterization of functionalized and polymer-grafted carbon nanotubes**

In general the characterization of carbon nanotubes after chemical functionalization is still developing. Up to now, there are several analytical techniques used to confirm the carbon nanotube chemical reaction, but also, the degree of functionalization.

Functionalized species on the carbon nanotube wall, can be characterized using spectroscopic techniques. Thus, Ultraviolet (UV), Infrared (IR) and Raman Spectroscopy

are used to analyze the changes in the carbon nanotube sidewall structure due to the presence of new chemical bonds.

Thermogravimetric Analysis (TGA) and X-Ray Photoelectron Spectroscopy (XPS) provide information related to the degree of functionalization.

Transmission Electron and Atomic Force Microscopy (TEM and AFM) show the sidewall structure and topological modifications and dispersion effectiveness.

$^1\text{H}$  NMR is not very informative, because of the traces of iron impurities (catalyst used during the synthesis) and the slow tumbling rates of carbon nanotubes that cause a signal broadening.

## 2.7. Conclusions

Experimental evidence supports that carbon nanotubes should be considered as a new macromolecular form of carbon with great potential in the development of novel devices. They could be soluble in organic solvents, by modifying the nanotube surface, thus changing their physico-chemical properties. In particular these chemical transformations could consider the surface functionalization by species covalently attached. Covalent attachment is preferred for applications, such as polymer-grafting, the focus of this work. In this study, radical functionalization and controlled radical polymer-grafting are proposed as preliminary stages to elaborate carbon nanotubes-polymer nanocomposites.

## References

1. Banerjee, S., T. Hemraj-Benny, and S.S. Wong, *Covalent surface chemistry of single-walled carbon nanotubes*. *Advanced Materials*, 2005. **17**(1): p. 17-29.
2. Sinnott, S.B., *Chemical functionalization of carbon nanotubes*. *Journal of Nanoscience and Nanotechnology*, 2002. **2**(2): p. 113-123.
3. Peng, H., P. Reverdy, V.N. Khabashesku, and J.L. Margrave, *Sidewall functionalization of single-walled carbon nanotubes with organic peroxides*. *Chemical Communications*, 2003: p. 362-363.
4. Hirsch, A., *Functionalization of single-walled carbon nanotubes*. *Angew. Chem. Int. Ed.*, 2002. **41**(11): p. 1853-1859.
5. Jin, Z., X. Sun, G. Xu, S.H. Goh, and W. Ji, *Nonlinear optical properties of some polymer multi-walled carbon nanotube composites*. *Chemical Physics Letters*, 2000. **318**(6): p. 505-510.
6. Shieh, Y.-T., G.-L. Liu, K.C. Hwang, and C.-C. Chen, *Crystallization, melting and morphology of PEO in PEO/MWNT-g-PMMA blends*. *Polymer*, 2005. **46**(24): p. 10945-10951.
7. Shieh, Y.-T. and G.-L. Liu, *Enhancement of PEO crystallization by PMMA-grafted multi-walled carbon nanotubes*. *PMSE Preprints*, 2004. **90**: p. 437-440.
8. Shaffer, M.S.P. and K. Koziol, *Polystyrene grafted multi-walled carbon nanotubes*. *Chemical Communications*, 2002: p. 2074-2075.
9. Tsubokawa, N., *Preparation and properties of polymer-grafted carbon nanotubes and nanofibers*. *Polymer Journal*, 2005. **37**(9): p. 637-655.
10. Sheiko, S.S. and M. Möller, *Visualization of macromolecules - A first step to manipulation and controlled response*. *Chemical Reviews*, 2001. **101**: p. 4099-4123.
11. Tasis, D., N. Tagmatarchis, A. Bianco, and M. Prato, *Chemistry of Carbon Nanotubes*. *Chemical Reviews*, 2006. **106**(3): p. 1105-1136.
12. Schmidt, G. and M.M. Malwitz, *Properties of polymer-nanoparticle composites*. *Current Opinion in Colloid and Interface Science*, 2003. **8**: p. 103-108.
13. Matyjaszewski, K., P.J. Miller, N. Shukla, B. Immaraporn, A. Gelman, B.B. Luokala, T.M. Siclován, G. Kickelbick, T. Vallant, H. Hoffmann, and T. Pakula, *Polymers at Interfaces: Using Atom Transfer Radical Polymerization in the Controlled Growth of Homopolymers and block Copolymers from Silicon Surfaces in the Absence of Untethered Sacrificial Initiator*. *Macromolecules*, 1999. **32**: p. 8716-8724.
14. Cao, A., V.P. Veedu, X. Li, Z. Yao, M.N. Ghasemi-Nejhad, and P.M. Ajayan, *Multifunctional brushes made from carbon nanotubes*. *Nature Materials*, 2005. **4**(7): p. 540-545.
15. Niyogi, S., M.A. Hamon, H. Hu, B. Zhao, P. Bhowmik, R. Sen, M.E. Itkis, and R.C. Haddon, *Chemistry of single-walled carbon nanotubes*. *Accounts of Chemical Research*, 2002. **35**: p. 1105-1113.
16. Ausman, K.D., H.W. Rohrs, M. Yu, and R.S. Ruoff, *Nanostressing and mechanochemistry*. *Nanotechnology*, 1999. **10**: p. 258-262.
17. Srivastana, D., D.W. Brenner, J.D. Schall, K.D. Ausman, M. Yu, and R.S. Ruoff, *Predictions of Enhanced Chemical Reactivity at Regions of Local Conformational Strain on Carbon Nanotubes: Kinky Chemistry*. *Journal of Physical Chemistry B*, 1999. **103**: p. 4330-4337.
18. Gulseren, O., T. Yildirim, and S. Ciraci, *Adsorption on Carbon Nanotubes*. *Physical Review Letters*, 2001. **87**: p. 116802-116806.
19. Park, S., D. Srivastana, and K. Cho, *Generalized Chemical Reactivity of Curved Surfaces: Carbon Nanotubes*. *Nanoletters*, 2003. **3**(9): p. 1273-1277.

20. Zhou, W., Y.H. Ooi, R. Russo, P. Papanek, D.E. Luzzi, J.E. Fischer, M.J. Bronikowski, P.A. Willis, and R.E. Smalley, *Chemical Physics Letters*, 2001. **350**: p. 6-14.
21. Georgaskilas, V., K. Kordatos, M. Prato, D.M. Guldi, M. Holzinger, and A. Hirsch, *Organic Functionalization of Carbon Nanotubes*. *Journal of American Chemical Society*, 2002. **124**(5): p. 760-761.
22. Yang, Q.-H., P.-X. Hou, M. Unno, S. Yamauchi, R. Saito, and K. Takashi, *Dual Raman Features of Double Coaxial Carbon Nanotubes with N-Doped and B-Doped Multiwalls*. *Nanoletters*, 2005. **5**(12): p. 2465-2469.
23. Terrones, M., P.M. Ajayan, F. Banhart, X. Blase, D.L. Carroll, J.C. Charlier, R. Czerw, B. Foley, N. Grobert, R. Kamalakaran, P. Kohler-Redlich, M. Rühle, T. Seeger, and H. Terrones, *N-doping and coalescence of carbon nanotubes: synthesis and electronic properties*. *Applied Physics A*, 2002. **74**: p. 355-361.
24. Bahr, J.L. and J. Tour, M., *Covalent chemistry of single-wall carbon nanotubes*. *Journal of Materials Chemistry*, 2002. **12**: p. 1952-1958.
25. Mawhinney, D.B., V. Naumenko, A. Kuznetsova, J.T.J. Yates, J. Liu, and R.E. Smalley, *Surface defect site density on single walled carbon nanotubes by titration*. *Chemical Physics Letters*, 2000. **324**: p. 213-216.
26. Jiang, K., A. Eitan, L.S. Schadler, P.M. Ajayan, and R.W. Siegel, *Selective attachment of gold nanoparticles to Nitrogen-doped carbon nanotubes*. *Nanoletters*, 2003. **33**(3): p. 275-277.
27. Bahr, J.L. and J.M. Tour, *Highly Functionalized Carbon Nanotubes Using in Situ Generated Diazonium Compounds*. *Chemical Materials*, 2001. **13**: p. 3823-3824.
28. Chen, Y., R.C. Haddon, S. Fang, A.M. Rao, P.C. Eklund, W.H. Lee, E.C. Dickey, E.A. Grulke, J.C. Perdergrass, A. Chavan, B.E. Haley, and R.E. Smalley, *Chemical attachment of organic functional groups to single-walled carbon nanotube material*. *Journal of Materials Research*, 1998. **13**(9): p. 2423-2431.
29. Mickelson, E.T., C.B. Huffman, A.G. Rinzler, R.E. Smalley, R.H. Hauge, and J.L. Margrave, *Fluorination of single-wall carbon nanotubes*. *Chemical Physics Letters*, 1998. **296**: p. 188-194.
30. Walbiner, M. and H. Fischer, *Rate constants for the addition of the benzyl radical to C60 in solution*. *Journal of Physico Chemistry*, 1993. **97**: p. 4880-4881.
31. Morton, J.R., K.F. Preston, P.J. Krusic, S.A. Hill, and E. Wasserman, *ESR studies of the reaction of alkyl radicals with C60*. *Journal of Physico Chemistry*, 1992. **96**: p. 3576-3578.
32. Donnet, J.B., *Structure and reactivity of carbons: from carbon black to carbon composites*. *Carbon*, 1982. **20**: p. 267-282.
33. Tsukagoshi, K., B. Alphenaar, and H. Ago, *Coherent transport of electron spin in a ferromagnetically contacted carbon nanotube*. *Nature*, 1999. **401**: p. 572-574.
34. Gallani, J.-L., L. Bonomme, A. Drury, and W.J. Blau, *Photosensitive magnetism of radicals coupled with carbon nanotubes*. *Organic Electronics*, 2003. **4**: p. 15-20.
35. Adronov, A., C.M. Homenick, Y. Liu, and Z. Yao, *Functionalization of single-walled carbon nanotubes with well-defined polymers*. *Polymer Preprints*, 2005. **46**(1): p. 201-202.
36. Hayashi, S., A. Naitoh, S. Machida, M. Okazaki, K. Maruyama, and N. Tsubokawa, *Grafting of polymers onto a carbon black surface by the trapping of polymer radicals*. *Applied Organometallic Chemistry*, 1998. **12**: p. 743-748.
37. Pena, J.M., *Analysis of radical content on carbon black pigments by electron spin resonance: influence of functionality, thermal treatment and adsorption of acidic and basic probes*. *Polymer Degradation and Stability*, 2000. **71**(1): p. 153-170.
38. Levy, M. and M.J. Szwarcz, *Methyl affinities of aromatic compounds*. *Chemical Physics*, 1954. **22**: p. 1621-1622.

39. Donnet, J.B., *Aroxylic structure of quinonic functions and free radicals on a carbon black surface. II. Thermal polymerization of styrene in the presence of carbon black*. Rev. Gen. Caoutchouc, 1962. **39**(4): p. 583-591.
40. Gessler, A.M., *Evidence for chemical interaction in carbon and polymer associations. Extension of original work on effect of carbon black structure*. Rubber Chemistry and Technology, 1969. **42**(3): p. 858-873.
41. Fujiki, K., *Graft polymerization of vinyl monomers initiated by azo groups introduced onto carbon black surface*. Polymer Journal, 1990. **22**: p. 661-670.
42. Tsubokawa, N., *Radical grafting from carbon black: graft polymerization of vinyl monomers initiated by peroxyester groups introduced onto carbon black surface*. Polymer Journal, 1988. **20**: p. 213-220.
43. Tsubokawa, N., *Cationic grafting from carbon black. I. Graft polymerization of styrene using CO+ClO<sub>4</sub><sup>-</sup> groups on the surface of carbon black*. Journal of Polymer Science, Part A: Polymer Chemistry, 1983. **21**: p. 705-709.
44. Tsubokawa, N., Polymer Bulletin, 1983. **10**: p. 62.
45. Ohkita, K., *Free radical polymerization of vinyl monomers in presence of carbon black*. Carbon, 1975. **13**: p. 443-448.
46. Ohkita, K., *The competitive reactions of initiator fragments and growing polymer chains against the surface of carbon black*. Carbon, 1978. **16**: p. 41-45.
47. Donnet, J.B., *Influence of the nature of carbon black on its free-radical character*. Comptes Rendus Physique, 1959. **249**: p. 97-98.
48. Mehrotra, S., A. Nigam, and R. Malhotra, *Effect of [60]fullerene on the radical polymerization of alkenes*. Chemical Communications, 1997: p. 463-464.
49. Camp, A.G., A. Lary, and W.T. Ford, *Free-Radical Polymerization of Methyl Methacrylate and Styrene with C<sub>60</sub>*. Macromolecules, 1995. **28**: p. 7959-7961.
50. Krusic, P.J., E. Wasserman, B.A. Parkinson, B. Malone, and E.R.J. Holler, *Electron Spin Resonance study of the radical reactivity of C<sub>60</sub>*. Journal of American Chemical Society, 1991. **113**: p. 6274-6275.
51. Wang, C., Z.-X. Guo, S. Fu, W. Wu, and D. Zhu, *Polymers containing fullerene or carbon nanotube structures*. Progress in Polymer Science, 2004. **29**: p. 1079-1141.
52. Baskaran, D., J.R. Dunlap, J.W. Mays, and M.S. Bratcher, *Grafting efficiency of hydroxy-terminated poly(methyl methacrylate) with multiwalled carbon nanotubes*. Macromolecular Rapid Communications, 2005. **26**(6): p. 481-486.
53. Liu, Y., J. Tang, and J.H. Xin, *Fabrication of nanowires with polymer shells using treated carbon nanotube bundles as macro-initiators*. Chemical Communications, 2004. **24**: p. 2828-2829.
54. Liu, Y., D.-C. Wu, W.-D. Zhang, X. Jiang, C.-B. He, T.S. Chung, S.H. Goh, and K.W. Leong, *Polyethylenimine-grafted multiwalled carbon nanotubes for secure noncovalent immobilization and efficient delivery of DNA*. Angewandte Chemie, 2005. **44**(30): p. 4782-4785.
55. Hu, H., Y. Ni, S.K. Mandal, V. Montana, B. Zhao, R.C. Haddon, and V. Parpura, *Polyethyleneimine Functionalized Single-Walled Carbon Nanotubes as a Substrate for Neuronal Growth*. Journal of Physical Chemistry B, 2005. **109**(10): p. 4285-4289.
56. Choi, J.-Y., D.H. Wang, L.-S. Tan, and J.-B. Baek, *Grafting of hyperbranched polyetherketones onto multi-walled carbon nanotubes via A<sub>3</sub> + B<sub>2</sub> approach*. Polymer Preprints, 2005. **46**(2): p. 753-754.
57. Oh, S.-J., H.-J. Lee, J.-Y. Choi, L.-S. Tan, and J.-B. Baek, *In-situ grafting of poly(etherketones) from ab monomers with varying multi-walled carbon nanotube loads*. Polymer Preprints (American Chemical Society, Division of Polymer Chemistry), 2006. **47**(1): p. 399-400.

58. Oh, S.-J., H.-J. Lee, D.-K. Keum, S.-W. Lee, S.-Y. Park, L.-S. Tan, and J.-B. Baek, *Polymerizations of 3- and 4-phenoxybenzoic acids onto carbon nanotubes via electrophilic substitution reaction in polyphosphoric acid*. *Polymer Preprints*, 2005. **46**(1): p. 216-217.
59. Baskaran, D., J.W. Mays, and M.S. Bratcher, *Polymer adsorption in the grafting reactions of hydroxyl terminal polymers with multi-walled carbon nanotubes*. *Polymer*, 2005. **46**: p. 5050-5057.
60. Gao, C., Y.Z. Jin, H. Kong, R.L.D. Whitby, S.F.A. Acquah, G.Y. Chen, H. Qian, A. Hartschuh, S.R.P. Silva, S. Henley, P. Fearon, H.W. Kroto, and D.R.M. Walton, *Polyurea-Functionalized Multiwalled Carbon Nanotubes: Synthesis, Morphology, and Raman Spectroscopy*. *Journal of Physical Chemistry B*, 2005. **109**(24): p. 11925-11932.
61. Xu, Y., C. Gao, H. Kong, D. Yan, Y.Z. Jin, and P.C.P. Watts, *Growing Multihydroxyl Hyperbranched Polymers on the Surfaces of Carbon Nanotubes by in Situ Ring-Opening Polymerization*. *Macromolecules*, 2004. **37**(24): p. 8846-8853.
62. Ku, B.-C., D.K. Kim, J.S. Lee, A. Blumstein, J. Kumar, and L. Samuelson, *Synthesis of water-soluble single-walled carbon nanotube-polyacetylene nanocomposites*. Abstracts of Papers, 231<sup>st</sup> ACS National Meeting, Atlanta, GA, United States, 2006. **POLY-301**.
63. Hsiao, C.-C., T.S. Lin, L.Y. Cheng, C.-C.M. Mar, and A.C.M. Yang, *The Nanomechanical Properties of Polystyrene Thin Films Embedded with Surface-grafted Multiwalled Carbon Nanotubes*. *Macromolecules*, 2005. **38**(11): p. 4811-4818.
64. Hill, D.E., Y. Lin, L.F. Allard, and Y.-P. Sun, *Solubilization of carbon nanotubes via polymer attachment*. *International Journal of Nanoscience*, 2002. **1**(3 & 4): p. 213-221.
65. Hill, D.E., Y. Lin, A.M. Rao, L.F. Allard, and Y.-P. Sun, *Functionalization of Carbon Nanotubes with Polystyrene*. *Macromolecules*, 2002. **35**: p. 9566-9571.
66. Ham, H.T., C.M. Koo, S.O. Kim, Y.S. Choi, and I.J. Chung, *Chemical modification of carbon nanotubes and preparation of polystyrene/carbon nanotubes composites*. *Macromolecular Research*, 2004. **12**(4): p. 384-390.
67. Huang, H.-M., I.-C. Liu, C.-Y. Chang, H.-C. Tsai, C.-H. Hsu, and R.C.-C. Tsiang, *Preparing a polystyrene-functionalized multiple-walled carbon nanotubes via covalently linking acyl chloride functionalities with living polystyryllithium*. *Journal of Polymer Science, Part A: Polymer Chemistry*, 2004. **42**(22): p. 5802-5810.
68. Li, H., F. Cheng, A.M. Duft, and A. Adronov, *Functionalization of Single-Walled Carbon Nanotubes with Well-Defined Polystyrene by "Click" Coupling*. *Journal of the American Chemical Society*, 2005. **127**(41): p. 14518-14524.
69. Nap, R. and I. Szleifer, *Control of carbon nanotube-surface interactions: the role of grafted polymers*. *Langmuir*, 2005. **21**(26): p. 12072-12075.
70. Park, S.J., M.S. Cho, S.T. Lim, H.J. Choi, and M.S. Jhon, *Synthesis and dispersion characteristics of multi-walled carbon nanotube composites with poly(methyl methacrylate) prepared by in-situ bulk polymerization*. *Macromolecular Rapid Communications*, 2003. **24**(18): p. 1070-1073.
71. Park, S.J., M.S. Cho, S.T. Lim, H.J. Choi, and M.S. Jhon, *Electrorheology of multiwalled carbon nanotube/poly(methyl methacrylate) nanocomposites*. *Macromolecular Rapid Communications*, 2005. **26**(19): p. 1563-1566.
72. Qin, S., D. Qin, W.T. Ford, J.E. Herrera, and D.E. Resasco, *Grafting of Poly(4-vinylpyridine) to Single-Walled Carbon Nanotubes and Assembly of Multilayer Films*. *Macromolecules*, 2004. **37**(26): p. 9963-9967.
73. Mylvaganam, K. and L.C. Zhang, *Nanotube Functionalization and Polymer Grafting: An ab Initio Study*. *Journal of Physical Chemistry B*, 2004. **108**(39): p. 15009-15012.
74. Viswanathan, G., N. Chakrapani, H. Yang, B. Wei, H. Chung, K. Cho, C.Y. Ryu, and P.M. Ajayan, *Single-step In-situ Synthesis of Polymer-grafted Single Wall Nanotube Composites*. *Journal of American Chemical Society*, 2003. **125**(31): p. 9258-9259.

75. Kong, H., C. Gao, and D. Yan, *Functionalization of Multiwalled Carbon Nanotubes by Atom Transfer Radical Polymerization and Defunctionalization of the Products*. *Macromolecules*, 2004. **37**(11): p. 4022-4030.
76. Ramirez, S.M. and D.Y. Sogah, *Nitroxide-Mediated Living Radical Polymerization from Carbon Nanotubes*. *PMSE Preprints*, 2004. **91**: p. 493-494.
77. Datsyuk, V., C. Guerret-Piecourt, S. Dagreou, L. Billon, J.-C. Dupin, E. Flahaut, A. Peigney, and C. Laurent, *Double walled carbon nanotube/polymer composites via in-situ nitroxide mediated polymerization of amphiphilic block copolymers*. *Carbon*, 2005. **43**(4): p. 873-876.
78. Hong, C.-Y., Y.-Z. You, and C.-Y. Pan, *Synthesis of Water-Soluble Multiwalled Carbon Nanotubes with Grafted Temperature-Responsive Shells by Surface RAFT Polymerization*. *Chemistry of Materials*, 2005. **17**(9): p. 2247-2254.
79. Cui, J., W. Wang, Y. You, C. Liu, and P. Wang, *Functionalization of multiwalled carbon nanotubes by reversible addition fragmentation chain-transfer polymerization*. *Polymer*, 2004. **45**(26): p. 8717-8721.
80. Adronov, A. *Functionalization of single-walled carbon nanotubes with polymers: New approaches to highly soluble nanotubes*. in *Abstracts of Papers, 227<sup>th</sup> ACS National Meeting*. 2004. Anaheim, CA, United States.
81. Baskaran, D., J.W. Mays, and M.S. Bratcher, *Polymer-grafted multiwalled carbon nanotubes through surface-initiated polymerization*. *Angewandte Chemie*, 2004. **43**(16): p. 2138-2142.
82. Choi, J.H., S.B. Oh, J. Chang, I. Kim, C.-S. Ha, B.G. Kim, J.H. Han, S.-W. Joo, G.-H. Kim, and H.-j. Paik, *Graft Polymerization of Styrene from Single-Walled Carbon Nanotube using Atom Transfer Radical Polymerization*. *Polymer Bulletin*, 2005. **55**(3): p. 173-179.
83. Qin, S., D. Qin, W.T. Ford, D.E. Resasco, and J.E. Herrera, *Functionalization of Single-Walled Carbon Nanotubes with Polystyrene via Grafting to and Grafting from Methods*. *Macromolecules*, 2004. **37**(3): p. 752-757.
84. Cheng, B., Y. Li, and C. Shen, *Polymerization of styrene from multiwall carbon nanotubes*. *Abstracts of Papers, 228<sup>th</sup> ACS National Meeting*, Philadelphia, PA, United States, 2004. **POLY-075**.
85. Fragneaud, B., K. Masenelli-Varlot, A. Gonzalez-Montiel, M. Terrones, and J.-Y. Cavailié, *Efficient coating of N-doped carbon nanotubes with polystyrene using atomic transfer radical polymerization*. *Chemical Physics Letters*, 2006. **419**(4-6): p. 567-573.
86. Gao, C., C.D. Vo, Y.Z. Jin, W. Li, and S.P. Armes, *Multihydroxy Polymer-Functionalized Carbon Nanotubes: Synthesis, Derivatization, and Metal Loading*. *Macromolecules*, 2005. **38**(21): p. 8634-8648.
87. Gao, C., H. Kong, and D. Yan, *Controlled functionalization of carbon nanotubes by in situ polymerization strategy*. *AIP Conference Proceedings*, 2004. **723(Electronic Properties of Synthetic Nanostructures)**: p. 193-196.
88. Li, L. and C.M. Lukehart, *Synthesis of Hydrophobic and Hydrophilic Graphitic Carbon Nanofiber Polymer Brushes*. *Chemistry of Materials*, 2006. **18**(1): p. 94-99.
89. Tsarevsky, N.V., W. Wu, J.L. Hudson, T. Kowalewski, J.M. Tour, and K. Matyjaszewski, *Grafting of well-defined polymers from the surface of functionalized single-walled carbon nanotubes via atom transfer radical polymerization and visualization of the polymer-nanotube hybrids by atomic force microscopy*. *Polymer Preprints*, 2005. **46**(1): p. 203-204.
90. Hong, C.-Y., Y.-Z. You, D. Wu, Y. Liu, and C.-Y. Pan, *Multiwalled Carbon Nanotubes Grafted with Hyperbranched Polymer Shell via SCVP*. *Macromolecules*, 2005. **38**(7): p. 2606-2611.
91. Kong, H., W. Li, C. Gao, D. Yan, Y. Jin, D.R.M. Walton, and H.W. Kroto, *Poly(N-isopropylacrylamide)-Coated Carbon Nanotubes: Temperature-Sensitive Molecular Nanohybrids in Water*. *Macromolecules*, 2004. **37**(18): p. 6683-6686.

92. Kong, H., P. Luo, C. Gao, and D. Yan, *Polyelectrolyte-functionalized multiwalled carbon nanotubes: preparation, characterization and layer-by-layer self-assembly*. *Polymer*, 2005. **46**(8): p. 2472-2485.
93. Kong, H., C. Gao, and D. Yan, *Constructing amphiphilic polymer brushes on the convex surfaces of multi-walled carbon nanotubes by in situ atom transfer radical polymerization*. *Journal of Materials Chemistry*, 2004. **14**(9): p. 1401-1405.
94. Liu, Y., Z. Yao, and A. Adronov, *Functionalization of Single-Walled Carbon Nanotubes with Well-Defined Polymers by Radical Coupling*. *Macromolecules*, 2005. **38**: p. 1172-1179.
95. Matyjaszewski, K., ed. *Controlled radical polymerization*. ACS Symposium Series 685. 1998, American Chemical Society: San Francisco, CA. 483.
96. Matyjaszewski, K. and T.P. Davis, *Handbook of radical polymerization*, ed. H. Wiley-Interscience. 2002: John Wiley & Sons Inc. 920.

# **Chapter 3.**

## **Polymer-carbon nanotube composites**

The chapter presents some of the fundamental ideas about nanocomposites especially focusing on polymers-carbon nanotubes composites. Among them, the processing methods, properties and characterization will be discussed. Particularly, the challenges found when carbon nanotubes are used as filler will be outlined. In the final of the chapter, an overview of carbon nanotube composites with polystyrene and polyethylene oxide, as polymer matrices will be present.

In particular, this thesis is interested in the preparation protocol of composites of PS, PEO and PS-PEO blends with carbon nanotubes. Thus, this chapter will give some of the main ideas, viable routes and tools to reach it.

### **3.1. Introduction**

A composite material is made of two or more constituents with significant different physical or chemical properties. They are distinguished by the nature of their constituents and by the geometry and arrangement of the disperse phase in the matrix. The properties of the new material are dependant upon the properties of the constituent materials, as well as the properties of the interface.

The composites are formed by the matrix, and the filler or reinforcement. The matrix of the composites could be formed by metals, ceramics or polymers materials.

In particular, the nanocomposites, i.e. materials formed with nano-sized fillers, display superior properties at lower loadings than conventional composites because of the filler nanometric size, huge specific surface areas, and their high aspect ratio. These characteristics are of fundamental importance in the understanding of the structure-property relationship of nanocomposites due to their effect on morphology. Thus, the

nanocomposites can be divided in three categories according to the reinforcement materials [1]: (i) particles (silica, metal and other organic and inorganic particles), (ii) layered materials (graphite, layered silicate, and other layered minerals), and (iii) fibrous materials (nanofibers and nanotubes).

### 3.1.1. Carbon nanotubes as nanofillers

Carbon nanotubes are ideal fillers for incorporation into composite systems, among them ceramics and polymer matrices materials, due to their high aspect ratio, extremely large surface areas [2], physico-chemical properties [3-5], together with the need for only small volume fractions to obtain desired properties. Carbon nanotubes [6] present high Young modulus, tensile strength, electrical conductivity and thermal conductivity, among other interesting properties (for a detail description of the nanotube properties see Chapter 1). Therefore, the composites prepared using carbon nanotubes as fillers could use for the development of advanced multifunctional materials.

According to the description a great kind of composite materials could be prepared changing the materials (matrix, the nanotube type, etc), and the processing methods.

### 3.1.2. Types of carbon nanotubes composites

The types of nanocomposites formed using carbon nanotubes according to their chemical compositions and structures, are summarized in Fig. 3.1.

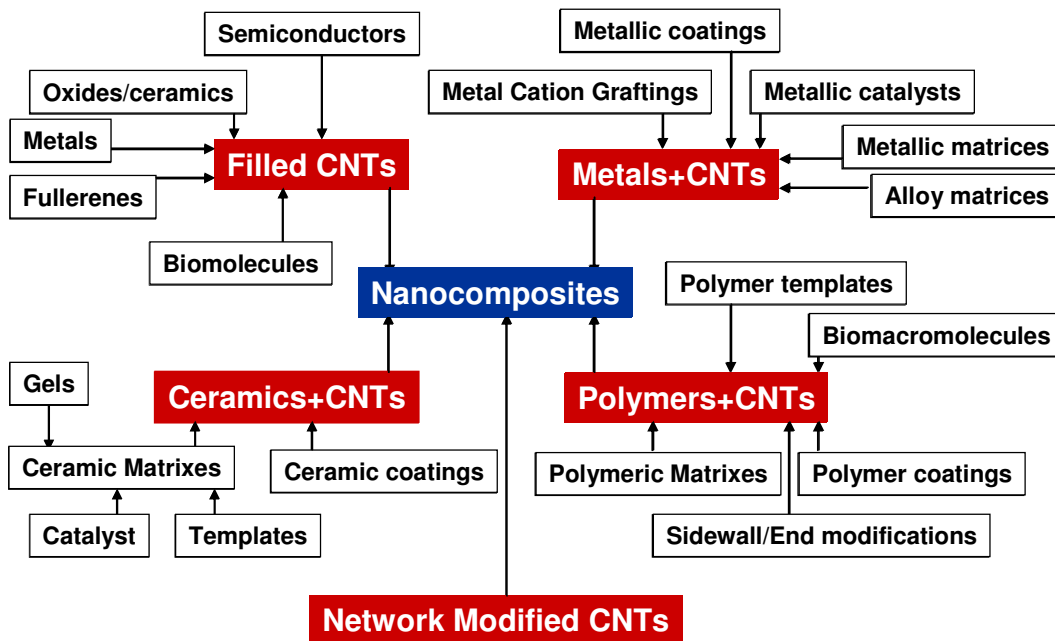


Fig. 3.1. Types of nanocomposites prepared using carbon nanotubes [7].

In particular, this thesis is focused on the study of polymer composites prepared with fibrous nanofillers, particularly nanotubes, where the nanotubes and the polymer matrices present a contrast in their thermal, electrical and mechanical properties.

## 3.2. Polymer-CNT composites

The reinforcement of polymers with nanofillers is a viable alternative to conventional filler-polymer systems and polymer blends. Polymer-nanotube composites combine the unique properties of nanotubes with the ease of processability of polymers.

In particular, SWNTs and MWNTs have been successfully used as filler in several polymeric matrices[8-16], including polyamides, polyesters, polycarbonates and their blends, polystyrene and high performance polymes such as polyphenylene sulphide (PPS), PEI, polyetheretherketone (PEEK), and polyolefins. In these composite materials, a variety of property enhancements were reported, such as the mechanical, electrical, optical and thermal when carbon nanotubes have been used as fillers in polymers.

Some of the advantages of polymer-CNT composites are the necessity of low fraction content of CNT as fillers, light in weight, and finally, the possibility to design multifunctional materials that combine structural, electrical, thermal and mechanical properties.

### 3.2.1. Processing methods of polymer-CNT composites

The main challenge in the polymer-CNT composite preparation is the implement of carbon nanotube amazing properties on a macroscale composite, combining the choice of materials with the appropriate processing methods.[17]

Different processing methods have been reported in literature to prepare polymer-nanotube composites; among them, melt mixing, *in situ* polymerization and solution processing are the main processes discussed. Using these different techniques a great number of polymer nanocomposites can be processed, either thermoplastic or thermoset, amorphous or semicrystalline.[18] In all processing cases it is important to keep the filler volume fraction as low as possible in order to maintain the mechanical properties and to control the viscosity increment which reduces processing ease.

#### *Preprocessing*

In the case of carbon nanotubes used as fillers, a preprocessing step has to be added to prepare the materials.

1. Purification of carbon nanotubes to eliminate non-nanotube material.
2. Deagglomeration of nanotube ropes for dispersing individual nanotubes.
3. Chemical functionalization of carbon nanotubes for improving nanotube/matrix interactions for processability and property enhancement.

All of these topics were mentioned in Chapter 2 in detail. Furthermore, additional commentaries about the chemical functionalization of carbon nanotubes to be used as nanofillers in polymer composites will be discussed in section 3.2.3.

### *Melt-mixing*

Carbon nanotubes could be incorporated into the polymer melt using mechanical shear.

Melt mixing is particularly desirable when thermoplastic polymers are used as matrices because of the speed, simplicity and availability of these processes in the plastic industry. In fact, the classical industrial processing techniques of extrusion and melt compounding are currently used for microsized and nanosized fillers. Additional advantages of the method involve that the system could be carried on free of solvents and contaminants presents in other processing methods. Recycling thermoplastic matrices could be also possible improving cost-benefit and diminishing the pollution.

In this technique, the viscosity increase due to nanoparticles can affect the incorporation process; nevertheless, it has been observed that melt flow is higher in CNT filler than using other nanofillers like carbon fibers.

### *In situ polymerization*

In this method the dispersion of the fillers is performed in the monomer or prepolymer before initiate polymerization step. The main advantage of method is improving dispersion and integration between the phases, but also that the reinforcement is obtained on a molecular scale.

### *Solution processing*

Solution processing use a solvent in which carbon nanotubes and polymers are first dispersed separately and then mixed together. Polar and non polar solvents could be used, depending on the polymer chemistry, but also in the carbon nanotube characteristics due to preprocessing.

In this technique the main challenge is to obtain a stable suspension of the fillers in the chosen solvent and during film forming. This stabilization depends on the chemical functionalities of carbon nanotubes and polymer. Some ways to improve the stabilization of the fillers are

- (i) by functionalization of the surface of the carbon nanotubes by low molecular weight or high molecular weight species (i.e. polymers), providing steric stabilization, or
- (ii) by adding surfactant molecules, either ionic for electrostatic repulsion or nonionic for steric stabilization.

In both cases, the modification of carbon nanotubes surface by covalent attachment, or addition of surfactant molecules modifies the final properties of the nanocomposite.

A variation of the solution processing method considers the mixture of various aqueous suspensions (colloids) with carbon nanotubes, as in the case of emulsion polymerization. Anyway, in all cases the final materials of solution processing methods have to be obtained by solution casting.

Solution processing have many advantages; among them, the low viscosities generated that facilitate mixing and dispersion of the CNTs, the use on both thermosets and thermoplastic polymers.

### 3.2.2. Critical issues in polymer-CNT composites processing

As was observed, several processing methods are available to produce polymer-CNT composites. Although the techniques are inherently different, all of them try to address the dispersion, interfacial bonding and alignment of nanofillers in the polymer matrix that directly affect the composite properties. In fact, the optimization of these critical issues was proposed to improve the polymer-CNT composite performance by an efficient exploitation of CNT properties. The main reason is that the magnitude of property enhancements predicted for nanotube-based polymer composite is not being achieved yet.[14, 19]

#### 3.2.2.1. Dispersion of nanotubes within the matrix

The effective utilization of CNTs in composite applications depends strongly on the ability to disperse them individually and uniformly throughout the matrix, without destroying their structure, or reducing their aspect ratio. Thus, appropriate dispersion of the nanotubes is essential to achieve required nanocomposite properties and isotropy.

The importance of dispersion process in nanocomposite materials was described by Chazeau *et al* [18] when they analyze the relation microstructure and composite properties. They stated several facts. First of all, in materials science is generally accepted that an increase in the developed interface allows an optimum mechanical stress transfer between the filler and the matrix. Some other reports described that the presence of certain amount of aggregates leads to an increase in the elastic properties. Nevertheless, the presence of large agglomerates is known to have a dramatic effect on the ultimate properties of the composite and a uniform dispersion of fillers in the matrix is needed to obtain homogeneous properties at a mesoscopic level. Thus they concluded that an optimum dispersion (uniform and without large aggregates) is needed in order to reach the best mechanical behavior.

Some of the nanofillers properties than impacts on their dispersability on the polymer matrix are the specific surface area (SSA) and the aspect ratio.

Even differences in the specific surface area (SSA) of SWNT (1300 m<sup>2</sup>/g) and MWNT revealed changes in the nanotube dispersability in polymers. Thus, according to Gogny *et al* [2] the SSA for SWNT causes agglomeration in polymer nanocomposite, whereas the smaller SSA of MWNT had shown better dispersability.

Furthermore, Martin *et al* [20] studied the influence of the nanotube aspect ratio in the dispersability and stability of CNT dispersions. They found that while the long nanotubes, i.e. high aspect ratio, remained well-dispersed, the shorter ones were found to have formed small agglomerates immediately after the stirring was stop. Even more, the agglomerates formed by the short nanotubes were much bigger than those consisting of the long nanotubes material.

Different procedures have been developed to efficiently disperse nanotubes in polymer matrices using the processing methods of nanocomposites, already commented. Some reported examples are melt-mixing [21-23], *in situ* polymerization under sonication

[24], solution process with the aid of ultra-sonication [25], acid treatment [26], or use of surfactants and processing aids, and the combination of solution-casting and melt mixing processing methods [22], among others.

From them, high energy sonication of solutions of disentangled nanotubes and polymers [25] appears to be one of the most efficient. This approach suggests that the nanotubes be soluble in the medium in order to achieve optimal dispersion. Hence surface modification of nanotubes to make them compatible with solution-processing methods becomes necessary. The determination of the practical conditions, like time and power, have to be made to avoid degradation of the fillers. On the opposite of ultrasonication method, the direct mixing polymer-nanotubes do not lead to homogeneity because of the lack of compatibility between the polymer chains and the nanotubes.

### **3.2.2.2. Interaction of nanotubes with the polymer matrix**

As was mentioned in the previous section, the filler dispersion is a fundamental issue in the preparation of polymer nanocomposites to obtain isotropic reinforced materials. However, the properties enhancement is also related to the interaction of the fillers with the polymer matrix at interface, i.e. interfacial bonding or interfacial strength. Inherently weak interactions between the nanotubes and polymer result in poor interfacial adhesion, which can lead to nanotube aggregation within the matrix and potentially weaken the composite mechanical performance. Therefore, the interfacial properties are fundamental for the macroscopic behavior of composite materials.

Several factors are related to an interaction polymer-matrix enhancement. The uniform and individual dispersion of carbon nanotubes in a polymer matrix by itself maximize their contact surface area with the matrix. Even more, the inherent filler SSA determines the extent of interface for stress-transfer.

High aspect ratio increases the filler interaction with itself. Thus, fiber-shaped fillers with higher aspect ratio than spherical particles exhibit better interaction at the same volume fraction [2]. For the case of carbon nanotubes an increasing nanotube length, i.e. aspect ratio, appears to decrease the percolation threshold, as well the maximum composite conductivity for a given filler weight fraction [20].

Furthermore, the modification of nanotube surfaces by the introduction of vacancies, defective sites, or functional groups on the nanotube surface have proved to enhance their interactions and gives interfacial strength of the materials. In addition, a tailored functionalization can lead to the formation of covalent bonds and/or additional dipole-dipole interactions between CNTs and the polymeric matrix, resulting in a strengthened interface and an improved wettability of the CNTs [27-29]. The effect of a linkage between the nanotubes and the polymer, which should lead to improved interfacial interactions with polymer, as was confirmed by the calculations of Frankland [29]. They found that functionalization of less than 1% would improve the interaction between nanotubes and the polymer without decreasing their strength significantly.

Several polymer-carbon nanotubes composite systems have been experimentally and theoretically studied in relation to the interaction of carbon nanotubes with polymers. Nevertheless, until now there is a lack of understanding in the area. Anyway, some of the

obtained experimental results and the main results on the polymer-CNT composite interface interaction are following exposed.

Various reports hint at the existence of strong adhesion at the nanotube-polymer interface, which would lead to effective stress transfer. This adhesion will be a strong function of physical and chemical influences, such as the polymer properties in the vicinity of the fiber and covalent bonding between the polymer, and defect or functionalized sites in the nanotube [19, 30]. In particular for PS-CNT [11, 19], epoxy-CNT [28, 31] and polyethylene butane-CNT [30] composite systems, among others, polymers adhere well to CNT at nanometer scale. Nevertheless, until now most of experimental measurements of the nanotube-polymer interaction has been indirect and in some cases only qualitative:

Polymer wetting of nanotubes have been observed in nanocomposite samples using TEM without giving the magnitude of the interfacial adhesion.

The deformation of nanotubes in a polymer, examination of individual nanotube fragmentation under composite loading and mechanical characterization of bulk nanotube-polymer nanocomposite systems have been followed using Raman spectroscopy [30].

The interfacial strength measurement among polymer and carbon nanotubes is still a difficult procedure, thus most of the results are obtained from theoretical predictions [29]. However, some works performed pull-out test to evaluate the interfacial strength. Among them, Cooper *et al* [31] made pull-out tests using an SPM for individual nanotubes from an epoxy matrix and they found high values for the interfacial shear strength comparing with those of the fiber-polymer interfaces ones. This behavior had been correlated using molecular dynamics to the existence of covalent bonding between nanotube and polymer that strengthen the interface, highlighting also the fact that the mechanical behavior the ultrathin polymer layer at the interface may be different than that of bulk polymers. The SPM technique had some problems in the interfacial strength determinations, as the pullout partial or complete, bending and breakage. Thus, the values could be higher than the real ones because involve the values to deform the polymer matrix.

Similar measurements were obtained by Barber *et al* [30]. They performed nano-pull out experiments for a polyethylene-butene/MWNT system using AFM. The obtained results stated that the polymer matrix near from the interface is able to withstand stresses higher than those supported by the bulk polymer. The relatively high stress values indicated physical, but also chemical interactions among filler and matrix.

Other reports, presented detaching results for individual SWNT and MWNT from an epoxy matrix using SPM and TEM. As in the previous case, composite materials of carbon nanotubes seemed to present higher interfacial strength than polymer-fiber composites (lower than 10 MPa) [32].

Theoretical results from simulation revealed also interesting phenomena. Whereas van der Waals interactions between reinforcement and polymer matrix produces an interfacial strength of polyethylene-CNT system 2 MPa [29], strong bonding like covalent interfacial strength can be as high as 100 MPa [33]. In the particular case of PS-CNT nanocomposites, Liao *et al* [33] found values of 160 MPa as shear-stress value between filler and matrix using molecular simulation. The authors considered that high interfacial shear stress could be attributed to the intimate contact between the CNT and the polymer matrix.

In general, in experimental and theoretical results an important enhancement in interfacial strength in polymer-CNT composites could be expected (from around hundred

of MPa) using functionalized nanotubes, because the measured separation stress of the tubes from the polymer was found to be remarkably high. This behavior indicates that carbon nanotubes are effective at reinforcing polymer with superior than most advanced microfiber reinforced nanocomposites.

### 3.2.2.3. Alignment and orientation of nanotubes within the matrix

Dispersion and interfacial strength were determinant in the macroscopic properties of nanocomposites. At the same manner, the alignment of nanotubes could enhance some polymer-nanocomposite properties at macroscopic level [25, 34].

The dispersion of nanotubes in a solvent, or matrix material is necessary for aligning and orienting them. In fact, in most of the processing methods, the nanotube alignment was observed to depend strongly on the quality of initial dispersion: well-dispersed and separated nanotubes could be aligned, while entangled non-separated nanotubes formed dense aggregates [35].

In general, there still exist a lack of control on the alignment and orientation of nanotubes in a polymer matrix due to the nano-sized scales. Thus, many modifications to the already known techniques for fibers have to be found.

Melt-mixing methods could be use to control the nanotubes alignment. Spinning of extruded melt samples could be used to make well aligned composites with well aligned nanotube dispersion. When using extrusion numerous fiber-aligning techniques have been developed, like increasing the residence time in the die channel, or altering the die design to control the orientation of the fibers. Injection molding was also found to induce significant alignment in some kind of polymers.

Alignment of CNTs could also be controlled in solution. Sometimes, the film formed could be mechanically stretched to align the nanotubes. Otherwise, electrospinning method, high voltage electric field generated between the polymer solution and a metallic screen, forms nanocomposite fibrils, which contain aligned CNTs. Electrophoresis may be applied as well by applying a voltage between a carbon fiber and a nanotube suspension that produces a SWNT fiber, which is subsequently spun through a polymer solution.

Additional techniques involve deposition of carbon nanotubes suspension under magnetic field, and synthesis of aligned nanotubes by deposition of nanotubes onto chemically modified substrate [36].

### 3.2.3. Modification of CNT for composite processing

As have been commented, the carbon nanotubes characteristics as nanofillers and their physico-chemical properties are ideal to produce polymer nanocomposites. Nevertheless, two main problems that difficult the production of nanocomposite materials appears: (i) the insolubility of carbon nanotubes in most solvents, and (ii) the weak interaction matrix-nanotube usually performed only through van der Waals forces leading poor interfacial adhesion and nanotube aggregation. In particular, the chemical functionalization of carbon nanotubes has been proposed [6, 26] to overcome these problems. Approaches to the chemical functionalization of nanotubes to promote the

adhesion and stress transfer among matrix and reinforcements consider [28, 29] (i) the low molecular weight functionalization [37, 38] with suitable groups, and (ii) the polymer attachment to nanotubes [1]. The polymer attachment ideally provides the best interface with the host polymer.

### 3.2.3.1. Group functionalization of CNT

It has been observed that blending of un-functionalized nanotubes with polymer matrix often does not offer significant improvements in composite performance [39]. On the contrary, the group functionalization of CNT is an efficient way of interface engineering to promote better polymer-carbon nanotubes interactions, like better dispersability [40], because of the steric and electrostatic repulsion of the functional groups [28].

Most of the chemical groups attached on nanotube surface have been described in section 2.3. Particularly, acid treatment, inducing oxidation, introduces a lot of defective sites in the nanotube structure leading to an uncontrolled loss of nanotube intrinsic properties [26, 28]. Other kind of functionalities [41], as amines [28, 42], aryl halide [43], diazonium compounds [40], fluoride [44], etc. have been intensively studied and could be performed in a controlled way to diminish the properties reduction. Sometimes, the attached functional groups have been used to also promote polymer-grafting [43, 45-47] by *in situ* polymerization or functional group reaction approach. Alternatively, doped-carbon nanotubes (nitrogen or boron) were also began to be used as reinforcing for polymer composites. Among the studied systems, Eitan *et al* [48] developed a technique to homogeneously disperse  $CN_x$  nanotubes in an epoxy matrix to prepared polymer composites. In addition, boron-doped carbon nanotubes in polystyrene nanocomposites [49] were also evaluated. In both cases, interesting and positive results had been obtained.

In general, the experimental results related to the performance of composites contained functionalized nanotubes are also supported by theoretical studies [50].

### 3.2.3.2. Polymer attachment on CNT surface

An alternative route to produce composites with enhanced interface properties, and that could not severely modify the properties of the individual tubes, is to graft polymer chains on the surface of the nanotube. It is desirable that the grafted-polymers could be selected to be compatible with the polymer matrix.

The grafting of the polymer could be prepared by several approaches like “grafting to”, “grafting from”, and functional group reaction, already commented in section 2.4.

As in the group functionalization case, the effect of polymer-functionalized nanotubes on composite performance has also been investigated and many experimental results were reported, along with various theoretical confirmations.

Among the reported systems, it could be possible to mention the mechanical properties (strength and toughness) enhancement of polypropylene-functionalized nanotubes composites of about 3.8 and 4.0, as well as in the storage modulus at room temperature of PMMA/PMMA-grafted MMWNT composites [51], the storage modulus, tensile strength, glass transition and load transfer properties enhancement in PMMA/functionalized MWNT [52], the good matrix-filler interaction in several cases on

PS-grafted SWNT by *in situ* polymerization [53, 54], among many others. In fact, many of the experimental results have been supported by theoretical calculations [29].

It is worth to mention that this thesis proposed the use of nitrogen doped carbon nanotubes (CN<sub>x</sub>) which could be subsequently chemically modified by polymer attachment to prepare polymer-CNT composites. The evaluation of the relation microstructure-properties will be also proposed for thermal, electrical and mechanical properties.

### 3.2.4. Physical properties of polymer-CNT composites

Carbon nanotubes have been incorporated into polymer matrices to enhance different polymer properties, like to improve thermal resistance, to improve mechanical strength, to impart conductivity, or to enhance the conductivity of the polymer and, many others like induce crystallization effects. Another goal is to overcome the drawbacks of carbon nanotube for large-scale applications, such as improve their solubility, their dispersibility, their reactivity, and enhance their interfacial interactions in composites.

The section below enumerates some of the properties observed in polymer composites as nanotubes were added. In all cases, it has to be emphasized that the morphological characteristics, i.e. microstructure of the materials had determined the properties.

#### 3.2.4.1. Morphological properties of polymer-CNT composites

The morphological properties of polymer-CNT composites strongly depend on the materials, processing and their critical processing issues. In the same manner, the morphology characteristics affect the material performance. Therefore, most of all of the reported results in composite production dedicate some effort to described the morphology of their products before characterize them physically.

The investigation of nanocomposite morphology needs techniques that can provide details down to a subnanometer size scale. The geometrical arrangement and sized of the polymer and nanofillers phases have to be observed (Table 3.1). The techniques could be divided in:

- (i) microscopies techniques that gives direct local observation. In this case a lot of observations have to be performed to obtain an average result, and
- (ii) scattering techniques that provide average characterization on a large volume, but require the use of various models and hypothesis.

Excellent discussions about the applications of each technique to the nanocomposite characterization could be found elsewhere.

#### 3.2.4.2. Thermal properties of polymer-CNT composites

The thermal properties of polymer-CNT composite were extensively studied. The addition of functionalized or non functionalized carbon nanotubes in most of the polymeric matrices seemed to result in a shift on the glass transition temperature (T<sub>g</sub>), depending on the filler type and content [55]. As the nanotube-polymer interaction was improved using

adequate functional groups, a stronger shift of the  $T_g$  was observed due to the formation of covalent bonds [56]. The  $T_g$  increment effect was explained in most of the literature reports as a reduction of the mobility of the polymeric chains around the surface nanotubes by the interfacial interactions. These observations were corroborated by Wei *et al* using classical molecular dynamics. They showed that addition of CNTs into a polymer matrix increases the  $T_g$ , but also thermal expansion, and diffusion coefficients in the composite above  $T_g$ .

Table 3.1. Microscopy and Spectroscopy techniques most used in morphological characterization of nanocomposites and their corresponding size range. [18]

Characterization technique	Size range
Wide-angle X-ray Scattering (WAXS)	0.01 nm - 3 nm
Small-angle X-ray or Neutron Scattering (SAXS, SANS)	1 nm - 200 nm
Transmission Electron Microscopy (TEM)	0.15 nm - 1000 nm
Scanning Electron Microscopy (SEM)	1 nm - 1 mm
Atomic Force Microscopy (AFM)	0.2 nm - 0.2 mm
Optical Microscopy (OM)	300 nm - 1 mm
Light Scattering	300 nm - 0.2 mm

Thermogravimetric Analysis (TGA) measurements from the thermal properties of functionalized nanotube-polymer composites revealed additional degradation curves, attributed to the species adsorbed, or covalently linked on nanotube surface. This degradation process is added to, and sometimes modify (by a retardation due to re-absorption of species during polymer decomposition for example [57]) the separately observed for nanotubes and bulk polymer chains. This behavior could be explained because the thermal stability is affected by the presence of the nanotubes and their high thermal conduction. They also interfere with the mobility and crystallization of the polymer chains. These results enable the composite to be used for high temperature applications.

Furthermore, the crystallization and morphology of semicrystalline polymers can be strongly affected by the addition of carbon nanotubes. Lozano and Barrera [58] showed that the addition of catalytically grown carbon nanofibers can promote nucleation of polypropylene. Similar observations were made by Valentini *et al* [59]. In general, the crystallinity of polymer has shown to be increased with the addition of carbon nanotubes [60]. Changes in the crystal structure of polymers can also be induced by nanotubes [61].

Finally, the high thermal conductivity and thermal stability of polymer-CNT composites has a number of applications particularly in heat sinks for electronics, motors and tires. These property is especially important in thermal management applications and in precision structures where thermally induced distortions reduce the ability to hold tolerances.

### 3.2.4.3. Electrical properties of polymer-CNT composites

Carbon nanotubes exhibit high aspect ratio, excellent electrical properties that make them suitable to use as conductive fillers in polymer composites. Additionally, nanotubes

present the tendency to become entangled into a three-dimensional interconnecting network that favors the connectivity and conductivity. In fact, it was reported conductivity at extremely low CNTs contents in a polymer matrix because of the large CNT aspect ratio [62].

The study of electrical conductivity in polymer composites due to the addition of conductive nanofillers begins to be understood. By the moment, two main approaches have to be considered, the statistical percolation theory and the colloids theory. Nevertheless, most of the literature reports on polymer-carbon nanotube composites use the percolation theory in terms of excluded volume (for non spherical fillers). Generalities from percolation and colloids theory could be found elsewhere. Some of the phenomena analysis involving polymer-CNT composites will be summarize below.

The experimentally observed percolation threshold values strongly depend on the particle shape and aspect ratio. Percolation threshold decrease significantly as the aspect ratio of the filler particles increases [63]. Thus fibril shaped filler particles such as conductive polymers have been an attractive choice in recent years.

The advantages of CNTs with their high aspect ratio (around 1000) leads to a lower percolation threshold compared to other spherical particles like carbon black the most common filler in polymers that require high loadings to provide appropriate level of conductivity.

In addition, the maximum composite conductivity that can be achieved is higher for carbon nanotubes than for carbon black. Such an increase is expected given the reduced number of filler-filler hops required to cross a given distance [64]. In the same manner, when comparing MWNT vs. SWNT, the firsts are preferred because they are always conductive. This is not the case for SWNTs which can be semi-conductive or metallic as a function of their chirality [10]. Even more, experimental percolation thresholds for both types of nanotubes cannot be explained by statistical percolation theories based on an excluded volume approach. The deviation observed is not a purely geometrical problem but rather relates to local improvements in nanotube contacts due to segregation [64]. In addition, it was observed that the resistivity of composite films with thicker nanotubes were generally higher than for films made with smaller diameter nanotubes due to the mean separation between nanotubes at same volume fraction [62].

It is important to notice that the percolation threshold depends upon the morphology of the conductive network, which again is influenced by the processing route. The highest efficiency can be reached by increasing the ionic concentration [65].

Respect to the critical issues when processing polymer-CNT composites, extremely uniform dispersion of the conductive filler could be disadvantageous if it is searching conductivity at low concentration. Anyway the quality of the initial nanotube dispersion has a pronounced effect on the percolation threshold

In some cases like extrusion processing materials, it was observed that the alignment of CNTs in the composite reduces the contact between the nanotubes thereby increasing the level of the percolation threshold. Thus, extruded fibers in general required higher concentration of nanotubes than solution casting films to achieve the percolation threshold [62]. Nevertheless, aligned carbon nanotubes have lower percolation threshold than entangled carbon nanotubes even though the maximum conductivity is the same.

The use of raw or functionalized nanotubes as conductive fillers remains as a challenge because even though in some cases the functionalization aid in their dispersion in

the matrix, sometimes reduces the quality and quantity of electrical contacts between the nanotubes because of the adsorbed or covalently attached layer of molecular species or polymer [57].

For economic reasons, the achievement of extremely low percolation threshold is important and has been a driving force behind much research.

Benoit *et al* [66] suggested that SWNTs network in the composite films behaves as a classical percolation network. The very small percolation threshold is indeed due to the strong anisotropy of the SWNTs. It confirms, according to the author, that the remaining particles (amorphous carbon, polyhedral particles, catalysts) from the starting material do not play a significant role in the transport process. Some deviations over pure statistical percolation model were observed by other authors when nanotubes were used as conductive nanofillers, because the formation of the conductive network is not a true statistical percolation process based on the random distribution of individual high aspect ratio fillers, but rather is attributed to the mutual attraction of the nanotubes [67].

A wide range of values has been reported for percolation thresholds and DC and AC conductivity of CNT composites, depending on the processing method, polymer matrix and nanotube type. Extremely low percolation thresholds (<5%) fabricated with non-covalently functionalized CNTs [68], as well that with functionalized CNTs have been reported, as opposed to carbon black composites (around 20%). These values could be attributed to the random orientation of the CNTs and formation of network structures. In general, higher conductivity values have been obtained for the case of nanotube fillers than carbon fiber fillers [69].

Watts *et al* [70] performed current-voltage measurements of polymer-carbon nanotube composites revealing that the composite films consisting of defective C nanotubes exhibit higher conductivity than do graphite C nanotubes. This novel finding contradicts previous results.

In relation with the fabrication method, Zang *et al* [24] fabricated composites by PS *in situ* polymerization in the presence of MWNT. They reported improve dispersion, higher conductivity and high sensitivity and rate response for vapors of good solvents of PS than the composites prepared by solution mixing of polystyrene with MWNTs.

Many other polymer systems and conditions have been reported to prepared polymer-CNT composites, such as PVOH/CNT [71], PS [24, 72], PP, PS and ABS [62], etc.

Finally electrically conductive polymers have applications in areas as: antistatic, electrostatic dissipative (ESD), electrostatic painting electromagnetic shielding and absorbing materials to prevent electronic equipment interference. These properties enable production of advanced on-board shielding of electronic components and flexible electronics, etc.

Thus, electronic discharge protection can be achieved by static dissipation if the surface resistivity of the polymer is in the range of  $10^5$  to  $10^{12} \cdot \Omega / square$ . Furthermore, in electromagnetic interference shielding a more conductive polymer is required with a surface resistivity of less than  $10^5 \Omega / square$ . Both kind of application could being obtained by the addition of MWNTs. [62]

#### 3.2.4.4. Mechanical properties of polymer-CNT composites

As for other applications, carbon nanotubes are excellent reinforcing in polymers, due to the high aspect ratio, the specific surface area and their intrinsic individual mechanical properties (extremely high Young's modulus (1-5 TPa), stiffness and flexibility). Thus, both SWNTs and MWNTs have been used as fillers in polymer systems of thermoset polymers (epoxy, polyimide, and phenolic), as well as thermoplastic polymers (polypropylene, polystyrene, poly (methyl methacrylate), nylon 12, and poly ether ether ketone (PEEK)) [1]. In all cases, the filler volume fraction has to maintain as low as possible in order to maintain the fracture toughness and the tensile properties of the matrix. An increment in the filler content also lead to an increase in the viscosity with disadvantages in the processing step.

Literature reports numerous studies on the mechanical properties of polymer-nanotube composites, most of them consider tension and compression properties [25, 62, 73-75]. In general, the results revealed that compression modulus is higher than the tensile modulus, indicating that the load transfer to the nanotubes in the composite is much higher in compression due to the interwall sliding [19, 73]

Reported results on mechanical behavior of polymer-CNT composites have shown that the macroscopic behavior of these materials depends on many factors such as the type of nanotubes, the nature of the polymer used (CNT can have a nucleating effect in semicrystalline matrices or can induce a modification in the crosslinking as in epoxy) and the processing method (*in situ* polymerization, solvent method, or melt mixing) [76]. Thus, depending on morphological and interfacial characteristics as, the homogeneous dispersion and the existence of good interfacial bonding for efficient load transfer across the filler-matrix interface. If these conditions are not satisfied mechanic problems could be produce. That is, when the interfacial adhesion between the phases is weak, the nanotubes behaves as holes or nanostructured flaws, inducing local stress concentrations, and the benefits of the CNTs properties are lost. In addition, if the nanotubes are poorly dispersed, the nanotubes will fail by separation of the bundle rather than failure of the nanotube itself, resulting in significantly reduced strength.

The failure mechanism or energy dissipation in a polymer-nanotube composite could proceed through (i) nanofibers pull-out, ii) nanofibers fracture, iii) debonded/cracked bridging, and (iv) matrix cracking. Fig. 3.2 shows schematically these mechanisms operating at a crack tip as well as the micrographs demonstrating the individual failure modes [1, 7]. During load transfer, failure of nanotubes can occur either by individual nanotube fracture or by collective tube effects.

As was commented at the beginning of the section, several efforts have been done to obtain mechanically reinforced materials using different polymer matrices. From them, it could be mentioned the mechanical properties enhancement in dispersion in PMMA, strength and stiffness in PP, PS and ABS [62], mechanical reinforced using ester-functionalized CNTs [77], microhardness enhance in PS-CNT [72], elastic modulus and break stress in PS-CNT [22, 75], elastic modulus and nanotube alignment in PE and PS composite materials [22], PEG, PMMA and nylon-SWNTs composites [78], tensile modulus and strain to failure of PS-MWNT films [25], finally elastic modulus and break stress of PS-CNT [75].

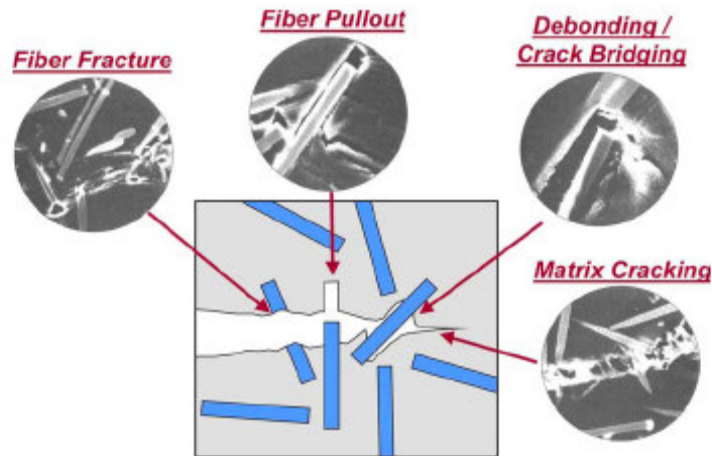


Fig. 3.2. Key mechanisms of energy dissipation have been identified in the fracture of short as well as continuous fiber-reinforced composites [1].

It is thought that the surfactants increase the dispersion of the nanotubes in the polymer and strengthen the interactions between the nanotube and polymer. However, all these composites fail by nanotube pullout. This is due to the shearing of the bundles in response to the applied stress and the weak van der Waals interactions between the nanotube and polymer chains. When nanotubes are functionalized, however, the nanotubes stick more strongly to the polymer matrix, as evidenced by the clumps of polymer still stuck to the outside of the nanotube.

In addition, simulations have been used to examine the mechanical properties of polymer-CNT composites with and without functionalization of the nanotubes [31, 74].

In the cases of non functionalized nanotubes it was observed no permanent stress transfer when the components held together by van der Waals bonds. When the same system is considered with a chemically functionalized nanotube, the material is found to have improved shear yield strength. Furthermore, according to the analysis of Visnawathan: “In the absence of atomic bonding between the nanotubes and the polymer, the interactions consists of micromechanical interlocking electrostatic and van der Waals interactions, deformation induced by these forces, as well as stress/deformation arising from a mismatch in the coefficients of thermal expansion. The strength of these non-bonded interactions depends on the system of interest” [79].

In all cases, until the moment the reported composite mechanical properties seem to be lower than expected because of transfer problems.

Some applications of the polymer-CNT composites due to their mechanical properties are aerospace structural panels, sporting goods, ultra-lightweight thin thin-walled space structures for use in space, among others.

#### *Mechanism of load transfer*

Load transfer depends on the interfacial shear stress between the fiber and the matrix. Schandler *et al* [73] established that a high interfacial shear stress will transfer the applied load to the fiber over a short distance, and a low interfacial shear stress will require a long distance.

There are three main mechanisms of load transfer from a matrix to filler. The first is micromechanical interlocking; this could be difficult in nanotube composites due to their atomically smooth surface. The second is chemical bonding between the nanotubes and the matrix. The third mechanism is a weak van der Waals bonding between the fiber and the matrix. Surface functionalization of CNT could increase the nanotube-polymer interfacial adhesion and chemical bonding, and further realize effective load transfer to the nanotubes.

Furthermore, there are two possible failure modes: breakage or pull-out. For poor nanotube-matrix bonding, under applied loads, MWNTs can act as defects within the material and consequently be sites for cracking and subsequent fracture. If the adhesion between the matrix and the nanotubes is strong, the external loads are then transferred to the nanotubes, resulting in high performance polymer-nanotube composites. [25]

A remaining open question: if the high modulus and strength predicted for nanotubes could be available in nanocomposites. Some answers determined that the weak coupling between the outer and inner layers of the nanotubes is responsible of the low load transfer that specially affects the tension loading. This is especially true under tensile loading when the load transfer occurs from the matrix to only the outer nanotube layer that is bonded to the polymer. SWNT composites may be similar since in the ropes only the peripheral tubes bonded to the polymer will be stressed. This will be different if the polymer infiltrates into the interstices of the nanotube ropes and creates strong interlocking. [73]

Helical polymer conformations around nanotubes and chemical bonds are ways to strengthen the interface between nanotubes and polymer matrices but it is also possible that functionalizing nanotube in composites may compromise properties such as tensile modulus and strength due to the introduction of sp<sup>3</sup> hybridized sites.

### **3.3. PS, PEO and PS-PEO blend and CNT composites**

Special interest has been taken for several years in polystyrene (PS) [11, 21, 25, 34, 69, 80], poly(ethylene oxide) (PEO) and their copolymer and polymer blends [81] as matrices medium to prepare nanocomposite materials. According to most of the results, the electrical conductivity and mechanical properties were enhanced when PS-nanotubes and PEO-nanotubes composites were prepared, indicating that MWNT could be homogeneously dispersed and could have strong interaction with the polymer matrix [2, 6, 8, 69, 78, 82-84]. The polymer blends of PEO-PS and their copolymers are especially interesting due to their incompatibility, the possibility to form an amphiphilic material, and the varied morphologies that the material could adopt. In addition, to the interesting properties deduced from their morphologies and compositions.

#### *Polymer blends filled with carbon black*

Several polymer blends, even more immiscible polymer blends, filled with carbon black have been prepared as composites since the last decade. These materials exhibited interesting electrical and mechanical properties. Some of the prepared systems were HIPS-EVA/CB [85], HDPE-EVA/CB [86], LDPE-EVA/CB [87], HDPE-PET/CB [88].

In all these cases, it was observed that CB was located in a preferentially way in one of the polymer phase, or at the interface. The location and the critical content for percolation threshold depends upon a balance between CB-polymer interactions, mixing kinetics, viscosity and polarity (surface tension) effects [85]. Furthermore, the characteristics of the original microstructure of the polymer blend related to the volume fraction of each component, the cristallinity, among others, could be modified and this change impact to the resultant electrical properties

Some of the observations about the CB behavior in most of the studied immiscible polymer blends are summarized below [86] [89] [85]:

- CB tends to accumulate within the amorphous regions of the polymer, the effective CB content within these regions increases, reducing the percolation threshold.
- High polarity induces polymer-filler interactions that could increase the percolation threshold due to the hinder of the formation of a segregated conductive network.
- A semicrystalline polymer promotes the formation of conductive structures, reducing the percolation point.
- In systems with high polymer-CB interfacial energy, the CB-CB interface is energetically probable and leads to the formation of a conducting network. On the contrary, if the polymer wet CB, the particles are completely dispersed and isolated. In the former a low percolation threshold are expected than in the last.
- CB locates preferentially within the phase in which it has a higher percolation threshold, being usually the polymer of higher surface tension value. This effect is so significant that occasionally migration of CB from one phase to another may be observed during melt mixing when the filler is initially incorporated within the polymer of lower polarity.
- The phases morphology and CB location determine the blend resistivity level. The double percolation concept, requiring continuity for the CB network, has been introduced and found necessary to obtain conductivity in CB-loaded polymer blends.
- The percolation threshold and resistivity values of the blend are lower than those depicted for the corresponding CB-filled individual polymers.
- CB tends to accumulate preferentially within one polymer phase, forming segregated structures, thus the conductivity of the blends is only obtained when double percolation was realized.

#### *Polymer blends filled with carbon nanotubes*

Very few reports on polymer blends filled with carbon nanotubes have been found in literature [8, 37, 90-92].

Zhang *et al* [87] stated that the theoretical percolation values in polymer loaded with conductive fillers might shift to a lower value with the use of polymer blends as matrix due to the multiple percolation resulting from heterogeneous distribution of conductive fillers in one phase of the blended matrix and/or at the interface of the polymers [89].

Furthermore, the low threshold also offers the possibility that good electrical and mechanical properties, as well as processability could be less deteriorated. Until now, very few efforts have been reported on the preparation of CNT filled polymer blends, their reproducibility and their modeling using multiple percolation theory. [86]

### 3.4. Conclusions

There is an increasing interest in the design and production of polymer-CNTs composites due to their potential amazing properties, close to those of carbon nanotubes; although, some difficulties have to be overcome before, like the inherent characteristics of insolubility and entanglement of carbon nanotubes, as well as the processability optimization conditions of dispersion, interface interaction and alignment of the materials. The already known approaches to trade with these facts have been discussed along the chapter.

At the final of this chapter, it is possible to say that the production of polymer-CNT composites is promising, especially when PS and PEO polymers and functionalized MWNT will be considered. These materials offer the opportunity to develop a new kind of reinforced polymers with electrical, mechanical and possible amphiphilic properties. This could be supposed after the analysis of the results of several polymer composite materials prepared with functionalized carbon nanotubes that presented desirable enhancement properties, as stiffness, retard in thermal degradation, and highly conductive materials, among others.

Some other trends for a future, like nanotube availability, high-purity and controlled intrinsic properties (length, diameter and chirality) at low-cost, high-yield and large-scale production have to be resolved. Furthermore, the appropriate development in the characterization techniques and theoretical simulation needs for the challenges of the new materials in the polymer-CNT composite field.

## References

1. Thostenson, E.T., *Nanocomposites in context*. Composites Science and Technology, 2005. **65**: p. 491-516.
2. Gojny, F.H., M.H.G. Wichmann, B. Fiedler, W. Bauhofer, and K. Schulte, *Influence of nano-modification on the mechanical and electrical properties of conventional fibre-reinforced composites*. Composites: Part A, 2005. **36**(11): p. 1525-1535.
3. Poncharal, P., Z.L. Wang, D. Ugarte, and W.A. de Heer, *Electrostatic deflections and electromechanical resonances of carbon nanotubes*. Science, 1999. **283**: p. 1513-1516.
4. Harris, P.J.F., *Carbon nanotubes and related structures New materials for the twenty-first century*. 2001, Cambridge: Cambridge University Press. 279.
5. Terrones, M., *Science and technology of the twenty-first century: synthesis, properties and applications of carbon nanotubes*. Annual Reviews Materials Research, 2003. **33**: p. 419-501.
6. Goh, H.W., S.H. Goh, G.Q. Xu, K.P. Pramoda, and W.D. Zhang, *Crystallization and dynamic mechanical behavior of double-C<sub>60</sub>-end-capped poly(ethylene oxide)/multi-walled carbon nanotube composites*. Chemical Physics Letters, 2003. **379**: p. 236-241.
7. Zeng, H.C., *Carbon nanotube-based nanocomposites*, in *Handbook of organic-inorganic hybrid materials and nanocomposites*, H.S. Nalwa, Editor. 2003, American Scientific Publishers. p. 151-180.
8. Zhou, C. and S. Kumar. *Study of interaction between various carbon nanotubes and polymer matrices*. in *Abstracts of Papers, 231st ACS National Meeting*. 2006. Atlanta, GA, United States: American Chemical Society.
9. Song, Y.S. and J.R. Youn, *Influence of dispersion states of carbon nanotubes on physical properties of epoxy nanocomposites*. Carbon, 2005. **43**: p. 1378-1385.
10. Allaoui, A., S. Bai, H.M. Cheng, and J.B. Bai, *Mechanical and electrical properties of a MWNT/epoxy composite*. Composites Science and Technology, 2002. **62**: p. 1993-1998.
11. Wong, M., M. Paramsothy, X.J. Xu, Y. Ren, S. Li, and K. Liao, *Physical interactions at carbon nanotube-polymer interface*. Polymer, 2003. **44**: p. 7757-7764.
12. Yao, Z., N. Braid, G.A. Botton, and A. Adronov, *Polymerization from the Surface of Single-Walled Carbon Nanotubes - Preparation and Characterization of Nanocomposites*. Journal of American Chemical Society, 2003. **125**: p. 16015-16024.
13. Chen, L., X.-J. Pang, M.-Z. Qu, Q.-T. Zhang, B. Wang, B.-L. Zhang, and Z.-L. Yu, *Fabrication and characterization of polycarbonate/carbon nanotubes composites*. Composites Part A, 2005. **37**(9): p. 1485-1489.
14. McNally, T., P. Potschke, P. Halley, M. Murphy, D. Martin, S.E.J. Bell, G.P. Brennan, D. Bein, P. Lemoine, and J.P. Quinn, *Polyethylene multiwalled carbon nanotube composites*. Polymer, 2005. **46**: p. 8222-8232.
15. Tong, X., C. Liu, H.-M. Cheng, H. Zhao, F. Yang, and X. Zhang, *Surface Modification of Single-Walled Carbon Nanotubes with Polyethylene via In Situ Ziegler-Natta Polymerization*. Journal of Applied Polymer Science, 2004. **92**: p. 3697-3700.
16. Doleman, B.J., R.D. Sanner, E.J. Severin, R.H. Grubbs, and N.S. Lewis, *Use of Compatible Polymer Blends To Fabricate Arrays of Carbon Black-Polymer Composite Vapor Detectors*. Analytical Chemistry, 1998. **70**: p. 2560-2564.
17. Breuer, O. and U. Sundararaj, *Big returns from small fibers: a review of polymer/carbon nanotube composites*. Polymer composites, 2004. **25**(6): p. 630-645.
18. Chazeau, L., C. Gauthier, G. Vigier, and J.Y. Cavail e, *Relationships between microstructural aspects and mechanical properties of polymer-based nanocomposites*, in *Handbook of organic-inorganic hybrid materials and nanocomposites*, H.S. Nalwa, Editor. 2003, American Scientific Publishers. p. 63-110.

19. Wagner, H.D., *Nanotube-polymer adhesion: a mechanics approach*. Chemical Physics Letters, 2002. **361**: p. 57-61.
20. Martin, C.A., J.K.W. Sandler, M.S.P. Shaffer, K.B. Schwartz, W. Bauhofer, K. Schulte, and A.H. Windle, *Formation of percolating networks in multi-wall carbon-nanotube-epoxy composites*. Composites Science and Technology, 2004. **64**: p. 2309-2316.
21. Choi, Y.-J., S.-H. Hwang, Y.S. Hong, J.-Y. Kim, C.-Y. Ok, W. Huh, and S.-W. Lee, *Preparation and Characterization of PS/Multi-Walled Carbon Nanotube Nanocomposites*. Polymer Bulletin, 2005. **53**(5-6): p. 393-400.
22. Hagenmueller, R., W. Zhou, J.E. Fischer, and K.I. Winey, *Production and characterization of polymer nanocomposites with highly aligned single-walled carbon nanotubes*. Journal of Nanoscience and Nanotechnology, 2003. **3**(1/2): p. 105-110.
23. Enomoto, K., T. Yasuhara, S. Kitakata, H. Murakami, and N. Ohtake. *Frictional properties of carbon nanotube reinforced polymer matrix composites*. in *NASA Conference Publication*. 2003.
24. Zhang, B., R.W. Fu, M.Q. Zhang, X.M. Dong, P.L. Lan, and J.S. Qiu, *Preparation and characterization of gas-sensitive composites from multi-walled carbon nanotubes/polystyrene*. Sensors and Actuators B, 2005. **109**(2): p. 323-328.
25. Safadi, B., R. Andrews, and E.A. Grulke, *Multiwalled carbon nanotube polymer composites: synthesis and characterization of thin films*. Journal of Applied Science, 2002. **84**: p. 2660-2669.
26. Niyogi, S., M.A. Hamon, H. Hu, B. Zhao, P. Bhowmik, R. Sen, M.E. Itkis, and R.C. Haddon, *Chemistry of single-walled carbon nanotubes*. Accounts of Chemical Research, 2002. **35**: p. 1105-1113.
27. Gojny, F.H., W.M.H. G., U. Köpke, B. Fiedler, and K. Schulte, *Carbon nanotube-reinforced epoxy-composites-enhanced stiffness and fracture toughness at low nanotube contents*. Composites Science and Technology, 2004. **64**: p. 2363-2371.
28. Gojny, F.H., J. Nastalczyk, Z. Roslaniec, and K. Schulte, *Surface modified multi-walled carbon nanotubes in CNT/epoxy-composites*. Chemical Physics Letters, 2003. **370**: p. 820-824.
29. Frankland, S.J.V., A. Caglar, D.W. Brenner, and M. Griebel, *Molecular simulation of the influence of chemical cross-links on the shear strength of carbon nanotube-polymer interfaces*. Journal of Physical Chemistry B, 2002. **106**: p. 3046-3048.
30. Barber, A.H., S.R. Cohen, and H.D. Wagner, *Measurement of carbon nanotube-polymer interfacial strength*. Applied Physics Letters, 2003. **82**(23): p. 4140-4142.
31. Cooper, C.A., S.R. Cohen, A.H. Barber, and H.D. Wagner, *Detachment of nanotubes from a polymer matrix*. Applied Physics Letters, 2002. **81**(20): p. 3873-3875.
32. Mader, E., K. Jacobash, K. Grundke, and T. Gietzelt, *Influence of an optimized interphase on the properties of polypropylene/glass fibre composites*. Composites Part A, 1996. **27**: p. 907-912.
33. Liao, K. and S. Li, *Interfacial characteristics of a carbon nanotube-polystyrene composite system*. Applied Physics Letters, 2001. **79**(25): p. 4225-4227.
34. Thostenson, E.T. and T.-W. Chou, *Aligned multi-walled carbon nanotube-reinforced composites: processing and mechanical characterization*. Journal of Physics D: Applied Physics, 2002. **35**(16): p. L77-L80.
35. Salalha, W., Y. Dror, R.L. Khalfin, Y. Cohen, A.L. Yarin, and E. Zussman, *Single-walled carbon nanotubes embedded in orientes polymeric nanofibers by electrospinning*. Langmuir, 2004. **20**: p. 9852-9855.
36. Dror, Y., W. Salalha, R.L. Khalfin, Y. Cohen, A.L. Yarin, and E. Zussman, *Carbon nanotubes embedded in oriented polymer nanofibers by electrospinning*. Langmuir, 2003. **19**: p. 7012-7020.

37. Zhang, W., S. Ge, Y. Wang, M.H. Rafailovich, O. Dhez, D.A. Winesett, H. Ade, K.V.P.M. Shafi, A. Ulman, R. Popovitz-Biro, R. Tenne, and J. Sokolov, *Use of functionalized WS2 nanotubes to produce new polystyrene/polymethylmethacrylate nanocomposites*. *Polymer*, 2003. **44**: p. 2109-2115.
38. Eitan, A., K. Jiang, D. Dukes, R. Andrews, and L.S. Schadler, *Surface Modification of Multiwalled Carbon Nanotubes: Toward the Tailoring of the Interface in Polymer Composites*. *Chemical Materials*, 2003. **15**: p. 3198-3201.
39. Niu, C., D. Moy, J. Ma, and A. Christi, *Modification of carbon nanotubes by oxidation with peroxide compounds*. 2002, Brevet WO02095098: USA.
40. Mitchell, C.A., J.L. Bahr, S. Arepalli, J.M. Tour, and R. Krishnamoorti, *Dispersion of Functionalized Carbon Nanotubes in Polystyrene*. *Macromolecules*, 2002. **35**: p. 8825-8830.
41. Andrews, R., J. Anthony, R. Bergosh, R.C. Haddon, C. Landis, F. McKenzie, M. Meier, and T. Rantell. *Carbon'01, An International Conference on Carbon*. 2001.
42. Zhu, J., H.Q. Peng, F. Rodriguez-Macias, J.L. Margrave, V.N. Khabashesku, A.M. Imam, K. Lozano, and E.V. Barrera, *Reinforcing epoxy polymer composites through covalent integration of functionalized nanotubes*. *Advanced Functional Materials*, 2004. **14**: p. 643-648.
43. Tour, J.M., J.L. Hudson, R. Krishnamoorti, K. Yurelki, and C.A. Mitchell, *Polymerization initiated at the sidewalls of carbon nanotubes*, in *PCT Int. Appl.* 2005, WO 2005030858 A2 20050407.
44. Geng, H., R. Rosen, B. Zheng, H. Shimoda, L. Fleming, J. Liu, and O. Zhou, *Fabrication and properties of composites of Poly(ethylene oxide) and functionalized carbon nanotubes*. *Advanced Materials*, 2002. **14**(19): p. 1387-1390.
45. Tsiang, R.C.-C. and I.-C. Liu, *Styrenic nanocomposite containing well-dispersed carbon nanotubes*. *Polymer Preprints*, 2005. **46**(1): p. 229-230.
46. Adronov, A., C.M. Homenick, Y. Liu, and Z. Yao, *Functionalization of single-walled carbon nanotubes with well-defined polymers*. *Polymer Preprints*, 2005. **46**(1): p. 201-202.
47. Curran, S.A., D. Zhang, W.T. Wondmagegn, A.V. Ellis, J. Cech, S. Roth, and D.L. Carroll, *Dynamic electrical properties of polymer-carbon nanotube composites: enhancement through covalent bonding*. *Journal of Materials Research*, 2006. **21**(4): p. 1071-1077.
48. Eitan, A., L.S. Schadler, J. Hansen, P.M. Ajayan, R.W. Siegel, M. Terrones, N. Grobert, M. Reyes-Reyes, M. Mayne, and H. Terrones. *Processing and thermal characterization of nitrogen doped MWNT/Epoxy composites*. in *Proceedings of the Tenth US-Japan Conference on Composite Materials*. 2002. Stanford, CA, United States: DEStech Publications, Inc.
49. Watts, P.C.P., W.K. Hsu, G.Z. Chen, D.J. Fray, H.W. Kroto, and D.R.M. Walton, *A low resistance boron-doped carbon nanotube-polystyrene composite*. *Journal of Materials Chemistry*, 2001. **11**: p. 2482-2488.
50. Namilae, S., N. Chandra, and C. Shet, *Mechanical behavior of functionalized nanotubes*. *Chemical Physics Letters*, 2004. **387**: p. 247-252.
51. Blake, R., Y.K. Gun'ko, J.N. Coleman, M. Cadek, A. Fonseca, J.B. Nagy, and W.J. Blau, *A generic organometallic approach toward ultra-strong carbon nanotube polymer composites*. *Journal of American Chemical Society*, 2004. **126**: p. 10226-10227.
52. Velasco-Santos, C., A.L. Martinez-Hernandez, F.T. Fisher, R. Ruoff, and V.M. Castano, *Improvement of thermal and mechanical properties of carbon nanotube composites through chemical functionalization*. *Chemistry of Materials*, 2003. **15**: p. 4470-4475.
53. Viswanathan, G., N. Chakrapani, H. Yang, B. Wei, H. Chung, K. Cho, C.Y. Ryu, and P.M. Ajayan, *Single-step In-situ Synthesis of Polymer-grafted Single Wall Nanotube Composites*. *Journal of American Chemical Society*, 2003. **125**(31): p. 9258-9259.

54. Liu, I.-C., H.-M. Huang, C.-Y. Chang, H.-C. Tsai, C.-H. Hsu, and C.-C. Tsiang, *Preparing a styrenic polymer composite containing well-dispersed carbon nanotubes: anionic polymerization of a nanotube-bound p-methylstyrene*. *Macromolecules*, 2004. **37**: p. 283-287.
55. Pham, J.Q., C.A. Mitchell, J.L. Bahr, J.M. Tour, R. Krishnamoorti, and P.F. Green, *Glass transition of polymer/single-walled carbon nanotube composite films*. *Journal of Polymer Science, Part B: Polymer Physics*, 2003. **41**(24): p. 3339-3345.
56. Gojny, F.H. and K. Schulte, *Functionalisation effect on the thermo-mechanical behaviour of multi-wall carbon nanotube/epoxy-composites*. *Composites Science and Technology*, 2004. **64**: p. 2303-2308.
57. Shaffer, M.S.P. and A.H. Windle, *Fabrication and characterization of carbon nanotube/poly(vinyl alcohol) composites*. *Advanced Materials*, 1999. **11**(11): p. 937-941.
58. Lozano, K. and E.V. Barrera, *Nanofiber-Reinforced Thermoplastic Composites. I. Thermoanalytical and Mechanical Analyses*. *Journal of Applied Polymer Science*, 2001. **79**: p. 125-131.
59. Valentini, L., J. Biagiotti, J.M. Kenny, and S. Santucci, *Morphological characterization of single-walled carbon nanotubes-PP composites*. *Composites Science and Technology*, 2003. **63**: p. 1149-1153.
60. Czerw, R., Z. Guo, P.M. Ajayan, Y.P. Sun, and D.L. Carroll, *Organization of Polymers onto Carbon Nanotubes: A Route to Nanoscale Assembly*. *Nanoletters*, 2001. **1**(8): p. 423-427.
61. Sandler, J., P. Werner, M.S.P. Shaffer, V. Demchuk, V. Altstadt, and A.H. Windle, *Carbon nanofiber-reinforced poly(ether ether ketone) composites*. *Composites Part A Applied Science and Manufacturing*, 2002. **33**: p. 1033-1039.
62. Andrews, R., D. Jacques, M. Minot, and T. Rantell, *Fabrication of carbon multiwall nanotube/polymer composites by shear mixing*. *Macromolecules Materials Engineering*, 2002. **287**: p. 395-403.
63. Munson-McGee, S.H., *Estimation of the critical concentration in an isotropic percolation network*. *Physical Review B*, 1991. **43**(4): p. 3331-3336.
64. Sandler, J.K.W., J.E. Kirk, I.A. Kinloch, M.S.P. Shaffer, and A.H. Windle, *Ultra-low electrical percolation threshold in carbon-nanotube epoxy composites*. *Polymer*, 2003. **44**: p. 5893-5899.
65. Schueler, R., J. Petermann, K. Schulte, and H.-P. Wentzel, *Agglomeration and electrical percolation behavior of carbon black dispersed in epoxy resin*. *Journal of Applied Polymer Science*, 1997. **63**(13): p. 1741-1746.
66. Benoit, J.M., B. Corraze, S. Lefrant, W.J. Blau, P. Bernier, and O. Chauvet, *Transport properties of PMMA-Carbon Nanotubes composites*. *Synthetic Metals*, 2001. **121**: p. 1215-1216.
67. Kilbride, B.E., J.N. Coleman, J. Fraysse, P. Fournet, M. Cadek, A. Drury, S. Hutzler, S. Roth, and W.J. Blau, *Experimental observation of scaling laws for alternating current and direct current conductivity in polymer-carbon nanotube composite thin films*. *Journal of Applied Physics*, 2002. **92**(7): p. 4024-4030.
68. Ramasubramaniam, R., J. Chen, and H. Liu, *Homogeneous carbon nanotube/polymer composites for electrical applications*. *Applied Physics Letters*, 2003. **83**(14): p. 2928-2930.
69. Yang, Y., M.C. Gupta, K.L. Dudley, and R.W. Lawrence, *The fabrication and electrical properties of carbon nanofibre-polystyrene composites*. *Nanotechnology*, 2004. **15**(11): p. 1545-1548.
70. Watt, P.C.P., W.-K. Hsu, H.W. Kroto, and D.R.M. Walton, *Are bulk defective carbon nanotubes less electrically conducting?* *Nano Letters*, 2003. **3**(4): p. 549-553.

71. Shaffer, M.S.P. and A.H. Windle, *Analogies between Polymer Solutions and Carbon Nanotube Dispersions*. *Macromolecules*, 1999. **32**: p. 6864-6866.
72. Yang, Z., B. Dong, Y. Huang, L. Liu, F.-Y. Yan, and H.-L. Li, *Enhanced wear resistance and micro-hardness of polystyrene nanocomposites by carbon nanotubes*. *Materials Chemistry and Physics*, 2005. **94**(1): p. 109-113.
73. Schadler, L.S., S.C. Giannaris, and P.M. Ajayan, *Load transfer in carbon nanotube epoxy composites*. *Applied Physics Letters*, 1998. **73**(26): p. 3842-3844.
74. Qian, D. and E.C. Dickey, *In-situ transmission electron microscopy studies of polymer-carbon nanotube composite deformation*. *Journal of Microscopy*, 2001. **204**: p. 39-45.
75. Qian, D., E.C. Dickey, R. Andrews, and T. Rantell, *Load transfer and deformation mechanisms in carbon nanotube-polystyrene composites*. *Applied Physics Letters*, 2000. **76**(20): p. 2868-2870.
76. Dalmas, F., L. Chazeau, C. Gauthier, K. Masenelli-Varlot, R. Dendievel, J.Y. Cavail  , and L. Forr  , *Multiwalled carbon nanotube/polymer nanocomposites: processing and properties*. *Journal of Polymer Science: Part B: Polymer Physics*, 2005. **43**: p. 1186-1197.
77. Sen, R., B. Zhao, D. Perea, M.E. Itkis, H. Hu, J. Love, E. Bekyarova, and R.C. Haddon, *Preparation of Single-Walled Carbon Nanotube Reinforced Polystyrene and Polyurethane Nanofibers and Membranes by Electrospinning*. *Nano Letters*, 2004. **4**(3): p. 459-464.
78. Liu, J., T. Liu, S.T. Veedu, J.E. Leisen, and S. Kumar. *Polymer/SWNT wrapping behavior*. in *Abstracts, 55th Southeast Regional Meeting of the American Chemical Society*. 2003. Atlanta, GA, United States: American Chemical Society.
79. Viswanathan, G., *Polymer grafted single-walled carbon nanotube composites*. 2004, Rensselaer Polytechnic Institute: Troy, NY, USA. p. 163.
80. Bellayer, S., J.W. Gilman, N. Eidelman, S. Bourbigot, X. Flambard, D.M. Fox, H.C. De Long, and P.C. Trulove, *Preparation of homogeneously dispersed multiwalled carbon nanotube/polystyrene nanocomposites via melt extrusion using trialkyl imidazolium compatibilizer*. *Advanced Functional Materials*, 2005. **15**(6): p. 910-916.
81. Galloway, J.A. and C.W. Macosko, *Comparison of Methods for the Detection of Cocontinuity in Poly(ethylene oxide)/Polystyrene Blends*. *Polymer Engineering and Science*, 2004. **44**(4): p. 714-727.
82. Loos, J., A. Alexeev, N. Grossiord, C.E. Koning, and O. Regev, *Visualization of single-wall carbon nanotube (SWNT) networks in conductive polystyrene nanocomposites by charge contrast imaging*. *Ultramicroscopy*, 2005. **104**(2): p. 160-167.
83. Yang, M., V. Koutsos, and M. Zaiser, *Interactions between Polymers and Carbon Nanotubes: A Molecular Dynamics Study*. *Journal of Physical Chemistry B*, 2005. **109**(20): p. 10009-10014.
84. Chatterjee, T., K. Yurekli, V.G. Hadjiev, and R. Krishnamoorti, *Single-walled carbon nanotube dispersions in poly(ethylene oxide)*. *Advanced Functional Materials*, 2005. **15**(11): p. 1832-1838.
85. Breuer, O., R. Tchoudakov, M. Narkis, and A. Siegmann, *The Interrelation Between Morphology, Resistivity, and Flow Properties of Carbon Black-Containing HIPS/EVA Blends*. *Journal of Applied Polymer Science*, 1998. **73**: p. 1655-1668.
86. Foulger, S.H., *Reduced Percolation Thresholds of Immiscible Conductive Blends*. *Journal of Polymer Science: Part B: Polymer Physics*, 1999. **37**: p. 1899-1910.
87. Zhang, M.Q., G. Yu, H.M. Zeng, H.B. Zhang, and Y.H. Hou, *Two-Step Percolation in Polymer Blends Filled with Carbon Black*. *Macromolecules*, 1998. **31**: p. 6724-6726.
88. Mallette, J.G., L.M. Quej, A. M  rquez, and O. Manero, *Carbon Black-Filled PET/HDPE Blends: Effect of the CB Structure on Rheological and Electric Properties*. *Journal of Applied Polymer Science*, 2001. **81**: p. 562-569.

- 
89. Breuer, O., R. Tchoudakov, M. Narkis, and A. Siegmann, *Segregated Structures in Carbon Black-Containing Immiscible Polymer Blends: HIPS/LLDPE Systems*. Journal of applied polymer science, 1996. **64**(6): p. 1097-1106.
  90. Pukanszky, B., *Interfaces and interphases in multicomponent materials: past, present, future*. European Polymer Journal, 2005. **41**: p. 645-662.
  91. Wu, M. and L. Shaw, *Electrical and Mechanical Behaviors of Carbon Nanotube-Filled Polymer Blends*. Journal of Applied Polymer Science, 2005. **99**: p. 477-488.
  92. Wu, G., S. Asai, and M. Sumita, *Entropy Penalty-Induced Self-Assembly in Carbon Black or Carbon Fiber Filled Polymer Blends*. Macromolecules, 2002. **35**: p. 945-951.

# Chapter 4.

## Materials, methods and characterization techniques

This chapter describes the materials, synthesis methods and characterization techniques used to functionalize and polymer-graft carbon nanotubes, as well as the use of these tube materials to produce polymer nanocomposites.

### 4.1. Nanocomposite materials

The materials used in the preparation of the nanocomposites are described below in addition with some of their raw characteristics.

#### 4.1.1. Carbon nanotubes

Multi-walled carbon nanotubes (MWNT) and nitrogen-doped multi-walled carbon nanotubes ( $CN_x$ ) were produced at IPICYT [1] by pyrolysing solutions of ferrocene ( $Fe(C_5H_5)_2$ ) and/or benzylamine ( $PhCH_2NH_2$ ) at 850 °C under an Argon atmosphere.

Fig. 4.1 shows SEM images of as-produced  $CN_x$  nanotubes. The obtained material consists of bundles by a pyrolytic self-assembly process. The nanotube composition is  $C_9N_x$  ( $x \leq 1$ ) with a typical nitrogen concentration around 1.6%, whereas the oxygen concentration corresponded to 2.4%. Characteristic dimensions are <80 nm in diameter and 80  $\mu m$  in length, in agreement with data reported elsewhere [1]. The overall morphology exhibits a carpet-like structure that sometimes shows a metal layer of iron catalyst (Fig. 4.1 (a) and (b)).

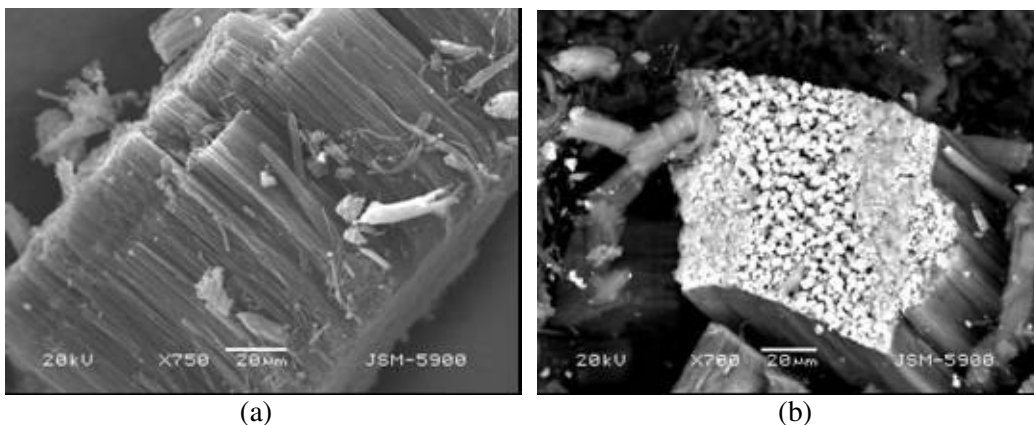


Fig. 4.1. SEM images of raw  $\text{CN}_x$  nanotubes: (a) nanotube bundles and (b) top-view of flakes showing the catalyst particles at the free ends of the nanotubes.

In order to get details on the structure, Fig. 4.2 depicts HRTEM images of as-produced  $\text{CN}_x$  nanotubes dispersed in ethanol thanks to ultrasonic technique. It can be observed that several kinds of morphologies of  $\text{CN}_x$  nanotubes are produced at the same time by the pyrolytic method, (general view in Fig. 4.2 (a)). Nevertheless, the most typical nanotube structure synthesized by this pyrolytic method is the multiwalled bamboo-type structure exhibiting diameters ranging from 20 to 80 nm, eventually covered by an amorphous carbon layer with a typical thickness of 3-5 nm (Fig. 4.2 (b)).

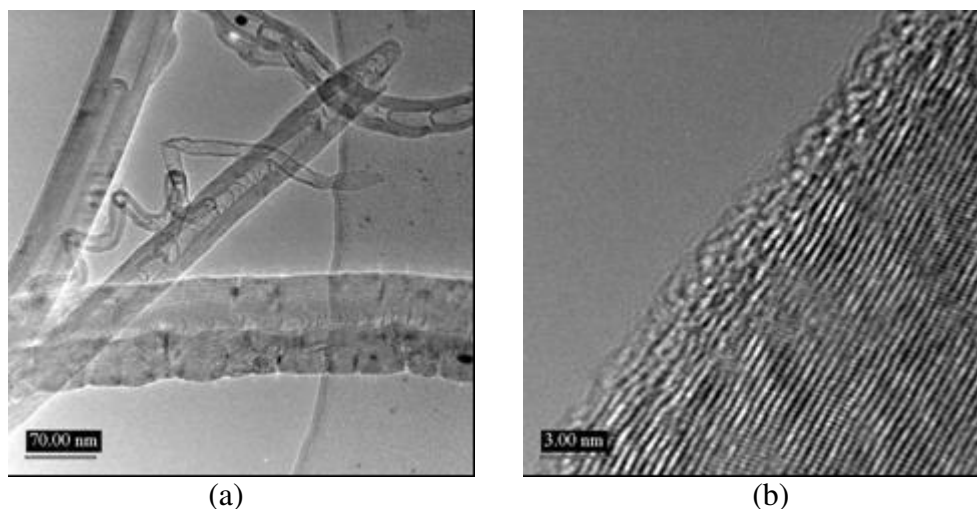


Fig. 4.2. HRTEM images of raw  $\text{CN}_x$  nanotubes after sonication in ethanol: (a) overall view, (b) nanotube crystalline planes and carbon amorphous layer.

As illustrated in Fig. 4.2 (b), it appears from several TEM observations that the  $\text{CN}_x$  nanotubes used in this study exhibit generally a good tubular perfection with several graphitic walls. Because of the low nitrogen concentration, the  $\text{CN}_x$  nanotubes used in this work are expected to have a low proportion of pyridine-like N sites. It has been previously reported that the pyridine-like nitrogen sites in the predominant graphitic walls are known

to be responsible for the roughness and for interlinked morphologies observed in the doped nanostructures [2, 3]. Moreover, it was reported (using EELS and *ab initio* calculations based on local density approximation of density functional theory and tight binding calculations) that nitrogen was predominantly in pyrolytic and coordinated N atoms replacing C atoms within graphene sheets. Using this information, it was concluded that the reactivity of carbon nanotubes is related to the low roughness of the nanotube layers.

Complementary studies using EELS were performed on carbon nanotubes. In the EEL spectra of the  $\text{CN}_x$  nanotubes (Fig. 4.3), it can be clearly observe the ionization edge at ca. 284.5 eV, corresponding to the C K-edge. The C-K edge exhibits bands for the  $1s \rightarrow \pi^*$  and  $1s \rightarrow \sigma^*$  transitions at 285.5 eV and 293 eV, respectively. The fine structure of the C-K edge confirms that nanotubes consist in a graphitic network with the typical  $sp^2$ -type bonding. In addition, the almost negligible ionization edges at ca. 400 eV corresponding to the N K-edge can be detected with intensity dependent on the N concentration. Previous studies reported [2] a splitting in the  $\pi^*$ -type peak of the nitrogen K edge exhibits two features at ca. 398.7 eV and 400.7 eV, corresponding to highly coordinated N atoms replacing C atoms within the graphene sheets (ca. 401-403 eV) and pyridinic nitrogen (ca. 399 eV). In this work, the N edge was very little because the analysis conditions were not good enough to observe it. This substitution of N could create radical sites in the graphene sheet, which, in the case of the outer layer, might be saturated with suitable reactants [3].

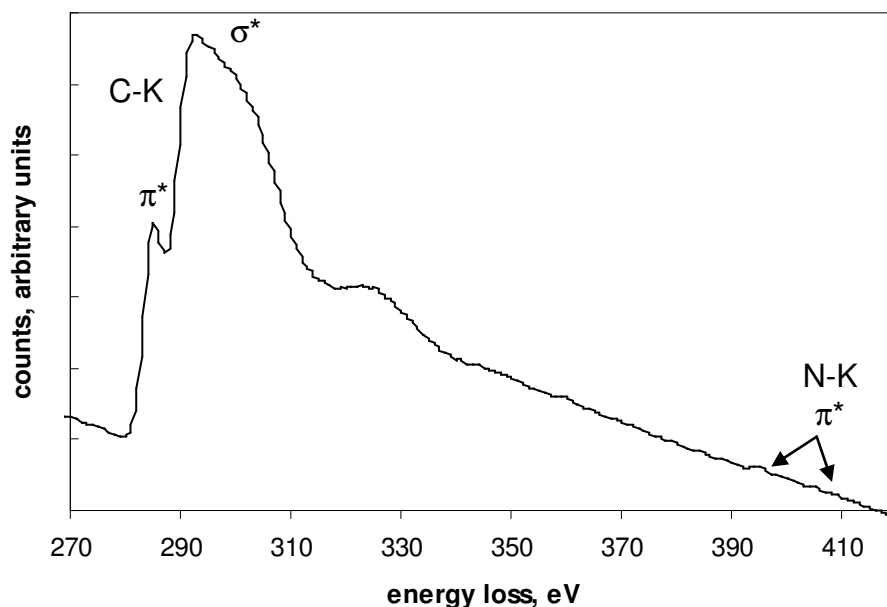


Fig. 4.3. Core-loss EEL spectra of the as prepared- $\text{CN}_x$  nanotubes, showing the C and N edges.

Raman Spectra of several samples of  $\text{CN}_x$  nanotubes (Fig. 4.4) were recorded in order to determine the average position of peaks D and G, and their relative intensities. The selected samples exhibited the peak D at  $1358 \text{ cm}^{-1}$ , the peak G at  $1579 \text{ cm}^{-1}$ , and an intensity ratio  $I_D/I_G$  of 0.36. Due to the low intensity ratio  $I_D/I_G$ , these kinds of nanotubes

are considered to be highly crystalline with a little amorphous carbon layer, which is in agreement with HRTEM observations (Fig. 4.2).

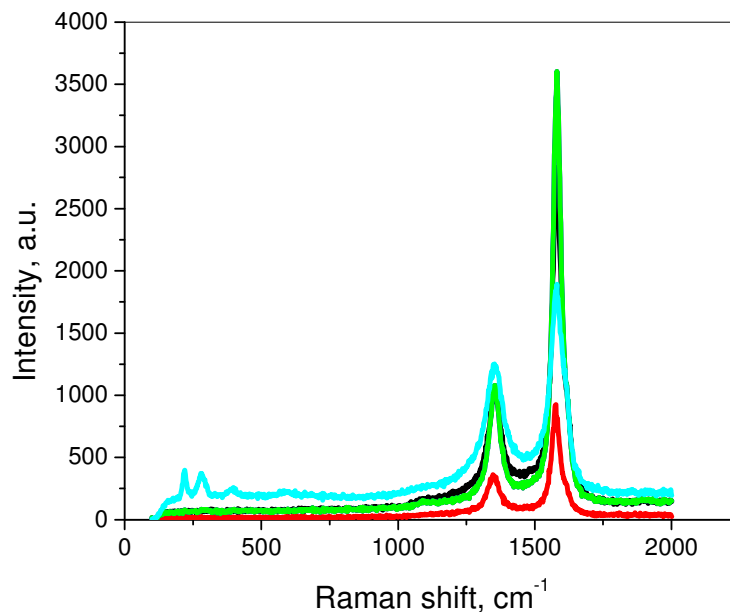


Fig. 4.4. D and G peak position and their relative intensities ( $I_D/I_G$ ) of  $CN_x$  nanotubes Raman Spectra from samples of different batches production.

In addition, as can be seen in Fig 4.5, MWNTs and  $CN_x$  nanotubes globally present a good thermal stability up to 700°C under  $N_2$  atmosphere. Below this temperature, it can be noticed that MWNTs start losing weight at temperatures below 200°C, which is expected to be only due to the loss of adsorbed molecules onto the surface of the MWNTs. Contrarily, for  $CN_x$  nanotubes the weight loss begins at 200°C, and could be associated to some attached molecules on the higher reactive surfaces of the  $CN_x$  nanotubes. When comparing both thermograms, it is observed that the doping of MWNTs (at least at low values, i.e. ~2%) does not change significantly their global average extent of thermal degradation. Indeed, only slight differences (around 2%) in weight losses of MWNTs and  $CN_x$  nanotubes were observed.

#### 4.1.2. Polymerization monomer, initiator and controllers

Styrene was chosen as the monomer of interest in the polymer-brushes synthesis due to the commercial importance of polystyrene, and also due to the well established nitroxide mediated radical polymerization protocols. Styrene (Aldrich, >98%) was purified of the inhibitor by a sodium hydroxide aqueous solution (10%) in a vol. ratio of 3:1 and subsequently cleaned with distilled water, the water molecules were removed with anhydrous sodium sulfate before used.

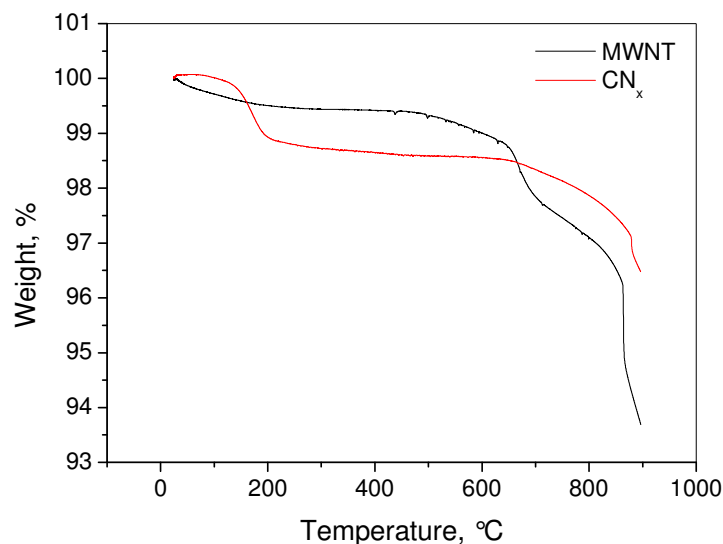


Fig. 4.5. Weight loss and degradation temperatures of as received carbon nanotubes: a) MWNTs, b) CN<sub>x</sub> nanotubes.

In this work, the reaction conditions to functionalize the carbon nanotubes and to synthesize the polystyrene-grafted carbon nanotubes were selected using a combinatorial experimental design. The nitroxide mediated radical polymerization requires the choice of a solvent, a controller and an initiator.

TEMPO type nitroxides are considered as efficient controllers in PS polymerization. Thus, this work has considered the evaluation of several molecular configurations of nitroxide controllers to determine the more convenient reactant for the carbon nanotube system. Three different controllers/regulators for the controlled free radical polymerization have been evaluated, namely TEMPO (2,2,6,6-tetramethyl-piperidine-1-oxyl, C<sub>9</sub>H<sub>18</sub>NO), OH-TEMPO (C<sub>9</sub>H<sub>18</sub>NO<sub>2</sub>), and PR CGX 505 (an experimental nitroxide from Ciba Specialty Chemicals).

BPO is known as an efficient initiator in free radical polymerization reactions, especially for styrene. In this work, benzoyl peroxide (BPO) supplied by Baker was used to create the initial free radical sites used during the grafting of polystyrene chains. Several solvents, such as toluene, benzene, xylene, were also supplied by Baker. All reagents were used as received.

#### 4.1.3. Polymer matrices

A second route to prepare carbon nanotube-polymer nanocomposites has been also used, based on the so-called solvent route. Several polymers have been investigated (i) an organic soluble polystyrene (PS) homopolymer which is amorphous, (ii) a water soluble polyethylene oxide (PEO) homopolymer, known to be semicrystalline, and (iii) a polymer blend of the two homopolymers.

The polymer blends were prepared using commercial polystyrene (PS HH104) from Resirene (Mw=46,000 gr/mol), and polyethylene oxide PEO14000 from Polioles and PEO1-5M from Rita Corporation (PEO14k of Mw=14,000 gr/mol and PEO210k of Mw=200,000 gr/mol, respectively) and blending them in a solution using toluene (Aldrich, >98%), as solvent.

## 4.2. Preparation methods

The functionalized  $CN_x$  nanotubes, polymer-grafted  $CN_x$  nanotubes and polymer-carbon nanotubes nanocomposites are prepared in two separate steps that will be described in the following sections.

### 4.2.1. PS-grafted $CN_x$ nanotubes

PS-grafted  $CN_x$  nanotubes (PS-g- $CN_x$ ) are synthesized by *in situ* radical polymerization via NMRP of styrene, as described in Dehonor *et al* [4].

The MWNT and  $CN_x$  raw tubes are dispersed ultrasonically in benzene for 60 min in order to eliminate the nanoparticles and decrease the catalyst moieties. Subsequently, the nanotube suspension is precipitated, filtered (0.5 $\mu$ m PTFE filter) and dried in vacuum at 60°C for 4 h.

First, the functionalization reactions to create polymer brushes have been carried out by a variable screening through combinatorial chemistry, and then by batch reactions in glass reactors or vials.

The initial screening of radical functionalization and polymer-grafting conditions has been realized using combinatorial design experiments in a Parallel Polymerization Reactor (PPR equipment) [5]. The investigated variables were carbon nanotube type ( $CN_x$  and MWNT), solvent type (xylene or benzene), controller type (TEMPO, OH-TEMPO, and PR-CGX505), initiator concentration (0.05 molar% or 0.1 molar %), and temperature (80 or 130°C). In all cases, BPO was used as initiator and the amount of sonicated carbon nanotubes was 10 mg. The initiator: controller molar ratio was set to 1:1.3, whereas the monomer: initiator molar ratio was chosen equal to 96:1, and finally the monomer:solvent molar ratio of 2:3 in volume. Also, the PPR equipment operated at 120 rpm in an  $O_2$  atmosphere, in two steps of respectively 3 and 24 hr of reaction. At the end of this screening study, the best conditions have been retained to scale up the reaction using batch conditions with 100 mg of carbon nanotubes in glass containers.

As indicated above, the overall reaction including radical functionalization and polymer-grafting involves two steps to produce (PS-g- $CN_x$ ), as shown in Fig. 4.6.

The first step, i.e. the radical functionalization, corresponds to the upper part of Fig. 4.6.. The previously purified  $CN_x$  nanotubes are mixed with initiator and controller solutions to functionalized carbon nanotubes with free radical sites (hereafter called  $CN_x-R\bullet$  and  $CN_x-RNO_x$ ). Then, the reactor is heated up to 130°C and maintained for 3 h. The functionalized nanotubes are then filtered using a 0.5 $\mu$ m PTFE filter and repeatedly washed using toluene to eliminate remaining dissolved species of initiator and controller.

The second step concerns the polymer-grafting as illustrated in the lower part of Fig. 4.6. Either the radical functionalized or the unreacted carbon nanotubes are added to monomer-solvent (volumetric ratio 2:3) solutions to proceed to the *in situ* polymerization of polystyrene at 130°C during 24 hr. After the reaction completion, the materials (PS-*g*-CN<sub>x</sub>), obtained in solution, are precipitated in methanol and vacuum dried during 24 h at 60°C.

The vacuum dried grafted-CNTs were redissolved in toluene and then the products are separated by solvent filtration (PTFE filters of 0.5 μm) and repeatedly washed.

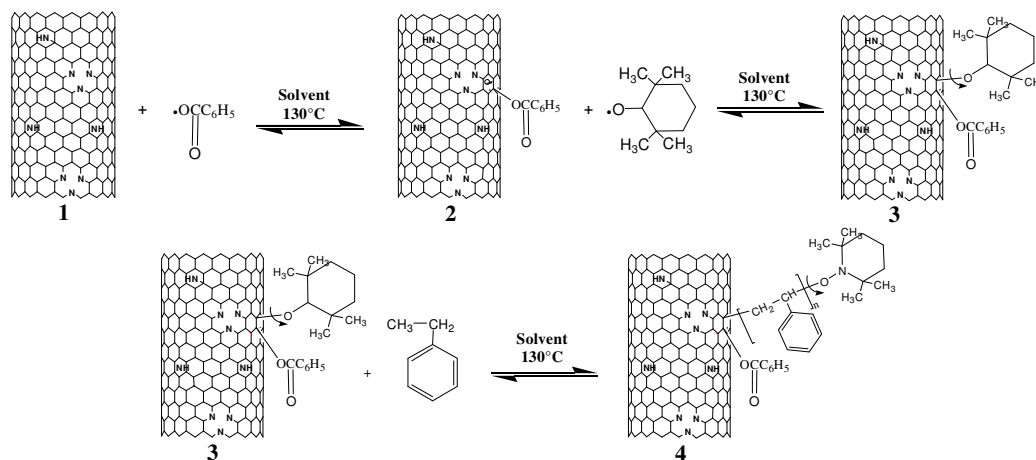


Fig. 4.6. Polymer brushes reaction scheme: functionalization of CN<sub>x</sub> nanotubes (**1**) with the NMRP initiator (**2**) and controller (**3**), and synthesis of polymer brushes of polystyrene (**4**).

#### 4.2.2. PS-PEO blend nanocomposites preparation

The polymer-nanocomposites are prepared with 40 ml of toluene and 2 g of the corresponding polymer matrix (PS, PEO and PS-PEO) and the different kinds of nanotubes (MWNT, CN<sub>x</sub> and PS-*g*-CN<sub>x</sub>) at several concentrations (0.1, 0.3, 0.5, 0.7, 1.0, 2.0 and 5.0 w%).

PS-based nanocomposites solutions are mixed in toluene at 130°C during 30 min. Then, films are prepared by solution casting over aluminum layers. After a solvent evaporation step at low temperature (20°C), the materials are dried in a vacuum oven at 60°C for 24 hrs and in an oven at 150°C for 4 hrs in order to remove all the residual toluene solvent. After these drying steps, the samples are pressed at 180-190°C and 13.79 MPa (2000 lb) for 10 min.

PEO and PS-PEO (35:65 w %) based nanocomposites are prepared in toluene at 130°C for 30 min. Films are also prepared by solution casting. After the solvent evaporation at low temperature (20°C), the materials are dried in a vacuum oven for 24 hrs at 60°C. Then, they are pressed at 150-160°C and 13.79 MPa (2000 lb) for 10 min, and then quenched in cold water at 55°C, maintained for crystallization during 2 min. The formed samples are approximately 0.5 mm thick.

The morphological and physical characterization of these materials will be presented in chapter 6.

### 4.3. Nanocomposite characterization

The synthesized materials, i.e. functionalized carbon nanotubes, polymer-grafted carbon nanotubes, and carbon nanotubes-polymer nanocomposites have been characterized using several techniques to determine their morphology, structure and composition, as well as their thermal, electrical and mechanical properties.

#### 4.3.1. Morphology, structure and composition characterization

Carbon nanotubes show a strong dependence of their properties (electronic, vibrational and other physical properties) with their geometrical structure often characterized through parameters such as  $(n,m)$  or  $(d_t, \theta)$ . Consequently, the structural characterization of carbon nanotubes is very important. Several microscopic techniques have been used to characterize the morphology, structure and composition of the nanosized polymer brushes and polymer-nanocomposites. Electron microscopy and related techniques High-Resolution Transmission Electron Microscopy (HRTEM), Transmission Electron Diffraction (ED), Electron Energy Loss Spectroscopy (EELS), Energy-filtered Transmission Electron Microscopy (EFTEM), Scanning Electron Microscopy (SEM), were selected. SEM is a versatile and widely used technique for characterizing the morphology of carbon nanotubes and their architectures, but is not adapted to study the structure of SWNT.

Note that overall morphological observations can also be performed using Scanning Tunneling Microscope (STM) and Atomic Force Microscopy (AFM). Imaging by AFM could give information about exfoliation of carbon nanotubes in organic solvents after chemical functionalization. In addition, AFM along with TEM were used to study the dispersion of nanotubes in the polymer matrix for the case of nanocomposites.

##### 4.3.1.1. Electron Microscopy and allied techniques

TEM and SEM have been extensively used to characterize carbon-nanotubes composites; nevertheless, and to the best of our knowledge other associated techniques such as EELS and EFTEM have been scarcely used by the time of the research. They can be useful to probe the chemical attachment of small molecules and to study polymer grafting via chemical bonding on the carbon nanotube surface. Thus, this work proposes the use of these techniques to investigate differences between as-produced  $CN_x$  carbon nanotubes, radical functionalized  $CN_x$  nanotubes, polystyrene-brushes of  $CN_x$  nanotubes, and finally physical blend of  $CN_x$  nanotubes and PS. The potential usefulness of these techniques to determine the structures, morphologies, chemical composition, and chemical bonding of carbon nanotubes with low molecular species and polymers will be addressed.

### Principles

In Transmission Electron Microscopy, a high energy electron beam is directed to a material sample. The incident electrons ( $e^-$ ) with energy  $E_0$  can encounter three types of interaction with the sample atoms, as represented in Fig. 4.7,

- (i) *Elastic scattering*, when  $e^-$  interact with the nucleus atom and continues with the same energy ( $E_0$ );
- (ii) *Inelastic scattering*, when  $e^-$  interact with electrons leading to an energy loss ( $E_0 - \Delta E$ ). The value of the energy loss,  $\Delta E$ , gives information on excitation energy for the inner-shell, valence or conduction electrons in the materials.
- (iii) *Element-specific X-rays*. Collisions with material electrons are responsible for the emission of X-rays. The energies of the emitted X-rays give information about the elements present in the material sample.

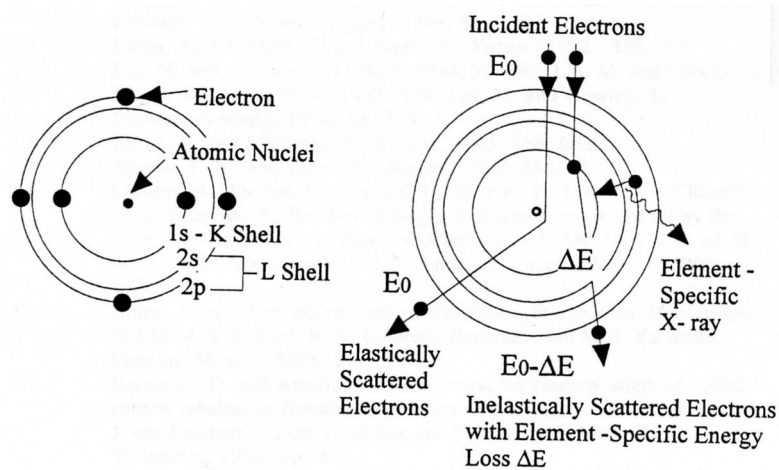


Fig. 4.7. Elastic and Inelastic Interactions between incident electron beam and atom [6].

### Experimental Technique

Fig. 4.8 shows a typical scheme of an electron ray path of a TEM equipped with an in-column EELS filter (for EFTEM experiments). In the experimental set up, imaging filter lens consists in a double magnetic prism, or  $\Omega$  omega filter (purely magnetic filter lens). Alternatively, an energy post-column imaging spectrometer, Gatan Imaging Filter (GIF) is also used and set under the fluorescent screen.

A Transmission Electron Microscope provides a two-dimensional intensity distribution of the electrons interacted with the specimen that can be recorded on a 2D detector as image, diffraction, or spectra. The imaging filter separates the electrons dispersed by the sample in elastically ( $E_0$ ) and inelastically scattered electrons ( $E_0 - \Delta E$ ). EELS pattern are formed by inelastically scattered electrons signal, separated by the differences between their respectively bends. Energy-filtering is used to obtain electron spectroscopic images (ESI) with an energy selecting slit in the energy dispersive plane. With this information, the zero loss images can be obtained and zero-loss diffraction eliminated the inelastic component; better contrast images taken at different energy losses, and elemental distribution (mapping) using energy-lost electrons at the ionization edges. Options of high resolution and high energy images have been used to obtained better image information.

*Applications to carbon nanotubes and nanocomposites*

Electron Microscopy studies devoted to carbon nanotubes include:

- (i) longitudinal-direction and cross-sectional observations using HR-TEM,
- (ii) structural analysis by Transmission Electron Diffraction (ED), and
- (iii) electronic structures evaluation by EELS

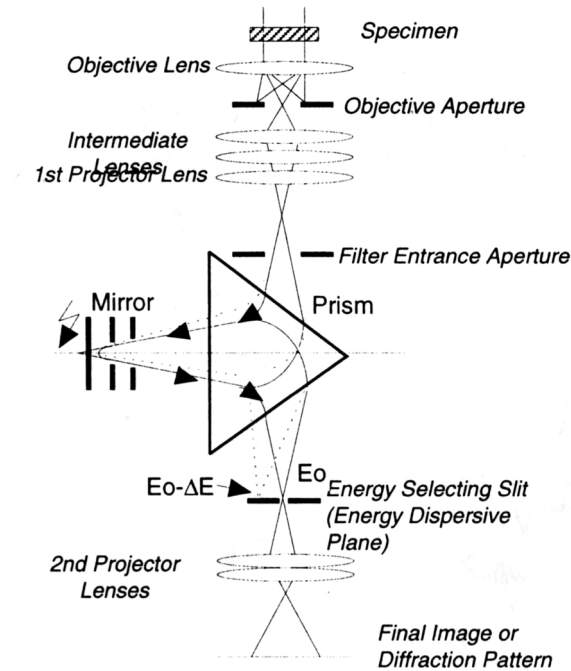


Fig. 4.8. Electron ray path of a Transmission Electron Microscope equipped with an in-column energy filter [6].

Electron Microscopy has also been applied to study the microstructure of polymer nanocomposites. Additional studies involve the adhesion of carbon nanotubes to a polymer matrix [7]. The nanotube adhesion to polymer matrices can be qualitatively observed by the interaction remaining between them in composite films after cutting, or even more, by pull-out experiments.

In the following, some of the main bibliographic studies concerning electron microscopy investigations are commented with a special attention to EEL results.

TEM reveals details of the internal structure of carbon nanotubes, and can provide information about the graphitic lattice such as the lattice points distance, orientation and tube chirality. Structural defects in multi-walled carbon nanotubes can be also determined using TEM, as well as their diameter distribution and packing configuration. Furthermore, the morphology and dispersion of carbon nanotubes inside the composites could also be observed.

EEL Spectra of carbon nanotubes can be taken at low and high energy loss. In the low-loss energy region, there are two peaks for graphite and carbon nanotubes: (i) the one at 5-8 eV is assigned to the  $\pi$  plasmon caused by the transition between  $\pi$  and  $\pi^*$  electron energy states, and (ii) the other at 20-28 eV is related to the collective excitation of all the

valence electrons ( $\pi+\sigma$  plasmon). In the core-loss region, there are also two peaks for the materials: (i)  $\pi^*$  ( $1s$ ) excitation peak at 285eV, and (ii) unoccupied  $\sigma^*$  levels at 292 eV. Carbon nanotubes exhibiting  $sp^2$  bonding present  $\pi^*$ -excitation peak lower than the  $\sigma^*$ -excitation peak.

The comparison of EEL spectra of CNTs with that of graphite (Fig. 4.9) reveals that  $\pi$  peak is at lower energy loss for CNTs than for graphite. That indicates a loss of valence electrons and a change in band gap due to the curvature of graphitic sheets. The peak width follows: SWNTs>MWNTs>graphite. That is related to the energy states of excitation caused by the curvature of graphitic sheets and the effect of the bundle formation.

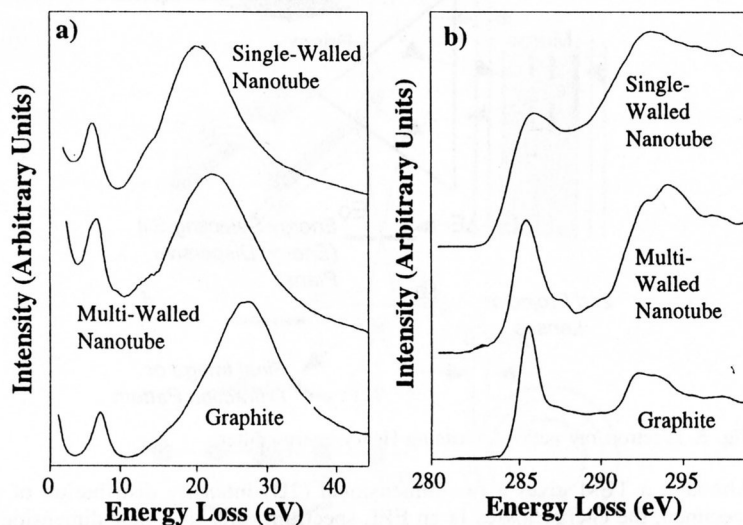


Fig. 4.9. Comparative EEL spectra of graphite, bundle of SWNTs and MWNTs in energy ranges of (a) 0 to 45 eV (plasmon region) and (b) 280-300 eV (carbon K-edge) [6].

The signature of chemical bonding can be distinguished in the core-loss region of EELS patterns, beyond the ionization edge, i.e. the energy-loss near-edge structure (ELNES). The height and width of peaks in this region depend on the density of excited states and the width of them, respectively.

#### *Experimental conditions*

In this thesis, two different Scanning Electron Microscopes, Jeol 5900 LV and a FEI ESEM XL 30, have been used under vacuum at accelerating voltage of 0.8 and 20kV. The samples have been observed without any conducting coating (such as gold coating) and images have been obtained by collecting the secondary electrons. Either the powdered materials or the fracture solid materials have been investigated in the case of polymer-grafted carbon nanotubes. In the case of nanocomposites, observations have been conducted on either the fractured solid materials or pressed films.

For HRTEM, EELS, EFTEM, and STEM, specimen preparation includes the dispersion or dissolution of solid materials (polymer-grafted carbon nanotubes) in ethanol or xylene and a ultrasonication step of 2 to 10 min. A drop of the solution is then deposited

on a copper grid covered by a lacey carbon film. The nanotubes are then observed and analyzed in the holes of the lacey carbon film.

In general, carbon nanotubes HRTEM images were obtained with a JEOL 2010F high-resolution electron microscope (Field Emission Gun, 200kV) equipped with a Gatan CCD slow-scan camera and a Gatan Digiscan EELS Spectrometer. Bright field images were acquired with a Gatan Slow Scan CCD camera. EEL Spectra at high spatial resolution were obtained with a probe size diameter of 2.4 nm. EEL spectra of larger areas were obtained with probe sizes of 50 nm. The collection angle was set to 31 mrad and the convergence angle was neglected (diffraction mode). The energy resolution was measured on the zero-loss peak and was equal to 1 eV FWHM. All spectra were corrected by the dark noise and the gain, and then deconvoluted using Fourier-log or Fourier ratio procedures to obtain the spectra of an ideally thin specimen. When it was possible, the spectra were further deconvoluted by the zero-loss peak to improve the energy resolution.

EFTEM was performed on a Leo 912 Microscope (in column Omega filter). The microscope operates in the image-spectrum mode at an accelerating voltage of 120 eV. The slit size was set to 6 eV. Image series of at least 20 images were acquired with an energy step of 2eV. The elemental maps were then calculated using a three image power-law subtraction.

STEM images were obtained in a Scanning Electron Microscope FEI XL30 SFEG. The samples were directly observed in solid.

Statistical measurements of carbon nanotubes diameters were performed on a Jeol 200 CX Electron Microscope operating at an accelerating voltage of 200 kV. Fifteen conventional bright field images were acquired all over the specimens. The diameters were then measured on at least 150 nanotubes.

Low-resolution TEM images of polymer-grafted carbon nanotubes and nanocomposites were obtained with a JEOL 200 CX (Field Emission Gun, 200kV). The samples were prepared by dispersion or dissolution of solid materials in the case of polymer-grafted materials and ultramicrotomy in the case of nanocomposites. The nanocomposite films of 50 nm were cut at  $-75^{\circ}\text{C}$  and 0.3 mm/s. The cuts were collected with a drop of an aqueous solution of 4 mol % of sucrose, deposited on a copper grid and then rinsed with distilled water. The films were tinted with  $\text{RuO}_4$  vapors (4 w% aqueous solution) during 5 min.

AFM measurements were obtained using a JEOL Microscope Model SPM 5200. The samples were prepared by 2-10 min of ultrasonication in toluene. After sonication, a drop of the nanotube dispersion was placed on a freshly cleaved  $1\text{ cm}^2$  mica wafer while spinning at 750 rpm. A subsequent drying step was taken place in an oven at  $100^{\circ}\text{C}$ .

#### **4.3.1.2. Raman Spectroscopy**

Raman spectroscopy is the measurement of the wavelength and intensity of inelastically scattered light from molecules. Recently, the technique was used to characterize the structure of nanotubes, and to determine chemical changes at their surfaces due to functionalization. In this work, the technique was proposed to analyze the as-produced  $\text{CN}_x$  nanotubes, the products from the radical functionalization, and the polymer grafting of  $\text{CN}_x$  nanotubes to conclude about the proceeding of the reaction, as well as the preservation of the overall nanotube structure.

### Introduction

Raman spectroscopy is based on the Raman effect, which is the inelastic scattering of photons by molecules, discovered by C. V. Raman and K. S. Krishan in 1928. The Raman effect concerns a very small fraction, about 1 to  $10^{-7}$  of the incident photons. Moreover, scattering events occur in around  $10^{-14}$  seconds or less [8].

In Raman scattering, the energies of the incident and scattered photons are different, in opposite to the Rayleigh scattering where both incident and scattered energies are equal (nearly 99%). Raman effect is divided in two phenomena: (a) Stokes lines, where the energy of the scattered radiation is lower than that of the incident radiation, and (b) anti-Stokes lines, where the energy of the scattered radiation is higher than that of the incident radiation (Fig. 4.10). The energy increase or decrease compared to the excitation is related to the vibrational energy spacing in the ground electronic state of the molecule. Therefore, the wavenumber of the Stokes and anti-Stokes lines are a direct measure of the vibrational energies of the molecule. The anti-Stokes shift spectrum has always less intensities than that for the Stokes spectrum. The frequency shift, that is the difference between the frequencies of the Raman lines and the exciting line, are independent of the frequency of the light. Furthermore, the lines are related to rotational and vibrational molecular transitions.

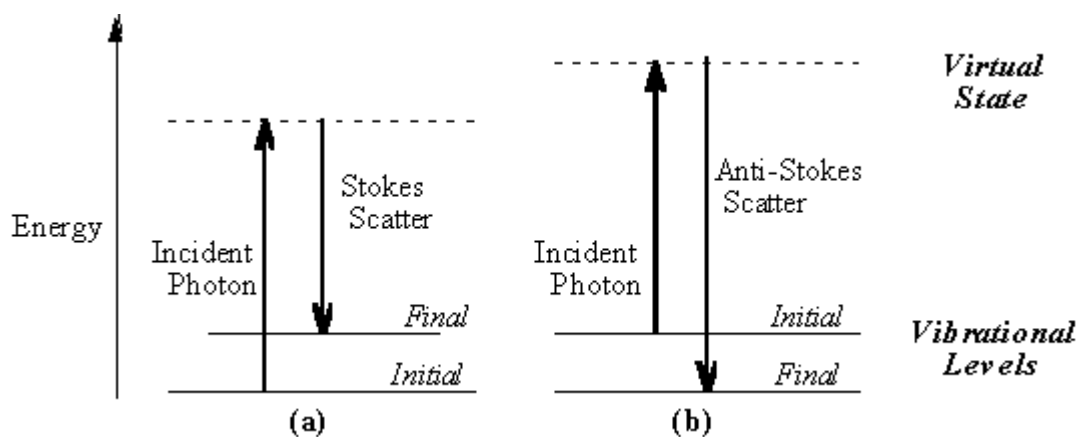


Fig. 4.10. Energy level diagram for Raman scattering: (a) Stokes Raman scattering, and (b) anti-Stokes Raman scattering [9].

### Principles

The difference in energy between the incident photon and the Raman scattered photon is equal to the energy of a vibration of the scattering molecule. A Raman spectrum is a plot of intensity of scattered light versus energy difference. The energy differences between the initial and final vibrational levels,  $\nu$ , or Raman shift in wave numbers ( $\text{cm}^{-1}$ ) is calculated through,

$$\nu = \frac{1}{\lambda_{\text{incident}}} - \frac{1}{\lambda_{\text{scattered}}} \quad [4.1]$$

in which  $\lambda_{\text{incident}}$  and  $\lambda_{\text{scattered}}$  are the wavelength of the incident and scattered Raman photons.

For a vibration to be active in Raman, the polarizability of the molecule must change with the vibrational motion. The induced dipole can be calculated as,  $p = \alpha E_i$ ,

where  $p$  is the induced dipole,  $E_i$  is the electromagnetic field of the incident radiation, and  $\alpha$  is referred to as the polarizability of the molecule. This induced dipole moment then emits a photon, leading to either Raman or Rayleigh scattering. The energy of this interaction is also dependent on the polarizability,  $E_{\text{interaction}} = -\frac{1}{2}\alpha E^2$ . The change in polarizability during the vibration is  $\frac{\partial\alpha}{\partial Q} \neq 0$ , where  $Q$  is the normal coordinate of the vibration. Scattering intensity is proportional to the square of the induced dipole moment, that is to say the square of the polarizability derivative.

The differences between the incident and inelastically scattered radiation are determined by the material molecule structure and environment, i.e. atomic mass, bond order, molecular substituents, molecular geometry and hydrogen bonding. Typical strong Raman scatterers are moieties with distributed electron clouds, such as carbon-carbon double bonds. The  $\pi$  electron cloud of the double bond is easily distorted in an external electric field. Bending or stretching the bond substantially changes the distribution of electron density, and strongly modifies the induced dipole moment.

Vibrational Raman spectroscopy is not limited to intramolecular vibrations. Crystal lattice vibrations and other motions of extended solids can be Raman-active. In crystalline solids, the Raman effect deals with phonons, instead of molecular vibration. Raman scattering by a crystal provides information on the crystal orientation.

#### *Experimental Technique*

Experimentally, only the Stokes shifts are observed in the Raman spectrum. Thus, the Stokes lines will be observed at higher wavelengths than the exciting light. High power excitation, monochromatic and polarized source are needed because Raman scattering is not very efficient and the measurement of the differences between the excitation and Stokes lines are searched. In addition, Raman spectroscopy is conventionally performed with green, red or near-infrared lasers with wavelengths below the first electronic transitions of most molecules (e.g. Ar<sup>+</sup>, Kr<sup>+</sup>, Nd:YAG, He-Ne, etc).

In Raman Spectroscopy, a laser beam is used to irradiate a sample. Light from the illuminated spot is collected with a lens and sent through a monochromator. Wavelengths close to the laser line (due to elastic Rayleigh scattering) are filtered out and those in a certain spectral window away from the laser line are dispersed onto a detector.

The advantages of Raman spectroscopy are that the pretreatment of samples is not necessary, samples are not destroyed, and the interference with water is weak.

#### *Applications to carbon nanotubes*

Carbon nanotubes present active vibrational modes to infrared and Raman Spectroscopy. For all kinds of nanotube chirality and symmetry, 7 to 8 FTIR active modes (A<sub>2u</sub>, E<sub>1u</sub>) and 15 to 16 Raman active modes (e.g. A<sub>1g</sub>, E<sub>1g</sub>, E<sub>2g</sub>) have been identified. An extended review of the nomenclature could be retrieved from the technical literature. The number of IR and Raman active modes is independent of the nanotube diameter for both SWNT and MWNT. However, the frequencies of these modes do vary with diameter [10].

In particular, many groups have reported Raman spectra for SWNTs in which they assigned observed Raman modes with specific (n,m) CNTs. They showed that the Raman

signal from the rope consists in the graphite related  $E_{2g}$  (or  $E_g$ ) modes and  $E_{1g}$ ,  $E_{2g}$  and  $A_{1g}$  modes of carbon nanotubes with different diameters, these modes occur in the high frequency around 1550 and 1600  $\text{cm}^{-1}$ . Moreover Raman spectra for SWNT also contain a low frequency (50-300  $\text{cm}^{-1}$ )  $A_{1g}$ -active mode that is not observed in graphite. This mode is known as the CNT radial breathing mode. In the intermediate frequency region (400-1350  $\text{cm}^{-1}$ ) weak signals are also observed [6]. Raman intensity for graphite in the 1300-1600  $\text{cm}^{-1}$  range is sensitive to sample quality, through the relative intensity of the D- and the G-band. This signal may come from a symmetry-lowering effect due to defects or nanotube caps, bending of the nanotube, and to the presence of carbon nanoparticles and/or amorphous carbon [11].

The Raman spectra of functionalized SWNT present additional peaks, and broadening or shift in characteristic radial breathing modes of raw carbon nanotubes. For instance, the characteristic radial breathing mode, observed at 250  $\text{cm}^{-1}$  for SWNT, is no longer present in the case of highly functionalized single-walled nanotubes. In addition, the disorder mode at 1290  $\text{cm}^{-1}$  is increased when carbon nanotubes are functionalized. Actually, disorder mode does not increase in non covalent functionalization unless aggressive processing methods alter the structure, causing defects [12].

Although the SWNT structure is extensively reported in literature, MWNTs, as well as doped-nanotubes have been less studied. In this context, Raman spectroscopy has proved to effectively determine vibrational modes attributed to the nanotube structure. As a consequence, we have used Raman spectroscopy in this work to analyze functional carbon nanotubes and to assess that the nanotube structure modification through chemisorption (bond formation) and the degree of roping left in the nanotubes. In fact, if chemical addition to the tube wall occurs in an ordered fashion, narrow, weak lines are expected in the Raman and IR spectra, depending on the symmetry and the fraction of tubes that have been functionalized.

Furthermore, Raman spectroscopy could be used to monitor the deformation of nanotubes in a polymer, to investigate individual nanotube fragmentation under composite loading, and mechanical characterization of bulk nanotube-polymer composite systems [13].

#### *Experimental conditions*

In this work, Raman Shift values were obtained using a Renishaw Raman Spectrometer with a Laser lamp of Ar (514 nm, 100 mW and resolution 1  $\text{cm}^{-1}$ ) in solid samples at room temperature. The integration time was 100s. The incident laser beam was focused onto the specimen surface through a 100x objective lens forming a laser spot of approximately 2 mm in diameter. The Raman spectra were obtained in the range of 100 to 2000  $\text{cm}^{-1}$ . Charge coupled detector CCD was used as detector and data were processed with the subtraction of laser-induced background luminescence using a personal computer.

#### **4.3.1.3. Infrared Spectroscopy (FTIR)**

Infrared Spectroscopy is the measurement of the wavelength and intensity of the absorption of infrared light by a sample. FTIR technique is useful to characterize the chemical structure of materials (chemical bonds and functional groups). Specially, the

nature of functional moieties introduced into the nanotube backbone as a consequence of the purification procedures, or chemical functionalization has been analyzed using FTIR.

The technique was used in this work to identify attached molecules and chemical bond differences between as produced  $CN_x$  nanotubes, radically functionalized and polymer-grafted  $CN_x$  nanotubes. Hence, it is expected to obtain information about the several chemical reaction carried out.

### Introduction

At temperatures above absolute zero, all the atoms in molecules are in continuous vibration with respect to each other. When the frequency of a specific vibration is equal to the frequency of the incident IR radiation directed on the molecule, the molecule absorbs the radiation. Among the normal modes of vibration of the molecule, those that produce a net change in the dipole moment may result in an IR activity and those that give polarizability changes, may give rise to Raman activity. Some vibrations can be both IR and Raman active.

### Principles

Molecules can exhibit translational, rotational and vibrational motion. Each molecular vibrational motion occurs with a frequency characteristic of the molecule and of the particular vibration (Fig. 4.11). The energy of a vibration is measured by its *amplitude* (the distance moved by the atoms during the vibration), so the higher the vibrational energy, the larger the amplitude of the motion. According to quantum mechanics, only certain vibrational energies are allowed to the molecule (this is also true for rotational and translational energies), so only certain amplitudes are allowed. Associated with each vibrational motion of the molecule is a series of energy levels (or vibrational energy states). The molecule may go from one energy level to a higher one by absorption of a quantum of electromagnetic radiation, such that  $E_{\text{final}} - E_{\text{initial}} = h\nu$ . Undergoing the transition, the molecule gains vibrational energy, and the amplitude of the vibration increases. The frequency of light required to cause a transition for a particular vibration is equal to the frequency of the vibration, so we may detect the vibrational frequencies by measuring the frequencies of light absorbed by the molecule. Since most vibrational motions in molecules occur at frequencies of about  $10^{14} \text{sec}^{-1}$ , light of wavelength  $\lambda = c/\nu = 3 \times 10^{10} \text{cm/sec}/10^{14} \text{sec}^{-1}$  is required to cause transitions. Light of this wavelength lies in the infrared region of the spectrum. IR spectroscopy, then, deals with transitions between vibrational energy levels in molecules.

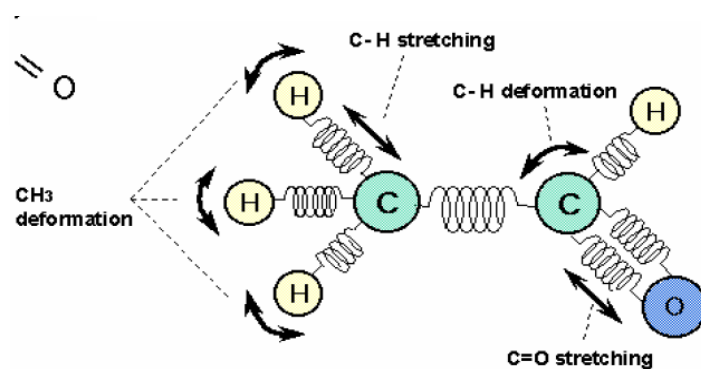


Fig. 4.11. Schematics of molecular vibration of polyatomic molecules.

An IR spectrum is displayed as a plot of the energy of the infrared radiation (usually expressed in wave numbers) versus the percentage of light transmitted by the compound

The spectrum of the molecule appears as a series of broad absorption bands of variable intensity, each of them providing structural information. Each absorption band in the spectrum corresponds to a vibrational transition within the molecule, and gives a measure of the frequency at which the vibration occurs. The frequencies which are absorbed are dependent upon the functional groups within the molecule and the symmetry of the molecule. The exact frequency at which a given vibration occurs is determined by the strengths of the bonds involved and the mass of the component atoms. Furthermore, the number of observed absorptions may be decreased by molecular symmetry, spectrometer limitations, and spectroscopic selection rules. The infrared spectrum can be divided into two regions, one called the functional group region and the other the fingerprint region. The functional group region is generally considered to range from 4000 to approximately 1500  $\text{cm}^{-1}$  and all frequencies below 1500  $\text{cm}^{-1}$  are considered characteristic of the fingerprint region. The fingerprint region involves molecular vibrations, usually bending motions that are characteristic of the entire molecule or large fragments of the molecule: hence the origin of the term. Used together, both regions are very useful for confirming the identity of a chemical substance. The functional group region tends to include motions, generally stretching vibrations, that are more localized and characteristic of the typical functional groups found in organic molecules. In fact a great number of functional groups are displayed in tables to analyze the spectra [14].

#### *Experimental Technique*

An IR spectrometer consists of a continuum radiation source of light, interferometer, and detector (Fig. 4.12). The common radiation source is an inert solid heated electrically to 1000 to 1800°C. The considered frequency range is  $10^{12}$ - $10^{14}$  with their corresponding wavenumber of 13000 to 10  $\text{cm}^{-1}$ . The most frequently used is the mid-IR region, between 4000 and 400  $\text{cm}^{-1}$ . Infrared is energetic enough to excite molecular vibrations to higher energy levels.

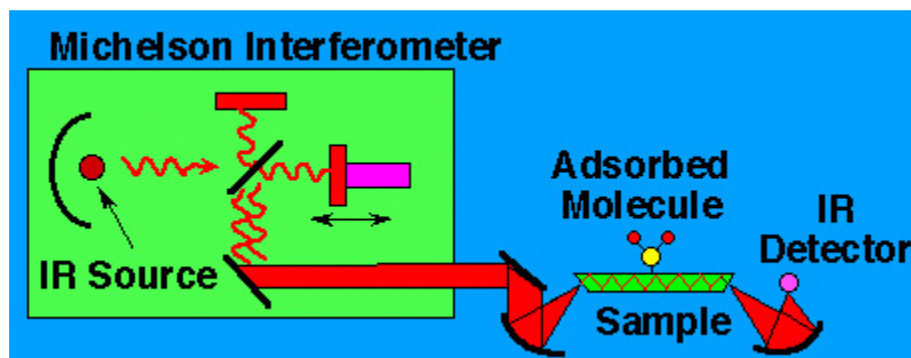


Fig. 4.12. FTIR experimental set up. [15]

In a typical dispersive IR spectrometer, radiation from a broad-band source passes through the sample and is divided and recombined after the split beams travel different optical paths to generate constructive and destructive interference by an interferometer.

The most used interferometer is the Michelson Interferometer. Then the beams fall on the detector, which generates an electrical signal and results in a recorded response. In a Fourier Transform IR all frequencies are examined simultaneously. The standard infrared spectrum is calculated from the Fourier-transformed interferogram, giving a spectrum in percent transmittance (%T) vs. light frequency ( $\text{cm}^{-1}$ ). Samples could be analyzed in solid, liquid or gas state. It is considered as a non destructive method.

Attenuated Total Reflectance (ATR) is useful for obtaining IR spectra of difficult samples that cannot be examined by normal transmission method. They are suitable for studying thick or highly absorbing solid and liquid materials.

#### *Applications to carbon nanotubes and nanocomposites*

The typical applications of the technique are in structure determination, multicomponent qualitative analysis, and quantitative analysis

FTIR can be used to compare pristine carbon nanotubes and nanotubes with functionalized open ends and/or functionalized sidewalls. The technique is more difficult to carry out in the case of functionalization restricted to nanotube ends.

Some of the absorption characteristic bands associated to functionalized CNTs are presented in summary [16] in Table 4.1.

Table 4.1. Characteristics bands associated to functionalized CNTs.

Wavelength $\text{cm}^{-1}$	Vibrational mode
2843-2922	C-H stretch modes
1646	Amide C=O stretch
1590	amide N-H motion
1540	amide C-N stretch
1427-1454	amide N-H bend
1332	amide C-N stretch
1187-1257	out-of-plane N-H motion

Traditional FTIR is used until the limit imposed by the high molar absorptivity of carbon nanotubes. Some specialized techniques, as Attenuated-Total-Reflectance (ATR) and reflection, have been applied to avoid spectra acquisition problems.

#### *Experimental conditions*

In this thesis, FTIR spectra were recorded on a Nicolet 20SXB Fourier-transform infrared spectrophotometer at room temperature. Thin films suitable for FTIR were prepared by casting 2% (w/v) solution in toluene directly on a ZnSe plate. Film thickness was adjusted so that the maximum adsorbance was about 1.0. The films were dried until most of the solvent was evaporated. Using this technique, 32 scans were made for each sample at a resolution of 2 and 4  $\text{cm}^{-1}$ . The spectra were taken over the range of 4000 to 700  $\text{cm}^{-1}$ .

### 4.3.2. Thermal properties characterization

The thermal analysis comprises a series of methods, which detect the changes in the physical and mechanical properties of a substance and/or its reaction products by the application of heat or thermal energy. The physical properties include mass, temperature, enthalpy, dimension, dynamic characteristics and others.

Thermal properties characterization are used to determine the purity, integrity, crystallinity and thermal stability of the chemical substances under study. Sometimes it is used in the determination of the composition of complex mixtures and/or material inspection [8].

In this thesis, the selected techniques to the study of nanotube polymer-brushes and polymer-nanocomposites were Thermogravimetric Analysis (TGA) and Differential Scanning Calorimetry (DSC).

#### 4.3.2.1. Thermogravimetric Analysis (TGA)

TGA is an analytical technique used to measure any reaction involving mass change. Some applications are to determine the material stability, its fraction of volatile components by monitoring the weight change that occurs as a specimen is heated.

The TGA technique has been extensively used to investigate the chemical modification of carbon nanotubes, as well as the thermal stability of polymer nanocomposites made off them. In this thesis, the technique was selected (i) to determine the effect of the purification and disentanglement steps on the as-produced carbon nanotubes, (ii) to verify that the proposed functionalization and polymer grafting of carbon nanotubes took place, (ii) to select the process variables and conditions and to measure the reaction efficiencies in the polymer brushes synthesis, and finally (iii) to determine the composition and thermal stability of the polymer-nanotube composites prepared with polymer brushes.

##### *Experimental Technique*

In TGA the change in sample weight is measured while the sample is heated or cooled at a constant rate. The Fig. 4.13 presents a simplified diagram for the thermogravimeter instrumentation.

A sample of the tested material is placed into a high alumina cup that is supported on, or suspended from an analytical balance located outside the furnace chamber. The balance is zeroed, and the sample cup is heated according to a predetermined thermal cycle. The balance sends the weight signal to the computer for storage, along with the sample temperature and the elapsed time. The TGA curve plots the TGA signal, converted to percent weight change on the Y-axis against the reference material temperature on the X-axis [17].

The measurement is normally carried out in air or in an inert atmosphere, such as helium or argon, and the weight is recorded as a function of increasing temperature (usually linear temperature ramp). The maximum temperature is selected so that the specimen weight is stable at the end of the experiment, implying that all chemical reactions are

completed. This approach provides information of the ash content (residual mass,  $M_{res}$ ) and oxidation temperature ( $T_0 = dm/dT_{max}$ ).

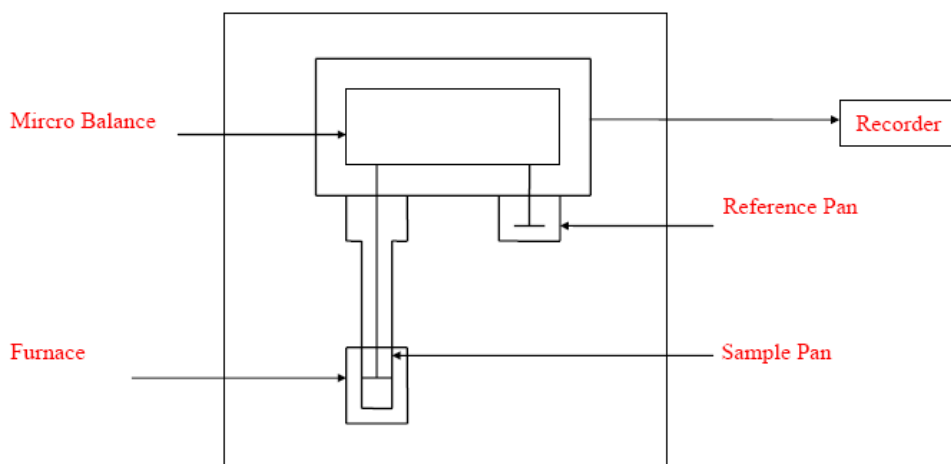


Fig. 4.13. Experimental set up of a Thermogravimeter.

The furnaces of commercial thermo balances cover the temperature range of 25 to 1700°C.

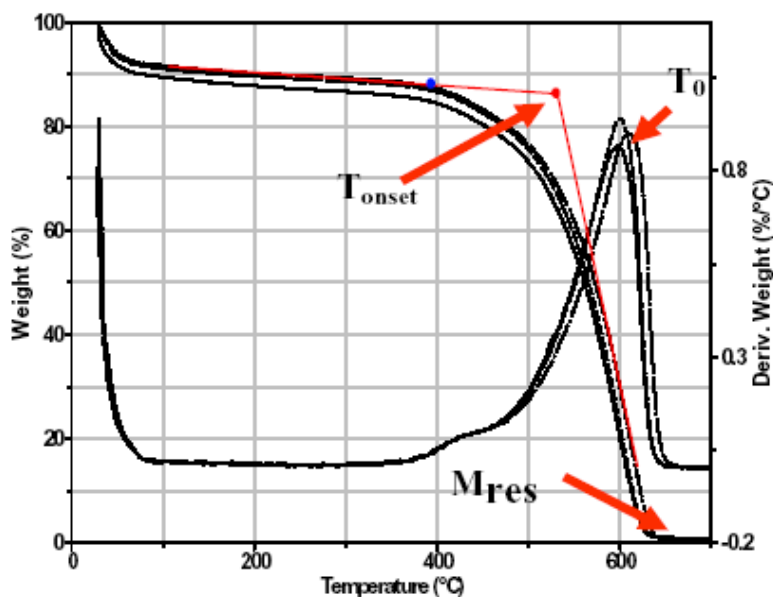


Fig. 4.14. TGA of purified SWNTs.

#### *Applications to carbon nanotubes and nanocomposites*

The TGA were used to determine the level of purification of raw carbon nanotubes [18] (Fig. 4.14). Thermograms present material weight losses after heat treatment. Organic moieties are first removed, just remaining carbon nanotubes. At higher temperatures, the weight change in an air atmosphere is typically a superposition of the weight loss due to

oxidation of carbon into gaseous carbon dioxide and the weight gain due to oxidation of residual metal catalyst into solid oxides. Oxidation temperature,  $T_o$ , is basically a measure of the thermal stability of nanotubes in air and depends on a number of parameters (diameter, defects and derivatization moiety, active metal particles, etc.) It is impossible to distinguish these contributions, but, nevertheless, thermal stability is a good measure of the overall quality of a given nanotube sample. Higher oxidation temperature is always associated with purer, less defective samples.

In addition, the modified nanotubes were analyzed using TGA to quantitatively determine the amount of attached molecules. For this application, TGA appears as a complementary technique to FTIR (that also detects the presence of these attached molecules and can be used to characterize the changes that occurred chemically) and DSC (sometimes reported to detect changes that occurred between reactive functional groups and the nanotube surface) [19]. The characterization by TGA, once covalent functionalization is confirmed, provides accurately results related to the degree of functionalization if the material is free of impurities [12, 20-22].

In order to obtain additional confirmation of both nanotube content and of the structure of the material, as well as to investigate the effects of the nanotubes on the thermal stability of the matrix, TGA was performed on composites [23]. In nanocomposites, the remaining polymer amount was determined by TGA [24].

#### *Experimental conditions*

In this thesis, TGA was carried out in a TA Q500 from 20°C to 900°C at 10°C/min in a N atmosphere.

### **4.3.2.2. Differential Scanning Calorimetry (DSC)**

#### *Introduction*

DSC measures the amount of energy absorbed or released by a sample when it is heated, cooled (or hold at a constant temperature) as a function of temperature (or time). Practically all physical and chemical processes involve changes in enthalpy or specific heat, and the applicability of DSC to condensed-phase systems is almost universal. A DSC measurement gives the rate of change of enthalpy, so that the area between a DSC curve and its extrapolated baseline indicates the total heat of the reaction.

Differential Scanning Calorimetry is the dominant technique for the thermal analysis of polymeric materials. Thus, in this work, the DSC has been used to determine differences in thermal properties of polymer matrixes used to produce carbon nanotube composites. Glass transition ( $T_g$ ), melting ( $T_m$ ) and crystallization temperatures ( $T_c$ ) were determined at several filler concentrations. In addition, a determination of changes in the miscibility of the polymer blend PS-PEO could be deduced from  $T_g$  measurements.

#### *Experimental Technique*

When a sample undergoes a physical transformation (such as melting, crystallization and glass transition), heat will be needed to maintain both the reference and the sample at the same temperature, depending on the type of process exothermic or endothermic. By observing the difference in heat flow between the sample and reference,

DS calorimeters are able to measure the amount of energy absorbed or released during such transitions.

A typical DS calorimeter (Fig. 4.15) consists of two sealed pans (reference and sample pan). These pans are often covered by or composed of aluminum, which acts as a radiation shield. The two pans are heated, or cooled, uniformly while the heat flow is monitored. This can be done isothermally or by changing the temperature at constant rate. The result is a plot of the differential heat flow as a function of temperature: a DSC curve. Generally, the differential heat flow is calculated by subtracting the sample heat flow from the reference heat flow. Thus in this case, exothermic processes will show up as positive peaks, while peaks resulting from endothermic processes are negative.

The sample is generally placed in an aluminum sample pan in the sample cell. The reference consists of a matched empty aluminum sample pan (high thermal conductivity) placed in the reference cell. Samples sizes generally range from 0.1 to 100 mg. Experiments could be performed under variable pressures and atmospheres.

Commercial DSC instruments operate from  $-200^{\circ}\text{C}$  to about  $900^{\circ}\text{C}$ . This range covers most applications for polymeric materials. Purge gases of helium, argon, nitrogen, or oxygen may be circulated through the calorimeter chamber. The temperature can be maintained isothermally or programmed at heating or cooling rates from  $0.1^{\circ}\text{C}/\text{min}$  to about  $20^{\circ}\text{C}/\text{min}$ .

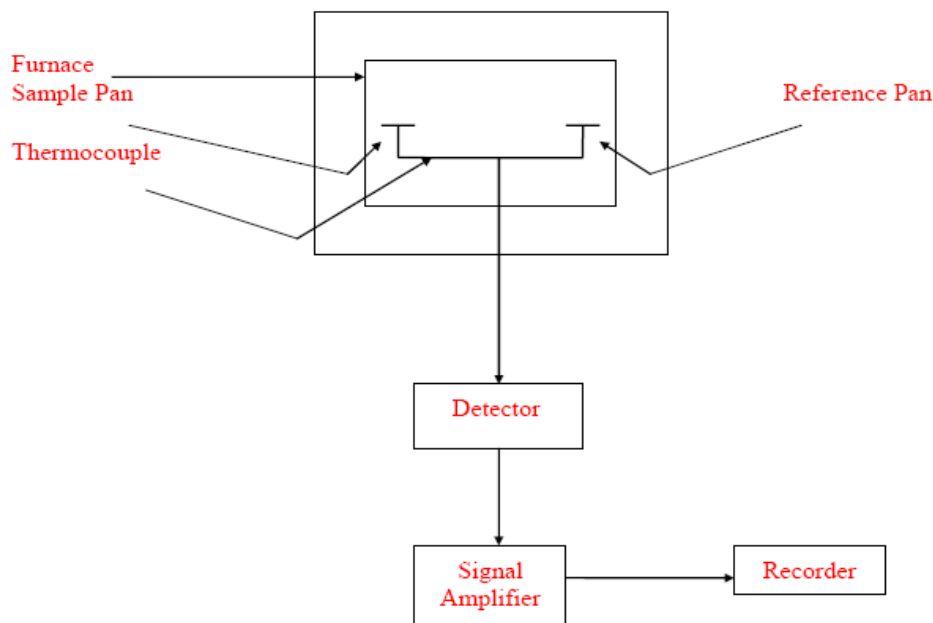


Fig. 4.15. Experimental device of a DS Calorimeter.

A DSC trace for a polymer at constant heating and cooling rates (Fig. 4.16) shows the main thermal events: glass transition temperature ( $T_g$ ), temperature of crystallization ( $T_c$ ) and its enthalpy and temperature of melting ( $T_m$ ) and its enthalpy. The result of a DSC experiment is a heating or cooling curve. This curve can be used to calculate enthalpies of transitions, by integrating the peak corresponding to a given transition.

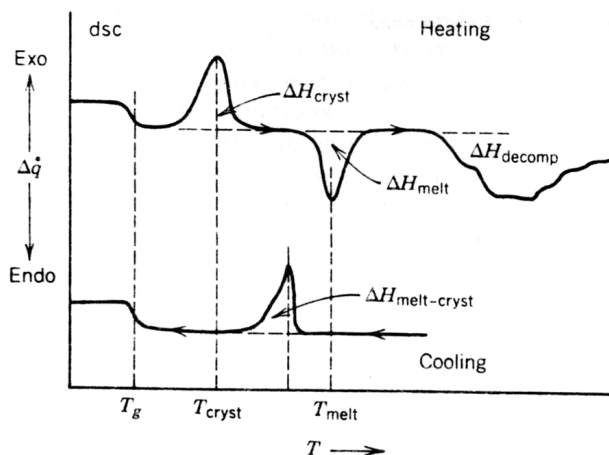


Fig. 4.16. Differential Scanning Calorimetry curve for a polymer which shows the glass transition temperature ( $T_g$ ), crystallization temperature ( $T_c$ ), melting temperature ( $T_m$ ), heat of crystallization ( $\Delta H_{cryst}$ ), heat of melting ( $\Delta H_{melt}$ ), heat of degradation ( $\Delta H_{decomp}$ ) and heat of crystallization from the melt ( $\Delta H_{melt-cryst}$ ) [8].

#### *Applications to nanocomposites*

A DSC trace may be interpreted to obtain information about the previous thermal and mechanical history of a polymer sample. DSC is often used to study the effects of thermal pretreatment on polymer morphology. Additionally, the fraction of crystallinity can be determined by dividing the enthalpy per gram calculated from the areas under the melting or crystallization peaks by the enthalpy of fusion.

DSC is widely used to investigate the properties of polymer blends. It is especially useful for distinguishing compatible and incompatible polymers; the former have a glass transition temperature intermediate between those of the two components, whereas the latter exhibit the two individual glass transitions. Effects of varying component fraction on the melting temperatures of the blends are determined as well, so that phase diagrams can be developed showing regions of incompatibility, solution and eutectics, and interaction parameters can be calculated.

Many inert additives have a dilution effect and diminish physical transformations as measured by DSC in proportion to their concentrations. Others, such as plasticizers, decrease the glass transition temperature. DSC studies of composite materials help in the interpretation of the interactions among polymers and additives.

As  $T_g$  is sensitive to quite a series of factors, it is suited to be used in microstructural and phase-behavioral studies in polymer blends and composites. In polymer blends,  $T_g$  has been used as a parameter to determine thermodynamic component miscibility. In composite materials,  $T_g$  has been proved useful in the study of the effects related to the polymer adhesion at the interface. Thus, the shift in the  $T_g$  value is commonly associated to a difference in the polymer chain mobility due to the presence of filler. In the last case, a controversy between the lower and higher shift values comparing to raw material remains. In both cases,  $T_g$  shifts towards higher or lower temperatures which allows the related effect to be inferred. In general the decrease of glass transition temperature in polymer composites is interpreted as an improvement of adhesion at the filler polymer interface in accordance with the general theory of polymer composites.

### *Experimental conditions*

Differential Scanning Calorimetry was performed using a TA Instruments DSC 2920. The nanocomposite samples were allowed to equilibrate at 20°C before being heated at 10°C/min to 120°C for PS, PEO and PS-PEO blends materials. The temperature was held for 2 min, then cooled at 10°C/min to 20°C for the case of PS materials and to -70°C for the case of PEO and PS-PEO materials. The samples were held at this temperature for 2 min before being reheated until 20°C. This cooling and heating method was adopted to ensure complete melting of the crystalline fraction for the case of crystalline materials and to remove the thermal history of the samples. The glass transition temperature ( $T_g$ ), the melting temperature ( $T_m$ ) and the crystallization temperature ( $T_c$ ) were measured using this non-isothermal method. The endothermic peak temperature was taken as the melting temperature and the weight percentage crystallinity was calculated using an equilibrium heat of fusion for PEO of 213.7 J/mol.

## 4.3.3. Electromagnetic and electrical properties characterization

### 4.3.3.1. Electron Spin Resonance (EPR)

Electronic Paramagnetic Resonance was used to study the chemical interaction of radical solutions with carbon nanotubes. Particularly, the EPR characterization is devoted to (i) the confirmation of the radical trapping behavior of  $CN_x$  nanotubes that was observed in other carbon structures and (ii) the determination of the reaction mechanism of carbon nanotubes with radicals, i.e. radical resonance or scavenging. Furthermore, the differences in the interaction of carbon nanotubes with peroxides and nitroxides were explored, as well as the differences between MWNTs and  $CN_x$  nanotubes in the radical uptake, i.e. effect of doping.

### *Introduction*

The electronic spin and its interactions with its microscopic neighborhood provide a unique tool for the study of the structure and dynamics of paramagnetic centers. In order to exhibit paramagnetic resonance absorption a specimen must contain unpaired electrons. Paramagnetism occurs: (a) in all atoms and molecules having a net odd number of electrons, e.g. atomic hydrogen, nitrogen, molecular NO, etc.; in a few molecules with an even number of electrons but which still exhibit a resultant magnetic moment; (b) in the transition elements where unfilled inner electron shells results in unpaired electrons; (c) in conductors or semiconductors where the paramagnetism is due to the conduction electrons; and (d) in crystals or glassy materials whose normal bonds have been modified or broken [25]. Electron Paramagnetic Resonance (EPR) or Electron Spin Resonance (ESR) spectroscopy is a technique applicable only to systems with a net electron spin angular momentum, like species containing one or more unpaired electrons, like radicals. Thus, detail analysis of the EPR spectrum frequently make possible to deduce not only the gross chemical structure of a radical but also its conformation [26].

### *Principles*

The electron with the corresponding spins has an associated magnetic moment. Consequently, the electron will precess in an applied magnetic field with a precise precessional frequency and will undergo transitions between spin states if energy of the correct frequency is applied (Zeeman effect). The difference in energy of these spin states is given by the equation

$$\Delta E = h\nu = g\mu_B B \quad [4.2]$$

where  $g$  is a dimensionless proportionality constant (g-factor),  $\mu_B$  is the Bohr magneton, and  $B$  is the magnetic induction. In addition,  $\mu_B = eh/4\pi m_e$ , where  $e$  and  $m_e$  are the charge and the mass of electron respectively and  $h$  is Planck's constant [26].

### *Technique*

EPR concerns the resonant absorption of microwaves for a material submitted to a magnetic field. The technique involves placing a specimen in a strong magnetic field and observing resonance effects in a radar circuit surrounding the specimen. EPR spectrometers could measure absorptions at (a) fixed frequency, varying the magnetic induction, or at (b) fixed magnetic induction, varying the frequency. Particularly, organic radicals are determined at the former conditions. The measurements are carried out at microwave frequencies range of 9-10 GHz range (X-band) and variable magnetic induction. At resonance, some of the incident microwave radiations are absorbed. The value of  $B$  for resonance is typically about 330-350 mT [27]. Sufficiently high steady-state concentrations of radicals for ESR studies are achieved by the generation of radicals in a matrix at very low temperatures, or by temperature increment, ultraviolet or X-ray irradiation of a radical solution.

The EPR spectrometers record the first derivative of the absorption rather than the absorption curve itself. This gives greater sensitivity and better resolution. The sensitivity of the method enables radical concentration of  $10^{-8}$  M to be detected [26]. The intensities of the absorption spectra are a measure of the number of electrons participating in the resonance absorption, whereas their shapes provide information about the local chemical environment of the electron. Thus, the area under the absorption curve is proportional to the number of the spins in the sample, i.e. the radical concentration. The radical concentration is determined by comparison with a sample with a known radical concentration.

EPR spectra are characterized by three parameters: g-factors, hyperfine splitting constants, and line widths [26].

For a given frequency, radicals have different g-factors, and consequently resonate at different field strengths. The differences in the g-factors of a radical and a free electron give information about the radical structure. The spin-orbit coupling of the electron in a radical depends on the orientation of the radical with respect to the applied magnetic induction. Nevertheless in solution, the calculated g-factor value of the radicals is time-averaged because of their rapid tumbling. The measured g-factor of a free electron spin yields  $g=2.002319$ . In real materials,  $g$  may differ from this value, depending on variations in coupling, between spin and orbital angular momentum. The  $g$  values of organic free radicals are usually close to the free-electron value [8].

The hyperfine splitting characteristic of EPR spectra elucidates the structure and the shape of the studied radical. It arises from the interaction between the unpaired electron and neighboring magnetic nuclei. The hyperfine coupling constant or splitting constant is the

separation between two spectra absorption lines and it is measured in milliTesla (mT) or in Gauss (1 mT=10 Gauss). In general, interaction with  $n$  equivalent protons gives  $n+1$  lines which relative intensities are given by the coefficients of the binomial expansion. Interaction of the unpaired electron with a nucleus of spin  $I$  gives  $(2I+1)$  lines. In particular, the ESR spectrum of a radical centered on nitrogen ( $I=1$ ), like nitroxides, consists of a 1:1:1 triplet. The magnitude of the nitrogen coupling constant is also sensitive to the type of radical trapped. Thus, some nitrogen compounds were used as spin trapping to form nitroxides (stable radical). Spin traps have also been used quantitatively to determine rate constants for radical processes.

Theoretical EPR spectra are often constructed using either Gaussian or Lorentzian line shapes. The derivatives of the Gaussian and Lorentzian line shapes are expressed by

$$I_G = \frac{4I_0(H - H_0)}{(\Delta H)^2} \exp \left[ -2 \left( \frac{H - H_0}{\Delta H} \right)^2 \right] \quad [4.3]$$

$$I_L = \frac{I_0^2 (\Delta H)^2 (H - H_0)}{[(\Delta H)^2 + (H - H_0)^2]^2} \quad [4.4]$$

where  $I_0$  is the peak amplitude of the absorption line,  $H_0$  is the magnetic field, and  $\Delta H$  is the linewidth [25].

#### *Applications to carbon nanotubes and nanocomposites*

It was observed that EPR is sensitive to both itinerant (conduction electrons) and localized spins (defective sites). Thus, EPR experiments could determine the metallic transport properties in order to clarify the electronic structure and defective sites in carbon nanotubes. Additional information indicative of the preparation methods and the purification procedures could be also obtained.

In addition, EPR is a tool to probe experimentally the molecular occurrences associated with mechanical damage and failure of polymers [8].

#### *Experimental conditions*

In this work, EPR solution measurements were performed on a JEOL TE300 spectrometer, using a cylindrical cavity (TE<sub>011</sub> mode) operating at X-band frequencies (near 9.17 GHz) with 100 kHz field modulation and using a microwave power around 1 mW. All spectra, recorded at different temperatures, were obtained using the JEOL DVT variable temperature system. Quartz tubes (2.5 mm ID, 13 mm height) were used for the ESR measurements. To avoid the distortion of the spectrum, the modulation amplitude was kept at less than or equal to one-third of the peak-to-peak linewidth. The number of spins (radicals) in each sample was obtained by double numerical integration of the first derivative of the resonance signal, according with the equation:  $A = \int_{HA}^{HB} dH \int dH' S(H')$  where  $HA$  and  $HB$  are the initial and final magnetic fields of the resonance curve, respectively, and  $S(H')$  is the absorption at magnetic field  $H$ . The spin (free radical) concentrations were measured by comparison with a standard solution of TEMPO and of known concentration. The software for the data processing was Sprit-382. All spectra were recorded under identical conditions.

Sample observations were performed in organic solution/dispersion. Initiator and controller solutions at known concentrations were prepared prior addition to solid materials.

Nanotubes samples were dispersed by 10 min of ultrasonication using benzene, toluene or xylene, and then an amount of initiator/controller solution was added. For the measurements, liquid dispersions were placed into EPR quartz tubes centered into the regular cavity.

Additional, EPR spectra of solid materials were obtained in a spectrometer at 9.42 GHz with 20 DB of microwave power. Spectra of all samples were recorded applying both a wide scan covering a range of 1000G centered at 3500G.

#### 4.3.3.2. Dielectrical measurements

The dielectric spectroscopy (sometimes called impedance spectroscopy) consists of studying the frequency dependent complex dielectric permittivity of insulator materials. It is based on the interaction of an external electrical field with the dipole moment of the sample. In this thesis, the dielectric spectroscopy has been used to determine the dependence of the electrical behavior of carbon nanotube-polymer composites with the nanotube type and concentration.

##### *Introduction*

There are a number of different dielectric mechanisms, related to the reaction of the material to the applied alternating field. In general dielectric mechanisms can be divided into relaxation and resonance processes. The dielectric spectroscopy is used for physical and chemical analysis of material, because it enables investigation of dielectric relaxation processes in an extremely wide range of characteristic times ( $10^6 - 10^{-12}$  s). As the frequency decreases from  $10^{17}$  Hz the phenomena involved are: electronic polarization, atomic polarization, dipole relaxation and ionic relaxation, as shown in Fig. 4.17.

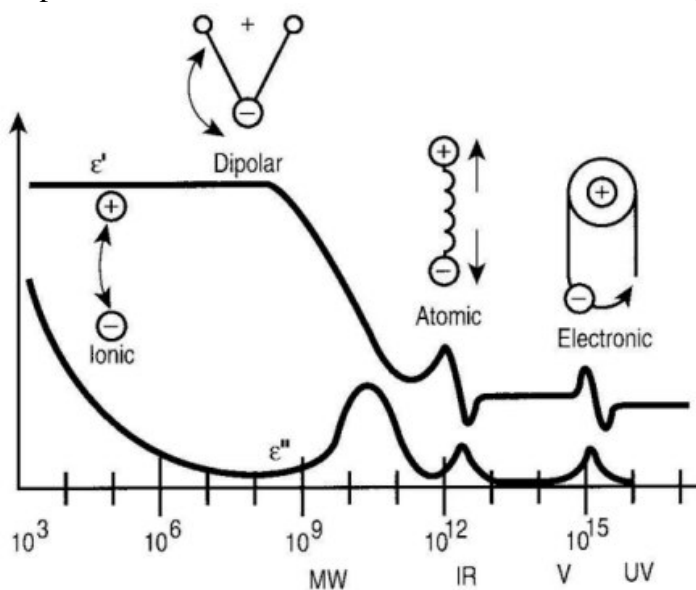


Fig. 4.17. Dielectric relaxation processes as a function of the frequency [28].

The application of an electric field to a material produces the polarization and eventually the apparition of an electrical charge flux. This behavior could be approached by a perfect conductor (Ohm Law),

$$j = \sigma E \quad [4.5]$$

where  $j$  is the electrical flux,  $E$  the applied electrical field and  $\sigma$  the conductivity. In addition for a perfect dielectric material,

$$P = \epsilon_0 \chi E \quad [4.6]$$

where  $P$  is the polarizability, and  $\chi$  is the susceptibility.

For an isotropic and homogeneous material at low frequency the polarization of the material is proportional to the electrical field applied. The polarization could be expressed as the impedance spectrum or the frequency-dependent complex permittivity and conductivity that characterizes the charge-density fluctuations within the sample. Such fluctuations generally arise from the reorientation of the permanent dipole moments of individual molecules or from the rotation of dipolar moieties in flexible molecules, like polymers. The timescale of these fluctuations depends on the sample and on the relevant relaxation mechanism. Dielectric spectroscopy is able to monitor cooperative processes and thus provides a link between molecular spectroscopy and bulk properties of the sample, especially viscoelastic and rheological behavior. Materials dielectric properties are determined by its molecular structure, if the molecular structure changes, its dielectric properties changes.

#### *Principles*

The conductivity of a material is measured by the application of a sinusoidal tension of the form:

$$U = U_0 \sin(\omega t) \quad [4.7]$$

resulting in a sinusoidal current with a dephased angle  $\phi$ ,

$$I = I_0 \sin(\omega t + \phi) \quad [4.8]$$

Using low electrical fields (in the order of Volt/cm), the polarization and conductivities are proportional to the electrical field. The conductivity  $\sigma^*$  could be defined as the ratio among the current and the tension in the sample and is a complex number,

$$\sigma^* = \frac{I}{U} \quad [4.9]$$

Thus, the real and imaginary parts of the conductivity are  $\sigma' = |\sigma^*| \cos \phi$  and  $\sigma'' = |\sigma^*| \sin \phi$ . The ratio between the real and the imaginary conductivity,  $\tan \phi = \sigma'' / \sigma'$  represents a dissipative energy by Joule effect.

The dielectric spectroscopy in an homogeneous medium could permit the study of the relaxations in the polymer. Furthermore, the evolution of the real and imaginary parts of the conductivity a low frequency in a blend insulant-conductor could be followed [29].

Figure 4.18 shows the conductivity zones of a material:

1. *Dielectric zone*. The composite behavior corresponds to an insulating material. The measured phase is near  $90^\circ$  and the conductivity is almost the same as the matrix.
2. *Transition zone*. The conductivity suffers considerable variations due to the formation of a percolating network.

3. *Conductive zone.* This zone corresponds to the increment of the density of the conductor network.

#### *Experimental Technique*

In dielectric spectroscopy or AC impedance spectroscopy, the sample is disposed between two parallel electrodes, constituting, hence, a capacitor during AC measurement. The sample is subjected to a sinusoidal perturbation of intensity in V with variable frequency. The analyzer detects the current (intensity and phase) through the sample at each frequency. Complex impedance is calculated as a function of frequency. The impedance can then be separated into the frequency dependent conductivity and relative permittivity [30].

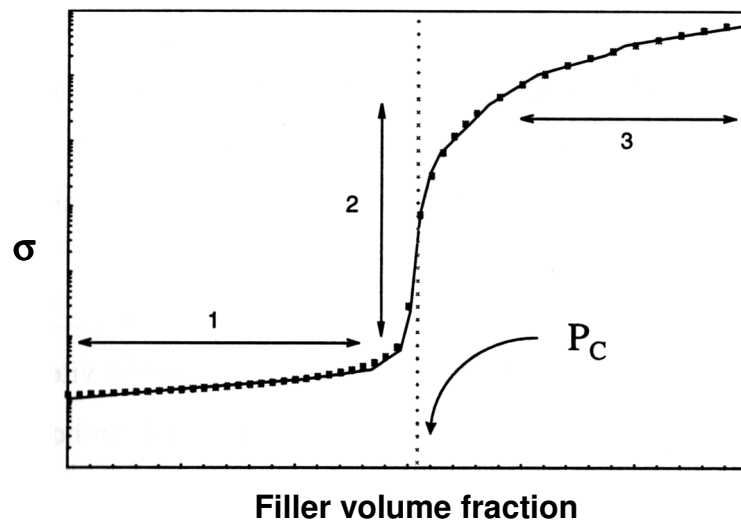


Fig. 4.18. Conductivity zones of a material.

From the AC impedance spectroscopy [31] performed at room temperature, the real and imaginary parts of the impedance ( $Z^*$ ) can be obtained as a function of the frequency. The complex admittance ( $Y^*=1/Z^*$ ) of the nanocomposites can be modeled as a parallel resistor (R) and capacitor (C) and written as a function of angular frequency ( $\omega$ )

$$Y^*(\omega) = Y' + jY'' = \frac{1}{R} + j\omega C \quad [4.10]$$

The specific AC conductivity of the nanocomposites as a function of frequency  $\sigma(\omega)$  is calculated from the modulus of the complex admittance, and was used as a means of comparing the frequency behavior

$$y(\omega) = |Y^*| \frac{d}{A} \quad [4.11]$$

where  $d$  is the sample length or distance between the electrodes, and  $A$  is the contact area. Values of AC conductivity were determined from the real part of the complex admittance

$$\sigma = Y' \frac{d}{A} \quad [4.12]$$

The pure insulating behavior as indicated by the frequency-dependent increase in conductivity with a slope of unity on the log-log plot of specific conductivity against frequency. This behavior is typical of a dielectric material, which for frequencies

$$f > \frac{\sigma_0}{2\pi\epsilon_0\epsilon'} \quad [4.13]$$

gives a conductivity of

$$\sigma = 2\pi f \epsilon' \epsilon_0 \quad [4.14]$$

where  $\epsilon_0$  is the permittivity of the vacuum and  $\epsilon'$  is the real part of the dielectric constant [32].

A material permittivity is usually normalized to the permittivity of vacuum. The real part of permittivity,  $\epsilon'$ , is a measure of the energy stored and is called the dielectric constant. The imaginary part of permittivity,  $\epsilon''$ , is a measure of the energy loss and called the loss factor. In addition, loss tangent is the imaginary part divided by the real part vs. frequency.

Many materials are a mixture of different sized molecules. The permittivity of these mixtures of materials will depend on the interaction of these molecules, their mass, charge and charge distributions.

#### *Applications to carbon nanotubes and nanocomposites*

The relaxational dynamics of soft matter in polymers is characterized by a large frequency range. Dielectric spectroscopy can provide information about the segmental mobility of a polymer by probing its dielectric properties.

Studied materials are among others: polymers, polymer blends, polyelectrolytes, normal and supercooled liquids, and solid state materials.

#### *Experimental conditions*

The AC conductivity measurements were performed at room temperature in the range of frequencies of 1mHz to 1MHz with a voltage of 0.1 and 1 V using a Solartron 1226 bridge system composed by an analyzer of frequencies and a dielectric interphase with a reference module controlled by a computer. The complex admittance  $Y^*$  was recorded versus time. From this admittance, the conductivity  $\sigma$  can be deduced with the equation 4.11.

### 4.3.4. Dynamical Mechanical Analysis (DMA)

#### *Introduction*

The mechanical dynamical analysis or mechanical spectroscopy permits the study of the viscoelastic properties of a material by a measurement of the dynamic module as a function of the temperature (isochrones measurements) or the solicitation frequency (isotherm measurements).

### Principles

Polymer are described as viscoelastic materials, which behavior is intermediate between a perfect elastic solid material (Hooke Law), where the deformation  $\varepsilon$  is proportional to the stress  $\sigma$ :

$$\varepsilon = \sigma / E \quad [4.15]$$

$E$  is the Young modulus, and the ideal viscous liquid (Newton Law), where the deformation speed  $\dot{\varepsilon}$  is proportional to the stress  $\sigma$ :

$$\dot{\varepsilon} = \sigma / \eta \quad [4.16]$$

$\eta$  is the Newtonian viscosity.

The relative importance of these parts is dependent of the stress time application (or frequency) and of the temperature. The Fig. 4.19 describes the typical evolution of the viscoelastic modulus of a polymer with the temperature:

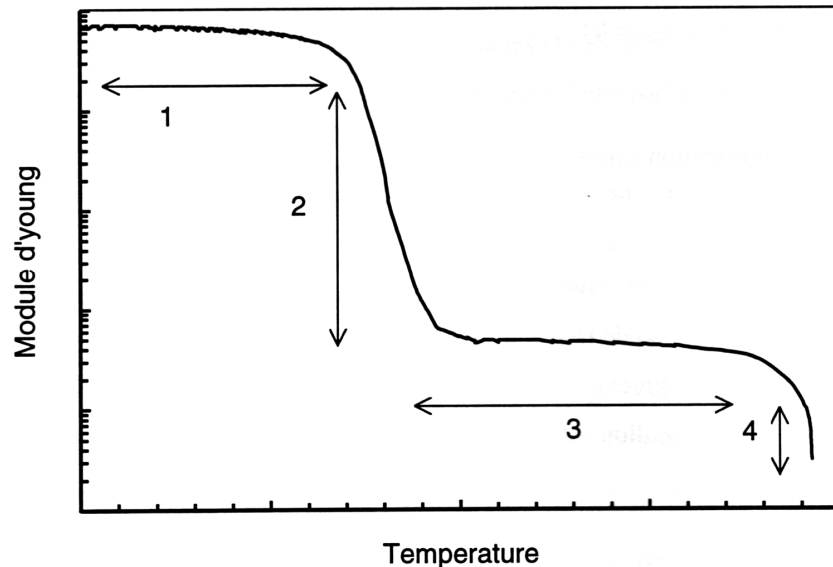


Fig. 4.19. Polymer modulus evolution as a function of the temperature [29].

The four zones corresponds with:

1. *Glassy state*. The polymer is in the vitreous state. Its elastic behavior is from enthalpic origin.
2. *Principal relaxation*. The behavior becomes viscoelastic. The module changes rapidly with the temperature.
3. *Rubery state*. The polymer could perform considerable elongations. Its elastic behavior is entropic in nature.
4. *Flux*. The polymer behaves like a viscous fluid.

### Technique

The mechanical spectroscopy (or Dynamical Mechanical Analysis (DMA)) permits the characterization of the viscoelastic properties of a polymer by the measurement of its Dynamic Module in function of the temperature (isochrones measurements) or the

solicitation frequency (isotherm measurements). The sample is solicited by the application of a stress, which varies periodically,

$$\sigma = \sigma_0 \sin(\omega t) \quad [4.17]$$

resulting in a sinusoidal deformation of the sample,

$$\varepsilon = \varepsilon_0 \sin(\omega t + \phi) \quad [4.18]$$

The deformation amplitude is from the order of  $10^{-6}$  and  $10^{-4}$  to coincide with the linear domain, where the Hooke and Newton laws are verified.

The dynamic module  $E^*$  considers the ratio between the stress applied and the deformation of the sample measured,

$$E^* = \sigma^*(i\omega) / \varepsilon^*(i\omega) = E' + iE'' \quad [4.19]$$

Additionally,  $E' = |E^*| \cos \phi$  and  $E'' = |E^*| \sin \phi$ . Thus,  $E' = (\sigma_0 / \varepsilon_0) \cos \phi$  and  $E'' = (\sigma_0 / \varepsilon_0) \sin \phi$ .

Furthermore, the desphase between the stress and the deformation could be measured as  $\tan \phi = E'' / E'$ . This coefficient is also named frictional interior coefficient and represents the proportion of the dissipated energy in the form of heat in the sample in relation with the elastic energy involved in a deformation cycle. The variations of the complex module  $G^*$  and the  $\tan \delta$  in temperature function or the frequency permit the identification of the associated relaxations to the several freedom degrees of the polymer chains.

In homogeneous systems, the variations in the dynamic module as function of the temperature (or the frequency) corresponds with the relaxation phenomena characteristics of a polymer. These relaxations have their origin in the mobility of the polymer chains at the molecular scale and their molecular motions depending on the temperature and the characteristics of the polymer (as the molecular weight). In the case of polyphase systems, the mechanical behavior depends additionally of the domain sizes and the morphology.

#### *Experimental conditions*

DMA tension mode experiments were performed over polymer nanocomposite films at 1 Hz of frequency and 20 to 120°C in a TA Instrument equipment.

### **4.3.5. Other characterization techniques**

#### *Solubility*

Differences in solubility could be used in the separation of bounded and non-bounded functional groups to carbon nanotubes. In this thesis, the use of organic solvents was selected to determine differences among functionalized and non-functionalized carbon nanotubes.

#### *Size exclusion Chromatography (SEC, or Gel Permeation Chromatography)*

SEC operates on the hydrodynamic volume difference between polymer chains of various sizes. When a polymer solution (mobile phase) is forced through a column containing a nanoporous material (stationary phase), smaller polymer molecules tend to pass through the pores, whereas larger chain elute from the column faster due to entropic

exclusion effects. Thus, analyzing the column outlet using a UV-visible or refractive index detector as a function of time, the molecular weight (MW), the molecular weight distribution and the polydispersity of the polymer sample can be obtained.

In this thesis, polymer molecular weights and molecular weight distributions were determined by Gel Permeation Chromatography, using a Waters GPC equipment with a 717 plus Autosampler, a 996 RI detector, a 600 controller, a 600 pump, and equipped with two Styragel columns (HR3 and HR4). Polystyrene was used as calibration standard. THF was used as eluent at a flow of 1.0 ml/min at room temperature.

## 4.4. Conclusions

The materials and the methods used to prepare polymer-CNTs composites have been described. In addition, the principles of characterization techniques used in the research were considered. Some of the already known applications in the area of nanotubes and their composites were also depicted.

To sum up, some of the main techniques used in this study were: (a) Raman spectroscopy that is performed to ensure that the nanotube sidewalls are modified through chemisorption (bond formation). (b) TGA is made to provide an indication of the degree of functionalization. (c) TEM, SEM and AFM also show sidewall modifications and roping interactions. IR spectroscopy could be useful in the identification of the organic groups appended to the sidewalls of the nanotubes in combination with Raman spectroscopy. However in this case, NMR spectroscopy is usually not very informative, because traces of iron impurities, local field effects due to the nanotubes themselves, and the slow tumbling rates of the nanotubes that cause signal broadening [12].

Finally microscopy techniques were used to determine dispersion and morphological properties of the polymer-CNTs composites. Thermal, electric and mechanical behavior was also important to determine.

## References

1. Terrones, M., H. Terrones, N. Grobert, W.K. Hsu, Y.Q. Zhu, J.P. Hare, H.W. Kroto, D.R.M. Walton, P. Kohler-Redlich, M. Rühle, J.P. Zhang, and A.K. Cheetham, *Efficient route to large arrays of  $CN_x$  nanofibers by pyrolysis of ferrocene/melamine mixtures*. Applied Physics Letters, 1999. **75**(25): p. 3932-3934.
2. Terrones, M., P.M. Ajayan, F. Banhart, X. Blase, D.L. Carroll, J.C. Charlier, R. Czerw, N. Grobert, R. Kamalakaran, M. Mayne, M. Reyes-Reyes, M. Rühle, T. Seeger, and H. Terrones, *Exploring the carbon nanocosmos: doped nanotubes, networks, and other novel forms of carbon*. Proceedings of SPIE, 2003. **5118**: p. 1-.
3. Glerup, M., M. Castignolles, M. Holzinger, G. Hug, A. Loiseau, and P. Bernier, *Synthesis of highly nitrogen-doped multi-walled carbon nanotubes*. Chemical Communications, 2003: p. 2542-2543.
4. Dehonor, M., K. Masenelli-Varlot, A. Gonzalez-Montiel, C. Gauthier, J.Y. Cavaillé, H. Terrones, and M. Terrones, *Nanotube brushes: polystyrene grafted covalently on  $CN_x$  nanotubes by nitroxide-mediated radical polymerization*. Chemical Communications, 2005: p. 1-4.
5. Ng, H.T., B. Chen, J.E. Koehne, A.M. Cassell, J. Li, J. Han, and M. Meyyappan, *Growth of carbon nanotubes: a combinatorial method to study the effects of catalysts and underlayers*. Journal of Physical Chemistry B, 2003. **107**: p. 8484-8489.
6. Tanaka, K., T. Yamabe, and K. Fukui, *The science and technology of carbon nanotubes*. 1999, Amsterdam: Elsevier Science. 191.
7. Cooper, C.A., S.R. Cohen, A.H. Barber, and H.D. Wagner, *Detachment of nanotubes from a polymer matrix*. Applied Physics Letters, 2002. **81**(20): p. 3873-3875.
8. Kroschwitz, J.I., *Polymers: Polymer characterization and analysis*. Encyclopedia Reprint Series. 1990, New York: Wiley Intersciences. 957.
9. Institute, W.P., [www.wpi.edu/Academics/Depts/Chemistry/Courses/General/Infrared.html](http://www.wpi.edu/Academics/Depts/Chemistry/Courses/General/Infrared.html).
10. Harris, P.J.F., *Carbon nanotubes and related structures New materials for the twenty-first century*. 2001, Cambridge: Cambridge University Press. 279.
11. Saito, R., G. Dresselhaus, and M.S. Dresselhaus, *Physical properties of carbon nanotubes*. 1998, London: Imperial College Press. 279.
12. Dyke, C.A. and J.M. Tour, *Overcoming the insolubility of carbon nanotubes through high degrees of sidewall functionalization*. Chemical European Journal, 2004. **10**: p. 812-817.
13. Wagner, H.D., *Nanotube-polymer adhesion: a mechanics approach*. Chemical Physics Letters, 2002. **361**: p. 57-61.
14. Chickos, G.a.D.S., *Infrared Spectroscopy*  
[www.umsl.edu/%7Eorglab/documents/IR/IR2.html](http://www.umsl.edu/%7Eorglab/documents/IR/IR2.html).
15. [www.imb-jena.de/ImgLibDoc/fir/IMAGE\\_FTIR.html](http://www.imb-jena.de/ImgLibDoc/fir/IMAGE_FTIR.html).
16. Sinnott, S.B., *Chemical functionalization of carbon nanotubes*. Journal of Nanoscience and Nanotechnology, 2002. **2**(2): p. 113-123.
17. [www.si-mex.com.mx/PDFS/orthon/Thermal%20Gravimetric%20Analysis](http://www.si-mex.com.mx/PDFS/orthon/Thermal%20Gravimetric%20Analysis).
18. Chen, L., X.-J. Pang, M.-Z. Qu, Q.-T. Zhang, B. Wang, B.-L. Zhang, and Z.-L. Yu, *Fabrication and characterization of polycarbonate/carbon nanotubes composites*. Composites Part A, 2005. **37**(9): p. 1485-1489.
19. Eitan, A., K. Jiang, D. Dukes, R. Andrews, and L.S. Schadler, *Surface Modification of Multiwalled Carbon Nanotubes: Toward the Tailoring of the Interface in Polymer Composites*. Chemical Materials, 2003. **15**: p. 3198-3201.
20. Bahr, J.L. and J.M. Tour, *Highly Functionalized Carbon Nanotubes Using in Situ Generated Diazonium Compounds*. Chemical Materials, 2001. **13**: p. 3823-3824.

21. Tasis, D., N. Tagmatarchis, A. Bianco, and M. Prato, *Chemistry of Carbon Nanotubes*. Chemical Reviews, 2006. **106**(3): p. 1105-1136.
22. Viswanathan, G., N. Chakrapani, H. Yang, B. Wei, H. Chung, K. Cho, C.Y. Ryu, and P.M. Ajayan, *Single-step In-situ Synthesis of Polymer-grafted Single Wall Nanotube Composites*. Journal of American Chemical Society, 2003. **125**(31): p. 9258-9259.
23. Shaffer, M.S.P. and A.H. Windle, *Fabrication and characterization of carbon nanotube/poly(vinyl alcohol) composites*. Advanced Materials, 1999. **11**(11): p. 937-941.
24. Datsyuk, V., C. Guerret-Piecourt, S. Dagreou, L. Billon, J.-C. Dupin, E. Flahaut, A. Peigney, and C. Laurent, *Double walled carbon nanotube/polymer composites via in-situ nitroxide mediated polymerization of amphiphilic block copolymers*. Carbon, 2005. **43**(4): p. 873-876.
25. Weil, J.A., J.R. Bolton, and J.E. Wertz, *Electron Paramagnetic Resonance Elementary Theory and Practical Applications*, ed. I. John Wiley & Sons. 1994, New York: John Wiley & Sons, Inc. 568.
26. Nonhebel, D.C., J.M. Tedder, and J.C. Walton, *Radicals*. 1979, Cambridge: Cambridge University Press. 198.
27. Henry, Y. and A. Guisanni, *Contribution of spin-trapping EPR techniques for the measurement of NO production in biological systems*. ANALUSIS, 2000. **28**(6): p. 445-448.
28. Wikipedia: [www.wikipedia.com](http://www.wikipedia.com).
29. Flandin, L., *Etude expérimentale et modélisation microstructurale de l'évolution des propriétés électriques d'un matériau composite en cours de déformation*, in *Centre de Recherches sur les Macromolécules Végétales, CERMAV-CNRS Grenoble*. 1998, Joseph Fourier- Grenoble I: Grenoble. p. 211.
30. Allaoui, A., S. Bai, H.M. Cheng, and J.B. Bai, *Mechanical and electrical properties of a MWNT/epoxy composite*. Composites Science and Technology, 2002. **62**: p. 1993-1998.
31. Sandler, J.K.W., J.E. Kirk, I.A. Kinloch, M.S.P. Shaffer, and A.H. Windle, *Ultra-low electrical percolation threshold in carbon-nanotube epoxy composites*. Polymer, 2003. **44**: p. 5893-5899.
32. Martin, C.A., J.K.W. Sandler, M.S.P. Shaffer, K.B. Schwartz, W. Bauhofer, K. Schulte, and A.H. Windle, *Formation of percolating networks in multi-wall carbon-nanotube-epoxy composites*. Composites Science and Technology, 2004. **64**: p. 2309-2316.

# Chapter 5.

## Polystyrene-grafting on nitrogen-doped multi-walled carbon nanotubes by nitroxide-mediated radical polymerization

### 5.1. Introduction

As an introduction, we can recall that the overall reaction to produce polystyrene-brushes from nitrogen-doped carbon nanotubes is a two steps process including radical functionalization and polymer-grafting reactions. The theoretical mechanism proposed is shown in Fig. 5.1. The first step, that corresponds to the upper part of Fig. 5.1, considers the formation of initiator radicals by thermolysis in organic solution media, followed by their attachment on the nanotube surface to form radical macroinitiators ( $\text{CN}_x\text{-R}\bullet$ , **2**). Subsequently, the covalent reaction of the controller radicals with the radically activated nanotube surface takes place to form controlled-radical macroinitiators ( $\text{CN}_x\text{-RNO}_x$ , **3**). Finally, the controlled-radical nanotube macroinitiators, presumably formed, are separated from the solvent media by filtration, and repeatedly washed using toluene. In the second step (as illustrated in the lower part of Fig. 5.1), the reactor is fed with a constant amount of purified controlled-radical nanotube macroinitiators, solvent and monomer. At high temperatures, *in situ* radical polymerization begins in the solution media. After 24 hr of reaction polymer-brushes ( $\text{PS-g-CN}_x$ , **4**) are formed.

The different obtained products ( $\text{CN}_x\text{-R}\bullet$ ,  $\text{CN}_x\text{-NO}_x$ ,  $\text{CN}_x\text{-RNO}_x$ , and  $\text{PS-g-CN}_x$ ) have been characterized using Analytical Electron Microscopy, AFM, ESR, Raman Spectroscopy, FTIR, TGA, DSC, and GPC as described in the Chapter 4. Results are discussed in the following.

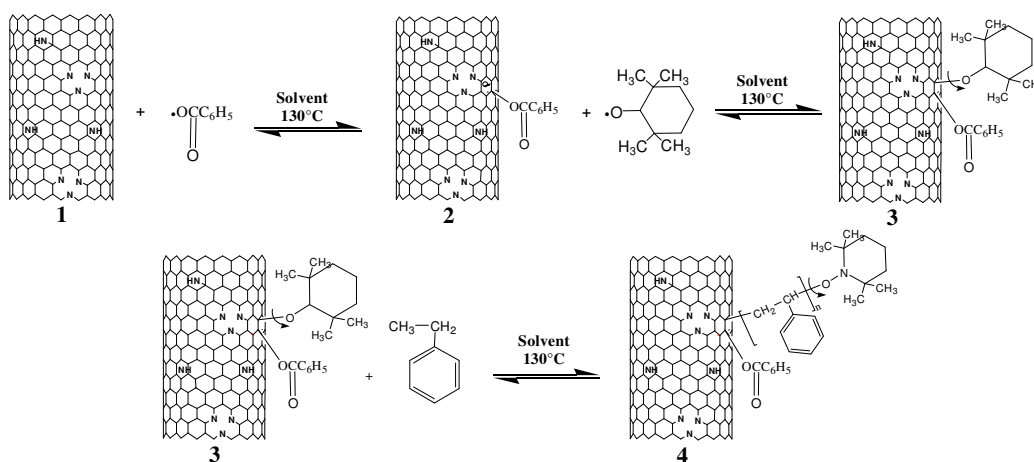


Fig. 5.1. Polymer brushes reaction scheme: functionalization of CN<sub>x</sub> nanotubes (1) with the NMRP initiator (2) and controller (3), and synthesis of polymer brushes of polystyrene (4).

## 5.2. Results and discussion

As can be thought, many chemical routes and some by-products could be formed during these reactions; therefore several physico-chemical characterization techniques have been performed to confirm the occurring of the chemical reactions, as well as the most probable chemical route. The synthesis and characterization results will be presented in chronological order: (i) as-produced CN<sub>x</sub> nanotube disentanglement and purification, (ii) radical functionalization of CN<sub>x</sub> nanotubes, and (iii) polymer-grafting of CN<sub>x</sub> nanotubes.

The first section presents the experimental results concerning the disentanglement of the nanotubes ropes and the purification step of as-produced nitrogen-doped carbon nanotubes.

In the second section, the general screening of the reaction variables performed in order to select the best conditions in the studied range is discussed. The radical functionalization products issued from selected reaction conditions are used for further synthesis and analysis. Some of the obtained results will be described.

Finally, the polymer brushes (PS-g-CN<sub>x</sub>) were analyzed using several characterization techniques.

The differences between physically adsorbed polymer and chemically attached polymer chains on the nanotube surfaces are also commented. Furthermore, a comparison between the overall behavior of multiwalled carbon nanotubes without atom doping, and the nitrogen-doped carbon nanotubes is highlighted.

The sample preparation, as well as the technical conditions of the products characterization, is given in Chapter 4.

### 5.2.1. Disentanglement, dispersion and purification of the as-produced CN<sub>x</sub> nanotubes

The disentanglement, dispersion and purification of as-produced carbon nanotubes ropes have been performed by sample ultrasonication in organic solvents (benzene, toluene or xylene), followed by filtration and drying processes. Several studies were performed to determine the effects of these steps on the CN<sub>x</sub> nanotubes structure. Some of the characterization techniques at this stage involved solubility tests, HRTEM images and TGA.

Solubility experiments of CN<sub>x</sub> and MWNTs after disentanglement, dispersion and purification combined processes reveal that stable dispersions of CN<sub>x</sub> nanotubes can be obtained in various solvents like benzene, toluene, and xylene. Conversely, MWNTs form swollen particles when organic solvents are used. These particles flocculate (sediment deposition) after some time. This difference in solubility is a first indication that there is strong reactivity differences between both kinds of nanotubes, i.e. CN<sub>x</sub> nanotubes are expected to be more reactive, and thus a better interaction with the solvent can take place. In addition, obtained HRTEM images, in agreement with Raman studies, reveal that the ultrasonication in the different solvents provides negligible structural damage in the crystalline structure of the walls (Fig. 4.2). Ultrasonication is thus an efficient way to disentangle nanotubes ropes, to individually disperse them, and to separate carbon particles and catalyst particles. Furthermore, the filtration step eliminates most of catalyst and carbon nanoparticles. Therefore, after ultrasonication/filtration/drying combined processes, a good enough purification seems to be reached and organic solvent dispersions of CN<sub>x</sub> nanotubes are obtained. However, it has to be noted that the length of the nanotubes could not be measured by TEM. It is known that sonication may induce some cutting of the nanotubes but this aspect can not be addressed at this point.

The effects of ultrasonication conditions, such as the type of solvent, the sonication time, and the drying time on the thermal stability of the CN<sub>x</sub> nanotubes were systematically studied using TGA. The experimental error on the weight loss measurements was estimated by measuring 5 samples of the same material. Our results indicate an estimated error of 0.06% in the weight loss calculation in these experiments.

The effect of the solvent type used in the sonication on the thermal stability of CN<sub>x</sub> nanotubes was studied for benzene and xylene. As explained in Chapter 4, the weight loss associated to these organic solvents (low molecular weight species) is assigned to the region from 200-400°C. A higher weight loss in this temperature interval was observed in the case of xylene when compared to benzene. In fact, for the case of xylene a 4.5 % of weight loss was measured vs. around 2 % of weight loss for benzene. This behavior can be related with the individual chemical interactions of benzene and xylene with the CN<sub>x</sub> nanotubes, i.e. molecular size and/or reactivity that determine their superficial adsorption or even more their chemical attachment. In other words, it appears that the extent of weight loss from CN<sub>x</sub> nanotube materials sonicated in organic solvents differs with the solvent used for sonication. As a result of this study, the benzene has been selected as solvent to carry out sonication to minimize the interaction with the CN<sub>x</sub> nanotubes in further treatment and during the chemical reaction steps.

Another important variable is the sonication time (chosen in our study from 1 to 5 hr). Our results point out that difference in this variable induced changes in the weight loss of the  $CN_x$  nanotubes (Fig. 5.2). These differences in the weight loss change can be associated to higher amorphous external layers degradation during the process: the longer the time the higher the degradation of these layers. So, one hour of sonication time has been selected to diminish the structural damage on carbon nanotubes structures.

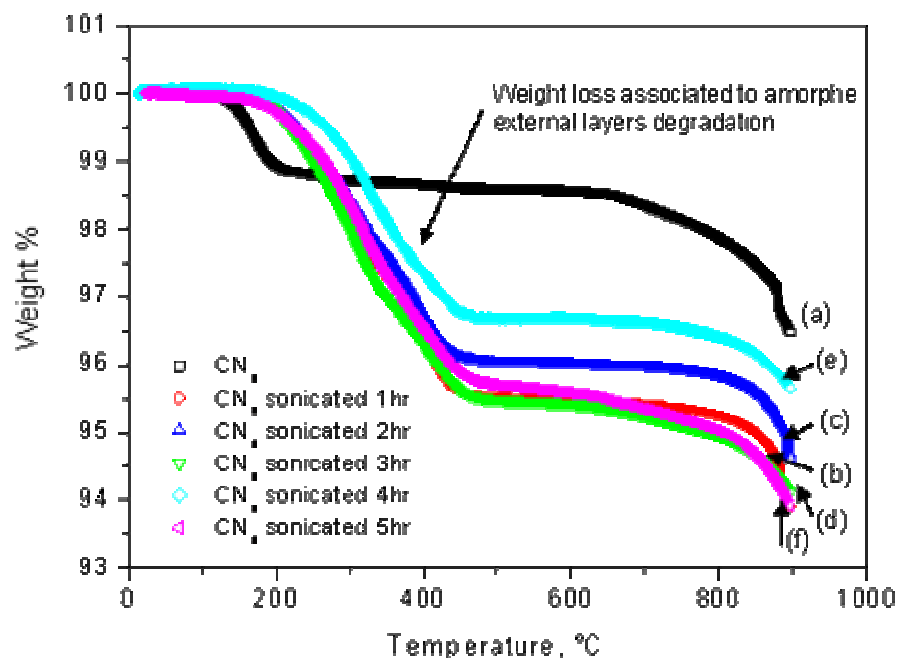


Fig. 5.2. Effect of sonication time in thermal degradation of  $CN_x$  nanotubes: samples were sonicated (a) 0, (b) 1, (c) 2, (d) 3, (e) 4 and (f) 5 hr in xylene and dried in a vacuum oven for 15 hrs at 70-80°C. TGA in N from 20-900°C at 10°C/min.

After the sonication step, a drying step is necessary. The effect of the drying time on sonicated samples has been determined using drying times from 2 to 15 hr in an oxygen atmosphere (Fig. 5.3). When the drying is performed on the as-produced  $CN_x$  nanotubes, an oxidation of the nanoparticles and  $CN_x$  amorphous (“defective”) layers takes place even at low temperatures (<100°C). This effect is illustrated in Fig. 5.3 for a drying step performed in oven for 15hr at 70-80°C (see samples at 2hr and 6 hr). Moreover, the ultrasonication of the  $CN_x$  nanotubes induces additional structural modifications (probably by cutting the nanotubes), thus after the drying step, a higher weight loss is observed. Increasing the drying time leads to higher weight losses. That indicates that the longer drying time eliminates adsorbed solvent molecules more efficiently, but could induce additional structural damage by oxidation. In this case, the drying time was selected to be 15 hrs.

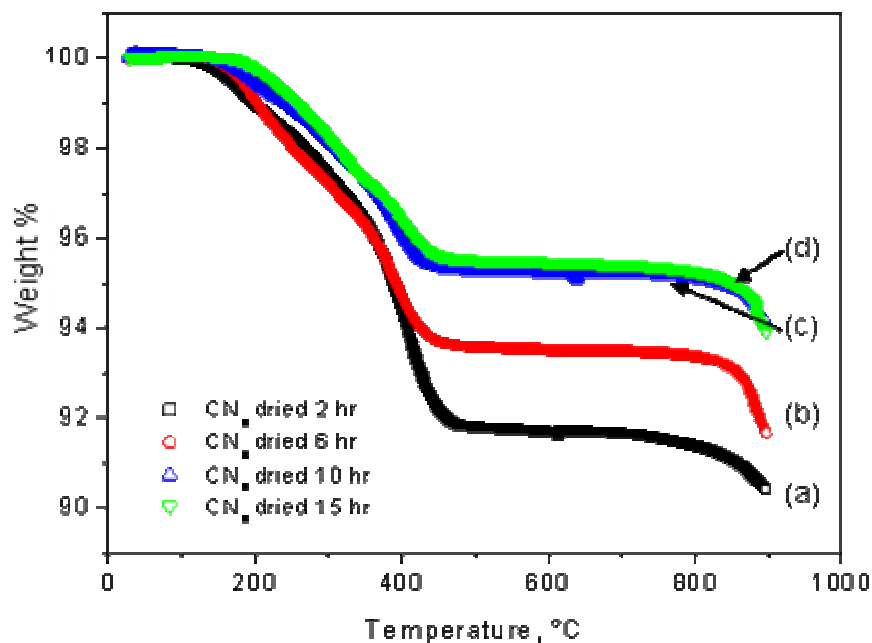


Fig. 5.3. Effect of the dried time in thermal degradation of CN<sub>x</sub> sonicated in xylene (1 hr) and dried for (a) 2, (b) 6, (c) 10 and (d) 15 hr in a vacuum oven at 70-80°C. TGA in N from 20-900°C at 10°C/min.

Fig. 5.4 shows the thermal degradation of samples of CN<sub>x</sub> nanotubes treated with several conditions. The curve of as produced CN<sub>x</sub> nanotubes (see curve (a)) reveals a weight loss below 200°C attributed to low molecular weight surface adsorbed species. The nanotubes remained thermally stable until around 600°C. As produced CN<sub>x</sub> nanotubes dried in a vacuum oven for 15 hr (see curve (b)) reveal a delay in the thermal degradation that begins at temperatures higher than 200°C and continues until 400°C. A similar behavior is observed when the sample was previously washed with xylene then dried (Fig. (c)). In these cases, the thermal degradation is attributed to the drying step degradation (i.e. CN<sub>x</sub> nanotubes and nanoparticles oxidation) without the presence of a solvent in the weight loss measurement. This absence of solvent was attributed to a low interaction of the solvent with nanotubes surface without the sonication step. Finally, CN<sub>x</sub> nanotube samples sonicated for 1 hr in xylene and dried during 15 hr (Fig. (d)) exhibited additional weight losses beginning at 200°C until 400°C. This weight loss was assigned to a double degradation process: (i) due to the drying step (i.e. CN<sub>x</sub> nanotubes and nanoparticles oxidation), and ii) induced by the solvent sonication.

From the observed thermal behavior of CN<sub>x</sub> nanotubes prepared under several conditions (Fig. 5.4), the average weight losses at each combined preparation process can be calculated. The values of weight loss assignment are summarized in Table 5.1. From these results, the total weight loss (4.5%) obtained when the CN<sub>x</sub> nanotubes undergo 1h sonication in xylene and 15h drying can be decomposed in three components: (i) loss of the adsorbed low molecular species, (ii) structural thermal degradation by oxidation in the drying step, and (iii) structural thermal degradation induced by solvent sonication and solvent molecular adsorption.

In the case of benzene, a lower weight loss value can be expected because of its lower molecular interaction (size/reactivity relation) observed in the weight loss measurements performed in 1 hr sonicated and 15 hr dried samples with both solvents (Benzene: 2.0% and xylene 4.5%), reported in a previous section.

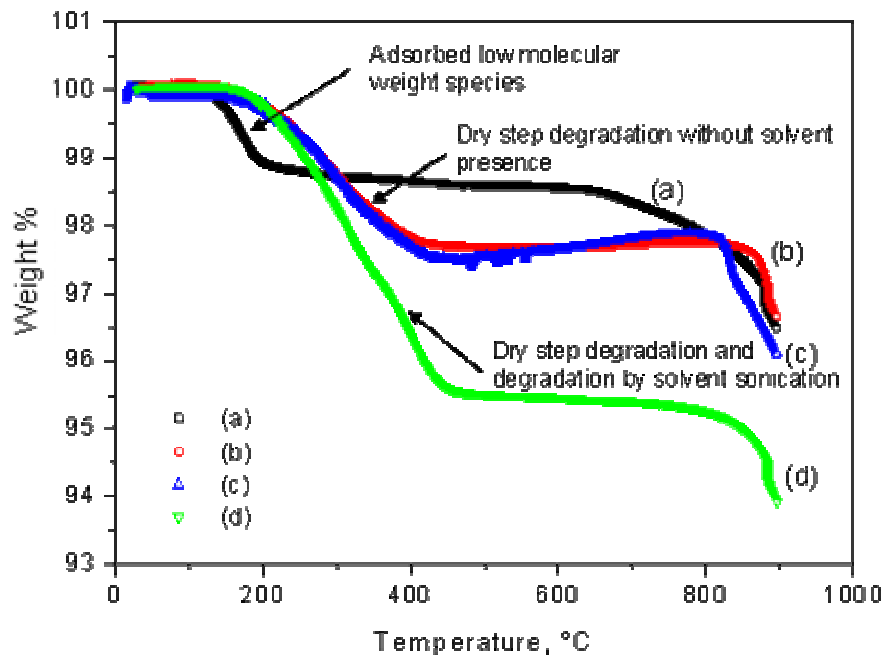


Fig. 5.4. Thermal degradation of: (a) as-received  $\text{CN}_x$  nanotubes, (b) dried  $\text{CN}_x$  nanotubes (15 hr), (c)  $\text{CN}_x$  nanotubes dispersed in xylene without sonication and dried (15 hr), (d)  $\text{CN}_x$  nanotubes sonicated in xylene (1 hr) and dried (15 hr).

The drying step was performed in oven for 15 hr at 70-80°C.

Table. 5.1. Values of the average weight losses at 600°C for ultrasonicated (1 hr in xylene), and dried (15 hr at 70-80°C) as-produced  $\text{CN}_x$  nanotube samples.

Weight loss assignment	%
Original adsorbed low molecular weight species	1.5
Thermal degradation of $\text{CN}_x$ amorphous layers and nanoparticles by oxidation in the dry step	1.0
Thermal degradation of $\text{CN}_x$ structure by solvent sonication and molecular solvent adsorption	2.0
Total:	4.5

To summarize, ultrasonication in organic solvents, followed by a filtration and drying process have been used to successfully disentangle, disperse and purify  $\text{CN}_x$  nanotubes without inducing extended structural damage on their surfaces, as it is usually the case when more aggressive reagents are used, like acids. However, a length decrease can be expected, due to nanotubes cutting. After this study, the more appropriate disentanglement and dispersion condition for  $\text{CN}_x$  nanotubes were determined to be 1 hr

sample sonication in benzene, filtration and vacuum dried at 70-80°C for 15 hr. Using these conditions the sonication time does not produce important structural damages of carbon nanotubes and almost all the adsorbed molecules could be detached without an extensive thermal oxidation. In addition, the selected solvent does not present a high interaction with the nanotubes. This preparation method has been used in this research to prepare the carbon nanotubes to further carry on the functionalization and grafting reactions.

### 5.2.2. Variables screening of functionalized CN<sub>x</sub> nanotubes

Chemical functionalization of carbon nanotubes has been carried out on purified CN<sub>x</sub> nanotubes as prepared in the previous section. As introduced in Chapter 4, the initial screening of radical functionalization and polymer-grafting conditions has been realized using combinatorial design experiments in a Parallel Polymerization Reactor (PPR equipment). The investigated variables were carbon nanotube type (CN<sub>x</sub> and MWNT), solvent type (xylene and benzene), controller type (TEMPO, OH-TEMPO, PR-CGX505, and without controller), initiator concentration (0.05 molar% and 0.1 molar %), and temperature (80 and 130°C). An example of the studied conditions using the Parallel Polymerization Reactor (PPR) is presented in the Fig. 5.5. In particular, columns 1 and 3 were prepared using benzene and 2 and 4 using xylene, as solvents. The use of both solvents was chosen to determine if the solvent behavior would vary with respect to the one found in the previous section for the sonication process.

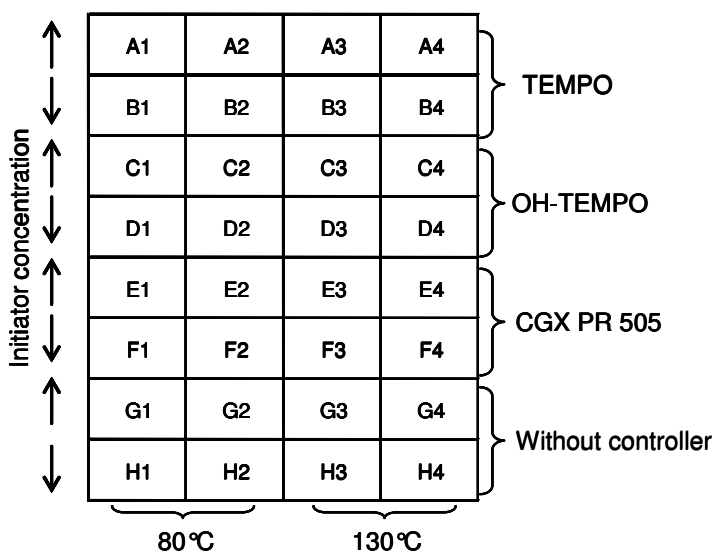


Fig. 5.5. Schematic experimental design.

For both reaction stages, i.e. radical functionalization and polymer-grafting, the inspection of the produced samples was realized to discriminate the experimental conditions.

First of all, it was observed that the products of the radical functionalization of CN<sub>x</sub> nanotubes (i.e. CN<sub>x</sub>-R•, and CN<sub>x</sub>-RNO<sub>x</sub>) at several conditions exhibit similar appearance of

black solids. Moreover, the inspection of the *in situ* polymerized final products (PS-*g*-CN<sub>x</sub>) reveals that higher and more homogeneous polymer-grafted materials of black color have been obtained when benzene and xylene were used at 130°C. This result is expected since 80°C is the lowest temperature to produce the thermolysis of the BPO molecule. Furthermore, the nitroxides remain stable at low temperature (<100°C), reducing the probability to react with the free radicals in the system. As a consequence, further analysis is made only in the samples synthesized at 130°C using benzene or xylene as solvents. The selection of the samples according to the type of solvent was chosen in order to limit the interaction of solvent in the reaction step and the inspection that the samples in benzene gave a high enough polymer yield in the presence of nanotubes. Furthermore, the inspected samples showed an apparent homogeneity in the distribution of the nanotubes within the polymer. Particularly, the systems using benzene have been screened in relation with the controller type and initiator concentration. The resulting materials have been characterized.

#### *Variable screening of benzene samples*

The screening of the controller type and the initiator concentration for theoretical high and low molecular weights has been performed on samples synthesized in benzene (A3 to H3).

The samples were analyzed by TGA to check that the reaction takes place, to measure the functionalization reaction efficiency, and to screen the process variables. Fig. 5.6 presents the effect of the nitroxide type and solution concentration in the weight losses of radical functionalized CN<sub>x</sub> nanotubes.

As can be seen, strong differences are observed as a function of the variables. As discussed previously (see Table 5.1), the interactions of solvent molecules with CN<sub>x</sub> nanotubes lead to a weight loss inferior to 4.5%, including the weight loss associated to the drying process. After reaction in the PPR equipment, all the materials exhibit weight losses superior to 4.5%; for example, sample F3 exhibits the higher weight loss about 10%. From this weight loss: 4.5% could be attributed to the preparation step (according to the section 5.2.1) and the rest could be attributed to the reaction step process. Furthermore, the solvent washing and the posterior drying processes were devoted to eliminate the remaining solvent, initiator and controller species in the solution. Thus, the weight losses could only be due to physically adsorbed or chemically bonded initiator and controller molecules to nanotube surfaces

Notably, thermograms in Fig. 5.6 show three changes of slopes, as shown for sample F3 in Fig. 5.7 with the first derivative of the weight loss vs. temperature. The values for all reactor samples (A3 to F3) are summarized in Table 5.2.

The first slope around 200°C could be associated to purely adsorbed low molecular species on the nanotubes; the second slope (between 200°C to 400°C), and the third change in weight loss (around 400°C) could be related to the detachment of initiators-controllers from the surface of the nanotubes, but also to the molecular degradation after their detachment. The temperature differences of the material degradation are related to the nature of organic bonding to be broken: O-O, O-N, O-C, C-C and C=C. In general, lower degradation energy is related to oxygen bonds. Thus, detachment of the initiator and controller from the nanotube surface could be related to the second slope, between 200 and 400°C.

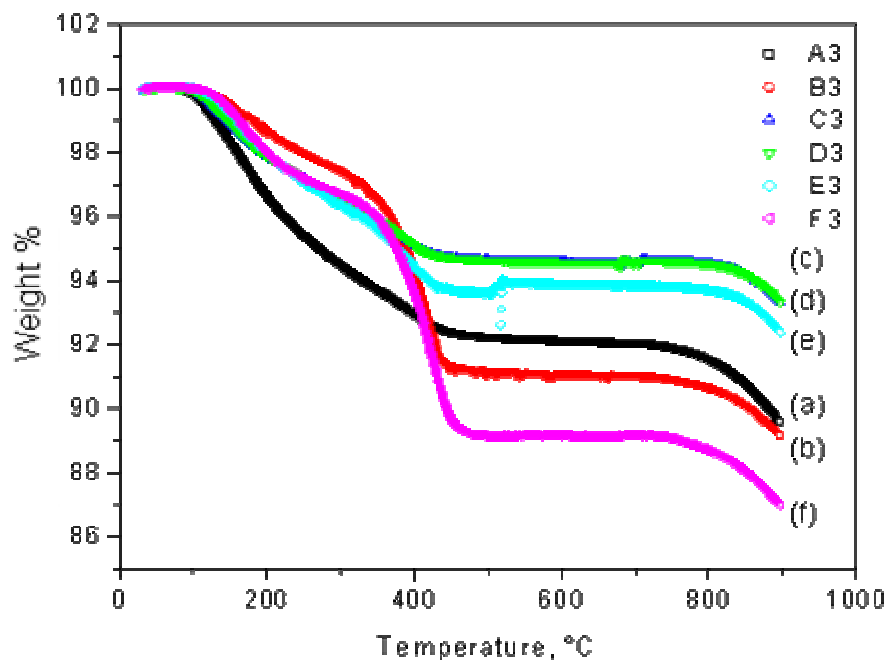


Fig. 5.6. Thermal degradation of radical functionalized reactor samples from the PPRs column 3, synthesized in benzene at 130°C using three nitroxides types: BPO/TEMPO ((a)A3 and (b)B3), BPO/OHTEMPO ((c) C3 and (d) D3) and PR CGX 505 ((e) E3 and (f) F3). A3, C3 and E3 consider high initiator concentration, whereas B3, D3 and F3 low initiator concentration.

Using the hypothesis of thermal degradation, the radical functionalization efficiency of CN<sub>x</sub> nanotubes (*eff*) can be estimated by comparing the experimental weight loss of the sample, associated to the controller and initiator ( $EWL_{BPO+NO_x}$ ), and the theoretical initiator and nitroxide added mass ( $TWL_{BPO+NO_x}$ ). The experimental weight loss of controller and initiator is adjusted with the weight loss due to adsorbed molecules and structural damage on carbon nanotubes ( $EWL_{CN_x}$ ). Thus,

$$EWL_{TOT} = EWL_{CN_x} + EWL_{BPO+NO_x}$$

Thus, the radical functionalization efficiency can be calculated as,

$$eff = \frac{EWL_{BPO+NO_x}}{TWL_{BPO+NO_x}} * 100$$

where  $EWL_{CN_x}$  for CN<sub>x</sub> nanotubes reacted in benzene could be 1.79% (according to previous section).

Table 5.2. Peak to peak analysis of weight losses of radical functionalized reactor samples from the PPRs column 3, synthesized in benzene at 130°C using two levels of initiator and three nitroxide types: BPO/TEMPO (A3 and B3), BPO/OHTEMPO (C3 and D3) and PR CGX 505 (E3 and F3).

Sample Description	Temperature °C	Weight loss %	Attribution
A3 CN <sub>x</sub> -BPO/TEMPO High initiator concn.	129.4	0.9247	
	171.03	1.453	Adsorbed low molecular weight
	393.4	4.562	Detachment and degradation of initiator-controller
	900	3.491	
	residue	89.5693	
B3 CN <sub>x</sub> -BPO/TEMPO Low initiator concn.	229.4	1.793	Adsorbed low molecular weight
	416.1	5.19	Detachment and degradation of initiator-controller
	900	3.904	
	residue	89.113	
	C3 CN <sub>x</sub> -BPO/OH-TEMPO High initiator concn.	157.32	1.31
381.4		3.406	Detachment and degradation of initiator-controller
900		2.014	
residue		93.27	
D3 CN <sub>x</sub> -BPO/OH-TEMPO Low initiator concn.		166.4	1.04
	415.6	5.968	Detachment and degradation of initiator-controller
	900	4.214	
	residue	88.778	
	E3 CN <sub>x</sub> -BPO/PR CGX505 High initiator concn.	172.9	1.361
397.4		4.116	Detachment and degradation of initiator-controller
900		2.134	
residue		92.389	
F3 CN <sub>x</sub> -BPO/PR CGX505 Low initiator concn.		167.73	1.13
	428.83	7.587	Detachment and degradation of initiator-controller
	900	4.342	
	residue	86.941	

\* All samples were reacted in benzene for 2 hr at 130°C with molar solutions of BPO and several nitroxides (1:1.3) for two molecular weights.

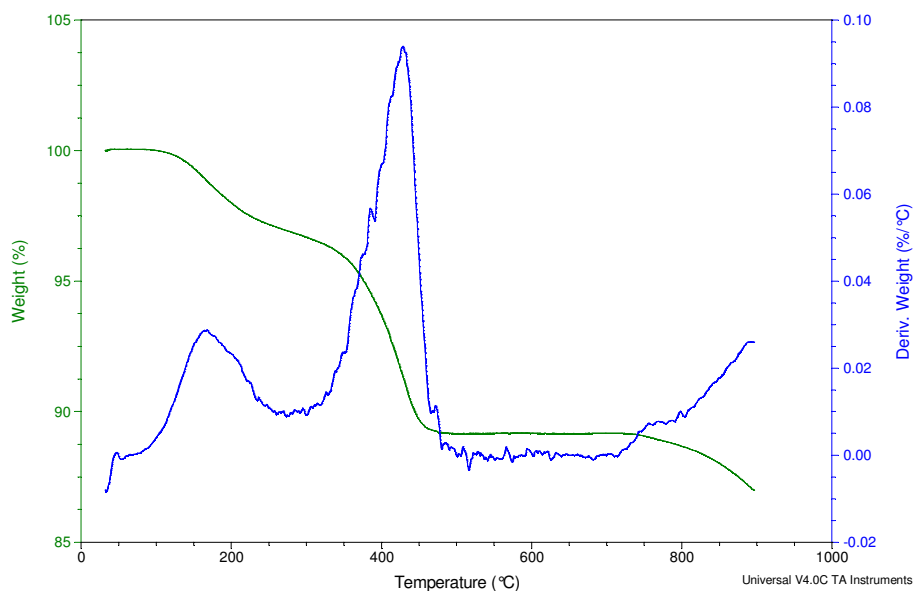


Fig. 5.7. Thermal degradation of radical functionalized reactor sample from the PPRs3, corresponding to F3 synthesized in benzene at 130°C using PR CGX 505 and low initiator concentration. The variables displayed are weight loss and its first derivative.

The radical functionalization efficiency of CN<sub>x</sub> nanotubes for each reactor was summarized in Table 5.3. From these results, it can be observed that systems with high initiator concentrations ( $[I]_{A3} > [I]_{B3}$ ,  $[I]_{C3} > [I]_{D3}$ ,  $[I]_{E3} > [I]_{F3}$ ) for the same nitroxide type are associated to lower radical functionalization efficiency of CN<sub>x</sub> nanotubes. The reason for this behavior can be related to the higher reaction probability of BPO with the nitroxides in solution in a higher concentrated system. In this case, the probability of radical attachment to the nanotube surface decreases. Furthermore, the best controller molecule to be attached to carbon nanotubes depends on the initiator concentration. According to these experiments, TEMPO controller presents higher attachment efficiency at higher initiator concentration, whereas PR CGX-505 presents the highest efficiency at lower initiator concentration. In cases, the polarity, the molecular mobility, and the steric hindrance of the controller molecules are relevant, but also their chemical reactivity toward styrene. Thus, for the first case the higher mobility of TEMPO molecules could favor the attachment to the surface in highly concentrated solutions. In the second case, the PR CGX-505 polarity and molecular conformation determine its more probable attachment to CN<sub>x</sub> nanotubes.

Table 5.3. Radical functionalization efficiency of reactor samples from the PPRs column 3, synthesized in benzene at 130°C using two levels of initiator and three nitroxide types: BPO/TEMPO (A3 and B3), BPO/OHTEMPO (C3 and D3) and PR CGX 505 (E3 and F3).

Sample	Description	Radical functionalization efficiency, %
A3	CN <sub>x</sub> -BPO/TEMPO High initiator concen.	10.9
B3	CN <sub>x</sub> -BPO/TEMPO Low initiator concen.	16.9
C3	CN <sub>x</sub> -BPO/OH-TEMPO High initiator concen.	6.1
D3	CN <sub>x</sub> -BPO/OH-TEMPO Low initiator concen.	16.4
E3	CN <sub>x</sub> -BPO/PR CGX505 High initiator concen.	7.2
F3	CN <sub>x</sub> -BPO/PR CGX505 Low initiator concen.	20.2

The radical attachment to carbon nanotube surface determines the formation of labile macroinitiators to initiate *in situ* polymer chains grafting. In consequence, the best yields of radical attachment could be related with the best yields of polymer grafting. Thus, the preliminary results favor further characterization of reactor F3 at each stage of the reaction (Table 5.3) Sample F3 (synthesized using PR CGX505 as a controller and lower concentrations of initiator-controller in solution) presents the highest efficiency, as could be expected from their nitroxide molecular structure (Ciba private information).

To summarize, the thermogravimetric results indicate that the radical functionalization of carbon nanotubes has taken place because of the observed weight losses (>9%) that are associated to the chemical interaction of the system initiator-

controller with the  $\text{CN}_x$  nanotubes. The radical functionalization efficiency varied between 9 and 20% depending on the nitroxide type used during functionalization (0.05 and 0.1 initiator molar %). The results indicate that higher concentrations of initiator-controller in the solution media increase competition between BPO- $\text{NO}_x$  (most favorable interaction) with  $\text{CN}_x$ - $\text{RNO}_x$  (surface less favorable interaction). In this case, the controller PR-CGX505 is observed as the most efficient to be bond to carbon nanotube surface. Because of these observations, this study continues with the analysis of F3 sample, but also with A3.

### 5.2.3. Radical functionalization of $\text{CN}_x$ nanotubes

The radical functionalized nitrogen-doped nanotubes at the reactors conditions A3 and F3 (as giving in Fig. 5.5) have been characterized using HRTEM and allied techniques, TGA, ESR, FTIR, Raman spectroscopy. These results are compared with those obtained with a physical blend of PS and  $\text{CN}_x$  nanotubes prepared in solution under the same conditions of composition and solvent.

At this point, it can be precised that the radical functionalization of carbon nanotubes could proceed through: (i) pure BPO radical attachment ( $\text{CN}_x\text{-R}\cdot$  or  $\text{CN}_x\text{-R}$ , i.e. radical stabilized or not), (ii) pure  $\text{NO}_x$  radical attachment ( $\text{CN}_x\text{-NO}_x\cdot$  or  $\text{CN}_x\text{-NO}_x$ , i.e. radical stabilized or not), and (iii) combined radical attachment of BPO and  $\text{NO}_x$  radicals ( $\text{CN}_x\text{-RNO}_x$ ). Also, a quantity of carbon nanotubes could remain un-reacted.

The produced samples that we analyzed could be formed by a combination of (i), (ii) and (iii) radical functionalized products. The differences between (i) and (ii) products can be explored using TGA, ESR and FTIR. Conversely, other characterization techniques do not distinguish between (i), (ii) and (iii) radical functionalized products, thus a generic  $\text{CN}_x\text{-RNO}_x$  name will be given. In particular, this study is interested in the formation of  $\text{CN}_x\text{-RNO}_x$  materials of type (iii) that could behave as macroinitiator for the polystyrene polymerization, therefore experimental pieces of evidence of their formation are searched for.

#### 5.2.3.1. Electron Microscopy and allied techniques

Microscopic techniques have been used to investigate the general arrangement of radical functionalized carbon nanotubes, their morphological differences in the amorphous and crystalline layers, as well as their changes in chemical composition related to as-produced  $\text{CN}_x$  nanotubes.

##### 5.2.3.1.1. Structure and morphology of radical functionalized carbon nanotubes

Examples of HRTEM images of  $\text{CN}_x$  nanotubes after the functionalization step with BPO and  $\text{NO}_x$  radicals are presented in Fig. 5.8 (a) and (b). As can be seen, the chemically modified carbon nanotubes (A3 and F3) exhibit some changes in their morphology in contrast with as-prepared  $\text{CN}_x$  nanotubes shown previously in Fig. 4.2.

The observed functionalized  $\text{CN}_x$  nanotubes disperse well in organic solvent media. Dispersed individual carbon nanotubes preserve their graphitic crystalline layers unchanged, but they present an inhomogeneous amorphous layer with an average thickness of 3.6 nm that could be associated to the initiator and controller species physically adsorbed

or chemically attached to nanotube surface. These evidences (even though the increase in the amorphous layer is low and may be considered as not significant) promote the need of further studies to determine if the radical functionalization of CN<sub>x</sub> nanotubes (CN<sub>x</sub>-RNO<sub>x</sub>) takes place on the surface of the CN<sub>x</sub> nanotubes.

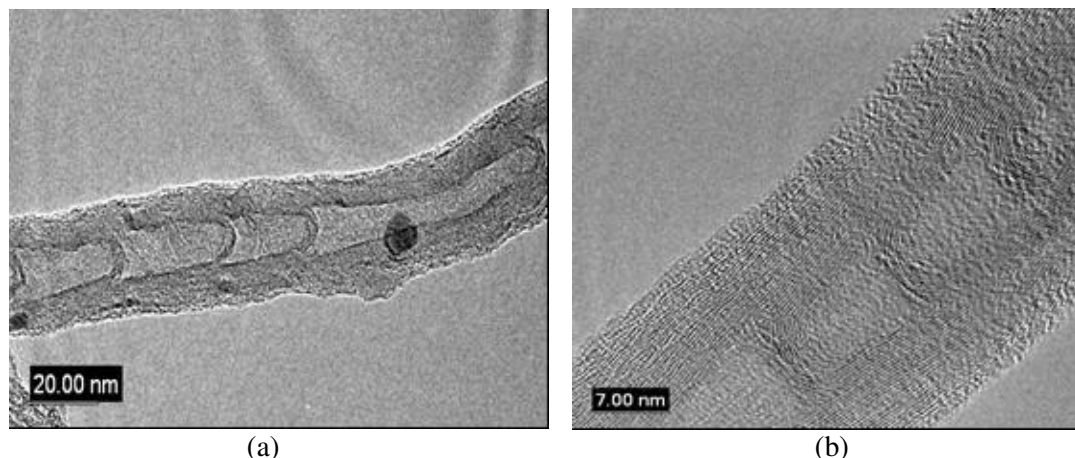


Fig. 5.8. HRTEM images of radical functionalized carbon nanotubes with BPO and TEMPO after dispersion by sonication in ethanol: (a) global view, (b) zoom.

#### 5.2.3.1.2. Chemical composition of radical functionalized carbon nanotubes

The CN<sub>x</sub>-RNO<sub>x</sub> materials were further analyzed by EELS at high energy losses and energy-filtrated TEM techniques (EFTEM) to determine their elemental composition. It is expected that the incorporation of molecules of initiator and controller to functionalized CN<sub>x</sub> nanotubes would increase their overall concentration of nitrogen and oxygen.

The relative concentration of nitrogen to carbon (N/C) and oxygen to carbon (O/C) elements in CN<sub>x</sub>-RNO<sub>x</sub> were determined by high loss EELS and the results are presented in Table 5.4.

#### *Relative N/C concentration*

From the Table 5.4, it can be seen that the CN<sub>x</sub> nanotubes seem to present higher N concentrations than MWNT because of the atom incorporation by doping in the nanotube synthesis step (as expected). Furthermore, the radical functionalized CN<sub>x</sub> nanotubes (3) seem to exhibit an increase of 27% in the relative N/C concentration, compared to as-produced CN<sub>x</sub> nanotubes. This N/C increment in the radical functionalized CN<sub>x</sub> nanotubes could only be explained by the incorporation of initiator-controller molecules (1 N atom per attachment site) to the nanotubes surface, and may indicate that at least the controller molecules are attached to the CN<sub>x</sub> nanotube surface (initiator does not have N atoms). Additionally, all the spectra were obtained after sample purification, therefore the NO<sub>x</sub> radical molecules could only remain if a chemical bond exists with the CN<sub>x</sub> nanotube. As a consequence, the obtained values for the relative N/C concentration, associated with NO<sub>x</sub>, correspond to a radical functionalization rate of around 27% on nitrogen-doped carbon nanotubes sites.

Table 5.4. N and O averages relative concentrations of as-produced (1), radical functionalized (3) and polymer-grafted carbon nanotubes (4) corresponding to F3 sample and measured by EELS at high energy losses.

Sample	N/C	±	O/C	±
MWNT	0.0059	0.00160	0.0016	0.00155
CN <sub>x</sub> , 1	0.0160	0.00600	0.0245	0.01350
CN <sub>x</sub> -RNO <sub>x</sub> , 3	0.0203	0.00233	0.0267	0.00233
PS- <i>g</i> -CN <sub>x</sub> , 4	0.0260	0.00600	0.0110	0.00470

#### *Relative O/C concentration*

As far as oxygen is concerned, the relative quantification in CN<sub>x</sub> nanotubes has a very high value, probably associated with a high number of molecules adsorbed onto the nanotube surface. This could be related to the as-produced sample preparation (without drying), and to the CN<sub>x</sub> nanotubes higher reactivity compared to MWNTs, that display O/C lower values. As a consequence, O/C results have to be carefully interpreted because of the high uncertainty in the measurement.

Considering the error in the O/C content quantification of CN<sub>x</sub> nanotubes, it may be possible to say that there is an increase in oxygen concentration in the radical functionalized carbon nanotubes (CN<sub>x</sub>-RNO<sub>x</sub>). This O/C increment could be associated with the oxygen atoms incorporated to CN<sub>x</sub> nanotubes sites due to the initiator-controller molecule. Unfortunately, in this case the value of the increment in O/C and the origin of the oxygen atoms were difficult to determine due to both initiator (two oxygen atoms as maximum), and nitroxide controller (one oxygen atom as minimum) contributions. It may also be possible that some other O atoms were incorporated to the nanotubes during the functionalization processes because of the CN<sub>x</sub> nanotubes reactivity. As in the case of N, the O atoms only could be present in the sample by chemical attachment due to the purification process.

Additional information have to be taken into account in the analysis of the relative concentration of N/C and O/C in CN<sub>x</sub> nanotubes, obtained from high energy-loss EELS measurements. Loiseau *et al* [1] found that N is mainly located in the internal layers and O in the external layers of MWNT when doped with nitrogen. Thus, in this case it is expected that N would be better determined than O because of the possible external chemical reactions or adsorption-desorption phenomena, but also because of the differences in the elemental concentration. Yet, it should be noticed that the low contents of N and O in the samples make the definition of the background difficult and hence most probably lead to uncertainties higher than those indicated by the Gatan EL/P software. Therefore, other characterization technique is needed to confirm the chemical composition of the radical functionalized CN<sub>x</sub> nanotubes.

The energy-filtered images in Fig. 5.9 show the zero loss images and elemental maps (C, N and O) for: i) CN<sub>x</sub> nanotubes, and ii) CN<sub>x</sub>-RNO<sub>x</sub> samples. Furthermore, Figs. 5.10 (a)-(c) and 5.11 (a)-(c) show the EELS series spectra for each element in both samples, as well as the calculation method parameters. Note that in all cases, the image series

concerning an element were all acquired varying the experimental conditions (illumination current, acquisition time, slit width, etc), so that it should not be possible to compare the intensities of the edges from one specimen to another.

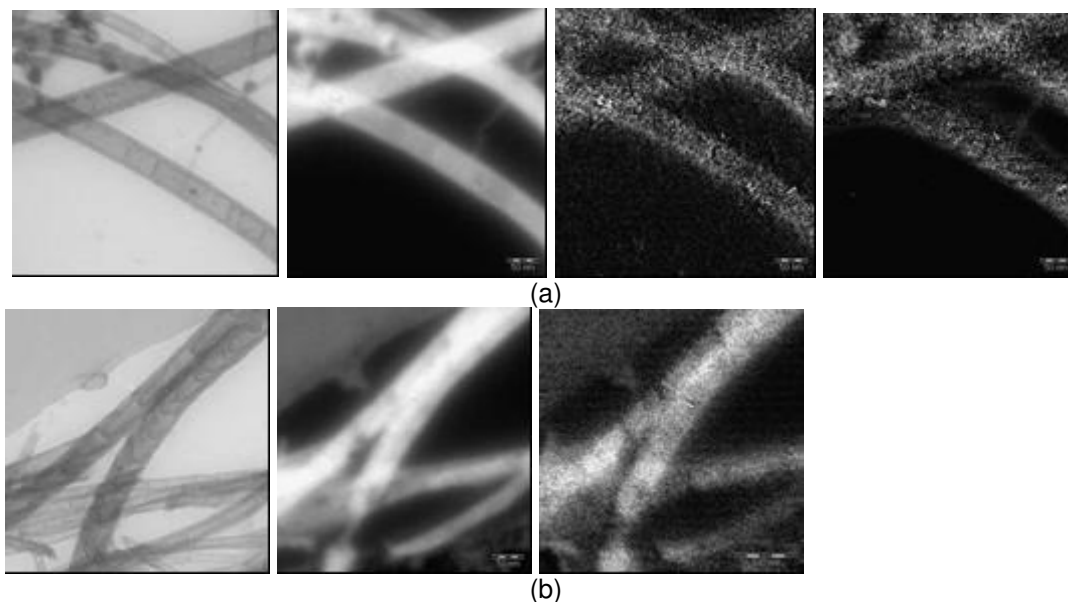


Fig. 5.9. Filtered images of (a)  $CN_x$  nanotubes, and (b)  $CN_x-RNO_x$ . Each group of images is presented in the following order: zero loss, carbon, nitrogen and oxygen maps.

Particularly, the chemical maps of C, N and O in  $CN_x$  nanotubes were obtained using the three image linear-law subtraction (Fig 5.10). The three images-linear law subtraction method is a conventional technique to analyze the elemental content of energy-filtered images. This method considers zones at the nanotube surface that are subtracted from the background zones of the same sample. The degree of the adjusting equation (i.e. linear, power or exponential) is determined according to the best fit.

The fitting procedure was relatively good in all cases and indicates that there are low quantities of N and O, as expected (high signal to noise ratio in the nitrogen and oxygen series). The elemental maps also reveal a quite homogeneous distribution of nitrogen and oxygen.

The  $CN_x-RNO_x$  sample was analyzed in a similar way. The three image-power law subtraction method could be used to calculate the carbon elemental map (Fig. 5.11). However, a good fit could not be obtained with the power law for nitrogen and oxygen, so exponential laws were used. The obtained maps also seem to indicate that nitrogen and oxygen have a quite homogeneous spatial distribution in the nanotube.

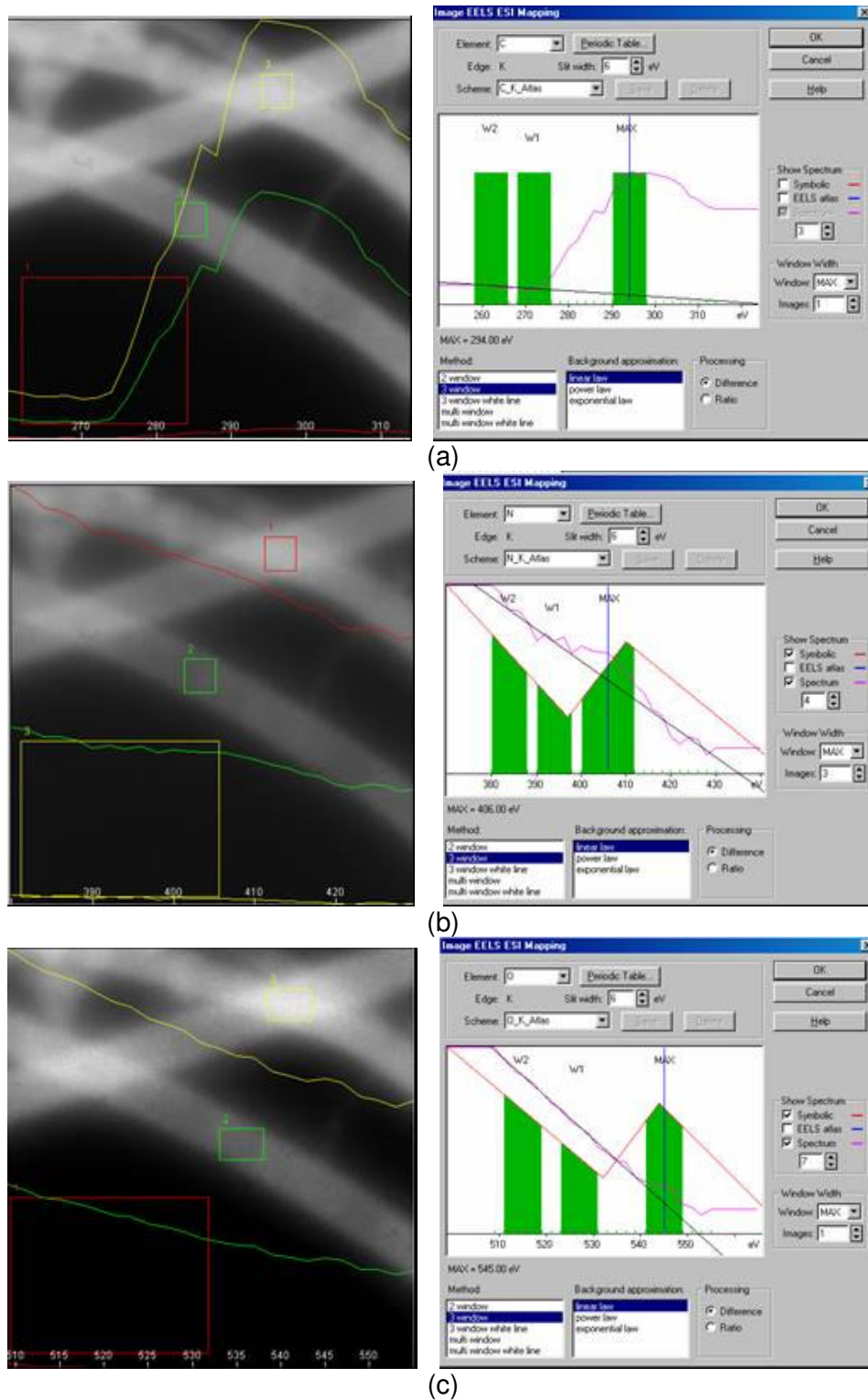


Fig. 5.10. EFTEM spectra extracted from the energy-filtered image series, sorted by element and the parameters used for the calculation of the elemental maps in  $CN_x$  nanotubes (1):  
 (a) carbon map, (b) nitrogen map and (c) oxygen map.

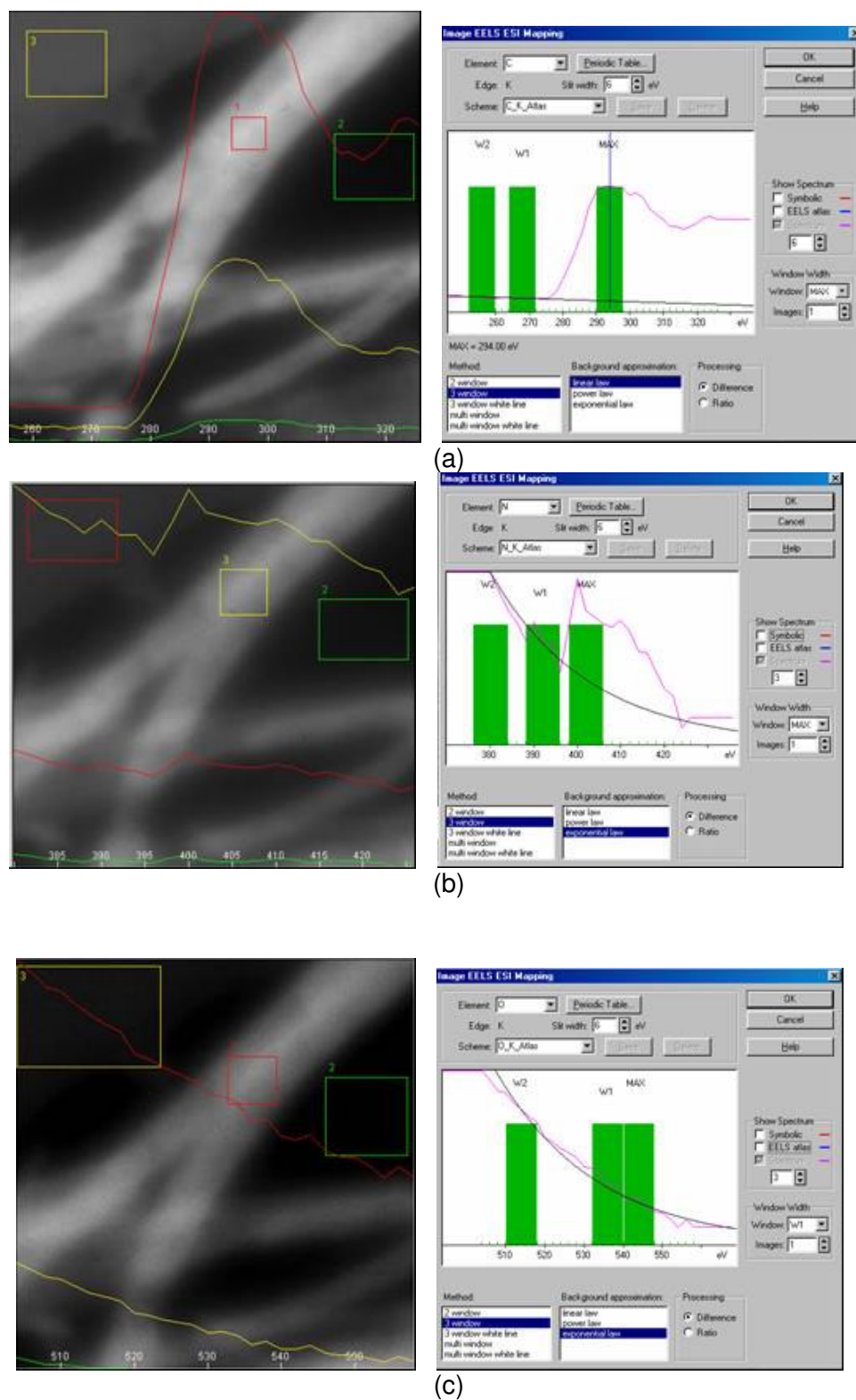


Fig. 5.11. EFTEM spectra extracted from the energy-filtered image series, sorted by element and the parameters used for the calculation of the elemental maps in CN<sub>x</sub>-RNO<sub>x</sub> (3):  
 (a) carbon map, (b) nitrogen map and (c) oxygen map.

In all the samples analyzed by EFTEM, it was found that N and eventually O (when detected) were homogeneously distributed on the nanotube. In fact, at the magnification chosen for the image acquisition, it was not possible to detect whether N was preferentially in the inner layers of the nanotubes or not, as observed by Loiseau *et al* [1]. It is thus assumed that the N and O coming from the initiator and the controller molecules are homogeneously distributed on the surface of the nanotube. This should favor the formation of a homogeneous PS layer during the polymerization step.

Comparing EELS and EFTEM results, it was observed that the concentration of nitrogen and oxygen were both increased in  $CN_x$ - $RNO_x$  materials. In addition, because the N concentration in the materials does not decrease, and supposing that the C concentration remains constant, the chemical functionalization could be proceeding by addition reactions at graphitic, pyridinic or pyrrolic sites. Furthermore, the relation between the nitrogen content in the N-doped carbon nanotubes and the chemical bonding was studied by Terrones *et al* [2]. They found that N could be: i) graphitic if  $N/C < 10\%$ , ii) pyridinic if  $N/C = 10-20\%$  and iii) pyrrolic if  $N/C > 20\%$ . Also the authors found that the pyridinic and pyrrolic groups are located in the internal layers, whereas the graphitic sites are in the external layers. Using this information, it is proposed that the radical functionalization could most probably proceed at graphitic sites by (i) radical addition reaction in the aromatic rings with radical resonance, or by (ii) radical trapping [3] of  $CN_x$  nanotubes. In the first case a controlled-macroinitiator could be formed if  $NO_x$  radicals further attached to the resonant radical. In the second case, the initiator and controller radical trapping is stronger than the creation and resonance of radicals by the initiator in the nanotube surface. This means that only controller molecules were attached to the  $CN_x$  nanotubes and that the polymerization over the surface begins by the radical monomer attachment, as was reported [4]. Using other characterization techniques a more detailed interpretation could be done.

In summary, the HRTEM, EELS at high energy losses and EFTEM results reveal that the morphology and elemental composition of the radical functionalized carbon nanotubes ( $CN_x$ - $RNO_x$ ) are modified after the radical functionalization step. That could be attributed to the incorporation of initiator-controller molecules onto the nanotube surface by chemical attachment.

In particular, the N increment in the  $CN_x$ - $RNO_x$  materials could be explained by the  $NO_x$  radical chemical bonding onto the nanotube surface with an estimated  $NO_x$  radical functionalization rate  $>25\%$ . The O increment in radical functionalized carbon nanotubes could be associated with the chemical bonding of the initiator-controller molecule. The EFTEM results determined a homogeneous N and O distribution in the  $CN_x$ - $RNO_x$  surfaces. This point is important as it can favor the formation of a homogeneous PS layer during the polymerization step.

Finally, the proposed mechanism is that radical functionalization of  $CN_x$  nanotubes could most probably proceed at graphitic sites by (i) radical addition reaction in the aromatic rings with radical resonance, or by (ii) radical trapping of  $CN_x$  nanotubes. To determine the extent and the mechanism of radical functionalization, other characterization techniques will be used.

### 5.2.3.2. Thermogravimetric Analysis

Previous results in TGA characterization (Fig. 5.4) reveal that the radical functionalization reaction of CN<sub>x</sub> nanotubes with initiator-controller combined system has taken place, thus a detailed characterization of the reaction is proposed to evaluate the interaction of carbon nanotubes with each kind of radicals at selected experimental conditions. Thus, thermograms from CN<sub>x</sub> nanotubes reacted with solutions of i) initiator, to give CN<sub>x</sub>-R or CN<sub>x</sub>-R•, ii) controller, to give CN<sub>x</sub>-NO<sub>x</sub> (using PR CGX505), and iii) initiator-controller, to give CN<sub>x</sub>-RNO<sub>x</sub> (using PR CGX505) have been obtained at same conditions and solutions concentration that F3 but with the double mass of CN<sub>x</sub> nanotubes (Fig. 5.12).

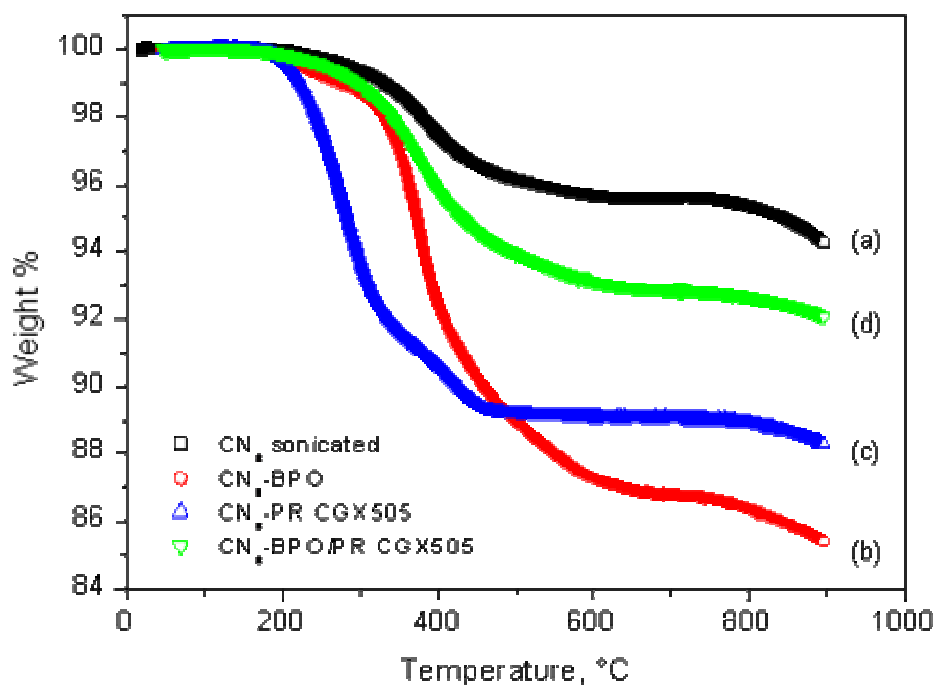


Fig. 5.12. Thermal degradation of CN<sub>x</sub> nanotubes reacted with solutions of (b) BPO, (c) PR CGX505 and (d) BPO-PR CGX505 at same reaction conditions than F3 sample, but with twice of CN<sub>x</sub> nanotubes.

Fig. 5.12 shows the differences between weight losses for each of the CN<sub>x</sub> nanotube products after reaction with initiator and controller radicals, separately. As can be seen, each curve presents different weight losses assignable to attached molecules. Interestingly, it can also be observed that the CN<sub>x</sub> nanotubes interacts with initiator and controller alone more than with the combined molecules solutions. This fact could be explained by the competition between heterogeneous and homogeneous radical reactions, but also due to differences in the chemical interaction nature of the components. Thus in the first case, it is expected that the most favorable radical reaction takes place in solution between low

molecular species. Furthermore, variables in the radical reactions, such as solvent cage effect, steric hindrance, radical persistence, and molecule mobility of low molecular species also determine the probability of radical reaction with carbon nanotubes.

The radical functionalization efficiencies of  $CN_x$  nanotubes were empirically determined using the weight loss values. Thus, the strongest interaction was observed in the system of  $CN_x$  nanotubes with BPO with a radical functionalization efficiency of 82%, followed by the  $CN_x$  nanotubes with PR CGX505 with 53%, and finally by the  $CN_x$  nanotubes with BPO and PR CGX505 with 13%. The last value associated to the  $CN_x$ - $RNO_x$  is slightly inferior to that obtained in the PPR with the F3 sample. This difference could be due to the double mass of carbon nanotubes labile to radical functionalization.

This experimental piece of evidence confirms that  $CN_x$  nanotubes react with both peroxide and nitroxide radicals. This radical functionalization could be explained by  $CN_x$  nanotubes radical scavenging properties, but also by radical addition reactions at nanotube reactive sites, as graphitic, “defective” and N-doped. Moreover, the existence of three kinds of products from the radical functionalization of  $CN_x$  nanotubes could be possible: (i)  $CN_x$ - $R\bullet$  or  $CN_x$ -R, (ii)  $CN_x$ - $NO_x\bullet$  or  $CN_x$ - $NO_x$ , and (iii)  $CN_x$ - $RNO_x$ .

After these results, it could be possible to select a simpler system composed only by the  $CN_x$  nanotubes radically functionalized with initiator or nitroxide controller to investigate the formation of  $CN_x$  polymer-brushes. Nevertheless, this study considers the use of controller macroinitiators synthesized in one chemical step by the BPO and PR CGX505, where a minor radical functionalization efficiency were formed (around 20% in weight), and also, where three kind of products could be formed.

### 5.2.3.3. FTIR Spectroscopy

The products of the radical functionalization of  $CN_x$  nanotubes were analyzed using FTIR to determine the presence of functional groups related to the initiator and controller chemically bonded to carbon nanotube surfaces.

#### 5.2.3.3.1. Carbon nanotubes spectra

In general, carbon nanotubes are difficult to analyze using FTIR because of their low absorption in the infrared region. In fact, carbon nanotubes spectra present around 97% of transmittance. Thus, several experimental techniques have been proposed to better determine the nanotubes absorption spectra. Among them, many reports consider mostly the Attenuated Total Reflectance (ATR) [5], solid state diffuse reflectance [6], as well as modified conventional FTIR [7] in order to enhance the detection of infrared absorption in nanotubes. In this work, FTIR in the modes of ATR, reflectance and conventional FTIR were tried. Good results were obtained in conventional FTIR using carbon nanotubes dispersed in toluene over a salt surface (SeZn), and in the ATR technique. The results of the conventional technique will be presented; the analysis is made always with the aid of the ATR results.

As-produced nitrogen-doped carbon nanotubes (Fig. 5.13) present some absorption bands at high wavenumber ( $>3500\text{ cm}^{-1}$ ), at  $2800\text{-}3000\text{ cm}^{-1}$ , and below  $1800\text{ cm}^{-1}$ , due to

C-H stretching vibrations and C-H deformation modes. The presence of toluene is not detected because there are no bands at 2000-1800 cm<sup>-1</sup>, neither at 700-800 cm<sup>-1</sup>.

#### 5.2.3.3.2. Radical functionalized carbon nanotubes

Radical functionalized carbon nanotubes with BPO, CGX505 and BPO/CGX505 have been analyzed separately. In general, it is observed that all the functionalized products present a diminution of the transmittance in relation with low molecular reactants spectra. Therefore, the attribution of each band remains difficult. Fig. 5.13 presents representative spectra of raw and radical functionalized with BPO/CGX505 CN<sub>x</sub> nanotubes. From the analysis of the differences between spectra, as well as the comparison with BPO and nitroxide spectra, the following absorption peaks can be highlighted:

- Bands between 3100 to 2900 cm<sup>-1</sup>, and 2000 to 1800 cm<sup>-1</sup> are attributed to the mono-substituted aromatic hydrocarbons due to BPO and nitroxide radical molecules. The first group of bands is relatively more intense than the corresponding bands in the original BPO. This fact could be related to the addition effect due to the presence of both radicals.
- Band at 1600 cm<sup>-1</sup> could be related to the C=C aromatic rings from the presence of BPO and nitroxide molecules, or to the carbonyl (-CO) bond between initiator-controller and carbon nanotubes.
- Intense bands at 1494 and 1451 cm<sup>-1</sup> are attributed to aromatic ring breathing modes, may be from BPO molecules after the comparison with its spectra.
- Band at 1260 cm<sup>-1</sup> and 1030 cm<sup>-1</sup> are related to the -CO vibrations from ethers which are attached to an aromatic ring of the carbon nanotube. These bonds occur when BPO and nitroxide molecules have effectively reacted with carbon atoms in the carbon nanotubes.
- Band at 1157 cm<sup>-1</sup> could be attributed to some kind of esters related to the formation of initiator-controller species preferentially over the nanotube because of the solvent washed of the material.
- Most of the bands among 1700 and 1500, at 1115 and 910 cm<sup>-1</sup> are related to the nanotube structure.
- Bands at 789 cm<sup>-1</sup>, 760 cm<sup>-1</sup>, and 700 cm<sup>-1</sup> in the fingerprint regions are attributed to BPO/nitroxide and nanotubes, respectively.
- Finally, it is very difficult to certainly attributed absorption peaks to nitrogen bonds, nevertheless: (i) the broad band at 3000-3500 cm<sup>-1</sup> could be attributed to N-H and C-H stretching vibrations, (ii) the peak at 1380 cm<sup>-1</sup> could be related to N-O stretch, and (iii) the combination band at 945 and at 1260 cm<sup>-1</sup> could be attributed to the N-O bond. Thus, it could be possible to say that the nitroxide molecule is present in the system.

- The bands attributed to carboxylic groups are absent from the spectra, indicating that BPO could be effectively bond to nanotubes.

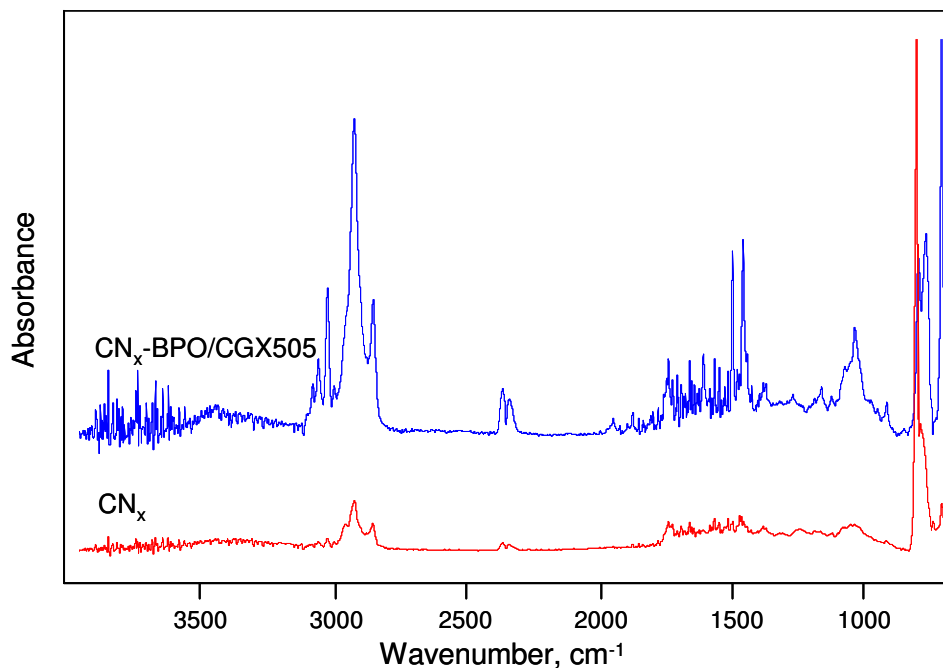


Fig. 5.13. FTIR spectra of  $\text{CN}_x$  nanotubes and radical functionalized  $\text{CN}_x$  nanotubes.

In summary, it is possible to say that the absorbance FTIR spectra of the radical functionalized carbon nanotubes are modified comparing to the as-produced and sonicated  $\text{CN}_x$  nanotubes. The first difference is related to the absorption intensity. Other is related to the presence to the C-O, COO, N-O and N-H due to BPO and nitroxide bonds. Furthermore, the presence of the bands due to ether and the absent of carboxylic groups could be evidences of the chemical bonding of initiator-controller onto the nanotube surface at reactive sites. The exact way of reaction remains unknown.

#### 5.2.3.4. Raman Spectroscopy

In this work, the Raman spectroscopy was used to characterize the bulk structure of nitrogen-doped carbon nanotubes samples, as well as to determine the structural changes that may be induced by radical functionalization. Moreover, Raman technique was used to discard the roping left by the chemical treatment. Consequently, some Raman experiments were developed on as-produced, purified, and radical functionalized  $\text{CN}_x$  nanotubes in solid state. Some of the results are reported below.

##### 5.2.3.4.1. Carbon nanotubes spectra

As can be seen from the Fig. 4.4, the absorption bands D and G of  $\text{CN}_x$  nanotubes present position dispersion, as well as a great variability in the  $I_D/I_G$  relation values. These variations can be associated to: (i) structural modifications due to the amorphous layer

extents, i.e. nitrogen functionalities, as observed in boron-doped nanotubes [8], and to (ii) CN<sub>x</sub> nanotube samples structural heterogeneity.

The first assumption is confirmed by the comparison with MWNT where a slightly lower intensity D/G relationship is obtained. The atom doping of carbon nanotubes decreases the graphitization, i.e. crystallinity of the carbon nanotubes. Furthermore, the I<sub>D</sub>/I<sub>G</sub> ratio is often used as a measure for the graphitic structure (amorphous carbon vs. graphite crystals), and degree of purity in nanotube samples [9]. Moreover, the shift of the G band was correlated with the decrease of electrical resistivity [10].

The second assumption is proposed in agreement with the work of Jiang *et al* [11], who observed the variations in carbon nanotube structural homogeneity upon excitation laser wavelength, and along the nanotube measured position.

In addition, as was reported for MWNT [12] the width of the G band could be related to the carbon nanotube size distribution, whereas the intensity of the D band decreases with the degree of graphitization of the tubes, related also with the number of defective sites. Nevertheless, some authors established that the D band intensity may also be due to polarization effects within aligned nanotube bundles [13]. Moreover, it was observed that less width in resonance peaks indicate less disorder carbon.

Resonance bands were observed in some CN<sub>x</sub> nanotube samples at around 221 cm<sup>-1</sup> and 283 cm<sup>-1</sup>, as shown in Fig. 4.4. In SWNT, these peaks are generally attributed to the radial breathing modes of carbon nanotubes. In this case, the shape, the position and the intensity of the resonance bands are strongly dependent on the tube diameter distribution [14, 15]. Nevertheless, in MWNT the radial breathing modes are almost unobservable, thus these bands are not completely understood. In general, the spectra of CN<sub>x</sub> nanotubes, as well as MWNT's, do not give detailed information about nanotube structure since they contain nanotubes with a variety of different sizes and structures.

Moreover, the second order Raman spectra, that were not obtained in this work, was reported to be more sensitive to small amounts of disorder within the graphite lattice (i.e. 2700 and 3241 cm<sup>-1</sup> highly ordered graphite and 2747 cm<sup>-1</sup> to disorder within graphite domains) [13].

Finally, some samples were chosen to carry out the functionalization reaction. The selected samples had an average position for the D peak at 1358 cm<sup>-1</sup>, for the G peak at 1579 cm<sup>-1</sup>, and a relation I<sub>D</sub>/I<sub>G</sub> of 0.36. Thus, these nanotubes are considered to be highly crystalline with little amorphous carbon layer, i.e. a high degree of perfection within the concentric graphene cylinders.

#### 5.2.3.4.2. Carbon nanotubes and radicals spectra

The reaction products of the radical functionalization using BPO/TEMPO (A3) and BPO/PRCGX505 (F3) were analyzed. The results are depicted in the Fig. 5.14 and summarized in the Table 5.5.

The appearance of D and G peaks in the spectra of radical functionalized carbon nanotubes revealed the prevalence of carbon nanotube structure, as was observed in the Fig. 4.4. Furthermore, an observable increase in the D and G peaks intensities, as well as the shift in their positions (positive and negative) comparing with CN<sub>x</sub> nanotubes, was obtained for the case of radically functionalized CN<sub>x</sub> nanotube samples (Table 5.5), as a result of nanotube structure modification. Moreover, the changes in the I<sub>D</sub>/I<sub>G</sub> ratio compared to CN<sub>x</sub> nanotubes could be attributed to the structural disorder increase at nanotube surface, due to functionalization reactions with initiator-controller radicals. All these facts are possible

indicators of the covalent modification, as it also reveals  $sp^3$ -hybridization or disorder within the nanotube framework, as was observed previously [16].

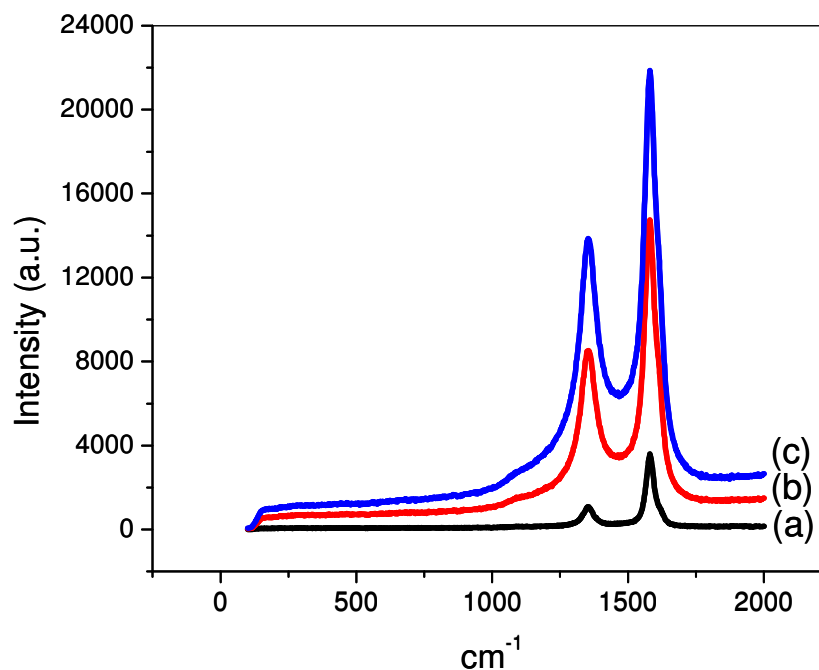


Fig. 5.14. Raman spectra of (a)  $CN_x$  nanotubes, and radical functionalized  $CN_x$  nanotubes with: (b) BPO/TEMPO and (c) BPO/PR CGX505 solutions.

Table 5.5. Parameters of Raman spectra of  $CN_x$  nanotubes and radical functionalized products using BPO/TEMPO (A3) and BPO/PR CGX505 (F3) radicals.

Peaks	$CN_x$		$CN_x$ -BPO/TEMPO (A3)		$CN_x$ -BPO/PR CGX505 (F3)	
	$cm^{-1}$	Intensity (a.u.)	$cm^{-1}$	Intensity (a.u.)	$cm^{-1}$	Intensity (a.u.)
X			1100.9	1384.1	1107.3	1296.4
D	1373.9	1047.6	1361.2	7311.4	1364.4	5187.9
G	1580.3	2831.7	1581.9	11182.0	1588.2	7144.5
D shift			12.7		-9.5	
G shift			-1.6		7.9	
$I_X/I_G$				0.12		0.18
$I_D/I_G$		0.36		0.65		0.73

As can be seen, a little higher increase in the disorder was obtained in F3 versus A3 samples, as shown by the  $I_D/I_G$  relation, being a qualitative reference of possibly higher radical functionalization in the system reacted with PR CGX505 nitroxide. This behavior can be compared with the results from TGA, where the same efficiency order was obtained after thermal mass degradation. In summary, the increase in the relative intensity of the disorder mode can be attributed to an increased number of  $sp^3$ -hybridized carbons in the nanotube framework and can be taken as a crude measure of the degree of functionalization

[17, 18] because there were no experimental evidences of nanotube destruction or degradation at the sidewalls. In fact, the disorder mode does not increase upon non-covalent functionalization unless processing cause new defect sites on the sidewalls of the nanotubes [19].

Consistent with the appearance of a disorder-induced peak in the Raman spectra of the chemically treated tubes, the samples also exhibit a small increase in the line width of the first-order bands, suggesting that functionalization of some of the tubes may have occurred, as was observed for other authors [20].

Additional analysis of the spectra implies the appearance of a new absorption peak at around 1100 cm<sup>-1</sup> in both A3 and F3 cases (band X). This band could be attributed to the (i) initiator-controller molecule bonding to the nanotube surface, and/or (ii) to disorder or sp<sup>3</sup>-hybridized carbons in the hexagonal framework of the nanotube walls. Both attributions are reported in the literature to this band.

In the first case, the functional groups from the initiator and controller used here could be bonded to nanotube surface, as was observed for nanotubes functionalized with nitrophenyl moieties [5]. The authors attributed the weakness of the signal, also observed in this case, to a less extent degree of functionalization or random orientation of the functional appendages rendering their detection. Some other cases of new excitation bands were observed in nanotube functionalization [20].

Related to the second case, some experimental reports have been done about the appearance of a disorder peak at around 1100 cm<sup>-1</sup> for carbon black samples [21] due to carbon atoms with sp<sup>3</sup> hybridization; and at around 1290 cm<sup>-1</sup> [22, 23] for carbon nanotubes due to the disruption of the graphene  $\pi$ -bonded electronic structure of the sidewalls suggesting their covalent functionalization.

Both assumptions are related because the introduction of covalently bound species could imply that a certain amount of sp<sup>2</sup> carbons could be converted to sp<sup>3</sup> hybridization. Thus, in the case of radical functionalization of CN<sub>x</sub> nanotubes using BPO and nitroxides (TEMPO and PR CGX505), it can be said that a successful reaction with unknown efficiency could have occurred, independently to the nitroxide type. The relation intensity of peaks X and G could be related quantitatively with the concentration of initiator-controller in the sample or with the carbon atom sp<sup>3</sup> hybridization, consequently to the extent of nanotube radical functionalization. As can be seen, the I<sub>X</sub>/I<sub>G</sub> relation has higher value for the F3 sample, meaning a probable higher radical functionalization over nanotubes using BPO/PR CGX505 radicals.

To conclude this experimental part it can be said that the Raman spectra were obtained for the nitrogen-doped carbon nanotube samples before and after radical functionalization. Some structural changes have been observed in both samples. Particularly, the intensity, width, and position of the resonance D and G peaks, as well as in the intensities ratios are modified. These differences could be attributed to the increase of structural disorder due to radical functionalization; because as reported in other cases [24], it was observed that the disorder-induced peak increase when functionalization of carbon nanotubes is carried on by chemical reaction. Furthermore, it is observed the appearance of a new band at 1100 cm<sup>-1</sup> that could be related to initiator-controller molecular bonding or to the carbon atom sp<sup>3</sup> hybridization. That confirms that structural change due to radical reaction have taken place in CN<sub>x</sub> nanotubes. This analysis assumes that the nanotube main

structure is preserved by the functionalization technique. That means also that, based on microscopy investigation on a variety of nanotubes, we state that structural degradation of carbon nanotubes during the purification and dispersion step is negligible. This is with no doubt the case for the sidewall of the nanotubes but is a approximation considering the fact that some tubes can be cut by the sonication process.

Nevertheless, we think that these Raman results are an element to claim the successful radical functionalization of  $CN_x$  nanotubes using BPO and nitroxides.

### 5.2.3.5. Electron Paramagnetic Resonance

Electron Paramagnetic Resonance (EPR) technique was used to study the interaction of carbon nanotubes with radicals (i.e. stabilization, neutralization, etc), as well as some magnetic properties of the radical functionalized  $CN_x$  nanotubes.

Several experiments were performed using X-band EPR. First experiments considered the differences in the EPR parameters, i.e. area under the absorption curve,  $g$ -factor, and hyperfine coupling constant, between radical functionalized  $CN_x$  nanotubes in relation to as-produced  $CN_x$  nanotubes. The area below the integrated ESR signal is a measure of total number of spins present in the sample. In addition, the  $g$ -factor were calculated using,  $h\nu = g\mu_B H$ , where  $g$  is a dimensionless proportionality constant ( $g$ -factor),  $h$  is the Planck's constant (6.62608 J•s),  $\nu$  is the frequency,  $\mu_B$  is the Bohr magneton (6.62608  $10^{-34}$ ), and  $H$  is the magnetic induction. The hyperfine coupling constant,  $B_{pp}$ , was geometrically obtained. Further experiments considered the dependence of material spectra characteristic with carbon nanotube type (MWNT and  $CN_x$ ), controller type (TEMPO and PR CGX505), measurement temperature (20, 80, 105, 120°C), and time (0-20 min). The samples analyzed are presented in Table 5.3 to 5.6.

#### 5.2.3.5.1. Nitroxides spectra

EPR spectra of solutions of nitroxide controllers and dispersions of nanotubes in organic solvents were measured at several temperatures.

It is known that nitroxide controllers are stable radicals with paramagnetic response. Thus, in particular TEMPO and PR CGX505 spectra at room temperature were formed by the characteristic triplet due to the presence of  $^{14}N$ . Furthermore, we observed that both nitroxides had different behaviors at higher temperature. Whereas TEMPO spectra presented a Lorentzian absorption curve at 105°C, PR CGX505 presented a triplet signal at all temperatures (20, 80 and 120°C). The possible explanation is found in the experimental observation that TEMPO tends to form a single line Lorentzian at high solution concentration or subzero temperature [25]. In addition, a lower peak-to-peak distance was obtained in the PR CGX505 sample as the temperature was increased. The EPR spectra of the PR CGX505 at experimental temperature conditions are shown in Fig. 5.15.

Furthermore, both nitroxides experienced a slight diminution of the spin concentration with temperature. Because no changes in spin concentration are expected due to the high stability of the nitroxide radicals, the minor changes observed in these samples could be due to the increment of the molecular mobility of radicals with temperature in the solution media.

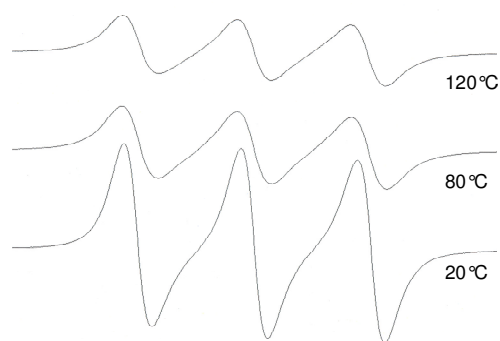


Fig. 5.15. EPR Spectra of PR CGX505 nitroxide recorded at several temperatures 20, 80 and 120°C in xylene as solvent.

#### 5.2.3.5.2. Carbon nanotubes spectra

Nitrogen-doped carbon nanotubes were analyzed in solid and liquid states by EPR technique.

Preliminary observations of CN<sub>x</sub> nanotubes in solid samples revealed a Lorentzian symmetric strong resonance at room temperature (293K). In this case, the *g*-factor was around 2.6. This *g*-factor value is in agreement with the *g*-factor for metallic Fe. Thus, in this case, the CN<sub>x</sub> nanotubes signal could be related to the resonance due to remained catalyst molecules from the CVD synthesis process. This signal could mask the carbon nanotube spectra, i.e. the metal content and the presence of graphitic particles seem to have the dominating effect on spectral appearance, as was observed by Shen *et al* [26].

Many authors confirmed that they do not observe any ESR signal for the pure nanotubes in solid state, neither at room temperature nor at low temperature [25]. This absence of observable ESR signal could be due to an increase in the relaxation time of the electrons upon interaction with residual metal catalyst particles and possibly a large proportion of semiconducting nanotubes. Other reports confirm the occurrence of Lorentzian and Dysonian curves for nanotube EPR spectra at several temperatures [26-28] in both solid and liquid states.

Alternative measurements are proposed in this work that considers the determination of the EPR spectra using purified and solvent dispersed carbon nanotubes in order to eliminate remaining metal particles from the sample, and to reproduce the system reaction conditions. Therefore, measurements of EPR absorption curves have been performed over purified MWNTs and CN<sub>x</sub>s nanotubes dispersed in benzene or xylene (Table 5.6 to 5.8). The CN<sub>x</sub> nanotubes were undamaged by the ultra-sound treatment (especially on their sidewall), as ascertained by numerous TEM observations, thereby limiting the generation of additional local electronic states.

It was observed that MWNT and CN<sub>x</sub> nanotubes dispersed in xylene do not exhibit EPR spectra in the studied solution concentrations at several temperatures (20, 80 and 120°C). On the contrary, CN<sub>x</sub> nanotubes dispersed in benzene exhibit a very slightly triplet signal that was integrated to obtain a *g*-factor of 2.006 and  $7.65 \times 10^{-5}$  spin concentration (Table 5.6). The line shape and the peak-to-peak value were difficult to discriminate because of the low signal intensity. First of all, the absence of EPR spectra for the xylene

samples could be related to the effect of nanotube purification [26], but also with the solvent used. In fact, it was reported that in some cases, the purification caused a slight decrease in signal intensity, a shift to lower field, and a change to a symmetric line shape. About the solvent type, it seems that benzene favors the observation of EPR spectra of pure carbon nanotubes, whereas xylene does not. After adequate corroboration, it could be possible that some chemical interaction with xylene could alter the radical measurement.

For the case of the benzene samples, the observed triplet line shape of the  $CN_x$  nanotubes spectra could be related to the three Lorentzian peaks related to the purification step, as was stated by Badow *et al* [29]. In fact, the authors observed differences between as-produced and purified nanotube samples produced by CVD method, and they interpreted these differences in terms of the electron conduction. They stated that agglomerated tubes electrons can transfer between the tubes, while for isolated nanotubes electrons only move around nanometer scale graphitic tube wall.

In the case of the nanotube  $g$ -factor, some typical reported values are 2.0189 [30], 2.011 [31], and 2.0114 [32] (calculated as  $g_{ave} = \frac{1}{3}(g_{\parallel} + 2g_{\perp})$ ) for multiwalled carbon nanotubes, and 2.002 [30] for boron-doped carbon nanotubes. Nevertheless, at the moment the  $g$ -factor of the  $CN_x$  nanotubes is not reported. In addition, the occurrence of a  $g$ -factor nearly of 2.0023, commonly associated to free electrons, could be attributed to paramagnetic impurities in the sample [31]. Furthermore, ESR signals that come from impurity or defect have been observed around  $g=2.001$  [33]. Graphitic particles also exhibited a  $g=2.02$  [31] and line widths of 10-25 G [26]. Thus, in this case the obtained  $CN_x$  nanotubes  $g$ -factor could be associated to the conduction electron spin system from metallic or semiconducting nanotubes with a small band gap, but also to the localized spins due to induced defects or impurities in doped carbon nanotubes. Furthermore, almost no paramagnetic impurities, metal content or graphitic particles seem to be observed in the EPR spectra of the sample.

Finally, the  $CN_x$  nanotubes revealed a low spin radical concentration that could be related with the presence of several junctions in the graphitic network (doping atoms or vacancies). For example, the negatively curved  $sp^2$ -bonded nano-regions in the carbon structure may cause spin frustration resulting in trapping of carbon radicals, as was postulated by Dubey *et al* [34].

#### 5.2.3.5.3. Carbon nanotubes and radical spectra in solution

Two experimental designs were proposed to determine the behavior of carbon nanotubes with radical solutions of peroxide initiator and nitroxide controllers. These experiments were developed to reproduce as much as possible the radical functionalization reaction media carried out in the PPR and batch experiments. The sample preparation of both experiments is described in Table 5.6 and 5.7. As can be seen, in both cases the radical solution concentrations differ to some extent from the reactors A3 and F3 concentrations; nevertheless, they could be indicative of the performed reactions. The EPR spectra for all samples were measured at several temperatures. In addition, a kinetic study was performed at high temperature.

Table 5.6. EPR sample preparation of sonicated-CN<sub>x</sub> nanotubes in benzene reacted with BPO and TEMPO. The experiment is made with dispersions of 10 mg of nanotubes in 15 ml of solvent and 1 ml of initiator/controller radical solution.

Sample	Radical solution concentration, mol/l	Initial no. radicals*
BPO	3.0E-02	3.9E-02
TEMPO	2.5E-02	2.5x10-2
CN <sub>x</sub> <sup>+</sup>	0	7.7E-05
CN <sub>x</sub> -BPO	2.7E-03	2.4E-03
CN <sub>x</sub> -TEMPO	2.2E-03	1.6E-03
CN <sub>x</sub> -BPO/TEMPO	2.7E-03	4.0E-03

\* Calculated radicals in the prepared solutions.

<sup>+</sup> Measured value using EPR

Table 5.7. EPR sample preparation of sonicated-MWNT and sonicated-CN<sub>x</sub> nanotubes in xylene reacted with BPO and PR CGX505. The experiment is made with dispersions of 1mg of nanotubes in 1 ml and 0.25 ml of initiator/controller radical solution.

Sample	Radical solution concentration, mol/l	Initial no. radicals*
BPO	6.60E-02	8.58E-02
CGX505	8.60E-02	8.60E-02
MWNT	0	-
MWNT-BPO	1.65E-02	2.15E-02
MWNT-CGX505	2.15E-02	2.15E-02
MWNT-BPO/CGX505	1.65E-02+2.15E-02	4.30E-02
CN <sub>x</sub>	0	-
CN <sub>x</sub> -BPO	1.65E-02	2.15E-02
CN <sub>x</sub> -CGX505	2.15E-02	2.15E-02
CN <sub>x</sub> -BPO/CGX505	1.65E-02+2.15E-02	4.30E-02

\* Calculated radicals in the prepared solutions.

#### *Nitrogen-doped carbon nanotubes and BPO/TEMPO in benzene*

The EPR spectra of CN<sub>x</sub> nanotubes samples with radical solutions of BPO and TEMPO were obtained. Experimental and calculated results for the spin concentration, the *g*-factor, and the B<sub>pp</sub>, for 20 and 105°C are summarized in Table 5.8. Line shape and symmetry were also observed.

As can be seen, the samples of CN<sub>x</sub> nanotubes with radicals in all cases reveal a lower spin concentration than the originally added by the initiator and/or radical solution, as a function of the temperature. That means that heating of the sample favors a diminution of the single unpaired electrons (spin concentration) in the sample, as it was observed before under light irradiation (without temperature increase) by Gallani *et al* [25]. The reason that can be envisaged to explain these observations is that the electrons in a higher energy level can pair with the single electron of a radical (from carbon nanotube or in solution media)

and cause the loss of a spin. Moreover, compared to as-produced carbon nanotubes, a higher concentration of radicals is observed in all samples. A possible explanation is that some resonant radicals could be generated over the nanotube surface. To quantify the loss of spins, the differences among theoretical and experimentally measured values (Dif, %) have been calculated for each sample. These values could be related empirically with the radical trapping of CN<sub>x</sub> nanotubes, as shown below.

Table 5.8. EPR spectra parameters of CN<sub>x</sub> nanotubes samples and BPO/TEMPO solutions reacted in benzene at several temperatures.

	Temp.	No. spins			g-value	H	□B <sub>pp</sub>	Line shape
	°C	Theoretical	Experimental	Dif, %		mT	mT	
BPO	20	3.90E-02	-		-	-	-	-
TEMPO	20	2.50E-02	2.50E-02		2.0066	327.421	1.3710	Triplet
	105	2.50E-02	2.39E-02		2.0067	327.421	-	Lorentzian
CN <sub>x</sub>	20	-	7.65E-05		2.0062	327.380	-	-
CN <sub>x</sub> -BPO	20	2.44E-03	1.41E-05	99.44	2.0063	327.236	1.5806	Triplet
	105	2.44E-03	2.15E-05	99.12	2.0060	327.300	-	No signal
CN <sub>x</sub> -TEMPO	20	1.56E-03	8.17E-04	48.42	2.0063	327.347	1.5903	Triplet
	105	1.56E-03	6.73E-04	71.72	2.0063	327.300	1.5349	Triplet
CN <sub>x</sub> -BPO/TEMPO	20	4.00E-03	2.04E-03	56.34	2.0063	327.277	1.5806	Triplet
	105	4.00E-03	1.19E-03	80.30	2.0062	327.321	1.5968	Triplet

For the sample CN<sub>x</sub>-BPO, a diminution of the 99% of BPO radicals from the solution is observed at both 20 and 105°C. At 20°C, this probably related to the fact that the thermolysis of the BPO has not take place because of the low temperature. Conversely, at 105°C the radicals were undoubtedly formed in solvent media. Thus, at this point, two explanations can be proposed: (i) almost all of the primary radicals are recombined with themselves because of the solvent cage effect, or (ii) almost all primary radicals react with the CN<sub>x</sub> nanotubes at reactive sites. The explanation of the phenomena only by the first assumption (i) cannot be admitted because the TGA results show that some BPO molecules have been added to nanotube materials, as measured by the corresponding weight losses. The assumption (ii) includes the fact that the radicals could be trapped by functional, defective, and radical nanotube surface sites, or could be resonant in the aromatic rings. If they are trapped (i.e. mainly radical-radical reaction), the radical concentration would decrease in the measurement. On the contrary, if they are resonant in the aromatic rings (i.e. radical addition reactions), the radicals would be measurable. This observation means that maybe in this case most of the BPO radicals could be radically trapped on the nanotube. This analysis contradicts some of the reported results that stated that BPO bonded to carbon structures can initiate *in situ* polymerizations. Thus, one explanation could be that some attachment-detachment process could take place in the former to also explain the low radical concentration measured in the samples.

Anyway, the most probable situation is that both (i) and (ii) taken place to some extent, but it becomes difficult to completely determine the exact mechanism of the

reaction with BPO radicals. It is supposed that both, radical resonance and radical trapping, took place for BPO radicals, that means that both CN<sub>x</sub>-R• and CN<sub>x</sub>-R were formed.

Similar spin concentration decrease was observed in the case of CN<sub>x</sub>-TEMPO. A main distinction in that case is that TEMPO is a stable radical that almost never react with itself. In this case, the diminution of 71% in the radical concentration could only be assigned to the radical interaction with carbon nanotube. The TEMPO molecules could be trapped, principally by radical-radical reactions, and less probably could be in resonance on the surface (CN<sub>x</sub>-NO<sub>x</sub>). The exact route of reaction at this moment is also unknown.

Furthermore, the CN<sub>x</sub>-BPO/TEMPO sample revealed a diminution of the 80% of spins number in the sample. This value could be related with a combination of pure BPO, pure TEMPO and BPO/TEMPO radicals interacting with carbon nanotubes. Thus, in BPO/TEMPO system the radicals could react separately with nanotubes, but also among them in the solution media. In this case, a competition between a heterogeneous vs. homogeneous reaction could take place, explaining the numeric result.

The comparison of the radicals decrease in the systems could led to: (i) the CN<sub>x</sub> nanotubes presented a high radical uptake behavior, as stated by CN<sub>x</sub>-BPO and CN<sub>x</sub>-TEMPO systems; (ii) the exact efficiency of radical uptake in CN<sub>x</sub>-BPO and CN<sub>x</sub>-BPO/TEMPO is difficult to be established because of the diversity of reactions that could take place; (iii) the radical addition behavior of CN<sub>x</sub> nanotubes, in particular in the case of BPO, could imply that the radicals are labile to radical reactions (i.e. to begin polymerization) on the nanotube surface only to some extent that will be conditioned by the radical bonding force.

The line shapes, symmetry and intensities of CN<sub>x</sub> nanotubes EPR spectra were analyzed (Table 5.8). First of all, a decrement of the resonance intensity was observed with the temperature that could be principally due to the radical attachment [26] in the CN<sub>x</sub>-radicals samples. In addition, the EPR line shapes of CN<sub>x</sub>-radical samples consist in symmetric triplets. These triplets could be assigned to the purified-CN<sub>x</sub> behavior, to the BPO-nanotube interaction, and/or to the TEMPO strong signal, according to each case. Furthermore, the symmetric line shapes could be related to localized spins (vs. itinerant spins due to conduction electrons) from the radical sites in the nanotube. No significant changes in shape or symmetry were observed after the reaction, that could reveal that the surface sites nanotubes were not saturated [26].

The main difficulty in the line shape comparison of the observed systems is that non observable changes are found. The positive result is that this characteristic also means that CN<sub>x</sub> nanotubes efficiently trap stable and instable radicals, i.e. peroxide and nitroxides.

Other derived results involved the *g*-factor and the Δ*B*<sub>pp</sub> values. First of all, only slight changes were observed in the *g*-factor between samples and as a function of the temperature. Concerning the Δ*B*<sub>pp</sub> values, a slight increase in the peak-to-peak distance is observed for samples with TEMPO radicals as temperature increased. The possible explanation is related with a change of molecular environment of TEMPO radicals that could be due to the chemical reaction with CN<sub>x</sub> nanotubes sites. Additionally, the

possibility of the triplets occurrence in purified carbon nanotubes could justify the  $B_{pp}$  values of  $CN_x$ -BPO from almost the same value as TEMPO samples.

Some authors agree in stating that the comparison of EPR parameters among samples, in particular the combination of the absence of changes in the  $g$ -factor, and the preservation of the line shape and symmetry, could be an indication of a weak radical coupling. Nevertheless, changes in intensity and peak-to-peak distances ( $\Delta B_{pp}$ ) of signals were also observed. They are related to the modification of the spin concentration and changes in the molecular environment of the molecules due to chemical attachment. To confirm both behaviors, it would be necessary to perform additional experiments.

#### *Carbon nanotubes and BPO/PR CGX505 radicals in xylene*

Very similar results in the EPR spectra and their parameters are obtained in the case of MWNT and  $CN_x$  nanotubes reacted with PR CGX505 in xylene. The main results are summarized in Table 5.9 and almost the same analysis and interpretation of parameters values could be done. In this case, the values of the  $g$ -factor and  $H$  were omitted because only slight differences were observed. The line shape and symmetry of the signal remain also unchanged. Finally, a decrease of the line intensity, spin concentration and  $\Delta B_{pp}$  parameters with temperature are also observed. Particularly, the radical trapping or scavenging properties of carbon nanotubes, measured as the difference among theoretical and experimental values, is determined. In this case, it is surprising that higher radical trapping is observed for MWNT. This behavior can be related to the type of chemical interaction between radical species and carbon nanotubes. First of all, it seems that a higher radical trapping (scavenging) and/or a higher stable chemical bonding with radicals are carried out at MWNT surfaces. Furthermore,  $CN_x$  nanotubes seem to have lower radical trapping (scavenging), higher surface radical resonance (stability), and/or less stable chemical bonding with radicals (irreversible reactions). The explanation of these behaviors is related to the number of available sites in nanotubes, but also with the chemical nature of sites. Because  $CN_x$  nanotubes are expected to have more sites than MWNT and with high chemical diversity and reactivity, a higher diversity of reactive mechanism is probably attained.

To summarize, for  $CN_x$  nanotubes the radical uptake from solution could be from both scavenging properties and radical resonance. The assignation to one behavior more than the other is difficult to establish using only this information. Nevertheless, if the hypothesis of  $CN_x$  nanotubes behavior is true, it could be possible that  $CN_x$  nanotubes would be a better material than MWNT to synthesized effective macroinitiators to perform *in situ* radical polymerization.

#### *Kinetic studies of the radical trapping behavior of carbon nanotubes*

Kinetic measurements of the spin concentration of MWNT, and  $CN_x$ -radical samples, reacted in benzene and xylene, were performed, and are depicted in Fig. 5.16 and 5.17. In all cases, it seems that the spin number decrement reaches an equilibrium value.

For the  $CN_x$ -TEMPO,  $CN_x$ -CGX505 and MWNT-CGX505, the equilibrium value could be related to (i) the limited number of radical species that can react with the nanotube

sites, or (ii) the limited number of available sites on nanotube surface to react with radicals. The first statement is closely related to controller molecule properties, as steric hindrance and polarity, and the second case with the nanotube surface radical reactivity. In this analysis several variables could take place: the solvent media, the controller molecule, and the radical solution concentrations. Thus, an exact explanation of the phenomena only could be done performing more experiments. Nevertheless, it seems that MWNT “trap” a higher number of spins from the solution.

Table 5.9. EPR spectra parameters of MWNT and CN<sub>x</sub> nanotube samples and BPO/PR CGX505 solutions reacted in xylene at several temperatures.

	Temp. °C	No. Spins			$\Delta B_{pp}$ mT	Line shape
		Theoretical	Experimental	Dif, %		
BPO	20	8.58E-02	-	-	1.5532	Triplet
CGX505	20	8.60E-02	8.60E-02	-	1.5000	Triplet
	80	8.60E-02	6.19E-02	-	1.4564	Triplet
	120	8.60E-02	5.15E-02	-	1.4541	Triplet
MWNT	20	-	-	-	-	No signal
MWNT-BPO	20	2.15E-02	-	-	1.5138	Triplet
	120	2.15E-02	-	-	1.5023	Triplet
MWNT-CGX505	20	2.15E-02	3.52E-03	83.6	1.5189	Triplet
	120	2.15E-02	1.92E-03	91.1	1.4959	Triplet
MWNT-BPO/CGX505	20	4.30E-02	3.25E-03	92.4	1.5000	Triplet
	120	4.30E-02	1.73E-03	96.0	1.4839	Triplet
CN <sub>x</sub>	20	-	-	-	-	No signal
CN <sub>x</sub> -BPO	20	2.15E-02	-	-	-	No signal
CN <sub>x</sub> -CGX505	20	2.15E-02	1.12E-02	47.9	1.5140	Triplet
	120	2.15E-02	7.48E-03	65.2	1.4867	Triplet
CN <sub>x</sub> -BPO/CGX505	20	4.30E-02	1.32E-02	69.3	1.4959	Triplet
	120	4.30E-02	9.17E-03	78.6	1.4799	Triplet

Generally, a higher equilibrium value was observed in CN<sub>x</sub>-BPO/TEMPO, CN<sub>x</sub>-BPO/CGX505 and MWNT-BPO/CGX505 than for the CNT-nitroxide systems. That means that some of the nitroxide that could react with nanotubes are reacting with BPO in solution. The remaining solution radicals are more available to further carry on reactions. In addition, because it is expected that attachment and detachment processes could be more probable in the homogeneous state, the measured average number of spins could be lower.

In addition, it was observed that the equilibrium values are lower for the system with nanotubes than pure radical solutions, as expected assuming that nanotubes exhibit a similar radical trapping behavior than with carbon black [35, 36].

Finally, more experiments and calculations could be realized to determine the rate of radical attachment in each system and study further the system. Particularly, it would be important to add the information about the BPO systems.

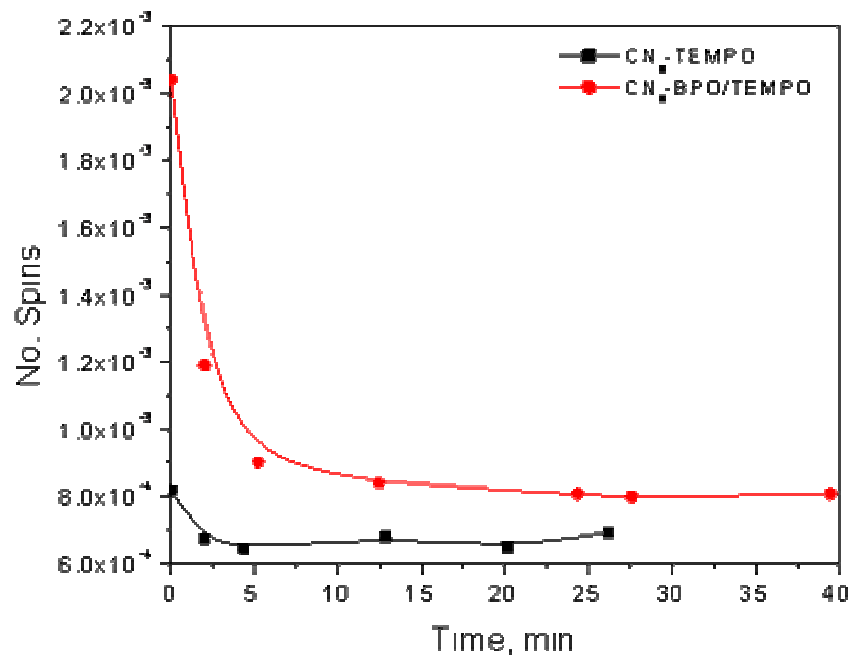


Fig. 5.16. Spin concentration as a function of time in samples of CN<sub>x</sub> nanotubes and BPO/TEMPO radicals reacted in benzene at 105°C.

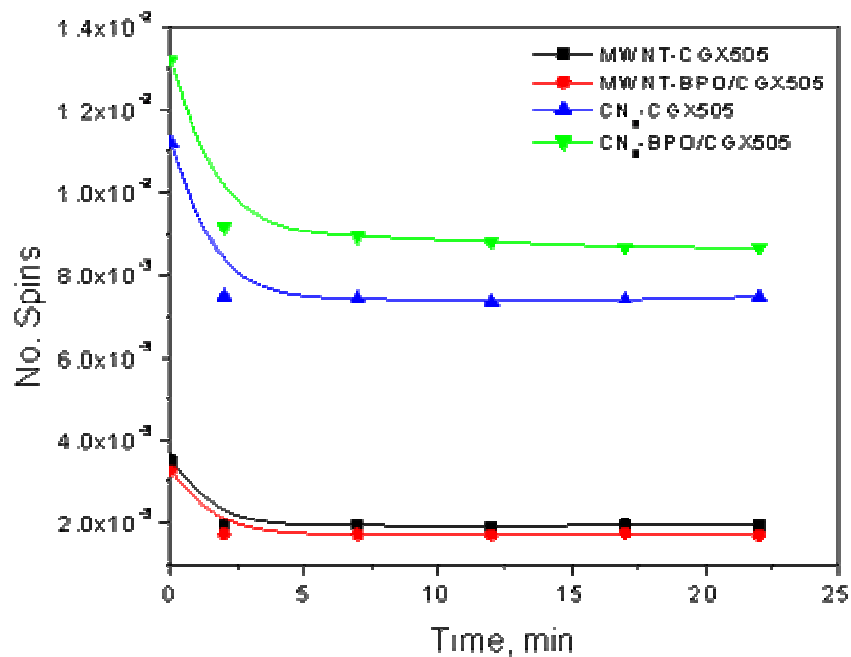


Fig. 5.17. Spin concentration as a function of time in samples of MWNT and CN<sub>x</sub> nanotubes with BPO/PR CGX505 radicals reacted in xylene at 120°C.

At this stage, it could be possible to say that MWNT and CN<sub>x</sub> nanotubes exhibit radical uptake from solution. The decreasing spin concentration values in both systems could be more related to the scavenging properties in the nanotubes than the formation of stable radicals in resonance over the surface. The differences among MWNT and CN<sub>x</sub> nanotubes trapping behavior could be explained by the fact that reactions were not preferentially performed on nitrogen type sites, (i.e. mostly radical-radical addition). On the contrary, nitrogen type sites favorably improved the radical resonance.

In addition, as was stated by other authors, like Gallani *et al* [25] in their results using photo-excitation, the heat of the sample causes a diminution of the number of single unpaired electrons in the sample. The process that can be envisaged is that (i) the thermal excitation promotes electrons in a higher energy level where they can pair with the single electron of a radical, or even more (ii) two radicals' coupling with the mediation of a photo-excited nanotube, both mechanisms caused the loss of a spin.

To summarize, Electron Paramagnetic Resonance (EPR) is a powerful tool to analyze the interactions of carbon nanotubes with radical in solution, because the technique is sensitive to both itinerant and localized spins, related to conduction electrons and "defective" of functionalized sites in carbon nanotubes.

In all cases, a high radical uptake is observed in MWNT and CN<sub>x</sub> nanotubes. Furthermore, the nanotubes efficiently trap stable and instable radicals from solution, i.e. nitroxides and peroxides. In particular, they exhibit a preference for BPO radicals more than nitroxides, according to the TGA results. Even though these characteristics were expected because of the previous results concerning other carbon structures, they were unmeasured in CN<sub>x</sub> nanotubes, becoming one of the goals of this study.

The analysis of EPR parameters for MWNT and CN<sub>x</sub> nanotubes could imply that the (i) radical attachment effectively takes place to some not saturated extent, (ii) a weak radical coupling (i.e. attachment and detachment) takes place between radicals and nanotubes; (iii) the radical environment could change to some extent, being an indication of nanotube surface radical reaction; (iv) the spin concentration decrement can be due to the reaction of the solution radicals with functional, vacancies or radical surface sites in nanotubes; (v) the radical trapping seems to be more probable than the resonance of radicals on the nanotube surface for BPO and undoubtedly for nitroxides; (vi) MWNT present higher radical uptake from solutions, that could imply that the radical bonding is more efficient or more stable in this case; and (vii) lower probability of radical trapping and higher radical resonance seems to be done over nitrogen sites.

These experimental results proved that CN<sub>x</sub> nanotubes easily reacted with radicals, as was already observed for SWNTs and MWNTs. Furthermore, all this analysis could imply that CN<sub>x</sub> nanotubes have better interaction properties with radicals to form macroinitiators to perform in situ radical polymerizations. Thus, it is theoretically expected that this macroinitiator could be formed by resonant BPO radicals over nanotube surface labile to react with the monomer and the nitroxides. In addition, it is expected that nitroxide controllers could be attached and detached from the nanotube surface, in particular from the radically activated sites on the nanotube due to BPO. Nevertheless, many other scenarios could take place; among them, it could be also possible that the radical type sites present on the nanotube surface could initiate radical polymerization by the uptake of thermally activated monomer radicals and that this chain could be controlled by nitroxide molecules.

In both cases, the possibility to nitroxide detachment is related to an effective polymerization control.

### 5.2.3.6. Discussion

At the end of this section in the Chapter 5, some general comments about the results can be made.

First of all, the radical functionalization of  $CN_x$  nanotubes seems to preserve the internal structure of the bamboo-type  $CN_x$  nanotubes, because only a narrow additional amorphous layer was observed by HRTEM. Furthermore, the N and O concentrations in  $CN_x$  nanotubes increase due to the incorporation of initiator and controller molecules, as revealed by elemental analysis by EELS and EFTEM. In addition, compositional mappings show homogeneous distribution of both elements over the surface, implying that a homogeneous radical reaction could take place.

Through thermal degradation experiments it is observed that the initiator and/or controller molecules could be chemically attached to  $CN_x$  nanotubes surface. Using measured values of the weight losses, the efficiency of the radical functionalization have been estimated. In particular, the better conditions and efficiency to functionalize nanotubes by radicals are obtained when the reaction of  $CN_x$  nanotubes with BPO and PR CGX505 is performed at 130°C in benzene.

Through FTIR it was observed that the chemical attachment of initiator and controller could take place due to the differences in the absorbance spectra of raw and radically functionalized carbon nanotubes. Furthermore, through the found possible bonding, i.e. C-O, COO, N-O and N-H, and the absence of carboxylic groups it could be possible to say that the initiator and controller radicals could react with the nanotube surface. The reacting mechanism remains difficult to determine because of the difficulty to certainly observe the absorption peaks.

The radical functionalization of  $CN_x$  nanotubes does not affect their overall structure, as determined by Raman Spectroscopy. Nevertheless, slight differences in the position and intensities of the characteristics D and G bands, as well as the apparition of a new band at 1100  $cm^{-1}$  could be related to the covalent attachment of initiator-controller species.

The corresponding mechanism is that radical reaction could take place at graphitic sites by radical addition reactions or radical trapping, according to the compositional results from Microscopy. Furthermore it has been proved by EPR that the BPO radicals could be resonant or trapped over the nanotube surface, forming  $CN_x-R\bullet$  and  $CN_x-R$  species, whereas nitroxide radicals are trapped, forming  $CN_x-NO_x$  species. The EPR results also reveal a weak radical coupling, but anyway an effective chemical attachment among radicals and  $CN_x$  nanotubes by both radical trapping and radical resonance. This chemical attachment could correspond with lower efficiency than the originally found by this technique due to the weak coupling or irreversibility process. Finally, the  $CN_x$  nanotubes

trapping behavior could be due to reactions that were not preferentially performed on nitrogen type sites, (i.e. mostly radical-radical addition). On the contrary, nitrogen type sites favorably improved the radical resonance.

Finally, it could be said that the radical attachment of BPO and nitroxides has effectively been carried out onto CN<sub>x</sub> nanotubes surfaces, as was determined by several characterization techniques. Furthermore, the radical attachment of initiator to carbon nanotube surface could lead to the formation of macroinitiators, or even more controlled macroinitiators labile to initiate *in situ* polymer-grafted chains.

### 5.2.4. Polystyrene-grafting of $CN_x$ nanotubes

The macroinitiators prepared by the radical functionalization of  $CN_x$  nanotubes using BPO and controlled radical initiator regulators (nitroxides  $CN_x-RNO_x$ ) have been used to carry out the *in situ* polymerization of PS, according to the second reaction step (Figs. 5.1 and 5.3). The obtained products, corresponding to the reactor conditions named A3 and F3 have been characterized by several techniques after their synthesis and purification/separation processes. Microscopy, spectroscopy, thermal properties and chromatography techniques have been used to determine if the *in situ* polymerization reaction in the presence of nanotubes, as well as the PS grafting-from on  $CN_x$  nanotubes (PS-*g*- $CN_x$ ), has taken place.

#### 5.2.4.1. Synthesis results

In all cases, the *in situ* polymerized  $CN_x$  nanotube samples have the appearance of homogeneous black polymer materials. Two different solid materials have been obtained after the purification steps through several precipitations and dissolutions in methanol and organic solvents followed by a filtration process. Under the filter, the purified material is uncolored and transparent, that could mostly correspond to polystyrene. Over the filter, a black sample is obtained that could be formed by a combination of different carbon nanotubes products and by-products. The probable products could be (i) un-reacted  $CN_x$  nanotubes, (ii) un-grafted radical functionalized  $CN_x$  nanotubes ( $CN_x-RNO_x$ ), (iii) polystyrene-grafted  $CN_x$  (PS-*g*- $CN_x$ ) nanotubes, and (iv) PS and  $CN_x$  nanotubes (PS- $CN_x$ ) physical blend. Thus, further characterization is required on these filtered materials to determine their nature and composition.

To do so, a physical blend of polystyrene (commercially available) and  $CN_x$  nanotubes has been prepared as a reference, in order to be able to identify the differences among the physically adsorbed PS on  $CN_x$  nanotubes prepared by blending (PS- $CN_x$ ) and the *in situ* polymerized  $CN_x$  nanotube samples prepared by NMRP. This physical blend has been purified/separated using the same conditions than those used for the *in situ* polymerized  $CN_x$  nanotube samples. Once again, in this case, two kinds of materials have been obtained, a polymeric sample under the filter and a black material that contains carbon nanotube over the filter.

After drying the black solids obtained over the filter in both *in situ* polymerization and physical blend routes, the obtained samples have been again solubilized in organic solvents. The dispersions obtained in toluene are presented in Fig. 5.18. As can be seen, the black solid component synthesized by *in situ* polymerization of PS in the presence of  $CN_x-RNO_x$  gives a stable homogeneous suspension in the solvent, in contrast to the physical blend appearance that is strongly inhomogeneous. In addition, another difference is observed concerning the time of dispersion stability: whereas the former solution is stable over weeks, the nanotubes in the second dispersion start to form aggregates and precipitates as soon as the agitation stops. These differences can be interpreted in terms of nanotube-polymer interface interaction i.e., the presence of grafted-PS on the  $CN_x$  nanotubes surface may help to the suspension stabilization. The improved solution stability can be related to the covalent bonding of the polystyrene chains onto the nanotube surface in the case of NMRP prepared  $CN_x$  nanotube samples, whereas in the case of the physical blend sample

the covalent bonding of the polymer to the nanotube is absent. The observed covalent attachment of polystyrene chains to the CN<sub>x</sub> nanotubes could also indicate efficient surface radical functionalization of the CN<sub>x</sub> nanotubes, and/or the *in situ* polymerization process by NMRP at surface radical present in the nanotubes due to their original structure.

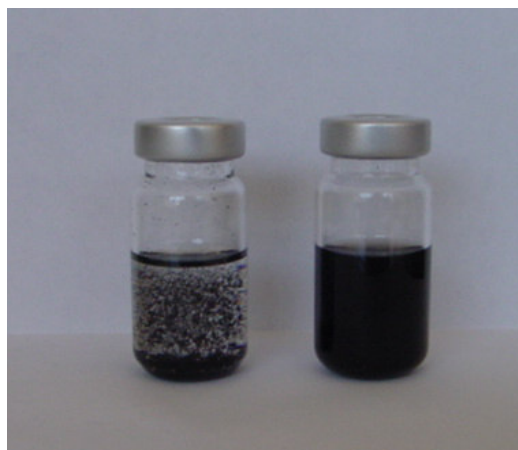


Fig. 5.18. Stability and solubility differences between (a) physical blend of PS and sonicated-CN<sub>x</sub> nanotubes, PS-CN<sub>x</sub>, (left hand side), and (b) *in situ* polymerized PS in the presence of radically functionalized CN<sub>x</sub> (right hand side) in toluene.

The former dispersion is not stable, whereas the second is stable over weeks.

#### 5.2.4.2. Thermogravimetric Analysis

Thermogravimetric Analysis (TGA) has been carried out on the materials arising from the filtration process (*in situ* polymerized and physically blended CN<sub>x</sub> nanotubes materials) to determine the amount of organic material and polymer present in each material.

##### *PS-grafting of CN<sub>x</sub> nanotubes: under-filter and over filter materials*

The thermogram of the under-filter material from the physical blend sample (not presented here) shows a 99% weight loss around 400°C, this behavior is unequivocally attributed to pure polystyrene. Comparatively, the over filter sample from the polymer blend presents a weight loss of only 0.5% after 600°C, indicating that this material is mainly composed of carbon nanotubes. Because this weight loss value corresponds exactly with the quantity of carbon nanotubes added at the beginning of the blending process, it can be said that the CN<sub>x</sub> nanotubes do not interact with the polystyrene and that the filtration process efficiently separates carbon nanotubes from polystyrene.

Fig. 5.19 presents the thermograms corresponding to both over and under filter products in the case of the *in situ* polymerized CN<sub>x</sub>-RNO<sub>x</sub> nanotubes. The curve corresponding to as-produced CN<sub>x</sub> nanotubes has been added for comparison. As can be seen from this figure, the under and over filter materials have a higher weight loss than CN<sub>x</sub> nanotubes. In addition, the under filter material displays no residual weight above 500, i.e. is entirely composed of polystyrene. Conversely, the over filter material presents a weight

loss of only 30%. This percentage is related to the thermal degradation of the radical functionalities previously introduced on carbon nanotubes surfaces, and to the polymer added in the *in situ* polymerization step. Because of the repeated purification of the products with different solvents (i.e. toluene and THF), the remaining polymer and initiator-controller mass in the sample has to be chemically bonded to the nanotube surface. Thus, the filtration method has separated the functionalized and grafted  $CN_x$  nanotubes from the PS. Further studies will be only performed on the over filter materials, i.e. on PS-grafted  $CN_x$ .

*PS-grafting of  $CN_x$  nanotubes at each reaction step*

Moreover, the weight losses for the over filter products from the *in situ* polymerized  $CN_x$  nanotubes can be used to determine the polymer-grafting reaction efficiency. To do so, we propose to compare the TGA results for the different products coming from each reaction step: (a) as-produced  $CN_x$  nanotubes, (b) radical functionalized  $CN_x$  nanotubes, and (c) polymer-grafted  $CN_x$  nanotubes (see Fig. 5.20). The radical functionalization of  $CN_x$  nanotubes (first stage reaction) is found to have an efficiency of 20% for the BPO/PR CGX 505 radicals (best case), whereas the combined first and second stages (polystyrene-grafted) reaction steps have a global efficiency of around 37% (in the best case) using the same initiator-controller system. Thus, the difference between these two steps, i.e. 17 weight % of increment in the weight loss is attributed to the polymer grafted onto the  $CN_x$  nanotube surface. Similar results of around 10% of polymer grafting were observed by other authors [37]. The weight loss value could be used to calculate a degree of polymerization of the superficially attached monomer.

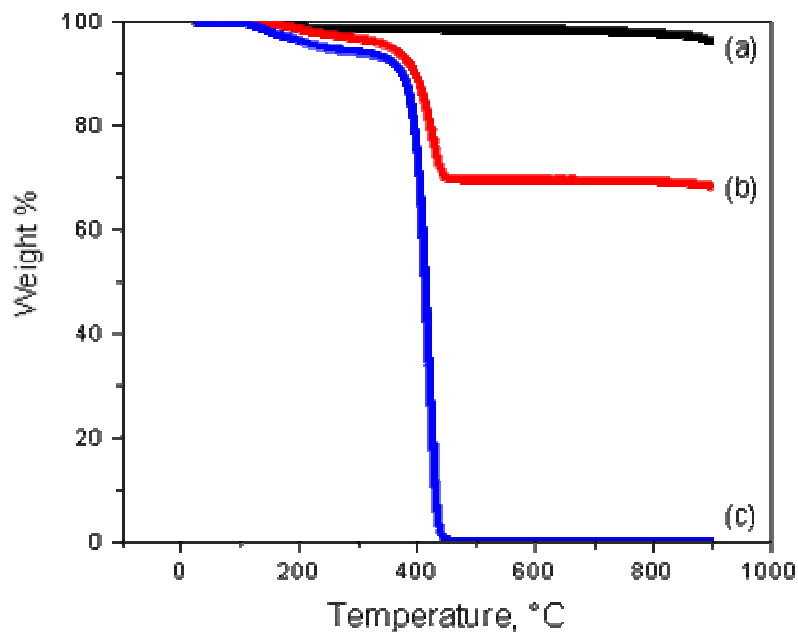


Fig. 5.19. Thermal degradation of reaction products of *in situ* polymerized  $CN_x$  nanotubes using BPO/PR CGX 505 (reactor F3), separated by filtration: (a) as-produced  $CN_x$  nanotubes, (b) over filter sample, corresponding to the PS-grafted from radical functionalized  $CN_x$  nanotubes, and (c) under filter sample, corresponding to PS.

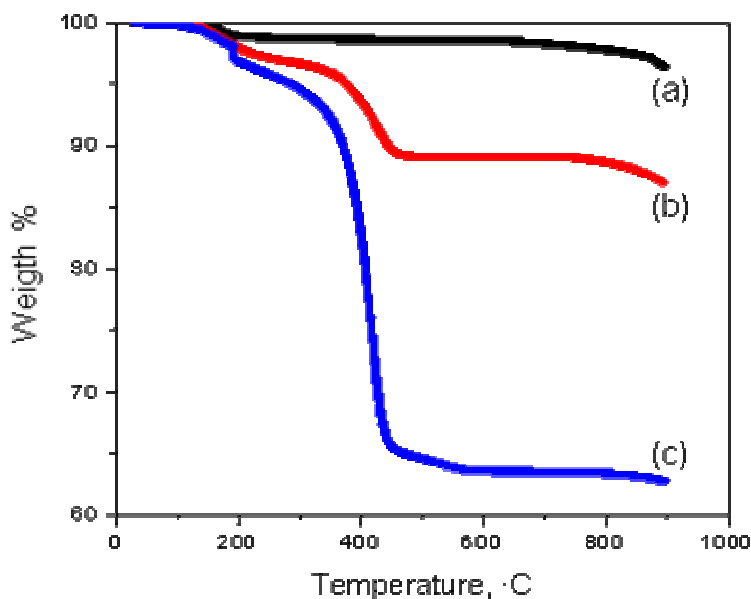


Fig. 5.20. Thermal degradation of reaction products of functionalized and polymer-grafted CN<sub>x</sub> nanotubes (reactor F3): (a) as-produced CN<sub>x</sub> nanotubes, (b) radical functionalized-CN<sub>x</sub> nanotubes (CN<sub>x</sub>-RNO<sub>x</sub>), where the weight loss mainly corresponding to the BPO/PR CGX505 attachment, and (c) polymer-grafted-CN<sub>x</sub> (PS-g-CN<sub>x</sub>) nanotubes where the weight loss corresponded to polymer attachment.

To sum up, we trust that these TGA measurements clearly reveal that some PS has been covalently attached to CN<sub>x</sub>-RNO<sub>x</sub> nanotubes. These results need confirmation coming from other characterization techniques in order to assess the true degree of polymer grafted to the surface of the nanotubes.

#### *PS-grafting of CN<sub>x</sub> nanotubes in initiator, controller and initiator/controller systems*

The *in situ* polymerization of radically functionalized CN<sub>x</sub> nanotubes have been performed with (i) BPO initiator, (ii) PR CGX505 controller, and (iii) BPO/PR CGX505 radicals. The corresponding thermograms showed in Fig. 5.21 reveal that there are differences in the polystyrene grafting onto the nanotube surface depending on the radical functionalization of CN<sub>x</sub> nanotubes. For instance, the presence of BPO in the system enhances the attachment of PS chains because the presence of about 40% of polymer is measured. This fact could support the hypothesis that the BPO attached to nanotubes acts as effective surface initiator to initiate the PS polymerization. In the case of CN<sub>x</sub>-NO<sub>x</sub> nanotubes, after the polymerization step, a very low weight loss (around 10%) is measured. The obtained value is in fact of the order of the one obtained just after the radical functionalization step. This indicates that the surface functionalization with nitroxide radical does not effectively initiate the polymerization of styrene on the nanotubes. Finally, an intermediate weight loss (around 15%) is obtained for the *in situ* polymerized sample with BPO/PR CGX505. This could be related to the lower radical functionalization of the nanotube surface, but also it could be due to a certain degree of control of the reaction

because of the nitroxides. It could reveal that the kinetics of the reaction become slower inducing a low degree of polymerization.

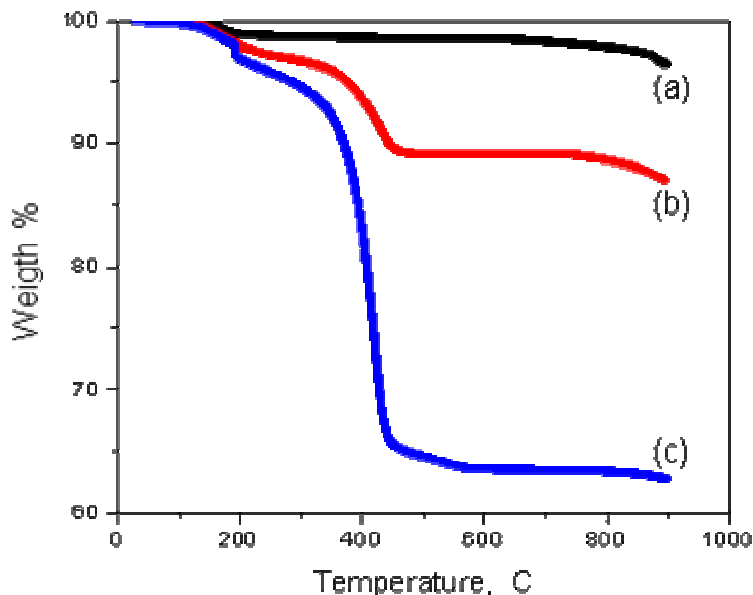


Fig. 5.21. Thermal degradation of reaction products of polymer-grafted  $\text{CN}_x$  nanotubes at the conditions of reactor F3 using several radical functionalized samples: (a)  $\text{CN}_x$ -BPO ( $\text{CN}_x$ -R), (b)  $\text{CN}_x$ -PR CGX505 ( $\text{CN}_x$ - $\text{NO}_x$ ), and (c)  $\text{CN}_x$ -BPO/PR CGX505 ( $\text{CN}_x$ - $\text{RNO}_x$ ).

In summary, the TGA characterization provides several evidences of molecular (initiator-controller) and macromolecular attachment (PS) over nanotube surface for the *in situ* polymerized  $\text{CN}_x$  nanotube samples, indicating the formation of  $\text{PS-g-CN}_x$  species. Furthermore, the differences in the weight loss between the *in situ* polymerized samples coming from the different radically functionalized  $\text{CN}_x$  nanotubes are consistent with the results obtained in the radical functionalization study. Actually, the lower degree of polymer grafting is obtained for the system with  $\text{CN}_x$ - $\text{RNO}_x$ . That could be related to a lower degree of radical functionalization, or a certain degree of control of the polymerization reaction (grown chain) due to a reduction in the reaction rate that produces also a better control, and consequently a low degree of polymerization.

#### 5.2.4.3. Electron Microscopy and allied techniques

Electron Microscopy techniques have been used to investigate the general arrangement, as well as the structural and compositional properties of the  $\text{PS-g-CN}_x$  materials. HRTEM and STEM images, and EELS and EFTEM spectra are used to verify the surface polymer grafting by chemical bonding ( $\text{PS-g-CN}_x$ , **4**) on the radical functionalized carbon nanotubes ( $\text{CN}_x$ - $\text{RNO}_x$ , **3**) when Nitroxide Mediated Radical Polymerization (NMRP) were used. The reaction products are analyzed and compared with the physical blend of PS and  $\text{CN}_x$  nanotubes.

#### 5.2.4.3.1. Arrangement and morphology of PS-grafted CN<sub>x</sub> nanotubes.

First results concern STEM observations of PS-g-CN<sub>x</sub> films. It appears that some groups of *in situ* polymerized CN<sub>x</sub> nanotubes stay together in the sample (Fig. 5.22). These images also reveal that the polymer-grafted nanotubes are almost completely disentangled, and also curved. This observed appearance is really different from that of the as-produced CN<sub>x</sub> nanotubes, and also of the radical functionalization products.

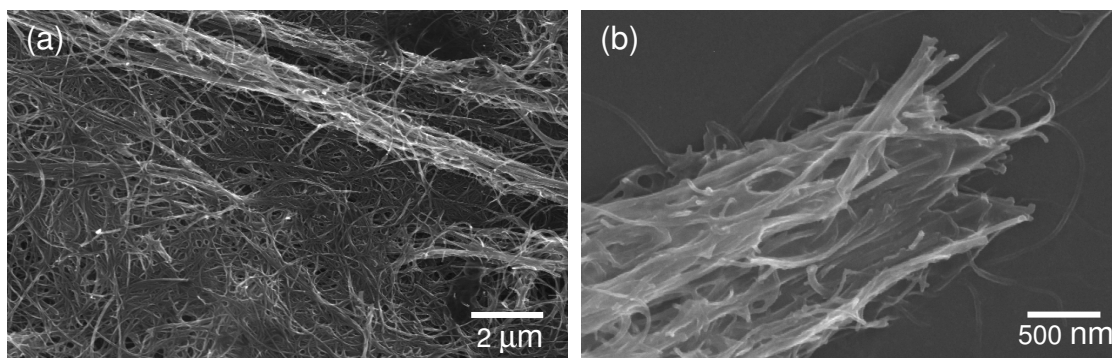


Fig. 5.22. STEM images of *in situ* polymerized PS-g-CN<sub>x</sub> nanotube samples at magnifications (a) 32676X and (b) 8000X.

Furthermore, HRTEM images showed in Fig. 5.23 (a)-(d) depict general differences in the amorphous layer surrounding the nanotubes depending on the processing method, i.e. *in situ* polymerization or physical blend. First of all, whereas the as-produced CN<sub>x</sub> nanotubes exhibit an outer surface without any coating or at most a 3 nm thick layer of amorphous carbon (Fig. 4.2), the *in situ* polymerized materials in Fig. 5.23 (a) and (b) present the formation of an amorphous layer coating the CN<sub>x</sub> nanotube of about 7 nm. The composition of this amorphous layer in the *in situ* polymerized materials has been probed by EELS. Low-loss EELS characterization has shown that the amorphous composition corresponds to PS (see analysis below).

The images of the *in situ* polymerized PS and CN<sub>x</sub> nanotubes revealed that the CN<sub>x</sub> nanotubes are coated with a continuous amorphous layer of about 7 nm. The images of the physical blend showed that PS wets only partially the CN<sub>x</sub> nanotubes. As described in the schemes. In Fig. 5.23 (a) and (b), PS wets the nanotubes homogeneously, in contrast with the samples produced by physical blending (Fig. 5.23 (c) and (d)), in which the nanotubes are not uniformly coated with PS.

Further now, it is possible to claim that the physical or chemical functionalization of CN<sub>x</sub> nanotubes modifies the nanotube morphology, especially the thickness of the amorphous layer, as seen by HRTEM. In addition, PS-grafting produces a thick regular film surrounding the nanotubes in opposition to what happens with the physical blend. Thus a better surface adhesion between polymer and CN<sub>x</sub> nanotube materials can be ensured if the nanotubes are previously radical functionalized and polymerized *in situ* by NMRP. In fact, these observations can be interpreted as a additional proof for the grafting of PS onto CN<sub>x</sub> nanotubes.

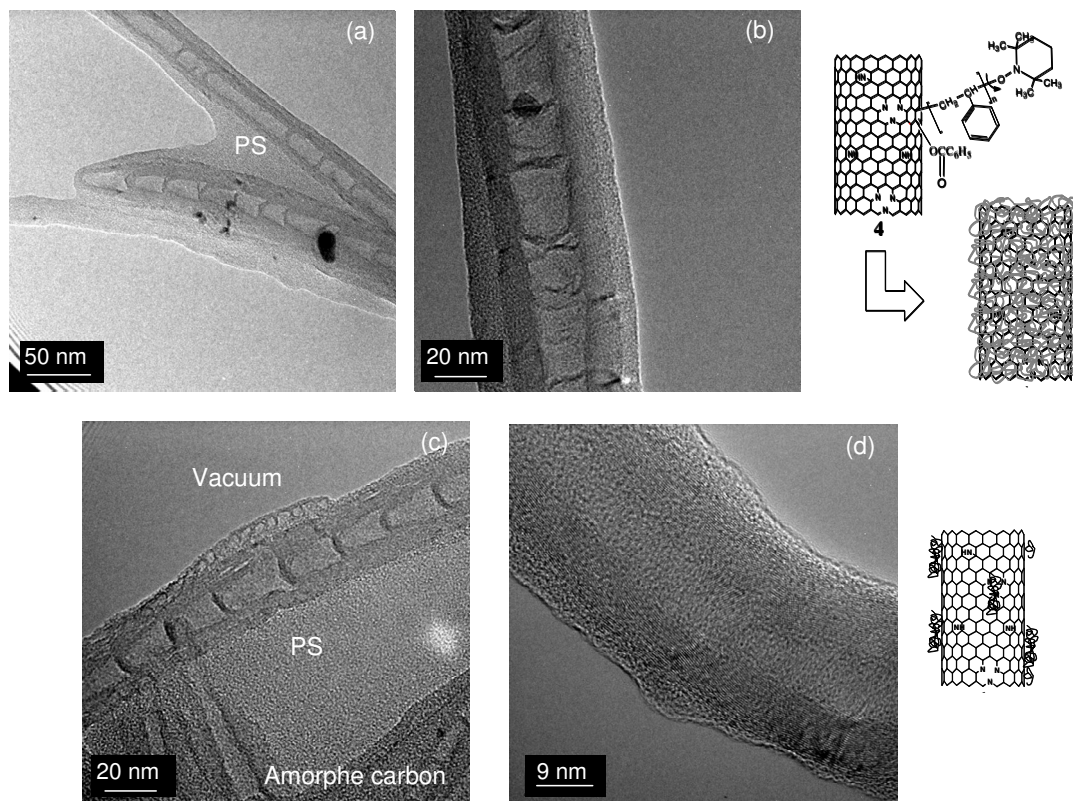


Fig. 5.23. HRTEM micrographs of the (a) and (b) *in situ* polymerized PS in the presence of CN<sub>x</sub> nanotubes produced using the NMRP method, and (c) and (d) physical blend of PS with CN<sub>x</sub> nanotubes.

#### 5.2.4.3.2. Chemical composition of PS-grafted CN<sub>x</sub> nanotubes.

The PS-g-CN<sub>x</sub> materials have been further analyzed by EELS at low and high energy losses, and by energy-filtrated TEM technique (EFTEM) to determine the nature of the bonding and the differences in the elemental composition in respect to the as-produced CN<sub>x</sub> nanotubes and CN<sub>x</sub>-RNO<sub>x</sub>.

Low energy loss spectra have been performed over i) as-produced CN<sub>x</sub> nanotubes (1), ii) pure PS, PS-g-CN<sub>x</sub> nanotubes using (iii) NO<sub>x</sub>=TEMPO (sample A3) (4), iv) NO<sub>x</sub>=PR CGX 505 (sample F3), and v) physical blend of PS and sonicated-CN<sub>x</sub> nanotubes. Some of the obtained spectra are shown in Fig. 5.24.

As can be seen, the Fig. 5.24 reveals characteristic peaks at 5.4 eV due to the  $\pi \rightarrow \pi^*$  excitation of the C=C conjugated bonds in the carbon nanotubes spectra [38], and at 6.8 eV due to the  $\pi \rightarrow \pi^*$  excitation of the C=C aromatic rings in PS spectra [39]. Both edges appear when the physical blend of nanotubes and PS is analyzed. In contrast, when analyzing the amorphous layer covering the NMRP reacted sample, there is only a peak at 6.6 eV that can be associated with a new excitation response in PS-grafted CN<sub>x</sub> (4).

The comparative curves (not shown here) of the *in situ* polymerized products synthesized using TEMPO and PR CGX505 as controllers reveal that the peak at 6.6 eV is observed in both samples. Moreover, the position and the form of the curve is the same in

both cases. This fact could mean that both controllers produce the polymer-grafting from radical functionalized CN<sub>x</sub> nanotubes, implying at same time the formation of polymer brushes.

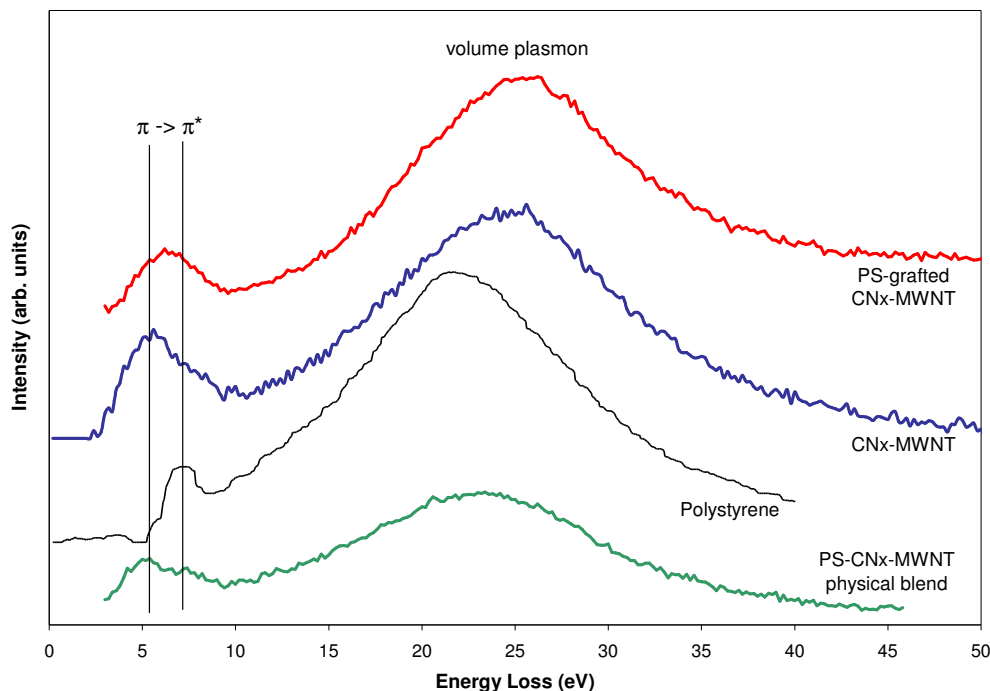


Fig. 5.24. EEL comparative spectra of the PS, raw CN<sub>x</sub> nanotubes, PS-*g*-CN<sub>x</sub>, and the physical blend of PS and CN<sub>x</sub> nanotubes.

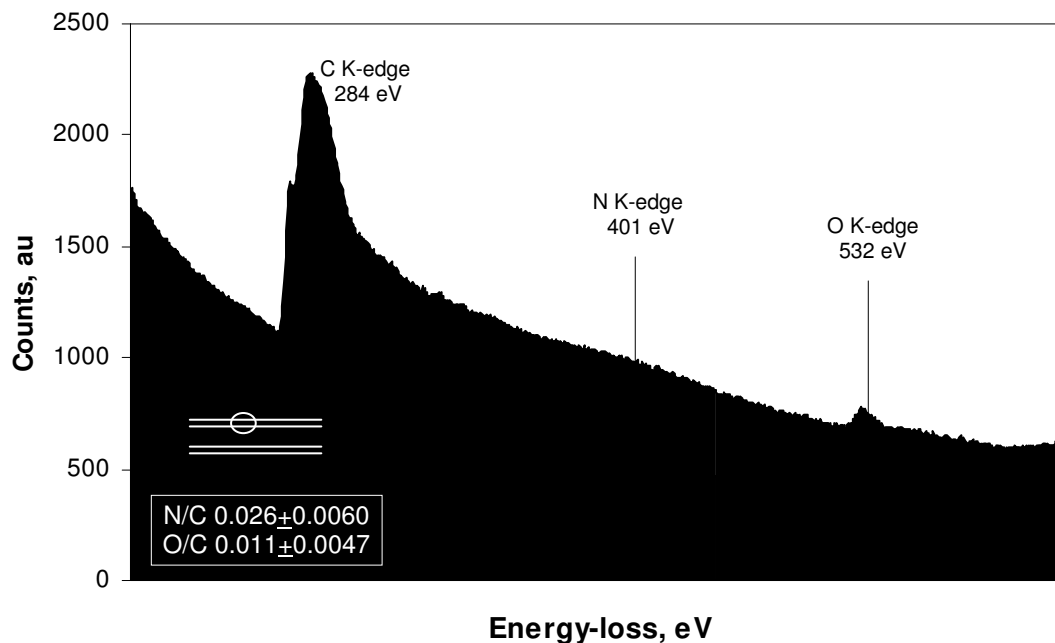


Fig. 5.25. High energy-loss EELS spectra of PS- CN<sub>x</sub> amorphous layer and relative elemental composition.

In the case of the amorphous layer coating the nanotubes in the PS-*g*-CN<sub>x</sub> samples, the EELS spectrum obtained at high energy losses, reveal the presence of bands associated with C-K edge (284 eV), N-K edge (401 eV) and O-K edge (532 eV) (Fig. 5.25). Consequently, EELS calculations of the relative concentration N/C and O/C are obtained and shown in Table 5.2. The obtained average values correspond to different zones and a variable number of nanotubes. For instance, the quantification in PS-*g*-CN<sub>x</sub> has been realized over the amorphous layer using the high spatial resolution of the microscope (probe size diameter equal to 2.4 nm). In all other cases, the quantification was made for entangled carbon nanotubes (global views, probe size diameter of about 100 nm).

The values for N/C equal to 2.6% and O/C 1.1% exhibit changes in the chemical content of N and O compared to as produced CN<sub>x</sub> nanotubes and CN<sub>x</sub>-RNO<sub>x</sub> nanotubes that could be explained through (i) the total mass difference considering the PS attached, and (ii) the radical functionalization reaction and the polymer-grafted CN<sub>x</sub> (already observed by TEM).

The energy-filtered images in Fig. 5.26 show the zero loss images and elemental maps (C, N and O) of: a) PS-*g*-CN<sub>x</sub> and b) physical blend of PS and CN<sub>x</sub> nanotubes. The energy-filtered images (Fig. 5.23 (a)) show a relatively higher concentration of N and O, comparatively with as-produced CN<sub>x</sub> nanotubes (image not shown here, see Annexes). The increase in the N and O could be attributed to the incorporation of the molecules of initiator and controller to the CN<sub>x</sub> nanotubes in the composite.

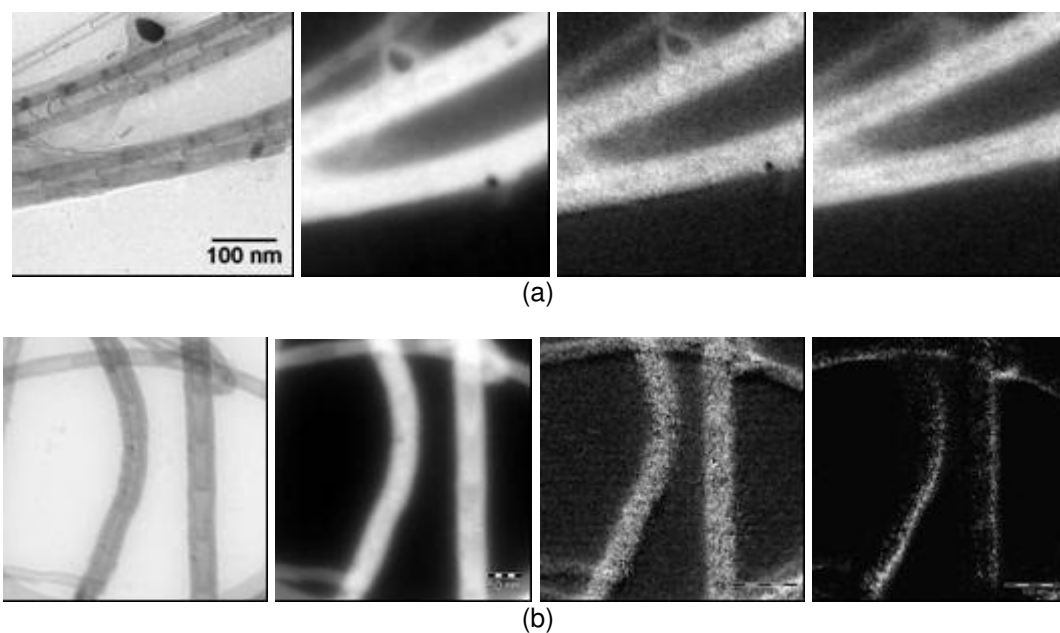


Fig. 5.26. Filtered images of (a) PS-*g*-CN<sub>x</sub> and (b) physical blend of PS and CN<sub>x</sub> nanotubes. Each group of images is presented in the next order: zero loss, carbon, nitrogen and oxygen maps.

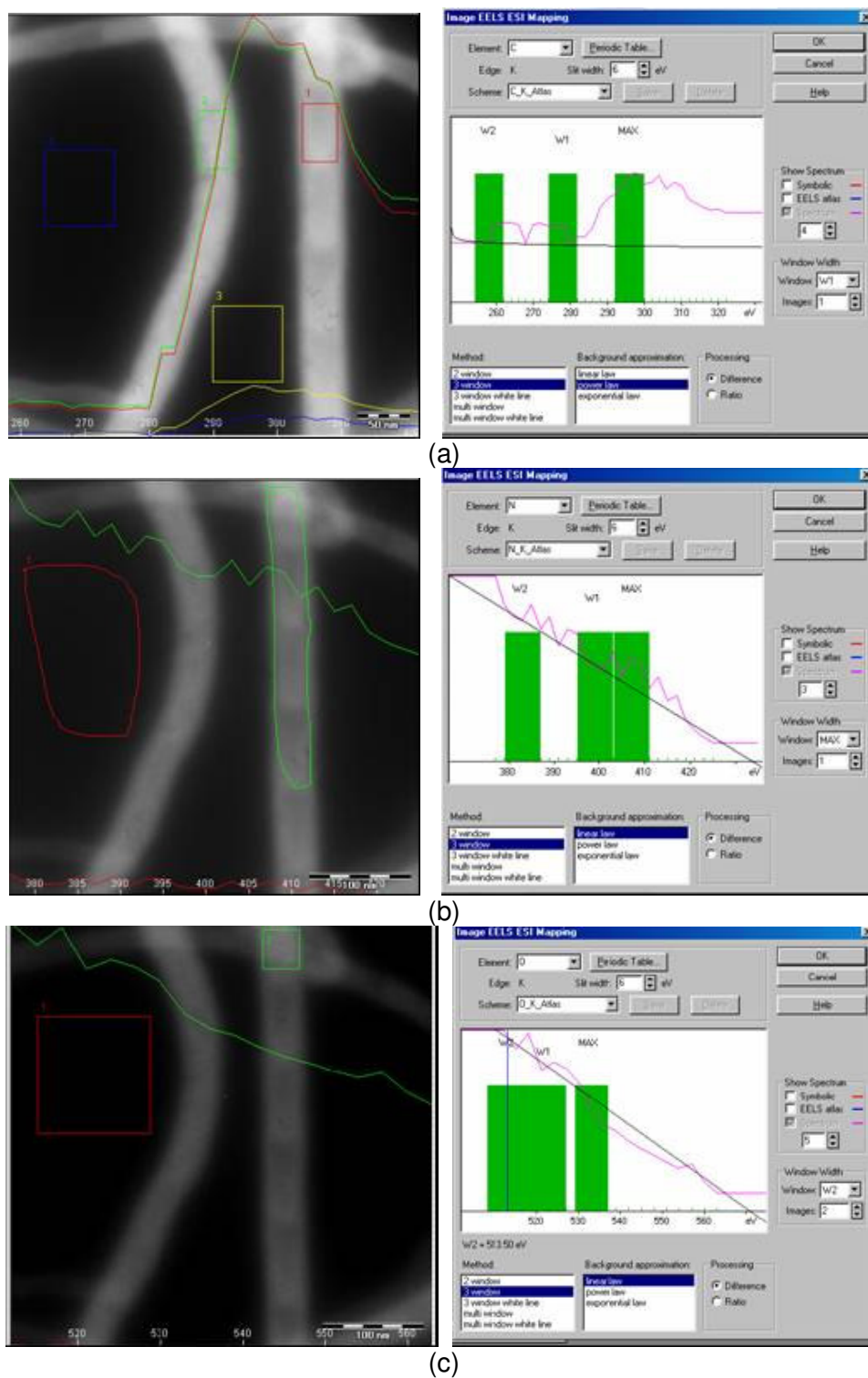


Fig. 5.27. EFTEM spectra extracted from the energy-filtered image series, and parameters used for the calculation of the elemental maps for the physical blend of PS and CN<sub>x</sub> nanotubes (PS/CN<sub>x</sub>): (a) carbon map, (b) nitrogen map and (c) oxygen map.

Fig. 5.27 (a) and (b) show the EEL series spectra for each element and the calculation method parameters for the same samples. Note that the image series concerning an element have been all acquired with the same experimental conditions (illumination current, acquisition time, etc), so that it should be possible to compare the intensities of the edges from one specimen to another. The analysis of PS-*g*-CN<sub>x</sub> was made using the conventional three image-power law subtraction methods (images not shown here). The degree of the adjusting equation (i.e. linear, power or exponential) is determined according to the best fit.

Energy-filtered images of the physical blend of PS and CN<sub>x</sub> nanotubes are depicted in Fig. 5.26 (b). The analysis of the spectra series have been developed using the three images-linear law subtraction method (Fig. 5.27), as in the PS-*g*-CN<sub>x</sub> case. In the frame of the calculation method, no significant increase in the N and O concentrations can be observed in the physical blend PS and CN<sub>x</sub> nanotubes respect to the raw CN<sub>x</sub> nanotubes, as expected from the processing method (simple blending). This reveals a weaker polymer interaction with the nanotube surface and means that the commercial polymer can not be attached onto nanotube surface.

Thus, energy-filtered images confirm in the case of PS-*g*-CN<sub>x</sub> that there is an increase in the N and O concentrations, most probably due to the chemical attachment of initiator and controller molecules on the nanotube surface. On the contrary, the physical blend presents a composition similar to that of CN<sub>x</sub> nanotubes, revealing no attachment of initiator and controller molecules on the nanotube surface.

In summary, all the microscopy techniques reveal that there are changes in the arrangement, the morphology, the elemental composition, and the polymer surface interactions in the case of the *in situ* polymerized PS in the presence of CN<sub>x</sub> nanotubes. That could be attributed to the presence of an important proportion of PS-grafted nanotubes (PS-*g*-CN<sub>x</sub>). This hypothesis is also confirmed by the presence of new bonding types found in the grafted material by EELS.

#### 5.2.4.4. Raman Spectroscopy

Raman Spectroscopy has been used to determine the structural effect of polymer-grafting from CN<sub>x</sub> nanotubes on their structures. The spectra of the CN<sub>x</sub> nanotubes and the *in situ* polymerized CN<sub>x</sub> nanotubes by NMRP are shown in the Fig. 5.28. As can be seen the Raman spectra of PS-*g*-CN<sub>x</sub> presents a combination of the CN<sub>x</sub> nanotubes and PS peaks, revealing the presence of both “kinds” of materials in the reaction products. The Table 5.10 details the intensity and Raman shift values attributed to each kind of signals for the A3 and F3 samples.

Let's first comment on the D and G peaks observed in the PS-*g*-CN<sub>x</sub> products that can give information on the preservation of the overall nanotube structure.

In all the polymer-grafted products (coming from both A3 and F3 reactors) there is a Raman shift and a modification of the I<sub>D</sub>/I<sub>G</sub> ratio compared to raw CN<sub>x</sub> nanotubes probably due to a nanotube structure modification and the structural disorder increased in

the nanotube amorphous layers. This structure modification could be due to the PS covalent grafting onto the nanotube surface. Besides, the  $I_D/I_G$  ratio is higher in the case of A3 than F3. That may indicate a relatively higher structural modification in the A3 sample i.e. a higher functionalization.

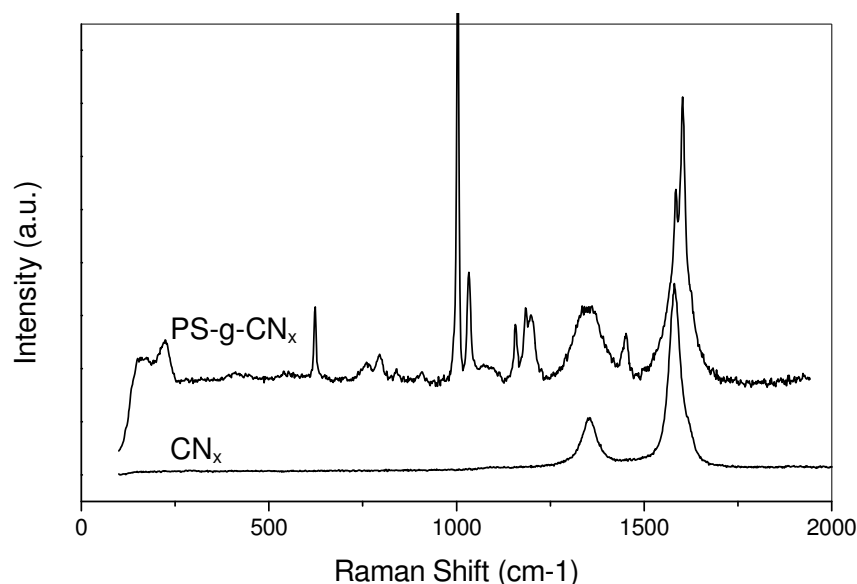


Fig. 5.28. Raman spectra of (a) raw CN<sub>x</sub> nanotubes, and (b) *in situ* polymerized CN<sub>x</sub> nanotubes (PS-g-CN<sub>x</sub>) due to F3 reactor.

Furthermore, the pure PS spectra (not presented here) shows typical intense bands. Among them, the bands at 1100 cm<sup>-1</sup> (band X) and 1600 cm<sup>-1</sup> (band Y) are especially interesting for this analysis.

Actually, we have already observed a band at 1100 cm<sup>-1</sup> (band X) for the radical functionalized carbon nanotubes (Table 5.7). This band X present higher intensity in the case of PS derived products. To probe if the band in the PS-grafted nanotubes sample corresponds to that of the pure PS, the intensity ratio ( $I_X/I_G$ ) has been calculated. In the case of radical functionalized samples,  $I_X/I_G$  ratios of 0.12 and 0.18 have been obtained (Table 5.7); whereas  $I_X/I_G$  ratios from 0.38 to 0.57 have been obtained in the case of PS-g-CN<sub>x</sub> nanotubes (Table 5.11). Thus, the level of intensity ratios favor to compare the last values mainly with the PS present in the grafted-samples. The decrease in intensities could be or not assigned to a structural change in the PS bonds due to the grafting over the nanotube surface.

Additionally, the band at 1600 cm<sup>-1</sup> (band Y) has been also found in PS-g-CN<sub>x</sub> nanotubes, thus a similar comparison to the  $I_X/I_G$  intensity ratios have been carried out for the band Y. The  $I_Y/I_G$  obtained values for PS and PS-g-CN<sub>x</sub> are presented in Table 5.11. Again, the PS-g-CN<sub>x</sub> presents lower intensity ratios than pure PS, thus these values corresponding to polymer-grafted materials are related to the polymer surrounding the nanotubes that also could be covalently attached to nanotube surface.

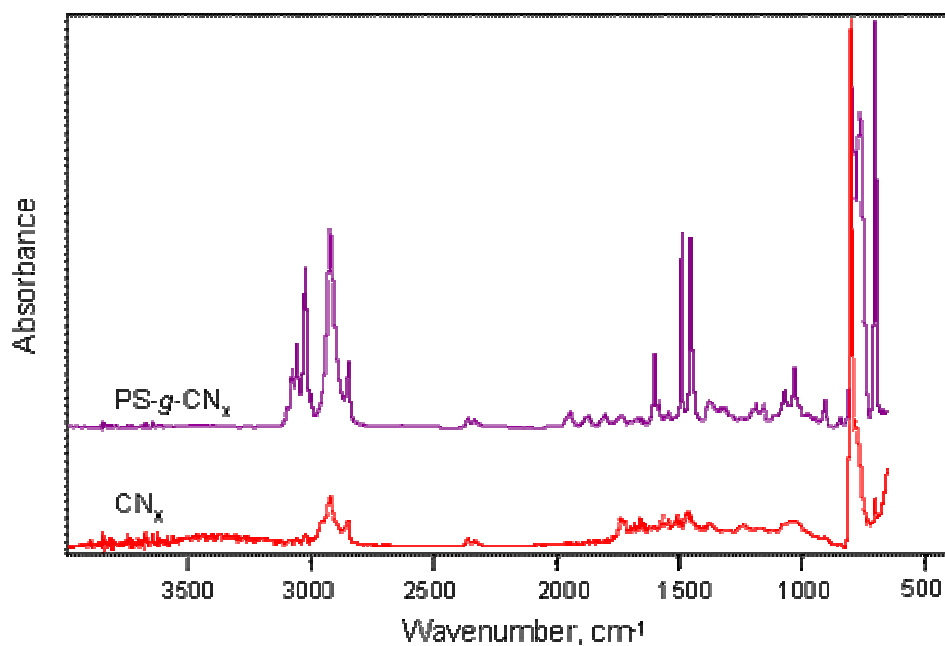
Table 5.10. Parameters of Raman spectra of  $\text{CN}_x$  nanotubes and polystyrene-grafted  $\text{CN}_x$  nanotubes.

Peaks	$\text{CN}_x$		PS		PS- <i>g</i> - $\text{CN}_x$ (A3)		PS- <i>g</i> - $\text{CN}_x$ (F3)	
	$\text{cm}^{-1}$	Intensity (a.u.)	$\text{cm}^{-1}$	Intensity (a.u.)	$\text{cm}^{-1}$	Intensity (a.u.)	$\text{cm}^{-1}$	Intensity (a.u.)
X			1104.1	21607	1104.1	8482	1105.1	2894.7
D	1373.9	1047.6	1342.2	26976	1369.2	11999	1366.0	5207.8
G	1580.3	2831.7	1597.0	37010	1593.0	14846	1596.1	7712.7
Y			1604.1	50347	1600.9	15862	1602.5	9353.6
D shift					4.7		7.9	
G shift					-12.7		-15.8	
I <sub>X</sub> /I <sub>G</sub>				0.58		0.57		0.38
I <sub>D</sub> /I <sub>G</sub>		0.36				0.81		0.68
I <sub>Y</sub> /I <sub>G</sub>				1.36		1.07		1.21

Raman spectra analysis indicates that the formation of PS-*g*- $\text{CN}_x$  products has occurred during the process and furthermore that the F3 sample displays a qualitatively higher radical functionalization, whereas the A3 sample has a higher polymer-grafting.

#### 5.2.4.5. FTIR Spectroscopy

The products of the *in situ* polymerization of PS in the presence of  $\text{CN}_x$  nanotubes have been analyzed using FTIR. The results could be used to determine the polymerization of PS in the presence of nanotubes and, if the case, the presence of functional groups related to the covalent attachment of PS.

Fig. 5.29. FTIR spectra of  $\text{CN}_x$  nanotubes and PS-*g*- $\text{CN}_x$  nanotubes.

The FTIR spectra of the samples are shown in the Fig. 5.29. As can be seen, the comparison of the PS-*g*-CN<sub>x</sub> with the as produced CN<sub>x</sub> nanotubes spectra reveals peak differences between them. These differences are attributed to the polymer presence in the sample after purification. This only could mean that (i) the polymerization of styrene monomer using NMRP has been successfully carried out in the presence of CN<sub>x</sub> nanotubes (radically functionalized or not) in the reaction media, and (ii) the polymer-grafting of PS chains from the CN<sub>x</sub> nanotubes surface has taken place.

The exact analysis of the peaks in the PS-*g*-CN<sub>x</sub> product becomes difficult because the bonding nature in PS is close to that already obtained in the radical functionalized nanotubes, corresponding to nanotube structure, and initiator-controller molecules bonds. In fact if the initiator-controller bonds remain in the polymerized sample (PS-*g*-CN<sub>x</sub>) the polymer-grafting could have proceed through the macroinitiator-controller (CN<sub>x</sub>-RNO<sub>x</sub>). Additional bands below 800 cm<sup>-1</sup> attributed to the nanotubes can be related to the PS grafting from the CN<sub>x</sub> surface.

#### 5.2.4.6. Separation

The measurements of the outer diameters of polymer-grafted CN<sub>x</sub> nanotubes have been carried out by TEM in the supernatant of PS-*g*-CN<sub>x</sub> solution separated by centrifugation. According to statistical tests performed over about 150 carbon nanotubes, the obtained diameter distribution of the PS-*g*-CN<sub>x</sub> (without taking into account the thickness of the PS layer) and as-received CN<sub>x</sub> nanotubes are depicted in Fig. 5.30. With a level of confidence of 95%, the mean diameters of the PS-*g*-CN<sub>x</sub> nanotubes and of the as-received CN<sub>x</sub> nanotubes are equal to 26 ± 2 nm and 35 ± 3 nm, respectively. With the same level of confidence, the standard deviations are equal to 14 ± 2 nm and 18 ± 2 nm, respectively. The data indicate a difference in the size distribution of the nanotubes before and after functionalization in the solution volume. This unambiguously shows that the PS-*g*-CN<sub>x</sub> are thinner than the as-received CN<sub>x</sub> nanotubes, probably because the thicker nanotubes are eliminated during the filtration and centrifugation steps. This result suggests a preferential separation of the CN<sub>x</sub>s nanotubes caused by the functionalization and grafting occurring on CN<sub>x</sub> nanotubes of certain diameter or by the subsequent precipitation of heavy species with or without polymer-grafted after centrifugation.

Some authors have reported several methods to isolate nanotubes from the mixture of graphitic particles using conjugated polymers [40]. Thus, it is important to highlight that the optimisation of this whole procedure may be a way to simultaneously graft polystyrene from the surface of the CN<sub>x</sub> nanotubes and control the diameter distribution of these nanotubes.

#### 5.2.4.7. Discussion

The analysis of the *in situ* polymerized CN<sub>x</sub> nanotubes products has been carried out by several techniques. From these different analyses, we can conclude that the polymer grafted-CN<sub>x</sub> nanotubes (PS-*g*-CN<sub>x</sub>) have been successfully formed using *in situ* NMRP.

Some of the experimental evidences of the PS-*g*-CN<sub>x</sub> production will be summarized below.

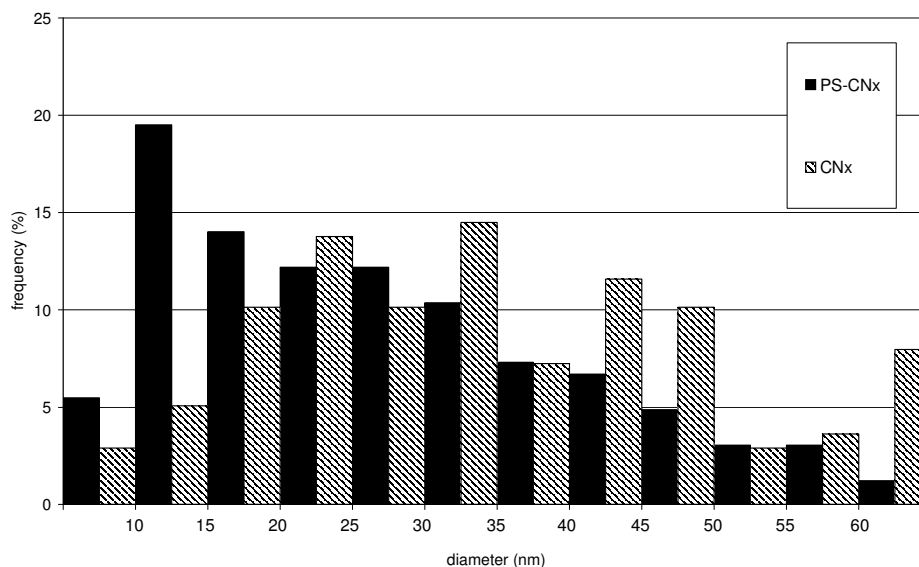


Fig. 5.30. Diameter distribution (150 nanotubes) of PS-*g*-CN<sub>x</sub> and CN<sub>x</sub> nanotubes measured by TEM.

Some of the changes in the properties of PS-*g*-CN<sub>x</sub> are related to enhanced solubility and stability in organic solvents. In fact, the comparison of PS and CN<sub>x</sub> physical blends with grafted PS-*g*-CN<sub>x</sub> systems determine strong differences in their behavior: the former material remains insoluble and instable in organic solvents.

Using TGA measurements, several observations could be done. The overall organic reactants and polymer presence in the PS-*g*-CN<sub>x</sub> materials was determined to be around 30%, according to the measured weight loss. From this quantity, the polymer grafting efficiency was estimated to be around 17%. In fact, we detect some weight losses at temperatures corresponding to polymer degradation, indicating that monomer polymerization takes place in the reaction media by the radical attachment (i.e. BPO molecules).

For instance, in isolated CN<sub>x</sub> nanotube systems reacted with BPO, NO<sub>x</sub> and BPO/NO<sub>x</sub>, the higher weight loss corresponds to BPO. This fact could support the hypothesis that the BPO attached to nanotubes acts as effective surface initiator to initiate the PS polymerization. However, even for this best case, the grafting efficiency calculated from the weight loss, seems to be low. This fact could be due to a low degree of polymerization or even more to low chain initiation. An additional possibility related to the control of the reaction by the nitroxides can be proposed. In all cases more studies have to be done to explain. In addition, the surface functionalization with nitroxide radical does not effectively allow the polymerization of styrene on the nanotubes.

Results of the electron microscopy techniques reveal differences in the arrangement of nanotubes in the polymer film (i.e. disentanglement, curvature). Besides, we observe that

the modification of the nanotube surfaces through the different steps of the process improve their solubility and stability in solvents. We also detect some changes in the amorphous layer surrounding the nanotubes. In fact, for PS-g-CN<sub>x</sub>, the polymer forms a more homogeneous and thicker amorphous layer compared to the original nanotubes. This behavior could be attributed to a better surface adhesion between polymer and CN<sub>x</sub> nanotube materials when CN<sub>x</sub> nanotubes were radically functionalized and polymerized *in situ* by NMRP.

Chemical bondings, obtained from EELS at low energy loss, are consistent with the assumption of PS-g-CN<sub>x</sub> formation. Even more, the C=C aromatic bonds due to a new excitation response in PS-grafted CN<sub>x</sub> are observed in the polymer-grafted CN<sub>x</sub>, probing the polymer attachment. Comparatively, PS and CN<sub>x</sub> physical blend samples do not present this new C=C response.

The high energy losses EEL spectrum at PS-CN<sub>x</sub> nanotube interface in PS-g-CN<sub>x</sub> materials revealed the presence of C, N and O that are attributed to the presence of BPO and NO<sub>x</sub> radicals in the PS-grafted samples. These results are verified by energy filtered images, where the same elements are found in PS-g-CN<sub>x</sub> nanotubes. PS-CN<sub>x</sub> polymer blend and CN<sub>x</sub> nanotubes present similar composition, revealing no attachment of initiator and controller molecules on the nanotube surface.

FTIR results also corroborate the presence of bonds attributed to both PS and CN<sub>x</sub> nanotubes, indicating a close relation between materials.

In addition, Raman spectra indicate that the overall nanotube structure is unchanged to unaltered some of the desirable nanotube properties (as mechanical modulus and conductivity). Nevertheless, slight changes in the Raman shift position and intensity of characteristic bands, as well as the presence of bands attributed to PS are related to the PS chains attachment to nanotubes.

Moreover, it seems that, through the different steps of our process (including the filtration), a separation of PS-g-CN<sub>x</sub> by diameter is possible. This separation may be originate from differences in the reaction efficiency for different nanotubes diameters.

All these observations can be interpreted as proofs for the grafting of PS onto CN<sub>x</sub> nanotubes using the NMRP *in situ* polymerization.

### 5.3. Conclusions

In this Chapter the radical functionalization and polymer-grafting of nitrogen-doped carbon nanotubes has been reported. As supported by the characterization results, the polystyrene grafting of nitrogen-doped carbon nanotubes has been successfully realized using *in situ* radical polymerization techniques, in particular NMRP.

According to the objectives proposed at the beginning of this Chapter:

The experimental results concerning the disentanglement of the nanotubes ropes and the purification step of as-produced nitrogen-doped carbon nanotubes have been outlined.

The most favorable preparation condition in the studied range has been determined. Furthermore, our work shows that these processes prepare the nanotubes to chemical functionalization without inducing extended structural damage.

The general screening of the reaction variables performed in order to select the best conditions in the studied range was discussed. The radical functionalization products issued from selected reaction conditions have been used for further synthesis and analysis.

The two step reaction procedure, i.e. radical functionalization of  $\text{CN}_x$  nanotubes and their polymer-grafting have been analyzed in detail.

First of all, the radical functionalization of  $\text{CN}_x$  nanotubes using initiator and controller radicals has been observed by the morphological differences among as-produced nanotubes and the final products using TEM. Further probes have been obtained by the measured changes in thermal degradation of materials (10 w% at 400°C) which are attributed to the presence of initiator-controller species in the final product. In addition, FTIR absorption bands attributed to the BPO and nitroxides reveal a chemical bonding from these species with nanotube surfaces. The scavenging properties of  $\text{CN}_x$  nanotubes have been confirmed by ESR technique, revealing the radical uptake of BPO and nitroxide from solution. All these results imply that  $\text{CN}_x$  radical macroinitiators are formed.

The next reaction step that considers the polymer-grafting of PS chains onto  $\text{CN}_x$  nanotubes radical macroinitiators has been proceeding. To begin, additional absorbance peaks have been recorded in FTIR spectra after reaction with monomer, these peaks imply that the polymerization reaction has taken place at the nanotube surface using the radically activated sites coming from the previous step. Moreover, Raman spectra modifications (changes in position and intensity in the nanotube characteristic peaks D and G) could be related to chemical reactions carried out at nanotube surface. TEM images reveal the presence of an amorphous layer surrounding the  $\text{CN}_x$  nanotubes after polymer grafting. The local analysis reveals that this amorphous layer contains aromatic rings and is thus composed of PS. Furthermore, new bond response were found at  $\text{CN}_x$  and PS interface. Finally, experiments of solubility, diameter separation of reacted- $\text{CN}_x$  nanotubes in solution, and dispersion preparation in polystyrene matrix confirms that the polystyrene-grafting of  $\text{CN}_x$  nanotubes took place and leads to significant improvements of several properties of  $\text{CN}_x$  nanotubes.

Moreover, the differences between physically adsorbed polymer and the chemically attached polymer chains on the nanotubes surfaces were described, as well as the comparison between the overall behavior of multiwalled carbon nanotubes without atom doping, and the nitrogen-doped carbon nanotubes.

Finally, the innovating PS-g- $\text{CN}_x$  nanotube materials could be use in the preparation of polymer nanocomposites, as will be described in Chapter 6 and 7.

## References

1. Lambin, P., A. Loiseau, C. Culot, and L.P. Biró, *Structure of carbon nanotubes probed by local and global probes*. Carbon, 2002. **40**: p. 1635-1648.
2. Terrones, M., *Synthetic routes to nanoscale B<sub>x</sub>C<sub>y</sub>N<sub>z</sub> architectures*. Carbon, 2002. **40**: p. 1665-1684.
3. Dehonor, M., K. Masenelli-Varlot, A. Gonzalez-Montiel, C. Gauthier, J.Y. Cavaillé, H. Terrones, and M. Terrones, *Nanotube brushes: polystyrene grafted covalently on CN<sub>x</sub> nanotubes by nitroxide-mediated radical polymerization*. Chemical Communications, 2005: p. 1-4.
4. Shaffer, M.S.P. and K. Koziol, *Polystyrene grafted multi-walled carbon nanotubes*. Chemical Communications, 2002: p. 2074-2075.
5. Bahr, J.L., Y. Yang, D.V. Kosynkin, M.J. Bronikowski, R.E. Smalley, and J.M. Tour, *Functionalization of Carbon Nanotubes by Electrochemical Reduction of Aryl Diazonium Salts: A Bucky Paper Electrode*. Journal of American Chemical Society, 2001. **123**: p. 6536-6542.
6. Koshio, A., M. Yudasaka, M. Zhang, and S. Iijima, *A Simple Way to Chemically React Single-Wall Carbon Nanotubes with Organic Materials Using Ultrasonication*. Nanoletters, 2001. **1**(7): p. 361-363.
7. Lin, T.S., L.Y. Cheng, C.-C. Hsiao, and A.C.M. Yang, *Percolated network of entangled multi-walled carbon nanotubes dispersed in polystyrene thin films through surface grafting polymerization*. Materials Chemistry and Physics, 2005. **94**: p. 438-443.
8. Chen, C.F., C.L. Tsai, and C.L. Lin, *The characterization of boron-doped carbon nanotube arrays*. Diamond and related materials, 2003. **12**: p. 1500-1504.
9. Strong, K.L., D.P. Anderson, K. Lafdi, and J.N. Kuhn, *Purification process for single-wall carbon nanotubes*. 2003.
10. Yang, Q.-H., P.-X. Hou, M. Unno, S. Yamauchi, R. Saito, and K. Takashi, *Dual Raman Features of Double Coaxial Carbon Nanotubes with N-Doped and B-Doped Multiwalls*. Nanoletters, 2005. **5**(12): p. 2465-2469.
11. Jiang, K., A. Eitan, L.S. Schadler, P.M. Ajayan, and R.W. Siegel, *Selective attachment of gold nanoparticles to Nitrogen-doped carbon nanotubes*. Nanoletters, 2003. **33**(3): p. 275-277.
12. Allaoui, A., S. Bai, H.M. Cheng, and J.B. Bai, *Mechanical and electrical properties of a MWNT/epoxy composite*. Composites Science and Technology, 2002. **62**: p. 1993-1998.
13. Harris, P.J.F., *Carbon nanotubes and related structures New materials for the twenty-first century*. 2001, Cambridge: Cambridge University Press. 279.
14. Laplaze, D., L. Alvarez, T. Guillard, J.M. Badie, and G. Flamant, *Carbon nanotubes: dynamics of synthesis processes*. Carbon, 2002. **40**: p. 1621-1634.
15. Chen, Y., R.C. Haddon, S. Fang, A.M. Rao, P.C. Eklund, W.H. Lee, E.C. Dickey, E.A. Grulke, J.C. Perdergrass, A. Chavan, B.E. Haley, and R.E. Smalley, *Chemical attachment of organic functional groups to single-walled carbon nanotube material*. Journal of Materials Research, 1998. **13**(9): p. 2423-2431.
16. Mitchell, C.A., J.L. Bahr, S. Arepalli, J.M. Tour, and R. Krishnamoorti, *Dispersion of Functionalized Carbon Nanotubes in Polystyrene*. Macromolecules, 2002. **35**: p. 8825-8830.
17. Bahr, J.L. and J.M. Tour, *Highly Functionalized Carbon Nanotubes Using in Situ Generated Diazonium Compounds*. Chemical Materials, 2001. **13**: p. 3823-3824.
18. Dyke, C. and J.M. Tour, *Solvent-Free Functionalization of Carbon Nanotubes*. Journal of American Chemical Society, 2003. **125**: p. 1156-1157.

19. Dyke, C.A. and J.M. Tour, *Overcoming the insolubility of carbon nanotubes through high degrees of sidewall functionalization*. Chemical European Journal, 2004. **10**: p. 812-817.
20. Chen, Y., R.C. Haddon, S. Fang, A.M. Rao, P.C. Eklund, W.H. Lee, E.C. Dickey, E.A. Grulke, J.C. Pendergrass, A. Chavan, B.E. Haley, and R.E. Smalley, *Chemical attachment of organic functional groups to single-walled carbon nanotube material*. Journal of Materials Research, 1998. **13**(9): p. 2423-2431.
21. Pantea, D., H. Darmstadt, S. Kaliaguine, L. Sümchen, and C. Roy, *Electrical conductivity of thermal carbon blacks Influence of surface chemistry*. Carbon, 2001. **39**: p. 1147-1158.
22. Peng, H., P. Reverdy, V.N. Khabashesku, and J.L. Margrave, *Sidewall functionalization of single-walled carbon nanotubes with organic peroxides*. Chemical Communications, 2003: p. 362-363.
23. Qin, S., D. Qin, W.T. Ford, D.E. Resasco, and J.E. Herrera, *Polymer Brushes on Single-Walled Carbon Nanotubes by Atom Transfer Radical Polymerization of n-Butyl Methacrylate*. Journal of the American Chemical Society, 2004. **126**(1): p. 170-176.
24. Mickelson, E.T., I.W. Chiang, J.L. Zimmerman, P.J. Boul, J. Lozano, J. Liu, R.E. Smalley, R.H. Hauge, and J.L. Margrave, *Solvation of Fluorinated Single-Wall Carbon Nanotubes in Alcohol Solvents*. Journal of Physical Chemistry B, 1999. **103**: p. 4318-4322.
25. Gallani, J.-L., L. Bonomme, A. Drury, and W.J. Blau, *Photosensitive magnetism of radicals coupled with carbon nanotubes*. Organic Electronics, 2003. **4**: p. 15-20.
26. Shen, K., D.L. Tierney, and T. Pietra, *Electron spin resonance of carbon nanotubes under hydrogen adsorption*. Physical Review B, 2003. **68**: p. 165418-1 a 165418-6.
27. Likodimos, V., S. Glenis, N. Guskos, and C.L. Lin, *Magnetic and electronic properties of multiwall carbon nanotubes*. Physical Review B, 2003. **68**: p. 045417-1.
28. Chen, Y., J. Chen, H. Hu, M.A. Hamon, M.E. Itkis, and R.C. Haddon, *Solution-phase EPR studies of single-walled carbon nanotubes*. Chemical Physics Letters, 1999. **299**: p. 532-535.
29. Bandow, S., S. Asaka, X. Zhao, and Y. Ando, *Purification and magnetic properties of carbon nanotubes*. Applied Physics A, 1998. **67**: p. 23-27.
30. Hsu, W.K., S.Y. Chu, E. Muñoz-Picone, J.L. Boldú, S. Firth, P. Franchi, B.P. Roberts, A. Schilder, H. Terrones, N. Grobert, Y.Q. Zhu, M. Terrones, M.E. McHenry, H.W. Kroto, and D.R.M. Walton, *Metallic behaviour of boron-containing carbon nanotubes*. Chemical Physics Letters, 2000. **323**: p. 572-579.
31. Coleman, J.N., D.F. O'Brien, A.B. Dalton, B. McCarthy, B. Lahr, R.C. Barklie, and W.J. Blau, *Electron paramagnetic resonance as a quantitative tool for the study of multiwalled carbon nanotubes*. Journal of Chemical Physics, 2002. **113**(21): p. 9788-9793.
32. Chauvet, O., L. Forro, W. Bacsá, D. Ugarte, B. Doudin, and W.A. de Heer, *Magnetic anisotropies of aligned carbon nanotubes*. Physical Review B, 1995. **52**(10): p. R6963-R6966.
33. Ishii, S., N. Aoki, K. Miyamoto, N. Oguri, K. Horiuchi, and Y. Ochiai, *CESR in multi walled carbon nanotubes*. Physica E, 2003. **17**: p. 386-388.
34. Dubey, P., D. Muthukumaran, S. Dash, R. Mukhopadhyay, and S. Sarkar, *Synthesis and characterization of water-soluble carbon nanotubes from mustard soot*. Pramana Journal of physics, 2005. **65**(4): p. 681-697.
35. Hayashi, S., A. Naitoh, S. Machida, M. Okazaki, K. Maruyama, and N. Tsubokawa, *Grafting of polymers onto a carbon black surface by the trapping of polymer radicals*. Applied Organometallic Chemistry, 1998. **12**: p. 743-748.
36. Tsubokawa, N., K. Fujiki, and Y. Sone, *Polymer-grafted carbon black with a higher percentage of grafting: graft polymerization of vinyl monomers onto unsaturated polyester-grafted carbon black surfaces*. Kobunshi Ronbunshu, 1987(44): p. 8.

37. Viswanathan, G., N. Chakrapani, H. Yang, B. Wei, H. Chung, K. Cho, C.Y. Ryu, and P.M. Ajayan, *Single-step In-situ Synthesis of Polymer-grafted Single Wall Nanotube Composites*. Journal of American Chemical Society, 2003. **125**(31): p. 9258-9259.
38. Terrones, M., P.M. Ajayan, F. Banhart, X. Blase, D.L. Carroll, J.C. Charlier, R. Czerw, N. Grobert, R. Kamalakaran, M. Mayne, M. Reyes-Reyes, M. Rühle, T. Seeger, and H. Terrones, *Exploring the carbon nanocosmos: doped nanotubes, networks, and other novel forms of carbon*. Proceedings of SPIE, 2003. **5118**: p. 1-.
39. Masenelli-Varlot, K. PhD thesis #98-45, Ecole Centrale de Lyon, Lyon, France (1998).
40. Coleman, J.N., *Carbon nanotube-conjugated polymer composites; a model study in nanoscale engineering*. 2002, Trinity College Dublin.

# **Chapter 6.**

## **Preparation and morphological characterization of nanocomposites of PS-PEO polymer blends and PS-grafted CN<sub>x</sub> nanotubes.**

### **6.1. Introduction**

Poly (ethylene oxide) (PEO) is a highly soluble water polymer that could form polymer electrolytes by addition of salts. Considering these properties, PEO appears as an appropriate candidate for biological and electrical applications. However, some challenges are still opened to satisfy simultaneously the electrical and mechanical performance requirements in growing fields of applications. Many efforts have been done to improve the PEO performance. Among the different routes are the synthesis of PEO polymer blends [1], or PEO block copolymer electrolytes [2, 3], as well as the addition of fillers.

Polymer blends and copolymer materials generally consist in chemically dissimilar polymers with complementary properties [4]; for example, high conductivity [5] and dimensional stability. In several works, a conductive phase as for instance PEO was combined with a stiff high-T<sub>g</sub> phase, such as poly(styrene) [6-8], to impart dimensional stability to the material associated with a continuous ion-conducting pathway [2]. In addition, copolymers and polymer blends of PEO and PS are especially interesting due to their immiscibility, leading to phase separation at equilibrium, and to the possibility to form an amphiphilic material [9]. These materials aggregate forming micelles in a selective solvent of one phase, and in the bulk, they adopt several morphologies depending on the volume fraction of each component (spherical domains, lamellae, cylinders, etc) and the processing conditions. Several efforts to incorporate immiscible polymers, like PS and PEO, have been made to produce polymer blend

materials since 1968 [10], like intense mixing during processing, the use of compatibilizers and additives, and the preservation of a non equilibrium morphology.

The optional addition of inorganic salts [2, 11], nanoclays [12], carbon black [13] and carbon nanotubes [14-17], among other fillers, has also been suggested to enhance the PEO performances. Several advantages can be expected from the introduction of an inorganic/organic component in a PEO polymer matrix. A main benefit is an increase in the strength of the polymer composite. Another advantage is the possibility to influence the crystallinity of the PEO, by changing conditions for polymer chain folding. An additional opportunity is the possibility to influence electrochemical properties of the polymer electrolytes [13, 14].

Another kind of examples involves the combined use of additives and amorphous polymers (PEO-LiBF<sub>4</sub> and PS) in PEO for special applications, as Li secondary batteries, flexible electrochromic displays and smart windows [18, 19]. In this case, the mechanical properties of the immiscible polymer blends were reduced, thus a filler, as carbon nanotubes, was used to enhance them. In addition, the carbon based filler could be preferentially located in one of the phases, or at the polymer-blend interface with the aim to reduce the percolation threshold of the material [20].

Many works on polymer-nanocomposites of PEO and PS using several processing methods can be found in the literature.

Nanocomposites of MWNTs embedded in PEO using amphiphiles (sodium dodecyl sulfate or a highly branched polymer) were prepared by Dror *et al* [9]. Dispersions of SWNTs in PEO assisted by a lithium-based anionic surfactant were produced and demonstrate low electrical percolation and a geometrical percolation [21]. Other works in the area considered also PEO nanocomposites with MWNTs [22] and C<sub>60</sub>-PEO-C<sub>60</sub> with MWNTs [16]. In addition, SWNT/PEG composites using various solvents were studied by Liu *et al* [23] where the authors found the interaction between polymer and SWNT as a major factor influencing the physical and mechanical properties of polymer-nanotube composites.

For the case of PS matrices, the ultrasonication in solution was used to uniformly disperse MWNTs in order to incorporate them into composites of PS without chemical pretreatment [24-26]. Melt blending by a twin-screw extruder was used to achieve dispersion of multi-walled carbon nanotubes in polystyrene matrices in several researches [27], some of them using additional compatibilizers [28, 29]. Polymer latex mixed with carbon nanotubes were also prepared [30].

Furthermore, it is well known that the chemical functionalization of carbon nanotube could enhance their chemical compatibility and dissolution properties. The modification of carbon nanotubes with polymers could in addition improve the interfacial interaction to polymeric matrices in its composites [15]. Some reported cases involve the *in situ*-polymerization process to prepare nanocomposites [31, 32].

In this thesis, the search of interesting electrical properties in polymer-nanotube composites has been focused on the synthesis of nanocomposites of PS, PEO and PS-PEO polymer blends using several kinds of nanotube as fillers. Among the fillers, multiwalled carbon nanotubes (MWNT) sonicated nitrogen-doped carbon nanotubes (CN<sub>x</sub>) and polymer-grafted nitrogen-doped carbon nanotubes (PS-*g*-CN<sub>x</sub>) were considered. The nanocomposites were prepared in solution. The morphology of the

nanocomposites, as well as the thermal properties were studied. Subsequent chapters discuss the physical and mechanical properties of the materials.

## 6.2. Results and discussion

The polymer nanocomposites of PS, PEO and PS-PEO blends and different kinds of carbon nanotubes (MWNT, CN<sub>x</sub> and PS-g-CN<sub>x</sub>) were prepared as described in Chapter 4 and schematized in Fig. 6.1. The materials were analyzed before and after producing films of 0.1-0.5 mm of thickness.

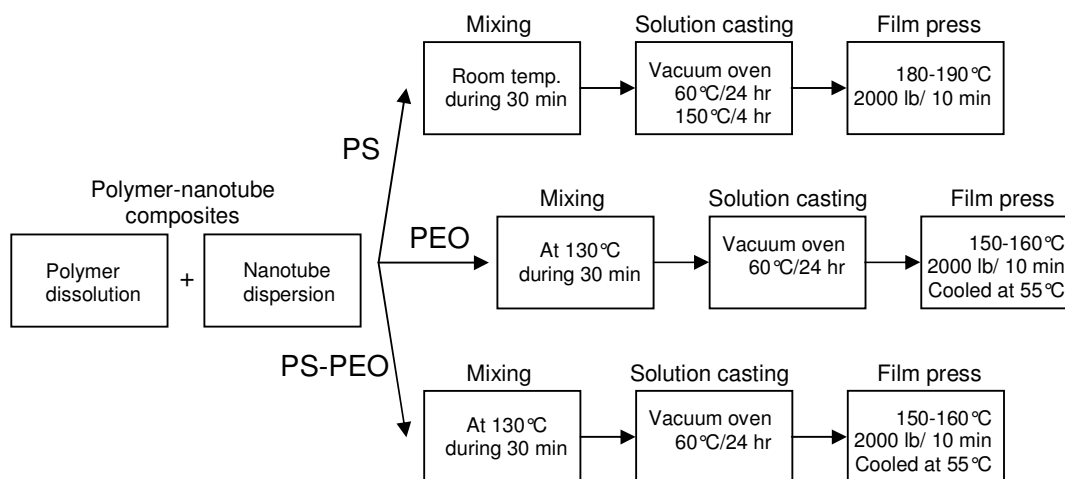


Fig. 6.1. Reaction scheme of the preparation steps of the polymer-nanotube composites.

In the following sections, the characterization of these materials is reported according to the polymer matrix of the nanocomposite. The morphological properties of the materials are determined using SEM and TEM in order to qualitatively study the filler dispersion, the nature of the contact among matrix and filler (i.e. polymer wetting of CNTs) and the interfacial adhesion strength. Additionally, the thermal properties are characterized using DSC and related to the microstructure of the nanocomposites. The electrical and mechanical properties will be discussed in the next chapter.

### 6.2.1. PS-based nanocomposites

#### 6.2.1.1. PS-nanotube composites processing

All the PS-nanocomposites have been prepared in toluene solutions with 2 gr of polymer and different amounts of pre-sonicated nanotube fillers (MWNT, CN<sub>x</sub> and PS-g-CN<sub>x</sub>) in order to obtain films at several concentrations (i.e. 0.1, 0.3, 0.5, 0.7, 1.0, 2.0 and 5.0 wt%). In particular, PS-based nanocomposite solutions were mixed with a magnetic shaker at room temperature during 30 min. The speed of mixing was not measured but it was considered the same for all materials. Films were prepared by solution casting. After the solvent evaporation at low temperature (20°C), the materials were dried in a vacuum oven at 60°C for 24 hrs and in an oven at 150°C for 4 hrs in

order to remove all the toluene solvent. After the drying step, the samples were pressed at 180-190°C and 2000 lb (8896 N) for 10 min, as described in Fig. 6.1.

Before hot-pressing, the PS-nanocomposite films presented variable nanotube dispersions according to the filler nature and the concentration. By macroscopic inspection, the PS-*g*-CN<sub>x</sub> nanotubes seemed to be better dispersed in PS when compared to the others at all concentrations. The level of filler dispersion for the other kind of nanotubes seemed to follow: CN<sub>x</sub>>MWNT. In any case, the differences of dispersion with the filler concentration are not easily understood only by this macroscopic observation of the samples. Morphological study of the obtained samples will be discussed in part 6.2.1.3. Before, the thermal properties will be described in the next part.

### 6.2.1.2. PS-nanotube composites thermal properties

PS-based nanocomposites have been characterized by DSC technique in order to determine changes in the T<sub>g</sub> of the polymer matrix with the filler type and the filler concentration. In this research, the analyzed composite samples by DSC were PS/MWNT (0.1-5.0 wt%), PS/CN<sub>x</sub> (0.1-5.0 wt%), and PS/PS-*g*-CN<sub>x</sub> (0.1-5.0 wt%).

First of all, it can be noticed that DSC is a suitable technique to assess that no solvent remains from both the solution casting and hot-pressing processes. After complete evaporation, for a given filler type, no change in T<sub>g</sub> with the nanotube filler concentration is observed. In other words, the T<sub>g</sub> of the PS/MWNT, PS/CN<sub>x</sub> and PS/PS-*g*-CN<sub>x</sub> nanocomposites reveal no changes whatever the concentration (graph not shown here).

To go further, the T<sub>g</sub> values for the nanocomposites can be compared to that of the pristine PS matrix (102.9°C). In the case of MWNTs no difference in T<sub>g</sub> is observed between the polymer matrix and the PS/MWNT nanocomposite (not shown in the Fig.). A similar result is obtained for PS/CN<sub>x</sub> composites as shown in Fig. 6.2. Thus, if the DSC measurements are accurate enough, and since no changes are noticed in the glass transition temperature measured by DSC could be related to the interaction between the carbon nanotube surface and the PS chains. As no covalent attachment of carbon nanotube surfaces with the polymer is expected in both cases, it can be proposed that these interactions are almost the same and not strong enough to modify the polymer chain mobility. Thus, it can be stated that PS/MWNT and PS/CN<sub>x</sub> nanocomposites could exhibit weak polymer-nanotube interaction in agreement with the unchanged value of T<sub>g</sub> with the filler concentration. Additional explanations are related to the high molecular weight of the polymer matrix that could produce only limited changes in the mobility of the polymer chains in interaction with nanotubes. Actually, it was reported that the magnitude of the T<sub>g</sub> change in the nanocomposites decreased for higher molecular weights of the matrix. [33]

For the PS/PS-*g*-CN<sub>x</sub> composite, we can first point to the fact that the modified nanotubes (PS-*g*-CN<sub>x</sub>) display a modified T<sub>g</sub>, equal to 101.3°C (Fig. 6.2). This lower value compared to pristine PS is related to the molecular weight of the attached polymer. In fact, it was observed that the grafted-PS of around 40,000 gr/mol exhibited a T<sub>g</sub> lower than that of the matrix [34]. In our case, the molecular weight of the polymer matrix around 70,000 gr/mol gave a slightly decrease in T<sub>g</sub>. In both cases, the nanotubes act as plasticizers within the matrix.

In general the analysis of the T<sub>g</sub> value of a nanocomposite could be related with its interfacial behavior with the filler : the decrease in mobility of the chains results from intimate interactions between PS and the nanotube surface. Thus, in some cases, a T<sub>g</sub> increment was observed in nanocomposites and attributed to the constraint of polystyrene chains due to their attachment to a solid surface [27, 35].

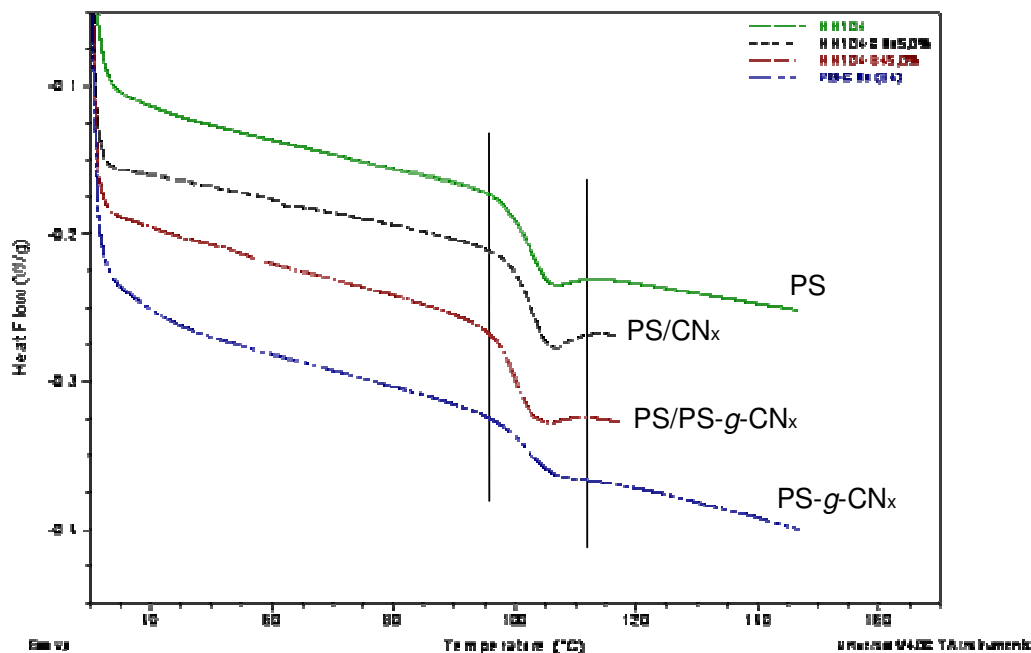


Fig. 6.2. Glass transition temperature of PS matrix, PS-grafted CN<sub>x</sub> nanotube fillers alone (PS-g-CN<sub>x</sub>) and the PS-based nanocomposites with either CN<sub>x</sub> (PS/CN<sub>x</sub>), or PS-grafted CN<sub>x</sub> fillers (PS/PS-g-CN<sub>x</sub>) at 5 wt%.

Now, let us consider the case of the PS/PS-g-CN<sub>x</sub> nanocomposites. In that case, whatever the composition, no change in the glass transition temperature has been measured. In the literature, the increase of T<sub>g</sub> is reported to depend on the filler content, even in nanocomposites at low filler concentration [36]. Furthermore, it was observed that the attachment of polymer chains to the nanotube surfaces promoted better matrix-nanotube adhesion [36]. Finally, higher increments in T<sub>g</sub> values were observed for functionalized-MWNT than for pristine-MWNT [36]. On the contrary, in other cases several authors found no effect of carbon nanotubes on the T<sub>g</sub> of PS-based nanocomposites, even at filler concentrations higher than 10 wt% [37, 38]. Even more, the absence of T<sub>g</sub> signal was obtained by DSC and it was considered as a result of the chemical reaction with polymers, as in the case of epoxide-based nanocomposites [39].

With all this information, several explanations can be proposed for the observed T<sub>g</sub> values of PS/PS-g-CN<sub>x</sub> nanocomposites. First, the value of T<sub>g</sub> is a result from a competition between anchoring and plasticizing effects of the filler within the matrix, as was already observed [40]. Thus, the unchanged T<sub>g</sub> of PS/PS-g-CN<sub>x</sub> could be a result from some plasticizing effects of the polymer brushes that compensate the expected increase in covalent attachment nanocomposites; but in this case, the PS-g-CN<sub>x</sub> nanotubes alone did not reflect the increment in the T<sub>g</sub> through a covalent attachment. Hence, it could most probably be related to the close values from the T<sub>g</sub> of the polymer

matrix and the  $T_g$  of the PS-grafted  $CN_x$  nanotubes (as shown in Fig. 6.2), even though a good interface interaction between materials was verified in the scanning electron microscopy images.

To summarize, the thermal properties of the PS-based nanocomposites, we can conclude that the PS-based nanocomposites exhibit unchanged values of  $T_g$  as a function of the type of filler and filler concentration. For PS/MWNT and PS/ $CN_x$ , the main causes of a constant  $T_g$  could be related to weak polymer-nanotube interactions leading to little changes in the chain mobility, or even more because of the molecular weight of the polymer matrices. For PS/PS- $g$ - $CN_x$  composites, it seemed that the main reason of an unobservable change in the  $T_g$  is related to values close to the  $T_g$  of the components.

### 6.2.1.3. PS-nanotube composites morphology

As already said, the PS-nanocomposite films have been first observed by macroscopic inspection before hot-pressing. According to the filler nature, the level of filler dispersion seems to follow: PS- $g$ - $CN_x$  >  $CN_x$  > MWNT.

After film pressing at high temperatures, homogeneous black films are obtained in all cases. In these materials, no clear evidence of any difference in the macroscopic dispersion is identified. Therefore, the morphology of the films is further investigated by electron microscopy. Fractures of these films are characterized by SEM, and microtomed films are analyzed by TEM. The samples are fractured and cut at low temperature. Films at 2 wt% of filler concentration (MWNT,  $CN_x$  and PS- $g$ - $CN_x$ ) are compared. PS-based nanocomposites are analyzed by SEM and TEM microscopy and the material morphology is discussed in terms of degree of filler dispersion and filler-matrix interaction.

#### *PS/MWNT nanocomposites*

SEM images of the film fracture of PS/MWNT nanocomposites at 2 wt% have been obtained at several magnifications. At low magnification, an homogeneous surface is observed (not shown here). If the surface of the sample is zoomed, the formation of polymeric “fibers” can be noticed, and associated to the fracture procedure (Fig. 6.3 (a)). At this scale (2500X), it is difficult to discriminate the fibers from the nanotubes. At higher magnifications and low scans (Fig. 6.3 (b)), some individual and bundles of MWNTs are observed as they exit from the surface of the fracture. From this image, it seems that the polymer matrix fracture is accompanied to a large extent of nanotube slippages. In addition, the presence of some holes around the nanotubes and emerging nanotubes from the surface indicate a possible poor interface polymer-nanotube interaction (pull-out).

TEM observations are consistent with these first conclusions (Fig. 6.4): images of microtomed films also reveal the pull-out of some nanotubes because of the cutting effects of the diamond knife. Thus, in some cases the images reveal the prevalence of carbon nanotubes in the polymeric material, but in other cases only the holes remain after cutting. This phenomenon, again, can be related to a poor polymer-nanotube interaction.

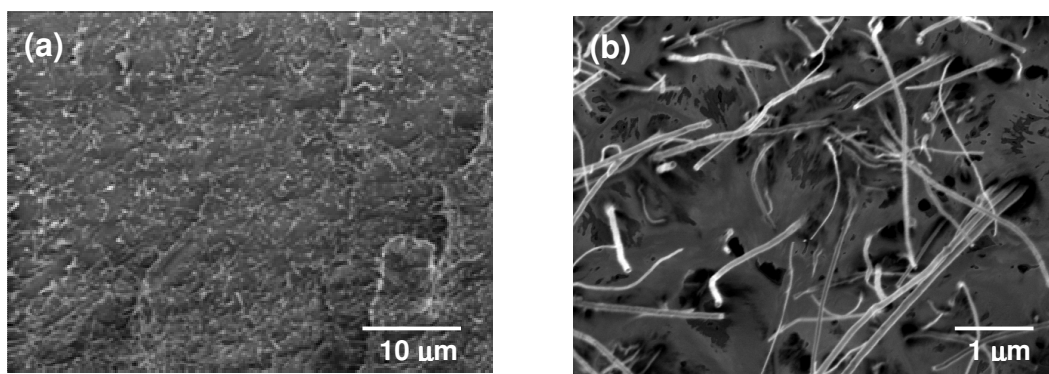


Fig. 6.3. SEM images of film-fractured polymer nanocomposites of PS and 2 wt% of MWNTs prepared by solution casting and high temperature pressing at several magnifications and scan velocities: (a) high scan, (b) low scan.

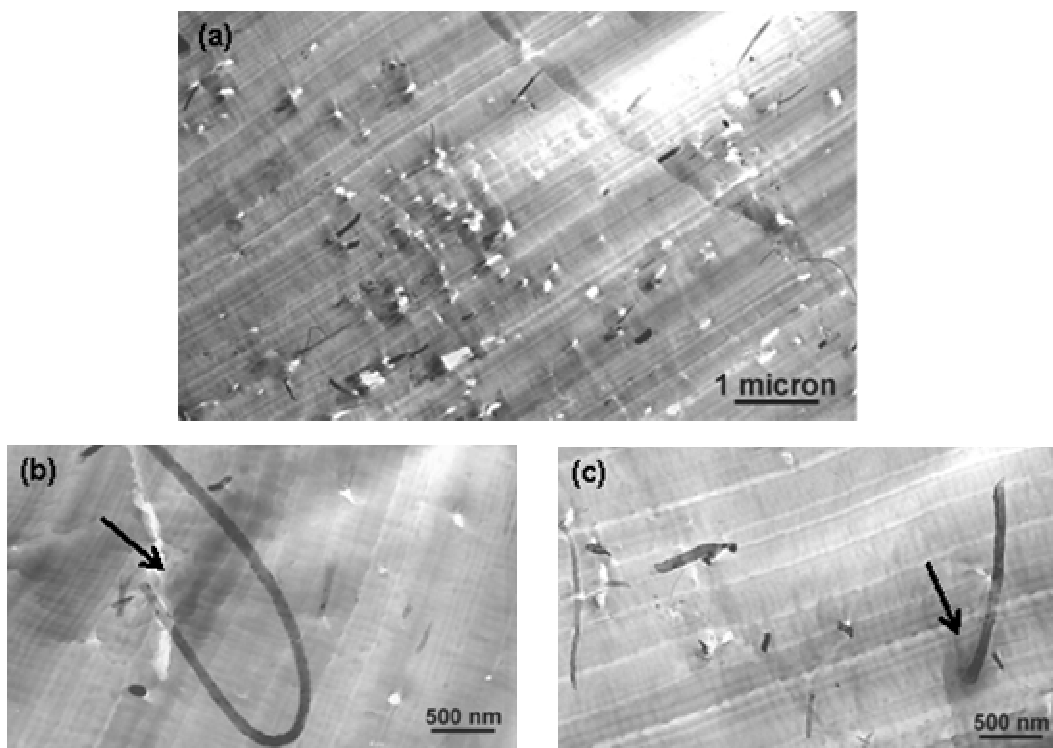


Fig. 6.4. TEM images of microtomed films of polymer nanocomposites of PS and 2 wt% of MWNT prepared by solution casting and high temperature pressing.

In summary, the observed morphology of PS/MWNT nanocomposites is characterized by a good general dispersion even though the presence of some bundles in the polymeric matrix is observed. This good dispersion after nanocomposite processing can be associated to the initial good dispersion of nanotubes in the organic solvent after sonication. Nevertheless, the low chemical reactivity of the MWNT surfaces leads to low interactions with the polystyrene matrix (and probably low interfacial strength) as evidenced by the pull-out of the nanotubes from the microtomed films.

*PS/CN<sub>x</sub> nanocomposites*

SEM images at very low magnification (not shown here) indicate that the PS-based nanocomposites with CN<sub>x</sub> nanotubes (PS/CN<sub>x</sub>) at 2 wt% display a homogeneous macro dispersion through the film section. Nevertheless, at higher magnification, it appears that the preparation of the surface by cryo-fracture leads to distinct zones with either a great quantity of polymer “fibers” formed, or a low quantity of fibers noticed. In the zone with a large amount of polymer “fibers” (Fig. 6.5 (a)), both individual nanotubes and bundles are present. The nanotubes seem to be perpendicular to the surface, and in some cases a little dark zone around them is also noted (Fig. 6.5 (b)). These characteristics can be related to a higher interfacial strength between the polymer matrix and CN<sub>x</sub> nanotubes, which is believed to be higher than for the case of PS/MWNT.

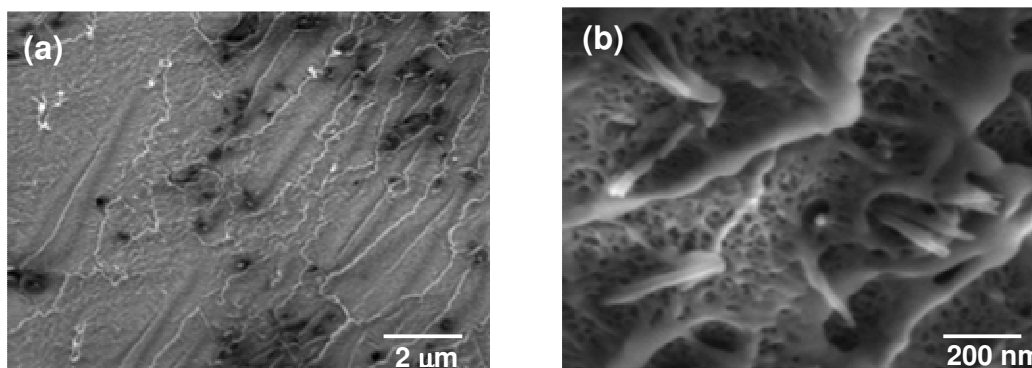


Fig. 6.5. SEM images of film fractured polymer nanocomposites of PS and 2 wt% of CN<sub>x</sub> nanotubes prepared by solution casting and high temperature pressing.

Complementary information is obtained by TEM images shown in Fig. 6.6. Microtomed-films present dispersed individual nanotubes (Fig. 6.6 (a)). In addition, the length of the tubes seems to be smaller than the original. This fact could be attributed to the mechanical cut of the nanotubes by the diamond knife. At higher magnifications, details of the effect of the cut on the tubes is observed (Fig. 6.6 (b) and 6.6 (c)). It seems that, in some cases, the nanotubes are moved from their initial position occasioning some holes near from the nanotube tips. This zone corresponds to the dark zone around the tips reported from SEM observations. In almost all cases, there are isolated holes present; indicating that the nanotubes remain in the polymer matrix even though the sample was cut. This fact only could be due to the higher strength of the polymer-CN<sub>x</sub> interactions.

In summary, the PS/CN<sub>x</sub> nanocomposites reveal once again a good dispersion but this time added to good properties of contact between polymer matrix and filler. Thus, a good interfacial strength can be expected. These properties are attributed to the enhanced chemical reactivity of CN<sub>x</sub> nanotubes than leads to better interactions with organic solvents or reactants.

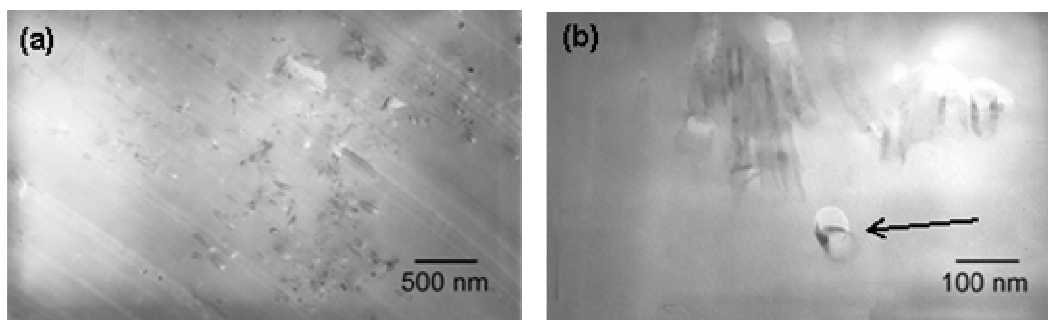


Fig. 6.6. TEM images of polymer nanocomposites of PS and 2 wt% of CN<sub>x</sub> nanotubes prepared by solution casting and high temperature pressing.

#### *PS/PS-g-CN<sub>x</sub> nanocomposites*

The PS-based nanocomposites based on PS-grafted CN<sub>x</sub> nanotubes (PS/PS-g-CN<sub>x</sub>) have also been analyzed by microscopy techniques. SEM images of the fracture film surfaces are presented in Fig. 6.7. Particularly, Fig. 6.7 (a) shows an homogeneous appearance of the nanocomposite at low magnification and slow scan. Thus, it could be expected a relatively homogeneous dispersion of the nanotubes in the nanocomposite. At higher magnifications, some polymer “fibers” and the presence of nanotube tips are observed (Fig. 6.7 (b)). Here again, the polymer “fibers” seemed to appear at the fracture time. Moreover, the nanotubes seem to enter and exit from the polymer surface as shown in Fig. 6.7 (c). Details of the nanotube interaction with the polymer matrix are depicted in the Fig. 6.7 (d). We believe that the nanotubes have a good interaction with the polymer matrix. In fact, lateral sustaining or attaching of nanotubes by polymer “fibers” are observed. In addition, holes around nanotubes after fracture are no more observed, as in the previous cases. Consequently, the PS grafted-CN<sub>x</sub> nanotubes seem to present the best interactions and contact with the PS matrix. Finally, a low tortuosity of the PS-grafted nanotubes embedded in the polymer matrix is observed.

TEM images (Fig. 6.8) show the presence of nanotubes individually distributed. Furthermore, the film is not mechanically cut near carbon nanotubes, revealing that a higher interfacial strength takes place.

At last, the PS/PS-g-CN<sub>x</sub> nanocomposites display good filler dispersion, contact and interfacial strength between the polymer and PS-g-CN<sub>x</sub> materials. This compatibility with the matrix seem to be higher that for the cases of CN<sub>x</sub> and MWNT fillers. These characteristics could be related to the compatibility of polystyrene-grafted on the nanotube surfaces with the polystyrene matrix, as expected. Thus, the preparation of polymer-grafted nanotubes could serve as a way of preparing nanotube-polymer nanocomposites with enhanced mechanical and conducting properties.

#### **6.2.1.4. Dispersion, adhesion and thermal behavior of PS-nanotube composites**

In summary, the comparison of the PS-based nanocomposites through electron microscopy reveals several differences attributed to the filler type. In Table 6.1 some of the most important results are reported.

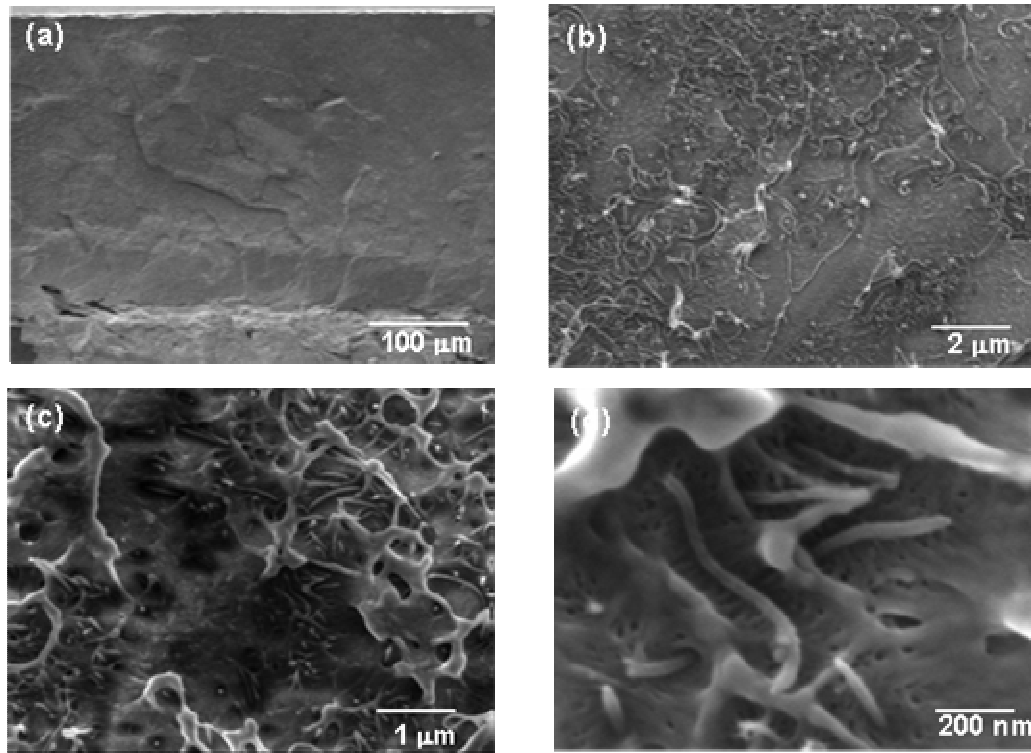


Fig. 6.7. SEM images of polymer nanocomposites of PS and 2 wt% of PS-grafted  $CN_x$  nanotubes (PS-g- $CN_x$ ) prepared by solution casting and high temperature pressing.

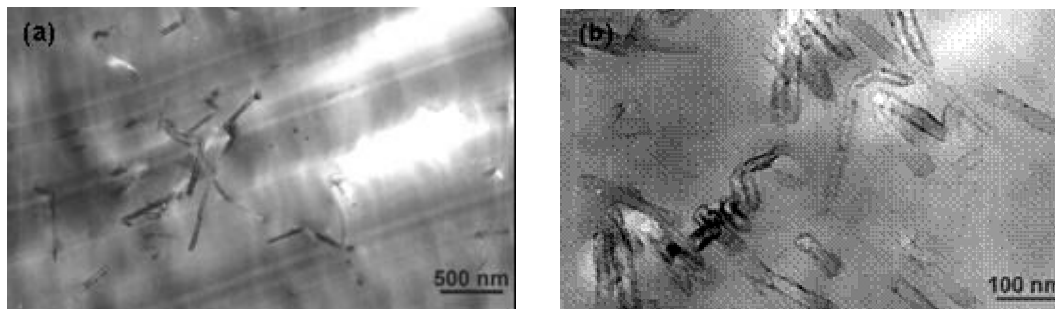


Fig. 6.8. TEM images of polymer nanocomposites of PS and 2 wt% of PS-grafted  $CN_x$  nanotubes (PS-g- $CN_x$ ) prepared by solution casting and high temperature pressing.

First of all, the chemical reactivity of carbon nanotubes has determined differences in the dispersion and adhesion between the fillers with the polystyrene matrix, as observed by microscopy. Thus, as expected, nitrogen-doped carbon nanotubes exhibited enhanced adhesion properties when compared to multiwalled nanotubes. Nevertheless, by DSC it was not possible to detect important differences in the  $T_g$  of the MWNT and  $CN_x$  nanotubes based materials to confirm and estimate the strength of the nanotube-polymer adhesion. Further characterization of these materials will highlight the nanocomposite microstructure properties and their relationships with other physical measurements.

Table 6.1. Characteristics of PS-based nanocomposites at several observational scales.

<b>Level</b>	<b>Characteristics</b>	<b>Scale</b>
Macro	Film homogeneous appearance after pressing In general, little group of particles with the relative size: PS/MW > PS/CN <sub>x</sub> > PS/PS- <i>g</i> -CN <sub>x</sub>	Visible
Micro	Almost homogeneous aspect of the transversal section, according to: PS/CN <sub>x</sub> < PS/PS- <i>g</i> -CN <sub>x</sub> ~ PS/MW Particle distribution homogeneity: PS/MW ~ PS/PS- <i>g</i> -CN <sub>x</sub> ~ PS/CN <sub>x</sub>	SEM
Nano	Interfacial strength and adhesion of nanotubes: PS/MW < PS/CN <sub>x</sub> < PS/PS- <i>g</i> -CN <sub>x</sub>	TEM

Furthermore, the polymer-grafting of carbon nanotubes seems to enhance the filler properties of CN<sub>x</sub> nanotubes. Clearly, dispersion efficiency differences were revealed between PS/CN<sub>x</sub> and PS/PS-*g*-CN<sub>x</sub> nanocomposites. In the second case, a more homogeneous nanocomposite was produced. Moreover, the interfacial adhesion strength between the PS matrix and non-grafted CN<sub>x</sub> nanotubes is weak. The interfacial adhesion strength seems to be greatly improved when using PS-grafted CN<sub>x</sub> nanotubes since the images do not show any partially pulled-out nanotube. Thus, PS/PS-*g*-CN<sub>x</sub> materials present good dispersion and adhesion between polymer and filler, as fortunately revealed by microscopy images. Furthermore, low tortuosity is induced in the nanotubes after nanocomposite preparation. Thus, the polystyrene-grafting of CN<sub>x</sub> nanotubes could be an efficient way to enhance the surface energy between the filler and the polymer matrix and therefore improve both the dispersion of nanotubes in a matrix and the interfacial adhesion strength. Even though, measurements of the T<sub>g</sub> values do not revealed important changes This property of polymer-grafted CN<sub>x</sub> nanotubes is very promising for achieving an enhancement of mechanical and electrical properties of polymer/nanotube nanocomposites. These combined properties let us establish that the polymer-grafting of nanotubes could serve as a way to prepare nanocomposites with enhanced physical properties, as well as polymer blends compatibilizers.

We believe that the preparation of PS-based nanocomposites could be enhanced by studying and optimizing the conditions of sonication of carbon nanotubes (time and drying), the conditions of nanocomposite synthesis and film preparation (time, vol. solvent, shaking, drying, pressure and temperature (hot-pressing)). Moreover, studies could also consider the intermolecular interaction energy between PS and CNTs in these composites, as some previous works report for other systems [41].

## 6.2.2. PEO-based nanocomposites

### 6.2.2.1. PEO-nanotube composites processing

Polymer nanocomposites of poly(ethylene oxide) and different kinds of carbon nanotubes have been prepared by the solvent route. PEO based nanocomposites have been prepared in toluene at 130°C for 30 min. After the solvent evaporation at low temperature (20°C), the materials were dried in a vacuum oven for 24 hrs at 60°C. Then, they were pressed at 150-160°C and 2000 lb (around 8896 N) for 10 min, and then cooled with cold water down to 55°C, then maintained for crystallization during 2 min. Film samples of approximately 1-4 mm of thickness were formed (See Fig. 6.1).

Toluene was selected as solvent of PEO at high temperatures, although it cannot dissolve the polymer at room temperature. This choice is justified by the fact that we decided to use a unique solvent in the preparation of all the nanocomposites. Thus, solutions of PEO and nanotubes were mixed at high temperature (solvent m.p.). Unfortunately in all cases, a phase separation in the materials has been observed as the solvent gets cold. In fact, a combination of white and black powders was obtained. Non observable differences have been seen in these films with any filler; nevertheless, the effect of concentration was observed as revealed by a more or less intense black coloration of powders.

After film pressing at high temperature, fragile black-white films are obtained for all materials. In these materials the macroscopic homogeneity is lower than for the PS-based nanocomposites. Detailed studies of the morphology of the PEO-based nanocomposites have been carried out on fracture samples using SEM and microtomed films by TEM at 2 wt% concentrations. As in the previous case, a comparison between the different filler types is performed. In addition, thermal studies of the glass transition temperature ( $T_g$ ) and crystallization temperature ( $T_c$ ) of the polymer matrix in nanotube composites is performed.

#### 6.2.2.2. PEO-nanotube composites thermal properties

PEO-based nanocomposites have been analyzed by DSC to determine possible differences in  $T_g$ ,  $T_c$  and  $T_m$  of the polymer matrix in the presence of nanotubes. The DSC measurements were performed over film sections and taken once after an appropriate drying process. Furthermore, it is possible that the effect of the morphology of the materials and the inherent inhomogeneities in the film reduce the measurements representativity. In addition, the samples were evaluated only once in DSC, thus an appropriate repetition of them could aid to also determine the representativity of the phenomena. Anyway, Table 6.2 summarizes the thermal properties of the PEO-based composites as a function of filler type and content obtained at these conditions.

##### *Glass transition temperature, $T_g$*

According to the reported values shown in Table 6.2, the glass transition temperature,  $T_g$ , presents no observable change in the PEO/MWNT, PEO/CN<sub>x</sub> and PEO/PS-g-CN<sub>x</sub> nanocomposites with the filler type or concentration, at least in the studied conditions. These results could be explained by (i) the nanocomposite morphology, particularly the increment in the polymer cristallinity in the presence of nanotubes, (ii) the inhomogeneity of the film materials that could induce measurement difficulties (by lack of representativity), or (iii) the low interfacial interaction between PEO and carbon nanotubes in these nanocomposites. The first statement could be possible in systems with great changes in cristallinity, but in this case the cristallinity has changed on a slight manner, making the argument negligible. Furthermore, the last statement will be further discussed thanks to microscopy observations. Finally, additional characterization will be needed to assess the proposed explanations at least; the measurement of more samples will be helpful to increase the representativity of each value.

##### *Melting temperature, $T_m$*

The melting temperature,  $T_m$ , for PEO/MWNT nanocomposites decreases with the filler content (Fig. 6.2). The higher difference is around 5°C for 2 wt% of MWNT,

with respect to the pure PEO matrix. This behavior could be related to the high thermal conductivity of MWNTs and their relatively good individual dispersion in the polymer matrix, as already observed with other crystalline matrices. However, it could be also related with the spherulite formation in the semicrystalline matrix that modifies the heat propagation.

Table. 6.2. Thermal properties of PEO-based nanocomposites<sup>†</sup>.

Nanocomposite	wt%	wt% funct*	T <sub>g</sub> , °C	T <sub>m</sub> , °C	T <sub>c</sub> , °C	ΔH <sub>c</sub> , J/g	Crystallinity, %
PEO	0		-54.3	69.9	43.6	131.7	0.62
PEO/MWNT	0.5		-52.4	65.2	47.1	150.8	0.71
	2.0		-54.5	64.5	43.7	136.6	0.64
PEO/CN <sub>x</sub>	0.5		-53.1	63.7	45.4	146.0	0.68
	2.0		-53.2	65.3	46.9	143.5	0.67
PEO/PS- <i>g</i> -CN <sub>x</sub>	0.5	0.2	-53.8	64.7	45.0	140.3	0.66
	2.0	0.7	-55.5	65.1	47.3	138.3	0.65

\* Filler weight % addition of functionalized carbon nanotubes according to the PS-grafting efficiency values.

<sup>†</sup> Estimated temperature precision: ±0.1°C.

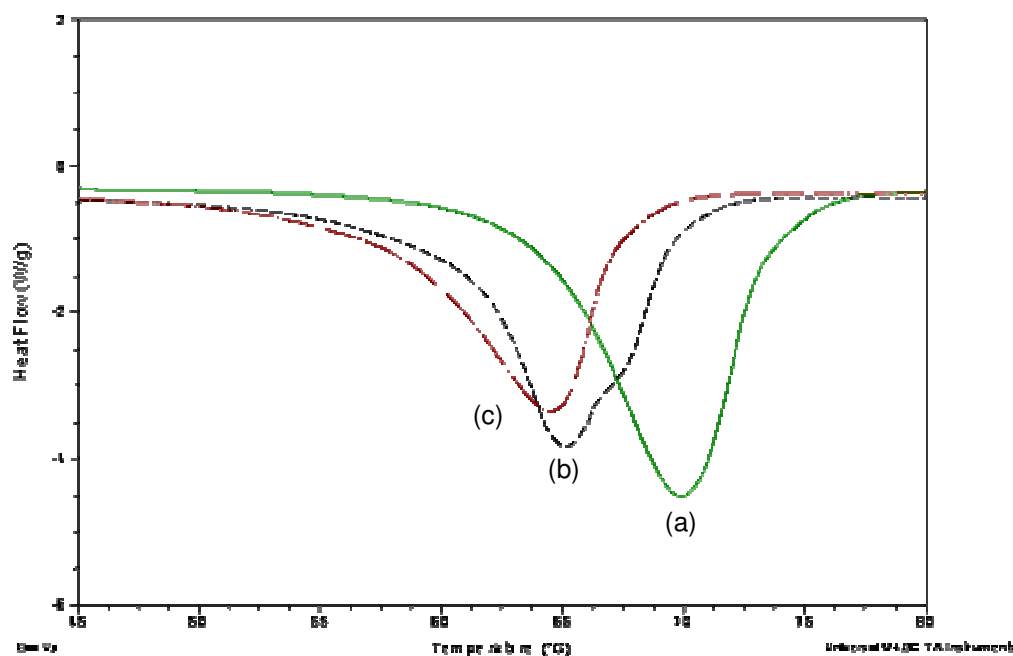


Fig. 6.9. Melting temperature of (a) PEO polymer matrix, and PEO/MWNT nanocomposites at several filler contents: (b) 0.5 wt% and (c) 2.0 wt%.

In the case of the PEO/CN<sub>x</sub> and PEO/PS-*g*-CN<sub>x</sub> nanocomposites, the melting temperature of PEO also decreases of about 5°C. However, this decrease, in opposite to the PEO/MWNT case, is more or less independent of the nanotube concentration, as can be seen in Fig. 6.10 (b)-(d). In this case, even though the carbon nanotubes have good thermal conductivity properties, the dispersion of individual filler may be worse and the presence of carbon nanotubes agglomerates could be responsible of a lower thermal conduction within the nanocomposite. Thus, it seems that a lower filler content has been better dispersed when compared to a higher filler content. This result may be related to

the lower chemical compatibility of  $CN_x$  and PS-g- $CN_x$  nanotube fillers with the PEO matrix, and also due to the choice of the organic solvent in the preparation method.

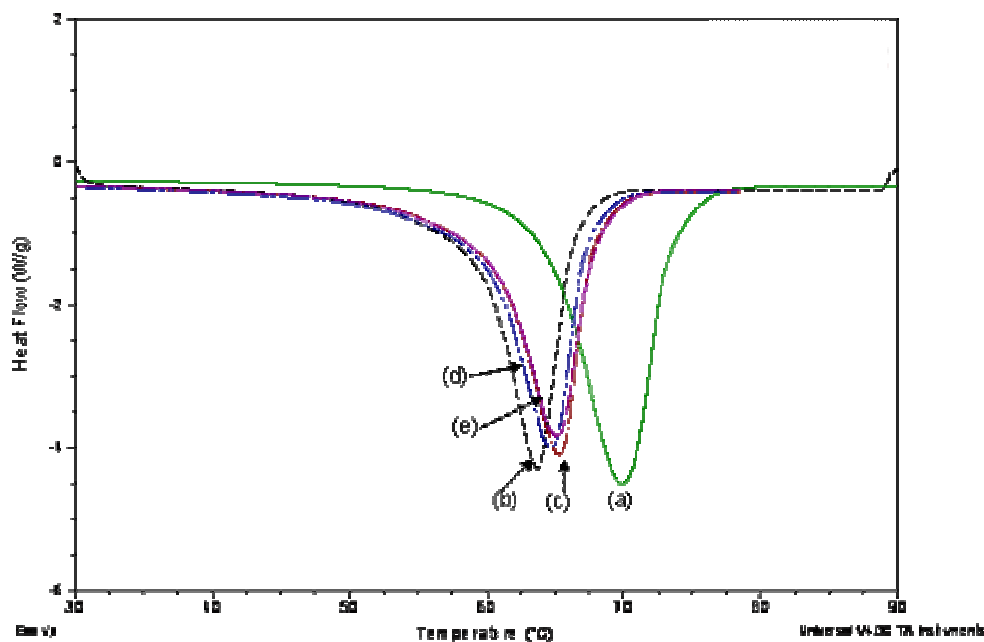


Fig. 6.10. Melting temperature of (a) PEO polymer matrix, and PEO-based nanocomposites: (b) PEO/ $CN_x$  at 0.5 wt%, (c) PEO/ $CN_x$  at 2.0 wt%, (d) PEO/PS-g- $CN_x$  at 0.5 wt%, and (e) PEO/PS-g- $CN_x$  at 2.0 wt%.

Comparing these results with those reported in the literature for crystalline and semicrystalline polymer matrices and carbon nanotubes as fillers, it was observed that poly(ethylene) (PE) [42] and poly(propylene) [43] nanocomposites using MWNTs revealed no significant changes in the  $T_m$  of the polymer matrix. Additionally, the incorporation of MWNTs resulted in a decrease of  $T_m$  with no obvious trend in the  $T_m$  values for functionalized-PEO with MWNTs nanocomposites [16].

#### *Crystallization temperature, $T_c$*

PEO-based nanocomposites present effects on the crystallization temperature,  $T_c$ , in relation with the filler type and filler concentration. In addition, it is important to comment that two differences in the crystallization temperature were observed. One is related to the temperature at the peak maximum ( $T_c$ ), and the other is related to the temperature at the beginning of the crystallization phenomenon ( $T_{onset}$ ), in both cases due to a modification in the crystallization behavior of the materials. The following paragraphs will comment the results in  $T_c$  values of the nanocomposites.

First of all, in PEO/ $CN_x$  and PEO/PS-g- $CN_x$  nanocomposites, an increase in  $T_c$  with the filler content is observed (Fig. 6.11). The maximum increase is noted for 2 wt% of filler, and corresponds to around 4°C. This increase in  $T_c$  could be associated to a nucleating effect of the  $CN_x$  and PS-g- $CN_x$  nanotubes in the PEO matrix that could be corroborated by the increment in the percentage of crystallinity, reported in Table 6.2. The crystallization percentage ( $X_c$ ) is measured based on the ratio of the heat of

melting from DSC results and the value of 213.7 J/g, which was reported for the melting enthalpy of 100% crystalline PEO. Thus,

$$X_c = \frac{\Delta H_m}{\Delta H_{m,PEO}} \times 100\% \quad (6.1)$$

From Fig. 6.11 and Table 6.2, it is possible to observe that the changes in the crystallinity for the PEO/CN<sub>x</sub> samples is higher than for the PEO/PS-g-CN<sub>x</sub> ones. This result could imply that the nucleating effect is higher in the case of the CN<sub>x</sub> filler than in the case of the PS-g-CN<sub>x</sub>.

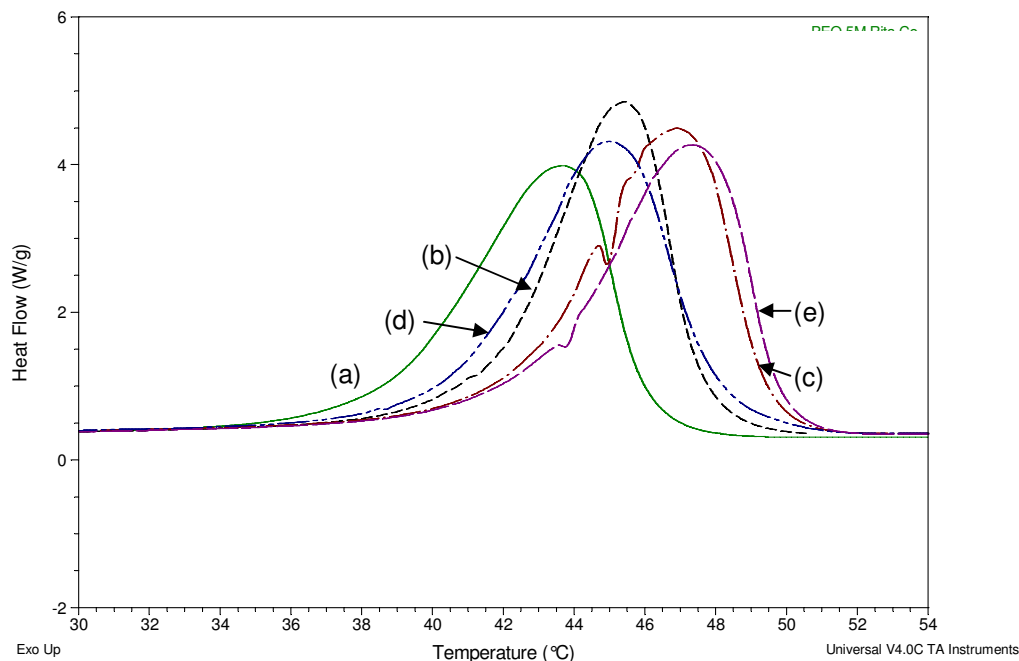


Fig. 6.11. Crystallization peak for (a) PEO polymer matrix, and PEO-based nanocomposites: PEO/CN<sub>x</sub> (b) with 0.5 wt%, and (c) with 2.0 wt%, PEO/PS-g-CN<sub>x</sub> (d) with 0.5 wt% and (e) with 2.0 wt%.

In addition, the PEO/MWNT nanocomposites (Fig. 6.12) present a similar behavior to that of the other PEO-nanocomposites, i.e. an increment in T<sub>c</sub> and in crystallinity. MWNTs act as a nucleating agent. In fact, a high efficiency in nucleation of semicrystalline polymers was already observed with MWNTs, more than with CN<sub>x</sub> nanotubes and PS-g-CN<sub>x</sub> nanotube fillers. However, the dependence with the filler concentration in the case of PEO/MWNT nanocomposite is less clear. Actually, a higher crystallinity % is obtained with 0.5 wt% of MWNTs.

Similar results in the T<sub>c</sub> values for semicrystalline polymer-based nanocomposites were reported for poly(ethylene) [42], poly(propylene) [16, 43] and poly(ethylene oxide)-salt systems. For example in the case of PE nanocomposite, the temperature of crystallization was increased by about 8°C for the nanocomposite containing 10 wt% of MWNTs. It was also observed that the relative shift of the T<sub>c</sub> occurred even at low nanocomposite content with a continuous increase with nanotube concentration in the composite. Opposite results were obtained when adding up to 7

wt% of acid-treated MWNTs to functionalized-PEO. In this system a slightly decrease (1°C) in the  $T_c$  of the PEO nanocomposite was reported. [16]. Thus, the incorporation of acid-treated MWNTs was claimed to have no significant effect on the crystallization behavior of functionalized PEO matrix.

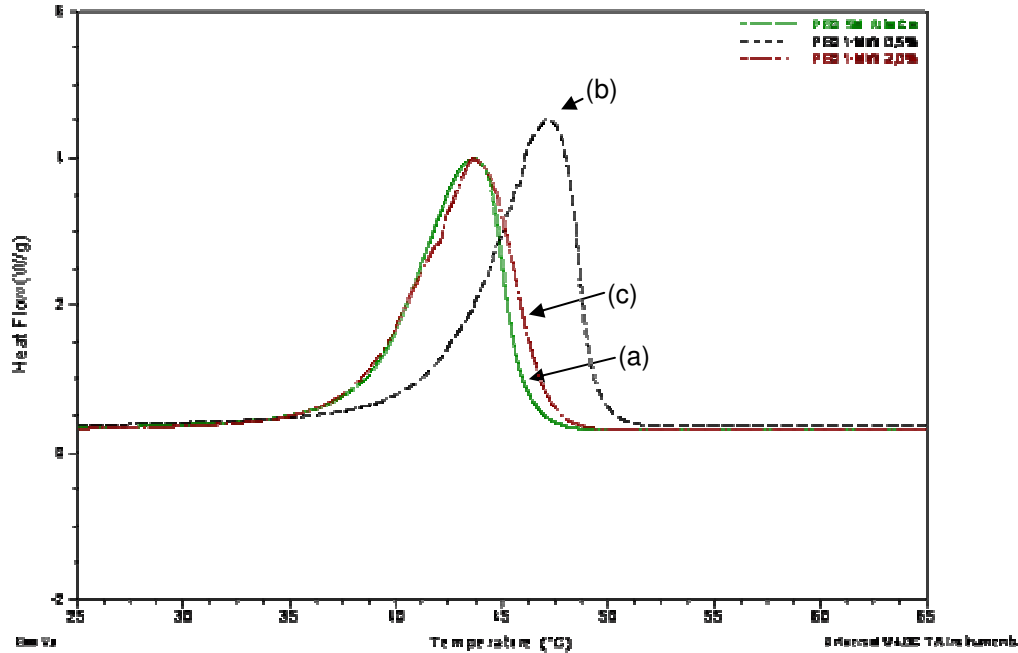


Fig. 6.12. Crystallization temperature of (a) PEO polymer matrix, and PEO/MWNT nanocomposites at several filler content: (b) 0.5 wt% and (c) 2.0 wt%.

The modification of the  $T_c$  is an indicative that in all these cases MWNTs or even carbon fibers behave as nucleating agents [17]. In general in the cited cases, the effect of nucleation seems to be not linearly dependent on the nanotube content.

As can be seen, most of the reported results are similar to those obtained in this thesis. Thus, it can be summarized that the behavior of the  $T_c$  in the PEO-based nanocomposites could suggest that carbon nanotubes can act as nucleating agents, influencing the crystallization process. Furthermore, the increase in  $T_c$  is associated with an increased number of nuclei for crystallization. Additionally, the amount of crystallinity and even the crystalline morphology of the polymer in polymer composites can be influenced by the fillers. When the crystallinity takes inverse values respect to the filler concentration (i.e., PEO/MWNT), it may be stated that while the concentration of fillers increases, the tubes start to act as restricting sites for the crystalline growth. Finally, the study of thermal properties is highly important because the alteration of the matrix crystalline structure may limit the influence of the reinforcing properties of nanofillers, affecting the mechanical behavior of the nanocomposite. In the case of crystalline or semicrystalline polymers, crystallization can be influenced by the fillers and additives to reduce its effectiveness as a composite matrix.

### 6.2.2.3. PEO-nanotube composites morphology

A homogeneous appearance of the fracture surface is observed for PEO nanocomposites based on MWNTs (PEO/MWNT) at low magnifications. At higher magnifications, the presence of “fibers” related to the polymer, or even more to the specimen preparation (fracture mode), are observed (Fig. 6.13 (a)), as in the case of the polystyrene matrix. In order to evaluate the dispersion of nanotubes, SEM images of the same zone have been taken at slow scan (Fig. 6.13 (b)). Using these images, two different zones could be distinguished: (a) one with high nanotube concentration, and (b) another one with low nanotube concentrations, indicating dispersion inhomogeneities. In zones with high nanotube concentrations (Fig. 6.13 (c)), the appearance of some fibers and nanotubes coming out from the polymer surface is observed. The nature of the interactions between MWNTs and PEO is revealed in Fig. 6.13 (d). Here, the MWNTs remain in the PEO polymer matrix, indicating a good interfacial contact; nevertheless the interfacial strength was probably not strong enough to promote the cut of the nanotubes, only their pull-out from the other part of the fractured sample.

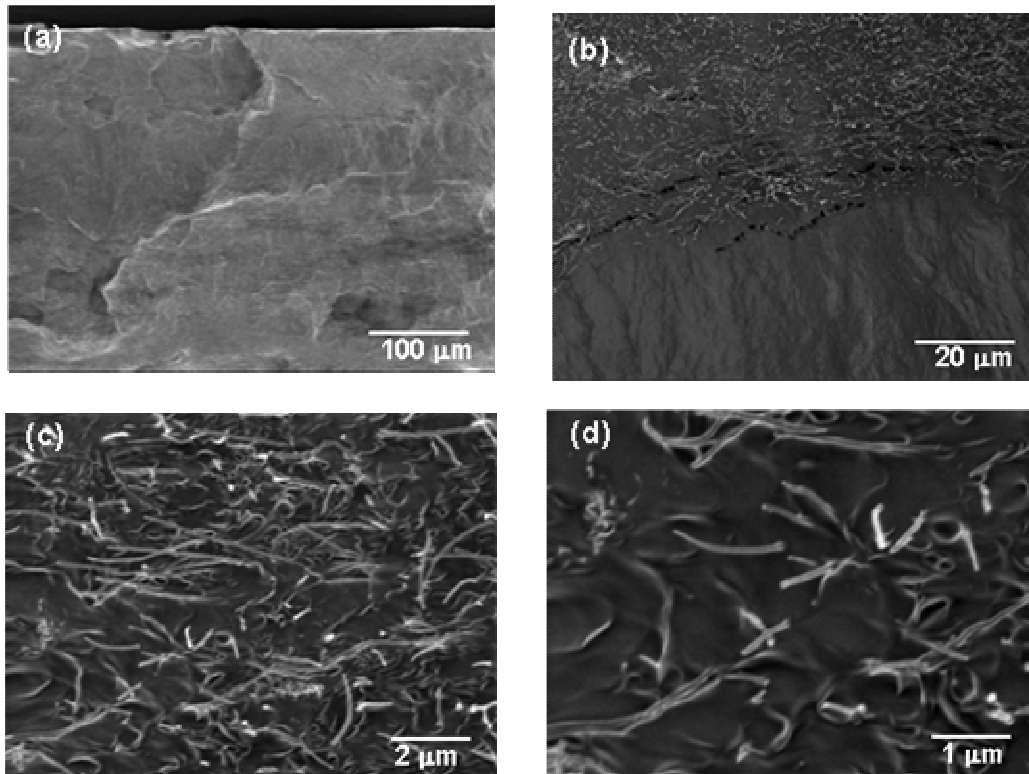


Fig. 6.13. SEM images of polymer nanocomposites of PEO and 2 wt% of MWNTs nanotubes prepared by solution casting and film pressing. Images (a) and (c) taken at normal scan and (b) and (d) at slow scan.

Therefore, it can be stated that the PEO/MWNT nanocomposite morphological studies reveal good contact properties although some dispersion inhomogeneities also appear.

SEM images at low magnification of the fractured films of PEO/CN<sub>x</sub> nanocomposites reveal a homogeneous appearance (not shown here). Nevertheless, at higher magnification an inhomogeneous dispersion is noticed (Fig. 6.14 (a)). In some cases, the presence of nanotube bundles is located (Fig. 6.14 (b)). Disentanglement of CN<sub>x</sub> nanotubes in the nanocomposite seem to be less efficient than for MWNT nanocomposites. This behavior could be related to the polarity differences between PEO and CN<sub>x</sub> that makes them more incompatible. Again in this case, the presence of some fibers in the images was observed. These kinds of fibers disappear when slow scan is used. The interaction of individual CN<sub>x</sub> nanotubes with the polymer matrix through SEM images seems to be as good as with MWNTs (Fig. 6.14 (c) and (d)).

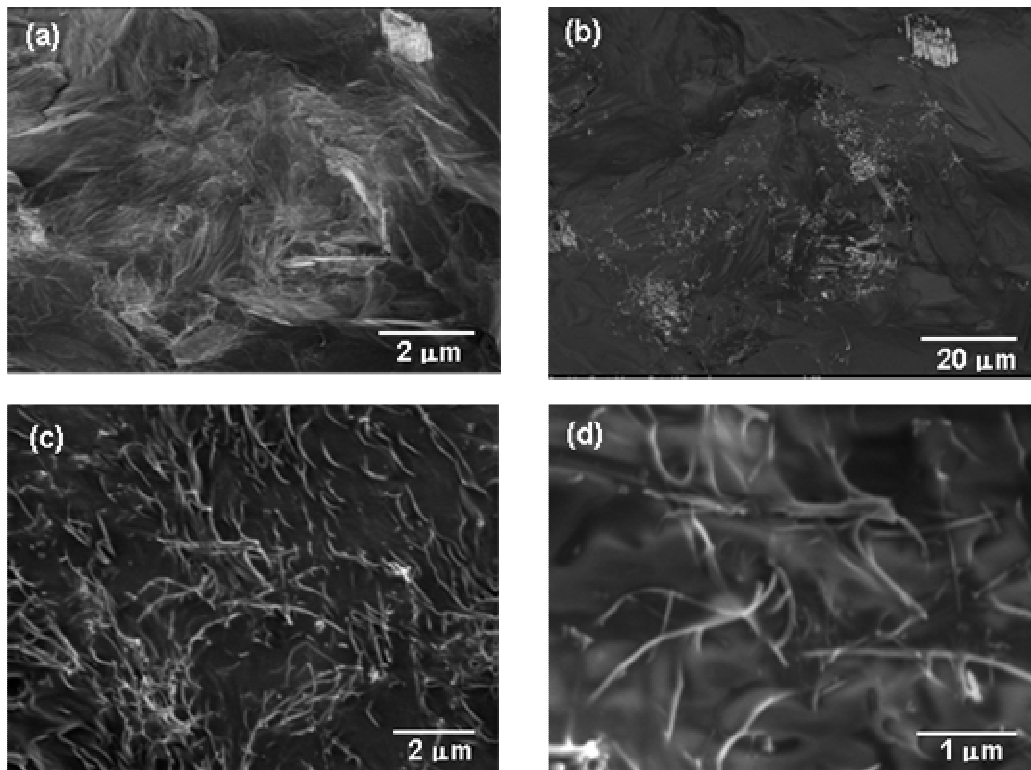


Fig. 6.14. SEM images of polymer nanocomposites of PEO and 2 wt% of CN<sub>x</sub> nanotubes prepared by solution casting and film pressing. Images (a) and (c) taken at normal scan and (b) and (d) at slow scan.

Additional images of TEM presented in the Fig. 6.15 clearly show two well differentiated zones, according to the nanotubes concentration (Fig. 6.15 (a)). It seems that the CN<sub>x</sub> nanotubes have some problems to interact with the matrix of PEO, on the contrary to the observations by SEM. The explanation could be related to Fig. 6.15 (b) where a stable dispersion of individual nanotubes is observed, indicating that the nanotubes prefer to stay together, but when CN<sub>x</sub> nanotubes are individually observed in the matrix, a very good interaction could be formed. Low magnification images reveal that most of the CN<sub>x</sub> nanotubes are arranged in bundles in the material. That means that the polymer can not efficiently wet the nanotubes in order to separate them. (Fig. 6.15 (c)).

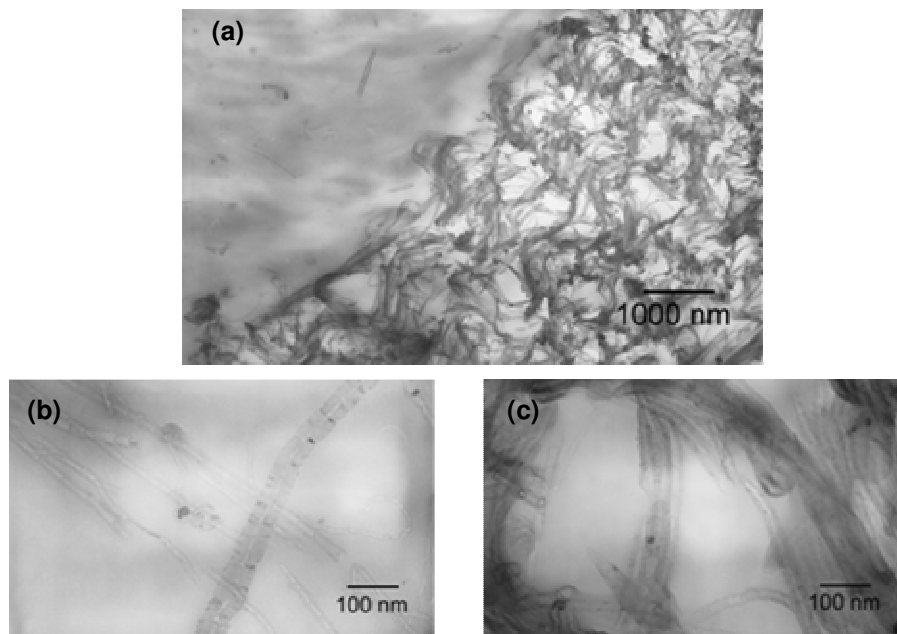


Fig. 6.15. TEM images of polymer nanocomposites of PEO and 2 wt% of CN<sub>x</sub> nanotubes prepared by solution casting and film pressing.

In PEO/CN<sub>x</sub> nanocomposites, the CN<sub>x</sub> nanotubes seem to have poor interactions with the PEO polymer. This fact causes dispersion problems. In addition, the presence of nanotube bundles of CN<sub>x</sub> nanotubes reveals clear differences in compatibility between PEO/CN<sub>x</sub> and PEO/MWNT, due to chemical characteristic and reactivity of fillers. In addition, dispersion inhomogeneities could be attributed to the effect of the organic solvent with both nanotube types.

Let us now consider the case of polymer nanocomposites of PEO and PS-grafted CN<sub>x</sub> nanotubes. SEM observations reveal clear differences in dispersion at the fracture surface (Fig. 6.16 (a)). Two distinct morphological zones exist with higher and lower quantity of grafted-CN<sub>x</sub>, along with, once again, the apparition of “fibers” due to the polymer fracture or technical difficulties (Fig. 6.16 (b)). Slow scan images reveal the exact location of nanotube tips. In zones with higher nanotube concentrations (Fig. 6.16 (c)) it seems that some polymer surrounds the nanotubes. A detail of the nanotubes embedded by polymer is shown in Fig. 6.16 (d). Nevertheless, it seems that the polymer in this image correspond to PS from the nanotube grafting. In any case, a poor dispersion is observed but also some adhesion and contact problems are expected.

TEM images of microtomed films present low concentration of nanotubes attributed to the fracture zone where individual nanotubes were found (not shown here). Even though a good interaction between matrix and nanotubes is observed, it is not a generalized behavior. Unfortunately, no TEM images have been taken from the other zone, but we expected similar images as in the PEO/CN<sub>x</sub> nanocomposites.

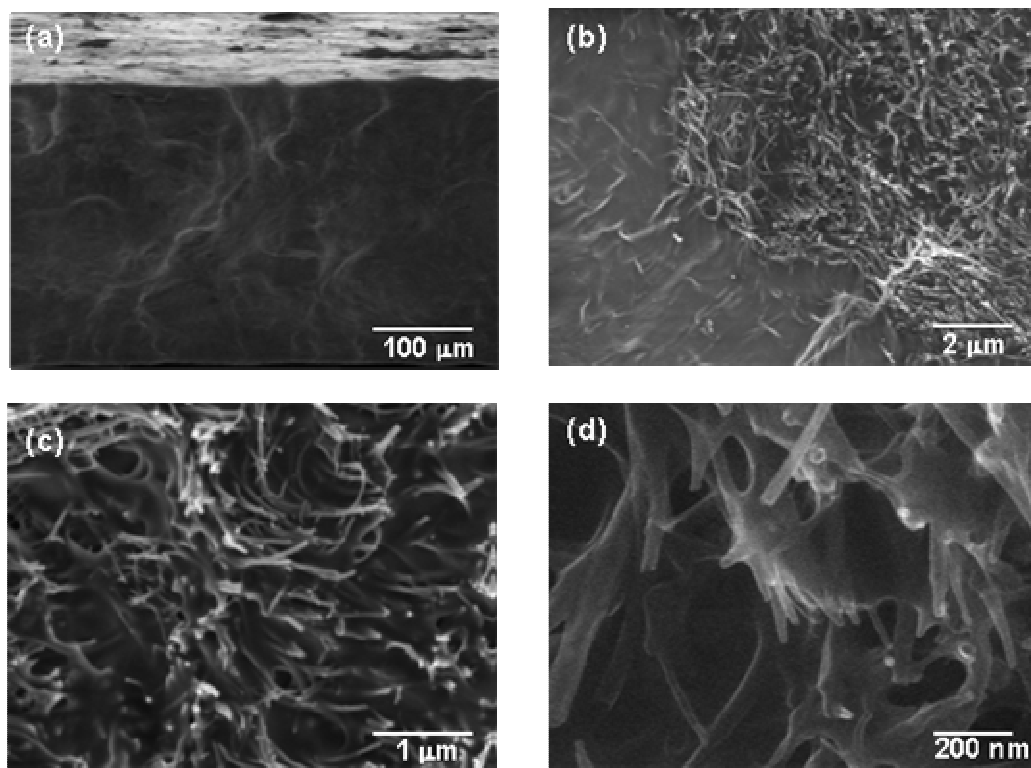


Fig. 6.16. SEM images of polymer nanocomposites of PEO and 2 wt% of PS-*g*-CN<sub>x</sub> nanotubes prepared by solution casting and film pressing.

#### 6.2.2.4. Dispersion, adhesion and thermal behavior of PEO-nanotube composites

From the comparison of PEO-based nanocomposites with several kinds of nanotubes some characteristics can be summarized as in Table 6.3.

Table 6.3. Characteristics of PEO-based nanocomposites at several observational scales.

Level	Characteristics	Scale
Macro	Film inhomogeneous appearance before and after pressing In general, phase separation and group the particles were observed	Visible
Micro	Inhomogeneous aspect of the transversal section Two zones of filler content, where: Group of nanotubes (bundles): PEO/MW < PEO/CN <sub>x</sub> Polymer-nanotubes agglomerates: PEO/PS- <i>g</i> -CN <sub>x</sub>	SEM
Nano	Inhomogeneous nanotubes distribution: In low filler content, apparently good contact with PEO matrix and low tortuosity In high filler content, poor contact with PEO matrix and high tortuosity	TEM

The results reported here reveal that the chemical reactivity or even more the polarity of nanotubes could determine the differences among PEO-based nanocomposites with the different studied fillers. Due to these filler differences, PEO/MWNT present the best dispersion, because of the better contact properties

between matrix and filler. Thus, it is expected that a relatively good interface strength could be obtained.

PS-grafted CN<sub>x</sub> nanotubes present the worse dispersion and interfacial contact in PEO matrices of other nanotube fillers. This fact is entirely attributed to the immiscibility of the grafted polymer (PS) with the PEO matrix. A limited solubility of PEO in toluene could also explain this behavior and favor the phase separation. It is also expected that properties derived from the interfacial contact, as the electrical and mechanical properties, will be worse in that case. Nevertheless, in the goal of preparation of a PS-PEO copolymer, a selective location and arrangement in bundles of grafted-CN<sub>x</sub> nanotubes in PS phase could be obtained. This kind of material could be specifically used in some applications.

About the thermal properties, it is possible to say that:

The absence of changes in the T<sub>g</sub> of almost all the PEO-based nanocomposites is attributed to weak interactions between polymer and fillers; but also, to the non homogeneity of the measured samples measured due to the inherent morphology of the material.

The melting temperature decreases with the filler content in the PEO-based nanocomposites. This behavior is associated to the filler content, but also with the type of filler. Furthermore, the type of filler influences the degree of individual nanotube dispersion in the polymer matrix and the presence of agglomerates that could be responsible for a better or worse thermal conductivity in the nanocomposite. In this case, the use of carbon nanotubes, known as good thermal conductors, favors the possibility of enhancing the heat conduction, but depending on the nanotubes dispersion.

Crystallization temperature of PEO-based nanocomposites decreases in relation with the filler type and the filler content. Considering the crystallinity percentage, it is possible to state that the nucleating effect of the carbon nanotubes follows: MWNT > CN<sub>x</sub> > PS-g-CN<sub>x</sub>.

### 6.2.3. PS-PEO blend nanotube composites

#### 6.2.3.1. PS-PEO nanotube composites processing

Nanocomposites based on PS-PEO blend (35:65 wt%) have been prepared by mixing a toluene solution of homopolymers with several kinds of nanotube fillers (MWNT, CN<sub>x</sub> and PS-g-CN<sub>x</sub>). Materials with different concentrations (i.e. 0.1, 0.3, 0.5, 0.7, 1.0, 2.0 and 5.0 wt%) were obtained. Films were prepared by solution casting and, after solvent evaporation, by pressing at high temperatures. The main processing conditions are depicted in Fig. 6.1.

Before pressing, the cast material had an appearance of white-black combined powder and suffered a phase separation. After pressing, in all cases the films exhibit a continuous combination of white and black bands associated to each one of the components: PEO and PS with nanotubes in some of the polymer phases. In fact, in some materials little black points can be distinguished in one of the polymer phases. The obtained films seem to be less granulated and less fragile than the PEO-based nanocomposites. Furthermore, the homogeneity of the sample appears difficult to establish. No macroscopic differences can be correlated with the filler type and concentration. Thus, the obtained materials have been further characterized in relation

with their morphology using electron microscopy techniques and with respect to the thermal properties using DSC.

### 6.2.3.2. PS-PEO nanotube composites thermal properties

The PS-PEO based nanocomposites with CNTs have been analyzed using DSC. The thermal properties of the materials, T<sub>g</sub>, T<sub>c</sub> and T<sub>m</sub> have been measured and reported in Table 6.4. As in the case of PEO nanocomposites, the materials are strongly inhomogeneous; that may induce some difficulties for the analysis of the thermal properties. Even more, the measurements consider only one sample after a drying process. Considering these facts the analysis of the results is presented below.

Table 6.4. Thermal properties of the PS-PEO blend nanocomposites with MWNT, CN<sub>x</sub> and PS-*g*-CN<sub>x</sub> carbon nanotubes<sup>†</sup>.

Nanocomposite	w%	wt% funct*	T <sub>g</sub> , °C		T <sub>m</sub> , °C	T <sub>c</sub> , °C	ΔH <sub>c</sub> , J/g	Crystallinity, %
			PEO	PS				
PS	0			102.9				
PEO	0		-54.3		69.9	43.6	131.7	0.62
PS-PEO	0		-52.0	103.4	63.3	46.1	89.6	0.42
	0		-52.0	103.4	63.3	46.1	89.6	0.42
PS-PEO/MWNT	0.5		-53.5	105.1	63.7	46.8	100.6	0.47
	2.0		-54.1	104.4	64.0	47.3	98.1	0.46
	0		-52.0	103.4	63.3	46.1	89.6	0.42
PS-PEO/CN <sub>x</sub>	0.5		-52.8	104.3	66.2	47.2	98.2	0.46
	2.0		-51.1	103.3	65.0	46.6	82.7	0.39
	0		-52.0	103.4	63.3	46.1	89.6	0.42
PS-PEO/PS- <i>g</i> -CN <sub>x</sub>	0.5	0.2	-52.7	105.2	62.7	46.7	90.0	0.42
	2.0	0.7	-53.4	105.3	65.2	51.8	99.2	0.46

\* Filler weight % addition of functionalized carbon nanotubes according to the PS-grafting efficiency values.

<sup>†</sup> Estimated temperature precision: ±0.1°C.

T<sub>g</sub> is often used as a parameter to determine thermodynamic component miscibility in polymer blends and to study the effects related to filler-polymer adhesion properties in the case of composites. In both cases, T<sub>g</sub> can shift towards higher or lower temperatures. In general the decrease of the glass transition temperature in polymer composites is interpreted as an improvement of adhesion at the filler-polymer interface in accordance with the general theory of polymer composites. [44]

From the analysis of the DSC signal, it is observed that the materials present two glass transitions, associated respectively to the PEO and the PS phases, a melting phenomenon, and a crystallization one. The analysis of each phenomenon will be explained in the next paragraphs.

#### *Glass transition temperature, T<sub>g</sub>*

The T<sub>g</sub> value, attributed to the PEO phase in the PS-PEO blend, presents a slightly higher value compared to the T<sub>g</sub> of the pristine PEO polymer. This increment could be related to the addition of a PS phase to the PEO phase, but also to the addition of carbon nanotubes.

The shifts in T<sub>g</sub> of the homopolymers in a given blend, that tend to form only one signal, is a measure of the miscibility of the materials. In our case, the little change in T<sub>g</sub> can be associated to a slight miscibility. Furthermore, the shape of the signal in the polymer blend is generally narrower and weaker than in the case of the homopolymer. This kind of change is related to the modification in the heat capacity, but also could be related with a low adhesion between polymer materials.

From Table 6.4, it can be seen that the T<sub>g</sub> associated to PEO in PS-PEO/MWNT nanocomposites is around -53°C. In that case, a slight decrease in the T<sub>g</sub> associated to the PEO phase with the MWNTs content is observed. This behavior is consistent with the possible improvement of the interfacial MWNT-PEO interaction. Almost no changes are observed in the PEO T<sub>g</sub> value on PS-PEO/CN<sub>x</sub> and PS-PEO/PS-*g*-CN<sub>x</sub> composites. C. del Rio, *et al* [44] reported comparable results when carbon black was added in immiscible polymer blends.

In all nanocomposite materials, the signal of the T<sub>g</sub> associated to the PEO matrix in the polymer blend (PS-PEO) nanocomposite seems to be more extended and with a less pronounced slope than for the corresponding PEO-based nanocomposite. This fact could interestingly be associated to the diminution of the heat capacity (C<sub>p</sub>) and the effect of the nanotubes on the polymer miscibility. Thus, maybe the filler, independently to its type, promotes a better mixing of polymers. That kind of compatibilization effect was reported for CB added to incompatible crystalline polymer blends. [45]

The PS-PEO blend present a T<sub>g</sub> value associated to the PS polymer phase around 103°C. This value is of the same order of magnitude than the one measured for the PS homopolymer. This low difference of T<sub>g</sub> can be attributed to the high molecular weight of the PS phase and to the high thickness of the polystyrene phase in PS-PEO material, as was confirmed by the morphology studies (described in the following section). However, the size, extension and slope of the signal presented a diminution (as in the case of the T<sub>g</sub> associated to the PEO phase), that can be associated to a diminution in the heat capacity. [46]

In the case of PS-PEO/MWNT nanocomposites, from the comparison of the PS-PEO blends with and without nanotubes, we note that the presence of the MWNTs makes the T<sub>g</sub> signal weaker. This behavior is also observed in PS-PEO/CN<sub>x</sub>. Behind the variations in the curve shape, the slight shifts of T<sub>g</sub> values from the PS phase could be associated to a restriction in the chain mobility of this phase due to filler. Furthermore, in both PS-PEO/MWNT and PS-PEO/CN<sub>x</sub> nanocomposites, as T<sub>g</sub> tends to disappear, an increase in the miscibility of the polymer blends might be evoked.

Conversely, for PS-PEO/PS-*g*-CN<sub>x</sub> nanocomposites, the T<sub>g</sub> evolution is close to that observed for the PS-PEO pure blend,. This point could be attributed to the presence of PS-grafted onto the nanotubes that increases the immiscibility as in the case of the PS-PEO pure blend.

#### *Melting temperature, T<sub>m</sub>*

The melting temperature of the PS-PEO blend is lower than the one corresponding to the PEO matrix. Furthermore, from the analysis of the T<sub>m</sub> values of the PS-PEO/MWNT, PS-PEO/CN<sub>x</sub> and PS-PEO/PS-*g*-CN<sub>x</sub> nanocomposites (not shown here), it appears that no significant changes in T<sub>m</sub> are observed compared to the pristine PS-PEO blend, even though good thermal conducting fillers (CNTs) are added. This

behavior is related to and proves the immiscibility of the polymer phases, as well as their inhomogeneous morphology.

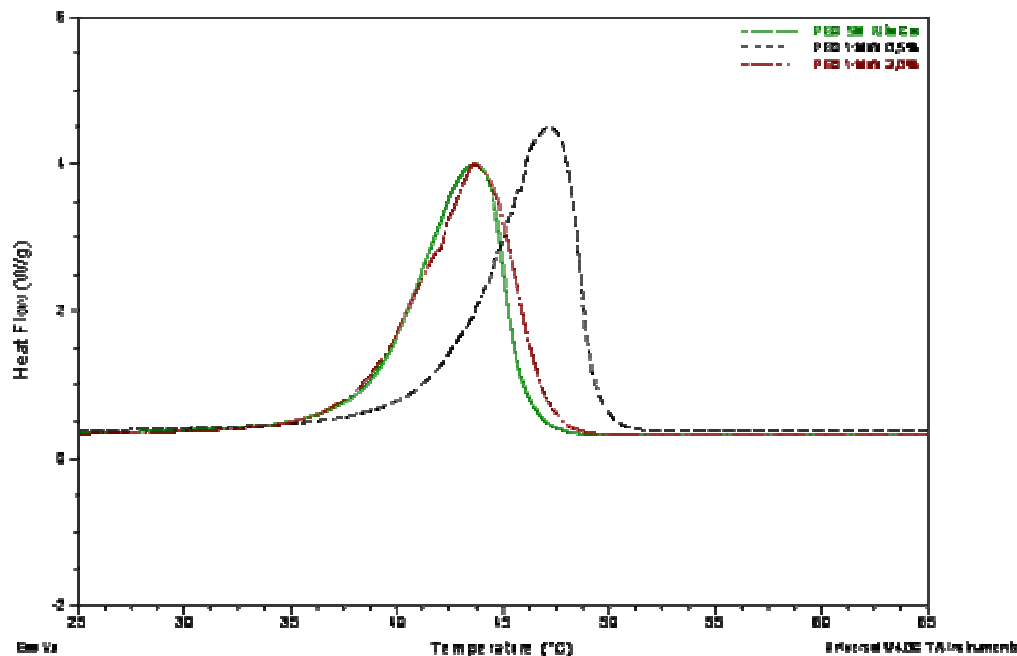


Fig. 6.17. Melting temperature of (a) pure PS-PEO polymer blend, and PS-PEO/MWNT nanocomposites at several filler content: (b) 0.5 wt% and (c) 2.0 wt%.

#### *Crystallization temperature, $T_c$*

A slight increase of the PEO crystallization temperature ( $T_c$ ) is observed compared to the PEO homopolymer, when PS-PEO blends are prepared. Thus, the presence of PS restricts the PEO crystallization.

Furthermore, little changes in the crystallization temperature of the PEO phase in PS-PEO/MWNT, and PS-PEO/CN<sub>x</sub> polymer blend nanocomposites is observed. This fact could be related to a bad dispersion of CNTs limiting their role as nucleating agents. However, a higher change in the  $T_c$  is observed in the case of PS-g-CN<sub>x</sub> nanotubes in addition with a clear dependence versus the nanotube content.

Chen *et al* [47] studied the properties of a polymer blend with C<sub>60</sub> and MWNTs. They observed the appearance of a new second-order transition characteristic of isolated C<sub>60</sub> dispersed in the polymer matrix. In this research, additional signals were not found.

Lastly, it can be noticed that the crystallization percentage has been modified (as reported in Table 6.4). This modification could be related to the presence of PS and nanotubes in the nanocomposite. The bad dispersion of both materials within the PEO could be related to a decrement in the formation of crystallites, particularly if nanotubes (known as crystallization agents) are present.

#### **6.2.3.3. PS-PEO nanotube composites morphology**

The morphological properties of the PS-PEO matrix without CNTs have been analyzed using SEM, and results at several magnifications are given in Fig. 6.18. The

high incompatibility between the PS and PEO phases is observed even at low magnification as revealed by the presence of stratus and holes in the material, as well as fractures in the structure (Fig. 6.18(a)). A kind of fractal morphology is observed (Fig. 6.18 (b) to (d)) with the presence of circumferences or ovals from one polymer containing circumferences from the other polymer. From the characteristics induced in the surface by the sample fracture, the identification of the different phases can be proposed as follows: PS appears as the “fibrous” type surface, whereas PEO presents clearer cut (both according to previous experiments). Thus, it seems that the continuous phase corresponds to PEO and the discrete phase to PS, that in fact is in agreement with the weight composition. Moreover, Fig. 6.18 (c) shows the polymer interface separation or rupture due to the immiscibility of PEO and PS. In addition to miscibility, the preparation method that involves the use of a room temperature solvent for PS but not for PEO, and the mechanical shaking conditions probably also helps to induce PS-PEO phase separation during evaporation. Clearly, an efficient preparation, may be involving copolymers, is necessary to produce specific and controlled morphologies. Thus, this study could be considered an precursor to further material developments.

Therefore after these observations, it is expected that the use of PS-PEO blends to produce nanotube nanocomposites looks like an important challenge.

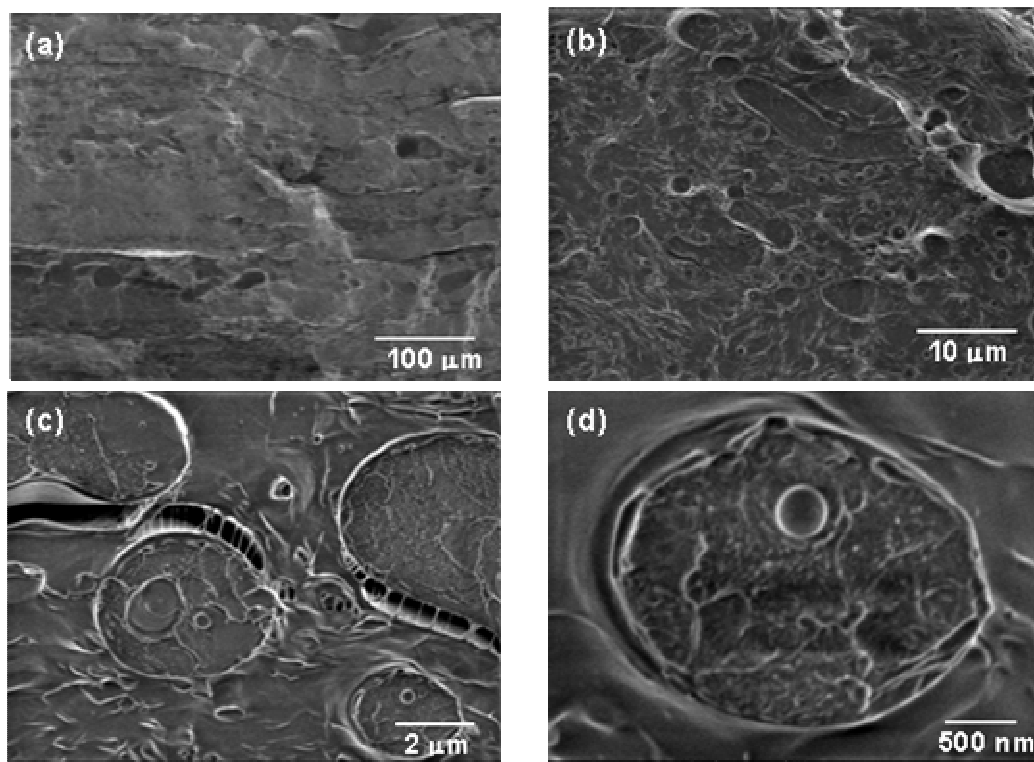


Fig. 6.18. SEM images of PS and PEO polymer blends at 35:65 wt% relation.

Nevertheless, the introduction of MWNT fillers in the PS-PEO blend (PS-PEO/MWNT) induces important morphological changes. First modifications are observed at the surface after sample fracture. In this case low magnification reveals an apparently homogeneous material, composed by granules (Fig. 6.19(a)). At higher magnification, the separation in zones with high and low nanotube concentration is

observed, but surprisingly no polymer separation of PS and PEO is detected. Conglomerates of nanotubes appear at slow scan (Fig. 6.19 (b) and (c)). Thus, from these results it could be possible to say that the dispersion and interaction of nanotubes with polymers are more complicated than in homopolymer nanocomposites. From the previous results, higher interactions are expected in PEO/MWNT than in PS/MWNT. Nevertheless, at the moment no clear conclusions about the location of nanotubes could be done, especially because the TEM images are missing. Anyway, it seems that nanotube dispersion is more difficult in PS-PEO/MWNT than in the PS and PEO-based nanocomposites, due to polymer immiscibility, added to difficulties in nanocomposite preparation (diffusion). It is not surprising that the optimization of the polymer blend preparation is fundamental.

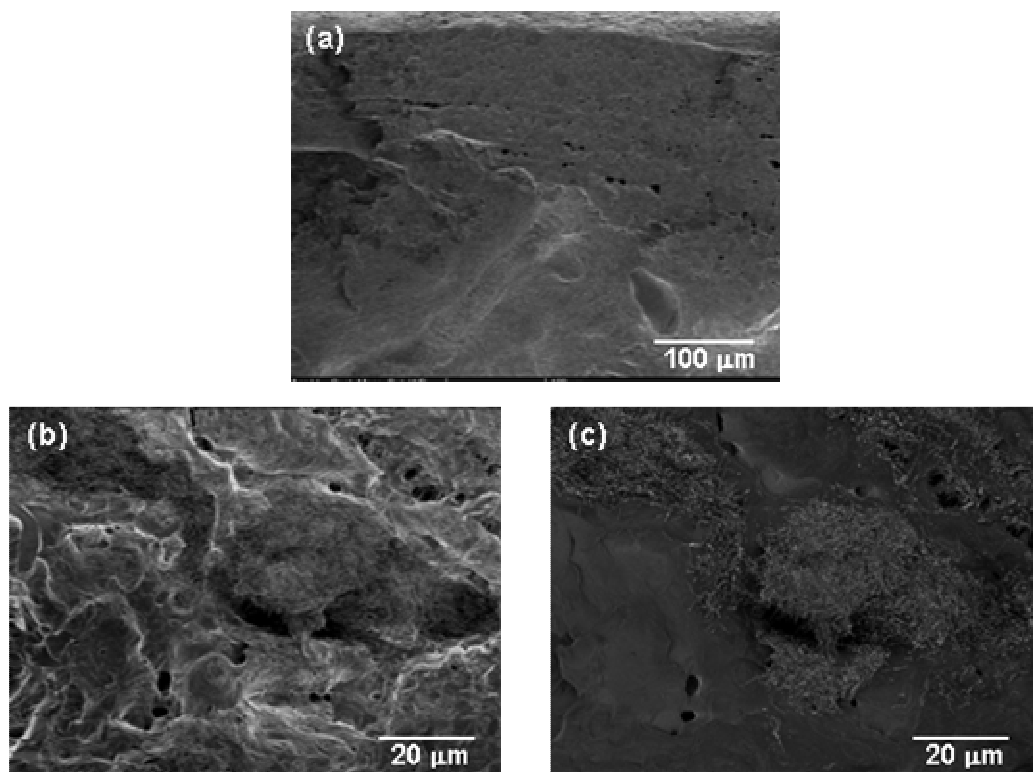


Fig. 6.19. SEM images of polymer nanocomposites of PS and PEO polymer blends (35:65 wt%) and 2 wt% MW nanotubes.

Images (a) and (b) were taken at normal scan, whereas image (c) is at slow scan.

In the case of  $CN_x$  nanotubes, SEM images of fractured surface (Fig. 6.20) reveal even stronger dispersion problems than that observed with the case of MWNTs. That time, a huge zone of the film is occupied by nanotubes agglomerates. Zoomed images show different nanotube arrangements, i.e. entangled nanotube bundles and enrolled disentangled nanotubes (Fig. 6.20 (b) and 6.20 (c), respectively).

It can be added that the nanotubes seem to contribute to the stabilization of the polymer blend morphology, even though an isotropic material is obtained due to nanotube phase separation. Actually, the polymer blend zone in this nanocomposite

does not reveal the clearly differentiated morphology of the PS-PEO observed in the absence of CN<sub>x</sub> nanotubes.

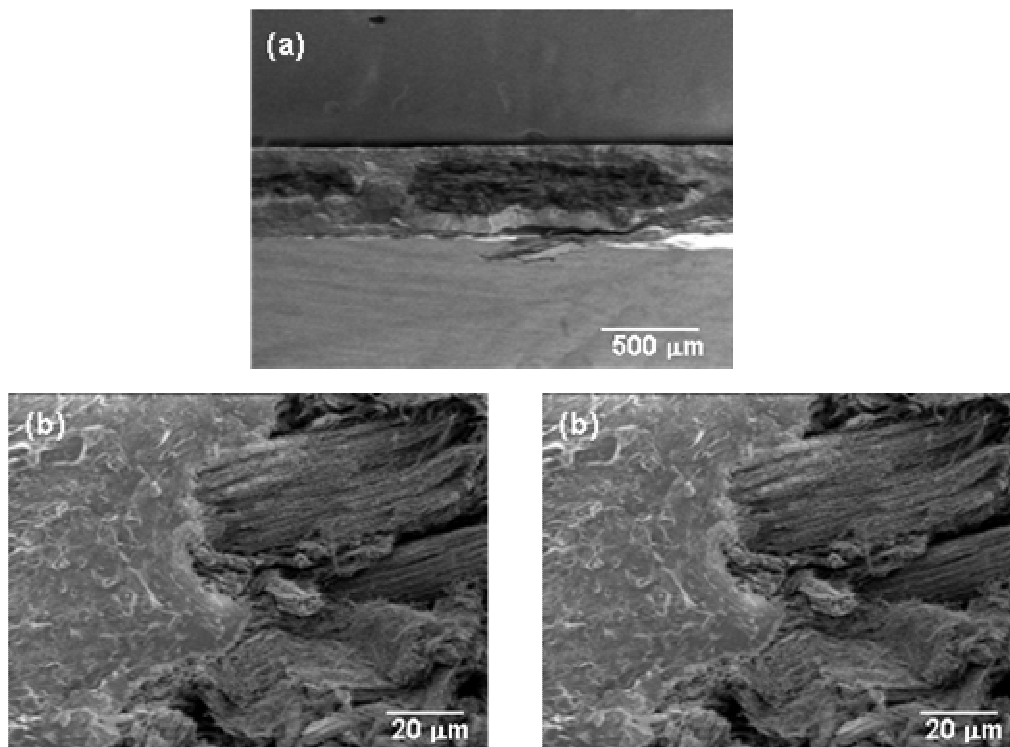


Fig. 6.20. SEM images of polymer nanocomposites of PS and PEO polymer blends (35:65 wt%) and 2 wt% CN<sub>x</sub> nanotubes.

In the case of CN<sub>x</sub> nanotubes, complementary information can be drawn from TEM images. It is important to say that the sample preparation involves the capture of microtomed films with an aqueous solution of sucrose, followed by a rinsing with distilled water. However, PEO is known to be a water soluble polymer. Thus we notice that PEO phase is dissolved from the ultramicrotomed thin film, before the TEM observation, as illustrated on Fig. 6.21 where a film with an enriched CN<sub>x</sub> nanotubes PS phase coexists with holes due to PEO phase absence. As can be seen, the nanotubes seem to follow the PS phase morphology whereas the holes seem to occupy little zones in proportion that is compatible with the blend composition (PS:PEO 35:65 wt%). Actually, we can assume that the film was cut in a PS rich zone. This observation confirms that the CN<sub>x</sub> nanotubes better interact with PS, as concluded from the PS-based nanocomposites study.

In summary, it appears that strongly inhomogeneous PS-PEO/CN<sub>x</sub> nanocomposites have been prepared due to nanotube dispersion difficulties. Polymer phase separation, as well as preferential location of nanotubes at PS phase is clearly demonstrated.

The last case concerns the PS-PEO/PS-g-CN<sub>x</sub> nanocomposite where an apparently homogeneous fractured surface is displayed (Fig. 6.22 (a)). At higher magnifications, a clear phase separation is observed with high concentration of grafted-CN<sub>x</sub> nanotube is located separately from polymer phase. These nanotubes seem to be

mostly disentangled and rolled, and surrounded by polymer (Fig. 6.22 (b) and (c)), presumably PS.

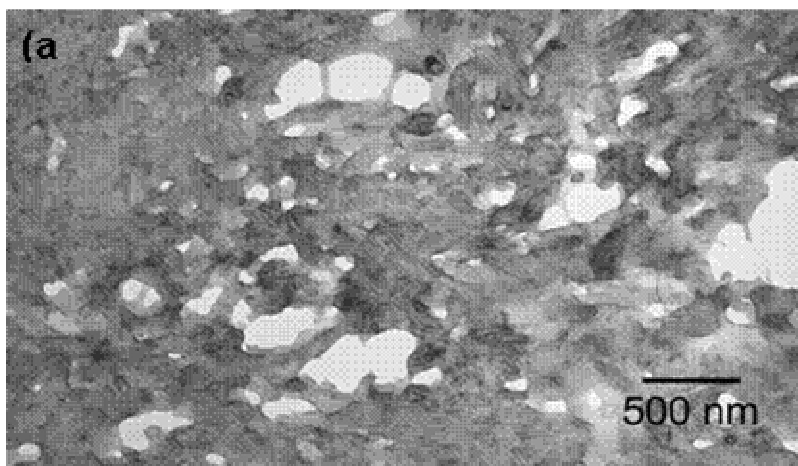


Fig. 6.21. TEM images of polymer nanocomposites of PS and PEO blends (35:65 wt%) and 2 wt% of  $CN_x$  nanotubes.

A complicated morphology is once again composed by (i) an enriched nanotube zone, (ii) a polymer blend with a slightly similar morphology of the raw PS-PEO, and (iii) an inter-phase fracture structure with some good interaction. As illustrated in Fig. 6.22 (d), this last zone clearly shows that the polymer-grafted or the polymer surrounding the  $CN_x$  nanotubes presents polymer fibers formation. This fact was not observed in previous nanocomposites and results from a good interaction of this polymer with one polymer blend phase. It is highly supported that PS could be this polymer.

In TEM images of PS-PEO filled with grafted nanotubes, the different zones namely (i), (ii) and (iii) are obvious. Fig. 6.23 (a) and (b) show the differences between the polymer blend enriched zone where the PEO has disappeared because of the sample preparation, and the nanotube enriched zone, respectively. The Fig. 6.23 (c) (zoom 6.23 (a) image) represents the low concentration of CNTs in the PS phase. The nanotubes that remain in this phase after processing and TEM observation preparation seem to have a good interaction with the polymer.

Fig. 6.23 (d) presents an image of the nanotube-polymer inter-phase-zone (iii). As can be seen, an evolving polymer is observed surrounding the nanotube, indicating a good interaction and contact between them. Thus, the PS of the nanocomposite interacted with PS-grafted  $CN_x$  nanotubes.

In this case, like in the others PS-PEO nanocomposites, strong dispersion problems were not overpassed. The immiscibility of the polymers in the blend leads to a non homogeneous separated phase morphology with the PS-grafted  $CN_x$  nanotubes preferentially located in the PS phase. Even more, different nanotube concentrations were locally observed in the material.

#### 6.2.3.4. Dispersion, adhesion and thermal behavior of PS-PEO blend nanotube composites

Semicrystalline polymer blends usually show richness in morphology due to the competition between microphase separation and crystallization. In our case, the immiscibility of the polymer blend and the polymer blend nanocomposites was evidenced by the presence of two Tg's in the material, one for each polymer phase. This immiscibility of the PS and PEO phases determines a strongly heterogeneous phase separated morphology. This polymer phase separation undoubtedly comes from a non optimized processing route. Moreover, in all cases, the PS-PEO based nanocomposites present nanotube dispersion problems. All these difficulties are associated to the nanocomposite preparation because of the immiscibility of the polymers, the solvent used [48], and the type of nanotube as filler. The optimization of the processing protocol is thus required to obtain more homogeneous materials.

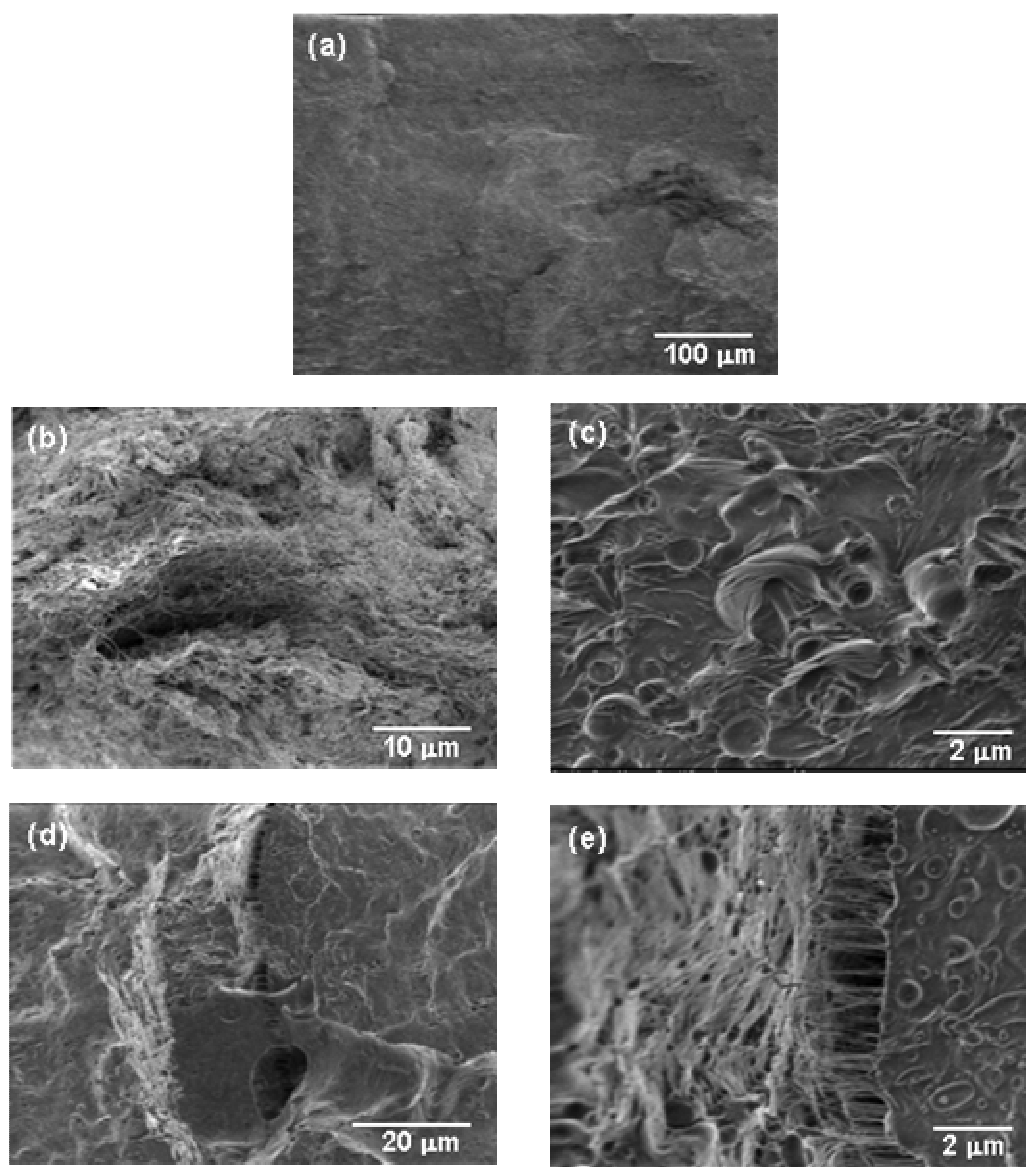


Fig. 6.22. SEM images of polymer nanocomposites of PS and PEO blends (35:65 wt%) and 2 wt% of polymer grafted nanotubes (PS-g-CN<sub>x</sub>).

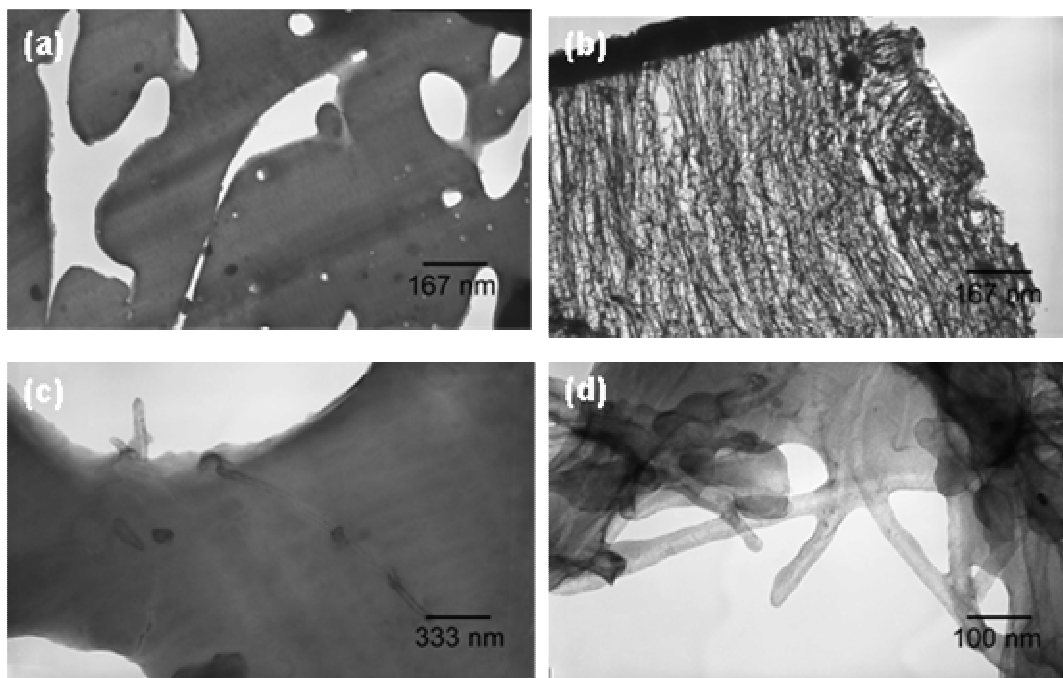


Fig. 6.23. TEM images of polymer nanocomposites of PS and PEO blends (35:65 wt%) and 2 wt% of polymer grafted nanotubes (PS-*g*-CN<sub>x</sub>) at several magnifications.

Nevertheless, some interesting results can be obtained from these preliminary investigations:

- In all the materials, the nanotubes formed agglomerates. These agglomerates, for the case of CN<sub>x</sub> and PS-grafted CN<sub>x</sub> nanotubes, are preferentially located in the PS phase, in agreement with the observations in the case of PS-based nanocomposites. Nevertheless, the best inter-phase contact was obtained when PS-*g*-CN<sub>x</sub> nanotubes are used as fillers. In that last case, nanotubes seem to be aligned and clearly embedded by a polymer phase (PS).
- The incorporation of nanotubes modifies the polymer blend morphology in the nanocomposite compared to the original polymer blend. These differences are revealed by thermal properties measurements, even if their accuracy suffers from the inhomogeneity of the samples. To be short, we observe that, in presence of nanotubes, the T<sub>g</sub> signal attributed to PEO and PS tend to disappear probably due to an slight increase in the miscibility of the samples due to CNTs fillers. The T<sub>g</sub> of the PS and PEO polymer phases in the PS-PEO blend was increased slightly, maybe due to the diminution of the chain mobility of each polymer phase due to the addition of the nanotubes and for the case of PEO by the addition of a rigid polymer phase. In most of the cases, the PS-*g*-CN<sub>x</sub> nanotube filler seems to be less efficient in the improvement of the miscibility of the polymers in the blend nanocomposite.
- Generally speaking, non significant changes of PEO crystallization have been observed in our different samples. The melting temperature T<sub>m</sub> of the pure PS-PEO blend and PS-PEO nanocomposites are comparable.

T<sub>m</sub> is mainly affected by the nanocomposite preparation and the immiscibility of the homopolymers, even though good thermal conductors were added. The crystallization temperature T<sub>c</sub> of the nanocomposites presents also slight changes only comparing to the PS-PEO polymer blend.

### 6.3. Conclusions

The preparation of PS, PEO and PS/PEO nanocomposites has been carried on following the solvent route and using several kinds of CNTs (MWNT, CN<sub>x</sub> and PS-*g*-CN<sub>x</sub>). The analysis of the materials gives interesting results about the preparation method and the inherent nanocomposite morphological properties. Among them, the homogeneity, dispersion, adhesion and tortuosity of the samples were considered and the main conclusions of our analysis are recalled below.

The homogeneity of the samples (in terms of filler dispersion) is higher for the homopolymer nanocomposites (PS-based and PEO-based) than for the polymer blend (PS-PEO based nanocomposite) independently of the kind of nanotubes. This characteristic undoubtedly influences directly the thermal properties measurements. The homogeneity of the material follows:

PS-based composites > PEO-based composites > PS-PEO-based composites

To go further, we can add that the best dispersion of fillers is obtained in the case of PS-based nanocomposites where individual nanotubes are observed. Furthermore, in the PEO-based nanocomposites the nanotubes form groups of particles which sizes are dependent on the type of filler. A completely bad dispersion and selective location of the nanotubes in the PS phase is observed for the PS-PEO based nanocomposites. Thus, considering nanotubes dispersion aspects, the following order is observed for each type of filler:

PEO/MWNT > PS/MWNT >> PS-PEO/MWNT  
 PS/CN<sub>x</sub> > PEO/CN<sub>x</sub> >> PS-PEO/CN<sub>x</sub>  
 PS/PS-*g*-CN<sub>x</sub> > PEO/PS-*g*-CN<sub>x</sub> >> PS-PEO/PS-*g*-CN<sub>x</sub>

For the last two fillers, it was observed that CN<sub>x</sub> nanotubes are dispersed easier than PS-*g*-CN<sub>x</sub> nanotubes, due to the better adhesion of grafted-CN<sub>x</sub> among themselves.

Some information about what we called adhesion of the nanotubes with the polymer matrices can be obtained indirectly from morphological observations. This parameter seems to vary according to polymer and filler types. For the case of PS in the homopolymer and polymer blend composites, a strong adhesion and good interaction is observed with PS-*g*-CN<sub>x</sub> nanotubes. An intermediate level of interaction was found for CN<sub>x</sub> with PS in both nanocomposites. At last, in the case of PEO polymer, only the MWNT<sub>x</sub> seem to have a good interaction. To sum up, the adhesion relations are as follows:

PEO/MWNT > PS/MWNT > PS-PEO/MWNT  
 PS/CN<sub>x</sub> > PS-PEO/CN<sub>x</sub> > PEO/CN<sub>x</sub>  
 PS/PS-*g*-CN<sub>x</sub> ~ PS-PEO/PS-*g*-CN<sub>x</sub> > PEO/PS-*g*-CN<sub>x</sub>

According to these adhesion properties, the  $CN_x$  and PS- $g$ - $CN_x$  nanotubes strongly prefer the PS phase in both homopolymer and polymer blend nanocomposites. For these kinds of material, interesting properties are expected.

Finally, the tortuosity of nanotubes seems to increase according to the polymer matrix and according to the local nanotube concentration, i.e. in general tortuosity varies as:

PS-based nanotubes < PEO-based nanotubes < PS-PEO-based nanotubes.

About the thermal properties of the nanocomposites, we observed that the PS-based nanocomposites exhibit unchanged values of the  $T_g$  as a function of the type of filler and filler concentration. This phenomenon could be related to either slight polymer-nanotube interactions that impede the measurement of some chain mobility changes or because of the high molecular weight of the polymer in the case of PS/MWNT and PS/ $CN_x$ . For PS/PS- $g$ - $CN_x$ , the unchanged  $T_g$  could be related to the near  $T_g$  values of the components, i.e. polymer matrix and polymer grafted on CNTs.

Weak interactions between polymer and filler could be also proposed to explain the absence of  $T_g$  change in the case of the PEO-based nanocomposites. Other explanation deals, for instance, with the inhomogeneous section of the film. On the other hand, a clear decrease of the melting temperature is observed. It is attributed to the enhancement of thermal conductivity due to the presence of CNTs, but always depending on the type and content of filler and the degree of dispersion. Finally, the CNTs behave as nucleating agents in the PEO-based nanocomposites.

Other explanations can be added as for instance. The PS-PEO based nanocomposites present miscibility problems (two observed  $T_g$  temperatures and  $T_c$  slightly changes) that are slightly diminished by the nanotubes addition. This behavior is confirmed by the absence of changes in the  $T_m$  values for all cases, even though good thermal conductors are added.

Unfortunately, the processing of PS-PEO composites suffers some preparation problems leading to inhomogeneous and bad dispersed materials. Thus, an optimization of the conditions of production *is thus required to obtain more homogeneous materials*.

The PS-grafted  $CN_x$  nanotubes display significant differences compared to  $CN_x$  nanotubes in terms of interaction with polymer matrices. These modifications can be with no doubt attributed to the grafted polymer and could be indicative of the successful synthesis of the polymer brushes. Therefore, we expect that the evaluation of the electrical and mechanical properties of the corresponding nanocomposites could be interesting. The next chapter will be devoted to their analysis and to the establishment of the structure-properties relationships.

## References

1. Mao, H., P.L. Arrechea, T.S. Bailey, B.J.S. Johnson, and M.A. Hilmyer, *Control of pore hydrophilicity in ordered nanoporous polystyrene using an AB/AC block copolymer blending strategy*. Faraday Discussion, 2004. **128**: p. 149-162.
2. Soo, P.P., B. Huang, Y.-I. Jang, Y.-M. Chiang, D.R. Sadoway, and A.M. Mayes, *Rubbery Block Copolymer Electrolytes for Solid-State Rechargeable Lithium Batteries*. Journal of the Electrochemical Society, 1999. **146**(1): p. 32-37.
3. Yuan, J., Z. Xu, S. Cheng, and L. Feng, *The aggregation of polystyrene-*b*-poly(ethylene oxide)-*b*-polystyrene triblock copolymers in aqueous solution*. European Polymer Journal, 2002. **38**: p. 1537-1546.
4. Galloway, J.A., M.D. Montminy, and C.W. Macosko, *Image analysis for interfacial area and cocontinuity detection in polymer blends*. Polymer, 2002. **43**: p. 4715-4722.
5. Moriya, S., K. Adachi, and T. Kotaka, *Effect of electric field on the morphology of a poly(ethylene oxide)-polystyrene blend*. Polymer Communications, 1985. **26**(8): p. 235-237.
6. Khan, I., D. Fish, Y. Delaviz, and J. Smid, *Makromolekulare Chemie*, 1989. **190**: p. 1069.
7. Giles, J.R.M., F.M. Gray, J.R. McCallum, and C.A. Vincent, *Polymer*, 1987. **28**: p. 1977.
8. Gray, F.M., J.R. McCallum, C.A. Vincent, and J.R.M. Giles, *Macromolecules*, 1988. **21**: p. 392.
9. Dror, Y., W. Salalha, R.L. Khalfin, Y. Cohen, A.L. Yarin, and E. Zussman, *Carbon nanotubes embedded in oriented polymer nanofibers by electrospinning*. Langmuir, 2003. **19**: p. 7012-7020.
10. Atkinson, E.B., *Fibrillated monofilaments*. 1968, GB 1104694 19680228.
11. Saibaba, G., D. Srikanth, and A. Ramachandra Reddy, *Preparation and study of conductivity in lithium salt complexes of mixed MEEP : PEO polymer electrolytes*. Bulletin of Materials Science, 2004. **27**(1): p. 51-55.
12. Gao, F., S. Chen, and J.B. Hull, *Layer expansion of layered silicates in solid polymer matrices by compression*. Journal of Materials Science Letters, 2001. **20**(19): p. 1807-1810.
13. Bronstein, L.M., R. Karlinsey, A. Ryder, C.-G. Joo, and J.W. Zwanziger, *Nanostructured solid polymer electrolytes: influence of material structure on property enhancement*. Polymeric Materials: Science & Engineering, 2001. **85**: p. 615-616.
14. Hayashi, S., A. Naitoh, S. Machida, M. Okazaki, K. Maruyama, and N. Tsubokawa, *Grafting of polymers onto a carbon black surface by the trapping of polymer radicals*. Applied Organometallic Chemistry, 1998. **12**: p. 743-748.
15. Jin, Z., X. Sun, G. Xu, S.H. Goh, and W. Ji, *Nonlinear optical properties of some polymer multi-walled carbon nanotube composites*. Chemical Physics Letters, 2000. **318**(6): p. 505-510.
16. Goh, H.W., S.H. Goh, G.Q. Xu, K.P. Pramoda, and W.D. Zhang, *Crystallization and dynamic mechanical behavior of double-C<sub>60</sub>-end-capped poly(ethylene oxide)/multi-walled carbon nanotube composites*. Chemical Physics Letters, 2003. **379**: p. 236-241.
17. Zhao, F., M. Wang, and S. Dong, *Conductive property of multiwall carbon nanotubes-PEO-salt nanocomposite film*. Electrochemical and solid-state letters, 2004. **7**(11): p. E48-E50.
18. Momma, T., H. Ito, H. Nara, H. Mukaibo, S. Passerini, and T. Osaka, *Characteristics of interpenetrate d polymer network system made of polyethylene oxide-LiBF<sub>4</sub> complex and polystyrene as the electrolyte for lithium secondary battery*. Electrochemistry, 2003. **71**(12): p. 1182-1186.
19. Christie, A.M., S.J. Lilley, E. Staunton, Y.G. Andreev, and P.G. Bruce, *Increasing the conductivity of crystalline polymer electrolytes*. Nature, 2005. **433**: p. 50-53.

20. Wu, M. and L. Shaw, *Electrical and Mechanical Behaviors of Carbon Nanotube-Filled Polymer Blends*. Journal of Applied Polymer Science, 2005. **99**: p. 477-488.
21. Chatterjee, T., K. Yurekli, V.G. Hadjiev, and R. Krishnamoorti, *Single-walled carbon nanotube dispersions in poly(ethylene oxide)*. Advanced Functional Materials, 2005. **15**(11): p. 1832-1838.
22. Gojny, F.H., M.H.G. Wichmann, B. Fiedler, W. Bauhofer, and K. Schulte, *Influence of nano-modification on the mechanical and electrical properties of conventional fibre-reinforced composites*. Composites: Part A, 2005. **36**(11): p. 1525-1535.
23. Liu, J., T. Liu, S.T. Veedu, J.E. Leisen, and S. Kumar. *Polymer/SWNT wrapping behavior*. in *Abstracts, 55th Southeast Regional Meeting of the American Chemical Society*. 2003. Atlanta, GA, United States: American Chemical Society.
24. Safadi, B., R. Andrews, and E.A. Grulke, *Multiwalled carbon nanotube polymer composites: synthesis and characterization of thin films*. Journal of Applied Science, 2002. **84**: p. 2660-2669.
25. Yang, Y., M.C. Gupta, K.L. Dudley, and R.W. Lawrence, *The fabrication and electrical properties of carbon nanofibre-polystyrene composites*. Nanotechnology, 2004. **15**(11): p. 1545-1548.
26. Wong, M., M. Paramsothy, X.J. Xu, Y. Ren, S. Li, and K. Liao, *Physical interactions at carbon nanotube-polymer interface*. Polymer, 2003. **44**: p. 7757-7764.
27. Thostenson, E.T. and T.-W. Chou, *Aligned multi-walled carbon nanotube-reinforced composites: processing and mechanical characterization*. Journal of Physics D: Applied Physics, 2002. **35**(16): p. L77-L80.
28. Bellayer, S., J.W. Gilman, N. Eidelman, S. Bourbigot, X. Flambard, D.M. Fox, H.C. De Long, and P.C. Trulove, *Preparation of homogeneously dispersed multiwalled carbon nanotube/polystyrene nanocomposites via melt extrusion using trialkyl imidazolium compatibilizer*. Advanced Functional Materials, 2005. **15**(6): p. 910-916.
29. Choi, Y.-J., S.-H. Hwang, Y.S. Hong, J.-Y. Kim, C.-Y. Ok, W. Huh, and S.-W. Lee, *Preparation and Characterization of PS/Multi-Walled Carbon Nanotube Nanocomposites*. Polymer Bulletin, 2005. **53**(5-6): p. 393-400.
30. Dalmás, F., L. Chazeau, C. Gauthier, K. Masenelli-Varlot, R. Dendievel, J.Y. Cavailié, and L. Forró, *Multiwalled carbon nanotube/polymer nanocomposites: processing and properties*. Journal of Polymer Science: Part B: Polymer Physics, 2005. **43**: p. 1186-1197.
31. Yang, Z., B. Dong, Y. Huang, L. Liu, F.-Y. Yan, and H.-L. Li, *Enhanced wear resistance and micro-hardness of polystyrene nanocomposites by carbon nanotubes*. Materials Chemistry and Physics, 2005. **94**(1): p. 109-113.
32. Enomoto, K., T. Yasuhara, S. Kitakata, H. Murakami, and N. Ohtake. *Frictional properties of carbon nanotube reinforced polymer matrix composites*. in *NASA Conference Publication*. 2003.
33. Viswanathan, G., N. Chakrapani, H. Yang, B. Wei, H. Chung, K. Cho, C.Y. Ryu, and P.M. Ajayan, *Single-step In-situ Synthesis of Polymer-grafted Single Wall Nanotube Composites*. Journal of American Chemical Society, 2003. **125**(31): p. 9258-9259.
34. Fragneaud, B., *Synthesis and characterization of polymer/carbon nanotube composites: Impact of the CNx MWNT surface polymer grafting on mechanical and electrical properties*. 2006.
35. Yao, Z., N. Braid, G.A. Botton, and A. Adronov, *Polymerization from the Surface of Single-Walled Carbon Nanotubes - Preparation and Characterization of Nanocomposites*. Journal of American Chemical Society, 2003. **125**: p. 16015-16024.
36. Gojny, F.H. and K. Schulte, *Functionalisation effect on the thermo-mechanical behaviour of multi-wall carbon nanotube/epoxy-composites*. Composites Science and Technology, 2004. **64**: p. 2303-2308.
37. Dufresne, A., M. Paillet, J.L. Putaux, R. Canet, F. Carmona, P. Delhaes, and S. Cui, *Processing and characterization of carbon nanotube/poly(styrene-co-butyl acrylate) nanocomposites*. Journal of Materials Science, 2002. **37**: p. 3915-3923.

38. Xu, Y., B. Higgins, and W.J. Brittain, *Bottom-up synthesis of PS-CNF nanocomposites*. *Polymer*, 2005. **46**(3): p. 799-810.
39. Eitan, A., K. Jiang, D. Dukes, R. Andrews, and L.S. Schadler, *Surface Modification of Multiwalled Carbon Nanotubes: Toward the Tailoring of the Interface in Polymer Composites*. *Chemical Materials*, 2003. **15**: p. 3198-3201.
40. Cui, S., R. Canet, A. Derre, M. Couzi, and P. Delhaes, *Characterization of multiwall carbon nanotubes and influence of surfactant in the nanocomposite processing*. *Carbon*, 2003. **41**: p. 797-809.
41. Yang, M., V. Koutsos, and M. Zaiser, *Interactions between Polymers and Carbon Nanotubes: A Molecular Dynamics Study*. *Journal of Physical Chemistry B*, 2005. **109**(20): p. 10009-10014.
42. McNally, T., P. Potschke, P. Halley, M. Murphy, D. Martin, S.E.J. Bell, G.P. Brennan, D. Bein, P. Lemoine, and J.P. Quinn, *Polyethylene multiwalled carbon nanotube composites*. *Polymer*, 2005. **46**: p. 8222-8232.
43. Valentini, L., J. Biagiotti, J.M. Kenny, and S. Santucci, *Morphological characterization of single-walled carbon nanotubes-PP composites*. *Composites Science and Technology*, 2003. **63**: p. 1149-1153.
44. Del Rio, C., M.C. Ojeda, and J.L. Acosta, *Carbon black effect on the microstructure of incompatible polymer blends*. *European Polymer Journal*, 2000. **36**: p. 1687-1695.
45. Feller, J.F., I. Linossier, S. Pimbert, and G. Levesque, *Carbon Black-Filled Poly(ethylene-co-alkyl acrylate) Composites: Calorimetric Studies*. *Journal of Applied Polymer Science*, 2001. **79**: p. 779-793.
46. Xu, J.-T., J.-J. Yuan, and S.-Y. Cheng, *SAXS/WAXS/DSC studies on crystallization of a polystyrene-*b*-poly(ethylene oxide)-*b*-polystyrene triblock copolymer with lamellar morphology and low glass transition temperature*. *European Polymer Journal*, 2003. **39**: p. 2091-2098.
47. Chen, X.L. and S.A. Jenekhe, *Solubilization and Encapsulation of Fullerenes by Amphiphilic Block Copolymers*. *Langmuir*, 1999. **15**: p. 8007-8017.
48. Christopoulos, V., D. Papanagopoulos, and A. Dondos, *Towards a better mixing of two incompatible polymers by casting from solution without compatibilizer*. *Journal of Polymer Science, Part B: Polymer Physics*, 1998. **36**(6): p. 1051-1060.

# **Chapter 7.**

## **Electrical and mechanical characterization of nanocomposites of PS, PEO and PS-grafted CN<sub>x</sub> nanotubes**

### **7.1. Introduction**

There is a growing interest in improving the thermal, mechanical, electrical, barrier properties, among others, in polymers through the preparation of nanocomposite materials using carbon nanotubes. Furthermore, it is proposed that the optimal performance of nanotube-based polymer composites could be expected when the nanotubes are grafted with polymer, because of the enhanced dispersion and interfacial strength that could be obtained. In the previous chapters, nanocomposites, using un-functionalized MWNTs, CN<sub>x</sub> and polymer-grafted nitrogen-doped carbon nanotubes (PS-*g*-CN<sub>x</sub>) were prepared using solution-pressing procedure, and their morphological and thermal properties were reported. Thus, in this chapter, the electrical and mechanical properties of the different nanocomposites are characterized using dielectric spectroscopy and DMA, and analyzed.

The goal of this chapter is the evaluation of the effect of the type of filler (functionalized or non-functionalized), and the type of matrix (amorphous or crystalline) on the electrical and mechanical properties of materials in order to understand the relationships between the microstructure and properties of the prepared nanocomposites.

## 7.2. Results and Discussion

### 7.2.1. PS-based nanocomposites

#### 7.2.1.1. PS-nanotube composites electrical properties

The PS-based nanocomposites at several nanotube type and concentrations were characterized by dielectric spectroscopy using films. The films were cut in parallelepiped samples of  $0.40 \pm 0.03$ ,  $20.0 \pm 2.26$ , and  $5.25 \pm 0.22$  mm. In all cases, the real and imaginary conductivity values of PS-carbon nanotube composites were obtained. These values were also compared to approximated values of conductivity measurements of pure carbon nanotubes samples (section below).

##### 7.2.1.1.1. Carbon nanotubes conductivity measurements

The conductivity values of the different carbon nanotubes were measured. The samples were prepared by cold-pressing ultrasonicated, dried and powdered carbon nanotubes samples to form films. Due to the inherent difficulty to handle carbon nanotubes without a matrix, the film dimensions strongly varied from one material to another. Thus, even though the length and width remained almost similar to the values of the nanocomposite samples (6.4 mm and 20 mm in average), the thickness strongly varied from 0.7 to 1.0 mm.

The experiments were carried out with and without applying an arbitrary pressure along the film using additional tweezers. This pressure variation was performed in order to qualitatively determine the effect of the increment in the contact surface area (between probes and films), and of the applied force in the conductivity measurements of the nanotube samples without a matrix. In addition, it is known that disentangled nanotube samples without matrix present low cohesion between individual tubes. This lower cohesion decreases the contact between nanotubes that also could decrease the measured conductivity to values lower than the intrinsic conductivity of individual nanotubes.

Table 7.1 presents the comparison of the real conductivity ( $\sigma$ ) of carbon nanotubes (MWNT,  $CN_x$  and PS-g- $CN_x$ ) measured using pressured and non pressured samples at 1 Hz. As can be seen, in all nanotube types the conductivity of pressured samples of pure carbon nanotubes presents higher values. This behavior is due to the favored contact between individual tubes by limiting the free space (air) in the compacted films. The conductivity values of the pressured samples could be considered as a better approximation to the nanotubes inherent conductivity. In addition, the arbitrary selected pressure applied to the samples gave an approximation to “real conductivity values”, but it could be possible that higher pressures or contact area trough the probes could induce higher conductivity measures. Thus, the reported values have to be considered as approximated values, but not as conductivity absolute measurements of nanotube filler samples. This fact is evidenced when other researchers found higher conductivity values for CNTs, as in the case of MWNTs (1285 S/m) [1]. Further analysis and comparison with composites will consider only pressured samples.

In addition, the level of conductivity of nanotube samples follows:  $\sigma_{\text{MWNTs}} > \sigma_{\text{CN}_x} > \sigma_{\text{PS-g-CN}_x}$ , in both pressured and non pressured samples (Table 7.1). Therefore, this result reveals that the chemical functionalization (i.e. nitrogen-doping or polymer-grafting) of the carbon nanotubes decreases the measured conductivity, at least with this processing and measuring technique.

The conductivity measurement of pure nanotubes samples (MWNT and CN<sub>x</sub>) is mainly dependant on the intrinsic nanotube conductivity, but also on the contact between tubes. In the case of PS-g-CN<sub>x</sub> nanotubes, the conductivity measurement is strongly dependent on the number and resistance of contacts between grafted-nanotubes within the polymer, in addition to the intrinsic conductivity of double modified nanotubes.

The lower conductivity of the CN<sub>x</sub> nanotubes in comparison with the MWNTs could be attributed to the graphite crystalline deviation that could induce “defects” due to functionalization with nitrogen. These structural modifications could limit the charge density and transport in nanotubes. Indeed, it was reported in the literature that nitrogen doping over 2% diminished the conductivity. Furthermore, the decrease in conductivity from CN<sub>x</sub> to PS-g-CN<sub>x</sub> nanotubes can be attributed to the presence of the grafted polymer layer, which isolates the nanotubes from each other. In summary, in this last case, the decreases in conductivity concern the inherent nanotubes conductivity (because of the further chemical functionalization), but also the nanotubes network formation (including the kind of contacts between them).

The curves of real conductivity vs. frequency of nanotubes pressured samples are depicted in Fig. 7.1. In all cases the curves exhibit a constant value until high frequencies followed by a decrease. These results clearly demonstrate that carbon nanotube fillers behave as conductor materials.

For comparison in the same graph, the curves of PS/CNTs composites at 5 wt% of nanotube fillers are presented. The filler concentration in these composites was selected to be above the conductivity percolation threshold (as further discussed in the section), i.e. when the samples became conductive. In this section, we first discuss the values in the plateau, i.e. at 1 Hz (reported in table 7.1 ).

In each case, the presence of the PS matrix in composites leads to a large decrease of the conductivity values compared to the pure nanotube films. This behavior of PS/CNTs composites is related to the: (i) intrinsic conductivity of nanotube fillers, (ii) nanotube network formation (dispersion quality within the polymer matrix, schematically represented in Fig. 7.2), and (iii) type of nanotube filler contacts, thus number and resistance of contacts.

The intrinsic conductivity of nanotubes was commented previously and follows  $\sigma_{\text{MWNTs}} > \sigma_{\text{CN}_x}$ . In addition, further chemical functionalization, as in the polymer grafted nanotubes, is expected to decrease more the tube inherent conductivity because of the crystalline network modification through the chemical functionalization, independently of the insulating polymer layer formed around them.

Table 7.1. Conductivity values of sonicated CNTs and PS/CNTs composites filled at 5 wt% of filler with and without additional pressure on the films at 1 Hz.

Materials	Conductivity S/m	Conductivity S/m*
MWNT	900	971
CN <sub>x</sub>	148	221
PS- <i>g</i> -CN <sub>x</sub> <sup>#</sup>	141	168
PS/MWNT <sup>+</sup>	633	-
PS/CN <sub>x</sub> <sup>+</sup>	187	-
PS/PS- <i>g</i> -CN <sub>x</sub> <sup>~</sup>	6.12	-

\* Values measured when applying an additional pressure on the film.

<sup>#</sup> PS-grafted CN<sub>x</sub>, mass relation polymer:tubes 35:65

<sup>+</sup> PS/CNT composites at 5 wt% of nanotube filler

<sup>~</sup> PS/CNT composites at 5 wt% of filler (PS-*g*-CN<sub>x</sub>)

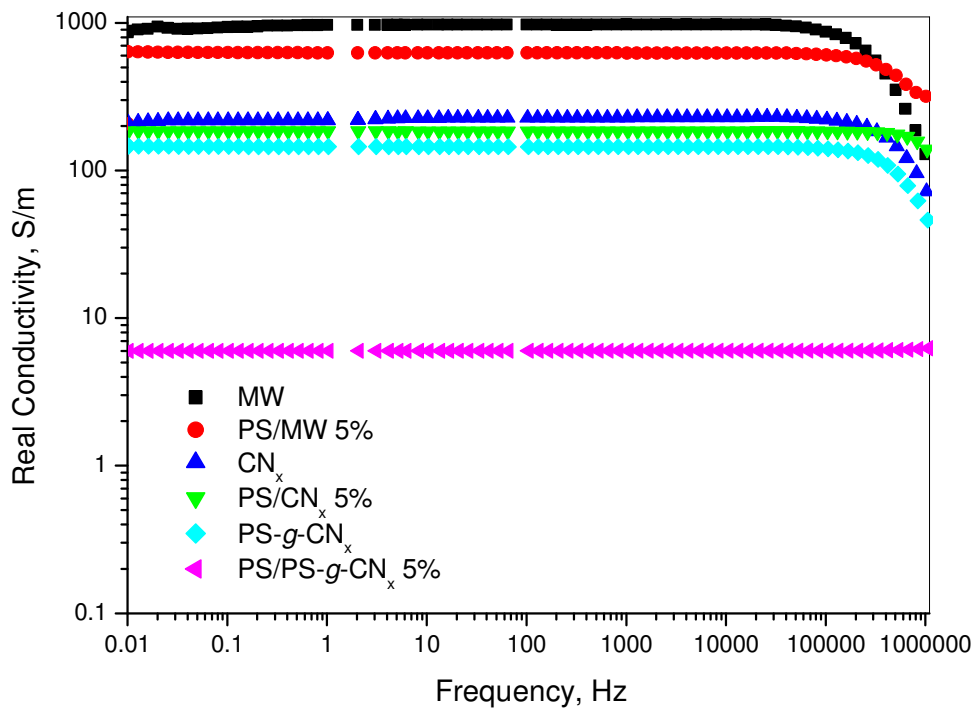


Fig. 7.1. Conductivity measures of several carbon nanotube fillers, and their correspondent PS-based nanocomposites filled at 5 wt% of filler.

The filler dispersion enhancement, follows PS-*g*-CN<sub>x</sub>>CN<sub>x</sub>>MWNT and determines the ease of the formation of a geometrical percolation network.

The type and resistance of contact between fillers in the percolating network can be summarized as follows: in MWNTs and CN<sub>x</sub> nanotubes are connected by direct tube-tube

contacts with lower electrical resistance and by dielectric polymer-polymer contacts in PS-g-CN<sub>x</sub>. The number of contacts is also concerned. Thus, the formation of a geometrical percolation network favors the probability, i.e. the number of contacts between dispersed conductive phase in the composite.

Thus, in the conductivity measurements, a competition between these different effects determined the observed values. In particular, in the case of the PS-g-CN<sub>x</sub> filler, even though the dispersion of the fillers is improved, the nanotubes are isolated from each other and the type of contact differs in a defavorable way. This last behavior was expected, and is a confirmation of the polymer-grafting of the nanotube surface. Alternatively, the coverage of nanotubes with conductive polymers could be a way to revert this phenomenon when for instance adequate polymer matrices like conjugated polymers are used.

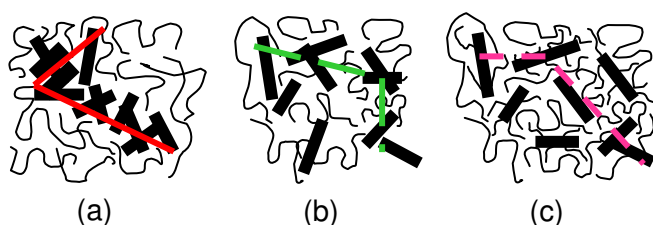


Fig. 7.2. Schematic representation of the percolation behavior dependence on the filler dispersion. Example of the (a) PS/MWNT, (b) PS/CN<sub>x</sub>, and (c) PS/PS-g-CN<sub>x</sub> nanocomposites.

#### 7.2.1.1.2. PS-nanotube conductivity measurements

The Fig. 7.3 and Fig. 7.4 show the evolution of the real and imaginary parts of the electrical conductivity of the PS/MWNT nanocomposites versus frequency for nanotubes content in the range (0-5%). Because the applied voltage was set to 0.1 V, the curves present some dispersed points at low filler content and low frequency. We have checked that measurements performed with a voltage of 1.0 V gave less dispersed curves, and that the values remained the same.

As far as the neat PS matrix is concerned, the increase of the real conductivity versus frequency is characteristic of a classical dielectric behavior. Indeed, the curve is in good agreement with the expression  $\sigma = \omega \varepsilon'' \varepsilon_0$  valid for dielectric materials, where  $\sigma$  is the conductivity,  $\varepsilon''$  is the imaginary part of the dielectric constant,  $\omega$  is the angular frequency, and  $\varepsilon_0$  is the vacuum permittivity. A similar dielectric behavior is observed at low loadings of carbon nanotubes (0.1 wt% of MWNTs). In this case, a percolating network of MWNTs has not yet been formed.

PS filled with 0.3 wt% of MWNT shows a behavior similar to that of the polymer matrix at low frequencies, nevertheless it presents a conductive behavior at higher frequencies. These curves are indeed characterized by a frequency independent conductivity  $\sigma_0$  up to a critical frequency, followed by a region of increasing conductivity. This frequency independent conductive behavior is indicative of nonzero dc conductivity, i.e. non dielectric behavior. This means that the composite displays a capacitive response. Thus, this material is identified as polymer-conductive filler composite below the

percolation threshold, where the electrical percolation threshold corresponds with the filler content value beyond which the composite behaves as conductive.

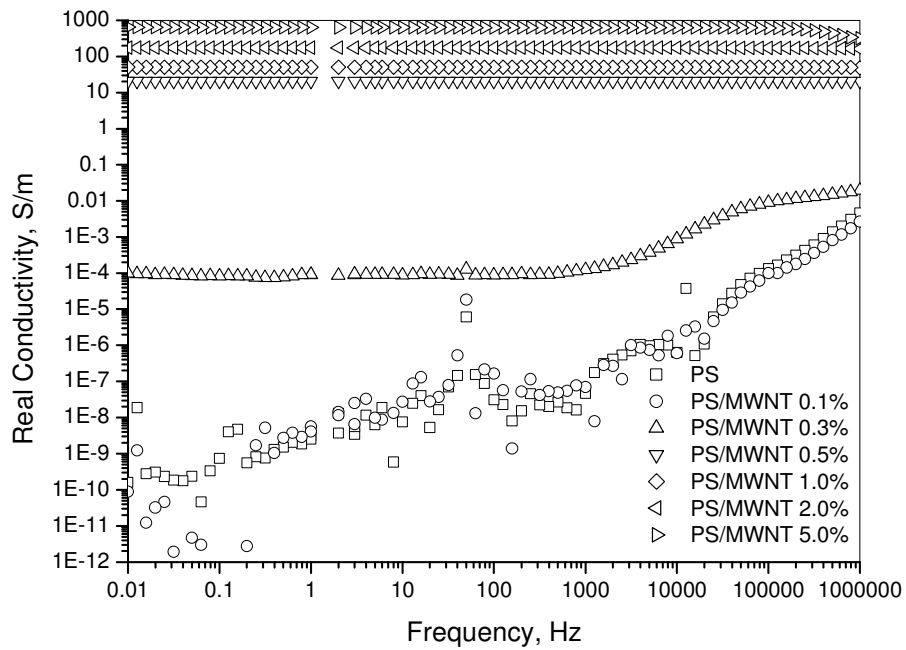


Fig. 7.3. Real conductivity of PS/MWNT nanocomposites vs. frequency at filler weight fractions of 0.1 to 5.0 wt% and applied voltage of 0.1 V.

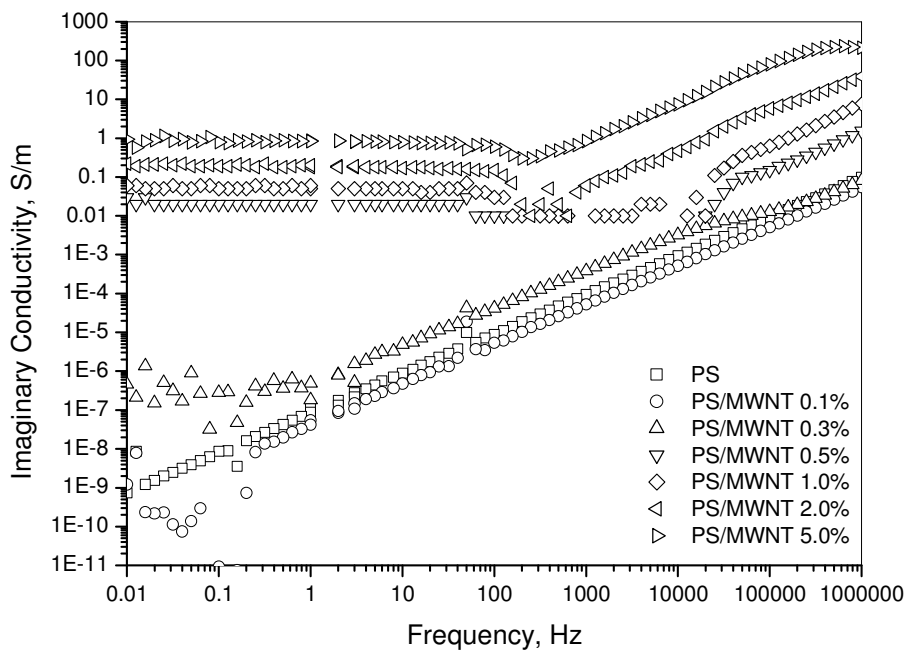


Fig. 7.4. Imaginary conductivity of PS/MWNT nanocomposites vs. frequency at filler weight fractions of 0.1 to 5.0 wt% and applied voltage of 0.1 V.

Nanocomposites with 0.5 wt% and higher loadings present a complete change in their behavior, becoming conductors with conductivity values ranging from 10 S/m to 630 S/m, as the filler content increases from 0.5 to 5.0 wt%. The conductive values remain constant with the frequency, thus the materials exhibit a pure real resistive behavior. In these cases, the materials are above the percolation threshold, and a connective network of nanotubes within the matrix has been formed.

The change from capacitive to conductive behaviors determines the percolation threshold of the material. Thus, for PS/MWNT nanocomposites, the percolation threshold is located between 0.3 and 0.5 wt%, equivalent to around 0.15 and 0.25 vol%. The percolation threshold is highly dependent on the filler dispersion state, and the value found here is lower than most of the reported for similar nanocomposite systems [1].

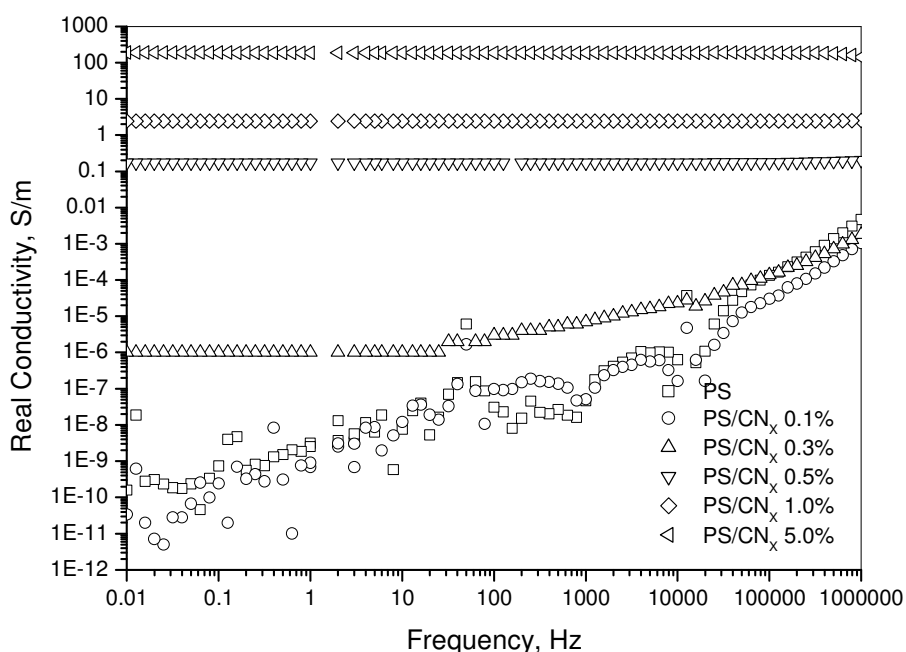


Fig. 7.5. Real conductivity of PS/CN<sub>x</sub> nanocomposites vs. frequency at filler weight fractions of 0.1 to 5.0 wt% and applied voltage 0.1 V.

Similar behaviors were observed for PS/CN<sub>x</sub> nanocomposites as shown in Fig. 7.5 and Appendix 7.1. In this case, the percolation threshold was observed, according to the graphs, between 0.3 and 0.5 wt%. Furthermore, the conductivity values were lower than those observed in PS/MWNT. The conductivity values range from 0.1 to 200 S/m as the CN<sub>x</sub> nanotube content increases from 0.5 to 5.0 wt%. For a given nanotube content, the conductivity values of PS/CN<sub>x</sub> are lower than those of PS/MWNT because of the lower conductivity of the CN<sub>x</sub> nanotubes (see Table 7.1).

As in the previous case, the PS/PS-g-CN<sub>x</sub> nanocomposite materials (Fig. 7.6) behave as conductive for values higher than 2.0 wt%, and also present a moderated

conductivity increment at the maximum loading of 5.0 wt%. The graphs are displayed in Appendix 7.1.

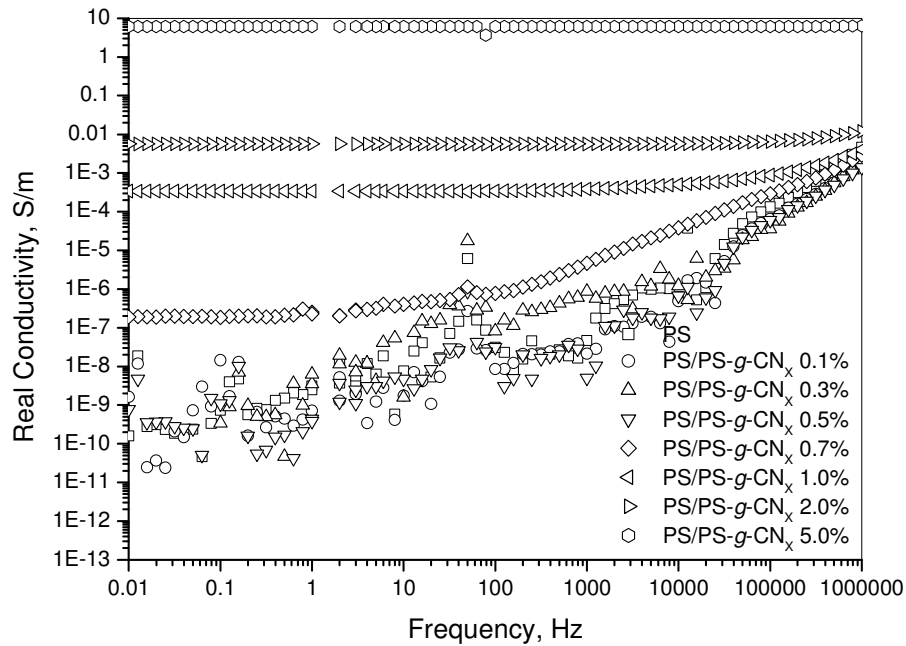


Fig. 7.6. Real conductivity of PS/PS- $g$ -CN $_x$  nanocomposites vs. frequency at filler weight fractions of 0.1 to 7.7 wt% and applied voltage 0.1 V.

#### 7.2.1.1.3. PS-nanotube composite conductivity modeling

Several models have been applied to describe the conductivity of polymer/filler composites, such as the simple mixing law [1], the statistical percolation theory [2-4], the insulator-conductor transition model [5-7], the fluctuation induced tunneling model [8], the temperature dependence of the conductivity [9], among others [10]. Particularly, several 2D and 3D approaches have been considered to determine the percolation threshold of composites filled with conductive fiber-type fillers. For example, Balberg *et al* [11] applied the Monte Carlo simulation method to sticks systems with aspect ratio and macroscopic characteristics. Munson-McGee [12] analyzed the geometry and the state of orientation of cylinders and focused on the aspect ratio.

From experimental data, it seems that the percolation phenomenon rules the electrical behavior measured for the different PS based nanocomposites. Thus, we decided to compare our measurements to the prediction of the percolation model. Note that the critical insulator-conductor model has also been tried (results are presented in Appendix 7.2) even though the better results have been obtained when percolation model was used.

#### Simple mixing law

First of all, it is confirmed that the conductivity of the systems PS/CNTs, whatever the type of nanotube (MWNT, CN $_x$  or PS- $g$ -CN $_x$ ) can not be well described by a simple mixing law,

$$\sigma_{comp} = V_{mat}\sigma_{mat} + V_{net}\sigma_{net} \quad [7.1]$$

where  $V_{net}$  is the volume fraction of the conductive network,  $V_{mat}$  is the volume fraction of the matrix,  $\sigma_{net}$  is the conductivity of the network, and  $\sigma_{mat}$  is the conductivity of the matrix. This observation has also been reported by other authors for similar polymer-CNTs composites, as Dalmás *et al.* [1]

Table 7.2 presents the results of the experimental and calculated values of conductivity at 1 Hz using the simple mixing law. The calculus was performed using the experimental values for PS and nanotube fillers (Table 7.1) and the equation 7.1. As can be seen, the theoretical values are more accurate for higher filler content than for lower ones; nevertheless, in general, the model does not correctly predict the conductivity of nanocomposites PS/CNTs.

Table 7.2. Experimental conductivity values measured for PS/CNTs composites compared with calculated values by the simple mixing law.

PS/MWNT		Conductivity		
wt%	vol. frac.	Experimental S/m	Theoretical S/m	$\Delta$ , %
0	0.0000	2.50E-09		
0.1	0.0005	5.64E-09	4.86E-01	-8.60E+09
0.3	0.0015	8.89E-05	1.46E+00	-1.64E+06
0.5	0.0025	20.57	2.43E+00	8.82E+01
1.0	0.0050	50.24	4.86E+00	9.03E+01
2.0	0.0100	173.61	9.71E+00	9.44E+01
5.0	0.0250	633.02	2.43E+01	9.62E+01

PS/CN <sub>x</sub>		Conductivity		
wt%	vol. frac.	Experimental S/m	Theoretical S/m	$\Delta$ , %
0.0	0.0000	2.50E-09		
0.1	0.0005	9.02E-10	1.11E-01	-1.23E+10
0.3	0.0015	7.36E-07	3.32E-01	-4.51E+07
0.5	0.0025	1.73E-01	5.53E-01	-2.20E+02
1.0	0.0050	2.42E+00	1.11E+00	5.44E+01
5.0	0.0250	1.88E+02	5.53E+00	9.71E+01

PS/PS-g-CN <sub>x</sub>			Conductivity		
wt%	tube wt%	vol. frac.	Experimental S/m	Theoretical S/m	$\Delta$ , %
0	0	0.0000	2.50E-09		
0.1	0.07	0.0005	7.10E-10	8.40E-02	-1.18E+10
0.3	0.20	0.0015	6.30E-09	2.52E-01	-4.00E+09
0.5	0.33	0.0025	3.84E-10	4.20E-01	-1.09E+11
0.7	0.46	0.0035	2.29E-07	5.88E-01	-2.56E+08
1.0	0.65	0.0050	3.41E-04	8.40E-01	-2.46E+05
2.0	1.30	0.0100	5.64E-03	1.68E+00	-2.97E+04
5.0	3.25	0.0250	6.12	6.47E+00	-5.67E+00

Statistical Percolation Theory

The statistical percolation theory predicts power law dependence for the conductivity above the percolation threshold

$$\sigma_e = \sigma_0 \left( \frac{p - p_c}{1 - p_c} \right)^t \quad [7.2]$$

where  $p_c$  is the percolation threshold,  $\sigma_0$  is a prefactor corresponding to the conductivity of the fillers and  $t$  is the universal exponent for the conductivity, usually close to 2 in 3D systems.

Fig. 7.7 depicts the electrical conductivity of PS/CNT composites as a function of the volume fraction of nanofillers. The volume fraction was calculated using the weight fractions of nanotubes and an estimation of their density ( $2.0 \text{ g/cm}^3$ ).

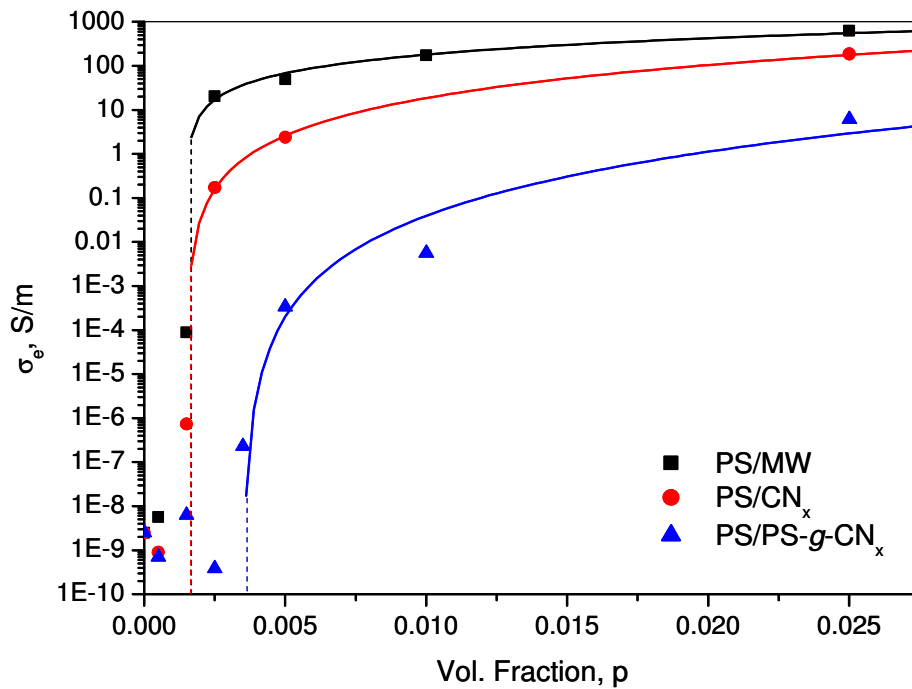


Fig. 7.7. Real part of the AC electrical conductivity at 1 Hz for nanocomposites of PS and nanotubes at several filler contents. Comparison with the statistical percolation theory (solid lines)

Using this modeling approach, the parameters of the fit are reported in Table 7.3, for each nanotube type. The detailed procedure to obtain the parameters is depicted in Appendix 7.3. The best fits were found by incrementally varying  $p_c$  until the best linear fit to the equation was found. The parameter analysis is described below.

Table 7.3. Conductivity exponent  $t$  and the percolation threshold  $p_c$  of PS/CNT composites using the statistical percolation model.

Nanocomposite	$p_c$ vol. frac.	Percolation Model			$\sigma_{\max}$ S/m
		$t$	$R^2$	$\sigma_0$	
PS					$2.49 \times 10^{-9}$
PS/MW	0.0015	1.10	0.9897	34538	633.02
PS/CN <sub>x</sub>	0.0015	2.22	0.9998	741241.97	187.83
PS/PS- <i>g</i> -CN <sub>x</sub>	0.0035	3.61	0.9562	2936973.3	6.12

#### Percolation threshold, $p_c$

Many parameters influence the percolation threshold, e.g. filler shape (aspect ratio), filler distribution, or filler/matrix interactions. Each one will be commented.

First of all, the percolation threshold strongly depends on the aspect ratio of the fillers, as was stated by Celzard *et al* [13]. Hence, the experiments performed using carbon nanotubes as conductive fillers generally result in low percolation thresholds for several polymer systems, as shown in Table 7.4. In fact, the obtained experimental values for PS/MWNT, PS/CN<sub>x</sub> and PS/PS-*g*-CN<sub>x</sub> materials are found to be in the observed experimental range for aspect ratios higher than 1000. Thus, another parameter has to be used to explain the different values obtained for the three types of nanotubes.

The percolation threshold obtained in materials is also dependent on the dispersion of fillers among the matrix. In fact, the dispersion state is a critical factor. In the case of (PS/MWNT and PS/CN<sub>x</sub>), the percolation threshold is low, which reveals the effects of a high aspect ratio (1333) and an efficient preparation/dispersion method of composites. Furthermore, from the microstructural observations, it seems that the best dispersed system is PS/PS-*g*-CN<sub>x</sub>; this system should thus have the lowest percolation threshold. However, the polymer-grafted nanotubes are more electrically isolated from each other by the PS layer and for that reason; PS/PS-*g*-CN<sub>x</sub> presents a higher percolation threshold compared to pure MWNT and CN<sub>x</sub>. In fact, it is expected that totally grafted fillers will form completely isolating composite materials. This fact is highly determinant for the percolation threshold behavior of PS/CNTs composites.

Moreover, due to van der Waals forces between nanotubes in lower stabilized dispersions, a re-agglomeration of the nanotubes may lead to the formation of conductive paths within polymer at lower filler contents. This re-agglomeration will be also dependent on the aspect ratio of the nanotubes and the mobility of the matrix. In our case, the MWNTs and CN<sub>x</sub> nanotubes could redistribute within the matrix during the solvent evaporation due to a worse dispersion properties of these fillers, explaining the lower percolation threshold in these PS/CNTs composites. Compared to PS-*g*-CN<sub>x</sub>, the non-functionalized CNTs have a higher tendency to re-agglomerate and form conductive paths, as shown Gogny *et al*. [14]. Even more, it was shown that the functionalization had led to a better and stabilized dispersion, due to improved intermolecular interactions between the polymer and the tube. Thus, the re-agglomeration of the PS-*g*-CN<sub>x</sub> is not likely to occur and the value of the percolation threshold is detrimentally influenced by a functionalization of carbon nanotubes.

The percolation threshold results could be compared to predictions based on the statistical percolation theory using an excluded volume argument. The excluded volume approach is particularly efficient in treating the problem of percolating systems in which the objects possess a large aspect ratio. In this notion, a composite can thus be considered as a conducting backbone with a certain packing density which differs from the conducting powder according to the particle morphologies. It was observed that the greater the aspect ratio, the less the packing density and the lower the expected critical volume concentration. [13]

The range of percolation thresholds expected from a purely statistical range of particles strongly differs from the ones obtained in Table 7.3 for PS/CNT systems, as well as for other composite materials as epoxy/MWNT composites (Table 7.4) [3]. These differences are attributed to the model which does not address the inter-tube or polymer-nanotube interactions. Thus, the effect of van der Waals forces and Coulomb interactions, among others, are neglected. In summary, the percolation of nanotubes is not a purely geometrical problem but also relates to the local improvements in nanotube contacts due to segregation.

#### *Conductivity exponent, $t$*

Usually the universal conductivity exponent,  $t$ , is related to the system dimensionality. Already observed experimental values generally range from 1.1 to 3.9 (as seen in Table 7.3), whereas theoretical values range from 1.6 to 2 [5].

In some cases, low  $t$  values were explained in terms of (i) charge transport through a two dimensional object, as a fractal of dimension around 2 [8], or (ii) an aggregation process of the carbon nanotubes during sample preparation, rejecting the formation of conductive networks through statistical percolation process. [15] These explanations could be useful for the case of PS/MWNT composites that exhibit a 1.1 as  $t$  value, and in which some aggregation could be possible (as seen during morphological observations). Also the formation of aggregates means that two dimensional objects could be formed.

Higher  $t$  values indicate transport in three dimensions, by analogy with last parameter value. Thus, for the case of PS/CN<sub>x</sub> nanotubes this hypothesis could be applied because of the relatively high  $t$  value of 2.2. Furthermore, PS/PS-*g*-CN<sub>x</sub> composites reveal a higher value of  $t$ . It is difficult to explain such a high value of  $t$ , but it seems that a distribution of contact resistances should be taken into account. Indeed, in PS-*g*-CN<sub>x</sub>, the properties of the PS grafted layer should be taken into account, since the deformation of the PS grafted layer, or even an interpenetration of two PS grafted layers, may occur. Similar results have been observed by Dalmas *et al* [1] with a solution prepared P(S-Abu)/MWNTs composite prepared through solvent route using surfactants. They obtained a  $t$  value of 3.9.

#### *Maximum conductivity, $\sigma_0$*

The maximum value of conductivity according to the model,  $\sigma_0$ , is determined by extrapolation when polymer is filled with high nanotubes loadings, i.e.  $p=100\%$ . In general, it was observed that in all cases the values are higher than the ones expected (calculated with a mixing law for example). This fact also reveals a great modeling problem for the case of these synthesized materials, particularly PS/CN<sub>x</sub> and PS/PS-*g*-CN<sub>x</sub> composites, where the polymer-nanotube and nanotube-nanotube interaction predominate.

Table 7.4. Literature reports of conductivity in composites modeling by percolation theory.

Nanocomposite	Preparation	Range filler Concentration	Percolation Theory		$\sigma$ max	Analysis method	Reference
			$p_c$	t			
Epoxy/fibre/CB	Calendaring		0.1-0.3 wt%	-	-	AC Imped. Spectr.	Gogny et al, 2005
Epoxy/fibre/DWNT				-	-	"	"
Epoxy/fibre/DWNT-NH <sub>2</sub>				-	-	"	"
Epoxy/MWNT	Solution casting		0.00015	-	-	AC Imped. Spectr.	Sandler et al, 1999
Epoxy/MWNT (aligned)	Solution casting	0.001-1 w%	0.0025 wt%	1.2	2 S/m	AC Imped. Spectr.	Sandler et al, 2003
Epoxy/MWNT (entangled)			~0.01 w%	-	~ 10 <sup>0</sup> S/m		
Epoxy/MWNT	Solution casting	1, 4 w%	<1.0 wt%	-	6x10 <sup>-2</sup> S/cm	DC Conductivity AC Imped. Spectr.	Allaoui et al, 2002
Epoxy/MWNT (10 $\mu$ m)	Solution casting	0.01-0.01 w%	0.0021 wt%	1.78	10 <sup>-2</sup> S/m	AC Imped. Spectr.	Martin et al, 2004
Epoxy/MWNT (17 $\mu$ m)			0.0025 wt%	-	-	"	"
Epoxy/MWNT (43 $\mu$ m)			0.0039 wt%	1.74	10 <sup>-4</sup> S/m	"	"
Epoxy/CB (no shear stirr)	Solution casting	0.06-0.9 vol%	0.9 vol%	-	-	DC Conductivity	Schueler et al, 1997
Epoxy/CB (shear stirr)			0.3 vol%	-	-	"	"
Epoxy/CB-CuCl <sub>2</sub>			0.06 vol%	-	-	"	"
Epoxy/CB	Solution casting	-	0.01	2.0 $\pm$ 0.2	-	DC Conductivity	van der Putten et al, 1992
Epoxy/CB	Solution casting		0.175	1.7	-		Fournier et al, 1997
			0.125	2	-		
Epoxy/Polypyrrole	Solution casting		0.035	2.6	-		
			0.03	3	-		
PMPV/MWNT	Spin casting	0.5-36 wt%	0.035	-	3 S/m		Coleman et al, 1998
PMMA/SWNT	Solution casting	0.1-10.0 wt%	0.33%	2.1 $\pm$ 0.1	30 S/cm	Electr. transport measurements	Benoit et al, 2001
PVA/CNT	Solution casting	5-60 w%	5-10 wt%	-	10 <sup>2</sup> S/m	AC Imped. Spectr.	Shaffer et al, 1999
PP/MWNT	Extrusion/	0.03-12.5 vol%	<0.25 vol%	-	100 ohm/sq		Andrews et al, 2002
PP/Nanofibers PG3	Injection/ Press		-	-	1E7 ohm/sq		
ABS/MWNT			-	-	1E11 ohm/sq		
PS/MWNT			<0.25 vol%	-	1000 ohm/sq		
PS/Nanofibers PG3			-	-	1E8 ohm/sq		
HIPS/MWNT			-	-	-		
PVA/MWNT	Solution casting	0.037-4.3 wt%	0.055 wt%	1.36	10 <sup>-3</sup>	DC Conductivity	Kilbride et al, 2002
PmPV/MWNT	spin coating					AC Imped. Spectr.	
PVA/MWNT	Solution casting	0.5-36 wt%	7-11 w%	-	3 S/m		
PmPV/MWNT	spin coating						
PS/MWNT	In situ polym. & Solution casting	< 30 wt%	4 wt%	-		AC Imped. Spectr.	Zhang et al, 2005
			9 wt%				

### *Comparison with other systems modeled by Statistical Percolation Theory*

To make a comparison of PS/CNT synthesized in solution with other polymer systems, several variables have to be taken into account: the measurement method, the sample dimensions to favor the contact, the processing differences that affect the dispersion, the interaction differences due to filler functionalities (chemical attachment of molecular species or polymer-grafting), among others.

Summarizing, according to the experimental observations, in all cases the PS/CNTs present a conductive behavior due to the functionalized and non functionalized nanotubes added to the material. The level of conductivity seems to be higher than most of the composites reported previously, probably because of a good dispersion state of the nanotubes in the matrices.

Modelization of the systems was performed by the statistical percolation model. With this model, good fits were obtained in all cases but for the PS/PS-*g*-CN<sub>x</sub>, a high value of the critical exponent  $t$  is obtained. In that case, this could mean that a distribution of contact resistances exists in the material, probably because of the deformable PS-grafted layer.

It is important to highlight that the percolation threshold ( $p_c$ ) is measured in the range of the reported values, or even at lower values. Nevertheless, differences in the model parameters were observed when comparing PS composites of as-produced nanotubes and polymer-grafted nanotubes. From the analysis of these parameter values, it could be possible to say that the PS/CNT composite behavior is dominated by the percolation/interaction, indicating the importance of dispersion and interfacial strength.

### **7.2.1.2. PS-nanotube composites mechanical properties**

The mechanical behavior of the PS/CNTs composites was studied using a DMA in tension mode. The storage and loss moduli were obtained at constant frequency as a function of the temperature. Dynamic Mechanical Analysis was performed to characterize the viscoelastic behaviors of pure polymer and polymer composites, as responses of the molecular relaxation processes.

The Fig. 7.8 to Fig. 7.14 and Appendix 7.4 show the storage modulus ( $G'$ ), loss modulus ( $G''$ ) and the loss factor ( $\tan \delta$ ) determined by DMA measurements for pure PS matrix and composite materials. In addition, Table 7.5 summarizes the measured mechanical properties.

#### **7.2.1.2.1. PS-nanotube composites DMA measurements**

Pure PS displays a typical viscoelastic behavior, as shown in Fig. 7.8. At low temperature, the material is in the glassy state (i.e. out of equilibrium) and the shear modulus  $G'$ , below  $T_g$  of PS, is about 1 GPa. In this temperature range, the stiffness is mainly due to the intermolecular van der Waals bonds. Then, a rapid decrease in the elastic modulus by more than three decades is observed, corresponding to glass-rubber transition. This modulus drop is attributed to an energy dissipation phenomenon involving cooperative motions of long chain sequences.

The PS/CNTs composites were analyzed comparing to pure PS. The results will be present according to the physical property measured.

#### *Storage Modulus, $G'$ , below $T_g$*

The elastic behavior is analyzed considering the storage modulus below and above  $T_g$ .

The measured storage modulus of the PS/CNTs composites in the glassy state (i.e. below  $T_g$ ) are almost the same, and close to that of pure PS matrix, as depicted in Figs. 7.8, 7.11 and 7.13. These results are difficult to accurately compare with pure PS due to the precision of DMA experiments (at most 10%) and the low number of composite samples analyzed to establish the reproducibility of the phenomena. At this respect, two procedures can be proposed:

(a) a normalization of all the curves to a given constant value in the glassy plateau (for instance 1 GPa) in order to analyze the differences in the storage modulus difference in the rubbery plateau

(b) a normalization of the curves in the glassy plateau using the prediction of Halpin-Kardos model.

The first procedure will be discussed in this section, whereas the second one will be commented in the section 7.2.1.2.1.2 corresponding to the PS/CNT systems modeling.

Considering the first procedure (a), it was observed that the normalization of the different curves in the glassy plateau for all PS/CNTs composites (not shown here) consequently affected, as expected, the storage modulus values in the rubbery plateau. Nevertheless, the  $G'$  measured values in the rubbery range did not present a direct correlation with the filler content. That means that this first procedure is not recommended.

Thus, in a first step, the values at the glassy plateau will be considered to be almost the same for all materials, i.e. within the accuracy of the  $G'$  measurements and we will discuss the modulus in the rubbery plateau as obtained. This is related to the fact that in nanocomposites, reinforcement is often higher above  $T_g$ , because of the great difference in the modulus of polymer and nanofillers.

Table 7.5 describes the storage values of PS/MWNT, PS/CN<sub>x</sub> and PS/PS-g-CN<sub>x</sub> below and above  $T_g$ . As was mentioned, the difference in the  $G'$  values in the glassy plateau will be disregarded. Further discussion of the reinforcement effect of nanotubes in the glassy plateau thanks to modeling approach will be found in section (7.2.1.2.2).

#### *Main relaxation temperature, $T_\alpha$*

At higher temperature, a strong decay of the modulus (around three orders of magnitude) is observed at the main relaxation temperature,  $T_\alpha$  (i.e. temperature at which  $\tan \delta$  is maximum). This relaxation is generally associated with an increase mobility of polymeric chains, i.e with the  $T_g$  of the material. The  $T_\alpha$  values for PS/CNTs composites are described in Table 7.5.

For pure PS, the temperature at which  $\tan \delta$  occurs is located at 124°C (see Table 7.5). The main relaxation temperatures of the composites with MWNTs from 0.1 to 0.5 wt% slightly decrease to 122°C, whereas from 1.0 to 5.0 wt% of MWNTs  $T_\alpha$  increases until 129°C. The slight decrease for low filler fractions has to be confirmed with further measurements.

Furthermore, the shift in the  $T_\alpha$  after 1.0 wt% seems to be a more general trend. In order to relate this evolution to the modification of the mobility of the polymeric chains, one should consider the curves of  $G''$  vs temperature. Loss modulus curves (Figs. 7.9 and Appendix 7.4) present the loss modulus ( $G''$ ) of the PS/MWNT, PS/CN<sub>x</sub> and PS/PS-g-CN<sub>x</sub> composites at several concentrations.

It is seems that the temperatures at the  $G''$  maximum ( $T_{G''}$ ) are not clearly dependent on the nanotube weight fraction. Thus, no clear indication of mobility change

is found. The evolution of  $T_\alpha$  versus filler weight fraction is then only a consequence of the increase of the  $G'$  value in the rubbery plateau.

In PS/CN<sub>x</sub> and PS/PS-g-CN<sub>x</sub> composites, the  $T_\alpha$  and  $T_{G'}$  values seem to be in the same order than the PS pure matrix following the level of uncertainty of the measure. This behavior reveals that the polymeric chain mobility has not been affected by the presence of carbon nanotubes. This also means that the interaction polymer-nanotube filler is weak.

In summary the slightly increase in  $T_\alpha$  in PS/MWNT composites was previously observed for other polymer-nanotube composite [1] and could be interpreted as an enhanced utilization temperature of composites compared to the unfilled PS samples. For the cases of PS/CN<sub>x</sub> and PS/PS-g-CN<sub>x</sub> composites, there was not observed an increase in  $T_\alpha$ .

Comparing the  $T_\alpha$  and Tg values obtained by DMA and DSC techniques, it has to be said that the  $T_\alpha$  determines the maximum energy dissipation in a dynamical essay and depends on the frequency used, whereas the Tg is the calorimetry measured temperature that depends on the variation of the temperature increment (dT/dt). Thus,  $T_\alpha$  values could be related with the Tg measured by DSC.

First of all, the  $T_\alpha$  measurements in DMA are more precise than the Tg measurements obtained by DSC. In the corresponding DSC section the Tg values of PS/CNTs revealed any changes due to weak interactions between nanotube and polymer; or even more, due to the similar properties of the polymer-grafted to CN<sub>x</sub>. After analysis of the complementary DMA measures, it could be possible state that the polymer-filler interactions in PS/MWNT are weak enough not to modify in great form the polymer chain mobility. This behavior is in agreement with the unchanged values of both Tg and  $T_{G'}$ . Weaker interaction between polymer and filler was evidenced in PS/CN<sub>x</sub> and PS/PS-g-CN<sub>x</sub> where both Tg and  $T_{G'}$  remained constant. To summarize, the interaction polymer-nanotube fillers follow: PS/MWNT > PS/CN<sub>x</sub> and PS/PS-g-CN<sub>x</sub>, according to their thermo-mechanical properties.

#### *Storage Modulus, $G'$ , above Tg*

Above  $T_\alpha$  the material is in the rubbery state until the material starts to flow, then it behaves as a viscous fluid and the experiment fails. In this temperature range ( $T_\alpha$  - flowing temperature), the thermal agitation makes the van der Waals bonds negligible, thus the entropic forces become predominant. Pure PS flows soon after  $T_\alpha$  as observed in Fig. 7.8. The presence and the length of the rubbery plateau is associated to the persistence of chain entanglements of the polymeric chains. In fact, for a entangled network, the  $G'$  value is given by  $G=NkT$  with N as the number of entanglements/m<sup>3</sup>. Moreover, the formation of a composite with strong interfacial strength is sometimes reported to influence the results in the rubbery plateau.

Actually, the possible persistence of the rubbery plateau versus temperature was not searched in this case. In fact, all the curves were stopped at the same temperature value. Nevertheless, other nanotube/polymer composites present the formation of a rubbery plateau, attributed to the formation of a connective network of CNTs within the polymer matrix. The entanglement level of this network, as well as the interface interactions (polymer-carbon nanotubes) have been proposed to explain the delay of the material flowing [1].

According to Fig. 7.8, the main observed phenomenon above  $T_{\alpha}$  is the increment in the storage modulus. For instance at 140°C, the  $G'$  modulus of the material is around thirty times higher than that of unfilled material for the composite with the highest filler content (PS/MWNT 5.0 wt%) (Table 7.5). Thus, higher MWNT concentrations produce a progressive change in the mechanical properties above  $T_g$ .

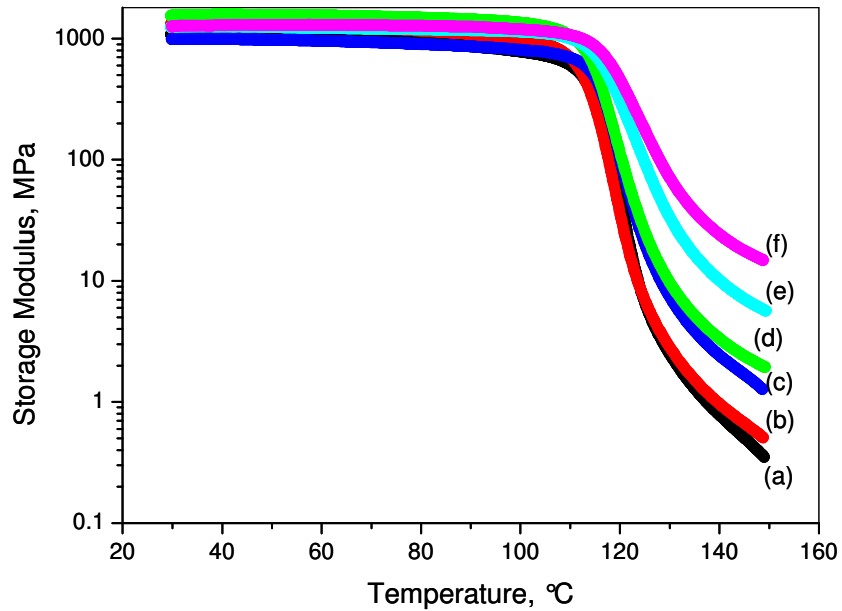


Fig. 7.8. Storage modulus of PS/MWNT nanocomposite vs. temperature at filler weight fractions of (a) 0, (b) 0.3, (c) 0.5, (d) 1.0, (e) 2.0 and (f) 5.0 wt%.

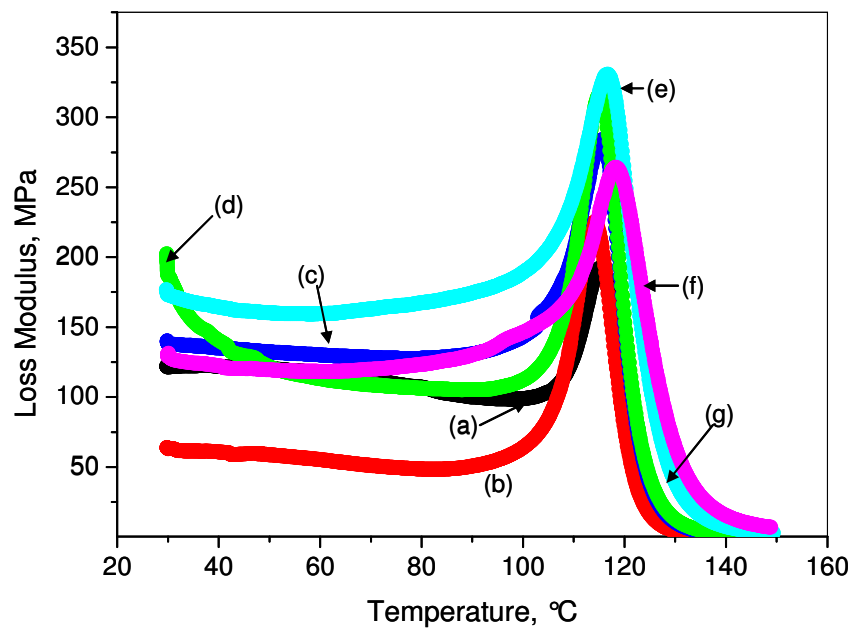


Fig. 7.9. Loss modulus of PS/MWNT nanocomposites vs. temperature at filler weight fractions of: (a) 0, (b) 0.3, (c) 0.5, (d) 1.0, (e) 2.0 and (f) 5.0 wt%.

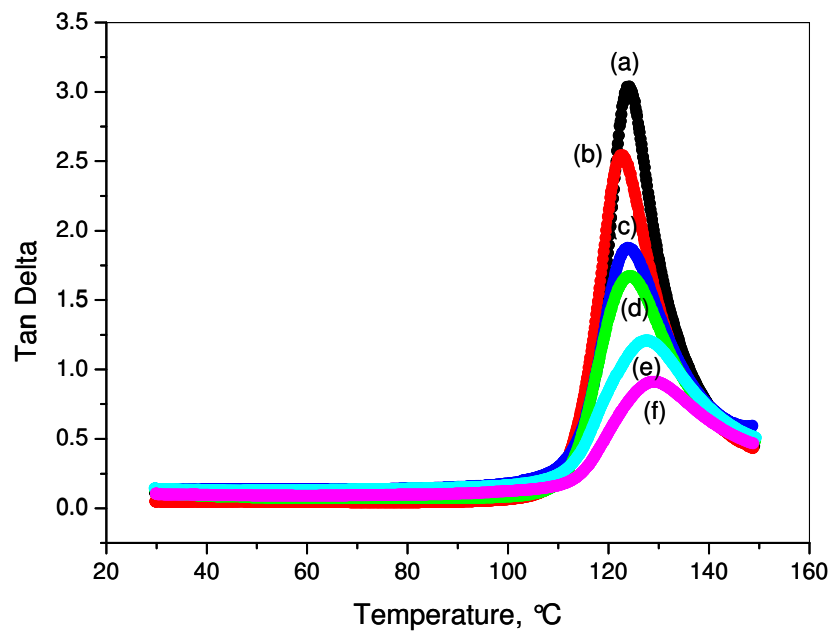


Fig. 7.10. Tan  $\delta$  of PS/MWNT nanocomposites vs. temperature at filler weight fractions of (a) 0, (b) 0.3, (c) 0.5, (d) 1.0, (e) 2.0 and (f) 5.0 wt%.

Table 7.5. Mechanical properties of PS/CNTs composites at several concentrations of MWNT, CN<sub>x</sub> and PS-g-CN<sub>x</sub> fillers.

PS/CNTs	Filler			Storage Modulus, G'		Loss Modulus G''		Tan δ	
	w%	v%	vol. frac.	Rubbery plateau*		Max, MPa	Temp, °C	Max.	Tα, °C
				MPa					
PS/MW	0	0	0	0.8		192.4	115.4	3.04	124.24
	0.3	0.15	0.0015	1.0		224.9	114.0	2.54	122.41
	0.5	0.25	0.0025	2.4		283.8	115.5	1.88	122.78
	1.0	0.5	0.0050	3.3		315.9	115.1	1.67	124.25
	2.0	1	0.0100	10.1		330.7	116.7	1.21	127.69
	5.0	2.5	0.0250	24.0		264.3	118.2	0.91	129.00
PS/CN <sub>x</sub>	0	0	0	0.8		192.4	115.4	3.04	124.24
	0.3	0.15	0.0015	0.8		316.5	112.4	3.05	121.19
	0.5	0.25	0.0025	1.0		214.3	114.2	2.50	123.39
	1	0.5	0.0050	1.9		244.8	114.2	1.89	123.37
	2	1	0.0100	2.1		241.4	118.0	2.07	126.53
	5	2.5	0.0250	8.9		262.6	115.9	1.20	124.96
PS/PS-g-CN <sub>x</sub>	0	0	0	0.8		192.4	115.4	3.04	124.24
	0.1	0.05	0.0005	0.8		243.0	115.9	3.16	124.12
	0.3	0.15	0.0015	0.7		326.0	113.3	3.20	122.20
	0.5	0.25	0.0025	0.8		279.8	113.2	3.12	121.89
	0.7	0.35	0.0035	0.9		275.9	113.6	2.85	122.48
	1	0.5	0.0050	1.3		222.3	114.9	2.46	123.90
	2	1	0.0100	1.4		220.7	114.3	2.23	122.99
	5	2.5	0.0250	2.6		177.8	115.7	1.68	125.20
	7.7	3.85	0.0385	3.8		246.7	115.5	1.62	123.81

\* Measured value at T of 140°C

~ Measured value at T of 60°C

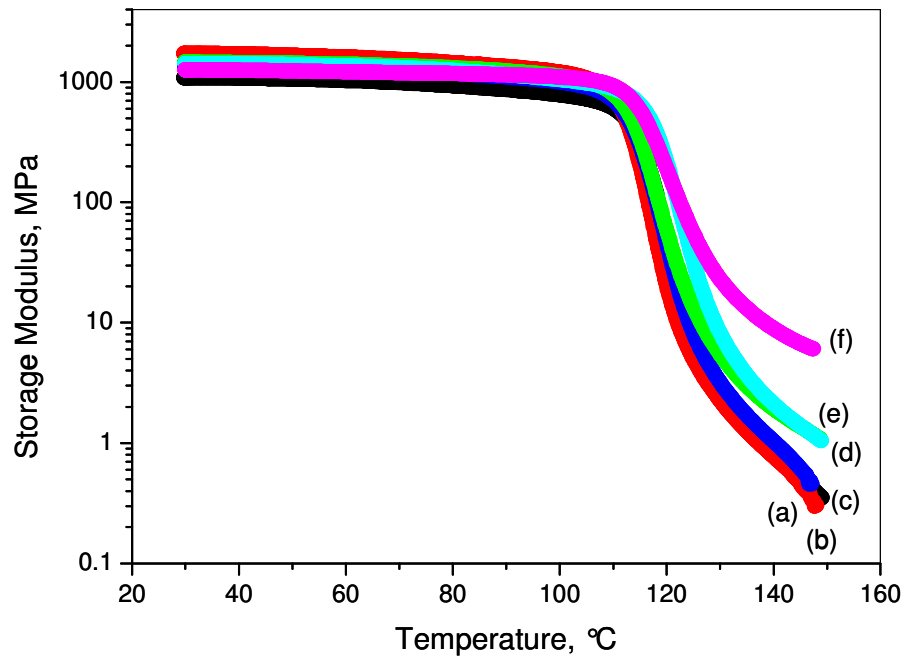


Fig. 7.11. Storage modulus of PS/CN<sub>x</sub> nanocomposites vs. temperature at filler weight fractions of (a) 0, (b) 0.3, (c) 0.5, (d) 1.0, (e) 2.0, and (f) 5.0 wt%.

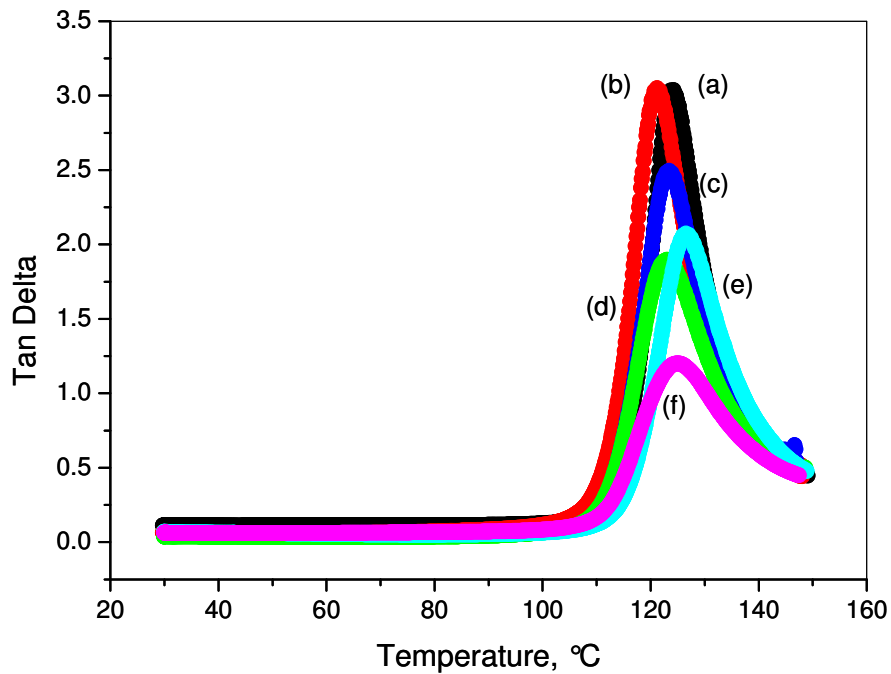


Fig. 7.12. Tan  $\delta$  of PS/CN<sub>x</sub> nanocomposites vs. temperature at filler weight fractions of (a) 0, (b) 0.3, (c) 0.5, (d) 1.0, (e) 2.0, and (f) 5.0 wt%.

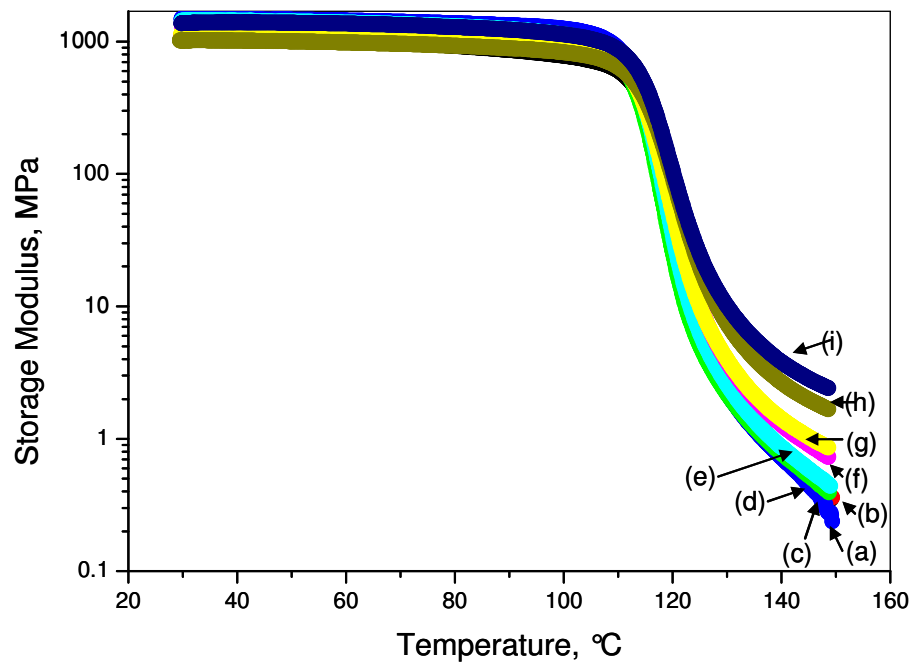


Fig. 7.13. Storage modulus of PS/PS-*g*-CN<sub>x</sub> nanocomposites vs. temperature at filler weight fractions of 0.1 to 5.0 wt%.

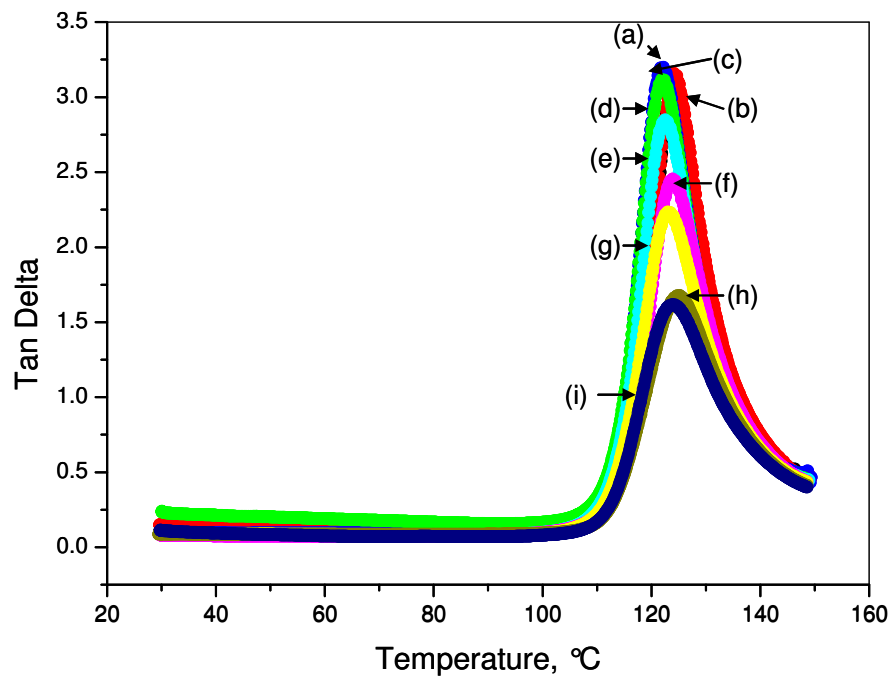


Fig. 7.14. Tan  $\delta$  of PS/PS-*g*-CN<sub>x</sub> nanocomposites vs. temperature at filler weight fractions of (a) 0, (b) 0.1, (c) 0.3, (d) 0.5, (e) 0.7, (f) 1.0, (g) 2.0, (h) 5.0, and (i) 7.7 wt%.

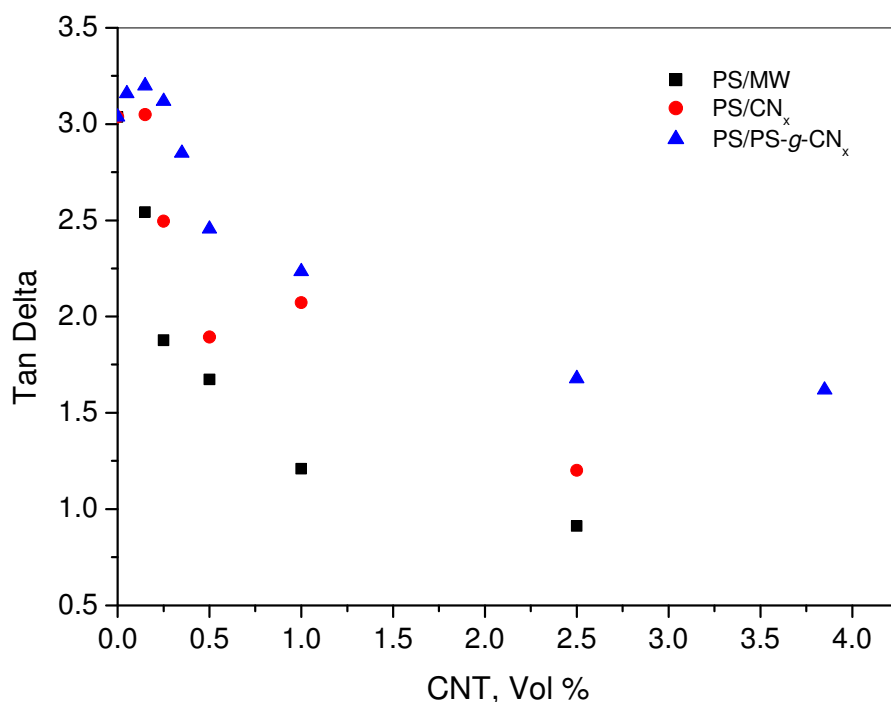


Fig. 7.15. Loss factor ( $\tan \delta$ ) of the PS/CNTs composites at several volume fractions of: ( $\diamond$ ) MWNT, ( $\square$ ) CN<sub>x</sub> and ( $\circ$ ) PS-g-CN<sub>x</sub> nanotubes.

Similar but lower increment in the  $G'$  above  $T_g$  was observed for the other composites PS/CN<sub>x</sub> and PS/PS-g-CN<sub>x</sub>. For instance, an increase of 11 and 5 times compared to the values of the PS were obtained in PS/CN<sub>x</sub> and PS/PS-g-CN<sub>x</sub> composite respectively. To sum up, the increment in  $G'$  follows the nanotube content, thus PS/MWNT > PS/CN<sub>x</sub> > PS/PS-g-CN<sub>x</sub>. According to literature, these differences in reinforcement could be associated to intrinsic modulus of each filler and morphology differences (dispersion, contacts, entanglements...).

#### *Loss factor, $\tan \delta$*

The loss factor ( $\tan \delta$ ) depicted in Fig 7.10, 7.12 and 7.14 reveals a classical decrease as a function of the filler concentration as shown in Fig. 7.15.

When comparing the different nanocomposites for a given filler content (5 wt%), it appears that above  $T_\alpha$ , the storage modulus increases from PS/PS-g-CN<sub>x</sub>, PS/CN<sub>x</sub> and finally to PS/MWNT, (Fig. 7.17). In the same time, the loss factor decreases as the storage modulus in the rubbery plateau increases (Fig. 7.18).

The measures in the rubbery plateau in all PS/CNTs cases are influenced for:

- (i) the matrix properties,
- (ii) the intrinsic properties of nanotubes (mechanical modulus, form factor, etc),
- (iii) the filler dispersion with the eventual formation of a percolant network, and

(iv) the interactions filler-filler and filler-matrix.

Analyzing each of the variables, first of all the PS is the matrix in all PS/CNTs composites, thus its behavior is expected to be the same.

In second time, the nanotubes modulus could be slightly different because of the functionalization of the nanotube surface. As was observed by DMA results the nitrogen doped and the polymer-grafting impacts the storage modulus of the fillers because the increase in modulus was observed higher when MWNT were used, following by CN<sub>x</sub> and finally PS-g-CN<sub>x</sub>. This behavior is explainable by the functionalization that could compromise the nanotube properties due to the introduction of sp<sup>3</sup> hybridized sites [16-19]. Anyway, the difference between polymers and nanotubes modulus remains almost the same. Therefore, this fact will less impact the modulus change.

In third place, the filler dispersion within the polymer matrix was more efficient in the case of PS-g-CN<sub>x</sub> then CN<sub>x</sub> and finally MWNT. In all cases, a percolating network was observed, evidenced by conductivity measurements. Nevertheless, the higher properties increase, as well as the theoretical modeling (section 7.2.1.1.3), determine that a more efficient percolating network was formed when MWNTs were used due to their dispersion properties.

Let's recall the scheme proposed to explain the electrical conductivity of PS/CNTs. When one consider the mechanical properties in the rubbery plateau, reinforcement can be also expressed in terms of entanglements of the nanotubes within the matrix. Higher entanglements might take place for the MWNT case, then CN<sub>x</sub> and PS-g-CN<sub>x</sub> nanotubes. The differences in the entanglements may be due to the stability of the nanotube dispersion. Thus, better dispersion was observed when functionalized and polymer-grafted nanotubes were used due to the better stability of these materials in the polymer matrix, i.e. better contact polymer-tube. In the case of MWNTs a better contact tube-tube was observed that determines a worse dispersion, and worse stability of the filler in the matrix.

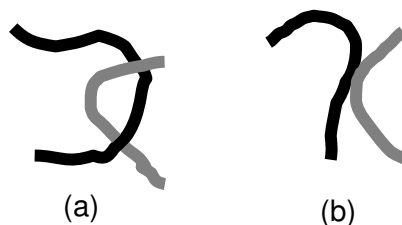


Fig. 7.16. Schematic representation of (a) the entanglement of the nanotube fillers, and (b) the contact between nanotube fillers (PS/MWNT, PS/CN<sub>x</sub>, and PS-g-CN<sub>x</sub>).

Furthermore, the increase in thermo-mechanical stability was understood not only by the interactions between the polymer chains and the nanotube surface, but also by the formation of a percolating entangled nanotube network. Thus entanglements (Fig. 7.16 (a)) between tubes explain the storage modulus measured in this large temperature range where the polymer behaves as a viscous fluid. Similar results were observed in polymer-nanotube composites of P(S-BuA) and MWNT [1] prepared by slow solvent evaporation and freeze-drying and hot pressing procedures.

The scheme 7.16 also explains the effect of the processing conditions on thermo-mechanical results. The processing conditions also aid in the formation of both kind of interactions between tubes, i.e. entanglement and contact. As was observed by Dalmas *et al* [1] the slow evaporation of solvent in the composite films favors the formation of more entanglement between tubes than tube contacts; nevertheless, in our case the posterior hot pressing could modify some entangled tubes to simple contact. This behavior was more frequently in PS-*g*-CN<sub>x</sub>, due to the polymer layer surrounding them, next in CN<sub>x</sub> because of the good polymer wetting, and finally in MWNTs. This means that in the case of MWNT more entangled tubes was obtained than simply contacts, followed by CN<sub>x</sub> and PS-*g*-CN<sub>x</sub> were less entanglement and more simply contact could be possible. Thus, in this experimental case, it seems that the simple contact of carbon nanotubes (b) was not enough to reinforce the polymer composites due to the filler. Furthermore, the entanglements between nanotubes appear to have low effect on the mechanical reinforcement, as was observed by the low increase in the elastic modulus of PS/CNTs composites.

We can be surprised that the surface functionalization of carbon nanotubes (N-doping, radical functionalization and even PS-grafting) does not improve the mechanical properties of the corresponding nanocomposites. It is thus difficult to evoke a difference in stress transfer efficiency, as it could be expected, i.e. stress transfer should be better in the case of the grafted nanotubes, because of the DMA results that did not give information about the stress transfer matrix-filler. Thus, using the technique information, in summary a possible interpretation of the thermo-mechanical behavior of PS/CNT composites can be based on the dispersion and polymer-filler interaction. These facts are related to the morphology, as proposed in the previous part (electrical properties). As the dispersion of the nanotubes increases, the nanotube network can be modified, i.e. less entangled. Thus, the rubbery plateau might be lower.

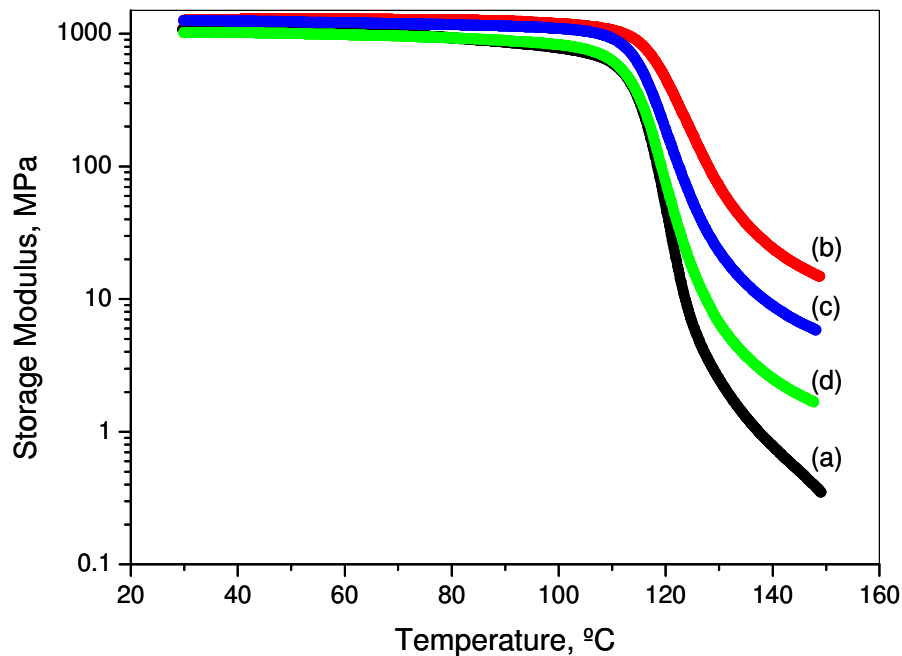


Fig. 7.17. Comparison of the Storage Modulus of (a) PS and PS-based composite with (b) MWNT, (c) CN<sub>x</sub> and (d) PS-*g*-CN<sub>x</sub> nanotubes at a concentration of 5.0 wt%.

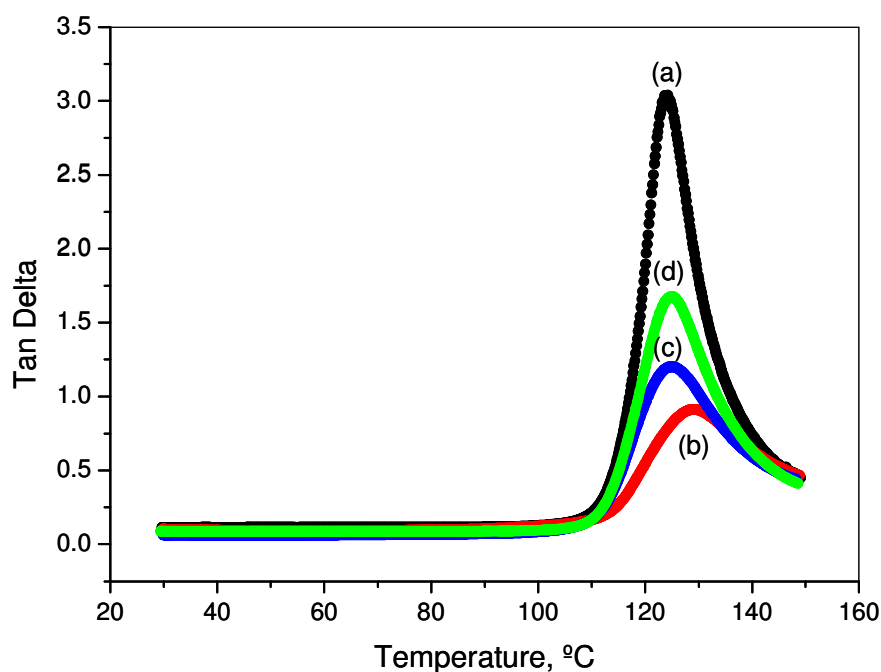


Fig. 7.18. Comparison of the Tan  $\delta$  of (a) PS and PS-based composite with (b) MWNT, (c) CN<sub>x</sub> and (d) PS-g-CN<sub>x</sub> nanotubes at a concentration of 5.0 wt%.

To sum up, some reinforcement in the storage modulus could be obtained below  $T_g$  that could not be observed due to the precision of the DMA measurements and because the lack of reproducibility tests. Above  $T_g$ , the measurement precision becomes less important because at this region (i) the difference in the nanotube and polymer modulus are higher, and (ii) the entanglements of nanotubes and polymer chains take an important place in the matrix reinforcement.

The addition of nanofillers (MWNTs, CN<sub>x</sub> and PS-g-CN<sub>x</sub>) to a polymer matrix revealed reinforcement in the rubbery plateau of the materials in all cases. Higher reinforcement have been obtained when MWNT are used, followed by CN<sub>x</sub> and PS-g-CN<sub>x</sub> nanotubes. This result is interpreted in terms of modification of nanotube entanglements.

In conclusion, DMA measurements show that there was a progressive increase in the storage and loss modulus with increasing nanofillers concentration over the observed range of temperature. Furthermore, an increment of the utilization temperature was obtained in the case of PS/MWNT due to the  $T_\alpha$  shifts with concentration. Thus, PS/MWNT are thermo-mechanically more stable.

At this point is important to say that the analysis of the load transfer between nanotubes and polymer could not be carried out using DMA technique in which only a linear region deformation could be applied to composite films.

### 7.2.1.2.2. PS-nanotube composites mechanical modeling

The DMA measurements of PS/CNTs were modeled using both the Halpin-Kardos Model and the Statistical Percolation Model, as other reports have been proposed.

#### *Halpin Kardos Model*

To understand the properties of the PS/CNTs composite materials, the Halpin Kardos model (mean-field approach for isotropic short fiber composites) was used:

$$\frac{M_c}{M_m} = \frac{1 + \xi\eta\psi}{1 - \psi} \quad [7.3]$$

where  $\psi$  is the filler volume fraction,  $M_m$ ,  $M_f$  and  $M_c$  are the matrix, fiber and composite

moduli,  $\xi$  is a form factor, and  $\eta = \frac{\frac{M_f}{M_m} - 1}{\frac{M_f}{M_m} + \xi}$ .

This model takes into account the modulus of each phase, as well as the geometry of the particles without considering the interaction of the particles between each other (i.e. effect of entanglements between nanotubes or polymer-nanofiller interactions). The parameters of the model are the modulus of the polymer matrix and filler, and the form factor.

The results of the modeling are depicted in Fig. 7.19. The calculations are carried out using some of the measured values, for example the PS matrix modulus (Table 7.5). Consequently, the fiber modulus is also used as a fitting parameter. The values corresponding to the better fit are as follows :  $M_{f \text{ MWNT}} = 1000$ ,  $M_{f \text{ CN}_x} = 300$  and  $M_{f \text{ PSgCN}_x} = 100$ .

As can be seen, in order to reproduce the modulus difference, we have to assume that nanofillers exhibit great differences in their modulus depending on their type. The high difference in filler modulus obtained by estimation using the Halpin Kardos model follows.  $M_{f \text{ MWNT}} > M_{f \text{ CN}_x} > M_{f \text{ PSgCN}_x}$ . This behavior is unexpected for bamboo type nanotubes of the same geometry and aspect ratio (MWNT and  $\text{CN}_x$ ), even when chemical functionalization (i.e. nitrogen doping) have take place (PS-g- $\text{CN}_x$ ). Thus, the probable explanations to the obtained differences in the calculated modulus are:

- (i) the intrinsic differences in the mechanical properties of the nanotube fillers by a combination of factors (as inclusion of defects in the nanotube structure, among others) and that have not been measured here, or
- (ii) the model is not capable to take into account the interactions between matrix and filler that modify the modulus measurement. These interactions became more important when the  $\text{CN}_x$  nanotubes are further functionalized by the chemical functionalization and polymer grafting procedure, as in PS-g- $\text{CN}_x$  fillers.

In this case, we consider that the most probable explanation of the obtained fiber modulus is the second one.

Furthermore, the calculated form factors,  $\xi$ , for MWNT, CN<sub>x</sub> and PS-g-CN<sub>x</sub> nanotubes that depend on the aspect ratio and the geometry of the fillers have values around 1300 in all nanotube cases.

At this point, it is possible to state that the Halpin-Kardos model is adequate to fit the experimental data and correctly describe the PS/CNTs composites behavior above T<sub>g</sub>, even though the model consider questionable hypothesis according to this system, as the use of stiff fibers as fillers (nanotubes are flexible) and the absence of matrix-filler interaction (observed by microscopy). Furthermore, the estimated modulus parameters ( $M_f$ ) seems to be present a high difference between each other, according to the similar geometry of nanotubes.

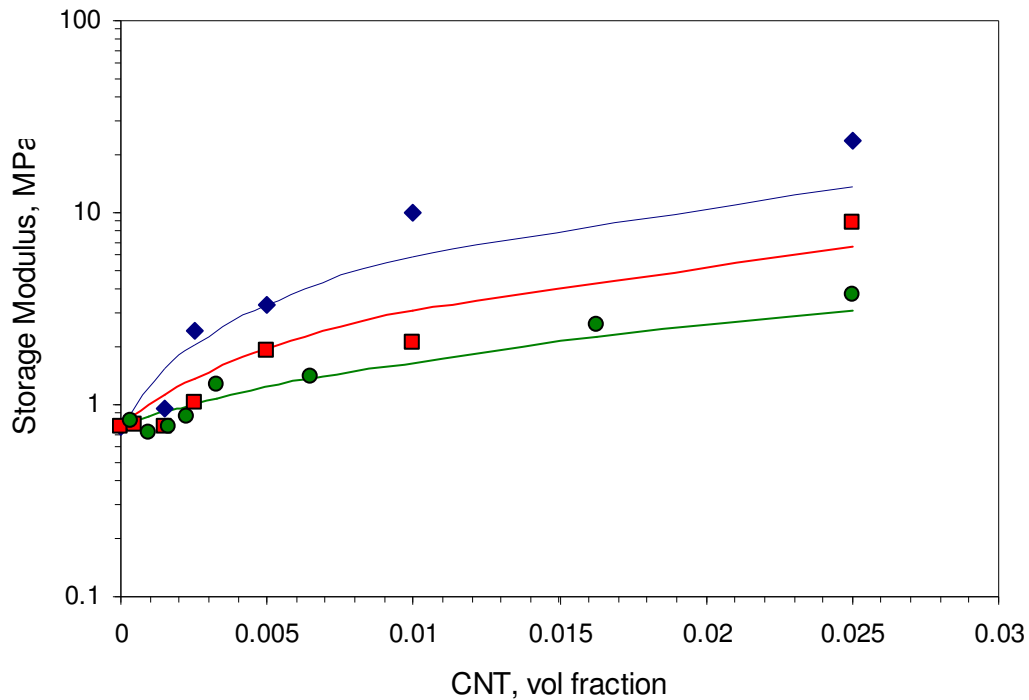


Fig. 7.19. Storage modulus of the PS/CNTs composites at several volume fractions of: (◇) MWNT, (□) CN<sub>x</sub> and (○) PS-g-CN<sub>x</sub> nanotubes. Lines show the Halpin-Kardos Model calculated values.

Table 7.6. Storage modulus of PS/CNTs composites at 60°C and several filler and nanotube content from 0 to 5.0 wt%.

PS/MWNT Vol. Frac.	Storage Modulus, MPa	
	Experimental	Calculated
0	1030.0	1030.0
0.00150	1252.8	1031.5
0.00250	957.9	1032.5
0.00500	1551.6	1035.0
0.01000	1223.0	1040.1
0.02500	1292.0	1055.6

Using the same calculated values for the aspect ratio and fiber modulus, as well as the experimental data for PS (Table 7.5), the composite modulus as a function of filler in the glassy plateau was estimated and described in Table 7.6.

Table 7.6. Storage modulus of PS/CNTs composites at 60°C and several filler and nanotube content from 0 to 5.0 wt% (cont.).

PS/CN <sub>x</sub> Vol. Frac.	Storage Modulus, MPa	
	Experimental	Calculated
0	1030.0	1030.0
0.00050	1368.3	1030.1
0.00150	1604.2	1030.4
0.00250	1283.0	1030.7
0.00500	1396.0	1031.5
0.01000	1352.7	1033.0
0.02500	1209.4	1037.7

PS/PS- <i>g</i> -CN <sub>x</sub>		Storage Modulus, MPa	
Filler Vol. Frac.	Nanotubes Vol. Frac.	Experimental	Calculated
0	0	1030.0	1030.0
0.0005	0.0003	1060.7	1030.0
0.0015	0.0010	1439.1	1030.1
0.0025	0.0016	1200.3	1030.1
0.0035	0.0023	1388.5	1030.2
0.0050	0.0033	1235.6	1030.3
0.0100	0.0065	1094.8	1030.6
0.0250	0.0163	984.6	1031.6
0.0385	0.0250	1364.1	1032.5

As can be seen, the calculated modulus values in the glassy plateau (60°C) are almost constant and around the measured moduli of PS matrix. Furthermore, higher variations are observed when MWNT were used as filler, and consecutively when CN<sub>x</sub> and PS-*g*-CN<sub>x</sub> nanotubes due to the fiber modulus used in calculations. From these results, it is observed that very low variation of calculated modulus versus volume fractions is expected. Thus, the differences with the experimentally data could be related to measurement difficulties (due to DMA precision), differences in the samples homogeneity and the number of samples evaluated, and, as in the previous case, to the limitation in the theoretical calculation due to the model hypotheses.

In any case, the prediction of the model established that almost constant values of the storage modulus at the glassy plateau are expected if the materials behave as the Halpin-Kardos model determines.

In summary, the behavior of the storage modulus of PS/CNTs composites and the restricted hypothesis of the Halpin-Kardos model indicate that it is necessary to consider additional parameters, as the existence of the interaction between the elements of the

system (polymer-polymer, polymer-nanotube and nanotube-nanotube) and the geometrical percolation [20].

The interactions are more important in the case of PS-grafted CN<sub>x</sub> < CN<sub>x</sub> < MWNT naturally because of the effect of the chemical functionalization and the polymer-grafted.

Furthermore, the geometrical percolation phenomena observed in PS/CNTs by electrical characterization requires additional efforts to understand the behavior of these composites. Therefore, the use of the Statistical Percolation Model applied to the mechanical model of PS/CNTs was carried out.

#### *Statistical Percolation Model*

The percolation model considers that the storage modulus can be calculated using the formation of a percolating network of fibers,

$$G = \left[ \frac{1 - 2P(\psi) + P(\psi)\psi G_s G_r + (1 - \psi)P(\psi)G_r^2}{(1 - \psi)G_r + (\psi - P(\psi))G_s} \right] \quad [7.4]$$

where  $P(\psi) = \left( \frac{\psi - \psi_c}{1 - \psi_c} \right)^b$ ,  $\psi$  is the volume fraction,  $\psi_c$  is the percolation threshold,  $G_s$  is the polymer matrix modulus and  $G_r$  is the filler modulus.

As in the previous case, the calculation of the storage modulus of PS/CNTs composites above T<sub>g</sub> is performed with fixed values for the polymer matrix modulus (measured values reported in Table 5), the experimental volume fractions, and adjusted values for the nanotube moduli and the percolation threshold. The calculated values were adjusted to obtain the better fit and are the model parameters.

In this case, the obtained filler modulus of nanotubes are  $G_{r, MWNT} = 1000$ ,  $G_{r, CN_x} = 150$ , and  $G_{r, PSgCN_x} = 15$ . Again, the estimated fiber modulus for each nanotube type is highly different compared to each other. This fact, as in the previous model, could be apparently due to their chemical functionalization. Nevertheless, the interaction between PS matrix and nanotubes and nanotubes-nanotubes was neglected and has to be considered in the modulus measurement.

The percolation threshold are  $\psi_{c, MWNT} = 0.0006$ ,  $\psi_{c, CN_x} = 0.0001$  and  $\psi_{c, PSgCN_x} = 0.0001$ . The values were estimated according to the experimental data.

Fig. 7.20 presents the comparison between experimental and calculated values for the PS/CNTs storage modulus using the Percolation model. As can be seen, the percolation model also fit well the experimental data.

#### *Comparison between models*

The Halpin-Kardos model establishes that the system could be understood as a mixing law of rigid fibers in a soft polymer matrix, when the modulus values of the nanotubes (MWNT, CN<sub>x</sub> and PS-g-CN<sub>x</sub>) are highly different and the aspect ratio is taken into account.

The Statistical Percolation Model is based on the assumption that the PS/CNTs composites form percolating networks that with an appropriate fiber modulus induce the

reinforcement effect. In this case, it seems that the percolation network was formed, in fact at low percolation thresholds, but maybe the fiber modulus was not enough to reinforce the system.

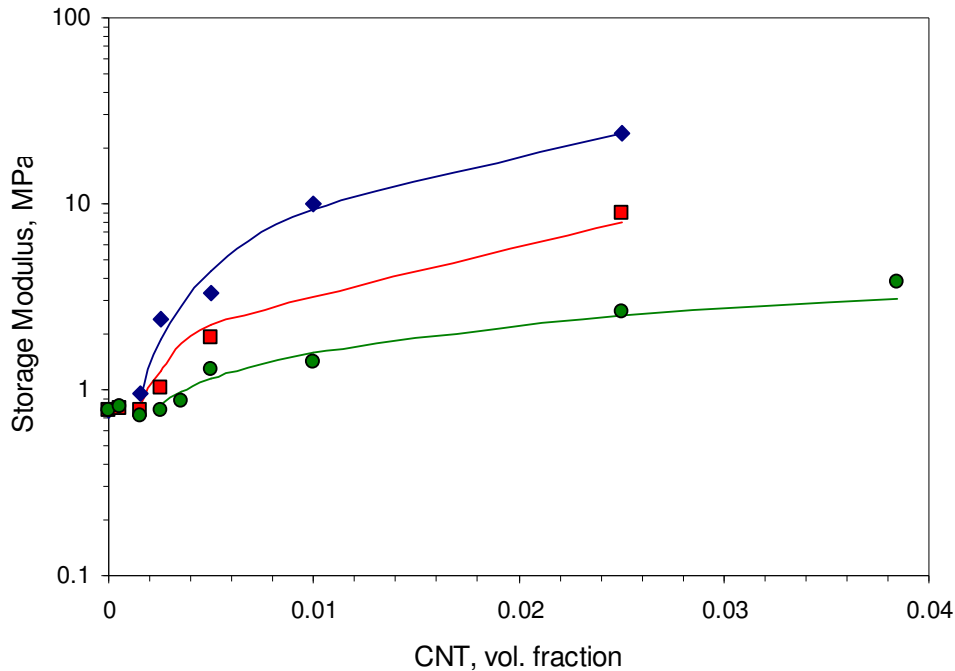


Fig. 7.20. Storage modulus of the PS/CNTs composites at several volume fractions of: ( $\diamond$ ) MWNT, ( $\square$ ) CN<sub>x</sub> and ( $\circ$ ) PS-g-CN<sub>x</sub> filler. Lines show the fits obtained with the Percolation Model.

After the comparison of both models, it can be said that the Halpin-Kardos and the percolation models describe appropriately the phenomena, at least in terms of the mathematical description. Nevertheless, in both cases, the interaction between nanotubes and fillers are neglected. Thus, the adjustment obtained through filler modulus modification that may be unrealistic. The lack in the hypotheses to correspond with the experimental phenomenon has to be overcome. It could be more convenient to search a special model for these PS/CNTs composite cases. Several additional models have been proposed, as the modeling approach based on the discretization of CNTs proposed by Dalmas *et al* [1]. In our case the proposition of a modelization of the phenomena is out of the scope of this thesis.

### 7.2.1.3. Analysis of the relation between the electro-mechanical properties and the microstructure of the PS-nanotube composites.

The combined analysis of the physical properties results for the PS/CNTs will be described in the following paragraphs.

### *PS/MWNT*

Thermal characterization of the composite revealed no changes in the  $T_g$  by DSC characterization. This behavior was attributed to a soft interaction between the nanotubes and PS (due to the absence of covalent attachment) that reflect no change in the polymer chain mobility. DMA results revealed a slight increment in the  $T_\alpha$  values of the composites, associated to an increase of  $G'$  in the rubbery plateau. However no clear trend in the maximum of the  $G''$  peak was observed as a function of the filler content, indicating only low effect on molecular mobility. Furthermore, the morphological analysis of PS/MWNT revealed a relatively good dispersion of individual nanotubes within the matrix, even though some nanotube bundles could also be observed. A low PS-nanotube interfacial strength was proposed from the observation of individual pulled-out nanotubes. All these material characteristics determine the measured conductivity and storage modulus values. First, the dispersion level of the nanotubes favors the formation of a percolating path within the materials that reflects high conductivity values and low percolation thresholds. Nevertheless, as far as the mechanical properties are concerned, the storage modulus was slightly impacted below  $T_g$  and more impacted above  $T_g$  as an increase in the modulus storage. These phenomena could be attributed to:

- (i) *Below  $T_g$* : to the unobserved reinforcement probably due to the near values of the fiber and matrix values. In addition, the technical and experimental challenges could also contribute to the impossibility to observe coherent modulus values.
- (ii) *Above  $T_g$* : the reinforcement observed in the rubbery plateau could be attributed, among other aspects, to the effect of the filler in the system by an increase in the entanglement of the polymer due to the presence of nanotubes.

The storage modulus behavior modeling of PS/MWNT also indicates that the formation of a geometrical percolation network with moderate interface interaction has taken place. This percolation is enough to enhance the conductivity and to slightly enhance the material stiffness in the rubbery plateau.

### *PS/CN<sub>x</sub>*

As in the case of PS/MWNT, the  $T_g$  of PS/CN<sub>x</sub> composites, measured by DSC, revealed no change. This behavior was confirmed when no change in the  $T_\alpha$  was obtained by DMA. The microstructure studies of PS/CN<sub>x</sub> qualitatively revealed a CN<sub>x</sub> nanotubes good dispersion with apparently good properties of contact between the polymer matrix and the filler. From these results only, a relatively good interfacial strength could be expected.

Complementary studies of the conductivity determined that raw CN<sub>x</sub> nanotubes exhibit a lower conductivity than raw MWNTs. This lower value is reflected in the composite conductivity measurements where a lower maximum conductivity was observed in comparison with MWNTs. In addition, the percolation threshold was observed at low content filler values which are explained by the formation of a percolating path within the polymer matrix (same percolation threshold values with CN<sub>x</sub> and with MWNTs). Finally, the interaction between the nanotubes and the polymer was analyzed using DMA. The obtained mechanical results revealed that the entanglement was lower when MWNTs were functionalized by nitrogen doping. Thus, it could be possible to establish that the enhanced chemical reactivity of CN<sub>x</sub> nanotubes that explain the better dispersion and interface interaction could be useful when a geometrical percolation is needed, but

undesirable if an efficient polymer chain entanglement is required. The conductivity and storage modulus measured values were lower than the MWNTs mainly because of the presumable inherent low conductivity and stiffness of  $CN_x$  nanotubes due to chemical functionalization. Additional explanations to the low increment in the storage modulus was focused on the lower entanglement obtained when  $CN_x$  nanotubes are present in the composite.

Thus, for  $CN_x$  nanotubes, it becomes necessary to determine the raw values to select an appropriate polymer matrix in order to obtain useful and desirable properties.

#### *PS/PS-g- $CN_x$ composites*

DSC and DMA measurements of the *PS/PS-g- $CN_x$*  composites revealed no changes in the  $T_g$  nor in the  $T_\alpha$ . In this case, the explanation to the unchanged  $T_\alpha$  seems to be related to a plasticizing effect of the nanotube brushes or the similarity in the molecular weight of the matrix and the attached chains. In this case, the microstructure corresponded to good dispersed materials with apparent good interfacial interactions. As in the previous case, it was expected that these characteristics were sufficient to obtain good mechanical properties.

As showed by the results, the *PS-g- $CN_x$*  fillers were less conductive than the raw  $CN_x$  nanotubes. Thus, the maximum conductivity values of the composites were lower than with other type of nanotubes. Nevertheless, an increase in the composite conductivity was attained, indicating that a geometrical percolation was achieved. A minor increase in the storage modulus of this material was observed in the rubbery plateau as compared to the others nanotube types, indicating that the polymer chain entanglement was weaker when *PS-g- $CN_x$*  fillers were present in the system. This behavior is explainable due to the type of contact between the polymer brushes and the polymer matrix, i.e. polymer-polymer. It seems that the high efficient reinforcement expected for polymer-grafted materials could not be obtained.

To summarize, two main effects of the CNTs on the mechanical behavior were observed in *PS/CNTs* composites: (i) an improvement in the thermo-mechanical stability (increase in the main relaxation temperature), and (ii) mechanical reinforcement above  $T_g$ . The reinforcement of the materials in the rubbery plateau seemed to follow:  $G'_{MWNT} > G'_{CN_x} > G'_{PS-g-CN_x}$ . Even though, the increase in modulus is quite low in comparison with other high aspect-ratio fillers.

These mechanical properties seem to be dependent on the filler dispersion with the eventual formation of a percolating network, and on the filler-filler and filler-matrix interaction.

Furthermore, the presence of carbon fillers (MWNT,  $CN_x$  and *PS-g- $CN_x$* ) in *PS/CNTs* allows the material to be electrically conductor at low filler contents.

For the case of  $CN_x$  and MWNTs, the differences in the percolation thresholds and in the extent of diminution of conductivity compared to pristine nanotubes could be related to the dispersion level that was better in  $CN_x$  fillers, but also the formation of agglomerates in MWNT that could be an impediment to the formation of the geometrical nanotube network. Particularly, for the case of *PS-g- $CN_x$*  filler a polymer coating, which prevents direct contact between nanotubes lower the maximum conductivity compared to the other

filler types. This value is lower also than the expected intrinsic nanotube conductivity. This result has also been observed by others [15].

One of the most relevant ideas is that in all three cases the materials exhibit a different behavior in their morphological and physical properties that evidenced the chemical functionalization of nanotubes. Thus, the optimization of the systems to obtain specialized properties becomes necessary, for example by using other types of grafting or of polymer matrices.

Finally, it was verified that the microstructure of the material strongly determines the thermal, electrical and mechanical properties of PS/CNTs composites.

## 7.2.2. PEO-based nanocomposites

### 7.2.2.1. PEO-nanotube composites electrical properties

Figs. 7.21 to 7.23 show the real conductivity of the PEO-based nanocomposites using PEO210k (MW=210,000 gr/mol). Numerical values are summarized in Table 7.5. Additional images for the imaginary conductivity of nanocomposites are displayed in Appendixs 7.5.

From Fig. 7.21 it is observed that the pure PEO sample exhibits a capacitive behavior. The conductivity value is around  $3.78 \times 10^{-7}$  S/m at 1 Hz. This value is comparable to those obtained before for almost similar systems [21, 22].

The addition of conductive nanofillers notably increases the conductivity of the samples. First of all, higher conductivity values were obtained when MWNTs are used as fillers, followed by CN<sub>x</sub> and then PS-g-CN<sub>x</sub> (Table 7.7). Even if the number of studied samples is low, it is clear that percolation thresholds are low and follow the same order as the high conductivity maximum values: percolation in PEO/MWNT is attained below 0.5 wt%, whereas it is observed in PEO/CN<sub>x</sub> between 0.5 and 2.0 wt%. Finally, PEO/PS-g-CN<sub>x</sub> materials do not present any percolation even at 2.0 wt%.

The conductivity behavior of PEO/CNT composites could be related to the:

- (i) Intrinsic conductivity of nanotubes that follows  $\sigma_{\text{MWNTs}} > \sigma_{\text{CN}_x} > \sigma_{\text{PS-g-CN}_x}$ , as was extensively commented previously,
- (ii) Type and resistance of contact between fillers in the percolating network, i.e. direct tube-tube contacts with lower electrical resistance or by dielectric polymer-polymer contacts, and the number of contacts,
- (iii) Dispersion of the nanotubes, that follows MWNT > CN<sub>x</sub> > PS-g-CN<sub>x</sub> as commented in morphology section, and the
- (iv) Crystallinity properties of the PEO matrix.

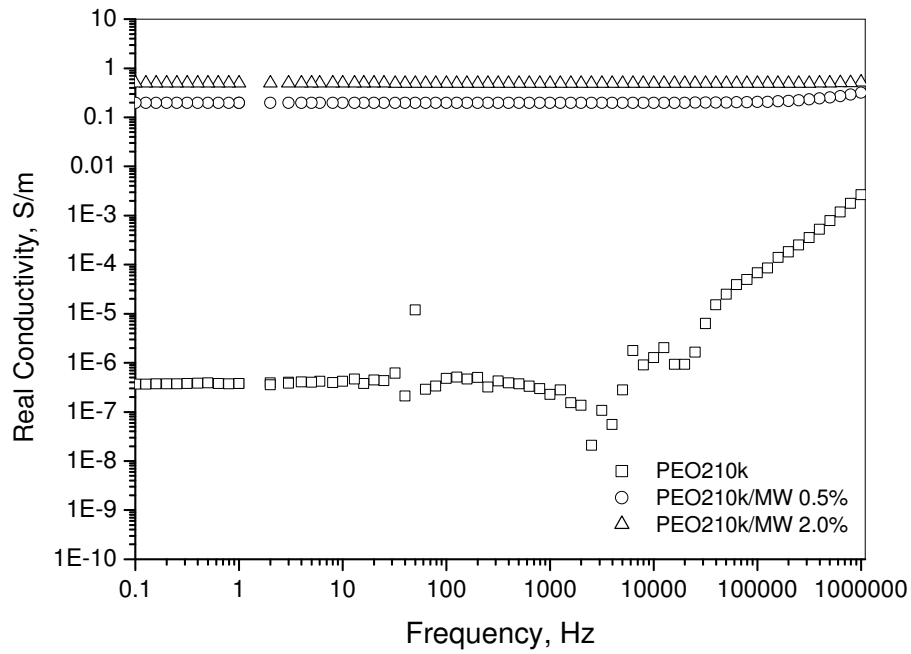


Fig. 7.21. Real conductivity of PEO210k/MWNT nanocomposites vs. frequency at filler weight fractions of 0.1 to 5.0 wt% and applied voltage of 0.1 V.

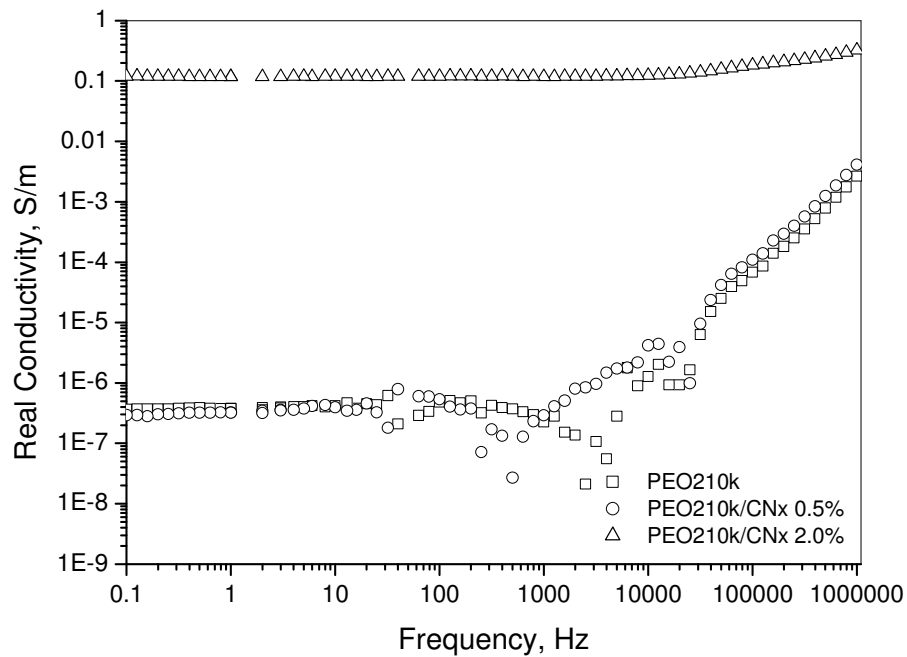


Fig. 7.22. Real conductivity of PEO210k/CN<sub>x</sub> nanocomposites vs. frequency at filler weight fractions of 0.1 to 5.0 wt% and applied voltage of 0.1 V.

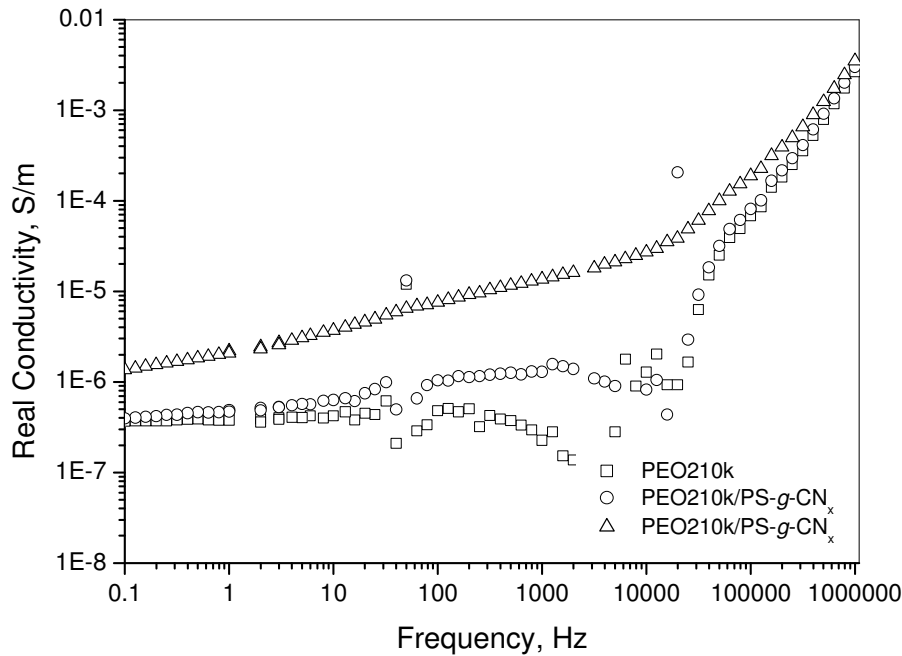


Fig. 7.23. Real conductivity of PEO210k/PS-*g*-CN<sub>x</sub> nanocomposites vs. frequency at filler weight fractions of 0.1 to 5.0 wt% and applied voltage of 0.1 V.

Table 7.7. Maximum conductivity values at 1 Hz and cristallinity for PEO210k/CNTs at 2 wt%.

Sample	$\sigma_{\max}$ S/m	Crystallinity
PEO210k	3.78E-07	0.62
PEO210k/MW	4.94E-01	0.64
PEO210k/CN <sub>x</sub>	1.18E-01	0.67
PEO210k/PS- <i>g</i> -CN <sub>x</sub>	2.08E-06	0.65

Indeed, the better dispersion was obtained in the case of MWNTs in PEO/MWNT, and a good dispersion could be associated in this nanocomposite to the formation of an efficient geometrical percolating conductive network at low filler contents. Furthermore, the cristallinity extent was only slightly increased when MWNTs were added to the system that also could aid in the conductivity of this system and in the formation of a percolating network. On the contrary, the quality of the dispersion was lower when CN<sub>x</sub> and PS-*g*-CN<sub>x</sub> nanotubes were used, and even more, the cristallinity of the PEO samples was higher than in the previous case (as can be seen in Table 7.7). Thus, the difference in conductivity of the PEO based nanocomposites can be associated mainly to both combined effects, dispersion quality, as well as some cristallinity changes in PEO.

Due to the mechanical fragility of the PEO210k/CNTs composites, it was not possible to have enough conductivity measurement points to model the system. Therefore, some other composite samples were prepared using PEO14k (MW=14,000 gr/mol).

The PEO14k/CNT composite films were cut in parallelepiped samples of  $0.48 \pm 0.02$ ,  $19.12 \pm 0.75$  and  $5.07 \pm 0.15$  mm. The analyzed PEO14k/CNTs composite samples corresponded with loadings of 0.1 to 5.0 wt%. The electrical conductivity as a function of frequency obtained by AC impedance for both nanotube loadings is presented in Appendix 7.5.

As for the case of PEO210k composites, the PEO14k/CNT materials exhibit capacitive and conductive behaviors depending on the filler content (below or above the percolation threshold, respectively) (Appendix 7.5). These behaviors are also dependent on the nanofillers type and concentration. As for PEO210k/CNT, higher values of the maximum conductivity are observed when MWNT are added to PEO14k, followed by  $CN_x$  and PS-g- $CN_x$  nanotubes, i.e.  $\sigma_{MWNT} > \sigma_{CN_x} > \sigma_{PS-g-CN_x}$ . This behavior can also be related with the expected morphology (i.e. dispersion level of the nanotubes) of the samples that can be predicted from the PEO210k results. It is expected that the MWNTs are better dispersed than  $CN_x$ , which are themselves better dispersed than PS-g- $CN_x$  nanotubes. As far as the PEO crystallinity is concerned, it could not be possible to argue anything due to the changes of the polymer matrix because the DSC measurements were performed over PEO210k. Thus, additional thermal measurement of PEO14k composite materials has to be done in detailed works on this special topic.

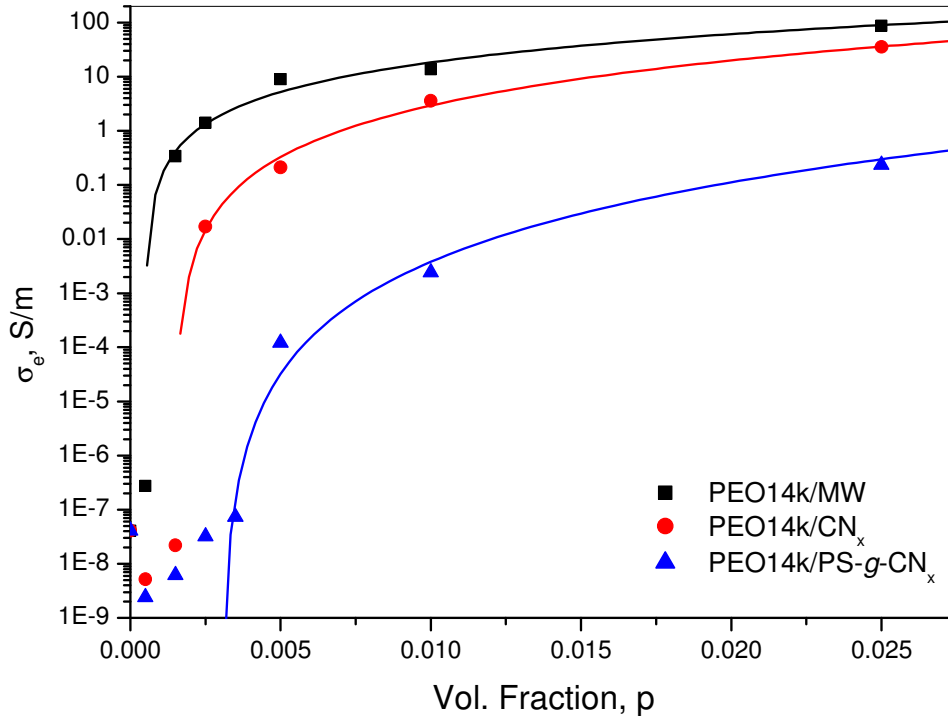


Fig. 7.24. Real part of the AC electrical conductivity at 1 Hz and 0.1 V for PEO14k/CNT at several filler contents. Comparison with statistical percolation theory (solid lines).

Fig. 7.24 displays the real conductivity of PEO14k-based composites at several volume fractions and their modeling using a statistical percolation model. Numerical values are summarized in the Table 7.8. The detailed procedure to obtain the parameters is depicted in Appendix 7.6. The best fits were found by incrementally varying  $p_c$  until the best linear fit to the equation was found.

Table 7.8. Experimental conductivity values and statistical percolation parameters for PEO14k/CNT composites.

Nanocomposite	$p_c$ vol. frac.	Percolation Model				$\sigma_{\max}$ S/m
		t	$\pm\Delta t$	$R^2$	$\sigma_0$ (100%CNT)	
PEO14k						4.09E-08
PEO14k/MW	0.0005	1.68	0.150	0.988	45569	87.03
PEO14k/CN <sub>x</sub>	0.0015	2.47	0.147	0.997	378879	35.51
PEO14k/PS- <i>g</i> -CN <sub>x</sub>	0.0030	3.82	0.412	0.989	609101.96	0.23

First of all, a main difference between the pure PEO210k and PEO14k conductivity values is detected (comparing Fig. 7.21 to 7.23). It seems that the molecular weight of the polymer matrix affects the maximum conductivity of the material. The higher molecular weight PEO indeed presents lower maximum conductivity. This difference could be explainable only by difference in cristallinity, but more experiments are necessary to explain this behavior. Thus, for the PEO14k/CNT composites, lower percolation values and higher maximum conductivity values are obtained than those measured for the PEO210k/CNT composites. In both cases, the presence of a geometrical percolation network of CNTs was established within the materials. Even though the lowest percolation thresholds seem to be obtained with MWNTs, PS-*g*-CN<sub>x</sub> can be described as a very good alternative to the conductivity increment of PEO14k matrices.

#### *Comparison of PEO/CNTs with PS/CNTs composites*

It has to be said that no extensive investigation of the electrical properties of the PEO-based nanocomposites has been performed. Nevertheless, the nanotubes seem to behave in the same way independently of the matrix (PS or PEO), provided that the same dispersion level is obtained, and in the case of PEO that the cristallinity remain almost constant. From the modeling, it was found that the dispersion level of the nanotubes greatly influences the value of the percolation threshold. Nevertheless, other factors are involved like the nanotubes intrinsic conductivity, the nature of the contact polymer-carbon nanotube, as was extensively commented in the PS/CNTs composites, and the matrix cristallinity.

The abnormally high value of the critical exponent t in the percolation model, found for both PS/PS-*g*-CN<sub>x</sub> and PEO/PS-*g*-CN<sub>x</sub> indicate that a distribution of contact resistances exists in the materials, most probably because of the deformable PS grafted layer.

In addition, Croce *et al* [23] reported that the glass transition temperature (T<sub>g</sub>) and the cristallinity of nanocomposite have a great effect on the conductivity. However, in this particular case, some homogeneity challenges in the materials did not allow to be

completely sure about the validity of thermal properties measured. Thus, a direct correlation could not be possible. Anyway, as was reported [21], when CNTs were added to the polymer matrices, the heat of melting and  $T_g$  decrease only slightly, which indicates that the polymer chain flexibility of the PEO/CNT systems is similar to that of the pure PEO system. These experiments were reported in order to check that a similar conduction phenomenon, as observed with PS, was obtained when carbon nanotubes are added to a semi-crystalline polymer matrix like PEO.

### 7.2.2.2. PEO-nanotube composites mechanical properties

The mechanical properties of the PEO/CNTs composites materials were obtained using a DMA in tension mode. The analyzed samples were PEO/MWNT, PEO/CN<sub>x</sub> and PEO/PS-g-CN<sub>x</sub> at 0, 0.5 and 2.0 wt%. Due to the lack of time, we only performed a preliminary study, in order to found the tendencies in the mechanical behavior of the materials. These preliminary results have not yet been confronted to models prediction.

The storage modulus and loss factor of the PEO/MWNT materials, as an example of all PEO/CNTs behavior, are depicted as a function of temperature at constant frequency in Fig. 7.25 and 7.26.

Polyethylene oxide is a semicrystalline polymer, i.e. consist of sequences of crystalline and amorphous lamellae. Its mechanical behavior could be understood as a composite system where the crystalline sections are considered as the fillers. Thus, when the material is filled with carbon nanotubes it is expected that the mechanical properties will be drastically modified depending on the (i) PEO morphology and (ii) the localization of the nanotubes at the crystalline or amorphous domains.

PEO mechanical behavior was studied between the range of -90°C to 20°C. In the glassy region, below  $T_g$ , the PEO exhibited a storage modulus of about 5GPa, which corresponds, at least for the order of magnitude, to values previously reported [24]. In this region the modulus decreases only slightly with increasing temperature. Furthermore, as in the case of PS, in this zone the polymer stiffness is associated to the intermolecular van der Waals bonds.

Variations in the modulus below  $T_g$  were observed as nanotubes were added to PEO (Fig. 7.25 and Table 7.9). In all cases, the storage modulus exhibited a decrease from that of the pure PEO, independently of the type of filler and content, i.e. MWNT, CN<sub>x</sub> or PS-g-CN<sub>x</sub>. This decrease in the modulus could reflect a decrease in the crystallinity percentage of the composite due to filler addition. In our case, the changes in crystallinity were low between types of filler, and furthermore, as presented in Chapter 6 the DSC measurements have to be carefully evaluated due to the number of samples measured (precision problems) and the poor homogeneity of the PEO/CNTs composites. Consequently, both the variations in the  $T_g$  and  $T_m$  of PEO/CNTs composites due to homogeneity and measurement problems, could not be certainly correlated to the modulus decrease. In fact, the decrease in the modulus nanotubes is inexplicable considering the crystallinity percentage and the addition of nanotubes. Other factors, as the density of the materials due to the introduction of air bubbles, have to be evaluated in further works. With

all these observations, it is difficult to offer a complete and coherent explanation to the modulus decrease below  $T_g$  of PEO/CNTs. Even more, the other mechanical properties are also affected by these measure difficulties. Thus, some general comments will be described.

Around the  $T_g$  the modulus in PEO dropped to a secondary, or rubbery plateau with storage modulus around 1 GPa until the  $T_m$  of PEO polymer (around 70°C). The decay is observed at the main relaxation temperature,  $T_\alpha$ . Moderate increments in  $T_\alpha$  (associated to  $T_g$ ) (shown for PEO/MWNT as an example of PEO/CNTs) from -42°C of pure PEO to around -37°C for nanocomposites with 2.0 wt% were obtained by DMA. Nevertheless, this result cannot be verified by  $T_g$  modifications, as measured by DSC. Thus, again it could be possible that the measure and homogeneity difficulties favor the apparition of errors in the measurements.

The modulus storage values of PEO/CNTs composites at 20°C exhibited also a decrement respect to the pure PEO. This behavior determines that a chain entanglement was not form in these systems independently of the filler type, and most that the interfacial interactions were poor. Slight differences in the storage modulus at this range with the nanotube content (i.e. 0.5 or 2.0 wt%) need a detail research to confirm the relation order of the materials. Only using this information the effect of the content could be related to anisotropic and/or inhomogeneous samples.

The loss factor ( $\tan \delta$ ) depicted in Fig 7.26 revealed also the measure problems. In fact, the curves presented noisy experimental points, attributed to an inhomogeneous distribution of the filler. Consequently, it cannot possible to established representative changes as compared to the pure PEO matrix.

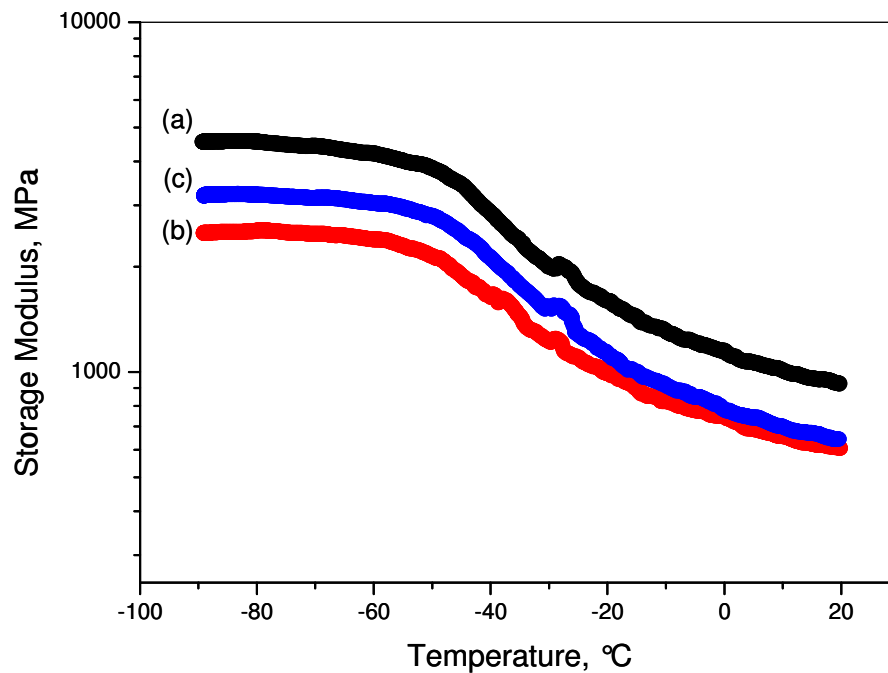


Fig. 7.25. Storage modulus of PEO/MWNT nanocomposite vs. temperature at filler weight fractions of (a) 0, (b) 0.5, and (c) 2.0 wt%.

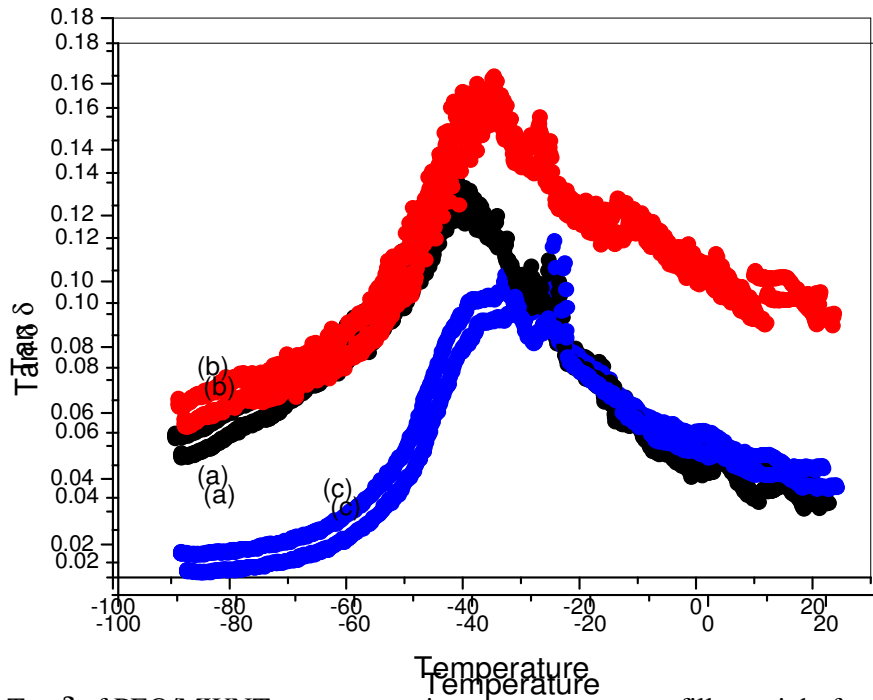


Fig. 7.26.  $\text{Tan } \delta$  of PEO/MWNT nanocomposite vs. temperature at filler weight fractions of (a) 0, (b) 0.5, and (c) 2.0 wt%.

Table 7.9. Mechanical properties of PEO/CNTs composites at several concentrations of MWNT,  $\text{CN}_x$  and PS- $g$ - $\text{CN}_x$  fillers.

PEO/CNTs	CNT, wt%	Storage Modulus, MPa		$T_w$ , °C	Tan $\delta$
		Below $T_g$	Above $T_g$ (20 °C)		
MW	0	4558.92	927.15	-42.04	0.13
	0.5	2498.45	606.29	-38.37	0.16
	2	3201.86	643.38	-37.27	0.10
$\text{CN}_x$	0	4558.92	927.15	-42.04	0.13
	0.5	3269.7	399.74	-54.89	0.17
	2	3011.72	800.786	-36.75	0.14
PS- $g$ - $\text{CN}_x$	0	4558.92	927.15	-42.04	0.13
	0.5	3723.63	818.313	-40.06	0.12
	2	2317.66	563.852	-37.45	0.13

A second decrease in the modulus (not observable in this graphs) is associated to the melting crystallites  $T_m$  (around 70°C) and thus again impacted by the experimental measurements. Between the  $T_\alpha$  and  $T_m$ , the modulus of a semicrystalline polymer is strongly dependent on the crystallinity (amount, dimension, texture of the crystalline phases), but in this case also affected by the homogeneity of the samples and quality of measurements due to the phase separation.

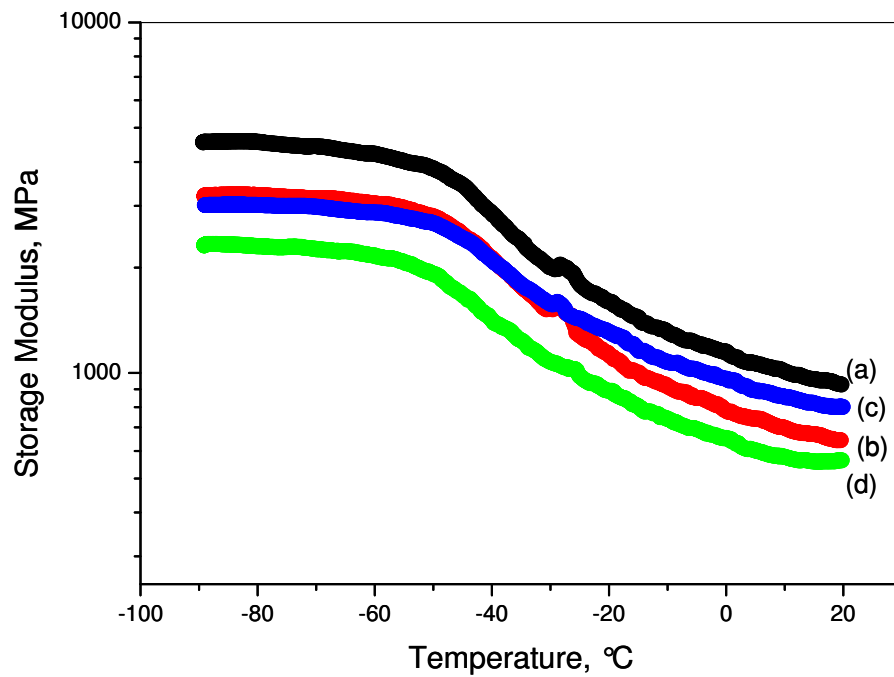


Fig. 7.27. Comparison of the Storage Modulus of (a) PEO and PEO-based composite with (b) MWNT, (c) CN<sub>x</sub> and (d) PS-g-CN<sub>x</sub> nanotubes at a filler concentration of 2.0 wt%.

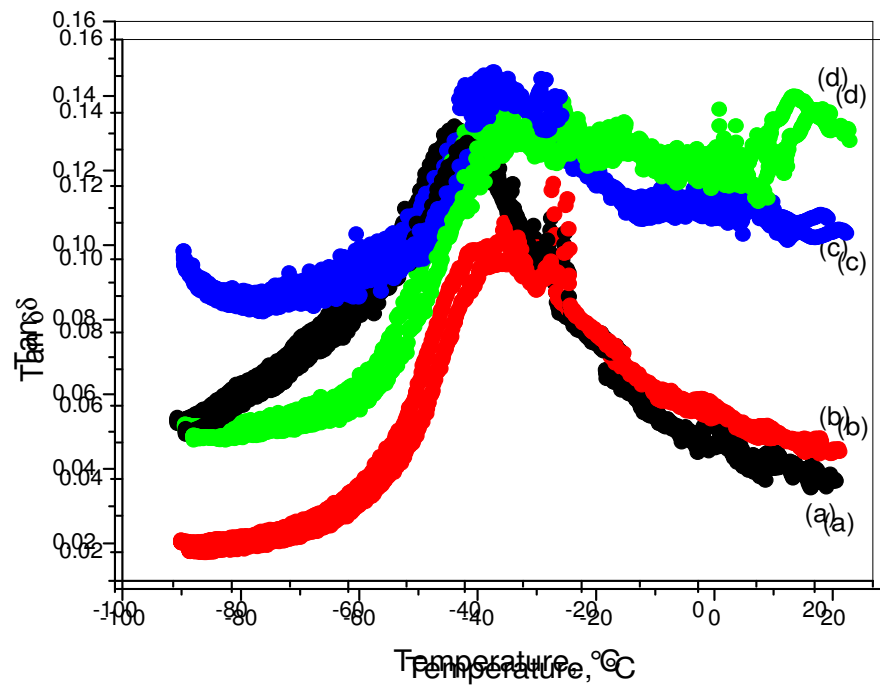


Fig. 7.28. Comparison of the Tan δ of (a) PEO and PEO-based composite with (b) MWNT, (c) CN<sub>x</sub> and (d) PS-g-CN<sub>x</sub> nanotubes at a concentration of 2.0 wt%.

Figs. 7.27 and 7.28 revealed the differences among the PEO/composites as a function of filler type. As can be seen, the modulus storage was lower as the functionalization of the nanotubes was increased. Thus, a better mechanical performance was obtained when PEO was charged with MWNT, then  $CN_x$  and finally PS-*g*- $CN_x$ . The explanation of this behavior is related to the microstructure of the materials defined by the interaction of each type of filler with the matrix that also affected the processing conditions of materials. In fact, it could be expected that stronger homogeneity problems are found due to the increasing immiscibility of the grafted PS within the matrix respect to MWNTs.

Furthermore, in Fig. 7.28 a strong alteration of the loss factor of the materials became evident as the functionalization of the nanotubes increase.

All these observed properties in the mechanical studies of PEO/CNTs composites determined that the polymer was not reinforced when nanotubes (MWNT,  $CN_x$  and PS-*g*- $CN_x$  nanotubes) were used as fillers. This phenomenon could be attributed mainly to several reasons, among them the (i) processing conditions that determine the material homogeneity and morphology, and (ii) the derivate measure problems (precision and reproducibility) in the properties of the material samples performed by DSC and DMA.

In summary, the PEO/CNTs composites exhibited one observable transition due to the beginning of the cooperative molecular motion. Furthermore, it seems that the nanotube filler do not affect the glass transition as the nanotube content was increased, as observed in DMA and DSC. In addition, the magnitude of the maximum of the  $\tan \delta$  peak was not modified by the presence of nanotubes in the composite. This fact evidences that the material exhibited some preparation problems compared to the expected result. The  $\tan \delta$  peak broadening was observed as the nanotubes were chemically modified. This curve behavior determined that some modifications in the interfacial interaction of the materials were obtained. Furthermore, a decrement in the storage modulus in the glassy and rubbery plateau was observed. The behavior could be attributed to inhomogeneity problems in the sample preparation. In addition, this fact altered the observable filler dispersion and the filler-matrix interfacial interactions and did not promote the mechanical reinforcement of the materials.

#### *Analysis of the mechanism*

In these PEO/CNTs composites several factors contribute to the macroscopic properties.

In general, the mechanical behavior of semicrystalline materials could be understood as those of nanocomposites, where the crystallites act as both filler and cross-linking nodes. The peculiar filler/matrix interactions are due to the tie molecules (molecules shared by an amorphous part and its two adjacent crystallites) and to van der Waals bonds between amorphous and crystalline parts. Composites of semicrystalline polymers and nanotubes involve additional interactions related to the interfacial strength of the nanotube fillers with each part of the PEO matrix, i.e. amorphous and crystalline.

Cristallinity increase could be a way to strengthen the semicrystalline polymers. In particular, the presence of the nanotubes in certain polymer systems was found to nucleate crystallization. This crystal growth is thought to enhance matrix-nanotube stress transfer. This extremely strong interfacial bonding in polymer-based composite has been manifested by the fracture of the polymer rather than the polymer-nanotube interface. [25] In our case,

the nanotubes also behave as nucleating agents, but the increase in crystallinity was not enough in extent and homogeneity to enhance the storage modulus ( $G'$ ) of the PEO/CNTs composites.

In general, it was observed that the study of semicrystalline polymers and their mechanical properties is difficult to model. Even more, the nanocomposites derived from semicrystalline polymers will be also complicated to model.

The modeling of the semicrystalline polymers are difficult because the modulus of the amorphous and crystalline parts are difficult to be known, the crosslinking effects depends on many parameters (tie molecules, crystallite size, etc), the microstructure is complex and must be considered at different scales: crystallite, spherulite, the materials are anisotropic giving anisotropic characteristics in materials, etc. [26] Additional complications will be obtained when the nanotubes are added to the system. Thus, a complete work is required to develop and validate composite models for semicrystalline polymers and their composites. In our case, important modifications in the processing of the samples have to be carried out to ensure the homogeneity of the materials before proceeding to the characterization and modeling of the PEO/CNTs behavior.

In summary, the measurements of mechanical modulus in all PEO/CNTs composites are influenced by several factors: (i) the matrix and filler intrinsic modulus, (ii) the filler dispersion with the formation of a percolating network, and (iii) the filler-filler and filler-matrix interactions.

Differences between PEO/CNTs composites can be first attributed to filler properties, as the nanotubes are expected to have different storage modulus according to their chemical modification. That means that nitrogen doping and polymer-grafting altered the mechanical response of MWNT. This effect was also observed and commented in detailed for PS/CNTs composites.

The dispersion level of filler within the PEO matrix was more efficient in the case of MWNT, followed by CN<sub>x</sub> and then PS-g-CN<sub>x</sub>. This phenomenon is explained by the chemical compatibility of materials, as in the last case, where the immiscibility of the matrices (i.e. PS surrounding the nanotubes and PEO) favor the phase separation. The dispersion factor, thus, alter the mechanical reinforcement due to the introduction of nanotube fillers in the polymer matrix. In PEO/CNTs composites a negative mechanical reinforcement seems to be obtained due to the addition of nanotubes to the systems, following  $G'_{PEO/MWNT} > G'_{PEO/CN_x} > G'_{PEO/PS-g-CN_x}$ . This apparent behavior is attributed to the inhomogeneity in the PEO/CNTs composite materials.

Finally, the filler-filler and filler-matrix interactions result in a better enhancement of the modulus in MWNT than in the other cases, at least at the observed conditions.

### **7.2.2.3. Analysis of the relation among electro-mechanical properties and microstructure of PEO-nanotube composites.**

It is known that due to the processing conditions and/or additives addition, like reinforced fillers, the composite materials are rarely isotropic or homogeneous. More over, their thermo mechanical properties are very sensitive to these variations in structure. Some of the methods to determine the influence of thermal and processing history on the behavior

of a material could be done using the dynamic mechanical techniques. Nevertheless, the homogeneity of the samples became a fundamental requisite, as was described. In the following paragraphs a relation among the physical properties of nanocomposites will try to be explained.

#### *PEO/MWNT*

The thermal properties of PEO/MWNT measured by DSC revealed no changes in the  $T_g$  values, a decrement in the  $T_m$ , and an increment in the  $T_c$  and percentage of crystallinity of the samples. This global behavior was related to several factors:

- (i) the nanocomposite morphology, because the MWNT behaved as nucleating agents, and their individual good dispersion, and
- (ii) the low interfacial interaction between PEO and carbon nanotubes.

Dispersion and interfacial interactions were also observed by microscopy experiments. Furthermore, electrical studies also determined that MWNT present good dispersion within the PEO matrix that could be associated to the formation of an efficient geometric percolating conductive network. This filler geometrical percolation was aided by the slight increment in the crystallinity and led to increase the conductivity of the system respect to the pure matrix.

In addition, the mechanical properties revealed that the geometrical percolation of the nanotubes within the polymer was not enough to enhance the storage modulus of the material (below or above the  $T_g$ ). This effect was mainly correlated to the inhomogeneity of the samples that produce measure problems that were evident when DMA measurements were performed. In fact, a decrement in the storage modulus revealed that heterogeneity and porosity took place in this material. Furthermore, carbon nanotubes entanglement was not observe in this case probably due to the same processing problem.

#### *PEO/CN<sub>x</sub>*

PEO/CN<sub>x</sub> nanocomposites properties also revealed no changes in the  $T_g$  values, a decrement in the  $T_m$ , and an slight increment in the  $T_c$  and in crystallinity percentage. These results are very similar to those obtained for MWNTs.

Morphological differences produced by a less efficient disentanglement of CN<sub>x</sub> nanotube ropes in the composite were observed compared to PEO/MWNT composites. This behavior was attributed to a less efficient interaction between polymer and CN<sub>x</sub> nanotubes due to polarity or chemical reactivity incompatibilities promoted by the processing conditions.

The dispersion quality, slight crystallinity percentage increment, and lower inherent conductivity could explain the different conductivity properties of PEO/CN<sub>x</sub> nanotubes. Anyway a geometrical percolating system was formed that was enough to promote the increment in conductivity of the PEO/CN<sub>x</sub> composite samples compared to pure matrix. These values were lower in comparison to the PEO/MWNTs due to the inherent lower conductivity of the filler and the morphological differences of both composites.

To determine the effect of the nanotube loading, the materials were submitted to DMA measurements. The results revealed unchanged  $T_g$ , a decrease in the storage modulus below and above  $T_g$ , and low entanglement of carbon nanotubes. These conditions along with the inhomogeneity of samples determine the non reinforcing of the composites by nanotube fillers.

Again, as in previous case, the overall thermo-mechanical behavior is mainly attributed to the morphological characteristics of the materials due to processing problems

#### *PEO/PS-g-CN<sub>x</sub>*

Thermal properties of the PEO/PS-g-CN<sub>x</sub> composite were similar to those of other nanotube filler. The differences in the crystallization percentage were minor. The morphology of the PEO/PS-g-CN<sub>x</sub> revealed a poor dispersion of polymer-grafted nanotubes due to adhesion between tubes.

Additional measurements of conductivity revealed that a geometrical percolation was obtained in the composite that became the polymer conductor (for the case of PEO14k), nevertheless the maximum conductivity values in all cases were lower than for the other composite types (i.e. PEO/MWNT and PEO/CN<sub>x</sub>).

More over, the results for the storage modulus measurements in DMA resulted lower than for the other composites, but also lower than the pure matrix.

All these results determined that the interfacial strength between PEO and PS-g-CN<sub>x</sub> was lower than for any other PEO-synthesized system. This fact is attributed to the immiscibility of grafted polymer (PS) with the nanocomposite matrix polymer (PEO). Additional facts to be considered like inhomogeneity in the system and the absence of entanglement of carbon nanotubes, even more than other factors, are crucial to explain the mechanical behavior of the materials.

In general, complications due to the inhomogeneity of the film materials in all composite cases, inducing measurement difficulties (lack of precision and representativity) were permanently present. These difficulties are coming from the choice of the solvent, that favor the phase separation. Thus, as predicted the properties derived from the dispersion and interfacial contact, as electrical and mechanical properties have presented a dependency to the morphology of the materials.

In the electrical properties, a percolating network seems to be formed improving the conductivity of the PEO/CNTs samples. Nevertheless, the mechanical properties of PEO/CNTs more sensible to the nanocomposite preparation methods, i.e. homogeneity and dispersion of fillers, presented a decrement in the modulus of the materials. Additional DMA measurement problems were always present.

### **7.3. Conclusions**

MWNTs, CN<sub>x</sub> and PS-grafted CN<sub>x</sub> nanotubes were dispersed as conductive and reinforcing fillers in PS and PEO matrices. The resulting electrical and mechanical properties were investigated by AC impedance spectroscopy and DMA. The results were analyzed according to the studied material microstructure and their thermal properties reported in previous chapter.

In general, the solution casting method to prepare polymer/CNT composite materials presents some challenges specifically due to the selected solvent and the processing conditions. In our cases, the method was efficient in the preparation of PS/CNTs composite but inefficient in the preparation of PEO/CNTs. In the last case the materials

presented strong dispersion and homogeneity problems that also produce measurements difficulties at least for mechanical behavior.

The more interesting results observed for PS/CNTs composites concern the enhancement in the conductivity, at low electrical percolation thresholds, in the storage modulus above  $T_g$ , and the thermo - mechanical stability. The mechanism explaining the composite behavior is related to the formation of a percolating network with different dispersion quality and entanglement density. The variations in properties between materials are explained by the nanotube intrinsic properties, the contact filler-filler and filler-matrix differences, and the dispersion characteristics. In the synthesized composites and at the studied conditions, the better performance in general was obtained when MWNT were used in comparison to  $CN_x$  and PS- $g$ - $CN_x$  nanotubes.

PEO/CNTs composites exhibit dispersion trends mainly due to the processing conditions. This fact determined inhomogeneity in samples that consequently produce precision and reproducibility problems. At these conditions, the level of properties enhancements was lower than for the PS case. In fact, only a geometrical percolation network was formed that increases the conductivity level of the insulating polymer matrix, but did not result efficient enough to enhance the mechanical properties. Therefore, with the obtained information it could be possible to establish a scheme of geometrical percolation network where the nanotubes were in general bad dispersed and low entangled. In this case, the nanotube intrinsic properties and the contact filler-filler and filler-matrix differences are hindered by the anisotropy of the measured samples.

Again in this system of composites at the studied range and processing conditions the MWNT nanotubes seemed to present the most enhanced properties.

The comparison of the carbon nanotube type in the preparation of nanocomposites reflects that each kind of nanotube behave differently. Thus, MWNT presented higher intrinsic conductivity and storage modulus;  $CN_x$  nanotubes presented higher chemical reactivity with a moderate decrement in the conductivity and storage modulus; and finally, PS- $g$ - $CN_x$  presented better chemical compatibility with a polymer miscible with PS.

When nanotubes were chemically modified some differences were also observed, as:

- (i) Interfacial interaction that affects the dispersion in the embedded polymer matrix, due to polarity, reactivity, functional sites, etc. and favor by the processing method.
- (ii) Nucleating promotion in a semicrystalline polymer that slightly modifies the crystalline level of the nanocomposite.

To conclude, several kind of composite polymer-nanotube materials were synthesized by a solution casting method: PEO/CNTs and PS/CNTs composites. All the nanocomposite materials exhibited differentiated electrical and mechanical properties. The most promising at the moment are those related with the PS/CNTs composites. In all cases, further studies become necessary to explain more accurately the behavior of these composite materials.

## References

1. Dalmas, F., L. Chazeau, C. Gauthier, K. Masenelli-Varlot, R. Dendievel, J.Y. Cavailié, and L. Forró, *Multiwalled carbon nanotube/polymer nanocomposites: processing and properties*. Journal of Polymer Science: Part B: Polymer Physics, 2005. **43**: p. 1186-1197.
2. Flandin, L., Y. Bréchet, and J.Y. Cavailié, *Electrically conductive polymer nanocomposites as deformation sensors*. Composites Science and Technology, 2001. **61**: p. 895-901.
3. Martin, C.A., J.K.W. Sandler, M.S.P. Shaffer, K.B. Schwartz, W. Bauhofer, K. Schulte, and A.H. Windle, *Formation of percolating networks in multi-wall carbon-nanotube-epoxy composites*. Composites Science and Technology, 2004. **64**: p. 2309-2316.
4. Kirkpatrick, S., *Percolation and conduction*. Reviews of Modern Physics, 1973. **45**(4): p. 574-588.
5. Fournier, J., G. Boiteux, G. Seytre, and G. Marichy, *Percolation network of polypyrrole in conducting polymer-composites*. Synthetic Metals, 1997. **84**: p. 839-840.
6. Coleman, J.N., S. Curran, A.B. Dalton, A.P. Davey, B. MacCarthy, W.J. Blau, and R.C. Barklie, *Percolation-dominated conductivity in a conjugated-polymer-carbon-nanotube composite*. Physical Review B, 1998. **58**(12): p. R7492-R7495.
7. Zhang, B., R.W. Fu, M.Q. Zhang, X.M. Dong, P.L. Lan, and J.S. Qiu, *Preparation and characterization of gas-sensitive composites from multi-walled carbon nanotubes/polystyrene*. Sensors and Actuators B, 2005. **109**(2): p. 323-328.
8. Kilbride, B.E., J.N. Coleman, J. Fraysse, P. Fournet, M. Cadek, A. Drury, S. Hutzler, S. Roth, and W.J. Blau, *Experimental observation of scaling laws for alternating current and direct current conductivity in polymer-carbon nanotube composite thin films*. Journal of Applied Physics, 2002. **92**(7): p. 4024-4030.
9. van der Putten, D., J.T. Moonen, H.B. Brom, J.C.M. Brokken-Zipj, and M.A.J. Michels, *Evidence for superlocalization on a fractal network in conductive carbon-black-polymer composites*. Physical Review Letters, 1992. **69**(3): p. 494-497.
10. Bueche, F., *Electrical resistivity of conducting particles in an insulating matrix*. Journal of Applied Physics, 1972. **43**(11): p. 4837-4838.
11. Balberg, I. and N. Binenbaum, *Percolation threshold in the three-dimensional Sticks System*. Physical Review Letters, 1984. **52**(17): p. 1465-1468.
12. Munson-McGee, S.H., *Estimation of the critical concentration in an isotropic percolation network*. Physical Review B, 1991. **43**(4): p. 3331-3336.
13. Celzard, A., E. McRae, C. Deleuze, M. Dufort, G. Furdin, and J.F. Marêche, *Critical concentration in percolating systems containing a high-aspect-ratio-filler*. Physical Review B, 1996. **53**(10): p. 6209-6214.
14. Gojny, F.H., M.H.G. Wichmann, B. Fiedler, W. Bauhofer, and K. Schulte, *Influence of nano-modification on the mechanical and electrical properties of conventional fibre-reinforced composites*. Composites: Part A, 2005. **36**(11): p. 1525-1535.
15. Sandler, J.K.W., J.E. Kirk, I.A. Kinloch, M.S.P. Shaffer, and A.H. Windle, *Ultra-low electrical percolation threshold in carbon-nanotube epoxy composites*. Polymer, 2003. **44**: p. 5893-5899.
16. Hirsch, A., *Functionalization of single-walled carbon nanotubes*. Angew. Chem. Int. Ed, 2002. **41**(11): p. 1853-1859.
17. Wagner, H.D., *Nanotube-polymer adhesion: a mechanics approach*. Chemical Physics Letters, 2002. **361**: p. 57-61.
18. Gojny, F.H., J. Nastalczyk, Z. Roslaniec, and K. Schulte, *Surface modified multi-walled carbon nanotubes in CNT/epoxy-composites*. Chemical Physics Letters, 2003. **370**: p. 820-824.

19. Song, Y.S. and J.R. Youn, *Influence of dispersion states of carbon nanotubes on physical properties of epoxy nanocomposites*. Carbon, 2005. **43**: p. 1378-1385.
20. Cui, S., R. Canet, A. Derre, M. Couzi, and P. Delhaes, *Characterization of multiwall carbon nanotubes and influence of surfactant in the nanocomposite processing*. Carbon, 2003. **41**: p. 797-809.
21. Zhao, F., M. Wang, and S. Dong, *Conductive property of multiwall carbon nanotubes-PEO-salt nanocomposite film*. Electrochemical and solid-state letters, 2004. **7**(11): p. E48-E50.
22. Saibaba, G., D. Srikanth, and A. Ramachandra Reddy, *Preparation and study of conductivity in lithium salt complexes of mixed MEEP : PEO polymer electrolytes*. Bulletin of Materials Science, 2004. **27**(1): p. 51-55.
23. Croce, F., L. Persi, B. Scrosati, E. Serraino-Fiory, E. Plitche, and M.A. Hendrickson, *Electrochim. Acta*, 2001. **46**: p. 2457.
24. Chaput, S., C. Carrot, M. Castro, and F. Prochazka, *Co-continuity interval in immiscible polymer blends by dynamic mechanical spectroscopy in the molten and solid state*. Rheological Acta, 2004. **43**: p. 417-426.
25. Cadek, M., J.N. Coleman, V. Barron, K. Hedicke, and W.J. Blau, *Morphological and mechanical properties of carbon-nanotube-reinforced semicrystalline and amorphous polymer composites*.
26. Chazeau, L., C. Gauthier, G. Vigier, and J.Y. Cavaillé, *Relationships between microstructural aspects and mechanical properties of polymer-based nanocomposites*, in *Handbook of organic-inorganic hybrid materials and nanocomposites*, H.S. Nalwa, Editor. 2003, American Scientific Publishers. p. 63-110.

# Conclusions and Perspectives

The enhancement of general performances of nanotube-based polymer composites is expected when the dispersion, contact and load transfer from filler to the matrix is optimized. According to several reports, these characteristics could be facilitated when the nanotubes are functionalized [1-4] and/or polymer-grafted [5-9] with molecules compatible with the host polymer matrix.

The main goal of the work reported in this thesis is devoted to the production of polymer composites of PS-grafted  $\text{CN}_x$  nanotubes. The synthesis of these materials involves:

- (i) the development of a novel chemical methodology to polymer grafted nitrogen-doped carbon nanotubes using a nitroxide-mediated radical polymerization (NMRP) approach. The NMRP is used with radical functionalized  $\text{CN}_x$  nanotubes to obtain macroinitiators that could overcome *in situ* solution polymerization to form polystyrene-grafted nanotubes.

Some advantages of the methodology involve the preparation of materials without an extended degradation of nanotube structure (like in the acid treatment); furthermore the *in situ* polymerization could favor the grafted polymer architecture, the density grafting control as well as the polymer chain polydispersity. In summary, radical functionalization and NMRP methodology represent an interesting approach to the synthesis of polymer brushes of carbon nanotubes. It is important to highlight that at the present time, some reports support the feasibility of the use of radical functionalization [3, 8, 10] and NMRP [11-13], independently, to functionalize carbon nanotubes. Nevertheless, an approach using both combined techniques has not being used before.

- (ii) the preparation by solvent-casting-pressing of polymer-carbon nanotubes composites using polymer-grafted  $\text{CN}_x$  nanotubes in order to improve the dispersion and interfacial adhesion between the filler and the matrix. Some of the desired properties involve the enhancement of the thermal, electrical and/or mechanical behavior of the original materials. This work, in addition, present an effort to use different polymer matrices as PEO and PS-PEO polymer blends, in addition to the already studied PS.

The preparation of polymer composites of PS-grafted  $CN_x$  nanotubes, thus, was delimited by the main objectives described in the introduction and the main results will be outlined in the following paragraphs.

First of all, the synthesis of polymer-grafted  $CN_x$  nanotubes, using a two step approaches (the initiator-controller attachment (radical functionalization), and the *in situ* polymerization via NMRP) was carried out as confirmed by several characterization techniques.

The radical functionalization of  $CN_x$  nanotubes by initiator-controller (BPO and nitroxides) radicals was achieved, proceeding by covalent attachment. It was observed that the functionalization reaction preserves the internal structure of the bamboo type nanotubes. Furthermore, an homogeneous radical reaction over the nanotube surface was evidenced. The attached radicals seem to be resonant or trapped over nanotube surface depending on the nanotube superficial group (based on nitrogen or any other). Thus, the radical attachment of initiator-controller radicals to carbon nanotube surface could determine the formation of macroinitiators, or even more controlled macroinitiators labile to initiate *in situ* polymer-grafted chains.

The polymer grafted- $CN_x$  nanotubes (PS-*g*- $CN_x$ ) have been successfully formed using *in situ* NMRP. The polymerization of PS takes place on radical functionalized carbon nanotube surfaces. The grafted polymer is covalently attached to carbon nanotubes, forming an amorphous layer surrounding the nanotubes. Some properties of the novel materials involve the enhancement of their solubility and stability in organic solvents. The comparison of PS and  $CN_x$  physical blends with grafted PS-*g*- $CN_x$  systems determine strong differences in their behavior, due to the nature of the attachment. Also, the importance of the reactivity of  $CN_x$  nanotubes in the polymer-brushes preparation was highlight in comparison with un-doped MWNTs.

Some of the main goals of this thesis in the polymer-grafting step involved: *the development of a novel methodology to attached polymer chains to the nanotube surface, the exploration of the synthesis conditions using a Parallel Polymerization Reactor (PPR) system, the chemical process to functionalized carbon nanotubes that does not induce extended nanotube structural damage, and finally the innovative PS-*g*- $CN_x$  nanotube materials properties that could be used in the preparation of polymer nanocomposites (enhancing the dispersion of the nanotubes within the matrix and the interfacial strength).*

As a second part of the work, the preparation of PS, PEO and PS/PEO nanocomposites of PS-grafted  $CN_x$  nanotubes was carried out by a solution-casting-pressing method. The analysis of the materials gives interesting results about the preparation method and the inherent nanocomposite morphology. The effect of the addition of polymer-grafted  $CN_x$  nanofillers was compared to the addition of MWNT and  $CN_x$  nanotubes.

In terms of morphology, the homogeneity of the samples (in terms of filler dispersion) is higher for the homopolymer nanocomposites (PS-based and PEO-based) than for the polymer blend (PS-PEO based nanocomposite) using several kinds of carbon nanotubes as fillers. In addition, the adhesion of the nanotubes with the polymer matrixes can be obtained indirectly from morphological observations. This parameter seems to vary according to polymer and filler types: for example a strong adhesion and good interaction

to PS is observed with PS-*g*-CN<sub>x</sub> nanotubes. Conversely, MWNTs display good interactions with PEO. Finally, the tortuosity of nanotubes seems to increase according to the polymer matrix and according to the local nanotube concentration, thus higher for polymer blend composites, followed by PEO and finally PS.

In general, the processing critical issues as dispersion and interfacial adhesion strongly vary between materials. The PS-based nanocomposites exhibited better properties due to the homogeneity of the samples, but also due to the compatibility of the polymer-grafted around nanotubes and the composite matrix. In the other polymer cases, some trends were highlighted in the preparation and processing of the samples. Therefore, an optimization of the process becomes necessary to obtain better composite materials when PEO and PS-PEO blends are used.

Additional results are related to the characterization of the composite samples in relation to their physical properties. The results vary according to the type of polymer matrix and filler, as well as filler content. Some relevant results are summarized below.

PS/CNTs composites revealed interesting results in the modification of the properties as the nanotubes were added: enhancement in the conductivity at low electrical percolation thresholds, a moderated increase in the storage modulus above T<sub>g</sub>, and a small improvement in the thermo-mechanical stability. Thus, the materials form percolating networks at different dispersion quality and where nanotubes present entanglements. In general, the synthesized composites at the studied conditions exhibit better performance when MWNT are used in comparison to CN<sub>x</sub> and PS-*g*-CN<sub>x</sub> nanotubes.

PEO/CNTs composites exhibit dispersion trends mainly due to the processing conditions. This fact determines inhomogeneity in samples that consequently produces precision and reproductibility problems. In these conditions, no clear enhancement was obtained. In fact, a geometrical percolation network was formed that increases the conductivity level of the insulating polymer matrix, but did not efficiently enhance the mechanical properties.

PS-PEO/CNTs composites presented even stronger problems in their physical performance due to inherent immiscibility of the homopolymers and the processing conditions. Thus, the experimental results of their characterization were not reported.

Finally, a close relation between morphology and physical properties were found. Thus, all the nanocomposite materials exhibited differentiated thermal, electrical and mechanical properties. In general, the properties enhancements due to the addition of carbon nanotubes to polymer matrices are good in the case of electrical properties, but moderate in the case of mechanical properties. The most promising at the moment are those related with the PS/CNTs composites.

In addition, very different properties modifications were induced by the use of PS-grafted CN<sub>x</sub> nanotubes compared to MWNT and CN<sub>x</sub> nanotubes in terms of interaction with polymer matrixes. These modifications can be with no doubt attributed to the grafted polymer and could be indicative of the successful synthesis of the polymer brushes.

At this point the main goals of the work concerning the polymer nanocomposite preparations are: *the synthesis and systematical study of several kinds of polymer-nanotube materials, particularly using PEO and PS-PEO polymer blends as matrices, and several*

*types of nanotubes including PS-g-CN<sub>x</sub> nanotubes and the preparation of novel composite materials with interestingly conductor properties and moderated mechanical properties.*

After all these commentaries, it can be possible to state that most of the thesis objectives were satisfied. At this point it has to be remarked the enormous utility from the basic and technological point of view of the developed nanomaterials.

The polymer-grafting of carbon nanotubes and the composite synthesis methodology presented hold immense promise for future work encompassing different areas. Some ideas regarding possible directions are described below.

#### *Polymer-grafting of carbon nanotubes*

1. As discussed in previous sections, the current NMRP grafting technique can be significantly improved, i.e. optimization of the synthesis processing variables of PS-g-CN<sub>x</sub> polymer brushes for highly specific applications. Among them, the evaluation of the control polymerization process in order to produce monodispersed and copolymer chains grafted from the nanotube surface; and the evaluation of several initiator-controller systems (like AIBN and alcoxiamines) and solvents. In addition, a theoretical study in terms of kinetics and modeling of the NMRP systems can be also performed.
2. The knowledge about the polymer-grafting of PS over nanotube surfaces could be extended to other polymers to enhance other polymer-composite systems. Thus a variety of thermoplastics can be synthesized and grafted to carbon nanotubes.
3. Additional studies in the use of several kinds of carbon nanotubes (i.e. MWNT, CN<sub>x</sub>) according to the polymer grafted and the specific applications could be carried out. Particularly, an optimization of the behavior of each nanotube system can be done.

#### *Polymer-carbon nanotubes composite preparation*

4. In relation to the nanocomposite preparation, the optimization of the production method can be done using several solvent systems and conditions for the solvent-casting-pressing method, or even more using alternative methods, as melt blending.
5. Studies of composites prepared by *in situ* polymerization using PS-g-CN<sub>x</sub> nanotubes or even non functionalized type can be suggested due to the apparently good dispersion properties.
6. Evaluation of several kinds of polymer matrices in the production of polymer/CNTs composites, like using different polymer blends with controlled morphology and/or specific physico-chemical properties (miscibility, amphiphilic, etc)
7. Several studies of the electrical behavior of polymer/CNTs composites, as:
  - (i) The enhancement of the electrical properties of the composites by the addition of inorganic salts in the case of PEO/CNTs systems.
  - (ii) the electrical evolution of nanocomposite materials, i.e. AC electrical conductivity, during tensile tests to understand microstructure, obtaining graphs of conductivity vs. strain;

- (iii) the evaluation of the current as a function of voltage to determine the Ohmic (linear) and non Ohmic (quadratic) behavior and thus the type of conductivity. In the linear region the current is dominated by carriers injected by the electrodes and known as space-charge limited current (SCLC). The quadratic behavior holds in the presence of shallow traps, or in the theoretical limit of no traps. This behavior could be described by the Child-Langmuir equation:  $J = 9\mu\varepsilon V^2 / 8l^3$ , where  $\mu$  is an effective mobility,  $\varepsilon$  the permittivity, and  $l$  the electrode spacing. The effective mobility is the product of the free carrier mobility and the fraction of free charge  $\theta$ . Hence the effective mobility of carriers from the current-voltage characteristics could be calculated;
- (iv) the temperature dependence of the conductivity using  $\ln\left[\frac{\sigma_p}{\sigma(T)}\right] = \left(\frac{T_0}{T}\right)^\gamma$  where  $\gamma$  is the temperature exponent,  $T_0$  is the reduction temperature.

7. Several studies respect to the mechanical properties of the materials, such as the evaluation of other mechanical properties of the materials.
8. The proposition of a specific model adapted to the polymer/CNT composite produced.

*As can be seen the future directions of the work presented in this thesis are enormous and diverse. In all cases it has to be highlighting the actual importance of nanocomposite materials that could also forward autoensambling and that present specifically design properties, like in the polymer/CNTs composites using high developed fillers.*

## References

1. Banerjee, S., T. Hemraj-Benny, and S.S. Wong, *Covalent surface chemistry of single-walled carbon nanotubes*. *Advanced Materials*, 2005. **17**(1): p. 17-29.
2. Sinnott, S.B., *Chemical functionalization of carbon nanotubes*. *Journal of Nanoscience and Nanotechnology*, 2002. **2**(2): p. 113-123.
3. Peng, H., P. Reverdy, V.N. Khabashesku, and J.L. Margrave, *Sidewall functionalization of single-walled carbon nanotubes with organic peroxides*. *Chemical Communications*, 2003: p. 362-363.
4. Hirsch, A., *Functionalization of single-walled carbon nanotubes*. *Angew. Chem. Int. Ed*, 2002. **41**(11): p. 1853-1859.
5. Jin, Z., X. Sun, G. Xu, S.H. Goh, and W. Ji, *Nonlinear optical properties of some polymer multi-walled carbon nanotube composites*. *Chemical Physics Letters*, 2000. **318**(6): p. 505-510.
6. Shieh, Y.-T., G.-L. Liu, K.C. Hwang, and C.-C. Chen, *Crystallization, melting and morphology of PEO in PEO/MWNT-g-PMMA blends*. *Polymer*, 2005. **46**(24): p. 10945-10951.
7. Shieh, Y.-T. and G.-L. Liu, *Enhancement of PEO crystallization by PMMA-grafted multi-walled carbon nanotubes*. *PMSE Preprints*, 2004. **90**: p. 437-440.
8. Shaffer, M.S.P. and K. Koziol, *Polystyrene grafted multi-walled carbon nanotubes*. *Chemical Communications*, 2002: p. 2074-2075.
9. Tsubokawa, N., *Preparation and properties of polymer-grafted carbon nanotubes and nanofibers*. *Polymer Journal*, 2005. **37**(9): p. 637-655.
10. Gallani, J.-L., L. Bonomme, A. Drury, and W.J. Blau, *Photosensitive magnetism of radicals coupled with carbon nanotubes*. *Organic Electronics*, 2003. **4**: p. 15-20.
11. Ramirez, S.M. and D.Y. Sogah, *Nitroxide-Mediated Living Radical Polymerization from Carbon Nanotubes*. *PMSE Preprints*, 2004. **91**: p. 493-494.
12. Adronov, A., C.M. Homenick, Y. Liu, and Z. Yao, *Functionalization of single-walled carbon nanotubes with well-defined polymers*. *Polymer Preprints*, 2005. **46**(1): p. 201-202.
13. Datsyuk, V., C. Guerret-Piecourt, S. Dageou, L. Billon, J.-C. Dupin, E. Flahaut, A. Peigney, and C. Laurent, *Double walled carbon nanotube/polymer composites via in-situ nitroxide mediated polymerization of amphiphilic block copolymers*. *Carbon*, 2005. **43**(4): p. 873-876.

# Appendix



## 1.1. Discovery of carbon nanotubes

Table 1.5. Progress in carbon allotropes until the discovery of carbon nanotubes [1, 2].

---

1890	Schützenberger and Schützenberger studied the vapor grown of carbon filaments [3].
1892	Thomas A. Edison prepared the first carbon fiber, showing filament growth from the thermal decomposition of hydrocarbons.
1924	J. D. Bernal successfully identified the crystal structure of graphite.
1940s	Developments of carbon alloys such as spheroidal graphite in cast iron were obtained.
1950s	Rosalind Franklin distinguished graphitizing and non-graphitizing carbons. Continuous carbon fibers based on polymer precursors were obtained.
1950-1970s	Carbon fibers were produced and developed for industrial applications. Also, carbon whiskers were grown.
1955	Diamonds and diamond thin films were synthetically produced by chemical vapor deposition.
1970	Morinobu Endo presented the first images of SWNTs and MWNTs by HRTEM [4].
1980	Sumio Iijima reported the existence of nested carbon nanocages (graphitic onions), tightly curved, closed nanoparticles and extended tube-like structures by HRTEM [5, 6].
1985	Harold Kroto, Richard Smalley and colleagues at Rice University observed by mass spectrometry C <sub>60</sub> -atom clusters during solid vaporizing experiments [7].
1989	Harold Kroto at Univ. Sussex and Ken McKay proposed the model of graphitic onions consisting of nested icosahedral fullerenes (C <sub>60</sub> , C <sub>240</sub> , C <sub>540</sub> , C <sub>960</sub> ) containing only pentagonal and hexagonal carbon rings.
1990	Wolfgang Krätschmer at Max Planck Institute, Donald Huffman at Univ. Arizona found that C <sub>60</sub> could be produced in macroscopic quantities, forming crystals, using and electrical carbon-arc discharge apparatus (x <sub>0</sub> -x <sub>1</sub> m length and 2.5-30 nm diam).
1991	Sumio Iijima from NEC laboratories discovered the existence of MWNTs consisting of graphene tubules. The nested tubes had 2-10 nm outer diameter, <5 μm in length and interlayer spacing of ca. 3.4 Å. They also observed several carbon nanotube helicities and chiralities [8].
1991	Thomas Ebbesen and Pulickel Ajayan synthesized MWNTs in bulk using arc-discharge technique [9].
1992	Kroto and coworkers at Sussex extracted C <sub>60</sub> and C <sub>70</sub> molecules by chromatography [10].
1990,1996	Theoretical researchers proposed the idea of introducing additional pentagonal, heptagonal or octagonal carbon rings into icosahedral carbon cages in order to form spherical onions.
1992	Daniel Ugarte observed the transformation of polyhedral graphitic particles into almost spherical carbon onions when he irradiated the specimens with fast electrons inside an electron microscope.
1992	Theoretical prediction proposed that electronic properties could depend on CNTs diameter and chirality.
1993	Sumio Iijima and Toshinari Ichihashi from NEC laboratories and Donald Bethune and colleagues from IBM Almaden Research Center independently reported the synthesis of SWNTs [11, 12].
1996	Smalley and his group present an alternative method to prepare SWNTs by laser-vaporization with high yields and unusually uniform diameters.

---

Table 1.6. Discovery of carbon nanotubes.

---

<b>Year</b>	<b>Discover</b>
1991	Discovery of multiwalled carbon nanotubes
1992	Conductivity of carbon nanotubes
1993	Structural rigidity of carbon nanotubes Synthesis of single-wall nanotubes
1995	Nanotubes as field emitters
1996	Ropes of single-wall nanotubes
1997	Quantum conductance of carbon nanotubes Hydrogen storage in nanotubes
1998	Chemical Vapor Deposition synthesis of aligned nanotube films Synthesis of doped carbon nanotubes Synthesis of nanotube peapods
2000	Thermal conductivity of nanotubes Macroscopically aligned nanotubes
2001	Integration of carbon nanotubes for logic circuits Intrinsic superconductivity of carbon nanotubes

---

## 1.2. Growth mechanisms of carbon nanotubes

The general mechanism of carbon nanotubes formation from chaotic carbon plasma, independently of the producing method, remains a great challenge. Nevertheless, many efforts have been devoted to model their growth behavior. In this section, some of the postulated theories will be presented in the case of the two main carbon nanotube production methods (i.e. arc discharge and pyrolysis).

*Growth mechanism of carbon nanotubes produced by electric-arc evaporation method.*

To explain the growth mechanism of carbon nanotubes produced by electric-arc evaporation, there are two main theories:

- i) *Nanotubes are always capped and the growth process involves a  $C_2$  absorption.* In this case the pentagonal defects of fullerene-type structures are labile to add new carbon atoms forming hexagonal structures that have to be rearranged to equilibrate the strain. The result is the continuous extension of an initial fullerene, see Fig. 1.17.

This theory is applied to synthesis methods with temperatures of  $\sim 1100^\circ\text{C}$ , and explains the SWNT growth but it has some problems to explain the multilayer growth.

- ii) *Nanotubes are open during the growth process and the carbon atoms are added to the open ends.* This method applies better for the case of electric-arc discharge. It explains the formation of chiral nanotubes, the carbon nanotube growth when higher temperatures (about  $3400^\circ\text{C}$ ) are involved; and the large aspect ratio of the nanotubes. The last implies that the technique proposes that growth in the tube axis is preferable than growth along the nanotube diameter, as it is observed. Fig. 1.18 depicts this mechanism.

In addition, some researches consider that the electric discharge has a predominantly role in this process, favoring the stability of the open structure of carbon nanotubes, and the fact that the tubes are only formed in the cathode.

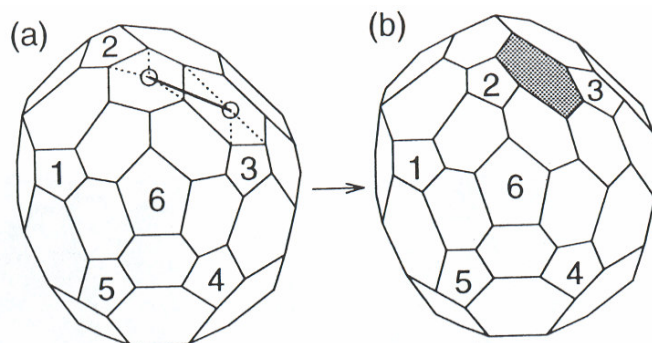


Fig. 1.17.  $C_2$  addition to a cap of nanotube. (a) Numbers from 1 to 6 indicate the position of the six pentagons on the hemispherical cap. If there is an addition of one  $C_2$  molecule, indicated by the open circles between 2 and 3, and if the new bonds denoted by dotted lines form, a new hexagon denoted in (b) by dark shading is obtained [3].

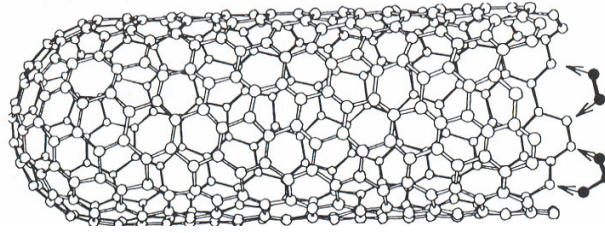


Fig. 1.18. Growth mechanism of carbon nanotubes at an open end by the absorption of  $C_2$  (dimers) and  $C_3$  (trimers) [3].

Many other models of carbon nanotubes formation by electric-arc discharge has been proposed. Most of them assume that the tubes nucleate and grow in the arc plasma. Some others predominantly consider the physical state of the plasma. Among the last ones, Gamaly and Ebbesen analyzed the density and velocity of carbon vapors in the cathode region. Using this piece of information, they explain the carbon nanotube growth process as a series of cycles comprising: seed formation, growth during stable discharge and termination and capping. Alternative models establish that tubes are formed on the cathode as a result of a solid-state transformation due to the rapid heating to high temperatures experienced for material deposited on the cathode [13]. Nevertheless, in all cases the models of carbon nanotubes growth by electric-arc discharge partially explain the phenomenon; also they do not consider all the variables involved. More analysis and experimental results are needed.

*Growth mechanism of carbon nanotubes by pyrolysis.*

Three main growth mechanisms are proposed for the case of carbon fiber formation using a catalyst by pyrolysis. All of them have been extended to explain the SWNTs and MWNTs growth:

- i) This mechanism was first proposed by Baker *et al.* In this case, fibers are produced by the diffusion of carbon (obtained from the decomposition of the hydrocarbon) through the catalyst with the subsequent precipitation and deposition on the other particle side (colder zone). The mechanism diagram is schemed in Fig. 1.19. As can be seen, the catalyst particle is separated from the substrate by the tube formation. Neutralization of the catalytic activity or the lack of carbon atoms determines the end of the growth.
- ii) Baird *et al* in 1974 and Oberlin *et al* [4] in 1976 were the firsts to propose that carbon atoms from the precursor could be diffused around the catalyst surface to generate the fibers in the other side. Also in this case the catalyst is put forward from the substrate, as illustrated Fig. 1.20.
- iii) Finally, in this method, carbon material diffuses through the particles and formed the fibers in the other side, but the catalyst remains over substrate (Fig. 1.21).

In all these cases, the parameters that determine the carbon-diffusion over and through are the dimensions of carbon particle, the physico-chemical properties of the catalyst, the process temperature, the hydrocarbons and the selected gases.

Finally, it can be stated that in both carbon nanotube production methods the tubes formation could be complementary understood taking into account the carbon-based thermal properties, i.e. the graphitization process (See section below). Because, by the moment, growth models of carbon nanotubes remains incomplete regard to temperature, gas presence and other particular processing conditions.

It is worth to mention that carbon nanotube synthesis process really change the growth mechanism and also, that a combination of mechanism could be present in a particular production case.

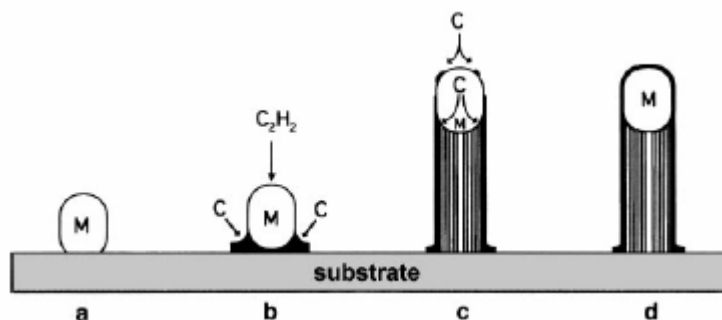


Fig. 1.19. Growth mechanism proposed by Baker *et al* for the formation of carbon nanotubes by pyrolysis. In this model, the carbon particles from the precursor, C, diffuse through metal catalyst, M, precipitating in the other side in the form of graphite. As can be seen, fiber formation take place in the substrate side [14].

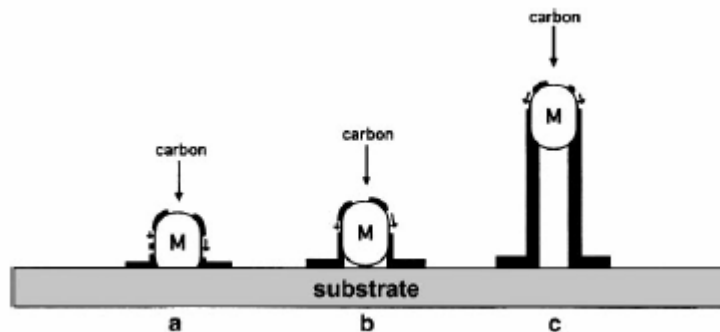


Fig. 1.20. Model representation of carbon nanotubes growth mechanism from a substrate by the carbon diffusion over the metal catalyst particle, M. Vertical fibers of graphite are formed between metal and substrate [14].

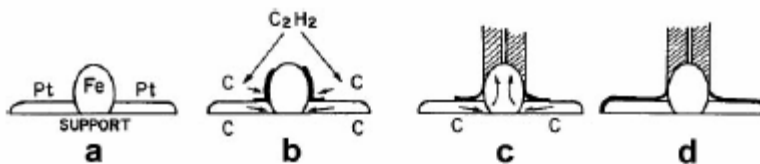


Fig. 1.21. Schematic diagram of fibrils growth from a substrate using pyrolysis method. In this particular case, carbon particles from the precursor Fe-Pt/C<sub>2</sub>H<sub>2</sub> diffuses the catalyst, but it remains close to the substrate [14].

## 5.1. EFTEM spectra from the energy-filtered image series of $CN_x$ NTs

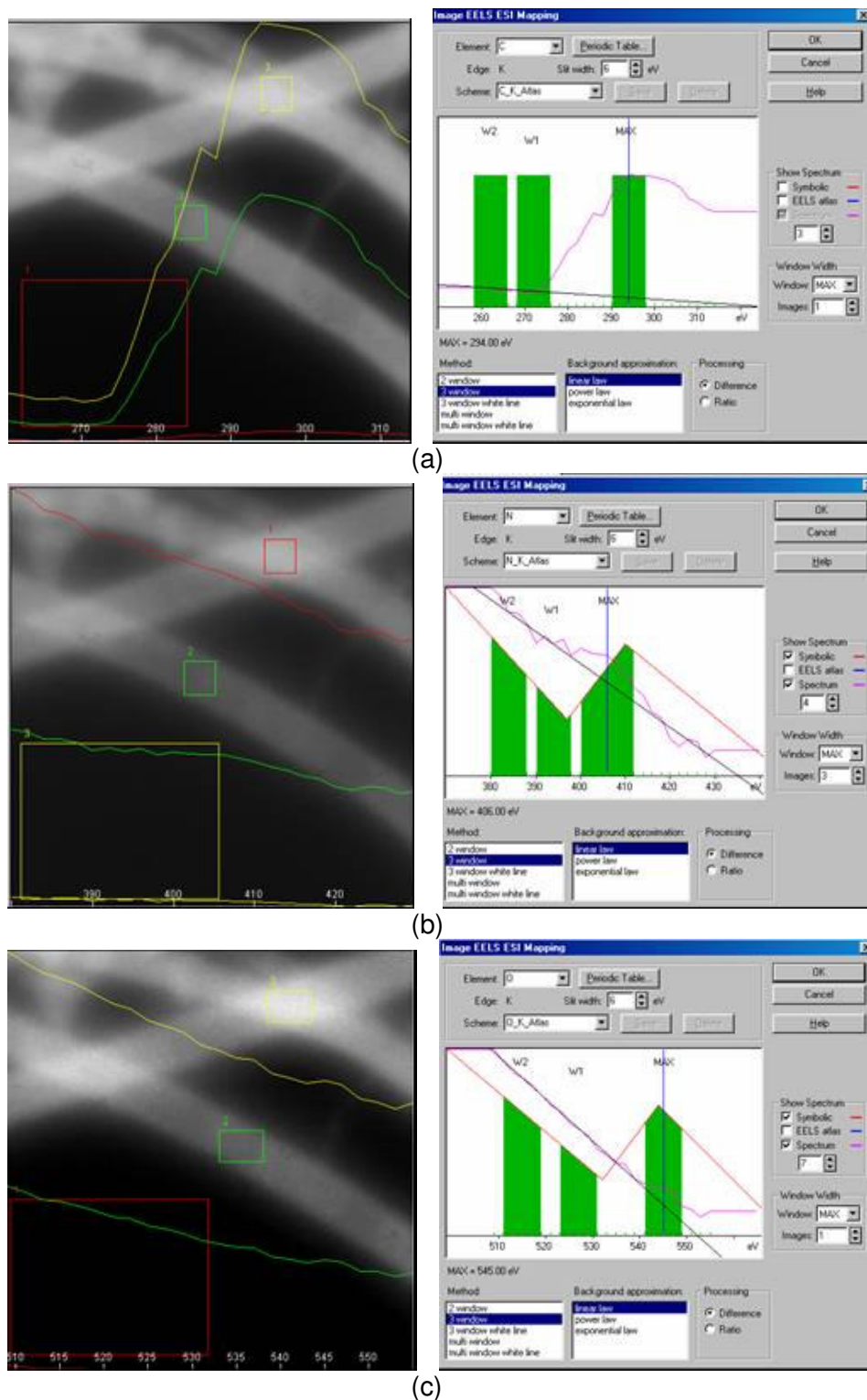


Fig. 5.31. EFTEM spectra extracted from the energy-filtered image series, sorted by element and the parameters used for the calculation of the elemental maps in  $CN_x$  nanotubes (1): (a) carbon map, (b) nitrogen map and (c) oxygen map.

### 7.1. Imaginary part of the conductivity AC measurements in PS/CNTs composites

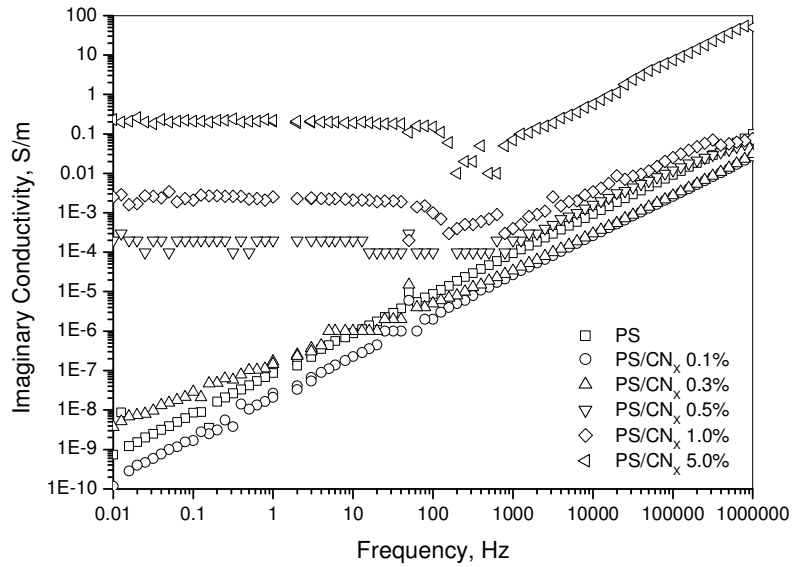


Fig. 7.29. Imaginary conductivity of PS/CNT<sub>x</sub> nanocomposites vs. frequency at filler weight fractions of 0.1 to 5.0 wt% and applied voltage of 0.1 V.

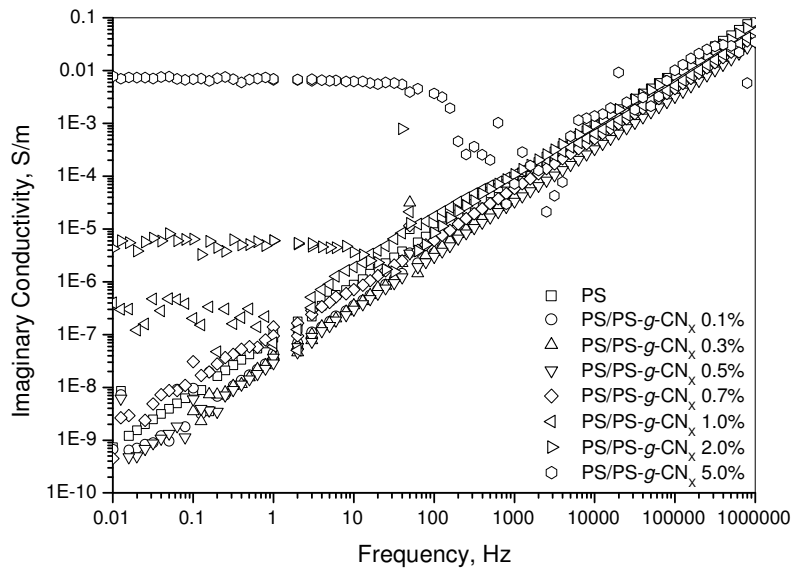


Fig. 7.30. Imaginary conductivity of PS/PS-g-CNT<sub>x</sub> nanocomposites vs. frequency at filler weight fractions of 0.1 to 5.0 wt% and applied voltage of 0.1 V.

## 7.2. Modeling of electrical behavior of PS/CNTs composites using the Insulator-Conductor Transition Model

Fournier *et al* [15] proposed the use of the Insulator-Conductor Transition Model to analyze the composite materials using polymer-carbon black, and polymer-polymer composites. Some other authors employed the same model for polymer blends along with a modelisation of the conductivity by a generalized effective medium equation that was valid at all volume concentrations and not only near the percolation transition.[16].

This transition model states

$$\log(\sigma_c) = \log(\sigma_n) + \frac{[\log(\sigma_p) - \log(\sigma_n)]}{[1 + \exp\{b(p - p_c)\}]} \quad [7.5]$$

where  $\sigma_p$ ,  $\sigma_n$  and  $\sigma_c$  are the conductivities of polymer, nanotubes and composites, respectively. Also  $b$  is an empirical parameter which leads to the change of conductivity at the percolation threshold  $p_c$ . The authors estimated that the expression is valid at all volume concentrations.

Other authors tried to use this model, among them Zhang *et al* [17] who evaluated the differences between *in situ* polymerized and solution processing methods for PS/MWNT. They found that the critical transition value took place at lower filler loadings *in situ* polymerized samples (4 wt%) than in solution case (9 wt%). Thus, they concluded that the MWNTs were less efficient to build up conductive networks in PS during solution mixing. The explanation was focused on the easier penetration of low-molecular weight monomers near from the nanotube surface, resulting in better dispersion of the fillers.

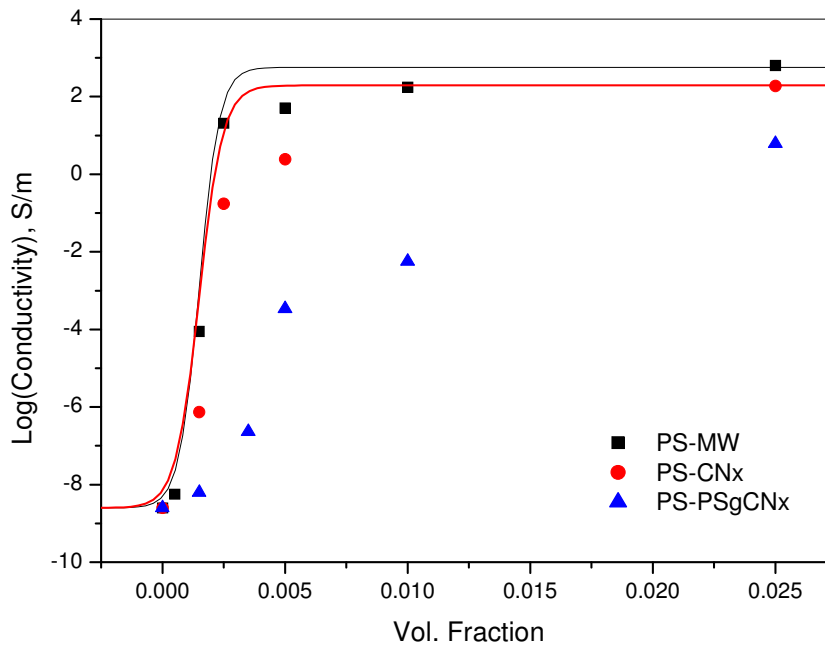


Fig. 7.31. Insulator-conductor transition model applied to PS/CNTs composites.

Fig. 7.31 presents the experimental results for the conductivity vs. volume fraction of nanofillers of PS/MWNT, PS/CN<sub>x</sub> and PS/PS-*g*-CN<sub>x</sub>, and the fits obtained with the insulator-conductor transition model. The parameters  $\sigma_p$ ,  $\sigma_n$ ,  $\sigma_c$  and  $p_c$  were set and the obtained parameter was  $b$ .

It seemed that the Insulator-Conductor Transition Model describes approximately the conductivity of PS/MWNT, nevertheless as the carbon nanotube fillers were chemically modified by nitrogen doping and further by polymer-grafting, the experimental values were not correctly fitted. This result mainly means that as the nanotubes become more functionalized the influence of the contact becomes more important and deviates the result from that of the sum of their parts. Therefore, the insulator-conductor transition model is not appropriate to model all the PS/CNTs synthesized here.

### 7.3. Conductivity exponent and the percolation threshold in PS/CNTs composites calculated using the statistical percolation model

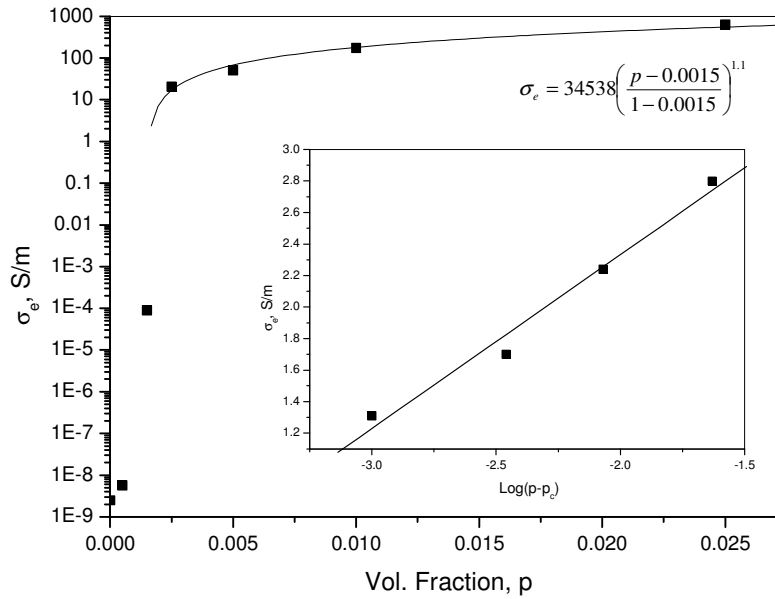


Fig. 7.32. Real part of the AC electrical conductivity at 1 Hz and applied voltage of 0.1 V for PS/MWNT at several filler contents. Comparison with statistical percolation theory (solid lines).

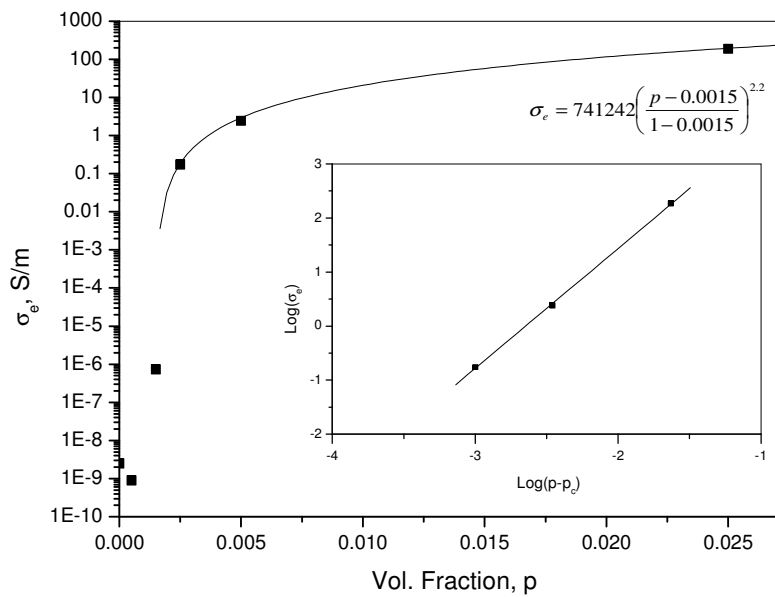


Fig. 7.33. Real part of the AC electrical conductivity at 1 Hz and 0.1 V for PS/CN<sub>x</sub> at several filler contents. Comparison with statistical percolation theory (solid lines).

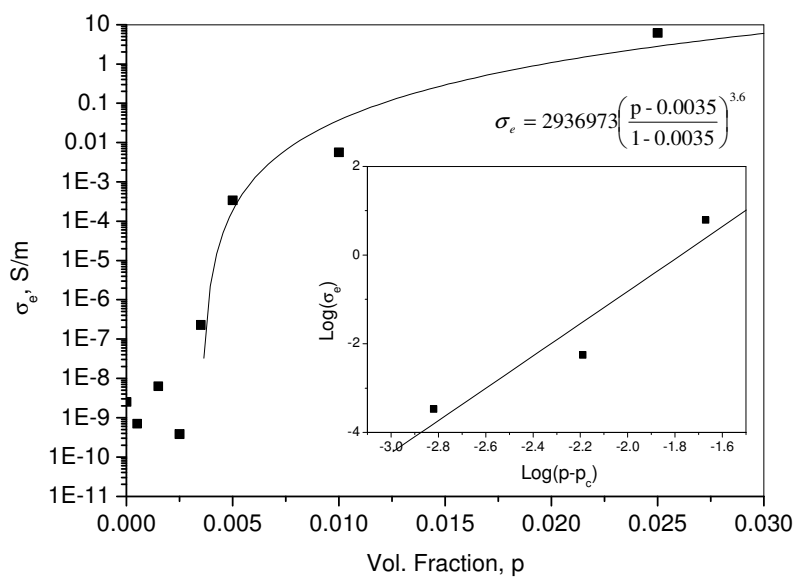


Fig. 7.34. Real part of the AC electrical conductivity at 1 Hz and applied voltage of 0.1 V for PS/PS-g-CN<sub>x</sub> at several filler contents. Comparison with statistical percolation theory (solid lines).

### 7.4. Loss modulus of PS/CNTs composites at several CNT concentration

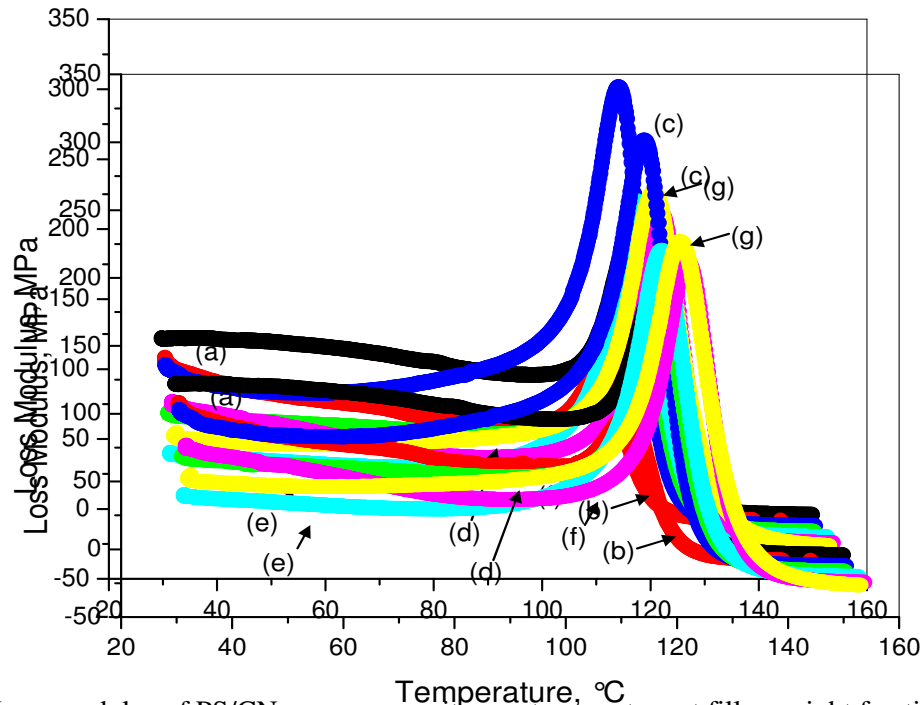


Fig. 7.35. Loss modulus of PS/CNT<sub>x</sub> nanocomposites vs. temperature at filler weight fractions of: (a) 0, (b) 0.1, (c) 0.3, (d) 0.5, (e) 1.0, (f) 2.0 and (g) 5.0 wt%.

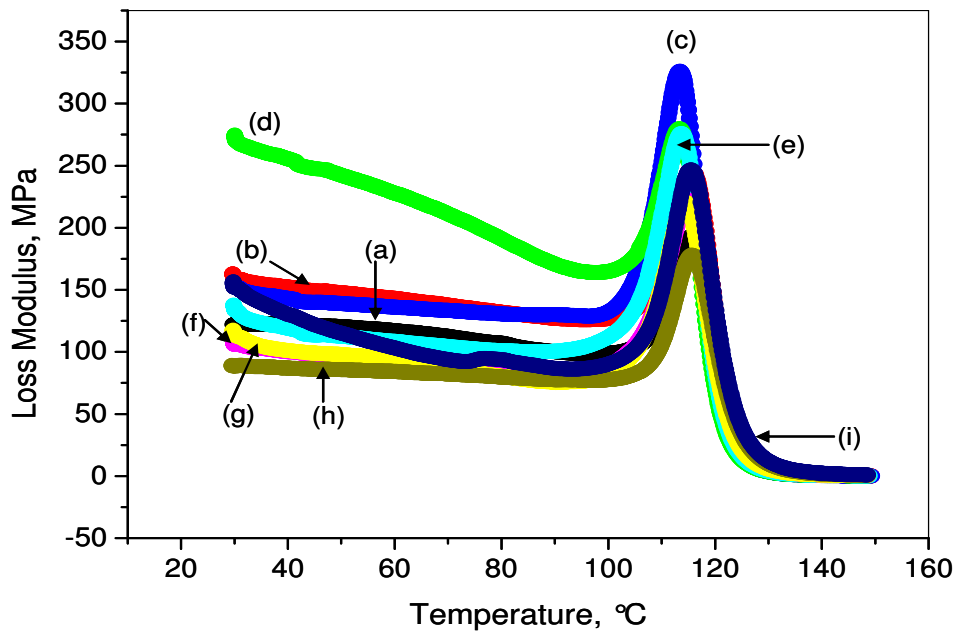


Fig. 7.36. Loss modulus of PS/PS-g-CNT<sub>x</sub> nanocomposites vs. temperature at filler weight fractions of: (a) 0, (b) 0.1, (c) 0.3, (d) 0.5, (e) 0.7, (f) 1.0, (g) 2.0, (h) 5.0 and (i) 7.7 wt%.

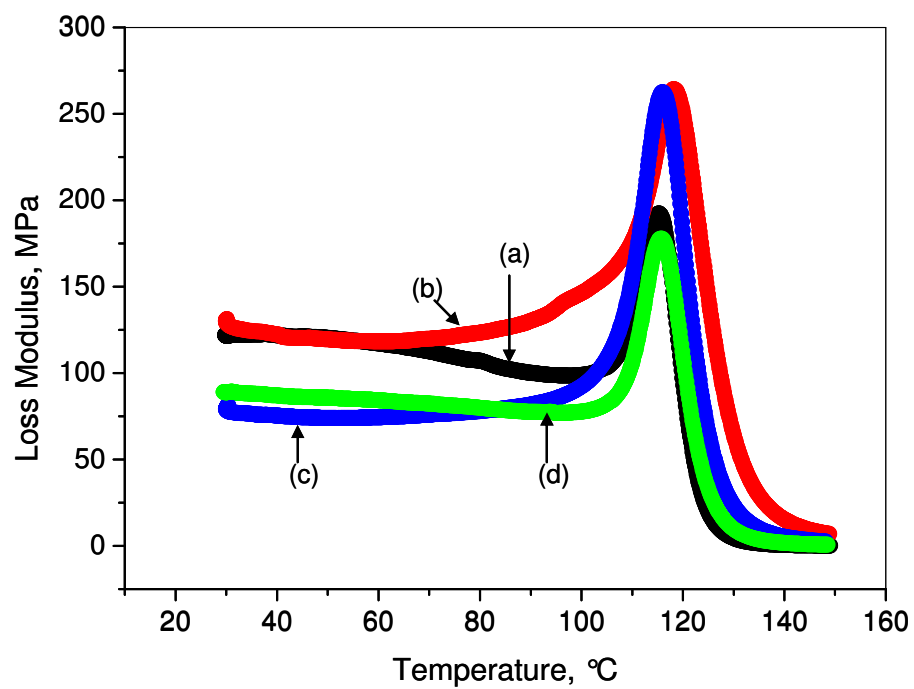


Fig. 7.37. Comparison of the loss modulus of (a) PS and PS-based composite with (b) MWNT, (c) CN<sub>x</sub> and (d) PS-g-CN<sub>x</sub> nanotubes at a concentration of 5.0 wt%.

### 7.5. Real and imaginary parts of the conductivity AC measurements in PEO210k/CNTs and PEO14k/CNTs composites.

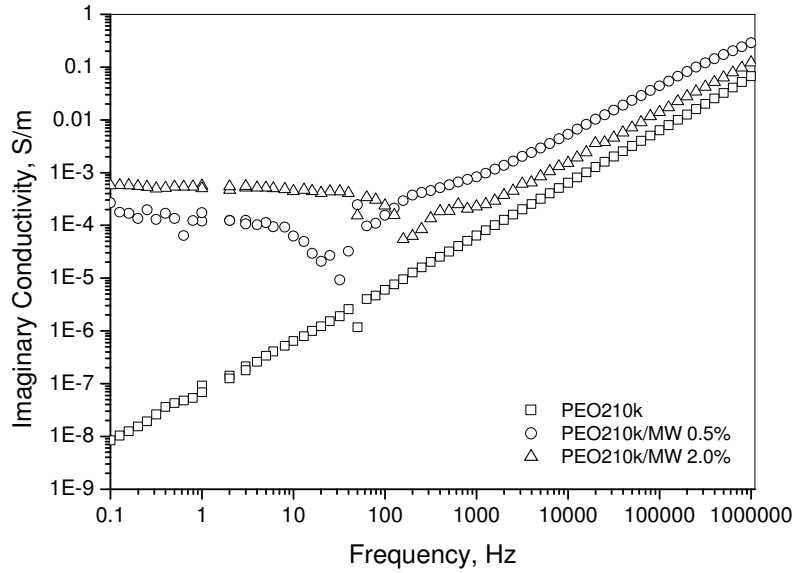


Fig. 7.38. Imaginary conductivity of PEO210k/MWNT nanocomposites vs. frequency at filler weight fractions of 0.1 to 5.0 wt% and applied voltage of 0.1 V.

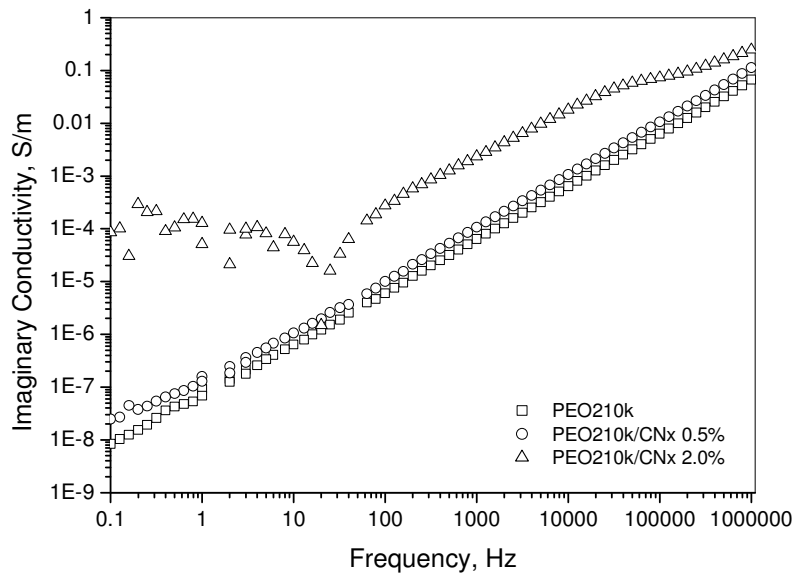


Fig. 7.39. Imaginary conductivity of PEO210k/CN<sub>x</sub> nanocomposites vs. frequency at filler weight fractions of 0.1 to 5.0 wt% and applied voltage of 0.1 V.

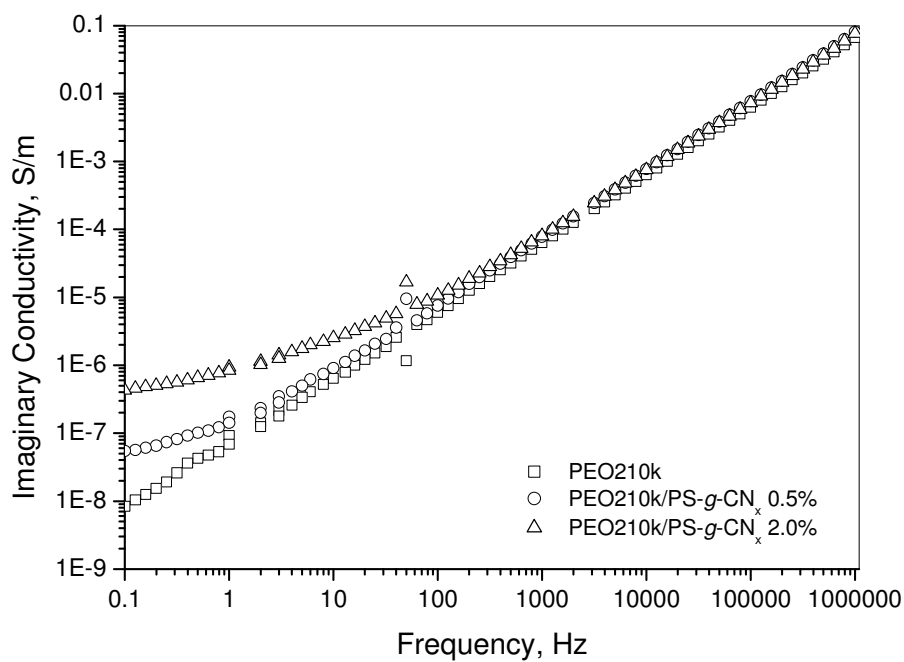


Fig. 7.40. Imaginary conductivity of PEO210k/PS-g-CN<sub>x</sub> nanocomposites vs. frequency at filler weight fractions of 0.1 to 5.0 wt% and applied voltage of 0.1 V.

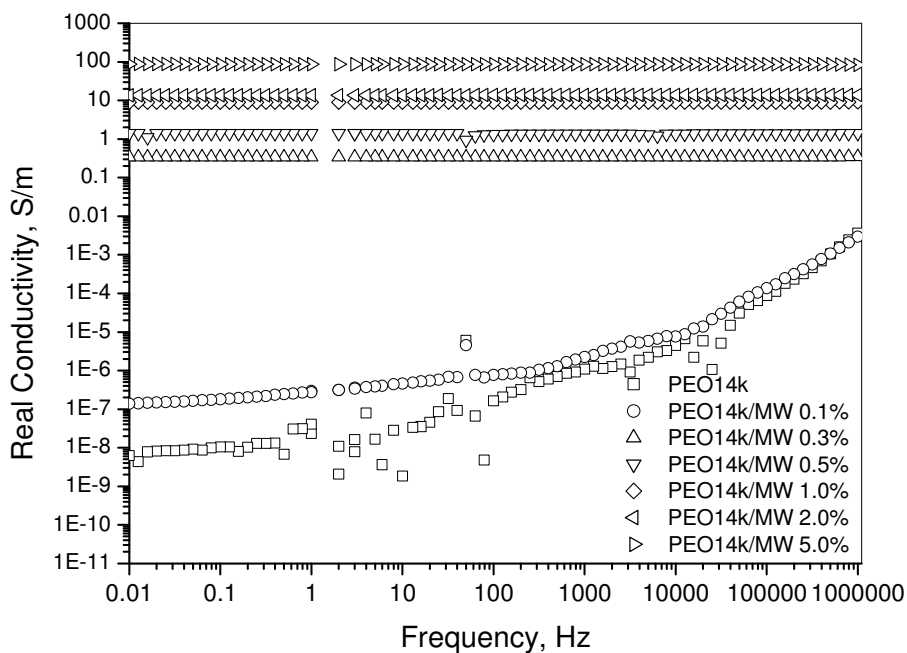


Fig. 7.41. Real conductivity of PEO14k/MWNT nanocomposites vs. frequency at filler weight fractions of 0.1 to 5.0 wt% and applied voltage of 0.1 V.

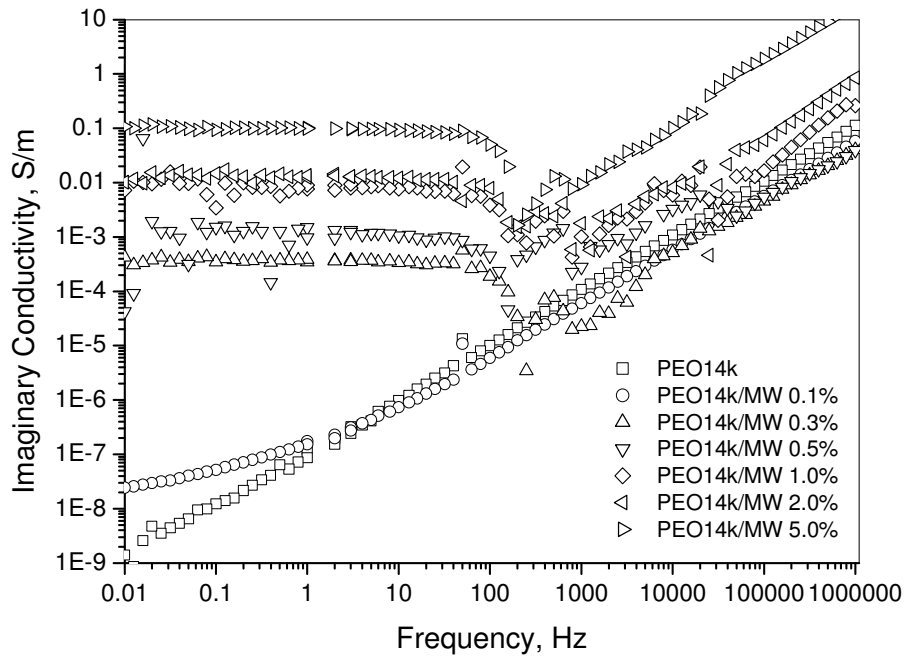


Fig. 7.42. Imaginary conductivity of PEO14k/MWNT nanocomposites vs. frequency at filler weight fractions of 0.1 to 5.0 wt% and applied voltage of 0.1 V.

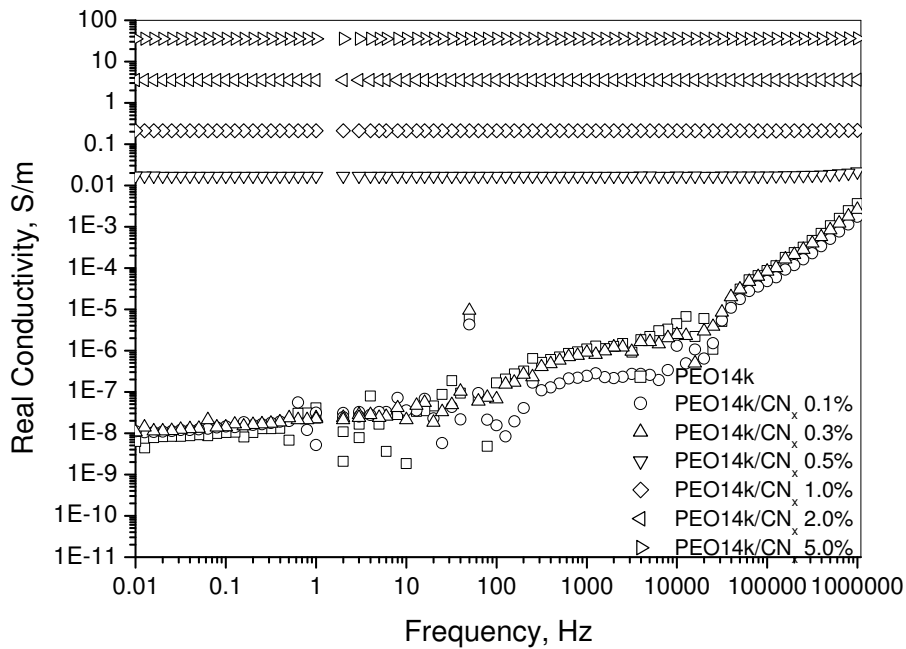


Fig. 7.43. Real conductivity of PEO14k/CN<sub>x</sub> nanocomposites vs. frequency at filler weight fractions of 0.1 to 5.0 wt% and applied voltage of 0.1 V.

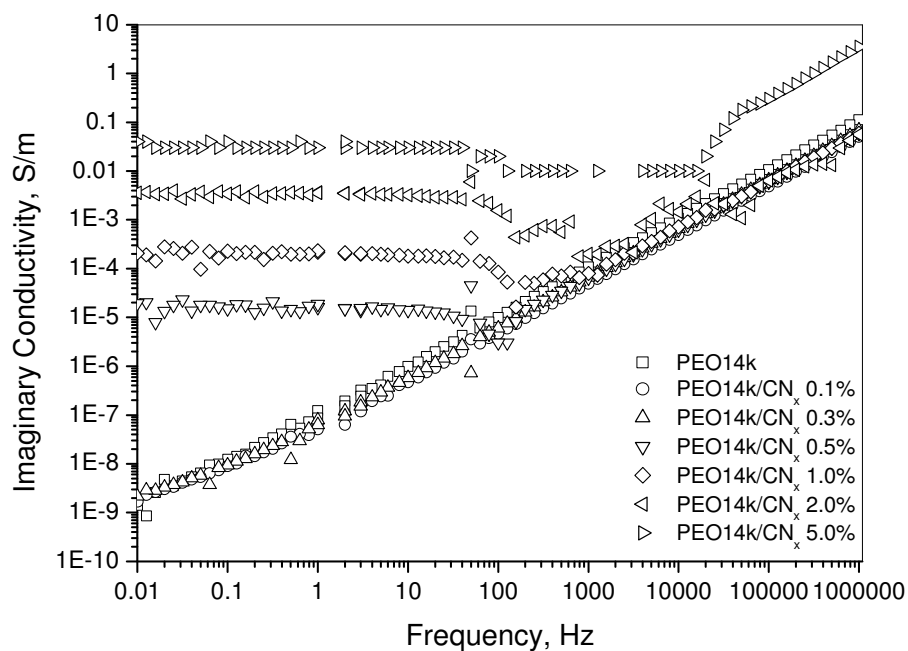


Fig. 7.44. Imaginary conductivity of PEO14k/CN<sub>x</sub> nanocomposites vs. frequency at filler weight fractions of 0.1 to 5.0 wt% and applied voltage of 0.1 V.

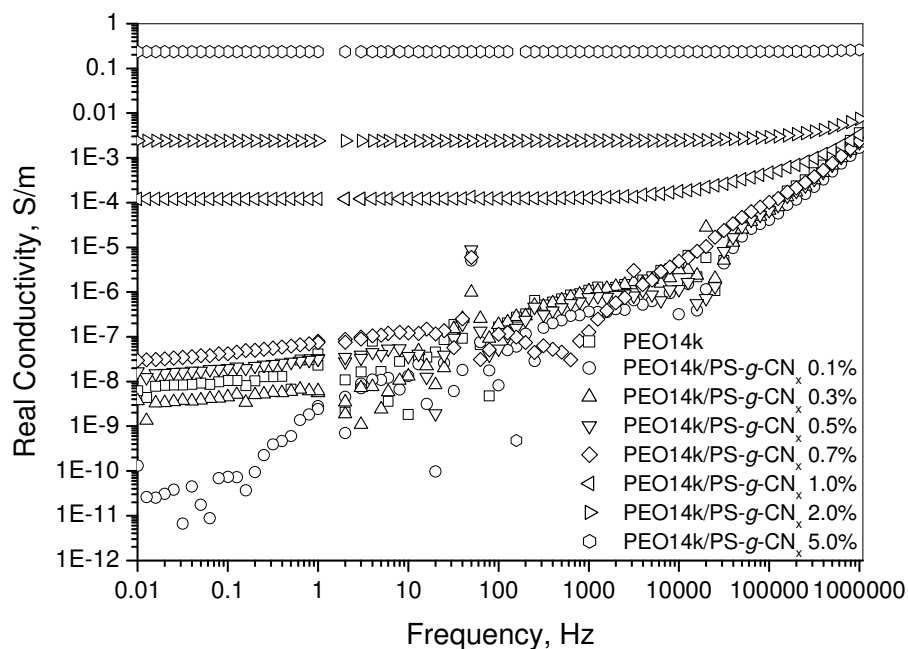


Fig. 7.45. Real conductivity of PEO14k/PS-g-CN<sub>x</sub> nanocomposites vs. frequency at filler weight fractions of 0.1 to 5.0 wt% and applied voltage of 0.1 V.

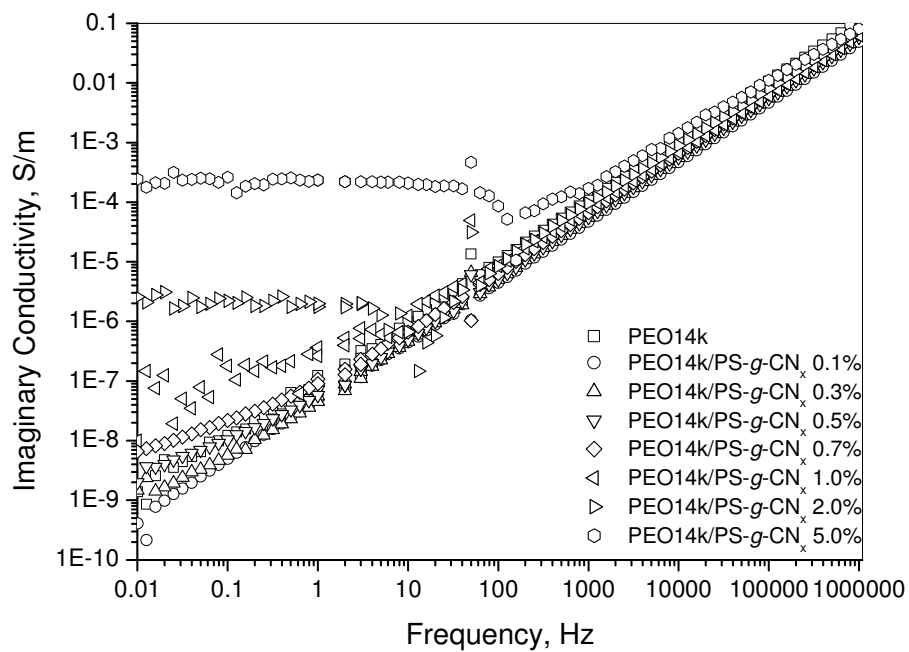


Fig. 7.46. Imaginary conductivity of PS- $g$ -CN $_x$  nanocomposites vs. frequency at filler weight fractions of 0.1 to 5.0 wt% and applied voltage of 0.1 V.

## 7.6. Conductivity exponent and percolation threshold in PEO14k/CNTs composites calculated using the Percolation Model

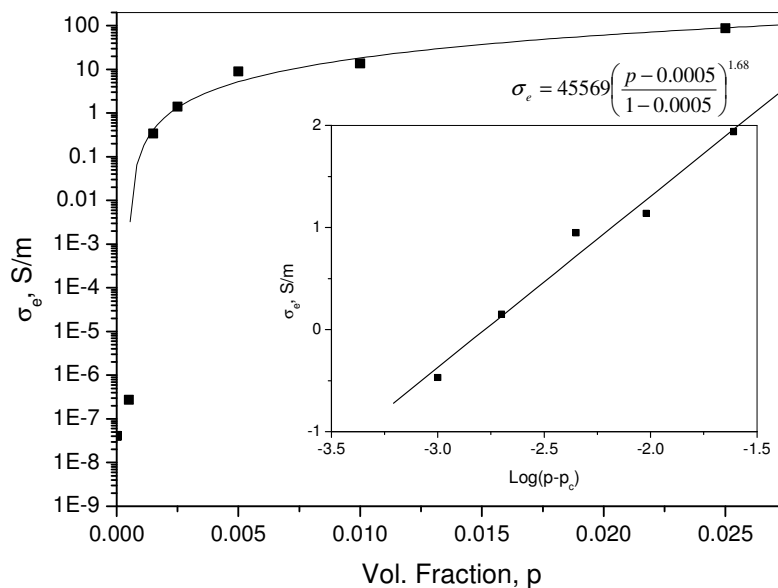


Fig. 7.47. Real part of the AC electrical conductivity at 1 Hz and applied voltage of 0.1 V for PEO14k/MWNT composites at several filler contents. Comparison with model (solid lines).

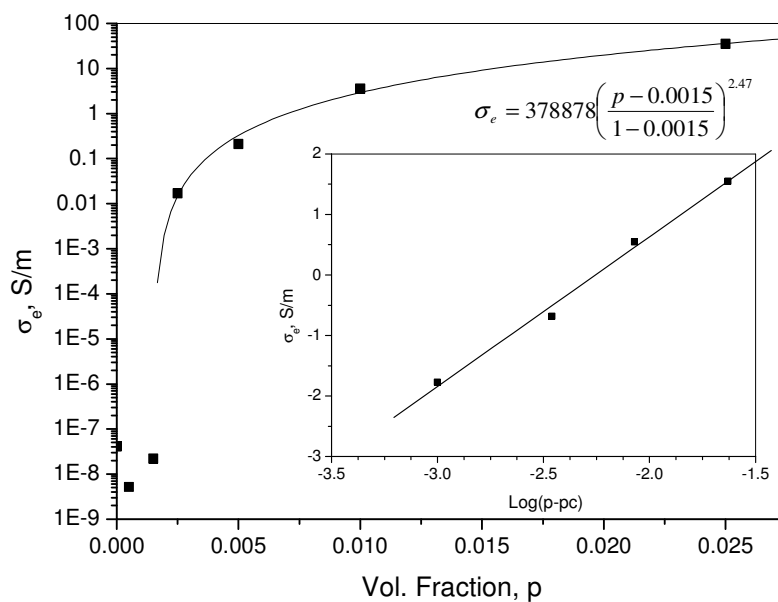


Fig. 7.48. Real part of the AC electrical conductivity at 1 Hz and applied voltage of 0.1 V for PEO14k/ $CN_x$  composites at several filler contents. Comparison with model (solid lines).

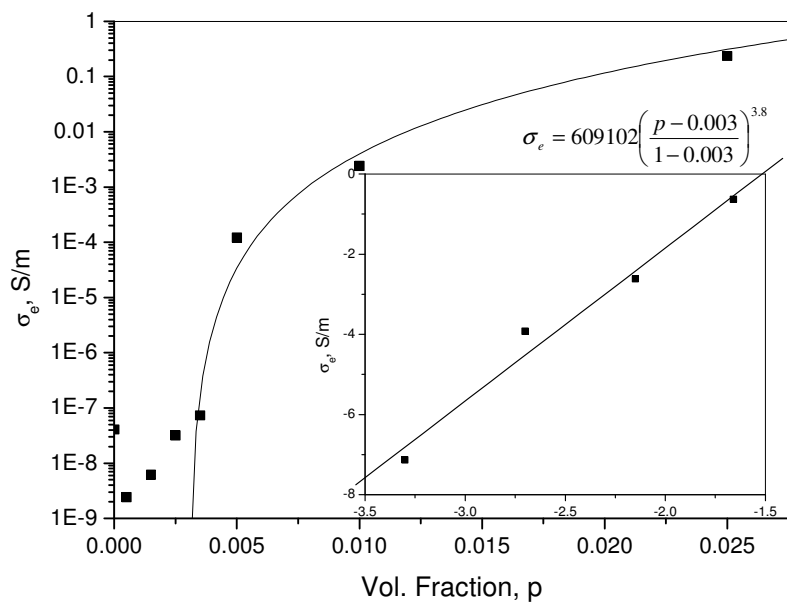


Fig. 7.49. Real part of the AC electrical conductivity at 1 Hz and applied voltage of 0.1 V for PEO14k/PS-g-CN<sub>x</sub> at several filler contents. Comparison with model (solid lines).

## References

1. Terrones, M. and H. Terrones, *The carbon nanocosmos: novel materials for the twenty-first century*. Philosophical Trans Royal Society of London A, 2003. **361**: p. 2789-2806.
2. Subramoney, S., *Novel nanocarbons-structure, properties and potential applications*. Advanced Materials, 1998. **10**: p. 1157-1171.
3. Saito, R., G. Dresselhaus, and M.S. Dresselhaus, *Physical properties of carbon nanotubes*. 1998, London: Imperial College Press. 279.
4. Oberlin, A., M. Endo, and T. Koyama, *Filamentous growth of carbon through benzene decomposition*. Journal of Crystal Growth, 1976. **32**: p. 335-349.
5. Iijima, S., *High resolution electron microscopy of some carbonaceous materials*. Journal of Microscopy, 1980. **119**: p. 99.
6. Iijima, S., *Direct observation of the tetrahedral bonding in graphitizing carbon black by high-resolution electron microscopy*. Journal of Crystal Growth, 1980. **50**: p. 675.
7. Heath, H.W., J.R. Heath, S.C. O'Brien, S.C. Curl, and R.E. Smalley, *C60 : Buckminsterfullerene*. Nature, 1985. **318**(6042): p. 162-163.
8. Iijima, S., *Helical microtubules of graphitic carbon*. Nature, 1991. **354**: p. 56.
9. Terrones, M., W.K. Hsu, H.W. Kroto, and D.R.M. Walton, *Nanotubes: a revolution in material science and electronics.*, in *In Fullerenes and related structures: topics in chemistry series*, A. Hirsch, Editor. 1998, Springer: Berlin. p. 189.
10. Dresselhaus, M.S., G. Dresselhaus, and P.C. Eklund, *Science of fullerenes and carbon nanotubes*, in *Science of fullerenes and carbon nanotubes*. 1996, San Diego: Academic. p. 1-505.
11. Iijima, S. and T. Ichihashi, *Single-shell carbon nanotubes of 1 nm diameter*. Nature, 1993. **363**: p. 603.
12. Bethune, D.S., C.H. Kiang, M.S. de Vries, G. Gorman, R. Savoy, J. Vasquez, and R. Beyers, *Cobalt-catalysed growth of carbon nanotubes with single-atomic-layers walls*. Nature, 1993. **363**: p. 605.
13. Harris, P.J.F., *Carbon nanotubes and related structures New materials for the twenty-first century*. 2001, Cambridge: Cambridge University Press. 279.
14. Terrones, M., *Science and Technology of the twenty-first century: synthesis, properties, and applications of carbon nanotubes*. Annual Reviews Materials Research, 2003. **33**: p. 419-501.
15. Fournier, J., G. Boiteux, G. Seytre, and G. Marichy, *Percolation network of polypyrrole in conducting polymer-composites*. Synthetic Metals, 1997. **84**: p. 839-840.
16. Lafosse, X., *Percolation and dielectric relaxation in polypyrrole-Teflon alloys*. Synthetic Metals, 1995. **68**: p. 227-231.
17. Zhang, B., R.W. Fu, M.Q. Zhang, X.M. Dong, P.L. Lan, and J.S. Qiu, *Preparation and characterization of gas-sensitive composites from multi-walled carbon nanotubes/polystyrene*. Sensors and Actuators B, 2005. **109**(2): p. 323-328.